How life flourishes in polar darkness *p. 1254*

An eco-research reboot for Guantanamo Bay *p. 1258*

The biggest methane leak in U.S. history *p. 1317*

# Science

$15
18 MARCH 2016
sciencemag.org
AAAS

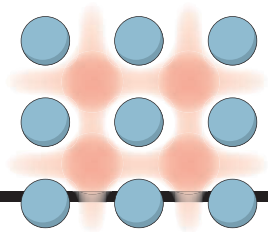


## *A new horizon*

The Pluto system seen up close

*pp. 1280–1293*

# CONTENTS



**1262 & 1314**
Hydride anions moving through oxides

18 MARCH 2016 • VOLUME 351 • ISSUE 6279

## NEWS

### IN BRIEF

1244 News at a glance

### IN DEPTH

**1248 GIANT ATOM-SMASHER GEARS UP TO CHASE WHIFF OF NEW PHYSICS**
Hints of a massive new particle at the Large Hadron Collider have physicists abuzz—and eager to follow up
*By A. Cho*

**1249 EFFORTS TO LINK CLIMATE CHANGE TO SEVERE WEATHER GAIN GROUND**
U.S. academies find researchers getting better at attributing heat waves, cold snaps, and other events to climate trends *By W. Cornwall*

**1250 FIVE MATINGS FOR MODERNS, NEANDERTALS**
Powerful genetic studies pin down multiple trysts on different continents *By A. Gibbons*
▸ B. VERNOT *ET AL.* 10.1126/science.aad9416

**1252 EUROPE ON COURSE FOR A NEUTRON DROUGHT**
Billion-euro accelerator won't make up for the shortfall, experts say
*By E. Cartlidge*

**1253 TESTS OF BLOOD-BORNE DNA PINPOINT TISSUE DAMAGE**
Assays spot cell death from diabetes, cancer, and more *By J. Kaiser*

### FEATURE

**1254 VOYAGE INTO DARKNESS**
Researchers are learning that Arctic organisms aren't dormant during the long polar night
*By E. Kintisch*

## INSIGHTS

### PERSPECTIVES

**1258 REBOOT GITMO FOR U.S.-CUBA RESEARCH DIPLOMACY**
Transform Guantánamo into a peace park and ecological research center
*By J. Roman and J. Kraska*

**1260 SQUEEZING INTO SUPERCONDUCTIVITY**
Synchrotron light sources can be used to probe superconductivity at extreme pressures *By V. Struzhkin*
▸ REPORT P. 1303

**1262 LARGE, SOFT, AND POLARIZABLE HYDRIDE IONS SNEAK AROUND IN AN OXYHYDRIDE**
A perovskite containing highly electropositive cations conducts hydride anions *By S. Yamaguchi*
▸ REPORT P. 1314

**1263 NEW MECHANISMS, NEW WORRIES**
The increasing spread of colistin resistance is resulting in untreatable infections *By M. Sprenger and K. Fukuda*

**1264 THE ENIGMATIC TUFT CELL IN IMMUNITY**
An intestinal cell stimulates the immune response to parasitic infections *By N. Harris*
▸ REPORT P. 1329

**1266 A RADICALLY UNEXPECTED MECHANISM**
Biosynthesis of the antibiotic nosiheptide proceeds via unforeseen radical intermediates *By J. Bridwell-Rabb and C. L. Drennan*
▸ REPORT P. 1320

**1267 QUANTUM DYNAMICS IN THE SMALLEST WATER DROPLET**
Two hydrogen bonds in a six-molecule water cluster break simultaneously in a concerted set of movements *By D. C. Clary*
▸ REPORT P. 1310

**1268 A SATIATING SIGNAL**
A glycosylation enzyme in specific brain neurons is a nutrient sensor that controls body weight
*By G. J. Schwartz*
▸ RESEARCH ARTICLE P. 1293

### BOOKS *ET AL.*

**1270 SCIENCE BLOGGING**
*C. Wilcox* et al., *Eds.*; *reviewed by A. D. Thaler*

**1271 HALF-EARTH**
*By E. O. Wilson, reviewed by C. J. Griffths*

### LETTERS

**1273 A WAVE OF INSPIRATION**
*By J. McNerney*

**1273 RISKS OF *WOLBACHIA* MOSQUITO CONTROL**
*By E. L. S. Loreto and G. L. Wallau*

**1273 CURBING IRAN'S ACADEMIC MISCONDUCT**
*By B. Ataie-Ashtiani*

**1274 TECHNICAL COMMENT ABSTRACTS**



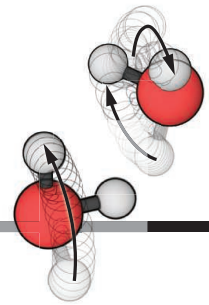

*Science* Staff ..... 1240
New Products ..... 1347
*Science* Careers ..... 1353

Downloaded from on March 17, 2016



Published by AAAS

# CONTENTS



1267 & 1310
Water shifting gears

18 MARCH 2016 • VOLUME 351 • ISSUE 6279

## RESEARCH

### IN BRIEF

**1276** From *Science* and other journals

### REVIEW

**1279 CHEMISTRY**
Designer protein delivery: From natural to engineered affinity-controlled release systems *M. M. Pakulska* et al.
REVIEW SUMMARY; FOR FULL TEXT: dx.doi.org/10.1126/science.aac4750

### RESEARCH ARTICLES

#### PLANETARY SCIENCE

**1280** The atmosphere of Pluto as observed by New Horizons *G. R. Gladstone* et al.
RESEARCH ARTICLE SUMMARY; FOR FULL TEXT: dx.doi.org/10.1126/science.aad8866

**1281** The small satellites of Pluto as observed by New Horizons *H. A. Weaver* et al.
RESEARCH ARTICLE SUMMARY; FOR FULL TEXT: dx.doi.org/10.1126/science.aae0030
▸ PODCAST

**1282** Pluto's interaction with its space environment: Solar wind, energetic particles, and dust *F. Bagenal* et al.
RESEARCH ARTICLE SUMMARY; FOR FULL TEXT: dx.doi.org/10.1126/science.aad9045

**1283** Surface compositions across Pluto and Charon *W. M. Grundy* et al.
RESEARCH ARTICLE SUMMARY; FOR FULL TEXT: dx.doi.org/10.1126/science.aad9189

**1284** The geology of Pluto and Charon through the eyes of New Horizons *J. M. Moore* et al.

#### FEEDING BEHAVIOR

**1293** The nutrient sensor OGT in PVN neurons regulates feeding *O. Lagerlöf* et al.
▸ PERSPECTIVE P. 1268

#### MICROBIOTA

**1296** The maternal microbiota drives early postnatal innate immune development *M. Gomez de Agüero* et al.

### REPORTS

#### SUPERCONDUCTIVITY

**1303** Observation of superconductivity in hydrogen sulfide from nuclear resonant scattering *I. Troyan* et al.
▸ PERSPECTIVE P. 1260

#### NANOMATERIALS

**1306** Formation of pseudomorphic nanocages from $Cu_2O$ nanocrystals through anion exchange reactions *H.-L. Wu* et al.

#### HYDROGEN BONDING

**1310** Concerted hydrogen-bond breaking by quantum tunneling in the water hexamer prism *J. O. Richardson* et al.
▸ PERSPECTIVE P. 1267

#### IONIC MATERIALS

**1314** Pure $H^-$ conduction in oxyhydrides *G. Kobayashi* et al.
▸ PERSPECTIVE P. 1262

#### GAS INFRASTRUCTURE

**1317** Methane emissions from the 2015 Aliso Canyon blowout in Los Angeles, CA *S. Conley* et al.

#### BIOCHEMISTRY

**1320** Fine-tuning of a radical-based reaction by radical *S*-adenosyl-L-methionine tryptophan lyase *G. Sicoli* et al.
▸ PERSPECTIVE P. 1266

#### NEUROINFLAMMATION

**1324** *C9orf72* is required for proper macrophage and microglial function in mice *J. G. O'Rourke* et al.

#### MUCOSAL IMMUNITY

**1329** Tuft cells, taste-chemosensory cells, orchestrate parasite type 2 immunity in the gut *M. R. Howitt* et al.
▸ PERSPECTIVE P. 1264

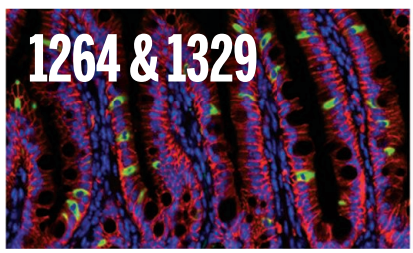
#### INFLAMMATION

**1333** Prostaglandin $E_2$ constrains systemic inflammation through an innate lymphoid cell–IL-22 axis *R. Duffin* et al.

#### EBOLA VIRUS

**1339** Protective monotherapy against lethal Ebola virus infection by a potently neutralizing antibody *D. Corti* et al.

**1343** Structural and molecular basis for Ebola virus neutralization by protective human antibodies *J. Misasi* et al.




### DEPARTMENTS

**1243 EDITORIAL**
Throwing deep
*By Michael S. Turner*

**1358 WORKING LIFE**
How I made my own opportunities
*By Ahmed Waqas*

### ON THE COVER




Pluto's surface, as seen by the New Horizons spacecraft. At left is the bright white Sputnik Planum, a plain of nitrogen ice. Its numerous surface pits are probably formed by sublimation. On the right are the dark red highlands of Krun Macula, rising 2.5 kilometers above the plains. To create this image, several exposures of the Long-Range Reconnaissance Imager were combined with color data from the Multispectral Visible Imaging Camera. See pages 1280 to 1293. *Photo: NASA/Applied Physics Laboratory/Southwest Research Institute; Image composition and processing by P. Engebretson*

**SCIENCE (ISSN 0036-8075) is published weekly on Friday, except the last week in December, by the American Association for the Advancement of Science, 1200 New York Avenue, NW, Washington, DC 20005.** Periodicals mail postage (publication No. 484460) paid at Washington, DC, and additional mailing offices. Copyright © 2016 by the American Association for the Advancement of Science. The title SCIENCE is a registered trademark of the AAAS. Domestic individual membership and subscription (51 issues): $165 ($74 allocated to subscription). Domestic institutional subscription (51 issues): $1522; Foreign postage extra: Mexico, Caribbean (surface mail) $55; other countries (air assist delivery) $89. First class, airmail, student, and emeritus rates on request. Canadian rates with GST available upon request, GST #1254 88122. Publications Mail Agreement Number 1069624. **Printed in the U.S.A.**
**Change of address:** Allow 4 weeks, giving old and new addresses and 8-digit account number. **Postmaster:** Send change of address to AAAS, P.O. Box 96178, Washington, DC 20090–6178. **Single-copy sales:** $15.00 current issue, $20.00 back issue prepaid includes surface postage; bulk rates on request. **Authorization to photocopy** material for internal or personal use under circumstances not falling within the fair use provisions of the Copyright Act is granted by AAAS to libraries and other users registered with the Copyright Clearance Center (CCC) Transactional Reporting Service, provided that $35.00 per article is paid directly to CCC, 222 Rosewood Drive, Danvers, MA 01923. The identification code for *Science* is 0036-8075. *Science* is indexed in the *Reader's Guide to Periodical Literature* and in several specialized indexes.



*Published by AAAS*

Science
AAAS
1200 New York Avenue, NW, Washington, DC 20005
Bateman House, 82-88 Hills Road, Cambridge, UK CB2 1LQ

**Editor-in-Chief** Marcia McNutt
**Executive Editor** Monica M. Bradford **News Editor** Tim Appenzeller
**Managing Editor, Research Journals** Katrina L. Kelner
**Deputy Editors** Barbara R. Jasny, Andrew M. Sugden(UK), Valda J. Vinson, Jake S. Yeston

## Research and Insights

**SR. EDITORS** Caroline Ash(UK), Gilbert J. Chin, Lisa D. Chong, Julia Fahrenkamp-Uppenbrink(UK), Pamela J. Hines, Stella M. Hurtley(UK), Paula A. Kiberstis, Marc S. Lavine(Canada), Kristen L. Mueller, Ian S. Osborne(UK), Beverly A. Purnell, L. Bryan Ray, Guy Riddihough, H. Jesse Smith, Jelena Stajic, Peter Stern(UK), Phillip D. Szuromi, Sacha Vignieri, Brad Wible, Nicholas S. Wigginton, Laura M. Zahn **ASSOCIATE EDITORS** Brent Grocholski, Keith T. Smith **ASSOCIATE BOOK REVIEW EDITOR** Valerie B. Thompson **ASSOCIATE LETTERS EDITOR** Jennifer Sills **CHIEF CONTENT PRODUCTION EDITOR** Cara Tate **SR. CONTENT PRODUCTION EDITORS** Harry Jach, Lauren Kmec **CONTENT PRODUCTION EDITORS** Jeffrey E. Cook, Chris Filiatreau, Cynthia Howe, Barbara P. Ordway, Catherine Wolner **SR. EDITORIAL COORDINATORS** Carolyn Kyle, Beverly Shields **EDITORIAL COORDINATORS** Joi S. Granger, Lisa Johnson, Anita Wynn **PUBLICATIONS ASSISTANTS** Aneera Dobbins, Jeffrey Hearn, Dona Mathieu, Le-Toya Mayne Flood, Shannon McMahon, Scott Miller, Caitlyn Phillips, Jerry Richardson, Rachel Roberts(UK), Alice Whaley(UK), Brian White **EXECUTIVE ASSISTANT** Anna Bashkirova **ADMINISTRATIVE SUPPORT** Janet Clements(UK), Lizanne Newton(UK), Maryrose Madrid, John Wood(UK)

## News

**NEWS MANAGING EDITOR** John Travis **INTERNATIONAL EDITOR** Richard Stone **DEPUTY NEWS EDITORS** Daniel Clery(UK), Robert Coontz, Elizabeth Culotta, David Grimm, David Malakoff, Leslie Roberts **CONTRIBUING EDITOR** Martin Enserink(Europe) **SR. CORRESPONDENTS** Jeffrey Mervis, Elizabeth Pennisi **NEWS WRITERS** Adrian Cho, Jon Cohen, Jennifer Couzin-Frankel, Carolyn Gramling, Eric Hand, Jocelyn Kaiser, Catherine Matacic, Kelly Servick, Robert F. Service, Erik Stokstad(Cambridge, UK), Emily Underwood **INTERNS** Hanae Armitage, Patrick Monahan, Nala Rogers **CONTRIBUTING CORRESPONDENTS** Michael Balter(Paris), John Bohannon, Warren Cornwall, Ann Gibbons, Mara Hvistendahl, Sam Kean, Eli Kintisch, Kai Kupferschmidt(Berlin), Andrew Lawler, Christina Larson(Beijing), Mitch Leslie, Charles C. Mann, Eliot Marshall, Virginia Morell, Dennis Normile(Shanghai), Heather Pringle, Tania Rabesandratana(London), Gretchen Vogel(Berlin), Lizzie Wade(Mexico City) **CAREERS** Donisha Adams, Rachel Bernstein(Editor) **COPY EDITORS** Julia Cole, Dorie Chevlen, Jennifer Levin (Chief) **ADMINISTRATIVE SUPPORT** Jessica Adams

**Executive Publisher** Rush D. Holt
**Interim Publisher** Bill Moran **Chief Digital Media Officer** Rob Covey

**BUSINESS OPERATIONS AND PORTFOLIO MANAGEMENT DIRECTOR** Sarah Whalen **PRODUCT DEVELOPMENT DIRECTOR** Will Schweitzer **PRODUCT DEVELOPMENT ASSOCIATE** Hal Moore **BUSINESS SYSTEMS AND FINANCIAL ANALYSIS DIRECTOR** Randy Yi **MANAGER OF FULFILLMENT SYSTEMS** Neal Hawkins **SYSTEMS ANALYST** Nicole Mehmedovich **ASSISTANT DIRECTOR, BUSINESS OPERATIONS** Eric Knott **MANAGER, BUSINESS OPERATIONS** Jessica Tierney **SENIOR BUSINESS ANALYST** Cory Lipman **BUSINESS ANALYSTS** Sandy Kim, Meron Kebede **FINANCIAL ANALYST** Robert Clark **DIRECTOR, COPYRIGHTS LICENSING SPECIAL PROJECTS** Emilie David **PERMISSIONS ASSOCIATE** Elizabeth Sandler **RIGHTS, CONTRACTS, AND LICENSING ASSOCIATE** Lili Kiser

**MARKETING DIRECTOR** Elise Swinehart **ASSOCIATE DIRECTOR OF ACQUISITION AND RETENTION** Julianne Wielga **MARKETING ASSOCIATE** Elizabeth Sattler **SR. MARKETING EXECUTIVE** Jennifer Reeves **ASSOCIATE DIRECTOR, CREATIVE SERVICES** Tzeitel Sorrosa **ART ASSOCIATE** Seil Lee **JR. ART ASSOCIATE** Kim Huynh **ASSISTANT COMMERCIAL EDITOR** Selby Frame **MARKETING PROJECT MANAGER** Angelissa McArthur **PROGRAM DIRECTOR, AAAS MEMBER CENTRAL** Peggy Mihelich **FULFILLMENT SYSTEMS AND OPERATIONS** membership@aaas.org **MANAGER, MEMBER SERVICES** Pat Butler **SPECIALISTS** Terrance Morrison, Latasha Russell **MANAGER, DATA ENTRY** Mickie Napoleoni **DATA ENTRY SPECIALISTS** Brenden Aquilino, Fiona Giblin

**PUBLISHER RELATIONS MANAGER** Catherine Holland **PUBLISHER RELATIONS, EASTERN REGION** Keith Layson **PUBLISHER RELATIONS, WESTERN REGION** Ryan Rexroth **SALES RESEARCH COORDINATOR** Aiesha Marshall **MANAGER, SITE LICENSE OPERATIONS** Iquo Edim **SENIOR OPERATIONS ANALYST** Lana Guz **FULFILLMENT ANALYST** Judy Lillibridge **ASSOCIATE DIRECTOR, MARKETING** Christina Schlecht **MARKETING ASSOCIATE** Isa Sesay-Bah

**WEB TECHNOLOGIES SR. DEVELOPER** Chris Coleman **DEVELOPERS** Dan Berger, Jimmy Marks, Ryan Jensen **SR. PROJECT MANAGER** Trista Smith **PROJECT MANAGER** Nick Fletcher

**DIGITAL MEDIA DIRECTOR OF ANALYTICS** Enrique Gonzales **DIGITAL REPORTING ANALYST** Eric Hossinger **SR. WEB PRODUCER** Sarah Crespi **WEB PRODUCER** Alison Crawford **VIDEO PRODUCER** Nguyen Nguyen **SOCIAL MEDIA PRODUCER** Brice Russ

**DIRECTOR OF OPERATIONS PRINT AND ONLINE** Lizabeth Harman **DIGITAL/PRINT STRATEGY MANAGER** Jason Hillman **QUALITY TECHNICAL MANAGER** Marcus Spiegler **PROJECT ACCOUNT MANAGER** Tara Kelly **DIGITAL PRODUCTION MANAGER** Lisa Stanford **ASSISTANT MANAGER DIGITAL/PRINT** Rebecca Doshi **SENIOR CONTENT SPECIALISTS** Steve Forrester, Antoinette Hodal, Lori Murphy, Anthony Rosen **CONTENT SPECIALISTS** Jacob Hedrick, Kimberley Oster

**DESIGN DIRECTOR** Beth Rakouskas **DESIGN EDITOR** Marcy Atarod **SENIOR DESIGNER** Garvin Grullón **DESIGNER** Chrystal Smith **GRAPHICS MANAGING EDITOR** Alberto Cuadra **SENIOR SCIENTIFIC ILLUSTRATORS** Chris Bickel, Katharine Sutliff **SCIENTIFIC ILLUSTRATOR** Valerie Altounian **SENIOR ART ASSOCIATES** Holly Bishop, Nathalie Cary, Preston Huey **PHOTOGRAPHY MANAGING EDITOR** William Douthitt **PHOTO EDITORS** Leslie Blizard, Christy Steele

**DIRECTOR, GLOBAL COLLABORATION, CUSTOM PUBLICATIONS, ADVERTISING** Bill Moran **EDITOR, CUSTOM PUBLISHING** Sean Sanders: 202-326-6430 **ADVERTISING MARKETING MANAGER** Justin Sawyers: 202-326-7061 science_advertising@aaas.org **ADVERTISING SUPPORT MANAGER** Karen Foote: 202-326-6740 **ADVERTISING PRODUCTION OPERATIONS MANAGER** Deborah Tompkins **SR. PRODUCTION SPECIALIST/GRAPHIC DESIGNER** Amy Hardcastle **SR. TRAFFIC ASSOCIATE** Christine Hall **SALES COORDINATOR** Shirley Young **ASSOCIATE DIRECTOR, COLLABORATION, CUSTOM PUBLICATIONS/CHINA/TAIWAN/KOREA/SINGAPORE** Ruolei Wu: +86-186 0082 9345, rwu@aaas.org **COLLABORATION/CUSTOM PUBLICATIONS/JAPAN** Adarsh Sandhu + 81532-81-5142 asandhu@aaas.org **EAST COAST/E. CANADA** Laurie Faraday: 508-747-9395, FAX 617-507-8189 **WEST COAST/W. CANADA** Lynne Stickrod: 415-931-9782, FAX 415-520-6940 **MIDWEST** Jeffrey Dembski: 847-498-4520 x3005, Steven Loerch: 847-498-4520 x3006 **UK EUROPE/ASIA** Roger Goncalves: TEL/FAX +41 43 243 1358 **JAPAN** Katsuyoshi Fukamizu(Tokyo): +81-3-3219-5777 kfukamizu@aaas.org **CHINA/TAIWAN** Ruolei Wu: +86-186 0082 9345, rwu@aaas.org

**WORLDWIDE ASSOCIATE DIRECTOR OF SCIENCE CAREERS** Tracy Holmes: +44 (0) 1223 326525, FAX +44 (0) 1223 326532 tholmes@science-int.co.uk **CLASSIFIED** advertise@sciencecareers.org **U.S. SALES** Tina Burks: 202-326-6577, Nancy Toema: 202-326-6578 **EUROPE/ROW SALES** Sarah Lelarge **SALES ASSISTANT** Kelly Grace **JAPAN** Hiroyuki Mashiki(Kyoto): +81-75-823-1109 hmashiki@aaas.org **CHINA/TAIWAN** Ruolei Wu: +86-186 0082 9345 rwu@aaas.org **MARKETING MANAGER** Allison Pritchard **MARKETING ASSOCIATE** Aimee Aponte

**AAAS BOARD OF DIRECTORS, CHAIR** Geraldine L. Richmond **PRESIDENT** Barbara A. Schaal **PRESIDENT-ELECT** Susan Hockfield **TREASURER** David Evans Shaw **CHIEF EXECUTIVE OFFICER** Rush D. Holt **BOARD** Cynthia M. Beall, May R. Berenbaum, Carlos J. Bustamante, Stephen P.A. Fodor, Claire M. Fraser, Michael S. Gazzaniga, Laura H. Greene, Elizabeth Loftus, Mercedes Pascual

**SUBSCRIPTION SERVICES** For change of address, missing issues, new orders and renewals, and payment questions: 866-434-AAAS (2227) or 202-326-6417, FAX 202-842-1065. Mailing addresses: AAAS, P.O. Box 96178, Washington, DC 20090-6178 or AAAS Member Services, 1200 New York Avenue, NW, Washington, DC 20005

**INSTITUTIONAL SITE LICENSES** 202-326-6730 **REPRINTS:** Author Inquiries 800-635-7181 **COMMERCIAL INQUIRIES** 803-359-4578 **PERMISSIONS** 202-326-6765, permissions@aaas.org **AAAS Member Services** 202-326-6417 or http://membercentral.aaas.org/discounts

*Science* serves as a forum for discussion of important issues related to the advancement of science by publishing material on which a consensus has been reached as well as including the presentation of minority of conflicting points of view. Accordingly, all articles published in *Science*—including editorials, news and comment, and book reviews—are signed and reflect the individual views of the authors and not official points of view adopted by AAAS or the institutions with which the authors are affiliated.

**INFORMATION FOR AUTHORS** See pages 624 and 625 of the 5 February 2016 issue or access www.sciencemag.org/authors/science-information-authors

**SENIOR EDITORIAL BOARD**
**Gary King,** *Harvard University,* **Susan M. Rosenberg,** *Baylor College of Medicine,*
**Ali Shilatifard,** *Northwestern University Feinberg School of Medicine*

**BOARD OF REVIEWING EDITORS** (Statistics board members indicated with **(S)**

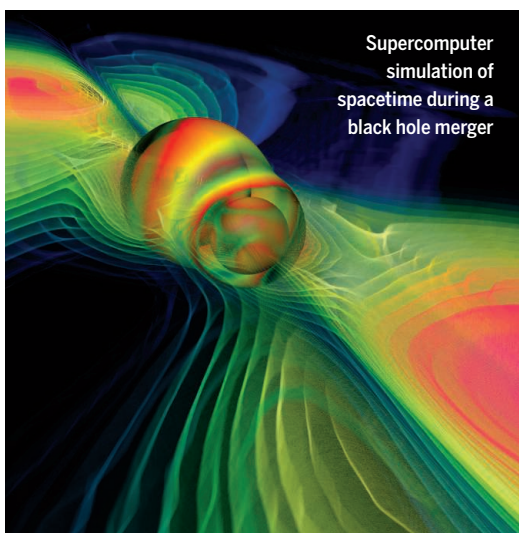
**Adriano Aguzzi,** *U. Hospital Zürich*
**Takuzo Aida,** *U. of Tokyo*
**Leslie Aiello,** *Wenner-Gren Foundation*
**Judith Allen,** *U. of Edinburgh*
**Sonia Altizer,** *U. of Georgia*
**Sebastian Amigorena,** *Institut Curie*
**Kathryn Anderson,** *Memorial Sloan-Kettering Cancer Center*
**Meinrat O. Andreae,** *Max-Planck Inst. Mainz*
**Paola Arlotta,** *Harvard U.*
**Johan Auwerx,** *EPFL*
**David Awschalom,** *U. of Chicago*
**Clare Baker,** *University of Cambridge*
**Jordi Bascompte,** *University of Zurich*
**Facundo Batista,** *London Research Inst.*
**Ray H. Baughman,** *U. of Texas, Dallas*
**David Baum,** *U. of Wisconsin*
**Carlo Beenakker,** *Leiden U.*
**Kamran Behnia,** *ESPCI-ParisTech*
**Yasmine Belkaid,** *NIAID, NIH*
**Philip Benfey,** *Duke U.*
**May Berenbaum,** *U. of Illinois*
**Gabriele Bergers,** *U. of California, San Francisco*
**Bradley Bernstein,** *Massachusettes General Hospital*
**Peer Bork,** *EMBL*
**Bernard Bourdon,** *Ecole Normale Supérieure de Lyon*
**Chris Bowler,** *École Normale Supérieure*
**Ian Boyd,** *U. of St. Andrews*
**Emily Brodsky,** *U. of California, Santa Cruz*
**Ron Brookmeyer,** *U. of California Los Angeles* **(S)**
**Christian Büchel,** *U. Hamburg-Eppendorf*
**Joseph A. Burns,** *Cornell U.*
**Carter Tribley Butts,** *U. of California, Irvine*
**Gyorgy Buzsaki,** *New York U. School of Medicine*
**Blanche Capel,** *Duke U.*
**Mats Carlsson,** *U. of Oslo*
**Ib Chorkendorff,** *U. of Denmark*
**David Clapham,** *Children's Hospital Boston*
**Joel Cohen,** *Rockefeller U., Columbia U.*
**James J. Collins,** *MIT*
**Robert Cook-Deegan,** *Duke U.*
**Lisa Coussens,** *Oregon Health & Science U.*
**Alan Cowman,** *Walter & Eliza Hall Inst.*
**Robert H. Crabtree,** *Yale U.*
**Roberta Croce,** *Vrije Universiteit*
**Janet Currie,** *Princeton U.*
**Jeff L. Dangl,** *U. of North Carolina*
**Tom Daniel,** *U. of Washington*
**Frans de Waal,** *Emory U.*
**Stanislas Dehaene,** *Collège de France*
**Robert Desimone,** *MIT*
**Claude Desplan,** *New York U.*
**Dennis Discher,** *U. of Pennsylvania*
**Gerald W. Dorn II,** *Washington U. School of Medicine*
**Jennifer A. Doudna,** *U. of California, Berkeley*
**Bruce Dunn,** *U. of California, Los Angeles*
**William Dunphy,** *Caltech*
**Christopher Dye,** *WHO*
**Todd Ehlers,** *U. of Tuebingen*
**David Ehrhardt,** *Carnegie Inst. of Washington*
**Tim Elston,** *U. of North Carolina at Chapel Hill*
**Gerhard Ertl,** *Fritz-Haber-Institut, Berlin*
**Barry Everitt,** *U. of Cambridge*
**Ernst Fehr,** *U. of Zurich*
**Anne C. Ferguson-Smith,** *U. of Cambridge*
**Michael Feuer,** *The George Washington U.*
**Toren Finkel,** *NHLBI, NIH*
**Kate Fitzgerald,** *U. of Massachusetts*
**Peter Fratzl,** *Max-Planck Inst.*
**Elaine Fuchs,** *Rockefeller U.*
**Daniel Geschwind,** *UCLA*
**Karl-Heinz Glassmeier,** *TU Braunschweig*
**Ramon Gonzalez,** *Rice U.*
**Julia R. Greer,** *Caltech*
**Elizabeth Grove,** *U. of Chicago*
**Nicolas Gruber,** *ETH Zurich*
**Kip Guy,** *St. Jude's Children's Research Hospital*
**Taekjip Ha,** *U. of Illinois at Urbana-Champaign*
**Christian Haass,** *Ludwig Maximilians U.*
**Michael Hasselmo,** *Boston U.*
**Martin Heimann,** *Max-Planck Inst. Jena*
**Yka Helariutta,** *U. of Cambridge*
**James A. Hendler,** *Rensselaer Polytechnic Inst.*
**Janet G. Hering,** *Swiss Fed. Inst. of Aquatic Science & Technology*
**Kai-Uwe Hinrichs,** *U. of Bremen*
**David Hodell,** *U. of Cambridge*
**David Holden,** *Imperial College*
**Lora Hooper,** *UT Southwestern Medical Ctr. at Dallas*
**Tamas Horvath,** *Yale University*
**Raymond Huey,** *U. of Washington*
**Fred Hughson,** *Princeton U.*
**Auke Ijspeert,** *EPFL Lausanne*
**Stephen Jackson,** *USGS and U. of Arizona*
**Steven Jacobsen,** *U. of California, Los Angeles*
**Kai Johnsson,** *EPFL Lausanne*
**Peter Jonas,** *Inst. of Science & Technology (IST) Austria*
**Matt Kaeberlein,** *U. of Washington*
**William Kaelin Jr.,** *Dana-Farber Cancer Inst.*
**Daniel Kahne,** *Harvard U.*
**Daniel Kammen,** *U. of California, Berkeley*
**Abby Kavner,** *U. of California, Los Angeles*
**Masashi Kawasaki,** *U. of Tokyo*
**V. Narry Kim,** *Seoul National U.*
**Joel Kingsolver,** *U. of North Carolina at Chapel Hill*
**Robert Kingston,** *Harvard Medical School*
**Etienne Koechlin,** *Ecole Normale Suprieure*
**Alexander Kolodkin,** *Johns Hopkins U.*
**Thomas Langer,** *U. of Cologne*
**Mitchell A. Lazar,** *U. of Pennsylvania*
**David Lazer,** *Harvard U.*
**Thomas Lecuit,** *IBDM*
**Virginia Lee,** *U. of Pennsylvania*
**Stanley Lemon,** *U. of North Carolina at Chapel Hill*
**Ottoline Leyser,** *Cambridge U.*
**Wendell Lim,** *U.C. San Francisco*
**Marcia C. Linn,** *U. of California, Berkeley*
**Jianguo Liu,** *Michigan State U.*
**Luis Liz-Marzan,** *CIC biomaGUNE*
**Jonathan Losos,** *Harvard U.*
**Ke Lu,** *Chinese Acad. of Sciences*
**Christian Lüscher,** *U. of Geneva*
**Laura Machesky,** *CRUK Beatson Inst. for Cancer Research*
**Anne Magurran,** *U. of St. Andrews*
**Oscar Marin,** *CSIC & U. Miguel Hernández*
**Charles Marshall,** *U. of California, Berkeley*
**C. Robertson McClung,** *Dartmouth College*
**Graham Medley,** *U. of Warwick*
**Tom Misteli,** *NCI*
**Yasushi Miyashita,** *U. of Tokyo*
**Mary Ann Moran,** *U. of Georgia*
**Richard Morris,** *U. of Edinburgh*
**Alison Motsinger-Reif,** *NC State U.* **(S)**
**Thomas Murray,** *The Hastings Center*
**Daniel Neumark,** *U. of California, Berkeley*
**Kitty Nijmeijer,** *U. of Twente*
**Pär Nordlund,** *Karolinska Inst.*
**Helga Nowotny,** *European Research Advisory Board*
**Ben Olken,** *MIT*
**Joe Orenstein,** *U. of California Berkeley & Lawrence Berkeley National Lab*
**Harry Orr,** *U. of Minnesota*
**Pilar Ossorio,** *U. of Wisconsin*
**Andrew Oswald,** *U. of Warwick*
**Steve Palumbi,** *Stanford U.*
**Jane Parker,** *Max-Planck Inst. of Plant Breeding Research*
**Giovanni Parmigiani,** *Dana-Farber Cancer Inst.* **(S)**
**John H. J. Petrini,** *Memorial Sloan-Kettering Cancer Center*
**Samuel Pfaff,** *Salk Institute for Biological Studies*
**Joshua Plotkin,** *U. of Pennsylvania*
**Albert Polman,** *FOM Institute AMOLF*
**Philippe Poulin,** *CNRS*
**Jonathan Pritchard,** *Stanford U.*
**David Randall,** *Colorado State U.*
**Felix Rey,** *Institut Pasteur*
**Trevor Robbins,** *U. of Cambridge*
**Jim Roberts,** *Fred Hutchinson Cancer Research Ctr.*
**Barbara A. Romanowicz,** *U. of California,Berkeley*
**Amy Rosenzweig,** *Northwestern University*
**Mike Ryan,** *U. of Texas, Austin*
**Mitinori Saitou,** *Kyoto U.*
**Shimon Sakaguchi,** *Kyoto U.*
**Miquel Salmeron,** *Lawrence Berkeley National Lab*
**Jürgen Sandkühler,** *Medical U. of Vienna*
**Alexander Schier,** *Harvard U.*
**Vladimir Shalaev,** *Purdue U.*
**Robert Siliciano,** *Johns Hopkins School of Medicine*
**Denis Simon,** *Arizona State U.*
**Uri Simonsohn,** *U. of Pennsylvania*
**Alison Smith,** *John Innes Centre*
**Richard Smith,** *U. of North Carolina* **(S)**
**John Speakman,** *U. of Aberdeen*
**Allan C. Spradling,** *Carnegie Institution of Washington*
**Jonathan Sprent,** *Garvan Inst. of Medical Research*
**Eric Steig,** *U. of Washington*
**Paula Stephan,** *Georgia State U. and National Bureau of Economic Research*
**Molly Stevens,** *Imperial College London*
**V. S. Subrahmanian,** *U. of Maryland*
**Ira Tabas,** *Columbia U.*
**Sarah Teichmann,** *Cambridge U.*
**John Thomas,** *North Carolina State U.*
**Shubha Tole,** *Tata Institute of Fundamental Research*
**Christopher Tyler-Smith,** *The Wellcome Trust Sanger Inst.*
**Herbert Virgin,** *Washington U.*
**Bert Vogelstein,** *Johns Hopkins U.*
**Cynthia Volkert,** *U. of Göttingen*
**David Wallach,** *Weizmann Inst. of Science*
**Ian Walmsley,** *U. of Oxford*
**Jane-Ling Wang,** *U. of California, Davis* **(S)**
**David A. Wardle,** *Swedish U. of Agric. Sciences*
**David Waxman,** *Fudan U.*
**Jonathan Weissman,** *U. of California, San Francisco*
**Chris Wikle,** *U. of Missouri* **(S)**
**Ian A. Wilson,** *The Scripps Res. Inst.* **(S)**
**Timothy D. Wilson,** *U. of Virginia*
**Rosemary Wyse,** *Johns Hopkins U.*
**Jan Zaanen,** *Leiden U.*
**Kenneth Zaret,** *U. of Pennsylvania School of Medicine*
**Jonathan Zehr,** *U. of California, Santa Cruz*
**Len Zon,** *Children's Hospital Boston*
**Maria Zuber,** *MIT*

**BOOK REVIEW BOARD**
**David Bloom,** *Harvard U.,* **Samuel Bowring,** *MIT,* **Angela Creager,** *Princeton U.,*
**Richard Shweder,** *U. of Chicago,* **Ed Wasserman,** *DuPont*

EDITORIAL

# Throwing deep

In a galaxy far, far away (a billion light years away, to be more precise), two massive black holes merged. Spacetime twisted, contorted, and rearranged itself in dramatic fashion, and ripples within its very fabric shot out across the cosmos. Occurrences like this happen hourly somewhere in the universe. What is notable is that on Earth, we detected these ripples, an event now known as GW150914. In the fraction of a second that we "heard" black holes shake up spacetime, a new window on the universe was opened where we hope to hear more black holes, cosmic phase transitions, and even the birth of the universe. The last big prediction of general relativity—the existence of gravitational waves—has been directly confirmed, and we now have a new way of advancing our understanding of gravity, the force that shapes our universe.



Supercomputer simulation of spacetime during a black hole merger

PHOTOS: (RIGHT) UNIVERSITY OF CHICAGO; (INSET) WERNER BENGER, ALBERT EINSTEIN INSTITUTE/ZUSE INSTITUTE BERLIN/CENTER FOR COMPUTATION & TECHNOLOGY AT LSU

Galileo Galilei urged, "Measure what is measurable, and make measurable what is not so." The team of scientists that built the Laser Interferometer Gravitational-Wave Observatory (LIGO) did the latter, big time. On 14 September 2015, during its first engineering run, spacetime ripples from GW150914 wiggled the separation of mirrors 4 km apart in the LIGO detectors, situated in Hanford, WA, and Livingston, LA, by about $10^{-16}$ cm, one-thousandth the size of a proton. They made the too-small-to-measure measurable by using interferometry, a technique invented by physicist Albert A. Michelson, the first Nobel Prize winner from the United States. Galileo must be smiling. GW150914 not only awed scientists but also captured the attention and imagination of much of humanity, which is no small feat.

This is big science well done. Researchers identified a lofty and worthy goal, and the U.S. National Science Foundation (NSF), in partnership with the California Institute of Technology and the Massachusetts Institute of Technology, funded and stuck with it until they succeeded, a timeline of almost 50 years. There were ups and downs. The brilliant invention of the first gravitational-wave antenna by physicist Joseph Weber was followed by false-alarm detections. NSF built LIGO in the face of skepticism by astronomers, and had to reorganize the project after an early management meltdown. Although the world of science today is more globally collaborative than competitive, there is still a place for national pride and strategic commitment. Just as Japanese scientists targeted neutrinos for their research in elementary particle physics and are proud of their great discoveries in that area (including a 2015 Nobel Prize in Physics), U.S. scientists can be proud of U.S. leadership in the discovery of gravitational waves.

*"GW150914...marked an extraordinary scientific milestone by a very curious species."*

In "The Chirp Heard Across the Universe," the *New York Times* editorial board argued that the justification for NSF's billion-dollar investment in LIGO was simply curiosity about our place in the universe, with no expectation that it would lead to "a better toaster." I agree, but that is not the whole story. Among federal science agencies, NSF is unique in its mission to fund discovery science; it is the throw-deep agency committed to satisfying the boundless curiosity of our species. And, if history is any guide, some of the new knowledge generated by these discoveries will result in future technological advances that transform our very existence. Michael Faraday's tinkering with magnetism in the 19th century led to the science that underpins everything that involves electricity and light, making good on his reply to British Chancellor of the Exchequer William Gladstone when asked about the utility of his research: "One day, sir, you may tax it."

GW150914 may have been an ordinary event in the larger cosmos, but here on Earth, it marked an extraordinary scientific milestone by a very curious species. And best yet, we still don't know where it will all lead. NSF, keep throwing deep!

**– Michael S. Turner**



*Michael S. Turner is director of the Kavli Institute for Cosmological Physics at the University of Chicago, Chicago, IL, and the former assistant director of NSF responsible for funding Advanced LIGO. E-mail: mturner@kicp.uchicago.edu*

10.1126/science.aaf662

Downloaded from on March 17, 2016



Published by AAAS

# NEWS

> “Never pick your career based on a Dustin Hoffman movie—but at least in my case, it’s worked out.”
>
> **Medical epidemiologist Jennifer Gardy** of the British Columbia Centre for Disease Control in Vancouver, Canada, to STAT last week, referring to the movie *Outbreak*.

## IN BRIEF

# Methane-sniffing mission heads to Mars



ExoMars lifted off from Baikonur, Kazakhstan, on 14 March.

The European/Russian Trace Gas Orbiter (TGO) mission, the first installment in the two-part ExoMars program, lifted off this week, beginning its 7-month trajectory to Mars. The TGO’s main aim is to detect and map emissions of methane around the Red Planet. A previous European Space Agency mission, Mars Express, detected methane in 2004 while circling the planet. Further detections—from orbit, on the surface, and by Earth-bound telescopes—have not determined whether the gas is produced by a geological process, by microbes that once lived on the planet, or even by microbes that survive today. A pair of highly sensitive spectrometers on the TGO may put the matter to rest. The mission also carries an experimental lander called Schiaparelli, designed to test landing technologies that will pave the way for part two of ExoMars: a rover to be launched in 2018 that can drill 2 meters below the surface in search of signs of life. Also in 2018, NASA will launch a Mars lander called InSight, the agency announced last week (http://scim.ag/InSightdelay). Designed to measure marsquakes, InSight was delayed because of a leak in the vacuum seal surrounding its seismometer.

AROUND THE WORLD

## China to create its own ‘DARPA’

BEIJING | China is putting military R&D under the oversight of the People’s Liberation Army (PLA), forming a new science and technology committee to manage defense R&D. That committee, in turn, is now creating a new agency it claims is modeled after the U.S. Defense Advanced Research Projects Agency. According to a spokesperson for China’s Ministry of National Defense, the committee, known in Chinese as *junweikejiwei*, is designed to meet the needs of China’s ongoing military modernization. China’s central government plans to spend $147 billion on defense this year; the amount allotted to defense R&D is a state secret. The new committee is headed by Liu Guozhi, an applied physicist and academician of the Chinese Academy of Sciences. An expert on high-power microwaves, he formerly commanded the Malan nuclear test base in Xinjiang, China, and was deputy director of the dissolved PLA General Armaments Department. The committee will strengthen management of defense science and technology, promote indigenous innovation in national defense, and coordinate integrated development of military and civilian technologies, the spokesperson says. http://scim.ag/ChinaDARPA

## Google AI wins Go battle

SEOUL | Google’s DeepMind computer program AlphaGo has beaten the human world champion, South Korea’s Lee Sedol, four games to one in the ancient game of Go. Although IBM’s chess program Deep Blue beat world chess champion Garry Kasparov in 1997, Go was considered far more difficult for artificial intelligence to crack: Its rules are simpler, but brute force computation is a less viable strategy because of the number of possible arrangements of the game’s black and white stones. However, this year, Google and a rival team at Facebook started to apply deep neural networks to Go, giving computers a way of learning by themselves. This week’s win earned DeepMind a $1 million prize and bragging rights—but the games themselves aren’t really the

PHOTO: STEPHANE CORVAJA/ESA

Downloaded from on March 17, 2016



Published by AAAS

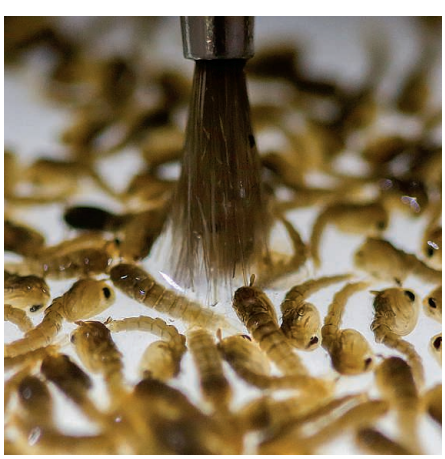
point. Google and Facebook will likely move on to other challenges, just as IBM did. "Where they're trying to get to is a [computerized personal assistant like] Siri that actually works," says Dave Sullivan, a deep neural net expert and CEO of Ersatz Labs in Pacifica, California. "That will be a game-changer."
http://scim.ag/AlphaGowins

## EPA to further limit methane

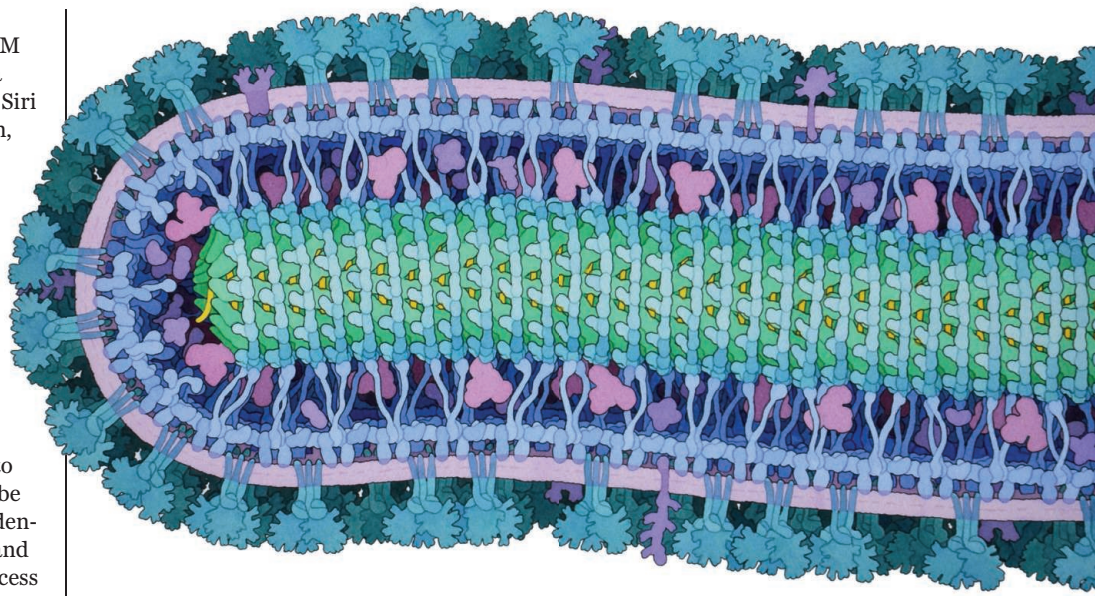
WASHINGTON, D.C. | The Obama administration announced plans last week to further reduce U.S. emissions of methane, a potent warming gas, by extending regulations that now apply to new oil and gas wells. Companies will be required to capture methane that accidentally leaks from wells on public lands and also to limit venting and burning of excess gas. Last August, the U.S. Environmental Protection Agency (EPA) in Washington, D.C., announced plans to regulate these emissions from new and modified wells as part of a plan to reduce overall methane emissions by at least 40% by 2025. But to reach that goal, existing wells must be included, said EPA Administrator Gina McCarthy on 10 March. "We intend to work quickly," McCarthy said, but it is unclear whether EPA can finalize the rule before a new president takes office in January 2017. Meanwhile, industry groups worry compliance will be expensive.

## FDA OKs GM mosquito trial

WASHINGTON, D.C. | A proposed field trial with genetically modified (GM) mosquitoes in Florida won't harm humans or the ecosystem, the U.S. Food and Drug Administration (FDA) says in a preliminary finding released on 11 March. A U.K. company named Oxitec plans to release millions of male *Aedes aegypti* unable to produce viable offspring in Key Haven, just east of Key West; the hope is that by breeding with local females, they will reduce local populations of the mosquito, which can transmit the viruses that cause dengue, chikungunya, and Zika. There's strong local opposition to the study, but FDA says Oxitec's mosquitoes are very unlikely to cause toxic reactions, contribute to insecticide resistance, or spread disease. The findings and Oxitec's own risk assessment are open for public comment for the next 30 days, after which FDA will release a final verdict.



At Oxitec, larvae of genetically modified mosquitoes surround a technician's brush.



## Ebola painting, baby light therapy photo win awards

Scientific visualizations often provoke viewers to recognize beauty even in the deadly or mundane. This detailed watercolor painting of an Ebola virus continues that tradition: It reveals elegant blue treelike proteins—which attach to cells the virus infects—sprouting from the pink membrane surrounding the virus; yellow RNA is encapsulated in its interior. The image, painted by molecular biologist David Goodsell of the Scripps Research Institute in San Diego, California, was named the overall winner of the 2016 Wellcome Image Awards at a ceremony 15 March at the Science Museum, London. Another winner shows a premature baby in an incubator, bathed in ultraviolet light, a treatment for jaundice. For this image, photographer David Bishop received the first Julie Dorrington Award for Outstanding Clinical Photography in a clinical environment. "It perfectly captured the vulnerability of a newborn, whilst keeping a respectful and discreet distance from the subject," wrote judge and BBC Medical Correspondent Fergus Walsh. Both images were chosen out of 20 selected images acquired by Wellcome Images (part of the London-based Wellcome Library).

NEWSMAKERS

## German minister keeps degree

German defense minister **Ursula von der Leyen**, who in August 2015 faced accusations of plagiarism in her 1990 dissertation (*Science*, 2 October 2015, p. 14), will be allowed to keep her doctor of medicine degree. An ethics committee at the Hannover Medical School (MHH) in Germany found that the work was indeed missing citations, but that the mistakes did not constitute misconduct. It concluded that the problems were mainly in the introduction, not in the description of her experimental work. On 10 March, the MHH Senate voted not to revoke her degree. Von der Leyen, who has been seen as a possible successor to Chancellor Angela Merkel, is the latest in a string of high-profile German politicians whose dissertations have been questioned by online plagiarism hunters.

## Three Qs

In January, science historian **Mark Carey** of the University of Oregon, Eugene, co-authored a paper in *Progress in Human*

CREDITS: (IMAGE) AP PHOTO/ANDRE PENNER; (PHOTO) DAVID S. GOODSELL/RCSB PROTEIN DATA BANK



Published by AAAS



*Timurlengia euotica's* keen hearing may have been the key to the large size of its later relative, *Tyrannosaurus rex*.

## A tyrannosaur 'missing link'

The earliest ancestors of *Tyrannosaurus rex* lived 170 million years ago and were just human-sized. By its heyday 68 million years ago, *T. rex* was up to 12 meters long. Efforts to track the evolution of modest-sized early tyrannosauroids into large tyrannosaurs have been stymied by a time gap in the fossil record between 100 million and 80 million years ago—but new 90-million-year-old fossils from Uzbekistan offer a clue to this dramatic increase in size, report paleontologist Stephen Brusatte of the University of Edinburgh in the United Kingdom and colleagues this week in the *Proceedings of the National Academy of Sciences.* The fossils, which include a skull, suggest that the species (*Timurlengia euotica*) was still only horse-sized. But the skull has an unusually complex inner ear apparatus, typical of later tyrannosaurs like *T. rex*, with a long cochlear duct, a canal in the inner ear associated with the ability to hear low-frequency sounds—such as prey creeping through the underbrush. That improved hunting ability gave the animals the calories they needed to maintain larger sizes, making them apex predators, the team suggests. **http://scim.ag/tyrannosaurears**

## BY THE NUMBERS

**13.1 million**

Number of people along the U.S. coast that could be at risk from flooding by 2100 if sea levels rise by 1.8 meters, an upper-end projection by the National Oceanic and Atmospheric Administration (*Nature Climate Change*).

**182**

Number of species listed by the U.S. Endangered Species Act that would have enough funds for protection if some money—$17 million—is transferred from endangered species that are declining despite being "overfunded" (*Proceedings of the National Academy of Sciences*).

**$37 million**

Public health money saved by the Centers for Disease Control and Prevention's food poisoning reporting system PulseNet, which prevented 2819 *Escherichia coli* cases and 16,994 salmonella cases from 1996 to 2009 (*American Journal of Preventive Medicine*).

*Geography* suggesting that more inclusion of research and narratives by women about glaciers—a "feminist glaciology framework"—would aid knowledge of the cryosphere. Now, Carey—a recipient of several National Science Foundation (NSF) grants over the years—has become the target of conservative bloggers, part of an ongoing controversy about NSF-funded research. **http://scim.ag/femglaciology**

**Q: How do you feel about the brouhaha?**
**A:** The good news is that people are talking about glaciers! But there's much more to the story. People and societies impose their values on glaciers when they discuss, debate, and study them. The attention during the last week proves our point clearly: that glaciers are, in fact, highly politicized sites of contestation. Glaciers don't have a gender. But the rhetoric about ice tells us a great deal about what people think of science and gender.

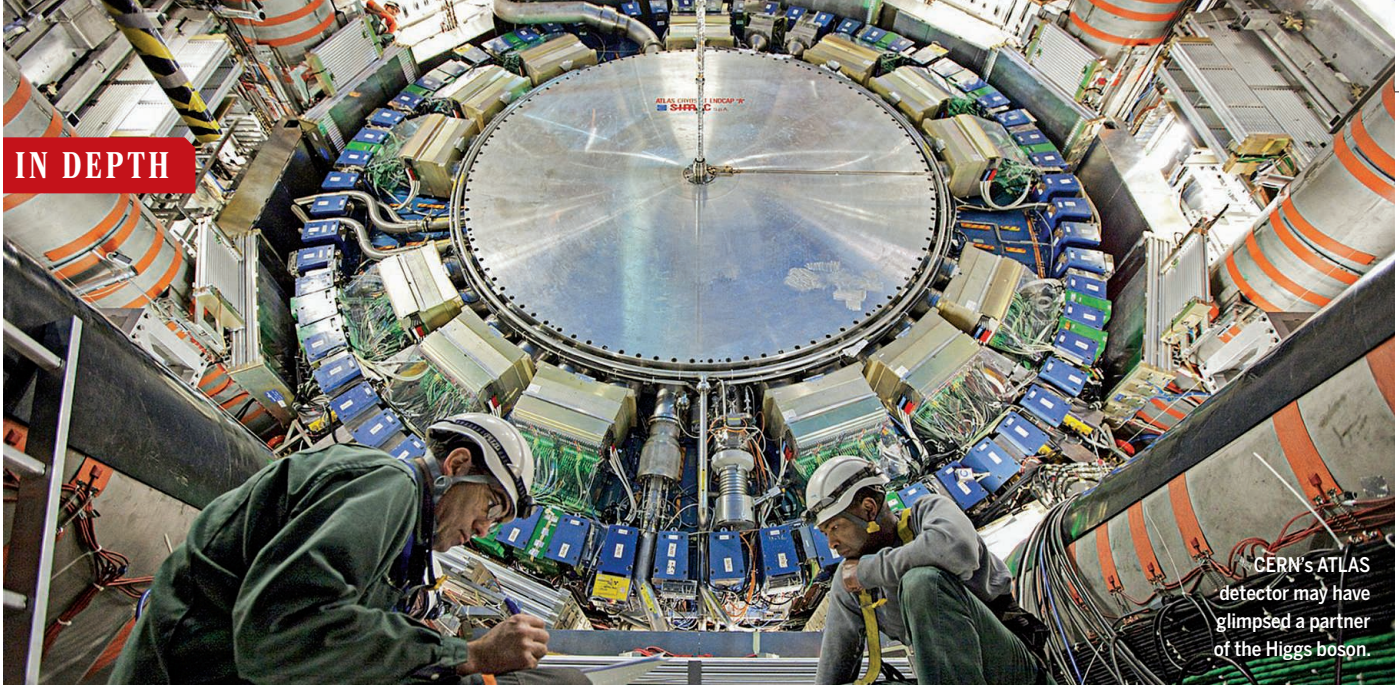
**Q: What is an example of feminist geography improving knowledge?**
**A:** If one goal of glacier research is to help the people living in places like the Alps and Alaska adapt to shrinking glaciers … then it is important to study more than the physical properties of ice. Our paper argues that social science and humanities research can contribute to the development of strategies … to adapt to change. A woman's experience securing post-disaster aid, rebuilding a home, and raising a family after a glacial lake outburst flood has destroyed her community is different than those of men.

**Q: A "man versus nature" framework is inherent in many geo-stories. How does it affect research?**
**A:** Our paper suggests that these broader societal classifications have historically influenced the reception of science [conducted by women]—with men's science more valued. Do we still privilege the heroic, risk-taking, conquest-oriented scientific projects (like data gathering in Antarctica) over "mundane" projects that don't involve adventure and risk into wild nature? Note that we are [not] talking about individual scientists, which is not the point.

ILLUSTRATION: TODD MARSHALL



Published by AAAS



CERN's ATLAS detector may have glimpsed a partner of the Higgs boson.

PARTICLE PHYSICS

# *Giant atom-smasher gears up to chase whiff of new physics*

## Hints of a massive new particle at the Large Hadron Collider have physicists abuzz—and eager to follow up

*By* **Adrian Cho**

Later this month, physicists will rev up the world's biggest atom-smasher—the Large Hadron Collider (LHC) at the European particle physics laboratory, CERN, in Switzerland—for this year's run. They are eagerly awaiting the first new data, due in May, as last year's run ended with a cliff-hanger. The LHC blasted out hints of a new fundamental particle—potentially the first in decades to come as a surprise—and thousands of physicists now want to see whether those signs will pay out.

Many urge caution. "If it's real, it is like opening a window onto a new world," says Beate Heinemann, an experimentalist at the University of California, Berkeley, who works on ATLAS, one of four particle detectors fed by the LHC. But, she adds, "by far the most likely explanation is that it's a statistical fluctuation." Sally Dawson, a theorist at Brookhaven National Laboratory in Upton, New York, agrees. "To me, it's a little underwhelming," she says. "We see bumps all the time and they come and they go."

If real, the new particle would resemble the LHC's previous big discovery, the famed Higgs boson—the last particle predicted by physicists' tried and true explanation of fundamental forces and particles, the standard model. The LHC smashes protons together at unprecedented energies. In December 2011, experimenters with both ATLAS and its rival, the CMS detector, reported signs that those collisions were blasting into existence a particle 133 times as massive as a proton, which quickly decayed into a pair of photons, just as the Higgs was expected to do. By July 2012, researchers had seen the particle decaying in other predicted ways and had enough data to claim a discovery.

The putative new particle would seem to be emerging in much the same way. Last December, the ATLAS and CMS teams reported hints of a particle that also decayed into two photons, but with a mass 800 times that of a proton, as deduced from the photons' energies. Those protosignals appear as "mass peaks" poking out of a background produced by pairs of random photons. There's a roughly one in 50 chance that a background fluctuation could produce a peak like ATLAS's—a chance far too large to allow the team to claim a discovery—and CMS sees an even smaller blip. Still, says Linda Carpenter, a theorist at Ohio State University, Columbus, "the thing that excites people is that both experiments see a similar bump at the same mass." (As *Science* went to press, both teams were planning to update their results on 18 March at a conference in La Thuile, Italy.)

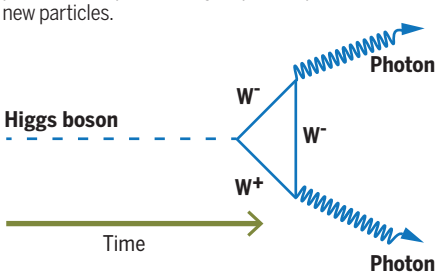
Some physicists think that the new beast is just another, heavier Higgs. The fact that it decays into two photons shows that it, too, is a boson and has spin equal to an integer multiple of a basic quantum called Planck's constant. Many theories that aim to extend the standard model posit multiple Higgs bosons, says Mayda Velasco, an experimentalist at Northwestern Universit, in Evanston, in Illinois, who works on CMS. "For me that would be the easiest way to explain it: that it is one of the extra Higgses that should be floating around," she says.

But other physicists say that the putative particle is not behaving like a Higgs. In addition to decaying into a pair of photons, the Higgs can also decay into a pair of particles called Z bosons or into a $W^-$ boson and a $W^+$ boson. Yet, so far, the LHC's new boson seems to decay only into photons.

One explanation for the absence of W and Z decays is the influence of still other undiscovered particles. To see how they might intervene, consider how the Higgs decays into photons. Photons interact only with charged particles, so the uncharged Higgs can't decay into them directly. Instead, it

### The Higgs, gone in a flash

A Higgs boson decays into photons through a "loop" of particles such as W bosons. The decay of the potential new particle may require loops with more new particles.




CREDITS: (PHOTO) 2011 CERN/CLAUDIA MARCELLONI; (DIAGRAM) H. BISHOP/*SCIENCE*

Downloaded from on March 17, 2016



Published by AAAS

spawns a charged particle and its antiparticle, such as a $W^+$ and a $W^-$, that instantly radiate the photons and annihilate each other (see figure, p. 1248). When the decay is sketched on paper, the $W^+$ and $W^-$ form a closed loop, so the decay is called a "loop process." The new boson would make photons in the same way, physicists assume. However, loop processes could also explain why the new particle doesn't decay to Zs or Ws: Other new particles could race around in loop processes that cancel out the decays into Zs or Ws.

Excited by the prospect of a bevy of new particles, theorists have wasted no time in trying to figure out how they might fit into theories that extend the standard model. In 3 months, some 300 papers addressing the LHC's bumps have appeared on the arXiv.org online preprint server. For example, Carpenter and colleagues apply a concept called supersymmetry, which posits that every standard model particle has a massive superpartner with a different spin. The simplest supersymmetric models won't cut it, she says, but so-called R-symmetric supersymmetry might. The new boson would be a hypothetical particle called a sbino, and the supporting cast of other particles would be superpartners to particles like the W.

But other theorists have explained the new particle in other ways: It could be a manifestation of extra spatial dimensions, a so-called axion (a particle invented to solve a certain technical problem in the theory of the strong nuclear force), an offshoot of string theory, or a new Z boson, to name a few. The list suggests that theorists can shoehorn the new particle into any existing beyond-the-standard-model theory. And the sheer number of different approaches shows that, even if the new particle is real, physicists may need years to figure out what's really going on. "Particles themselves don't tell you anything," Dawson says. "It's only when you put them together into the bigger picture" that insight comes.

Still, particle physicists would be delighted to have to puzzle over such things. After all, in 30 years they haven't spotted anything the standard model can't explain—except for the discovery that neutrinos have mass. Fortunately for them, they should soon know whether the new particle is real. Last year was the first in which the LHC ran full throttle instead of at half energy. Data taking started slowly, but it came on strong toward the end of the year. Physicists now expect to collect six times as much data this year, more than enough to put the supposed signals to the test, Velasco says. "If we start up where we left off—poom!—we will be able to tell in a few months." ■

CLIMATE SCIENCE

# *Efforts to link climate change to severe weather gain ground*

## U.S. academies find researchers getting better at attributing heat waves, cold snaps, and other events to climate trends

*By* **Warren Cornwall**

When record-setting rainstorms drenched the southern United Kingdom in early 2014, causing more than $500 million in damage, many wondered whether climate change had played a role. Two years later, scientists had an answer: Yes, it very likely did, they reported last month in *Nature Climate Change*, concluding that a warming planet had substantially raised the probability of such storms.

The finding is just one product of an emerging field known as event attribution science. Over the last dozen years, scientists have gone from saying it is impossible to link climate change to any single bout of bad weather to confidently declaring that, in certain cases, they can. Last week, the fledgling field got an independent vote of confidence from an expert panel assembled by the U.S. National Academies of Science, Engineering, and Medicine. "It is now possible to estimate [the] influence of climate change on some types of specific extreme weather events and in particular, heat and cold events, drought, and precipitation," said retired U.S. Navy Rear Admiral David Titley, the committee chair and director of the Pennsylvania State Center for Solutions to Weather and Climate Risk in University Park.

Although the panel warned against overstating current attribution capabilities, it noted that the field is advancing rapidly. Some research teams, for instance, are working to shorten the time it takes to make attributions from the years now required for the complex computer modeling and peer review to just weeks or days. Policymakers, meanwhile, are eyeing the possibility that attribution science could end up in the courtroom, as those harmed by climate-driven weather try to extract damage payments from those who produce greenhouse gases. "The dialogue becomes not 'Is climate change happening?' but 'Who's responsible for that?'" says attorney Lindene Patton in Great Falls, Virginia, a former insurance executive and an author of *Climate Change and Insurance*, a 2012 book from the American Bar Association.

The first major study that tried to link a specific weather event to climate change was published in *Nature* in 2004. That analysis found that global warming had at least doubled the chances of a 2003 heat wave associated with more than 70,000 deaths in Europe. To make the link, researchers relied on historic temperature records and computerized climate simulations. The simulations allowed the scientists to compare how different levels of warming gases affected the risk of heat waves. Since then, a string of similar studies have linked climate change to heat waves in Russia and Australia, several rounds of flooding in the United Kingdom, and a Texas drought, among other weather events.




Better climate models are revealing the role of climate change in severe weather events, such as heavy rains in the Philippines in 2015.

PHOTO: AP PHOTO/AARON FAVILA

Downloaded from on March 17, 2016



Published by AAAS

Today, advances in computer models have made it easier to do attribution analyses, says climate scientist Peter Stott, the lead author of the 2004 study and head of the Climate Monitoring and Attribution program at the Met Office in Exeter, the United Kingdom's weather service. New models have finer spatial resolution than past versions, improving from about 280 square kilometers to 60, making it easier to see how climate change might affect weather events that often are, by global standards, relatively compact. A growing number of competing global climate models also means scientists can run similar simulations in multiple models and then see whether the results agree. Stott notes his initial paper relied on just one model, but now "the sophistication has increased."

Still, some types of weather events are easier to attribute than others, the National Academies panel noted in its report, released on 11 March. Researchers can analyze with relatively high confidence how climate change contributes to heat waves and cold snaps, it concluded. Although a warming climate is expected to influence water cycles, intense rainfall is trickier to attribute because it's harder to produce accurate simulations, and droughts are subject to a host of variables, such as human alterations to the landscape.

> *"The dialogue becomes not 'Is climate change happening?' but 'Who's responsible for that?'"*
>
> **Lindene Patton**, insurance expert

Other events, such as hurricanes, still defy attribution, the panel found. In part, that's because even big hurricanes are still too small and complex to capture in global climate models, says Tom Knutson, leader of the Climate Impacts and Extremes group at the National Oceanic and Atmospheric Administration's Geophysical Fluid Dynamics Laboratory in Princeton, New Jersey. And although some researchers have argued that climate change should affect hurricane frequency or intensity, historical data are often too sparse to test those claims. One recent study, for instance, suggested that an uptick in the number of cyclones passing near the Hawaiian Islands in 2014 was connected to rising greenhouse gases. But Knutson isn't persuaded, saying "it doesn't have the buttressing of additional support of long-term observational trends."

Such issues mean attribution science still has "a lot of room for improvement," Titley said. One advance that scientists are pursuing is speeding up their analyses. The Met Office is gearing up to start offering conclusions immediately on the heels of some weather events by late 2017, Stott says. A similar initiative, called the World Weather Attribution (WWA) program, has already taken its first tentative steps. Last year, within a week of record-setting rainfall in the United Kingdom and a European heat wave, the group issued reports concluding that the odds of these weather patterns had increased.

To achieve this speed, researchers are doing the modeling in advance, by developing a wide range of weather scenarios and testing how climate change affects the odds of each one. Once a real event occurs—such as a heat wave—they can compare it to the scenarios to see whether climate change has made that particular freak event more likely.

This kind of prefabricated approach should allow scientists to provide the quick answers that the public, media, and policymakers often ask for, says Heidi Cullen, chief scientist for Climate Central, a Princeton, New Jersey–based nonprofit that promotes research and journalism on climate change. She is over seeing the WWA program, which also involves university and government scientists in Europe and Australia.

Ultimately, such efforts could have implications in legal settings and international diplomacy. The United Nations (U.N.) climate agreement struck last year in Paris notes the importance of exploring ways to compensate developing countries for the "loss and damage" caused by climate shifts. Some countries, such as small island nations threatened by sea-level rise, are already pressing for financial support from industrialized nations responsible for the bulk of greenhouse gas emissions. Those demands include compensation for extreme weather, too, says Friederike Otto, a scientist working on attribution at the University of Oxford in the United Kingdom. She's been contacted by a U.N. office preparing for a 2016 U.N. conference in Morocco, which is supposed to work out details of the loss and damage program.

Insurance companies are also monitoring the field, says Patton, the insurance expert. Architects, planners, and engineers, for instance, could be hit with lawsuits over whether they properly considered climate change when designing infrastructure such as flood-control levees, she says.

Some lawyers are also eyeing the possibility of pursuing weather-related damage claims against major carbon polluters, such as fossil fuel companies. In 2015, two attorneys for the London-based environmental firm ClientEarth took to the pages of *Nature Geoscience* to offer this advice to climate attribution scientists: "Be prepared to testify as an expert witness." ■



PHOTO: © JOE MCNALLY

HUMAN EVOLUTION

# *Five matings for moderns, Neandertals*

## Powerful genetic studies pin down multiple trysts on different continents

*By* **Ann Gibbons**

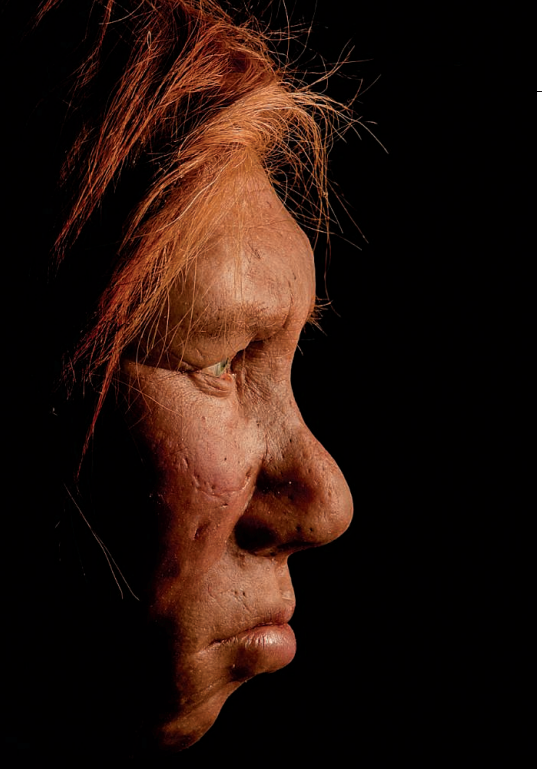
Only a bit of the DNA coiled inside the cells of Europeans and Asians comes from Neandertals, but those snippets have sparked a flurry of research. In the past few years, researchers have traced them to one or two ancient encounters with our extinct cousins. Now, a report published online in *Science* this week details a far richer sexual past for modern humans and their archaic cousins, one that played out at multiple times and places over the past 60,000 years.

By developing powerful new statistical methods, an international team has identified how often and on which continents modern humans, Neandertals, and a second kind of archaic human called Denisovans met and mated. The researchers conclude that if you're an East Asian, you have three Neandertals in your family tree; Europeans and South Asians have two, and Melanesians only one. (Africans, whose ancestors did not mate with Neandertals, have none.)

Downloaded from on March 17, 201



Published by AAAS



A genetic study uncovers the hidden Neandertals in the family tree of people from Europe and Asia.

Add in two additional liaisons known only from fossil DNA, and the ancestors of modern humans and Neandertals mixed it up at least five times. (Any matings that produced no offspring can't be traced.) Meanwhile, the Denisovans bred at least once with Melanesians. "It was apparently separate events, so not just one single happy party at some point," says evolutionary biologist Alan Cooper of the University of Adelaide in Australia, who was not part of the new study.

When researchers first spotted traces of Neandertal nuclear DNA in living people, they assumed that it must have come from a rare mating or two, likely when modern humans left Africa and first pushed into Neandertal territory in western Asia (*Science*, 7 May 2010, p. 680). But since then, the family history of modern humans and their cousins has grown tangled.

First, researchers found that Melanesians have inherited 2% to 4% of their DNA from the Denisovans, known from fossils at least 50,000 years old from Denisova Cave in Siberia, Russia. Then, they found that Denisovans had also interbred with Neandertals. Last year, researchers discovered that a 40,000-year-old modern human from Romania had a Neandertal great-great-great grandparent—but this Neandertal genome does not live on in present-day humans (*Science*, 22 May 2015, p. 847). Last month researchers reported modern DNA in a Neandertal toe bone, suggesting another early mating between the two types of humans, perhaps 100,000 years ago or so. And this week, the same team reports interbreeding between Denisovans and 440,000-year-old ancestors of Neandertals.

All this mixing has resulted in a patchwork of archaic DNA segments in modern human genomes. Tracing the source of each segment isn't easy, in part because Neandertals and Denisovans were closely related. In Melanesians, for example, "up to 20% of the time when we say a segment matches a Neandertal, it's Denisovan," says population geneticist Joshua Akey of the University of Washington, Seattle, who led the new study.

So Akey's team developed a statistical method to help identify and classify archaic DNA more reliably. They sequenced the genomes of 35 Island Melanesians, who carry more archaic DNA than any other group, and also analyzed the genomes of nearly 1500 other people around the world. They used the sequence data to find chunks of DNA likely inherited from archaic ancestors. Then they used new statistical methods to see how reliably they could classify the archaic DNA as Neandertal or Denisovan, and whether different populations had the same source of archaic DNA.

Akey expected that diverse Neandertal ancestors had contributed to Melanesian genomes, but that's not what the team found: Most of the Melanesians' archaic DNA turned out to be from Denisovans. What Neandertal DNA they have stems from a single liaison—the first one, soon after modern humans left Africa. A second Neandertal encounter shows up in the genomes of Europeans, South Asians, and East Asians, and likely happened in the Middle East before these populations diverged. Finally, the ancestors of East Asians had a third hookup with Neandertals, presumably somewhere in Asia (see graphic, below).

The most likely explanation, Akey says, is that Melanesians split from the ancestors of Europeans and Asians before the second encounter. Later, East Asians broke away from Europeans and South Asians and got a third pulse of Neandertal DNA as they went their separate way. Meanwhile, the ancestors of Melanesians picked up genes from Denisovans somewhere in Asia. The legacy of this ancient sex includes 21 chunks of archaic DNA bearing immune genes that recognize viruses, along with several metabolism genes, such as *GCG*, which increases blood glucose levels, and PLPP1, a cell membrane protein that breaks down fats. These genes may have helped modern humans adapt to new diseases, diets, and climates as they moved into Neandertal territory in Europe and Asia.

But the researchers also found "deserts"—stretches of the human genome where no archaic DNA appears. These genomic regions may once have carried the legacy of ancient encounters, but it no longer survives in living people. That suggests that these parts of the genome, which contain genes linked to language, brain development, and autism, are critical to a modern human's identity and reproductive fitness: Archaic gene variants can't be tolerated here.

Some researchers caution that modern DNA may not be a completely reliable guide to ancient matings. Groups like Melanesians may have simply lost archaic genes over time, so that their full mating history with Neandertals was erased. "It seems possible that the differences in Neandertal ancestry between present-day people could be due to differences in the efficacy of natural selection 'weeding out' Neandertal segments," says population geneticist Pontus Skoglund of Harvard University.

Still, he and others praise the power of the new method and the pace at which researchers are building a catalog of DNA inherited from archaic humans, which keeps adding new twists to the story of our origins. As evolutionary biologist Eske Willerslev of the University of Copenhagen and the University of Cambridge in the United Kingdom notes: "It seems like [ancient admixture] keeps getting more complicated." ■

## Mixing it up in the Pleistocene

After the ancestral population of humans divided, modern and archaic people mated several times (arrows), likely on different continents. Three encounters with Neandertals left DNA in living people, and Denisovans mated with the ancestors of today's Melanesians.

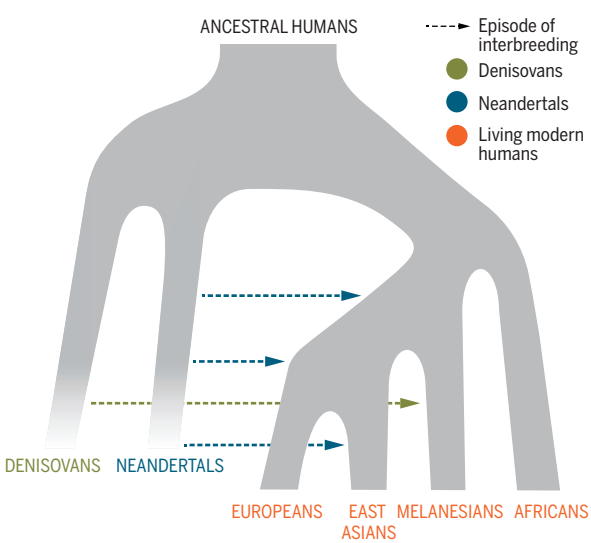



DIAGRAM: ADAPTED FROM VERNOT *ET AL.*/*SCIENCE*



Published by AAAS

RESEARCH FACILITIES

# Europe on course for a neutron drought

## Billion-euro accelerator won't make up the shortfall, experts say

*By* **Edwin Cartlidge**, *in Rome*

Neutrons may be ubiquitous in matter, but the intense, energetic neutron beams that scientists use to probe materials are a scarce commodity. In Europe, they will soon get a lot scarcer, according to a panel commissioned to assess the impact of the imminent closure of many of the continent's aging neutron reactors.

The panel, known as the Neutron Landscape Group (NLG), said last week that as the aging reactors shut down over the next 5 to 10 years, the number of neutrons available for research will fall by as much as half. A new, accelerator-based neutron source, the world's most intense, is due to turn on in Sweden by the end of the decade. But it will take years to reach full capacity, and in the meantime scientists who rely on neutrons will face a drought, unless the life span of some of the reactors can be extended. Multiple shutdowns "will have a traumatic effect on the neutron community," says NLG Co-Chair Colin Carlile of Uppsala University in Sweden. "But none of the owners or users want to talk about it in public."

The panel published its findings in the latest installment of a "road map" released last week by the European Strategy Forum on Research Infrastructures (ESFRI), which advises the European Union. The road map provides a rolling list of proposed pan-European facilities that ESFRI deems scientifically excellent and likely to start up within the next 10 years. This one includes five new projects—facilities studying the atmosphere, river-sea systems, and food security, as well as a solar telescope and a cultural heritage center—as well as others that have long been on scientists' wish lists.

It also includes NLG, which takes a special look at neutrons. Chaired by physicists Carlile and Caterina Petrillo of the University of Perugia in Italy, NLG points out that more than 6000 scientists and engineers in Europe use neutrons to study materials ranging from magnets and superconductors to plastics and proteins. However, it says, two-thirds of the continent's operating neutron sources were built in the 1960s and 70s, and most of those are due to close because of their age and antinuclear sentiment.

The €1.8 billion European Spallation Source (ESS) is meant to fill some of that gap. Under construction in Lund, Sweden, the ESS will use a proton accelerator to generate the world's most powerful beams of neutrons and is due to start operating in 2019. But limited initial funding means that the facility will have just 16 instruments up and running by 2028. That, NLG says, will leave researchers considerably worse off than they are today with the 40 instruments at the most powerful existing source, the Institut Laue-Langevin (ILL) research reactor in Grenoble, France.

The ILL is the wild card in the picture. The convention signed by the three countries that operate the ILL—France, Germany, and the United Kingdom—is due to expire in 2023, and neither the United Kingdom nor France has said whether they will extend the reactor's life. (Germany will likely want to finish its current license and so shut down in 2027.) Carlile says that this shortage would not only be devastating for current research, but would also make it much harder for younger researchers to gain experience in making neutron-based measurements. "People who use these facilities have no stepping stone to get there," he says, "unlike users of x-ray sources, which are available at universities."

According to the panel, neutron output over the next 15 years could be kept to within 20% of existing levels if the ILL and the other sources facing closure operate until at least 2030. These extensions, Carlile estimates, would cost about €200 million. But by 2030, he notes, the ILL reactor will be more than 50 years old.

Robert McGreevy, director of the ISIS neutron source in Oxfordshire, U.K., says his facility—one of the few existing accelerator-based sources—will operate at least until 2030 and perhaps beyond. But he believes there is little hope that two of the facilities that NLG wants to remain open, in Paris and Berlin, can be kept operating. The fate of both, he says, has already been announced by the respective national governments.

Meanwhile, uncertainty hangs over the ESS. Its director, James Yeck, says that it is currently being built on schedule and within budget, but he acknowledges the danger that one of the project's 17 member countries could pull out, as happened in 2003. The project's management has delayed a decision about whether to buy additional equipment that would increase the neutron beam power from 3 to 5 megawatts until 2017.

Carlile says that to secure the future of neutron research in the long term, Europe will need several new medium-flux neutron sources, costing about €500 million each. But McGreevy believes Europe's aversion to nuclear power means that any new mid-sized neutron sources will have to be accelerators rather than reactors which, he says, will be "technically very challenging."

And researchers may not be able to rely on the current mainstay, the ILL, even if the countries overseeing it decide to extend its life. McGreevy thinks that the ILL has done all it can to respond to new safety requirements imposed after the Fukushima nuclear disaster in Japan. But another major nuclear accident, he says, "would probably be the death knell for ILL." ■



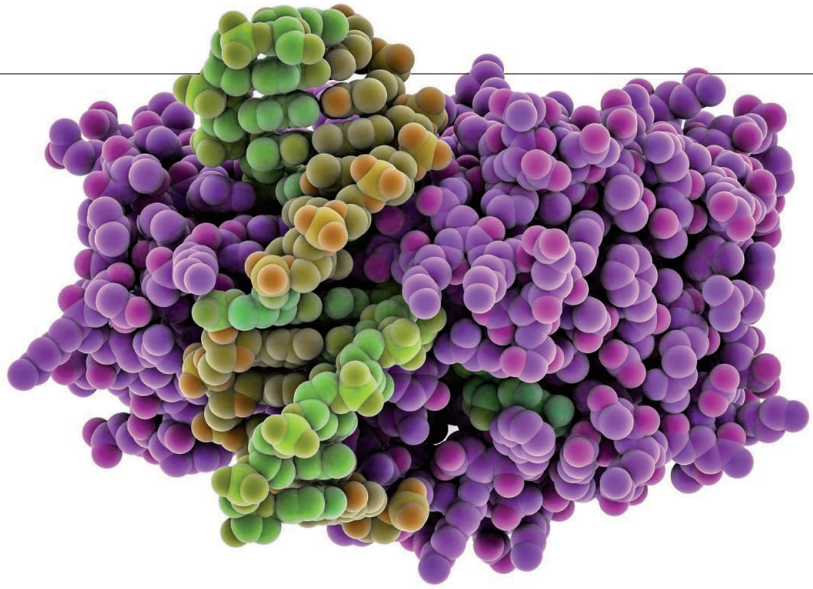
Architect's vision of the target station and instrument halls of the European Spallation Source in Sweden.

IMAGE: ESS/TEAM HENNING LARSEN ARCHITECTS

Downloaded from on March 17, 2016



Published by AAAS



The methyl groups placed on DNA (yellow, green) by an enzyme (purple) differ by tissue and can be used to locate where cell death occurs in a person's body.

IMAGE: LAGUNA DESIGN/SCIENCE SOURCE

DIAGNOSTICS

# *Tests of blood-borne DNA pinpoint tissue damage*

## Assays spot cell death from diabetes, cancer, and more

*By* **Jocelyn Kaiser**

In every living person, even the healthiest, death abounds. Cells throughout a person die naturally all the time, shedding fragments of DNA into the blood. When injuries or illness damage specific parts of a body, cell death generates even more of this so-called circulating DNA. Several research teams are now developing ways to trace it to the tissue from which it originated, hoping to detect early stages of a disease or monitor its progression.

"Noninvasive measurement of cell death is a superexciting area with endless applications," says developmental biologist Yuval Dor of the Hebrew University of Jerusalem. Dor's own group reports this week that its technique for tracing the origin of circulating DNA detected the expected type of cell death in people with pancreatic cancer, type 1 diabetes, multiple sclerosis, and brain injuries. Two more groups have reported preliminary but encouraging results for other cancers.

The published work does no more than prove the concept, says Alain Thierry, director of research at the National Institute of Health and Medical Research in Paris. The circulating DNA techniques still need to be vetted on a large scale, and they face competition from other diagnostic tests that rely on blood-borne hormones, metabolites, and other nongenetic molecules. Still, Thierry says, "having information from circulating DNA from a blood test could be very powerful" for detecting or tracking diseases.

A few assays based on circulating DNA are already in use. Since 2011, doctors can order a test for Down syndrome that analyzes DNA shed by a fetus into a pregnant woman's blood. Cancer researchers monitor circulating DNA carrying cancer-related mutations to follow patients' responses to targeted therapies and are working on similar tests for early signs of cancer. But those tests cannot identify the DNA's origins. For many other diseases that boost tissue-specific cell death, circulating DNA had little to offer.

One potential solution is to look at chemicals called methyl groups, which cells attach to certain genes to prevent them from being transcribed into proteins. Each cell type, whether muscle, neuron, or blood, has a distinct DNA methylation pattern. In October 2015, a group led by Dennis Lo of The Chinese University of Hong Kong reported in the *Proceedings of the National Academy of Sciences* (*PNAS*) that they could detect those distinctive patterns in circulating DNA. In liver cancer patients, for example, the team saw a rise in DNA traceable to dying liver cells. Their technique, however, relied on whole genome analysis of methylation that costs upward of $1000 per sample.

In *PNAS* this week, a team led by Dor, DNA methylation expert Ruth Shemer at the Hebrew University of Jerusalem, and endocrinologist Benjamin Glaser from the Hadassah Medical Center in Jerusalem offers a potentially simpler, and cheaper, approach. The group drew on known methylation signatures for various tissues to pick out methylated sites along the genome that provide unique fingerprints. They report that by scanning circulating DNA for those hotspots in people recently diagnosed with type 1 diabetes, they detected dying β cells—the insulin-producing cells in the pancreas—in all of the 11 people tested. Their test also revealed evidence of dying β cells in the blood of people who had received islet cell transplants—a potential sign of immune rejection of the islets.

Immunobiologist Kevan Herold of Yale University says the result bodes well for a circulating DNA test that could be used to screen people at high risk for type 1 diabetes before their pancreas is so damaged that blood sugar levels rise. "The hope is that we could intervene at an early stage and try to prevent progression," he says.

Circulating DNA can also flag other conditions, Dor and his colleagues showed. In blood from 14 out of 19 patients with relapsing multiple sclerosis, they detected circulating DNA shed by brain cells called oligodendrocytes, which the disease destroys. The team could also identify dying brain cells in blood samples from people who had brain damage due to head trauma or cardiac arrest. For pancreatic cancer, the team saw signs of pancreatic cell death in the blood of about half of 42 patients; the group even distinguished cancer from pancreatitis—which also raised cell-free DNA levels in seven of 10 patients—by incorporating a test for a cancer mutation.

Methylation isn't the only way to trace circulating DNA. In January, a team at the University of Washington, Seattle, described in *Cell* a test that relies on tissue-specific differences in how DNA is packaged in structures called nucleosomes. In three out of five people with advanced cancers, the team could use those nucleosome fingerprints to trace circulating DNA to the cancerous tissue.

Researchers now plan to test the nucleosome and methylation approaches in larger groups of people. Clinical biochemist Eleftherios Diamandis of the University of Toronto in Canada predicts that at least for initially diagnosing cancer, the tests may face an obstacle. In the early stages of cancer—just when the tests would be most useful—there may be little or no circulating tumor DNA in a person's blood.

"I am not sure if even the most fascinating technical developments will solve the issue of abundance," Diamandis says. Still, some were also once skeptical that Down syndrome could be reliably picked up from fetal DNA in a pregnant woman's blood, and now thousands of women a year use the screening tool. ■

Downloaded from on March 17, 2016



Published by AAAS

FEATURES






PHOTO: KAJETAN DEJA

# VOYAGE INTO DARKNESS

## Researchers are learning that Arctic organisms aren't dormant during the long polar night

*By* **Eli Kintisch**,
*on the* RV Helmer Hanssen*, northwest of Svalbard, Norway*

It is lunchtime, but the sun is nowhere in sight. Just the moon and stars illuminate a black sky above a blacker sea as we motor a small skiff along an island fjord. The five of us—three researchers, a crew member, and a reporter—are encased in bulky, full-body survival suits in deference to the sub-zero January temperatures here in the high Arctic. Our eyes acclimate slowly. Forty minutes into our foray, we see a green aurora above a majestic rock wall that appears, out of nowhere, along the shore. "Can you believe we're being paid for this?" one scientist marvels. A black-and-white seabird called a little auk emerges from the gloom. It dives nonchalantly into the shadows to hunt, pursuing tiny crustaceans the size of rice grains.




Not long ago, researchers would have considered such a scene unlikely. They generally believed marine life this far above the Arctic Circle was dormant during the long polar night, when temperatures plunge and the winter sun disappears below the horizon for roughly 4 months. "The thinking has been: Those who can, migrate out of the Arctic [in winter]. Those who can't … turn off," says marine biologist Jørgen Berge of the University of Tromsø - The Arctic University of Norway (UiT).

Now, Berge and other researchers are challenging that paradigm. On voyages deep into the polar night—when research vessels have traditionally stayed away—they're finding that Arctic waters can pulse with life, even in the dead of winter. They've documented foraging birds and fish, masses of surprisingly active zooplankton, and even signs that some animals are continuously growing and reproducing despite the cold and darkness. "We make fantastic discoveries every time we do a cruise," Berge says. Those findings are driving a "reevaluation" of how Arctic ecosystems behave during the polar night, writes marine biologist Geraint Tarling of the British Antarctic Survey in Cambridge, U.K.

Much about life in the polar winter still remains "essentially … a black box," Berge says. That is why, earlier this year, he led a 17-day research cruise from northern Norway into the Arctic Ocean, an environment he calls "the least known realm on the planet." The 28 researchers aboard the ship had goals that included testing new technologies for monitoring remote seas,



Published by AAAS



Northern lights bathe the high Arctic city of Tromsø, Norway, the departure port for a recent polar night cruise by the *RV Helmer Hanssen* (opposite page).

PHOTO: HINRICH BÄSEMANN/CORBIS

obtaining better measurements of the polar night's eerie "lightscape," and gaining a better understanding of how Arctic organisms cope with the sun's absence.

There was also a sense of urgency: Climate change is remaking the Arctic, and melting ice will allow more light to penetrate winter seas. "This will have a major impact on the ecology," Berge says. "So understanding the relationship between light and organisms is crucial to understanding the biological future of the Arctic."

**AS BERGE TELLS IT**, the emerging subfield of polar night biology was born almost by luck. The conventional wisdom was that the high Arctic only came alive each spring, after there was enough sunlight to fuel the growth of phytoplankton, the tiny marine plants that anchor the polar food web. As a result, biologists tended to launch their Arctic expeditions during the eight lighter months of the year—when the sun is sometimes above the horizon for 24 hours—and stay away during the roughly 4 months of constant night.

In 2007, however, Berge and colleagues retrieved some unexpected data from a sensor moored in a fjord off Svalbard, a rocky archipelago that sits about halfway between the Arctic Circle and the North Pole. The device used sound to track the movements of marine organisms, and readouts showed zooplankton periodically migrating up and down the water column. That's typical behavior during much of the year, when the creatures rise en masse to the surface at night and sink deep during the day, in part to avoid predators. But these movements were occurring in January, when Arctic zooplankton were expected to be dormant. "We were flabbergasted," recalls Finlo Cottier, a physical oceanographer with the Scottish Association for Marine Science (SAMS) in Oban, U.K.

Other surprises followed, sometimes aided by fate: In 2012, a cruise scheduled for November was delayed until January 2013 because of ship repairs, enabling biologists to discover unexpected bioluminescence and zooplankton at odd depths, whetting their appetite to learn more. Since then, each winter a tight-knit group of researchers—mostly Norwegian, British, and American—has reunited in Norway to sail into the dark.

The goal of this year's expedition was to explore several Svalbard fjords, as well as waters adjacent to the Arctic's floating sea ice. Our vessel was the 64-meter-long *Helmer Hanssen*, named for an early 20th century Norwegian who explored the region by wooden ship and ice sledge. In



*Published by AAAS*

contrast, we enjoyed cozy, quiet cabins, shockingly good Wi-Fi when the satellite cooperated, and hot Norwegian food, courtesy of a chef who jammed on his electric guitar off shift. The *Helmer Hanssen* also boasts well-stocked labs, cranes able to deploy sensor-laden buoys into the sea, trawl nets for sampling seafloor life, and autonomous undersea vehicles bristling with cameras and sensors.

Still, conditions can be harsh. Team members spent hours on icy decks wrangling wet nets and gear, or below decks fighting seasickness and claustrophobia in labs that often smelled like fish. ("I keep wanting to take a shower, but then I know there's a trawl coming up so I put it off again," said fish biologist and UiT graduate student Marine Cusa.) Cruise leaders had to cope with storms that repeatedly reshuffled their plans. Eventually, they stopped printing out revisions, opting instead to write changes on a whiteboard.

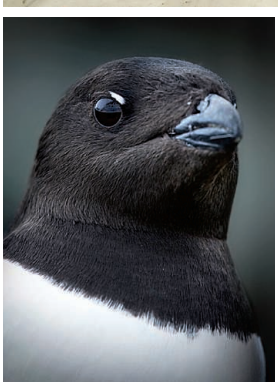
**WHEN I COMPLAIN** of seasickness during breakfast one morning, a researcher points to a porthole. "The best thing is to look out at the horizon," advises marine biologist Kim Last of SAMS. Everyone laughs, because there is nothing to see. During early January here, at about 79° north, the sun never rises; it stays at least 11° below the horizon. With luck, at high noon you might see a gorgeous but short-lived red and purple sky, caused by sunlight reflected around the curve of Earth.

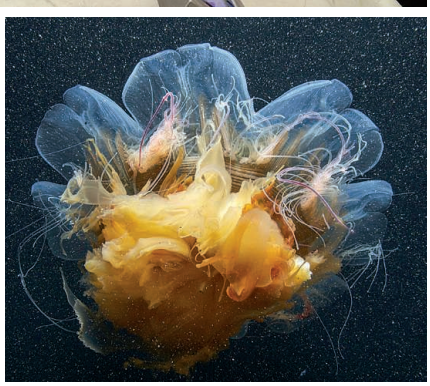
Scientists want to quantify that darkness, to know just how much light is available during the polar night. The measurements aren't easy. Satellite instruments, which rely on light reflected from land, and conventional light meters aren't sensitive enough to count the relatively few photons. So the researchers have hacked a device—originally designed to detect fluorescence in biomedical labs—that provides accurate readings.

One day, Last and biologist Jonathan Cohen of the University of Delaware (UD), Newark, pull on heavy winter gear and climb up to the top deck, above the bridge, to take a daily light measurement. The captain has turned off the radar so the scientists won't be exposed to its powerful microwaves. Crouched behind a bulwark as the wind howls, Cohen programs the sensor with a small keyboard. No flashlights, he warns bystanders.

Repeated measurements show that average winter light levels are tens of millions of times lower than those measured during the Arctic summer. Still, there are subtle patterns within the winter lightscape: "Fifty shades of gray," Berge jokes. Sunlight reflected from below the horizon makes the day a little brighter than the night, for example, and the aurora, the moon, and even the stars add measurable photons.







Polar night cruises give researchers a rare chance to study the winter habits of a wide range of marine organisms, including (from top, clockwise) fish such as cod, flamboyant cnidarians that sift food from the water column, and little auks.

**THOUGH SCARCE**, the rays are enough to shape the behavior of many Arctic organisms. In particular, studies of common, shrimplike crustaceans known as krill are yielding new insights into light sensitivity.

During a snow squall, one of the ship's cranes hauls up a net shaped like a dead giant squid. Kneeling, Last peers into a canister at the net's dripping bottom. Bioluminescent krill, collected from a depth of 100 m, coat the can with a blue glow. He wraps the container tightly in a black trash bag to protect the animals from light and hurries a few decks down to a darkened walk-in refrigerator. There a graduate student sorts the krill while wearing a headlamp that glows red, a wavelength the crustaceans can't see.

To study their light sensitivity, researchers glue live krill to an apparatus that uses electrodes to measure how their nerves respond to flashes of light of different wavelengths. Last year, Cohen showed that krill react most strongly to the bluish wavelengths that penetrate deepest into the water column, reaching a depth of 25 m even during the polar night. The experiments, combined with a model of the underwater light field, strongly suggest the krill can "cue upon ambient light during the dark polar night," Cohen and his colleagues reported in *PLOS ONE* last year.

Other research has highlighted the unexpected role of the moon's glow. One study by Last and his colleagues—dubbed "the werewolf paper"—analyzed several decades of acoustic data on the movements of krill and other zooplankton at 28 sites in the Arctic Ocean. They found that in December 2015 and January a daily migration can occur on a 24.8-hour cycle—which synchronizes the organisms' movements with the rising and setting of the moon—rather than a 24-hour, sun-based cycle. The zooplankton also performed a "mass sinking" to a depth of about 50 m every 29.5 days in the winter, which coincides with the brightest full moon, the researchers reported in January in *Current Biology*.

On this cruise, Last and his colleagues explore whether krill "have an inherent rhythm" shaping their ability to sense the subtle light differences between night and day during the winter. Many animals have biological clocks that keep track of the time of day, helping regulate gene activity and other functions. To see whether the crustaceans have similar internal clocks, the researchers keep some in cold storage until a time corresponding to the crustaceans "night"—say, 12 hours after a noontime capture—then measure their sensitivity to light. They do the same for another set, but take the measurement during the krill's "day."

Late one night near the end of the cruise, Cohen and Last sit reviewing data from the experiment on a laptop. Their eyes widen. Indeed, the numbers suggest the krill be-

PHOTOS: (TOP) KAJETAN DEJA; (BOTTOM, LEFT AND RIGHT) GEIR JOHNSEN/NTNU/UNIS



Published by AAAS

## Rhythms in the dark

In the Arctic fall and spring, krill and other zooplankton dive when the sun is out to avoid predators, and rise to the surface at night. During the polar night, the zooplankton tend to stay deeper in the water column. They rise and fall with lunar cycles, sinking deep to avoid the light of the full moon.

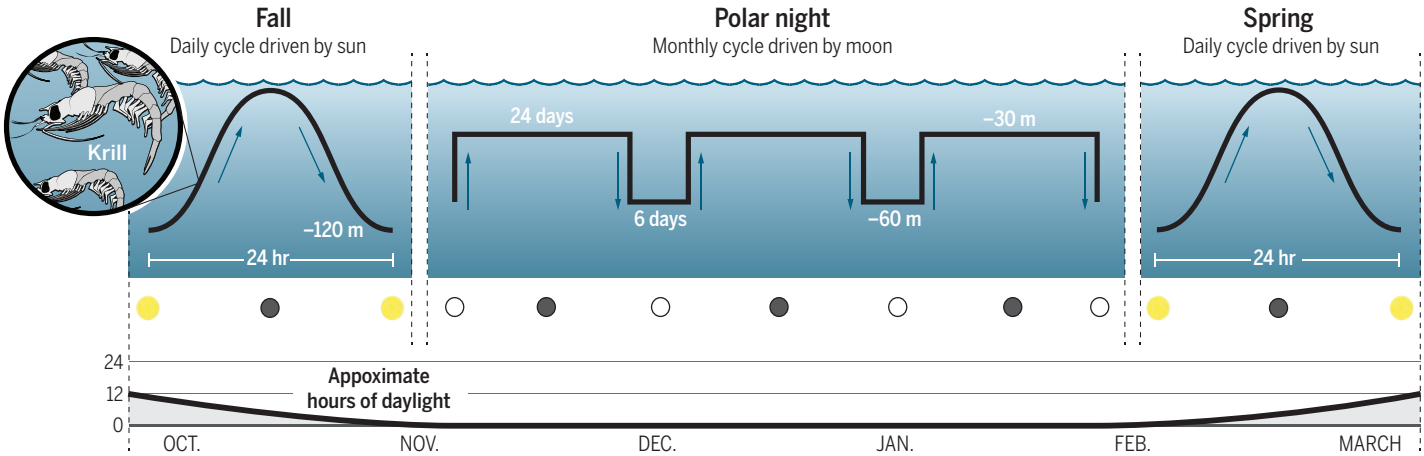



ILLUSTRATION: C. BICKEL/*SCIENCE*

come more sensitive to light during their night hours. "Yes!" shouts Cohen, as he and Last exchange a high-five. The finding may help explain how the creatures have evolved to most efficiently use what scant light exists here, a crucial aspect of survival.

**SCIENTISTS ARE** also examining how larger animals, such as cod and birds, can eat during the dark winter, when prey can be invisible. Deep in the ship, Marine Cusa, the fish biologist, spends a good chunk of the cruise cutting open the stomachs of cod collected by trawl nets and using a microscope to examine the contents. What she sees at first seems to confirm that the fish can use the meager light of polar night to hunt. Cod netted from a southern fjord that gets more winter light are stuffed with prey, but those caught farther north in Rijpfjorden, which gets less light, are nearly empty.

Later, she realizes that something is "really weird" about that pattern. On a winter cruise just 3 years ago, polar cod netted from Rijpfjorden had full bellies. What might explain the difference? Acting on a hunch, she climbs three flights up to the ship's instrument room—think laptops, body odor, and dirty coffee cups—and checks an online lunar calendar. "Please be full, moon, please be full," she pleads. Sure enough, the moon was full when researchers caught the 2013 batch of Rijpfjorden cod; on this year's cruise, it wasn't. "Dun-dun-dun," she announces later. "Maybe it's the moonlight that helps them hunt!"

Other creatures are also feeding in the darkness. Berge and his colleagues have found plenty of fecal pellets in the winter waters, apparently from krill and other zooplankton. "If there is shit in the water," he says, "someone is shitting, and if someone is shitting, someone is feeding."

That is true of the few species of Arctic birds that don't flee the polar night. In 2014 and 2015, the researchers observed six species actively foraging, including little auks. Many are known to rely on visual cues, but the darkness doesn't seem to bother them. When researchers caught several and examined their stomachs, they discovered plenty of prey; one guillemot had recently swallowed 214 krill. The birds also appeared to be specializing on specific organisms, not catching a random assortment. Such data "confirm active feeding by top predators," Berge wrote last year, but don't reveal how they're doing it.

**SUCH FINDINGS** are prompting new ways of thinking about the Arctic. One idea is that the existing notion of seasons, which focuses on temperature, should be expanded to include levels of light, especially in the water column. The middle of the dark polar night can be relatively warm compared with later months, for instance. In contrast, the spring bloom—which is triggered by increased light—often occurs when temperatures are still at a minimum.

Textbooks suggest that the bloom kicks off the growth and reproduction cycle of most Arctic organisms. But scientists have netted eggs and larvae that suggest the creatures are not only feasting in the darkness, but reproducing, too.

Such activity might mean that the Arctic has alternating ecological regimes, Berge says. In brighter months, it supports a food web that is driven from the bottom of the food web, by phytoplankton flourishing in the sun. But in winter it shifts to a "top-down" regime in which organisms thrive without primary production. "It could be a system that changes between two states," he says. The zooplankton's winter diet, however, is still a mystery. One scientist on the cruise was filtering seawater for microbes, which might be the missing source of energy.

Revising ecological dogma in the Arctic will require more data covering greater spans of ocean, over longer time periods. So polar researchers are designing instruments that could increase the data yield from each cruise. During this trip, for instance, scientists spent one afternoon testing a "jetyak"—an autonomous kayak that could be programmed to conduct biological surveys away from the light pollution of a ship. Although it performed what one researcher called some "crazy" turns, the team concluded it could be a useful platform.

**WHEN THE SHIP FINALLY DOCKS** at the Svalbard town of Longyearbyen, most of the scientists amble to a bar for a long-awaited drink. But Last and Cohen stay aboard, racing to complete preparations for a new experiment aimed at understanding the genes governing the krill's biological clock. At regular intervals, they freeze freshly caught krill in order to stop the ticking of the clocks at different points. Later, back in the lab, colleagues will run tests to see which genes are active at which times.

"If we hadn't learned what we did on this cruise we wouldn't have done this last experiment," a bleary-eyed Last says. He hopes it will reveal a little more about how the creatures survive their long night. If so, a journey into darkness will have shed a bit more light on the Arctic. ■

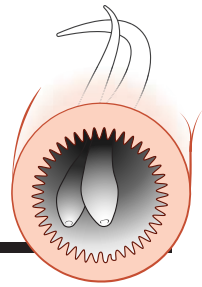


*Published by AAAS*

INSIGHTS

Oxides that conduct hydride anions *p. 1262*

Intestinal tuft cells provide protective immunity *p. 1264* ▸



PERSPECTIVES

SCIENCE DIPLOMACY

# *Reboot Gitmo for U.S.-Cuba research diplomacy*

## Transform Guantánamo into a peace park and ecological research center

*By* **Joe Roman**[1] *and* **James Kraska**[2]

Cuba has about 5000 km of coastline, including coral reefs, mangrove wetlands, seagrass beds, and tropical wet forests. Long stretches of coast remain undeveloped, with relatively high levels of fish biomass and marine biodiversity in marine parks that are unparalleled in the Caribbean (*1*, *2*). But on the eve of President Obama's visit to Cuba, we must consider whether normalization of relations between the United States and Cuba, with anticipated expansion of coastal development and return of industrial agriculture, might reverse Cuba's advances in ecological conservation. We propose an approach to protect Cuba's coastal ecosystems and enhance conservation and ecological research throughout the Caribbean. The United States should deliver on President Obama's recent plan to close the military prison at U.S. Naval Station Guantánamo Bay and repurpose the facilities into a state-of-the-art marine research institution and peace park, a conservation zone to help resolve conflicts between the two countries. This model, designed to attract both sides [similarly, see (*3*)], could unite Cuba and the United States in joint management, rather than serve as a wedge between them, while helping meet the challenges of climate change, mass extinction, and declining coral reefs.

POLICY

The U.S. presence at Guantánamo dates back more than a hundred years. The United States helped Cuba fight for independence from Spain in the 1890s and then occupied the island in 1898. As part of the Cuban-American Treaty, Cuba was granted independence in 1902, but the U.S. Platt Amendment required Cuba to rent Guan-



**Final approach?** Mangroves dot Guantánamo Bay with the U.S. naval base airstrip seen in the distance. Might the contentious base become a research and diplomatic centerpiece in U.S.-Cuba relations?

PHOTO: LUKE FRAZZA/AFP/GETTY IMAGES

Downloaded from on March 17, 2016

tánamo Bay to the United States as a coaling and naval station, a perpetual lease that could be broken only by mutual consent. Since the 1960s, the Cuban government has regarded the U.S. presence as illegal, refusing to cash the annual $4085 rent check. The Community of Latin American and Caribbean States recently called for returning the base to Cuba.

The Obama Administration has made it clear that diplomatic relations with Cuba and the transfer of detainees do not mean that it is willing to discuss the return of the 117 km$^2$ Guantánamo base to Cuba anytime soon (*4*, *5*). Although we believe that eventually giving the land back to Cuba would be a good outcome, we take the Administration at its word and propose a third path that would benefit Cuba, the United States, and beyond. The November 2015 agreement between the United States and Cuba on sister sanctuaries, including the Florida Keys National Marine Sanctuary and Guanahacabibes National Park on the west coast of Cuba, illustrates the current goodwill between the countries and could help foster dialogue to consider our proposal.

**"WOODS HOLE" OF THE CARIBBEAN.** Why would Cuba accept anything short of an immediate return of the base? A park that commemorates the history of the area and uses existing infrastructure for a research center would give global recognition to the country's conservation efforts. It would provide financial support, up-to-date facilities for ecological and environmental work, and an opportunity to build capacity and train Cuban scientists and students, especially those from the surrounding eastern provinces. A parcel of the land, perhaps on the developed southeastern side of the base, could become a "Woods Hole of the Caribbean," housing research and educational facilities dedicated to addressing climate change, ocean conservation, and biodiversity loss. With genetics laboratories, geographic information systems laboratories, videoconference rooms—even art, music, and design studios—scientists, scholars, and artists from Cuba, the United States, and around the world could gather and study. The new facilities could strive to be carbon neutral, with four 80-meter wind turbines having been installed on the base in 2005, and designed to minimize ecological damage to the surrounding marine and terrestrial ecosystems.



With a reduced U.S. footprint at Guantánamo, most of the land and sea could be returned to native wildlife. The area provides habitat for many endemic species, such as the vulnerable Cuban iguana (*Cyclura nubila*), and it may be a critical refuge for the West Indian manatee (*Trichechus manatus*) (*6*). It is an important nesting area for the endangered green turtle (*Chelonia mydas*) and critically endangered hawksbill turtle (*Eretmochelys imbricata*). The tropical dry forests on the base are relatively rare in Cuba, and the station hosts important Caribbean coastal habitats, such as sandy beaches, mangroves, coral reefs, and seagrass beds. The granadillo tree (*Brya ebenus*), spiny lobster (*Panulirus argus*), and several reef fishes have been overharvested and require better management. The two countries could work together to restore native species and fight noxious invasives, such as lionfish (*Pterois* spp.), African catfish (*Clarius gariepinus*), and marabou (*Dichrostachys cinerea*).

There are signs of progress in protecting Caribbean coastal ecosystems. Islands like Bermuda and Bonaire have moved forward on coral reef conservation, largely by protecting their reef fishes (*7*). After the 1992 Earth Summit in Rio de Janeiro, Cuba developed a strong tradition of environmental protection. More than an "accidental Eden" (*8*), Cuba has extensive protected areas, a constitution with strong environmental provisions, and an aggressive stance on climate change, putting it at the center of Caribbean conservation efforts. It has established the largest marine park in the Caribbean, the Jardines de la Reina (Gardens of the Queen), with abundant sharks and groupers (*9*).

**CONVERSION AND REDEMPTION.** The Guantánamo Naval Base serves the U.S. Fourth Fleet and is a hub for law enforcement and mass migration operations. Yet, as early as the 1970s, the base has been proposed as a bargaining chip to help normalize U.S. relations with Havana (*10*). By the end of the Cold War, the U.S. Department of Defense considered closing the base (*11*). As U.S. involvement in wars in Afghanistan and Iraq winds down and detainees are released or subject to criminal trial, perhaps the most compelling reason for the Pentagon to possess the base disappears. Although the station supports other missions, including regional counterdrug operations, maritime migration interdiction, search and rescue, and humanitarian assistance, Naval Air Station Key West, only 90 miles away, can meet most of these needs. Because Guantánamo is not in any U.S. congressional district, there would not be a fight over jobs at risk of being lost.

***"...the name Guantánamo could become associated with...efforts to preserve and repair...the planet."***

The move would extend a long tradition of U.S. naval support of marine scientific research and operational oceanography. More important, opening up Guantánamo would facilitate exchange, the two countries learning from each other. The peace park and research center would enhance capacity, technological transfer, and scientific facilities for Cuban researchers.

The world's first peace park is the Waterton-Glacier International Peace Park on the border of Canada and the United States, a symbol of goodwill between the countries (*12*). There have been successful transitions from military bases and conflict zones in other countries. After the United States left Fort Clayton to Panama, for example, part of the base was transformed into Ciudad de Saber (City of Knowledge), a government-sponsored complex that has attracted international scholars and the United Nations Development Program. Although the future of land along the corridor of the former Iron Curtain is uncertain, the European Green Belt initiative could transform the continent and help species such as lynx,

[1]Gund Institute for Ecological Economics, University of Vermont, Burlington, VT 05405, USA. [2]Stockton Center for the Study of International Law, U.S. Naval War College, Newport, RI 02841, USA. E-mail: jroman@uvm.edu



Published by AAAS

brown bears, and imperial eagles recover (*13*). Such international parks are signs that humans can respect each other, even after conflicts, and protect other species that share our planet. In transforming the base, we should not forget the past. Efforts such as the Guantánamo Public Memory Project (gitmomemory.org), which seeks to build awareness of U.S. history in the area, should be supported.

We hope that Pope Francis, who played an essential role in restoring relations between Cuba and the United States, will contribute to advancing a peaceful future for Guantánamo, in which both countries benefit. In the first papal encyclical on the environment, *Laudato Si'*, he called for an ecological conversion and the widespread protection of biodiversity, remarking on the decline of coral reefs, "Who turned the wonderworld of the seas into underwater cemeteries bereft of colour and life?" (*14*). Humans did, of course, through overfishing, deforestation, pollution, and burning fossil fuels (*15*). And humans can turn it around.

A first step in returning the land to Cuba, the Guantánamo peace park and research center would encourage nations to convert military bases and conflict zones into areas of creativity, cooperation, and biodiversity conservation. For the next generation, the name Guantánamo could become associated with redemption and efforts to preserve and repair international relations and the planet. ■

### REFERENCES AND NOTES


1. D. J. Whittle, O. Rey Santos, *Cuban Stud.* **37**, 73 (2006).
2. M. J. H. Newman, G. Paredes, E. Sala, J. B. C. Jackson, *Ecol. Lett.* **9**, 1216 (2006).
3. J. E. Schweig, *Cuba: What Everyone Needs to Know* (Oxford Univ. Press, New York, 2009).
4. M. Crowley, *Time*, 30 May 2013.
5. A. Holpuch, *The Guardian*, 4 February 2015.
6. G. Sedaghatkish, E. Roca, Eds., *U.S. Naval Station Guantánamo Bay Cuba: Rapid Ecological Assessment* (The Nature Conservancy, Arlington, VA, 1999).
7. J. Jackson, M. Donovan, K. Cramer, V. Lam, *Status and Trends of Caribbean Coral Reefs: 1970–2012* (Global Coral Reef Monitoring Network, IUCN, Gland, Switzerland, 2014).
8. D. Whittle, *MEDICC Rev.* **17**, 49 (2015).
9. F. Pina-Amargós, G. González-Sansón, F. Martín-Blanco, A. Valdivia, *Peer J.*, **2**, e274 (2014).
10. D. Binder, *The New York Times*, 30 August 1977.
11. M. Moore, *The Washington Post*, 25 April 1990.
12. S. H. Ali, Ed., *Peace Parks: Conservation and Conflict Resolution* (MIT Press, Cambridge, MA, 2007).
13. A. Terry, K. Ullrich, U. Riecken, *The Green Belt of Europe—From Vision to Reality* (IUCN, Gland, Switzerland, 2006).
14. Pope Francis, *Laudato Si', On Care for Our Common Home*, [encyclical] (2015); m.vatican.va.
15. J. M. Pandolfi *et al.*, *Science* **301**, 955 (2003).


### ACKNOWLEDGMENTS

We thank J. Brown, D. Greger, J. Jackson, L. Kaufman, and D. Whittle for comments and inspiration. Support was provided by the Mary Derrickson McCurdy Visiting Scholarship at Duke University Marine Laboratory, Ocean Doctor, the Rockefeller Foundation Bellagio Center, and the Sarah and Daniel Hrdy Visiting Fellowship in Conservation Biology at Harvard University.

10.1126/science.aad4247

PHYSICS

# Squeezing into superconductivity

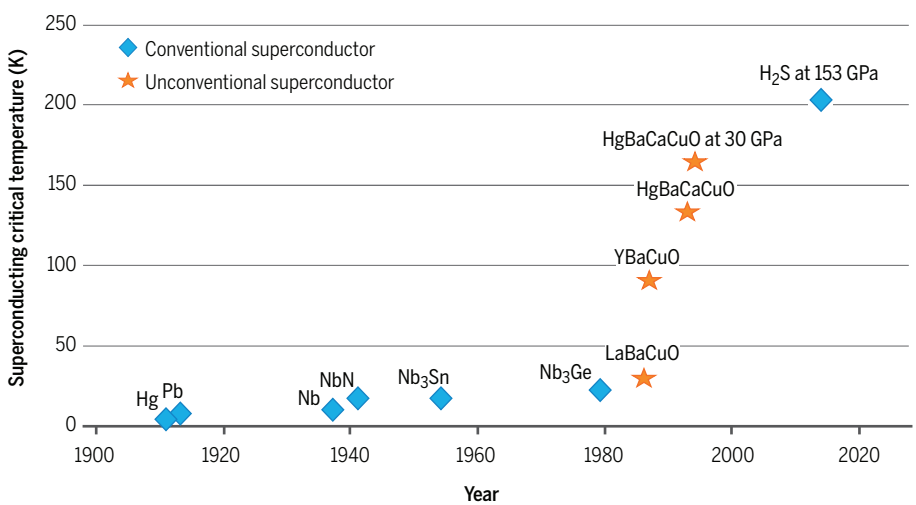
## Synchrotron light sources can be used to probe superconductivity at extreme pressures

*By* **Viktor Struzhkin**

The recent report of superconductivity in hydrogen sulfide ($H_2S$) by Drozdov *et al.* (*1*) at a record high superconducting critical temperature $T_c$ of 203 K and at high pressure (153 GPa) triggered excitement from both a fundamental and technological perspective. On page 1303 of this issue, Troyan *et al.* (*2*) confirm the finding by using an elegant and unexpected implementation of the Mössbauer technique at the third-generation synchrotron facility in Grenoble, France. They measured the Meissner effect (*3*)—the expulsion of magnetic field from the sample—thereby unequivocally confirming the existence of superconductivity. The new superconductor is believed to have a simple chemical formula, $H_3S$. The superconductivity in $H_3S$ was predicted theoretically by Duan *et al.* (*4*) before the first experimental findings were reported. The technique has great potential for future studies of tiny samples squeezed to extremely high pressure. This experimental advance paves the road to probing superconductivity in metallic hydrogen, which is expected to be a room-temperature superconductor above 500 GPa (*5*).

To understand the impact of the report by Troyan *et al.*, we should look deeper into the decades-long quest for a room-temperature superconductor. The most exciting development in superconductivity since its discovery by Kamerlingh Onnes in 1911 (see the figure) happened in 1987, when Bednorz and Müller found high-temperature superconductivity in materials based on copper-oxygen ($CuO_2$) layers, the layered structure being a necessary structural property of this new "unconventional" family of superconductors. The discovery of these so-called high-$T_c$ cuprate materials led to a stunning $T_c$ = 165 K at 30 GPa in a mercury-based cuprate material (*6*), which is higher than in a previous record-holding material ($Nb_3Ge$) by almost a factor of 7. The superconductivity mechanism in cuprates still defies theoretical understanding and remains the focus of intense research efforts by scientists around the world. This absence of theoretical understanding is a handicap preventing a guided search for new superconductors with even higher critical temperatures.

In contrast to the cuprate situation, there is a wealth of conventional superconducting




**Raising the critical temperature.** The highest-$T_c$ materials over the years since the discovery of superconductivity in mercury by Kamerlingh Onnes in 1911. The unconventional cuprate superconductors are marked by orange stars, the conventional ones by blue diamonds. Note that the highest $T_c$ values are observed in a compressed state at very high pressures. For useful applications, the effect of pressure must be understood theoretically, and this understanding should be used to design new materials with favorable parameters close to ambient conditions.

GRAPHIC: N. CARY/*SCIENCE*

Downloaded from on March 17, 2016



Published by AAAS



**Shining light on superconductors.** The European Synchrotron Radiation Facility in Grenoble, France.

PHOTO: © RGB VENTURES/SUPERSTOCK/ALAMY STOCK PHOTO

materials, where the accepted mechanism of superconductivity is driven by phonons (i.e., quanta of lattice vibrations) (*7*). Until recently, all of these conventional superconductors were not considered good candidates for high $T_c$, with the notable exception of hydrogen (*5*) and hydrogen doped with other elements, as in hydrides (*8*). Unfortunately, hydrogen requires very high pressures to get into a metallic state (*5*). To overcome this difficulty, doping of hydrogen with other elements was suggested as a means of lowering the pressure to a range more comfortable for experimentalists (*8*). This proposal was accepted by the high-pressure community, and several hydrides were tested in recent years [see (*9*) for a review]. The search resulted in the discovery of hydrogen sulfide with $T_c$ = 203 K (*1*). It is noteworthy that the finding of a new material was not accidental, but rather driven by a theory-guided search in a particular family of potential superconducting materials (hydrides). With recent progress in high-pressure research using double-stage diamond anvil devices that reach enormous static pressures above 750 GPa (*10*), the technique reported by Troyan *et al.* brings high-pressure researchers tantalizingly close to experimental proof of room-temperature superconductivity in metallic hydrogen.

The high-pressure advances described here are intellectually satisfying and form a solid basis for future research into novel material states that can be anticipated only by theoretical arguments. In terms of a wider societal impact, practical applications of these new materials require routes to sustaining such high critical temperatures at much lower pressures, possibly at ambient pressure. This task may be very difficult, perhaps impossible, and presents an even greater challenge than the search for superconductivity of metallic hydrogen. Such "materials by design," resulting from theoretical calculations, will drastically narrow the search for high-temperature superconductors based on hydrogen and other light elements in the top row of the periodic table.

Another message to be taken from the work of Troyan *et al.* is the complexity and power of modern synchrotron techniques in solving multiple problems in materials research. Present synchrotron-based Mössbauer techniques are operational down to scales of a few micrometers. Future upgrades of synchrotron facilities will allow much more tightly focused x-ray probes (submicrometer), allowing us to extend the pressure range to 1000 GPa. Such pressures exist in the interiors of giant planets and are expected to crush outer electronic shells of all the elements in the periodic table, drastically altering their chemistry in a very unintuitive way. The next generation of high-pressure science will rely on computational power and synchrotron techniques to investigate materials in such extreme environments. The x-rays generated by current and future synchrotron sources can be focused to a footprint just a few tens of nanometers across, allowing scientists to have a deep look into a realm of material properties down to the nanoscale. ■

*Carnegie Institution of Washington, 5251 Broad Branch Road, NW, Washington, DC 20015, USA. E-mail: vstruzhkin@ciw.edu*

## REFERENCES


1. A. P. Drozdov, M. I. Eremets, I. A. Troyan, V. Ksenofontov, S. I. Shylin, *Nature* **525**, 73 (2015).
2. I. Troyan *et al.*, *Science* **351**, 1303 (2016).
3. W. Meissner, R. Ochsenfeld, *Naturwissenschaften* **21**, 787 (1933).
4. D. Duan *et al.*, *Sci. Rep.* **4**, 6968 (2014).
5. J. M. McMahon, D. M. Ceperley, *Phys. Rev. B* **84**, 144515 (2011).
6. C. W. Chu *et al.*, *Nature* **365**, 323 (1993).
7. J. Bardeen, L. N. Cooper, J. R. Schrieffer, *Phys. Rev.* **108**, 1175 (1957).
8. N. W. Ashcroft, *Phys. Rev. Lett.* **92**, 187002 (2004).
9. V. V. Struzhkin, *Physica C* **514**, 77 (2015).
10. L. Dubrovinsky *et al.*, *Nature* **525**, 226 (2015).


10.1126/science.aaf2541



*Published by AAAS*

IONIC MATERIALS

# Large, soft, and polarizable hydride ions sneak around in an oxyhydride

## A perovskite containing highly electropositive cations conducts hydride anions

*By* **Shu Yamaguchi**

Ionic conductivity in solids, a field initiated by Faraday (*1*), has led to materials that help chemists spatially separate the oxidation and reduction steps of reactions, enabling technologies such as fuel cells. Many solid oxides are good oxygen ion ($O^{2-}$) conductors, but getting hydrogen ions, either protons ($H^+$) or hydride anions ($H^-$), to conduct through oxides has been a major challenge. A proton-conducting oxide reported in 1981 (*2*) marked the beginning of "oxide protonics," a materials science based on solid solutions of oxides and hydroxides. On page 1314 of this issue, Kobayashi *et al.* (*3*) report a material with pure $H^-$ conductivity (and yet an electronic insulator) in an oxyhydride system, which has been a "last frontier" in solid state ionics.

Except in the ionosphere, $H^-$ is exceedingly rare on Earth because of its extremely large $pK_a$ (acidity constant) for the deprotonation reaction of hydrogen. Efforts to discover $H^-$ conductors have primarily followed two strategies, one on oxide protonics—exploring oxyhydride materials (*4*)— and the other exploring metal hydride systems with strong ionic bonding characters, such as alkali-earth hydrides (*5*) and their analogs (*6*). Because metal hydrides have high electronic conductivity, it had been assumed that $H^-$ conductivity was negligible. Thus, the discovery of hydride ion conductivity in undoped $BaH_2$ was surprising, and was only revealed by the coincidence of the measured electromotive force (emf) for a hydrogen concentration cell with the theoretical one predicted by the Nernst equation for a pure $H^-$ conductor (*7*).

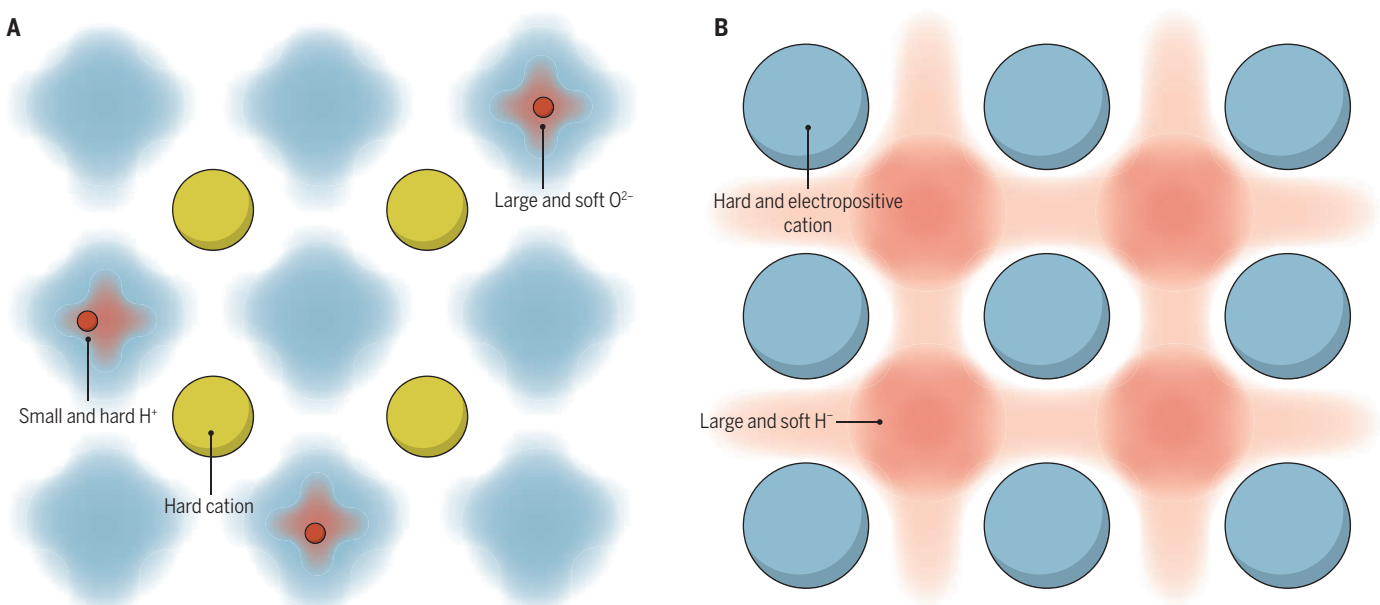
For oxyhydride systems, although $H^-$ was incorporated into perovskite oxides in a metastable condition that preserved the crystal framework (*8*, *9*), no clear evidence of $H^-$ conductivity could be obtained, except for a subtle trace, because of interference from the electron-predominant conductivity (*4*, *10*). The presence of $H^-$ in mayenite ($12CaO{\cdot}7Al_2O_3$ or C12A7) (*11*, *12*) shed light on the importance of chemical stability of C12A7 during heat treatment under an extremely reducing condition, in order to increase electron energy to stabilize $H^-$.

Several lines of experimental evidence support the report of Kobayashi *et al.* (*3*) of $H^-$ conductivity in $La_{2-x-y}Sr_{x+y}LiH_{1-x+y}O_{3-y}$. Detailed crystallographic analyses with neutron diffraction suggest an ordered arrangement of $H^-$ and oxide ion ($O^{2-}$) ions in the anion sublattice. The authors also performed electrochemical measurements of the conductivity and electrochemical polarization in the concentration cell with a protocol nearly identical to the so-called Tubandt method. The polarity, the magnitude of the cell emf, and consistent hydrogen transport all provide evidence for the transport of $H^-$ during direct-current (dc) polarization under blocking conditions for $O^{2-}$ transport.

What are the origins of $H^-$ conductivity in this material? First, all of the component cations—$La^{3+}$, $Sr^{2+}$, and $Li^+$—are extremely electropositive. They form very stable oxides and hydrides, and would produce donor states for electron ($e^-$) conductivity with great difficulty, even under extremely reducing conditions. Further, these oxides and halides form stable intermediate oxyhydride compounds with extended solid solubilities.

To obtain a pure $H^-$ conductor, electronic conductivity must be suppressed. Carrier mobility is typically more than 1000 times greater for electrons than for much larger

*Department of Materials Engineering, The University of Tokyo, Tokyo, Japan. E-mail: yamaguchi@material.t.u-tokyo.ac.jp*




**Stealthy hydride ions.** The two images contrast how (**A**) protons localize in an oxide, but (**B**) hydrides delocalize and conduct through an oxide with very electropositive cations.

ILLUSTRATION: P. HUEY/*SCIENCE*

Downloaded from on March 17, 2016



Published by AAAS

ions. The partial $H^-$ conductivity can be easily hindered even by a small amount of electrons formed by the reaction

$$H_H^x \rightarrow V_H^{\bullet} + e^- + \tfrac{1}{2}H_2$$

where $H_H^x$ and $V_H^{\bullet}$, expressed in Kröger-Vink notation, are the $H^-$ ion on a regular $H^-$ sublattice and its vacancy, respectively.

The origin of fast ion conduction in ionic solids is still unclear. Apparently, such materials should have defects that increase the chance of hopping—that is, the number of mobile ions and stable regular sites should not be equal. An easier way to introduce ionic defects is the introduction of anion vacancy by chemical doping of an acceptor, to avoid the electron formation discussed above. For example, electrons can be trapped by acceptors like $O^{2-}$, which suggests an important role for oxide ions. The faster $H^-$ migration is likely favored in the mobility competition between anions because $H^-$ has a lower charge density than $O^{2-}$ with a lower nominal valence and a similar ionic radius (1.46 Å for $H^-$ and 1.4 Å for $O^{2-}$). This explanation, however, needs further verification. The low charge density of $H^-$ may lead to a large polarizability, which provides an inspiration for the "sneaking" $H^-$ migration (see the figure). This feature contrasts with the extremely high charge density of protons.

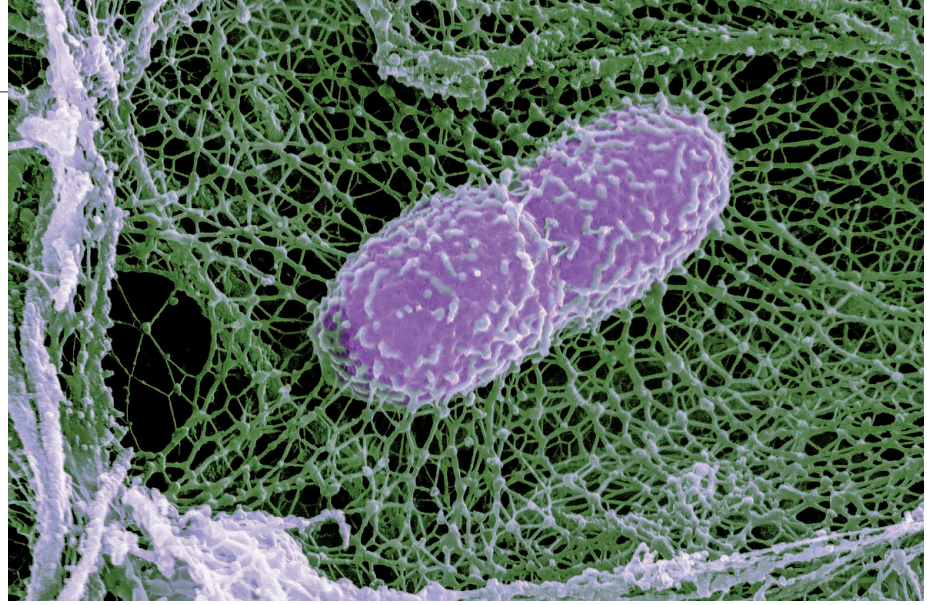
The result of Kobayashi *et al.* is just the beginning of a new materials science of $H^-$ conductivity in oxyhydride systems that will require further elaboration of the underlying mechanisms, as well as potential applications of the extremely reducing $H^-$ ion in chemical synthesis. A drawback of the current material is its chemical reactivity in oxidizing atmospheres, but this disadvantage may be overcome by various techniques, like surface protection coatings. These explorations of $H^-$ conductors now leave the question of what will be the next last frontier for solid state ionics. ■

## REFERENCES


1. K. Funke, *Sci. Technol. Adv. Mater.* **14**, 043502 (2013).
2. H. Iwahara, T. Esaka, H. Uchida, N. Maeda, *Solid State Ionics* **3–4**, 359 (1981).
3. G. Kobayashi *et al.*, *Science* **351**, 1314 (2016).
4. T. Norby, M. Widerøe, R. Glockner, Y. Larring, *Dalton Trans.* **2004**, 3012 (2004).
5. A. F. Andresen, A. J. Maeland, D. Slotfeldt-Ellingsen, *J. Solid State Chem.* **20**, 93 (1977).
6. F. Altorfer *et al.*, *Solid State Ionics* **70–71**, 272 (1994).
7. M. C. Verbraeken, C. Cheung, E. Suard, J. T. S. Irvine, *Nat. Mater.* **14**, 95 (2015).
8. M. A. Hayward *et al.*, *Science* **295**, 1882 (2002).
9. Y. Kobayashi *et al.*, *Nat. Mater.* **11**, 507 (2012).
10. M. Widerøe, R. Waser, T. Norby, *Solid State Ionics* **177**, 1469 (2006).
11. K. Hayashi, S. Matsuishi, T. Kamiya, M. Hirano, H. Hosono, *Nature* **419**, 462 (2002).
12. K. Hayashi, P. V. Sushko, A. L. Shluger, M. Hirano, H. Hosono, *J. Phys. Chem. B.* **109**, 23836 (2005).


10.1126/science.aaf3361

PHOTO: SPL/SCIENCE SOURCE



**Web of defense.** In this false-color scanning electron micrograph, a *Klebsiella pneumoniae* bacterium is caught in a web of extruded chromatin in a mouse lung. The web contains antimicrobial components that kill the bacterium. *K. pneumoniae* and other Enterobacteriaceae are increasingly becoming resistant to antibiotics, including last-resort compounds such as colistin.

ANTIMICROBIAL RESISTANCE

# *New mechanisms, new worries*

## The increasing spread of colistin resistance is resulting in untreatable infections

*By* **Marc Sprenger** *and* **Keiji Fukuda**

Growing levels of resistance to available antimicrobial medicines are causing tens of thousands of deaths each year across the world (*1*). By 2050, the overall costs associated with antimicrobial resistance (AMR) could reduce global gross domestic product (GDP) by 2 to 3.5% (*2*). One concern is the development of resistance to the carbapenem antibiotics among Gram-negative bacteria, in particular, the carbapenemase-producing Enterobacteriaceae (CPE) (see the image). Enterobacteriaceae are the source of community- and hospital-acquired infections and commonly cause opportunistic infections, including pneumonia, and sometimes death (*3*). CPE are resistant to nearly all available antibiotics, with the exception of colistin. Emerging resistance to colistin therefore has troubling implications for patient care.

Carbapenemase enzymes confer resistance to most β-lactam antibiotics, including carbapenem, making them particularly dangerous because they can inactivate a wide range of different antibiotics (*4*). Accurate detection of carbapenemase producers is therefore essential for infection control and management of antibiotic therapy (*5*). Carbapenemases are divided into three main classes, which differ in their mechanism of action. Class A includes the most common carbapenemase, *Klebsiella pneumoniae* carbapenemase. Class B carbapenemases are metallo-lactamases. An important member of this class is New Delhi metallo-beta-lactamase (NDM), which has spread widely since it was first described in 2009. Class D includes carbapenem-hydrolyzing oxacillinase-48 (OXA-48) (*6*), which is being reported with increasing frequency in outbreaks and case reports across the world (*7*). OXA-48 is particularly difficult to detect (*8*).

> **"E. coli *and* K. pneumoniae *are already increasingly resistant to all other available antibiotics; the transfer of colistin resistance to such bacteria can thus result in untreatable infections.*"**

Over the past 2 years, Enterobacteriaceae that produce OXA-48 and NDM have rapidly

*Antimicrobial Resistance Secretariat, World Health Organization, 1211 Geneva 27, Switzerland. E-mail: sprengerm@who.int; fukudak@who.int*

Downloaded from on March 17, 2016



Published by AAAS

spread through Europe (*9*). In 2015, 13 of 38 countries in Europe reported endemicity or interregional spread of CPE, compared with 6 countries in 2013. Concerns have also been raised over extensively resistant *Pseudomonas aeruginosa* in Belarus, Kazakhstan, and Russia (*10*). Almost all of these isolates were resistant to all antibiotics except colistin; a few were resistant even to colistin.

The resistance to colistin is particularly troubling. This polymyxin antibiotic was first used more than 50 years ago to treat Gram-negative infections, but its use declined on account of its severe effects on kidney function. Broad-spectrum beta-lactams (such as third-generation cephalosporins and carbapenems) were less toxic and easier to administer. However, as the incidence of multidrug-resistant infections has increased, so has—out of necessity—the use of colistin.

Colistin resistance arises through at least two known mechanisms, as illustrated by a recent report by Giani *et al*. on a large hospital outbreak of CPE *Klebsiella pneumoniae* infections in Italy (*11*). Resistance to colistin resulted in 93 bloodstream infections that were very difficult to treat. The outbreak was triggered by increased colistin consumption, underscoring the role of selective pressure generated by antibiotic use. However, the further development and spread of colistin-resistant mutants were mainly attributable to chromosomal mutations. This mechanism of colistin resistance facilitated the spread of resistant organisms within and between hospitals, but did not lead to the transfer of resistance between strains. Reinforcement of infection prevention and control measures was sufficient to limit the spread of these infections.

However, Liu *et al*. have recently documented a new mechanism of resistance to polymyxin antibiotics (colistin and polymyxin B) (*12*). They have discovered a plasma-mediated polymyxin resistance gene, *mcr-1*, in *Escherichia coli* isolated from animals housed in an intensive pig-farming operation in Shanghai. Further testing showed a high prevalence of the gene in *E. coli* isolates from raw pig and poultry meat at slaughterhouses and supermarkets in four provinces in China. The gene was also found in samples collected from hospital patients infected with *E. coli* and *K. pneumoniae* in two hospitals in two provinces. Researchers in Denmark and France have confirmed the presence of the *mcr-1* gene in stored samples of bacteria obtained from patients and poultry meat (*13*, *14*). These observations show that *mcr-1* is not confined to China.

These findings are deeply worrisome. Resistance to polymyxin antibiotics resulting from chromosomal mutations generally cannot spread to other bacteria. However, as Liu *et al*.'s study confirms, colistin resistance is transmissible between different bacteria because it involves a different mechanism, plasmid-mediated transfer. *E. coli* and *K. pneumoniae* are already increasingly resistant to all other available antibiotics; the transfer of colistin resistance to such bacteria can thus result in untreatable infections.

The study by Liu *et al*. leaves many questions unanswered, including the exact relationship between colistin use and the resistant bacteria found in animals, meat, and humans. This gap highlights the need for much better monitoring and reporting on the nature and extent of antibiotic use in animals and for further investigations. Nevertheless, there is a compelling public health need to take action now to slow the development of AMR.

In May of 2015, the World Health Assembly adopted a Global Action Plan against antimicrobial resistance (*15*). The plan reflects a global consensus on approaches to the problem but also a strong recognition that efforts to reduce AMR must extend beyond health. AMR cannot be addressed without the involvement of other sectors such as agriculture, development, economics, foreign affairs, and industry. The engagement of a broad range of sectors will require much greater awareness of the dangers posed by AMR, as well as political support.

Stewardship of existing antimicrobials within health and agriculture will be crucial for preserving the effectiveness of current antibiotics. At the same time, the ongoing evolution of new patterns of resistance will inevitably require the development of, and access to, new antimicrobial agents. Addressing AMR globally and across multiple sectors is a daunting challenge, but the consequences of not doing so will be far worse. ■

## REFERENCES AND NOTES


1. P. Phumart *et al*., *J. Health Syst. Res.* **6**, 352 (2012).
2. Review on Antimicrobial Resistance, *Antimicrobial Resistance: Tackling a Crisis for the Health and Wealth of Nations*, J. O'Neill, chair (UK, December 2014).
3. A. Borer *et al*., *Infect. Control Hosp. Epidemiol.* **30**, 972 (2009).
4. A. M. Queenan, K. Bush, *Clin. Microbiol. Rev.* **20**, 440 (2007).
5. V. Miriagou *et al*., *Clin. Microbiol. Infect.* **16**, 112 (2010).
6. L. Poirel, J. D. Pitout, P. Nordmann, *Future Microbiol.* **2**, 501 (2007).
7. N. T. Antunes *et al*., *Antimicrob. Agents Chemother.* **58**, 2119 (2014).
8. Y. D. Bakthavatchalam, S. Anandan, B. Veeraraghavan, *J. Global Infect. Dis.* **8**, 41 (2016).
9. B. Albiger, C. Glasner, M. Struelens, H. Grundmann, D. Monnet, *Euro Surveill.* **20**, 30062 (2015).
10. M. V. Edelstein *et al*., *Lancet Infect Dis.* **13**, 867 (2013).
11. T. Giani *et al*., *J Clin Microbiol.* **53**, 3341 (2015).
12. Y-Y. Liu, *Lancet Infect. Dis.* **16**, 161 (2016).
13. H. Hasman *et al*., *Euro Surveill.* **20**, 30085 (2015).
14. A. Perrin-Guyomard *et al*., *Euro Surveill.* **21**, 30135 (2016).
15. See www.who.int/drugresistance/global_action_plan/en/.


## ACKNOWLEDGEMENTS

We thank A. Andremont for his comments on this article.

10.1126/science.aad9450

IMMUNOLOGY

# The enigmatic tuft cell in immunity

## An intestinal cell stimulates the immune response to parasitic infections

*By* **Nicola Harris**

Helminth and protozoan parasites are the most common infectious agents of humans living in developing countries and represent an important disease burden, particularly through their ability to cause physical and intellectual growth retardation in young children (*1, 2*). Type 2 immune responses promote efficient expulsion of intestinal parasites such as helminths by driving a "weep and sweep" response that involves mucous production, fluid secretion, and increased intestinal motility. These same responses in susceptible individuals cause the symptoms of allergy after exposure to pollens and certain food antigens. The generation of type 2 immunity in response to helminth parasites requires the secretion of cytokines by intestinal epithelial cells, but the source and induction of cytokine secretion have been unclear. Three studies (*3*–*5*), including a report by Howitt *et al*. (*5*) on page 1329 of this issue, reveal a key role for a rare intestinal cell—the tuft or brush cell—in driving type 2 immunity.

***"Finding that tuft cells contribute to type 2 immunity...would likely prompt a close examination... in allergic diseases..."***

The intestinal epithelium is a specialized cell layer separating the intestinal contents from the underlying tissues. These epithelial cells function not only to absorb water and nutrients but also form an important barrier between the human host and the microbial,

*École polytechnique fédéreale de Lausanne, 1015 Lausanne, Switzerland. E-mail: nicola.harris@epfl.ch*

Downloaded from on March 17, 2016



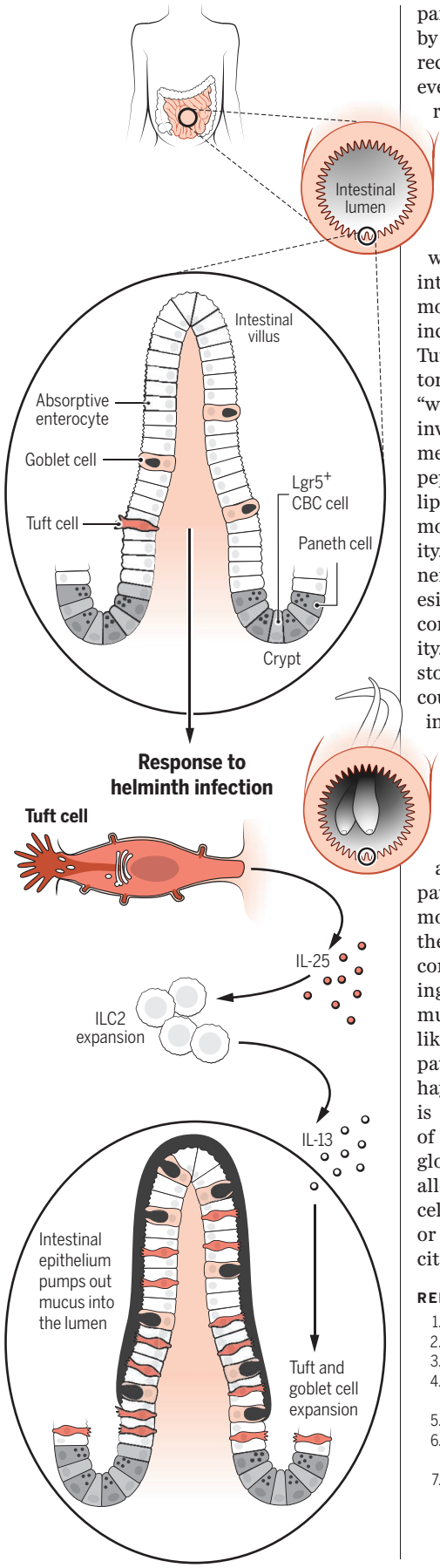
Published by AAAS

**Weep and sweep.** After infection with helminth or protozoal parasites, tuft cell–derived IL-25 leads to the activation of innate lymphoid cells (ILC2s) and initiates a feedforward loop in which ILC2s produce IL-13, which then acts on epithelial crypt base columnar (CBC) cells to promote further differentiation of tuft and goblet cells. Tuft cell responses following parasite infection require TRPM5-dependent chemosensation and are required for the goblet cell hyperplasia that contributes to parasite expulsion.

and potentially parasite-rich soup, of the intestinal lumen. The intestinal epithelium is made up of five main cell types: absorptive enterocytes and four secretory cells types including Paneth cells, goblet cells, enteroendocrine cells, and tuft cells. The first three secretory cell types release peptides that provide defense against bacteria, secrete mucus, or produce gastrointestinal hormones and peptides that regulate intestinal function and communication with other organs. By contrast, the function of tuft cells (which have a "tuft" of microvilli extending into the intestinal lumen) has remained largely elusive. The three new studies now report an important role for these cells in promoting immunity against parasitic helminths (*3*–*5*) or protozoa (*5*).

Each study identified tuft cells in the mouse small intestine as the sole intestinal source of an epithelial interleukin (IL), IL-25, which promotes the rapid expansion of an important immune cell called the type 2 innate lymphoid cell (ILC2). ILC2s in turn provide a crucial early source of the interleukin IL-13, which is key to the intestinal "weep and sweep" response that expels the parasite. Tuft cells take part in a feed-forward loop whereby tuft cell–derived IL-25 leads to the expansion of IL-13–secreting ILC2s. This, in turn, results in the formation of new tuft cells (see the figure). Disruption of tuft cell formation or function resulted in impaired type 2 immunity and delayed helminth expulsion. Of note, addition of IL-25 to mice lacking tuft cells could rescue ILC2 expansion and helminth expulsion, placing tuft cells at the beginning of the immune cascade.

Why and how parasites drive tuft cell expansion awaits further study. However, the findings of Howitt *et al*. raise an intriguing possibility. Tuft cells possess the machinery for chemosensory taste receptors that are responsible for the perception of sweet, bitter, and umami compounds in food. The authors used genetically modified mice lacking a key component of this pathway, the transient receptor potential cation channel subfamily M member 5 (TRPM5), and showed a crucial role for chemosensation in promoting tuft cell expansion in response to parasite infection. Should parasites secrete chemicals that are sensed by tuft cells, this would place chemosensory receptors as the most recent members of an ever-growing list of pathogen recognition receptor families.




The study of Howitt *et al*. emphasizes the concept that tuft cells are involved in the initiation of type 2 immunity. Whether tuft cell chemosensation promotes heightened IL-25 production, or whether early progenitor cells within the intestinal epithelium already possess chemosensory pathways and proliferate to increase IL-25 secretion, remains unclear. Tuft cells also possess an arsenal of mediators that could potentially contribute to the "weep and sweep" response that expels the invading parasite from the intestine. Such mediators include opioids (small bioactive peptides) and leukotrienes (inflammatory lipid mediators) (*6*, *7*), both of which promote fluid secretion and intestinal motility. Tuft cells also form close contacts with nerve cells (*7*), strengthening the hypothesis that they might regulate the muscle contractions that promote intestinal motility. Of note, tuft cells are also found in the stomach, and it seems plausible that they could also contribute to the expulsion of ingested toxins.

One question raised by the study of Howitt *et al*. is how parasites encountered within other bodily organs are sensed. A contribution by tuft cells may represent a common denominator as rare cells possessing chemosensory pathways and exhibiting a tuft cell–like morphology have also been described in the trachea, lower respiratory tract, and common bile duct of mammals (*6*). Finding that tuft cells contribute to type 2 immunity within other bodily organs would likely prompt a close examination of this pathway in allergic diseases, including hay fever and asthma. Even more likely is a role for tuft cells in the development of food allergy. Given the combined heavy global health burden of parasitic and allergic diseases, the unveiling of a new cell type involved in protective immunity or disease pathogenesis represents an exciting step forward. ■

ILLUSTRATION: K. SUTLIFF/*SCIENCE*

## REFERENCES


1. J. Bethony *et al.*, *Lancet* **367**, 1521 (2006).
2. P. J. Hotez *et al.*, *PLOS Negl. Trop. Dis.* **8**, e2865 (2014).
3. F. Gerbe *et al.*, *Nature* **529**, 226 (2016).
4. J. von Moltke, M. Ji, H. E. Liang, R. M. Locksley, *Nature* **529**, 221 (2016).
5. M. R. Howitt *et al.*, *Science* **351**, 1329 (2016).
6. F. Gerbe, C. Legraverend, P. Jay, *Cell. Mol. Life Sci.* **69**, 2907 (2012).
7. C. Bezencon *et al.*, *J. Comp. Neurol.* **509**, 514 (2008).


10.1126/science.aaf5215



*Published by AAAS*

BIOCHEMISTRY

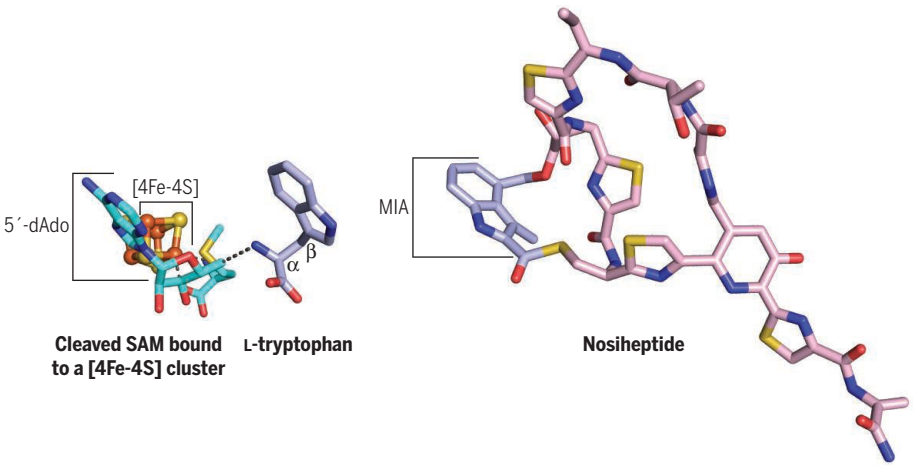
# A radically unexpected mechanism

## Biosynthesis of the antibiotic nosiheptide proceeds via unforeseen radical intermediates

*By* **Jennifer Bridwell-Rabb**[1,2,3] *and* **Catherine L. Drennan**[1,2,3]

The *S*-adenosylmethionine (SAM) radical enzyme superfamily plays a central role in the biosynthesis of many vitamins, cofactors, and antibiotics. Radical SAM enzymes catalyze challenging chemical reactions such as C-H bond activation (*1*), ring contraction (*2*), and molecular skeletal rearrangements (*3*, *4*). They overcome the difficulty of these reactions by forming a highly oxidizing radical species, 5′-deoxyadenosyl (5′-dAdo•), from SAM and a reduced iron-sulfur cluster (*5*). This radical species can selectively abstract a hydrogen atom from a substrate, enabling complex chemical transformations. There are more than 113,000 radical SAM enzymes, but only a small number are both biochemically and structurally characterized, and many of the reaction mechanisms remain enigmatic. On page 1320 of this issue, Sicoli *et al*. provide evidence for unexpected radical intermediates in the mechanism of the radical SAM enzyme NosL (*6*).

NosL catalyzes the rearrangement of the amino acid L-tryptophan into methylindolic acid (MIA). In doing so, it repurposes this amino acid to serve as a component of the bacterial warfare agent nosiheptide (*7*) (see the first figure), a ribosomally generated thiopeptide with potent activity against Gram-positive bacterial pathogens (*8*).



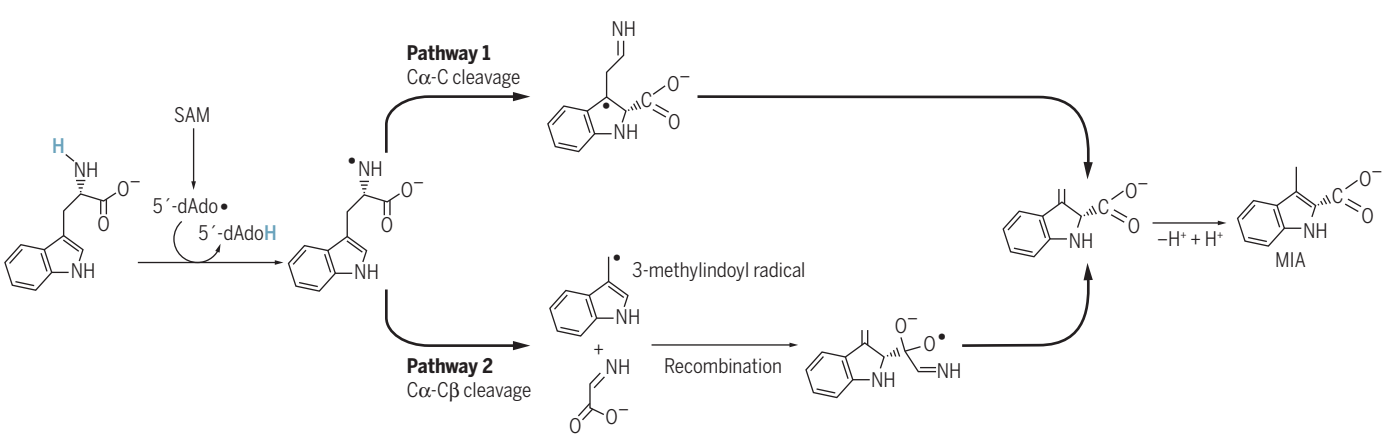

**From amino acid to bacterial warfare agent.** The radical SAM enzyme NosL catalyzes the transformation of L-tryptophan into MIA, a component of the antibiotic nosiheptide. NosL uses a [4Fe-4S] cluster and SAM to generate a 5′-dAdo• species. 5′-dAdo• abstracts a hydrogen atom from the amino moiety of L-tryptophan to initiate catalysis.

NosL is not the only radical SAM enzyme that uses an amino acid to make a new molecule. The ThiH, HydG, and CofH enzymes catalyze cleavage of the Cα-Cβ bond of L-tyrosine in the biosynthesis of thiamine (*9*), the H-cluster of hydrogenase (*10*), and the $F_{420}$ cofactor (*11*), respectively.

For ThiH and HydG, catalysis is thought to be initiated by abstraction of a hydrogen atom from the side-chain hydroxyl group of L-tyrosine (*9*, *10*). Zhang *et al*. have proposed that NosL similarly abstracts the hydrogen atom from the NH of the indole ring of L-tryptophan (*7*). However, Nicolet *et al*. have reported an L-tryptophan–bound NosL crystal structure in which the amino NH (rather than the indole NH) is positioned for hydrogen atom abstraction (*12*) (see the first figure).

Subsequent biochemical studies have supported the amino NH as the site of radical generation (*12*), prompting mechanistic proposals for NosL that involved radical-induced bond scission at either Cα-Cβ or Cα-C positions (see the second figure) (*13*). Literature precedence favored Cα-Cβ bond

[1]Department of Chemistry, Massachusetts Institute of Technology, Cambridge, MA 02139, USA. [2]Department of Biology, Massachusetts Institute of Technology, Cambridge, MA 02139, USA. [3]Howard Hughes Medical Institute, Massachusetts Institute of Technology, Cambridge, MA 02139, USA. E-mail: jb_rabb@mit.edu; cdrennan@mit.edu




**Unexpected mechanism.** Literature precedence favored a Cα-Cβ cleavage pathway for the biosynthesis of MIA from L-tryptophan, but the work of Sicoli *et al.* instead provides support for the unprecedented Cα-C cleavage pathway.

ILLUSTRATIONS: P. HUEY/*SCIENCE*

Downloaded from on March 17, 2016



Published by AAAS

scission to form a 3-methylindoyl radical species (*9*, *10*). However, formation of MIA from a 3-methylindoyl radical species would require a challenging recombination reaction and a second bond scission (*7*). Detection of shunt reaction products such as 3-methylindole could be indicative of this mechanism (*7*), but there was no evidence for the proposed 3-methylindoyl radical species or for other intermediates that would be consistent with the Cα-Cβ bond scission mechanism.

Sicoli *et al.* attempted to trap the proposed 3-methylindoyl radical species to provide support for the Cα-Cβ bond scission mechanism. Surprisingly, however, their investigations instead provide support for the Cα-C bond scission mechanism (see the second figure). This latter mechanism requires the specific and controlled migration of a carboxyl-fragment radical from Cα to C2, a rearrangement that has not previously been described. Observing radical reaction intermediates with spectroscopy is challenging, because they are short-lived. Nevertheless, by using numerous substrate analogs to prolong the lifetimes of the NosL reaction intermediates and computational methods to evaluate the nature of the intermediates, Sicoli *et al.* succeeded in providing support for a radically different mechanism.

The NosL reaction mechanism detailed by Sicoli *et al.* expands the list of complex chemical transformations accomplished by radical SAM enzymes. This work challenges the perception that the subset of radical SAM enzymes that cannibalize L-tryptophan and L-tyrosine all proceed via similar chemical mechanisms. As the saying goes, there is more than one way to skin a cat—and more than one way for radical SAM enzymes to perform their catalytic feats. ■


**REFERENCES**

1. P. Douglas, M. Kriek, P. Bryant, P. L. Roach, *Angew. Chem. Int. Ed. Engl.* **45**, 5197 (2006).
2. R. M. McCarty, A. Somogyi, G. Lin, N. E. Jacobsen, V. Bandarian, *Biochemistry* **48**, 3847 (2009).
3. N. C. Martinez-Gomez, D. M. Downs, *Biochemistry* **47**, 9054 (2008).
4. A. Chatterjee *et al.*, *Nat. Chem. Biol.* **4**, 758 (2008).
5. O. T. Magnusson, G. H. Reed, P. A. Frey, *Biochemistry* **40**, 7773 (2001).
6. G. Sicoli *et al.*, *Science* **351**, 1320 (2016).
7. Q. Zhang *et al.*, *Nat. Chem. Biol.* **7**, 154 (2011).
8. X. Just-Baringo, F. Albericio, M. Alvarez, *Mar. Drugs* **12**, 317 (2014).
9. M. Kriek, F. Martins, M. R. Challand, A. Croft, P. L. Roach, *Angew. Chem. Int. Ed. Engl.* **46**, 9223 (2007).
10. J. M. Kuchenreuther *et al.*, *Science* **342**, 472 (2013).
11. L. Decamps *et al.*, *J. Am. Chem. Soc.* **134**, 18173 (2012).
12. Y. Nicolet, L. Zeppieri, P. Amara, J. C. Fontecilla-Camps, *Angew. Chem. Int. Ed. Engl.* **53**, 11840 (2014).
13. D. M. Bhandari, H. Xu, Y. Nicolet, J. C. Fontecilla-Camps, T. P. Begley, *Biochemistry* **54**, 4767 (2015).


10.1126/science.aaf4942



PHOTO: © DESIGN PICS INC./ALAMY STOCK PHOTO

**Liquid complexity.** Water molecules in liquid water are held together by an everchanging network of hydrogen bonds.

CHEMISTRY

# *Quantum dynamics in the smallest water droplet*

## Two hydrogen bonds in a six-molecule water cluster break simultaneously in a concerted set of movements

*By* **David C. Clary**

Water plays a central role in scientific disciplines ranging from geology to astronomy to biology. Yet it is an extraordinarily difficult liquid to understand because of its complex, ever-changing patterns of hydrogen bonds. Studies of small water clusters have provided important insights into the concerted hydrogen-bond motions that can occur in water. These studies are also crucial for developing an accurate potential function for simulating the properties of liquid water and ice (*1*). On page 1310 of this issue, Richardson *et al.* (*2*) provide evidence for a concerted type of motion in which two hydrogen bonds in a water cluster are broken simultaneously (see the figure). The results have implications for many areas of scientific study, including the chemistry of polar solvents, the conformations of proteins, and the dissolution of ions in minerals.

Richardson *et al.* study the water hexamer $(H_2O)_6$, which is the smallest cluster with a three-dimensional geometry and has been dubbed the smallest water droplet (*3*). Advanced spectroscopic methods have yielded experimental information on its structure and properties (*4*). Accurate potential energy surfaces for the interaction of water molecules have been derived (*1*), and quantum dynamical methods have been developed for simulating the motion of the water molecules and calculating the spectral observables (*5*). Richardson *et al.* now show, based on experimental and theoretical evidence, that two hydrogen bonds rearrange simultaneously in a particular form of $(H_2O)_6$ that has the shape of a prism.

Until recently, the most precise experimental information on the structures of small water clusters came from far-infrared studies of their intermolecular vibrational modes (*4*). A broadband Fourier

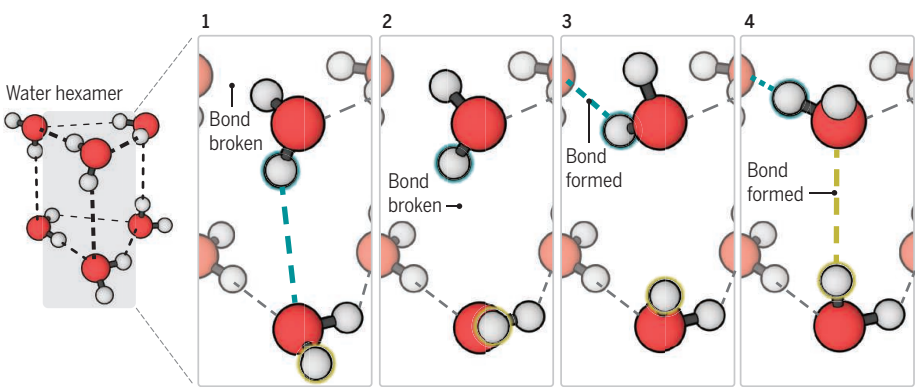
Downloaded from on March 17, 2016



Published by AAAS

Transform technique has now made it possible to study the rotational motion of these clusters directly in the microwave region (*6*). Richardson *et al.* report new results obtained using this method.

A water cluster such as $(H_2O)_6$ can have several different forms, which take the shapes of books, cages, and prisms (*3*). Each shape can be constructed with many different, energetically equivalent orientations of the hydrogen atoms in the water molecules. Each of these arrangements corresponds to a minimum on the potential surface. There is an energy barrier between equivalent minima, and rearrangements can thus occur via quantum tunneling. This feature leads to splittings of lines in the observed microwave spectrum, an effect that has been known for more than 60 years in fluxional molecules such as $NH_3$ (*7*). However, preparing weakly bound clusters for microwave observation and interpretation is much more complicated. The experiments are done with both the oxygen isotopes $^{16}O$ and $^{18}O$ in $(H_2O)_6$. This allows the lines observed in the microwave spectrum to be assigned to particular hydrogen-bond motions (*6*).




**Concerted motion.** Richardson *et al.* simulate concerted hydrogen bond breaking in the water hexamer prism.

These experimental spectra can only be understood with the help of quantum dynamical theory. This remains a real challenge for a system such as $(H_2O)_6$, which has 54 degrees of freedom. However, clever adaptation of Feynman's path integral theory (*8*) has provided a quantum dynamical method, ring polymer molecular dynamics (RPMD) (*9*), which is readily capable of calculating these tunneling spectra from the best available potential energy surfaces (*5*). This theory exploits the result that a classical treatment of a ring of an infinite number of copies of the system connected by harmonic springs maps on to the quantum mechanical system. However, in practice, a relatively small number of copies are needed to converge results for water clusters. The system can then be simulated using classical molecular dynamics, which is computationally inexpensive and readily applicable to many dimensions. Initially, the RPMD method was mainly used to study chemical reaction rates (*9*), but it can be adapted to calculate the tunneling splittings in the spectra of molecular clusters (*5*).

Previous theoretical studies identified hydrogen-bond rearrangements in water clusters that were either flips (with no hydrogen-bond breaking) or bifurcations (where one bond breaks) (*3*). Richardson *et al.* show that the hydrogen-bond dynamics in the prism form of $(H_2O)_6$ can involve the simultaneous breaking of two hydrogen bonds (see the figure). Such concerted bond breaking may be an important mechanism in the many systems—such as biological cells and mineral interfaces—where water molecules are found in confined environments. In addition, the excellent detailed agreement between the quantum dynamical calculations and experimental data shows that theory is getting much closer to a highly accurate description of water and, thus, to providing a detailed quantitative understanding of hydrogen-bond dynamics. ■

## REFERENCES


1. V. Babin, G. R. Medders, F. Paesani, *J. Phys. Chem. Lett.* **3**, 3765 (2012).
2. J. O. Richardson *et al.*, *Science* **351**, 1310 (2016).
3. K. Liu *et al.*, *Nature* **381**, 501 (1996).
4. F. N. Keutsch, R. J. Saykally, *Proc. Natl. Acad. Sci. U.S.A.* **98**, 10533 (2001).
5. J. O. Richardson, S. C. Althorpe, D. J. Wales, *J. Chem. Phys.* **135**, 124109 (2011).
6. C Pérez *et al.*, *Science* **336**, 897 (2012).
7. C. Townes, A. Schawlow, *Microwave Spectroscopy* (McGraw-Hill, New York, 1955).
8. R. P. Feynman, A. R. Hibbs, D. F. Styer, *Quantum Mechanics and Path Integrals* (Dover, Mineola, NY, 2010).
9. I. R. Craig, D. E. Manolopoulos, *J. Chem. Phys.* **122**, 084106 (2005).


*Department of Physical and Theoretical Chemistry, University of Oxford, Oxford OX1 3QZ, UK. E-mail: david.clary@chem.ox.ac.uk*

10.1162/science.aaf3061

NEUROSCIENCE

# A satiating signal

## A glycosylation enzyme in specific brain neurons is a nutrient sensor that controls body weight

*By* **Gary J. Schwartz**

The worldwide human obesity epidemic has provoked a great deal of experimentation to understand the biological controls of energy expenditure and food intake, two processes that together determine energy balance. Because food intake relies on feeding behavior that is determined by the brain, studies have focused on how the central nervous system receives and behaviorally responds to signals of metabolic status. On page 1293 of this issue, Lagerlöf *et al.* (*1*) report that a glycosylation enzyme serves as a neuronal nutrient sensor that is critical in the control of food intake and body weight.

Feeding behavior responds to metabolic need. Thus, food deprivation stimulates feeding, whereas signals arising from the biological consequences of food ingestion impinge on the central nervous system and lead to meal termination. These signals include sensorineural events generated by the gustatory, olfactory, and gastrointestinal properties of foods, neuroendocrine signals stimulated by food ingestion, and signals generated by nutrients themselves (*2*).

Nutrient sensing is critical for cellular viability in general, but in the central nervous system, it may serve a larger role in the control of whole-body energy balance by modulating food intake (*3*). Lagerlöf *et al.* have identified a new role for O-linked *N*-acetylglucosamine (O-GlcNAc) transferase (OGT) as a nutrient sensor in brain neurons for controlling food intake and body weight. OGT catalyzes the post-translational modification of proteins by O-GlcNAc (a monosaccharide derivative of glucose) and is regulated by nutrient access. Acute, inducible decreases in the expression of OGT in the adult mouse brain, under the control of the neuronal marker α–calcium/calmodulin-dependent protein

*Departments of Medicine & Neuroscience, Albert Einstein College of Medicine, Bronx, NY 10461, USA. E-mail: gary.schwartz@einstein.yu.edu*

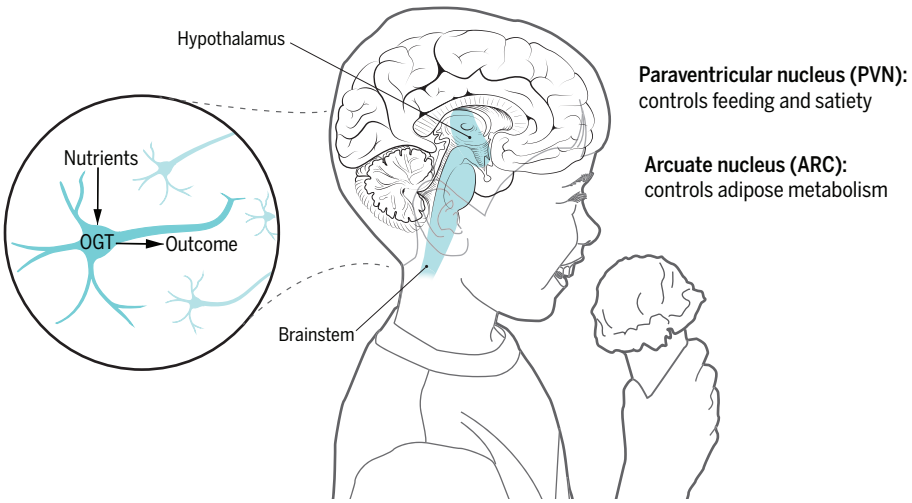
ILLUSTRATION: V. ALTOUNIAN/*SCIENCE*

Downloaded from on March 17, 2016



Published by AAAS

**OGT-expressing neurons as nutrient sensors in hypothalamus and brainstem**




**Heterogeneous function.** In the mouse, OGT in hypothalamic paraventricular nucleus (PVN) α-CAMKII neurons acts as a nutrient sensor by controlling overeating, whereas OGT in hypothalamic arcuate (ARC) agouti-related protein (AgRP) neurons controls the metabolic activity of adipose tissue. These OGT-expressing neuronal regions also exist in the human brain.

kinase type II (αCAMKII), rapidly produced pronounced overeating followed by massive weight gain and adiposity gain, with no gain in lean mass. Preventing this hyperphagia by pair-feeding animals to the levels of control subjects prevented the development of obesity, demonstrating that the hyperphagia produced by the absence of OGT expression is sufficient for the obese phenotype. The observed hyperphagia is characterized by both increased meal size and meal duration, with no change in meal frequency, supporting the interpretation that OGT signaling in brain neurons is critical for satiation.

The effect of reduced OGT expression was most pronounced in neurons of the hypothalamic paraventricular nucleus (PVN), a region implicated in controlling food intake and body weight (see the figure). An increase in blood glucose concentration after feeding increased the expression of OGT and the transcription factor c-Fos (a marker of neuronal activation) in PVN αCAMKII neurons, whereas reduced OGT expression blocked c-Fos activation and decreased excitatory synaptic input in these neurons. Deletion of the gene encoding OGT specifically in αCAMKII-expressing PVN neurons had the same effects as reducing expression in all αCAMKII-expressing neurons in the brain, and was accompanied by massive body weight gain and hyperphagia characterized by increased meal size. These findings show that a decrease in OGT action in PVN αCAMKII neurons is sufficient to mediate hyperphagia and obesity. Conversely, optogenetic stimulation of PVN αCAMKII neurons in mice acutely reduced food intake (smaller meals were consumed).

These are potent and neuroanatomically specific effects of OGT function on body weight. However, the localization of OGT expression in feeding-related neurons is not limited to the PVN. Multiple hypothalamic and brainstem regions implicated in the control of food intake express OGT, including the hypothalamic arcuate (ARC), ventromedial, dorsomedial, and lateral hypothalamic nuclei, as well as the brainstem nucleus of the solitary tract and the parabrachial nucleus (*1*, *2*). Indeed, the nutritional regulation of OGT function is heterogeneous across neuroanatomically and neurochemically distinct neuronal populations (*1*, *4*). Feeding and postfeeding blood glucose concentrations increased the amount of O-GlcNAc in PVN αCAMKII neurons, whereas fasting reduced the presence of this monosaccharide. By contrast, in ARC neurons expressing the orexigenic peptide agouti-related protein (AgRP), fasting increases OGT expression and the amount of O-GlcNAc in the cell (*4*). How fasting induces two opposite effects on neuronal OGT expression and activity remains unclear; the fasting-induced orexigenic gut peptide ghrelin increases O-GlcNAc amounts in AgRP neurons (*4*), but ghrelin action in PVN αCAMKII neurons has not been examined.

The metabolic consequences of reduced neuronal OGT for energy balance are also heterogeneous and appear to depend on the neurochemical and neuroanatomical phenotypes of the OGT-expressing neurons. Whereas adult-onset decreases in OGT expression in PVN αCAMKII neurons drives hyperphagia and obesity, constitutive reduction of OGT expression in ARC AgRP neurons leads to thermogenically effective browning of white fat, without observable changes in food intake or body weight, and protects against the development of obesity and glucose intolerance (*4*). Whether OGT action in PVN αCAMKII neurons is an important target in animal models of obesity and glucose tolerance remains to be determined.

Intriguingly, a decrease in OGT expression in ARC AgRP neurons or in PVN αCAMKII neurons reduces neuronal excitability, albeit through apparently distinct mechanisms. Reduced OGT in AgRP neurons also reduces the spontaneous action potential rate by blocking O-GlcNAcylation of inwardly rectifying Kv channels, whereas a decrease of OGT expression in PVN αCAMKII neurons reduces their miniature excitatory postsynaptic current frequency. Whether OGT modulates each of these two ionic determinants of neuronal excitability in both ARC AgRP neurons and PVN αCAMKII neurons is not known.

The identification of nutritionally regulated OGT expression in multiple neuron populations that control feeding sets the stage for elucidating how the consequences of OGT nutrient sensing are coordinated to determine both acute energy availability and long-term energy balance. Cerebrospinal fluid concentrations of multiple nutrients rise rapidly after meal ingestion and have simultaneous access to multiple brain nutrient-sensitive sites. For example, the amount of the essential branched-chain amino acid L-leucine in cerebrospinal fluid rapidly increases during the ingestion of a high-protein meal and activates both brainstem and hypothalamic sites (*5*). Local leucine administration to either of these sites in isolation rapidly decreases food intake through a selective reduction in meal size. Although these distinct effects appear to be redundant, they underscore the need for a more integrative experimental approach to understanding the role of neuronal nutrient sensors in the control of food intake, where meal-related nutrient stimuli have simultaneous access to multiple, neuroanatomically distributed nutrient-sensing sites. ■

## REFERENCES AND NOTES


1. O. Lagerlöf *et al.*, *Science* **351**, 1293 (2016).
2. G. J. Schwartz, L. M. Zeltser, *Annu. Rev. Nutr.* **33**, 1 (2013).
3. T. H. Moran, *Forum Nutr.* **63**, 94 (2010).
4. H. B. Ruan *et al.*, *Cell* **159**, 306 (2014).
5. C. Blouet *et al.*, *J. Neurosci.* **29**, 8302 (2009).


## ACKNOWLEDGMENTS


G.J.S. is supported by NIH grants DK 105441, DK 026687, and DK 020541.



10.1126/science.aaf5216


ILLUSTRATION: N. CARY/*SCIENCE*




*Published by AAAS*

BOOKS *et al.*

SCIENCE COMMUNICATION

# *Blogging for beginners*

## A new handbook offers approachable advice for aspiring science writers of all stripes

*By* **Andrew David Thaler**



**Science Blogging**
**The Essential Guide**
*Christie Wilcox, Bethany Brookshire, and Jason G. Goldman, Eds.*
Yale University Press, 2016.
286 pp.

One of the great ironies in attempting to formalize a guide to online outreach through traditional publication pathways is that by the time a book makes it onto the shelves, the content is already dated. The Internet is a dynamic place, and the past 2 years have seen major transitions in the way scientists use blogs, social media, and other online platforms to conduct outreach, education, and activism. *Science Blogging: The Essential Guide,* a new resource compiled by Christie Wilcox, Bethany Brookshire, and Jason G. Goldman, is conscious of this challenge and makes an admirable effort to overcome it. Although it does so better than many similar efforts, *Science Blogging* still feels firmly rooted in mid-to-late 2014. That is not to say that the book isn't an invaluable guide for aspiring science bloggers. It shines in the practical advice it offers to new entrants in the science blogging community.

Although often regarded as an easy path to science outreach, science blogging requires a skill set different from that of conventional writing and has its own challenges. Blog writing tends to be more conversational, with a focus on the author's unique voice, and often emphasizes, rather than minimizes, personal biases.

Wilcox, Brookshire, and Goldman have brought together some of the best science bloggers on the Internet to share their experience and expertise. The chapters that really stand out are timeless and extend far beyond the limits of science blogging. Janet Stemwedel's chapter on ethics and science blogging is an invaluable resource not just for bloggers but for all scientists, science writers, and science journalists. Glendon Mellow's chapter on science and art is broadly applicable to anyone seeking to incorporate visual media into their outreach plan, regardless of their platform of choice. Brian Switek's chapter on making the transition from writing online to writing books is an excellent resource for anyone preparing to make that leap. Kate Clancy's chapter tackles some of the most challenging issues facing female writers online, and Melanie Tannenbaum explores how to write persuasively while dealing with science deniers and trolls. These chapters alone make *Science Blogging* an essential resource for writers who work in online spaces, whether or not they fall within the vaguely defined criteria of "blogger."



Blogging can be a great form of scientific outreach—if you know what you're doing.

Indeed, different sections of the book seem to have different views on what constitutes science blogging. Although some clearly stick to a conventional view of science blogging as a static website with recent articles posted in reverse chronological order, other chapters consider microblogging platforms like Twitter, as well as video and podcasting outlets, to fall under the aegis of science blogging. This reflects the changing nature of online science communication, as bloggers and platforms adapt to changes in the way that audiences engage with content. However, this amorphous definition may leave some readers confused about what constitutes a blog.

Not all science blogging is about outreach to the general public. *Science Blogging* overlooks one of the major motivators for many scientists who blog: shaping the culture of science. Many sites exist purely to facilitate conversations among researchers. Absent from *Science Blogging* are such touchstones of the community as *Retraction Watch*, a blog run by Ivan Oransky that tracks and discusses retractions in the peer-reviewed literature. *Retraction Watch* has been instrumental in changing how journals publicize retractions and promoting greater transparency when important articles are retracted.

Had key chapters in *Science Blogging* been written today rather than late 2014 to early 2015, I'm certain that this guide would not have left out the societal effect of science blogging on the culture of science. In the past year, we have seen science bloggers shape the overall discussion about sexual harassment, racism, and discrimination within the scientific community and force institutions to confront entrenched and systemic abuses. Were it not for the freedom and visibility that online platforms provide, it is unlikely that we would be seeing the major revelations that have surfaced in the past several months. In that way, science blogging can be a powerful tool for change.

Despite its flaws, *Science Blogging* is an important and valuable guide for aspiring science writers of all stripes, with some specific advice for those building their online profile through blogging. Anyone interested in learning more about online outreach will find this guide approachable and insightful.

10.1126/science.aaf2417

*The reviewer is in the Department of Fisheries, Virginia Institute of Marine Science, Gloucester Point, VA 23062, USA, and at Southern Fried Science (www.southernfriedscience.com). E-mail: andrew@blackbeardbiologic.com*

PHOTO: M_A_Y_A/ISTOCKPHOTO

Downloaded from on March 17, 2016



Published by AAAS



The tabletop mountains in the Guiana Shield are largely unexplored "worlds unto themselves."

PHOTO: ©PHILLIP LEE HARVEY/CORBIS

ECOLOGY

# Back to nature

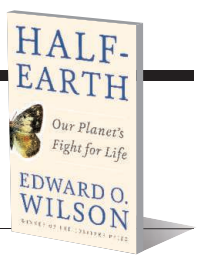
## Could committing half of Earth's surface to conservation stave off the next mass extinction?

*By* **Christine J. Griffiths**

Imagine a chain of uninterrupted wild landscapes spanning the savannas and forests of southern and central Africa, the woodlands of Poland and Belarus, and the tropical forests of Central and South America. By committing half of the planet's terrestrial and marine surface to nature, Edward O. Wilson believes that we can save millions of species, as well as humanity. This is Wilson's audacious proposal to stave off the coming biological apocalypse, the sixth mass extinction event, which he outlines in *Half-Earth: Our Planet's Fight for Life*.

According to Wilson, it's the "Darwinian propensity in our brain's machinery to favor short-term decisions over long-range planning" that has led us to ignore warning signs that we are nearing the irrevocable depletion of our natural resources. He vehemently attacks the views of "Anthropocene enthusiasts" who seem to believe that "what is left of nature should be treated as a commodity to justify saving it" and scathingly swipes at postmodern environmentalists who believe that conservationists should abandon their romantic opinions of "untrammeled wildernesses." Wilson argues that by framing humans as the masters of Earth, these alarming philosophies justify our current voracious exploitation of natural resources in the name of economic and development growth. Instead, he presents an impassioned and evidence-rich plea to assert nature's needs fearlessly, dismissing Anthropocene optimism that humanity can survive without nature and that ongoing extinctions can be balanced by de-extinction or the introduction of alien species.

**Half-Earth**
**Our Planet's Fight for Life**
*Edward O. Wilson*
Liveright, 2016. 261 pp.




Stemming the tide of species extinctions requires bold actions beyond current conservation targets. Wilson commends the conservation movement for its noble efforts in lowering the extinction rates of species by about 20% but points out that these figures fall drastically short of what is needed. Scientists and taxonomists have calculated that at least two-thirds of the species on Earth remain unknown and unnamed, suggesting that the magnitude of the problem may be far greater than we imagine. Complicating our ability to predict the impact of species extinctions is our poor understanding of how species interact with one another, especially in the oceans.

But why choose 50% when the Convention on Biological Diversity (CBD), an international legally binding treaty signed by 196 countries, stipulates a conservation goal to protect 17% of terrestrial and 10% of marine areas? Wilson, who together with Robert MacArthur formulated the theory of island biogeography (*1*), explains how confined landscapes, such as national parks, will inevitably lose species over time as environments change and animals and plants find that they cannot move freely to more hospitable habitats. Large, interconnected zones are needed. Indeed, more than a decade before the CBD's targets were set, scientific evidence suggested that some 25 to 75% of the world's lands and waterways would need to be protected in order to maintain biodiversity and ecological processes (*2*). *Half-Earth* offers a cautionary approach, moving away from individual species conservation and setting a single comprehensive goal to protect entire faunas and floras for perpetuity.

Given that conservation targets are constrained by global politics, is Wilson's vision realistic? Although every country in the world has a protected area system, in 2015 only 15% of land and 2.8% of marine areas held this designation. However, the area for potential nature conservation is much higher, because these figures fail to account for private reserves that represent key components of his proposed network. As more areas are declared protected, we must ensure that these are more than mere "paper parks," existing in name only.

Paying homage to extinct species, great and small, Wilson reminds us that it is the "little things that run the Earth." The book is enlivened with personal anecdotes, such as the joy so few will ever experience of encountering Sumatran rhinos. Naturally, because Wilson is the world's leading authority on ants, we learn about his lifelong fascination with these tiny creatures as well. Although the book emphasizes the grave nature of our current course, Wilson is optimistic that our ecological footprint will shrink as technological advances catalyze a shift from extensive to intensive economic growth, enabling us to be stewards of the planet, rather than destroyers.

*Half-Earth* challenges the reader to recognize that we each have an individual responsibility to ensure the survival of species and, ultimately, the biosphere. Considering the irreversible changes that have already taken place at human hands, Wilson leaves no doubt that half is the very least we can do, both for other species and for our descendants.

*The reviewer is at the School of Biological Sciences, University of Bristol, Bristol Life Sciences Building, 24 Tyndall Avenue, Bristol BS8 1TQ, England. E-mail: christine.griffiths@bristol.ac.uk*

### REFERENCES

1. E. O. Wilson, R. MacArthur, *The Theory of Island Biogeography* (Princeton Univ. Press, Princeton, NJ, 1967).
2. R. F. Noss, A. Y. Cooperrider, *Saving Nature's Legacy: Protecting and Restoring Biodiversity* (Island Press, Washington, DC, 1994).

10.1126/science.aaf1485

Downloaded from on March 17, 2016



Published by AAAS

# LETTERS

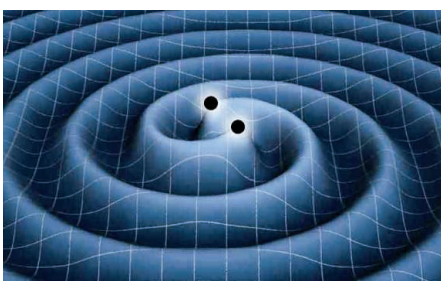
*Edited by* **Jennifer Sills**

## A wave of inspiration

SCIENTISTS HAVE NOW CONFIRMED the detection of gravitational waves, after the sensitive detectors emitted a chirp that represented two distant black holes colliding in space (*1*). This achievement allows us to see the universe in a whole new way.

I developed a fascination with gravitational waves while studying general relativity in graduate school. I wrote my dissertation in the field of differential geometry, the field of mathematics that is used to describe general relativity and model gravitational waves. It may sound geeky, but there's a definite beauty to the equations that give rise to gravitational waves.

The sensor that detected the waves involves high-precision lasers and massive data analysis, both of which are at the forefront of generating new technology. I hope this latest scientific discovery inspires a new sense of curiosity among students of all ages and encourages them to study math, engineering, and other technical fields that make such science possible.



An artist's conception of a binary black hole producing gravitational waves.

ILLUSTRATION: NASA

Our country has long stood at the forefront of scientific discovery, and I've always strongly supported federal funding for research to fuel scientific advancements. This latest discovery demonstrates the importance of investing in scientific research on a national level. Funding from the National Science Foundation, for example, was instrumental in developing and implementing the detectors that "heard" the chirp of the distant and massive astrophysical event that generated the gravitational waves.

This progress is the result of years of hard work and innovative research and experimentation. Now, with the capability to detect gravitational waves, we stand at a new frontier, with the opportunity to use this achievement to better understand this astonishing universe.

***Jerry McNerney***

U.S. House of Representatives, California's 9th Congressional District, USA.
E-mail: mcnerneypress@mail.house.gov

### REFERENCE

1. B. P. Abbott *et al.* (LIGO Scientific Collaboration and Virgo Collaboration), *Phys. Rev. Lett.* **116**, 061102 (2016).

## *Risks of* Wolbachia *mosquito control*

CONTROLLING INSECT CROP pests and disease vector populations is a huge challenge. A new control strategy involves releasing insects that have been deliberately infected by *Wolbachia*, a bacterium that induces modifications in host reproductive biology, such as male feminization (when a male develops as a female), cytoplasmic incompatibility (the inability to produce offspring), and reduced insect lifetimes (*1*). Caged and open-field experiments with infected mosquitoes are in progress (*2*–*4*). The Eliminate Dengue project (*5*) has released infected mosquitoes in Australia, Vietnam, and Brazil, and obtained promising results showing that the *wMel Wolbachia* strain is able to invade the *Ae. aegypti* population and block dengue transmission (*2*). Such results are very exciting, considering the number of people affected by malaria and arboviruses (dengue, chikungunya, zika, and related viruses) worldwide every year.

However, few have focused on the probability of *Wolbachia* strains being transferred to other insects and the potential environmental and economic impacts of this host shift. *Wolbachia* strains (including *wMel*-like strains) are capable of transferring horizontally among distantly related arthropods in a short evolutionary time (*6*, *7*). Moreover, some parasites are able to carry *Wolbachia* strains to other species (*6*).

The benefits of *Wolbachia* and risks of host shift must be weighed against the benefits and risks of other mosquito control strategies, such as chemical and bacterial pesticides. Pesticides also have environmental costs: They affect nontarget organisms and can lead to the development of resistant populations of insects (*8*). Unlike the effects of *Wolbachia*, the consequences of pesticide use are well known, and are regulated in several countries (*9*).

Although mosquitoes deliberately infected with *Wolbachia* could reduce the need for insecticide use, the consequences of *Wolbachia* host shift to native species are, for now, unpredictable. Arthropods present complex and poorly understood ecological relationships, and alterations in reproductive parameters of nontarget species can generate ecological disturbances. The Cartagena Protocol (*10*)—a United Nations safety regulation for transfer, handling, and use of genetically modified organisms, signed by 170 countries—is not applicable to *Wolbachia*-infected mosquitoes because the bacteria are considered nontransgenic (*11*). Therefore, the release of insects hosting *Wolbachia* was not subject to these regulations. In countries where *Wolbachia* release was allowed, veterinary, agricultural, and health legislation were used to evaluate its environmental risks (*11*). As far as we are aware, no country has regulations specifically pertaining to *Wolbachia*-infected insect release or mitigation strategies to deal with unexpected results. Even if a country enacts such legislation, it would not extend to other countries, whereas *Wolbachia*-infected insects, at least in theory, can easily cross political borders.

The release of insects hosting *Wolbachia* strains should be more carefully considered, and further studies of the potential impact of these bacteria on biodiversity should be undertaken, before this strategy can be widely used.

***Elgion Lucio Silva Loreto[1] and Gabriel Luz Wallau[2]****

[1]Departamento de Bioquímica e Biologia Molecular, Universidade Federal de Santa Maria, Rio Grande do Sul, Brazil. [2]Departamento de Entomologia, Centro de Pesquisas Aggeu Magalhães-FIOCRUZ-CPqAM, Recife, PE, Brazil.

*Corresponding author.
E-mail: gabriel.wallau@cpqam.fiocruz.br

### REFERENCES

1. E. P. Caragata, H. L. C. Dutra, L. A. Moreira, *Trends Parasitol.* **32**, 207 (2015).
2. T. Walker *et al.*, *Nature* **476**, 450 (2011).
3. L. O'Connor *et al.*, *PLOS Negl. Trop. Dis.* **6**, e1797 (2012).
4. T. H. Nguyen *et al.*, *Parasites Vectors* **8**, 563 (2015).
5. Eliminate Dengue Program (www.eliminatedengue.com/program).
6. B. D. Heath, R. D. J. Butcher, W. G. F. Whitfield, S. F. Hubbard, *Curr. Biol.* **9**, 313 (1999).
7. M. F. Ortiz, G. L Wallau, E. L. Loreto, *Mol. Genet. Genom.* **290**, 67 (2015).
8. N. Liu, *Annu. Rev. Entomol.* **60**, 537 (2015).
9. C. E. Handford, C. T Elliott, K. Campbell, *Integr. Environ. Assess. Manag.* **11**, 525 (2015).
10. The Cartagena Protocol on Biosafety (https://bch.cbd.int/protocol/).
11. J. M. Marshall, *AsPac J. Mol. Biol. Biotechnol.* **19**, 93 (2011).

## *Curbing Iran's academic misconduct*

IRAN AND CHINA are among the countries with the fastest growth rate of scientific publications in the world (*1*). Unfortunately, these countries are also home to more frequent publication misconduct (*2*). There is a growing publication bazaar in Iran, similar

Downloaded from on March 17, 2016



Published by AAAS

to the one in China (*3*). Agencies that guarantee publication for a price abound. The website of one such agency displays a price list based on the impact factor of the journal (*4*). For journals with impact factors below 0.5, between 0.5 and 1.0, and above 1.0, the price is about US$600, US$800, and US$1000, respectively.

Fortunately, the Iranian scientific community is raising awareness about this issue. In 2008, Iranian professors created the blog "Professors against plagiarism" (*5*) to discourage misconduct among faculty members and students. The blog provides updates on retracted papers and misconduct in academia, as well as information about unethical for-sale publications.

In response to the concerns of scientists and researchers, the Iranian government has recently proposed a draft piece of legislation to curb academic misconduct and plagiarism (*6*). The bill imposes severe penalties on faculty members and graduate students who are involved in academic misconduct, such as buying research papers and theses. It also aims to penalize paper- and thesis-selling agencies. Given that there is currently no specific law against academic misconduct in Iran, this is an important and positive step toward a better academic environment. I encourage the Parliament of the Islamic Republic of Iran (Majlis) to approve this legislation.

***Behzad Ataie-Ashtiani***

Department of Civil Engineering, Sharif University of Technology, 9313, Tehran, Iran.
E-mail: ataie@sharif.ir

**REFERENCES**

1. R. Van Noorden, *Nature* **480**, 426 (2011).
2. B. Ataie-Ashtiani, *Sci. Eng. Ethics*, 10.1007/s11948-016-9766-1 (2016).
3. M. Hvistendahl, *Science* **342**, 1035 (2013).
4. Easy Paper Scientific Research Papers (http://easypapers.ir/%D8%AA%D8%AF%D9%88%DB%8C%D9%86-%D9%88-%DA%86%D8%A7%D9%BE-%D9%85%D9%82%D8%A7%D9%84%D9%87-isi/) [in Persian].
5. Professors Against Plagiarism (http://pap.blog.ir/) [in Persian].
6. Islamic Republic News Agency (2015); http://www.irna.ir/fa/News/81848515/ [in Persian].

## TECHNICAL COMMENT ABSTRACTS

### Comment on "Unique in the shopping mall: On the reidentifiability of credit card metadata"

***David Sánchez, Sergio Martínez, Josep Domingo-Ferrer***

De Montjoye *et al.* (Reports, 30 January 2015, p. 536) claimed that most individuals can be reidentified from a deidentified transaction database and that anonymization mechanisms are not effective against reidentification. We demonstrate that anonymization can be performed by techniques well established in the literature.

Full text at http://dx.doi.org/10.1126/science.aad9295

### Response to Comment on "Unique in the shopping mall: On the reidentifiability of credit card metadata"

***Yves-Alexandre de Montjoye and Alex "Sandy" Pentland***

Sánchez *et al.*'s textbook *k*-anonymization example does not prove, or even suggest, that location and other big-data data sets can be anonymized and of general use. The synthetic data set that they "successfully anonymize" bears no resemblance to modern high-dimensional data sets on which their methods fail. Moving forward, deidentification should not be considered a useful basis for policy.

Full text at http://dx.doi.org/10.1126/science.aaf1578

TECHNICAL COMMENT

IDENTITY AND PRIVACY

# Comment on "Unique in the shopping mall: On the reidentifiability of credit card metadata"

David Sánchez,* Sergio Martínez, Josep Domingo-Ferrer

**De Montjoye *et al*. (Reports, 30 January 2015, p. 536) claimed that most individuals can be reidentified from a deidentified transaction database and that anonymization mechanisms are not effective against reidentification. We demonstrate that anonymization can be performed by techniques well established in the literature.**

De Montjoye *et al*. (*1*) concluded that, for most customers in a deidentified credit card transaction database, knowing the spatiotemporal features of four purchases by the customer was enough to reidentify her. Reidentification was measured according to "unicity" (*2*) (a neologism for uniqueness), which, given a number of personal features assumed to be known to an attacker, counts the number of individuals for whom these features are unique.

First, de Montjoye *et al*.'s reidentification figures are probably overestimated, because their database of 1.1 million customers seems only a fraction of the population of an undisclosed country (presumably, several millions). Unfortunately, they did not make their data set public, which prevents reproducing their results. As highlighted by Barth-Jones *et al*. (*3*), with a nonexhaustive sample, an individual's sample uniqueness/unicity does not imply population uniqueness and, hence, does not allow unequivocal reidentification; assuming otherwise clearly overestimates the reidentification risk. Moreover, not even population uniqueness automatically yields reidentification: The attacker still needs to link the records with unique features to external identified data sources (e.g., electoral rolls).

To reduce the high unicity in their database, de Montjoye *et al*. implemented some unreferenced "anonymization" strategies to coarsen data (such as clustering locations) that fell short of sufficiently reducing unicity. From this, de Montjoye *et al*. drew conclusions about the ineffectiveness of anonymization methods and highlighted the need for "more research in computational privacy."

We must recall that reidentification risk in data releases has been treated in the statistical disclosure control (*4*, *5*) and privacy-preserving data publishing (*6*) literatures for nearly four decades. As a result, a broad choice of anonymization methods exists. These usually suppress personal identifiers (such as passport numbers) and mask quasi-identifiers (QIs). The latter are attributes such as zip code, job, or birthdate, each of which does not uniquely identify the subject but whose combination may. Because QIs may be present in public nonconfidential data bases (like electoral rolls) together with some identifiers (like passport number), it is crucial to mask them to avoid reidentification. It is easy to see that reidentification through QIs [studied at least since 1988 (*7*) and popularized by the $k$-anonymity model (*8*)] is equivalent to the unicity idea rediscovered by de Montjoye *et al*. in 2013 (*2*)—that is, a subject whose QI values are unique in a data set risks being reidentified.

Data coarsening is indeed a method often used in anonymization to mask QIs (*8*). However, de Montjoye *et al*. concluded that their coarsening-based anonymization was ineffective. This is unsurprising because they coarsened attributes independently and used value ranges fixed ex ante, which is inappropriate for at least two reasons: (i) to offer true anonymity guarantees, coarsening should be based on the actual distribution of the data set (i.e., a fixed range may contain a single value among those in the data set); and (ii) independently coarsening each QI attribute cannot ensure that unique QI value combinations disappear (coarsening must consider all QIs together).

To illustrate the effectiveness of anonymization, the simple and well-known $k$-anonymity notion is enough. In a $k$-anonymous data set, records should not include strict identifiers, and each record should be indistinguishable from, at least, $k - 1$ other ones regarding QI values. Thus, the probability of reidentification of any individual is $1/k$. Hence, for $k > 1$, this probability is less than 1 for all records, thereby ensuring zero unequivocal reidentifications. Moreover, by tuning $k$, we can also tune the level of exposure of individuals.

We looked for a data set with similar structure and unicity/reidentification risk properties to de Montjoye *et al*.'s data (which were unavailable) to show the effectiveness of $k$-anonymity. We chose a synthetically generated version of a publicly available patient discharge data set (that we call SPD), which includes the nearly 4 million patients admitted in 2009 to California hospitals [see details at (*9*)]. This data set includes a set of spatiotemporal features of the patients and, unlike de Montjoye *et al*.'s data set, it covers the whole population of 2009 California patients; hence, uniqueness in this data set quantifies the population reidentification risk (*9*). As shown in Fig. 1 the high risk reached for the SPD data set when the attacker knows all the patient's features (75%) is coherent with the high (even though overestimated) unicities reported by de Montjoye *et al*..

We enforced $k$-anonymity by grouping records with similar QIs (census + spatiotemporal features) in clusters of $k$ or more and generalizing/coarsening their QI values to their common range (*9*).

Figure 2 compares the risk of unequivocal reidentification and correct random reidentification of $k$-anonymity versus a naïve coarsening similar to de Montjoye *et al*.'s, with "fixed" intervals covering 1/32, 1/16, and 1/8 of the domain ranges of the attributes (*9*). Unlike naïve coarsening, $k$-anonymity

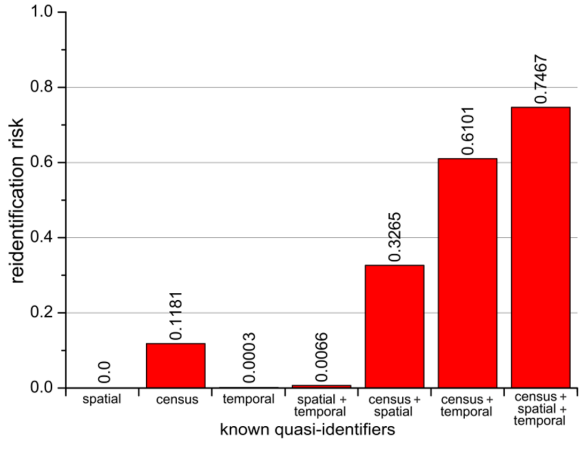



**Fig. 1. Reidentification risk in the SPD data set depending on the attributes known by the attacker.**

United Nations Educational, Scientific, and Cultural Organization (UNESCO) Chair in Data Privacy, Department of Computer Engineering and Mathematics, Universitat Rovira i Virgili (URV), Avenue Països Catalans, 26, E-43007, Tarragona, Catalonia.
*Corresponding author. E-mail: david.sanchez@urv.cat

Downloaded from on March 17, 2016

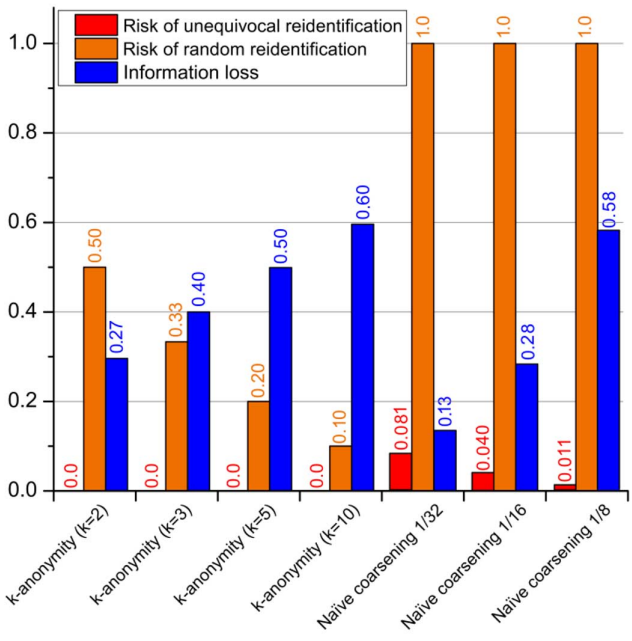



**Fig. 2. Reidentification risk and information loss for *k*-anonymity and naïve coarsening.**

yielded zero unequivocal reidentifications and a rate $1/k$ of correct random reidentifications when the attacker knows all QIs.

Furthermore, anonymized data should also retain analytical utility, which ultimately justifies data publishing. With *k*-anonymity, data utility is retained by grouping similar records together and by masking only those that do not fulfill the privacy criterion (de Montjoye *et al.*'s naïve coarsening fails to do either). Moreover, the trade-off between privacy and utility can be balanced by adjusting *k*. To illustrate, we have measured the information loss incurred by masking as the average distance between the SPD data set and its anonymized versions (*9*). Figure 2 shows that 2-anonymity not only yields less reidentifications but also less information loss than the safest naïve coarsening.

In addition to *k*-anonymity, there is much more in the anonymization literature. Specifically, extensions of *k*-anonymity [e.g., *t*-closeness (*10*)] also address attribute disclosure, which occurs if the values of the confidential attributes within a group of records sharing all QI values are too close. In (*9*), we report how *t*-closeness mitigates attribute disclosure by using the algorithm we proposed in (*11*). Moreover, the current research agenda includes more challenging scenarios, like big-data anonymization (in which scalability and linkability preservation are crucial) (*12*, *13*), streaming data anonymization (*14*), and local or co-utile collaborative anonymization by the data subjects themselves (*15*).

In conclusion, data owners and subjects can be reassured that sound anonymization methodologies exist to produce useful anonymized data that can be safely shared for research.

## REFERENCES AND NOTES

1. Y.-A. de Montjoye, L. Radaelli, V. K. Singh, A. S. Pentland, *Science* **347**, 536–539 (2015).
2. Y.-A. de Montjoye, C. A. Hidalgo, M. Verleysen, V. D. Blondel, *Sci. Rep.* **3**, 1376 (2013).
3. D. Barth-Jones, K. El Emam, J. Bambauer, A. Cavoukian, B. Malin, *Science* **348**, 194–195 (2015).
4. T. Dalenius, *Stat. Tidskr.* **5**, 429–444 (1977).
5. A. Hundepool *et al.*, *Statistical Disclosure Control* (Wiley, 2012).
6. B. Fung, K. Wang, R. Chen, P. S. Yu, *ACM Comput. Surv.* **42**, 14 (2010).
7. G. Paass, *J. Bus. Econ. Stat.* **6**, 487–500 (1988).
8. P. Samarati, L. Sweeney, "Protecting privacy when disclosing information: k-anonymity and its enforcement through generalization and suppression" (SRI International, 1998).
9. D. Sánchez, S. Martínez, J. Domingo-Ferrer, Supplementary materials for "How to avoid reidentification with proper anonymization." Available at http://arxiv.org/abs/1511.05957 (2015).
10. N. Li, T. Li, t-Closeness, in *IEEE 23rd International Conference on Data Engineering* (IEEE Computer Society, 2007), pp. 106–115.
11. J. Soria-Comas, J. Domingo-Ferrer, D. Sánchez, S. Martínez, *IEEE Trans. Knowl. Data Eng.* **27**, 3098–3110 (2015).
12. A. Machanavajjhala, J. Reiter, *XRDS: Crossroads* **19**, 20–23 (2012).
13. J. Soria-Comas, J. Domingo-Ferrer. Big data privacy: Challenges to privacy, principles and models. *Data Sci. Eng.* (published online Sep. 15, 2015); http://dx.doi.org/10.1007/s41019-015-0001-x
14. J. Cao, B. Carminati, E. Ferrari, K.-L. Tan, *IEEE T. Depend. Secure* **8**, 337–352 (2011).
15. J. Soria-Comas, J. Domingo-Ferrer, in *MDAI 2015-Modeling Decisions for Artificial Intelligence* (Springer, 2015), pp. 192–206.

## ACKNOWLEDGMENTS

Additional materials for this study are available at http://arxiv.org/abs/1511.05957. They detail the structure and synthetic generation of the SPD data set, describe the risk assessment and anonymization algorithms we used to obtain the reported results, and provide extended results and discussions. The SPD data set, with the synthetic quasi-identifiers, and its *k*-anonymous, *k*-anonymous and *t*-close, and coarsened versions can be found at http://crises-deim.urv.cat/opendata/SPD_Science.zip. The source code of the algorithms detailed in the additional materials is also available, together with some usage examples. These materials allow reproducing all results reported here and in the additional materials. Thanks go to J. Bambauer, A. Cavoukian, K. El Emam, K. Muralidhar, and V. Torra for useful reviews and discussions.
We gratefully acknowledge the following funding sources and grants: European Commission (H2020-644024 "CLARUS"), Spanish Government (TIN2012-32757 and TIN2014-57364-C2-1-R), Government of Catalonia (2014 SGR 537 and ICREA-Acadèmia award to J.D.-F.), and Templeton World Charity Foundation (TWCF0095/AB60). The opinions expressed in this paper are the authors' own and do not necessarily reflect the views of any funder or UNESCO.

23 November 2015; accepted 23 December 2015
10.1126/science.aad9295

TECHNICAL RESPONSE

IDENTITY AND PRIVACY

# Response to Comment on "Unique in the shopping mall: On the reidentifiability of credit card metadata"

Yves-Alexandre de Montjoye[1,2]* and Alex "Sandy" Pentland[1]

**Sánchez *et al.*'s textbook *k*-anonymization example does not prove, or even suggest, that location and other big-data data sets can be anonymized and of general use. The synthetic data set that they "successfully anonymize" bears no resemblance to modern high-dimensional data sets on which their methods fail. Moving forward, deidentification should not be considered a useful basis for policy.**

We believe that Sánchez *et al.* (*1*) fundamentally misunderstand the size and dimensionality of modern big-data data sets and how they are being used in industry and research. Making data available for socially beneficial applications is vitally important. We are therefore highly concerned by the failure of some in the "statistical disclosure control" community to reassess the limits of data anonymization (or deidentification) in the face of fast technological evolution. This insistence on sticking with "how we've done it for 40 years" risks (i) forcing us, as a society, to suffer either a dramatic loss of privacy or a sharp reduction in the availability and use of data in the coming decade, and (ii) preventing the development and adoption of modern privacy-through-security solutions for big data (*2*).

The textbook analysis presented by Sánchez *et al.* does not prove or even suggest that high-dimensional data sets, such as the one generated from credit cards, mobile phones, browsers, or the Internet of things, where hundreds or thousands of points are known for each individual across years, can be effectively anonymized. Specifically, the synthetic medical data set that Sánchez *et al.* successfully anonymize bears no resemblance to the high-dimensional data sets to which we refer in our studies (*3*, *4*) and which their textbook method would utterly fail to anonymize. Their data set contains a total of nine points, or quasi-identifiers (information that could be used to reidentify someone), per individual and cannot be used to track an individual across time.

Mobile phones typically record a person's location—also a quasi-identifier (*5*)—from every couple of hours to every 5 minutes, and payment systems up to a couple of times a day, often generating data sets that contain hundreds to thousands of points per individual across time. The intrinsic anonymizability of a data set is substantially driven by basic combinatorics. Showing that a method can anonymize a small (0.027 GB compressed) and low-dimensional data set of nine points does not prove anything about its ability to anonymize modern high-dimensional data sets containing hundreds or thousands of points per individual, such as a person's location in a country every 5 minutes for a year. In fact, the data set studied by Sánchez *et al.* is trivially anonymized by any method, including the one we used, which, when applying the least aggressive generalization, already decreases unicity from 0.7467 to 0.081 by Sánchez *et al.*'s calculations. In contrast, we showed that unicity only decreases very slowly with both spatial and temporal generalization in mobile phone and credit card data sets (*3*, *4*). We furthermore showed that an attacker can easily compensate for this decrease by collecting a few more external points: knowing that the person we are searching for was at a given place at a given time.

In addition, showing that a data set can be anonymized and still be useful for a specific application—which Sánchez *et al.* do not show—is not sufficient. The privacy guarantees offered by anonymization methods such as the one used by Sánchez *et al.* only hold if the data are anonymized one time (i.e., one anonymization method with one set of parameters per data set ever). The same mobile phone data are, however, already being used to study human mobility and behavior in cities (*6*), the geographical partitioning of countries (*7*), and the spread of information in social networks (*8*). To argue that sound anonymization methods are sufficient to protect people's privacy in mobile phone or credit card data, one would need to show that a single anonymization method can anonymize the data and yet allow for most present—and hopefully future—data uses. We currently have no reason to believe that such a method will ever exist for modern high-dimensional data sets.

Furthermore, Sánchez *et al.* claim that the anonymization method that we used is suboptimal. The choice of a specific anonymization method and set of parameters depends on how the data will be used. The one we picked—lowering the spatial and temporal resolution of the data—is both a general and a natural one. Although, by definition, one can never rule out the existence of a substantially more efficient anonymization method, the authors do not present evidence of one. Our analysis furthermore shows that, even if a new method were to be twice as effective as ours, one would still have to decrease the spatial and temporal resolution of the data by a factor of 15 to approach a reasonably low unicity knowing 10 points (*3*). This means that the location of an individual would only be known every 15 hours with an accuracy of roughly 15 $km^2$, raising doubts on the general utility of this data. In fact, one study that actually attempted to (*k*-)anonymize high-dimensional location data through trajectory-based clustering (nonorthogonal generalization) concluded that their results are in agreement with ours and "provide insights behind the poor anonimizability" of mobile phone data sets (*9*).

Finally, Sánchez *et al.* claim that our "reidentification figures are probably overestimated" because our data set contains "only a fraction of the population of an undisclosed country." This means that Sánchez *et al.* decide, when estimating the risk of an individual to be reidentified, that an attacker could never know whether the person he is searching for is in the data set—e.g., is a client of a specific carrier—or not. As we pointed out before, this arbitrary assumption artificially lowers the estimated, and thus perceived and potentially legally sanctioned, risk of reidentification without changing at all the actual risk for people in the released data set (*5*). Its reliance on such unscientific assumptions when protecting individuals' privacy is precisely why we, and others (*5*, *10*, *11*), have argued that deidentification is not a useful basis for policy.

To conclude, Sánchez *et al.*'s Comment arises from a fundamental misunderstanding of the size and dimensionality of modern big-data data sets and how they are being used. The textbook analysis they present does not prove, or even suggest, that high-dimensional data sets, such as the ones generated from credit cards, mobile phones, browsers, or the Internet of things, can be effectively anonymized. We have currently no reason to believe that an efficient enough, yet general, anonymization method will ever exist for high-dimensional data, as all the evidence so far points to the contrary. The current deidentification model, where the data are anonymized and released, is obsolete and should not be used for policy.

[1]Massachusetts Institute of Technology, Cambridge, MA 02139, USA. [2]Harvard University, Institute for Quantitative Social Science, Cambridge, MA 02138, USA.
*Corresponding author. E-mail: yvesalexandre@demontjoye.com

## REFERENCES

1. D. Sánchez, S. Martínez, J. Domingo-Ferrer, *Science* **351**, 1274 (2016).
2. C. Dwork, in *Encyclopedia of Cryptography and Security*, H. C. A. van Tilborg, S. Jajodia, Eds. (Springer US, 2011), pp. 338–340.

Downloaded from on March 17, 2016

3. Y. A. de Montjoye, C. A. Hidalgo, M. Verleysen, V. D. Blondel, *Nature* **3**, 1376 (2013).
4. Y. A. de Montjoye, L. Radaelli, V. K. Singh, A. S. Pentland, *Science* **347**, 536–539 (2015).
5. Y.-A. de Montjoye, A. S. Pentland, *Science* **348**, 195–195 (2015).
6. J. L. Toole, Y. A. de Montjoye, M. C. González, A. S. Pentland, in *Social Phenomena*, B. Gonçalves, N. Perra, Eds. (Springer International Publishing, 2015), pp. 15–35.
7. C. Ratti *et al.*, *PLOS ONE* **5**, e14248 (2010).
8. G. Miritello, E. Moro, R. Lara, *Phys. Rev. E Stat. Nonlin. Soft Matter Phys.* **83**, 045102 (2011).
9. M. Gramaglia, M. Fiore, On the anonymizability of mobile traffic datasets (2014); arXiv preprint; arXiv:1501.00100.
10. A. Narayanan, E. W. Felten, "No silver bullet: De-identification still doesn't work" (Princeton Center for Information Technology Policy, White Paper, Princeton CITP, 2014).
11. President's Council of Advisors on Science and Technology, Big Data and Privacy: A Technological Perspective (PCAST, Washington, DC, 2014), pp. 38–39.

25 December 2015; accepted 26 January 2016
10.1126/science.aaf1578

REVIEW SUMMARY

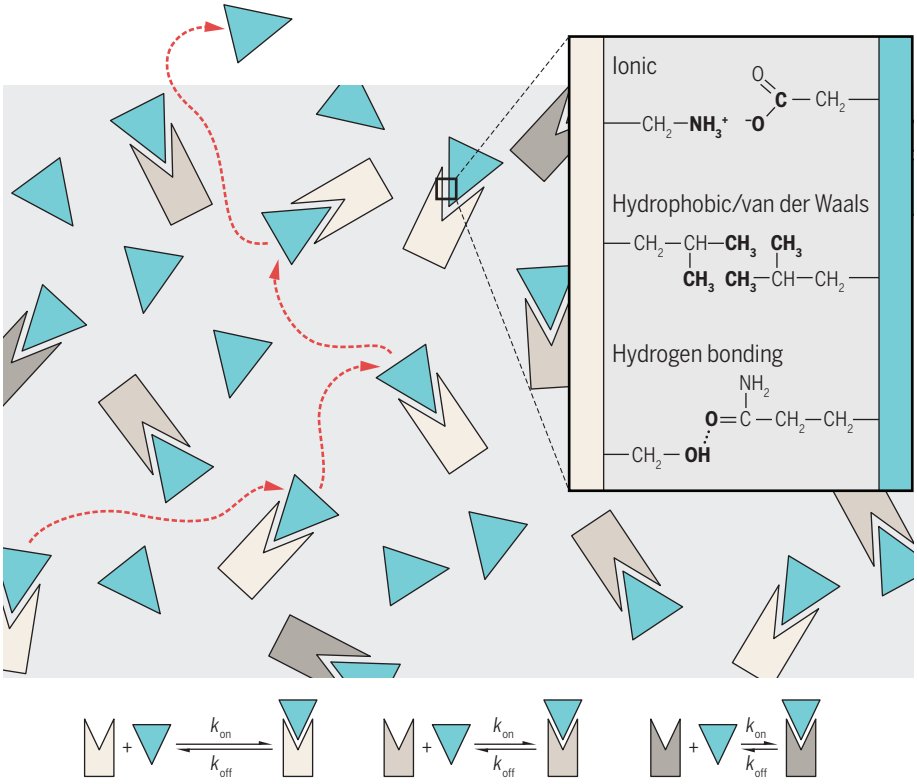
CHEMISTRY

# Designer protein delivery: From natural to engineered affinity-controlled release systems

Malgosia M. Pakulska, Shane Miersch, Molly S. Shoichet*

**BACKGROUND:** Protein therapeutics constitute a multibillion-dollar market, yet their formulation and sustained delivery still pose a substantial challenge. Controlled release strategies developed for small-molecule drugs, such as microparticle encapsulation, typically involve organic solvents and harsh processing conditions that are detrimental to protein structure and function. Affinity-controlled release has emerged as an alternative strategy for the sustained and tunable release of protein therapeutics in a neutral aqueous environment, thus reducing protein loss and improving loading.

Affinity-controlled release depends on a preferred noncovalent interaction between a protein therapeutic and a binding ligand. This binding ligand can be another protein, a peptide, or an oligonucleotide. Typically, the binding ligand is covalently linked to a polymer matrix, such as a hydrogel. Soluble protein is added, and equilibrium is established between free protein and ligand-bound protein. Whereas free protein is able to diffuse from the system, bound protein cannot. This equilibrium is dynamic and changes in response to local conditions. The rate of protein release from the system is therefore governed not only by protein diffusivity and the concentration gradient, but also by the concentration of the binding ligand, the strength of the interaction, and the binding kinetics. The challenge lies in finding binding ligands that afford the desired release profiles.




**Discovery of binding ligands for affinity-controlled release.** Ligands (peptides, proteins, or oligonucleotides; shown as polygons) that bind a protein therapeutic (triangles) through noncovalent interactions (ionic, hydrophobic, van der Waals, or hydrogen bonding; indicated in bold) can be discovered in nature, selected from a library, derived through in vitro evolution, or designed computationally. By choosing ligands with different affinities, represented by the size of the equilibrium arrows (bottom), and covalently linking them to a polymer matrix such as a hydrogel, one can control the diffusive release (dashed arrows) of a protein therapeutic.

**ADVANCES:** The earliest affinity-controlled release systems mimicked the extracellular matrix by using heparin to reversibly bind and control the release of various growth factors. Other natural interactions have since been used for affinity-controlled release, including albumin with small-molecule therapeutics and antibodies with cognate antigens. These systems have allowed for sustained release of protein therapeutics while maintaining protein activity; however, naturally occurring interactions are inherently limited in terms of available targets and binding strengths. In vitro selection and directed evolution are established techniques for isolation and engineering of binding partners against virtually any protein target. Harnessing these techniques for affinity-controlled release applications is now underway and has resulted in novel peptide-, protein-, and oligonucleotide-based binders for the sustained release of several growth factors.

ON OUR WEB SITE

Read the full article at http://dx.doi.org/10.1126/science.aac4750

**OUTLOOK:** Many opportunities exist for the discovery or design of binding ligands for affinity-controlled release. Computational techniques can help to identify protein backbones that have geometric and electrostatic complementarity to a target, reducing the screening required to isolate lead variants. Selection conditions can be tailored to isolate intermediate-strength binders, or iterative rounds of in vitro evolution can provide a series of related variants with a spectrum of affinities for a target. Competition selections can ensure selectivity for simultaneous yet independent release of multiple proteins from their corresponding binding ligands. On-demand affinity-controlled release has yet to be explored, but structure-switching aptamers and computational design of allosteric regulator sites show potential. These techniques, coupled with concurrent advances in accurate high-throughput measurement of binding constants, will allow for the creation of libraries of binding partners with various affinities for each target therapeutic. Such a standardized yet versatile controlled release strategy has the potential to improve reproducibility and accelerate optimization of protein delivery systems. ■

The list of author affiliations is available in the full article online.
*Corresponding author. E-mail: molly.shoichet@utoronto.ca
Cite this article as M. M. Pakulska *et al.*, *Science* 351, aac4750 (2016).
DOI: 10.1126/science.aac4750

Downloaded from on March 17, 2016

REVIEW

CHEMISTRY

# Designer protein delivery: From natural to engineered affinity-controlled release systems

Malgosia M. Pakulska,[1] Shane Miersch,[2] Molly S. Shoichet[1,3]*

**Exploiting binding affinities between molecules is an established practice in many fields, including biochemical separations, diagnostics, and drug development; however, using these affinities to control biomolecule release is a more recent strategy. Affinity-controlled release takes advantage of the reversible nature of noncovalent interactions between a therapeutic protein and a binding partner to slow the diffusive release of the protein from a vehicle. This process, in contrast to degradation-controlled sustained-release formulations such as poly(lactic-co-glycolic acid) microspheres, is controlled through the strength of the binding interaction, the binding kinetics, and the concentration of binding partners. In the context of affinity-controlled release—and specifically the discovery or design of binding partners—we review advances in in vitro selection and directed evolution of proteins, peptides, and oligonucleotides (aptamers), aided by computational design.**

Molecular medicine has allowed us to find and characterize the fundamental molecular or genetic causes of many diseases and injury pathologies. Although small-molecule drugs remain valuable, protein-based drugs have emerged as a way to correct such pathologies using innate processes. Examples include the use of insulin to treat diabetes (*1*), antibodies against vascular endothelial growth factor (VEGF) to treat hyperactive vasculature in wet age-related macular degeneration (*2*), and erythropoietin to treat anemia (*3*). The protein drug market was worth $151.9 billion in 2013 and is expected to reach $222.7 billion by 2019 (*4*). This includes proteins that directly serve a therapeutic purpose (e.g., insulin, antibodies), protein vaccines (e.g., the HPV vaccine), and protein-based diagnostics (e.g., technetium-labeled antibodies for imaging) (*5*).

Despite the commercial availability of protein drugs, their formulation and delivery still pose substantial challenges (*6*). Most protein drugs are currently administered by repeated injections and, to the best of our knowledge, only one sustained release protein formulation has been clinically approved (Nutropin Depot, Alkermes and Genentech) (*7*, *8*). With protein activity dependent on tertiary or even quaternary structure, sustained-release strategies developed for small-molecule drugs, such as encapsulation within poly(lactic-co-glycolic acid) microspheres, have proven difficult to translate. These microspheres are typically prepared using a double-emulsion solvent evaporation process, where organic solvents and shear stress can cause protein instability and consequent loss of function. Affinity-controlled release is an alternative sustained-release strategy that is attractive for protein drugs, because the components can usually be mixed together in a neutral aqueous environment with low losses and high loading.

Affinity is a general term used to refer to a preferred noncovalent interaction (electrostatic, hydrophobic, and/or van der Waals) between two binding partners, such as protein-protein, protein-peptide, or protein-polymer interactions. Affinity-controlled release takes advantage of these interactions to slow the diffusion of a drug from a release system. This is usually achieved by immobilizing a drug-binding ligand within a polymer matrix, often a hydrogel.

The challenge in affinity-controlled release is finding the right binding partners to achieve the desired release profile. Although many naturally occurring binding partners exist, the discovery and engineering of novel binding partners through advances in in vitro selection, directed evolution, and computational design have presented new possibilities for controlling biomolecule release using affinity (Fig. 1). A recent review of binding interactions used for affinity-controlled release (*9*) is a useful accompaniment to this review. Whereas the previous review focuses on the affinity-controlled release systems that have been used to date, this review aims to show how binding partners can be discovered or designed in order to make affinity-controlled release a convenient strategy for sustained drug release.

## Characterizing binding partners for affinity-controlled release

Affinity itself is not a novel concept: Scientists have been exploiting affinity between molecules for decades in enzyme-linked immunosorbent assay, immunostaining, and purification techniques, among others. To be successful, these laboratory techniques rely on strong and specific interactions that are often considered to be nearly irreversible. All affinity interactions, however, exist in equilibrium. This dynamic equilibrium is what makes affinity binding useful for controlled biomolecule release.

In a simple bimolecular affinity system, two molecules associate at a rate of $k_{on}$ to form a complex and dissociate at a rate of $k_{off}$ (Fig. 2). The ratio of these two rates determines the ratio of free and bound species at equilibrium and is defined as the equilibrium dissociation constant, $K_d$ (Eq. 1).

$$K_d = \frac{[\text{free species}]_{eq}}{[\text{bound species}]_{eq}} = \frac{k_{off}}{k_{on}} \quad (1)$$

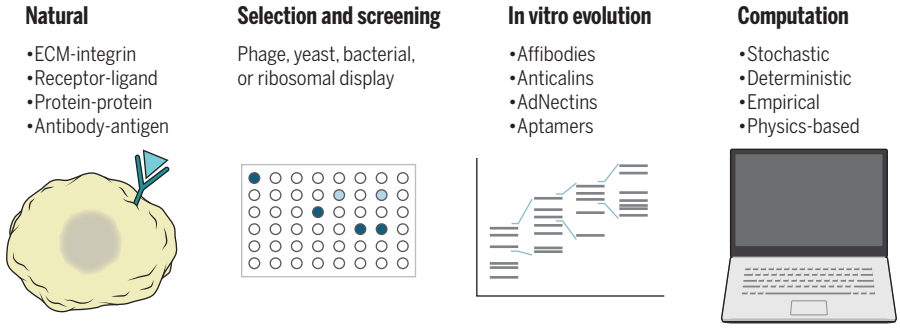



**Fig. 1. Interactions suitable for affinity-controlled release can be discovered or designed in different ways.** Naturally occurring interactions such as antibody-antigen or receptor-ligand binding (shown on the left) can be exploited for affinity-controlled release. Members of a protein or peptide library can be selected and screened for their ability to bind a target using display methods (e.g., phage, yeast, bacterial, or ribosomal) or yeast two-hybrid systems. In vitro selection can be combined with diversification steps (e.g., random mutagenesis) in multiple iterative rounds to obtain in vitro–evolved ligands that bind a specific target. Computational methods can be used to design sequences and structures that bind a target.

[1]Department of Chemical Engineering and Applied Chemistry, Institute of Biomaterials and Biomedical Engineering, and Donnelly Centre, University of Toronto, Toronto, Ontario, Canada. [2]Department of Molecular Genetics, University of Toronto, Toronto, Ontario, Canada. [3]Department of Chemistry, University of Toronto, Toronto, Ontario, Canada.
*Corresponding author. E-mail: molly.shoichet@utoronto.ca (M.S.S.)

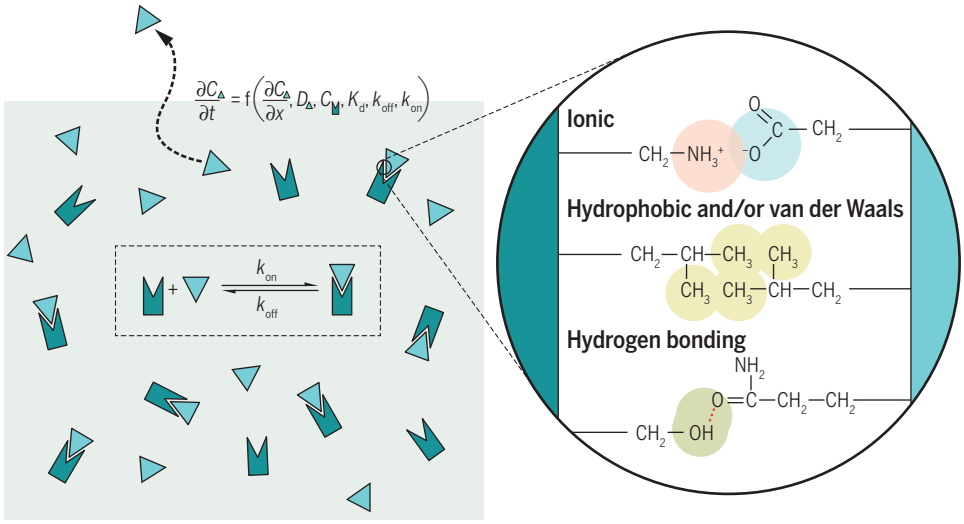



**Fig. 2. Schematic of an affinity-controlled release system.** A protein therapeutic (triangle) binds reversibly to an immobilized binding ligand (polygon) within a polymer matrix via electrostatic (ionic or hydrogen-bonding), hydrophobic, and/or van der Waals interactions. Diffusive release [the change in concentration ($C_{[triangle]}$) over time ($t$); dashed arrow] of the therapeutic from the hydrogel is governed by the protein concentration gradient ($dC/dx$), its diffusivity within the matrix ($D$), the concentration of the immobilized binding ligand ($C_{[polygon]}$), the equilibrium dissociation constant ($K_d$), and the binding kinetics ($k_{on}$ and $k_{off}$).

The rate of release from an affinity-controlled system is governed by both diffusion and the association-dissociation reaction (Fig. 2). Generally speaking, the stronger the interaction (smaller $K_d$) and/or the higher the concentration of the immobilized binding partner, the slower the release. In-depth analysis of how individual factors affect affinity-controlled release rates and release profiles can be found in (*10*–*12*).

To fully characterize a binding pair for affinity-controlled release, $K_d$ and either $k_{on}$ or $k_{off}$ must be known. The most commonly used methods for quantifying affinity binding interactions are isothermal titration calorimetry (ITC), surface plasmon resonance (SPR), quartz crystal microbalance (QCM), and spectroscopic methods, although only SPR and QCM provide kinetic data (*13*, *14*).

ITC is the most common approach for obtaining thermodynamic data for molecular interactions, but it provides no information about kinetics and is limited to solution-based equilibria (*15*). SPR and QCM are both powerful measurement methods because they give binding information in real time and provide kinetic as well as equilibrium data (*16*, *17*); however, they require the immobilization of one of the components, potentially affecting the binding interaction (*18*).

Spectroscopic methods include fluorescent correlation spectroscopy (*19*), fluorescence anisotropy (*20*, *21*), and Förster resonant energy transfer (FRET) (*22*). These methods can also provide insight into the nature of the binding site and the distance between fluorescent tags on the two bound molecules (*14*), but the presence of fluorophores or fluorescent tags can change the environment around the binding site, possibly resulting in inaccurate measurements. Spectroscopic methods usually have low sensitivity, requiring strong binding ($K_d < 10^{-6}$ M) or high concentrations (millimolar range) to be effective. Table 1 summarizes the characteristics of these techniques.

These current experimental methods to measure binding constants are time-consuming. For tunable release rates based on variable binding strength, we need methods to measure $K_d$ and kinetics in a high-throughput manner so that we can create libraries of molecules with a range of $K_d$ for the same drug target.

Several advances are being made in instrumentation for high-throughput screening of binding constants. Miniaturization of ITC instruments has decreased the sample size and measurement time required, although measurements are still performed in series. Array calorimetry, in which multiple measurements are performed in parallel, is an emerging technology but is not yet available commercially (*23*). SPR microscopy (SPRM) is essentially SPR with a charge-coupled device detector array, offering high spatial resolution for each binding event (*24*, *25*). This can be coupled with patterned microarrays of biomolecules or microfluidics (*26*) for a high-throughput method of measurement. Similarly, a QCM sensor array coupled with microfluidics could be used for high-throughput QCM measurements (*27*).

Spectroscopic methods can be combined with microfluidics for massively parallel measurements of binding kinetics. Geertz *et al.* (*28*) used mechanically induced trapping of molecular interactions in a microfluidic platform to simultaneously analyze the kinetics of transcription factors binding to their fluorescently labeled DNA ligands—a total of 223 unique interactions. These interactions have a range of $K_d$ values and tend to have high association rates and short half-lives, making them challenging to measure using standard techniques (*28*, *29*).

An additional challenge is quantifying the interaction of biomolecules immobilized to a polymer matrix, as is often the case in affinity-controlled release systems. In this sense, measurement methods where one of the molecules is immobilized, such as SPR and QCM, may best emulate the release conditions if the method of attachment is the same (*30*). Other methods include indirect measurement of binding constants by fitting experimental data to adsorption or diffusion models for molecules within the gel (*31*). For example, the binding constant for a protein immobilized to a gel was measured by observing the diffusion of its binding partner after wet-stamping it on specific sites on the gel surface (*32*). Indirect methods such as this, however, are not high-throughput, and SPRM coupled with microfluidics may be the current option that best mimics the affinity-controlled release environment.

Another important characteristic of a binding pair is specificity, especially in the context of the simultaneous release of multiple therapeutics. Interaction strength is often mistaken for high specificity, but these are different concepts (*33*). Interaction strength is the difference in free energy between bound and unbound states ($\Delta G$), whereas specificity is the difference in the $\Delta G$ of binding between two different binding pairs ($\Delta\Delta G$).

Although we think of bimolecular interactions as single binding events, each one is actually made up of many individual, interdependent events. Specificity can be independent of affinity if there are individual interactions that confer no energy change from the unbound to the bound state, such as if the decrease in the free energy of the interaction is exactly balanced by the increase in free energy caused by the removal of water. These interactions would then contribute to the specificity of binding but not to the overall strength (affinity) of the interaction (*34*). Similarly, one might think a higher complementary surface area would result in higher specificity, but this is not always the case. A major reorganization upon binding could lead to higher energy costs to the molecule that outweigh the benefits of a larger complementary interface. An alternative binding partner with a less desirable interface but with no requirement for reorganization might therefore preferentially interact (*35*).

## Affinity-controlled release inspired by nature

The noncovalent interaction between heparin in the extracellular matrix (ECM) and a series of growth factors serves as the inspiration for many of the affinity-controlled release systems pursued today. Within the ECM, heparin binds growth factors such as basic fibroblast growth factor

**Table 1. Comparison of methods used to quantify affinity binding interactions.** Data are from (13–22, 146). $\Delta H$ and $\Delta S$ are the enthalpy and entropy of binding, respectively.

| Method | ITC | SPR | QCM | Spectroscopic methods |
|---|---|---|---|---|
| $K_d$ range | $10^{-3}$ to $10^{-9}$ M | $10^{-3}$ to $10^{-12}$ M | $10^{-4}$ to $10^{-10}$ M | $< 10^{-6}$ M |
| Thermodynamic data ($\Delta H$, $\Delta G$, $\Delta S$)? | Yes | No | No | No |
| Kinetic data ($k_{on}/k_{off}$)? | No | Yes | Yes | No |
| Immobilization? | No | Yes | Yes | No |
| Modifications (e.g., fluorescent tag)? | No | No | No | Yes* |
| High-throughput potential | Array calorimetry | SPR microscopy coupled with microfluidics | QCM sensor array coupled with microfluidics | Coupled with microfluidics |

*Except for cases of innate fluorescence (e.g., tryptophan fluorescence).

(bFGF), VEGF, and nerve growth factor (NGF) with $K_d$ values ranging from $10^{-6}$ to $10^{-9}$ M (36). The earliest examples of affinity-controlled release used albumin-heparin microspheres to control the release of adriamycin, a cytostatic agent (37), or heparin-Sepharose beads within alginate microcapsules to control the release of bFGF (38, 39). There are now numerous studies that have taken advantage of heparin for affinity-controlled release of bFGF (40, 41), VEGF (41, 42), NGF (43), neurotrophin 3 (43, 44), brain-derived neurotrophic factor (43), and bone morphogenic protein 2 (45), among others. However, the heterogeneity and promiscuity of heparin make it challenging to reproduce and control binding.

Binding to heparin is primarily mediated by electrostatic interactions with sulfate groups that are negatively charged at physiological pH. Other anionic polymers, such as sulfated alginate (46, 47) and gelatin (48, 49), have also been used for affinity-controlled release because of their potential for electrostatic interactions. Gelatin can be produced recombinantly with specific isoelectric points, thus increasing control over binding strength (50). Molecular imprinting is another method to generate affinity for a specific molecule within a polymer. Molecularly imprinted polymers are synthesized in the presence of the imprinting molecule, thereby retaining pockets that specifically recognize this molecule. Although molecular imprinting has been used for affinity-controlled release of small molecules (51), the synthesis of polymers that can specifically recognize proteins remains a challenge because of protein size and flexibility and the necessity for aqueous conditions (52). Additionally, once imprinted, a polymer must remain intact, limiting injectability and the potential for minimally invasive application.

Other molecules with known binding partners, such as albumin (53) and antibodies (54), have also been used for affinity-controlled release. Proteins that do not have well-known binding partners have been recombinantly expressed as fusions with a binding domain. For example, Jeon *et al.* sustained the release of a FGF-collagen binding domain fusion protein from collagen matrices for up to 7 days to promote angiogenesis in ischemic organs (55). Other recombinant strategies have employed Src homology domain 3 and its binding partners to control the release of protein therapeutics such as bFGF, chondroitinase ABC, and insulin growth factor 1 fusion proteins from hydrogels for 7 days or more (56–58).

## In vitro selection and directed evolution of binding peptides and proteins

If an appropriate binding interaction for a therapeutic protein of interest is not known, in vitro selection and directed evolution can be used to identify and optimize novel protein-protein or protein-peptide interactions for use in affinity-controlled release. The process of designing affinity partners proceeds through (i) the creation of a combinatorial DNA library by means of mutagenesis of a known peptide sequence or protein scaffold; (ii) the display of the peptide or protein variants using phage, bacteria, yeast, ribosome, or mRNA display; and (iii) in vitro selection of variants from the displayed library through repeated rounds of exposure to the target of interest, capture, elution, and amplification. The term "scaffold" here represents a protein backbone within which mutations can be made, rather than a biomaterial for tissue engineering applications. Selected variants can then be characterized for affinity, specificity, and stability and stratified for application and/or continued engineering of desired attributes using directed evolution (Fig. 3). Efforts in this field have resulted in the identification of a wide variety of novel interactions that could be exploited for affinity-controlled release applications, and a database of affinity peptides (MimoDB) now exists (59).

Directed evolution offers a powerful means of modifying a protein to obtain desirable properties. These methods begin with a lead binding candidate and involve multiple iterative rounds of randomization, selection against a target under evolutionary pressures to eliminate undesirable clones, and characterization of variant properties (Fig. 3). Although examples of the directed evolution of antibodies are numerous (60, 61), their larger size, more complex architecture, and high binding affinities limit their utility for affinity-controlled release. Increasingly, smaller protein scaffolds (62, 63) are being designed for use as protein therapeutics, diagnostics, and imaging agents (62–64). Each step in the in vitro selection and directed evolution process is described below in the context of affinity-controlled release.

### Combinatorial libraries and randomization

The purpose of randomization is to sample as large a sequence space as possible in order to identify a variant with desired properties, while considering limitations imposed by the display platform and the approach to randomization.

For short peptides, randomization can be achieved by direct chemical synthesis using solid-phase split-mix synthesis. In this approach, a different amino acid is coupled to each pool of nascent peptide; the pools are then mixed and split again. The process is repeated, resulting in an exponential increase in the number of peptide variants with each round (65). Split-mix synthesis has been used to rationally design a combinatorial library of peptides to bind VEGF. In this instance, the amino acids were chosen to mimic the VEGF binding region of heparin and included four sulfated residues. Peptides that bound VEGF were selected using a microbead-based binding assay with fluorescently modified VEGF and characterized by SPR. The strongest resulting binding peptide bound VEGF with a $K_d$ of $3.1 \times 10^{-6}$ M (66). Although arguably simpler given the lack of intermediate organisms (e.g., bacteria or phage), this type of approach is limited to small peptides, which may not provide enough diversity to achieve a desired interaction.

Alternatively, for longer peptides and proteins, combinatorial libraries for use in in vitro selection can be generated by means of mutagenesis. Mutagenesis can be achieved by random position methods [(error-prone polymerase chain reaction (PCR)], mutagenic oligonucleotide–based methods [hard and soft randomization, custom codon (67), and di- and tri-nucleotide codons (68–70)], or recombination-based block-shuffling methods (71). Although error-prone PCR is a popular method, only one to three mutations are introduced per gene at random (72, 73), leaving little room for rational design. In contrast, mutagenic oligonucleotide–based methods offer more refined control over the position and type of mutations that are introduced, which can help to limit

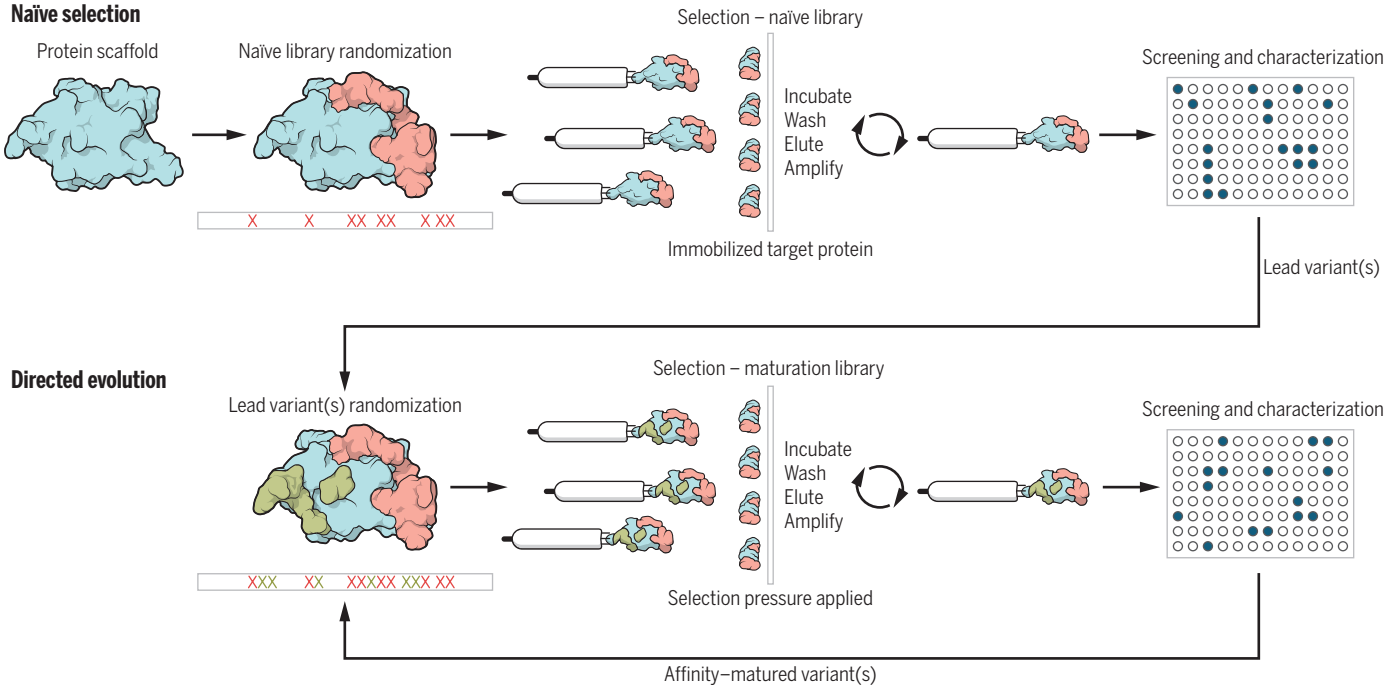



**Fig. 3. Naïve selection and/or directed evolution can be used to find and optimize novel binding partners for a target.** For illustration, regions of a protein scaffold displayed on the surface of a phage (depicted in white) are colored corresponding to mutations (a series of X's) shown in the primary sequence below the structure. Scaffold protein or peptide candidates are randomized to generate naïve libraries for use in in vitro selection against immobilized target proteins. Target-binding variants are captured and enriched from libraries in repeated rounds of selection, then characterized and ranked to identify lead variants. Successive rounds of protein or peptide lead randomization and selection under affinity-modifying pressures (antigen or competitor concentration, binder valency, and temperature) enable exploration of possible binding interfaces. By directing the evolution of binding properties, a system suitable for tunable affinity-controlled release can be achieved.

the number of nonfunctional variants in the library. Random position and oligonucleotide-based approaches are often viewed as complementary.

When developing randomization schemes, it is important to strike a balance between the theoretical diversity that can be introduced and the limitations of the display platform. For instance, hard randomization using NNN oligonucleotides (where N represents equal proportions of A, C, G, and T) in nine positions could create $20^9$ or $5.12 \times 10^{11}$ unique clones, approaching the limit of what can be captured with some display methods (discussed in the next section). The simple use of NNK or NNS oligonucleotides (where K indicates an equal proportion of G and T, and S indicates an equal proportion of C and G) still permits all 20 amino acids, while reducing the number of nonfunctional clones by eliminating two of the three stop codons (*67*). Redundancy in the genetic code may also result in various degrees of amino acid bias. Combinatorial approaches such as di- and tri-nucleotide block precursors (*68*, *69*, *74*) for oligonucleotide synthesis can further reduce or eliminate redundancy but may be prohibitively expensive for some laboratories. Novel combinatorial strategies are being devised to generate both cost-effective and nondegenerate mutagenic primers and have been assisted by computational efforts (*75*–*77*). Investigators should consider the type or scope of mutations incorporated and the potential forms of bias in each approach when developing selection and evolution strategies for a particular application (*74*).

For identification of novel binding pairs, numerous protein scaffolds have been shown to be amenable to randomization and the development of de novo binding interfaces (*78*–*81*). These efforts have been aided by the existence of structural information that can facilitate rational engineering choices regarding (i) the types of mutations that are likely to be tolerated by various regions and structures and (ii) the identification of residues and regions that contribute critically to binding interactions when randomizing the binding surface. Additionally, computational techniques such as protein docking can aid in identifying scaffold proteins with shape and electrostatic complementarity for a target (discussed below) (*82*). Currently, the majority of these engineered proteins function as antagonists, blocking interactions by binding receptors or soluble factors. If these molecules were immobilized in a polymer matrix, they could instead act as a depot for their selected binding partner and prolong therapeutic action. For example, a VEGF antagonist, Angiocal, is designed to treat solid tumors (*83*); however, one could reverse this strategy and use it for affinity-controlled release of VEGF, which has been studied as a therapeutic in numerous tissue-regeneration applications, including cardiac repair after infarction or heart failure (*84*). Thus, the same technology that is used to sequester VEGF could be leveraged to create a simple, well-defined, tunable VEGF delivery system.

### Display platforms

Display platforms translate the genetic information in the combinatorial library to peptides and proteins, effectively coupling genotype and phenotype, for subsequent exposure to the target of interest and the isolation and characterization of binding clones.

Phage display using a filamentous phage, such as M13, f1, or fd, is one of the most widely used display methods because of its high phage titers, library diversity ($10^9$ to $10^{11}$ variants), and easy access to encoding genes (*85*, *86*). The option of displaying proteins as either a fusion with pIII (monovalent) or pVIII (polyvalent) phage coat protein may be particularly useful for affinity-controlled release applications, because avidity effects during polyvalent display can promote the isolation of weaker binders. Peptides (*87*, *88*) and small and mid-size homo- or heteromeric proteins—such as fibronectin (Adnectin) domains (*81*), three-helical bundles (*89*, *90*), anticalins (*79*), and atrimers, among others (*62*, *80*)—have been successfully selected and engineered from phage-displayed libraries. Recent reports describe the use of a commercial phage-displayed peptide library to find short peptide sequences that bind heparin or NGF for subsequent use in affinity-controlled release; identified peptides were coupled

to fibrin matrices for controlled release of heparin and NGF (*91*) or NGF alone (*92*), with the rate of release being dependent on the strength of the interaction (*91*).

Cell-surface display methods are attractive because of their potential for coupling with fluorescence-activated cell sorting for high-throughput analysis and separation. Efforts to develop bacterial cell-surface display have demonstrated display levels sufficient to observe enrichment of binding variants (*93*), library sizes ranging from $10^9$ to $10^{10}$ (*94*), and suitability for use in isolating constrained peptides (*95*, *96*) and in antibody affinity maturation (*97*). Despite these efforts, challenges associated with presentation of displayed peptides and proteins on the outer membrane have thus far limited the utility of this approach (*95*, *96*). Additionally, bacteria are not capable of eukaryotic posttranslational modifications that are sometimes required for proper protein folding and function.

Yeast surface display is a eukaryotic alternative to bacterial display, circumventing the challenges faced during heterologous protein expression. The use of a variety of strains of yeast and approaches to membrane anchoring have been demonstrated (*98*, *99*); however, the Aga2p fusion system in *Saccharomyces cerevisiae* remains the most widely used (*100*). Library variants are expressed as an N- or C-terminal fusion with a secreted Aga2p subunit, which is then captured by means of disulfide linkages to a plasma membrane–anchored Aga1p subunit. One of the primary limiting factors of yeast surface display is library size, which usually ranges from ~$10^7$ to $10^9$ variants, although increased functionality due to eukaryotic expression may offset this limitation. Yeast surface display has been successfully used to isolate and engineer peptides (*101*), protein scaffolds (*102*), single-chain antibody fragments (scFvs) (*103*), and T cell receptors (*104*).

In contrast to the above platforms that rely on efficient DNA transformation and cellular propagation for display, ribosomal and mRNA display methods offer a fully in vitro alternative. Without the need for living cells, library sizes of $10^{12}$ to $10^{14}$ variants are frequently achieved. These two approaches are similar in that they generate mRNA transcripts and protein variants from the DNA library by in vitro transcription and translation. However, the means by which the translated protein variants are coupled to their encoding transcript for purification and use in selections differ (*105*). Ribosomal or mRNA display methods have been successfully used in the selection and evolution of various types of binders, including high-affinity cyclic peptides (*106*), serum-stable peptides (*107*), scFvs (*73*), and a growing body of protein scaffolds (*78*, *108*), which could conceivably be used for tunable affinity-controlled release.

### *Screening strategies for affinity-controlled release*

To promote the isolation of variants with desired properties, it is critical to optimize selection conditions, including the method of display, target concentration, presence of competitors, and time and temperature of incubation, among others. For example, off-rate selections with a long incubation period and a large excess of a soluble binding competitor enabled the isolation of a peptide-binding scFv clone with a $K_d$ of ~5 pM(*73*). This and other screening strategies for drug development are usually designed to isolate the strongest binders; however, for affinity-controlled release, a range of dissociation constants from the millimolar to the nanomolar scale would be desired. To achieve this, selection conditions favoring intermediate binders, such as high target concentrations and polyvalent display, may be favorable. Strategies that provide a progressive improvement in affinity, such as iterative rounds of in vitro evolution, would enable the isolation of a series of related variants with a spectrum of affinities that could then be explored for tunable affinity-controlled release.

Competition selections with soluble target competitors are a common method of applying selective pressure to enhance affinity by removing lower-affinity binders; similar approaches can also enhance the specificity of binding variants for a target. Enhanced specificity would be important for the simultaneous affinity-controlled release of multiple therapeutic proteins. This strategy was successfully demonstrated in the isolation of a variant of a serine protease inhibitor, ecotin, that bound plasma kallikrein with a $K_d$ of 11 pM but had equilibrium dissociation constants for five related proteases (FXa, FXIa, FXIIa, MT-SP1, and plasmin) that were four to seven orders of magnitude higher (*109*). The versatility of this strategy was further demonstrated by varying screening conditions to allow the isolation of other ecotin variants with specificities for other proteases.

Another strategy that is relevant for affinity-controlled release is the engineering of bispecificity in a protein scaffold. Nilvebrant *et al.* engineered the albumin-binding domain 3 of the streptococcal protein G both for high-affinity binding of ErbB2 and tunable binding to human serum albumin (*110*). Many of the novel protein scaffolds that have been described recently are below the renal filtration cutoff of 60 kDa and are rapidly cleared from circulation (*80*). Because it is an abundant and long-lived serum protein, binding to albumin can reduce the rate of clearance. Similarly, engineering a small protein scaffold to bind both a polymeric vehicle and a therapeutic target could provide tunable affinity-controlled release of the therapeutic from the vehicle. In this case, the engineered protein would act as an intermediate between the delivery vehicle and the therapeutic, allowing the same vehicle to be used for the delivery of a range of therapeutics.

## Directed evolution of oligonucleotides (aptamers)

Aptamers are short oligonucleotides that derive their name from the Latin word "aptus," meaning "to fit." They are selected by directed evolution to bind a specific target using a process termed SELEX (systematic evolution of ligands by exponential enrichment). Similarly to the directed evolution of proteins described above, the process begins by subjecting a random sequence pool of RNA or DNA to a binding assay with a target. The sequences that bind are selected, amplified by PCR, diversified, and resubjected to the same binding assay. This process is repeated until all the RNA or DNA ligands can bind to the target with high affinity (*111*, *112*). Theoretically, this method can be used to generate high-affinity ligands for any therapeutic protein target.

Aptamers have several advantages over antibodies, including no requirements for animals or cells, ease of synthesis, and the ability to select for binders under nonphysiological conditions (*113*); however, they suffer from short serum half-lives (*114*). Nevertheless, aptamers are being investigated for a variety of applications (*115*). Aptamer microarrays and photo–cross-linkable variants (*116*) allow screening for the presence of protein targets in diagnostic applications (*115*, *117*). Aptamers can also act as therapeutics, and at least one aptamer-based therapeutic is currently in clinical use (*118*). In drug delivery, aptamers are being investigated for their potential to enable targeted drug delivery to specific tissues, especially in cancer (*119*–*121*).

The use of aptamers for affinity-controlled release has emerged within the past 5 years. Aptamer affinity can be tuned by selection conditions, but most selection methods are designed to isolate high-affinity binders. An alternative approach is to select for a high-affinity aptamer and mutate the essential nucleotides to obtain a library of affinities. This technique has resulted in aptamers that bind platelet-derived growth factor (PDGF)–BB with affinities ranging from 11 to 350 nM. Conjugation of these aptamers to a series of hydrogels—agarose, poloxamer, and polyethylene glycol (PEG) diacrylate—resulted in the tunable release of PDGF-BB (*122*, *123*). High-throughput, parallel measurements of aptamer binding constants have generated large libraries of aptamers for a specific target (*124*).

Aptamers have also been evolved to bind non-protein targets such as peptides, small molecules, or nucleic acids (*115*). For example, aptamers selected to bind tetracycline with high affinity were conjugated to a PEG hydrogel, which increased tetracycline loading relative to unmodified gels. This resulted in increased and prolonged antibiotic release and ultimately decreased bacterial proliferation between 12 and 72 hours after treatment (*125*).

Structure-switching aptamers (SSAs) that are capable of controlled cargo release in response to allosteric binding of a specific target molecule have recently been reported (*126*). These SSAs selectively released a fluorescent cargo in response to allosteric binding of adenosine triphosphate (ATP) through a conformational change. The selection procedure involved isolating sequences that selectively unbound from a column containing the cargo in the presence of ATP. Such

ligands could provide a method for triggered affinity-controlled release.

## Computational design

Computational design of protein-protein interactions has the potential to generate binding partners for any therapeutic protein of interest. Although identification of new protein-protein interactions remains difficult and computationally intensive, completely new protein folds and topologies have been generated (*127*), as have enzymes with activities not found in nature (*128*) and proteins with entirely new binding interfaces (*129*–*131*).

Computational protein design has two main steps: (i) sampling of the conformational and sequence space and (ii) scoring of the resulting protein candidates (*132*, *133*). The pool of all possible conformations and sequences is initially reduced by starting with a fixed backbone conformation and/or through the a priori definition of fixed residues at the binding interface ("hotspots") (*130*). The chosen backbone conformation can be based on an existing three-dimensional (3D) structure or on a de novo design (*127*). Molecular docking simulations are often used initially to determine which backbone conformations exhibit reasonable geometric compatibility with the target of interest (*134*, *135*). The sequence-conformational space is then sampled within these restrictions using stochastic (e.g., Monte Carlo) or deterministic (e.g., dead-end elimination) (*136*) search algorithms. In designing a protein that binds a specific target, the focus is on optimization of the residues at the interface. Resulting candidates are filtered by scoring algorithms that can be knowledge-based (relying on empirical data collected from protein databases) or physics-based (derived from physical principles).

Computational design has not been used directly for affinity-controlled release to date, but it has been successfully used to design novel protein-protein (*82*, *131*) and protein–small molecule (*130*) binding pairs. Tinberg *et al.* (*130*) designed a protein that could bind the steroid digoxigenin (DIG), which is the deglycosylated form of digoxin, a cardiac glycoside used to treat heart disease (*137*). Digoxin has a narrow therapeutic window and could benefit from a controlled release strategy. Five predefined hotspot interactions, including hydrogen bonds to the polar groups on DIG and hydrophobic packing interactions among the steroid ring system, were placed at geometrically compatible sites in a set of scaffold protein structures. The rest of the binding site amino acids were then optimized for binding affinity and protein stability using RosettaDesign. Designs were scored based on interface energy, solvent-exposed surface area, binding orientation, shape complementarity, and binding site preorganization. Seventeen candidates were chosen for experimental testing, and the tightest binder bound DIG with a $K_d$ of 12.2 μM, determined by ITC. Directed evolution was then used to increase the binding affinity even further (*130*), yet even the initial affinity would be useful for affinity-controlled release. Computational design could also lead to more sophisticated affinity-controlled release systems. For example, a pH-dependent immunoglobulin G (IgG) binding protein has been generated using hotspot-guided computational protein interface design (*138*). This protein has a $K_d$ for IgG of 4.0 nM at pH 8.2 but only 3.8 μM at pH 5.5. If this protein was conjugated to a polymer scaffold, it could provide triggered affinity-controlled release of IgG upon exposure to a low-pH environment, such as that encountered in tumor tissues (*139*–*141*).

Despite this progress, many challenges still remain in the computational design of protein-protein interfaces. The extreme diversity of protein interfaces makes it difficult to predict energetically important interactions, especially because many proteins undergo substantial reorganization upon binding that may not be captured in traditional lock-and-key binding models (*132*, *142*). Solvent effects must also be considered, including energetically unfavorable desolvation of polar residues at the binding interface or the presence of explicit water molecules that are directly involved in binding interactions (*143*). Except in the case of truly de novo design, computational methods rely on 3D structures of homologous proteins as a starting point; thus, limited structural information can present a bottleneck. Global efforts in structural genomics (*144*) and advances in homology modeling methods (*145*) are accelerating determinations of macromolecular structure, thereby increasing the number of available structures and opening this bottleneck in the computational design of binding partners.

## Future outlook on affinity-controlled release

Affinity-controlled release provides significant advantages over traditional sustained drug-release strategies and is likely to be widely adopted in the drug delivery community. The elimination of organic solvents and high shear forces, which are typically used for protein encapsulation in synthetic water-insoluble polymers, enables higher active therapeutic loading for the same amount of polymer vehicle. Although there is still a certain amount of trial and error required to obtain the desired release profile from a protein encapsulated within polymeric micro- or nano-particles, mathematical modeling of affinity-controlled release has defined the variables important to control release profiles: For a known dose and characteristic diffusion length, the required $K_d$ and immobilized ligand concentration can be calculated (*12*).

Advances in computational design, in vitro selection, and directed evolution offer new ways to discover or design suitable binding partners for affinity-controlled release. Combining these methods will further increase efficiency. The use of computational techniques to identify scaffolds with geometric and electrostatic properties that are complementary to a target could reduce the upfront empirical screening required to isolate lead variants. Alternatively, in silico methods could also help identify critical binding interactions that can rationally guide mutagenesis and randomization. High-throughput measurement methods for $K_d$ and association rates would then be needed to create libraries of binding partners for a variety of therapeutics.

To effectively treat complex diseases, combinatorial drug strategies will probably be required. Ideally, a single delivery system could be designed to release multiple therapeutics, each with its own independent release profile. This is the next frontier for affinity-controlled release systems and requires affinity interactions that are specific and nonpromiscuous. For affinity-controlled release applications of multiple therapeutics, it will therefore be important to perform competitive selections to determine specificity and ensure independent control of the release rate.

On-demand drug release, using stimulus sensitivity, presents another opportunity for affinity-controlled release. Although systems such as structure-switching aptamers or computationally designed pH-dependent binding proteins have shown promise, this area is open to innovation.

Affinity-controlled release has great potential to be expanded in scope and provide fully customized delivery solutions. We envision a modeling program that would suggest a binding ligand from an existing library based on the desired release profile and protein therapeutic. This ligand would then be tested for affinity-controlled release of the protein therapeutic after covalent attachment to a well-defined polymeric vehicle.

## REFERENCES AND NOTES


1. K. Mane, K. Chaluvaraju, M. Niranjan, T. Zaranappa, T. Manjuthej, Review of insulin and its analogues in diabetes mellitus. *J. Basic Clin. Pharm.* **3**, 283–293 (2012). doi: 10.4103/0976-0105.103822; pmid: 24826038
2. A. Özkiris, Anti-VEGF agents for age-related macular degeneration. *Expert Opin. Ther. Pat.* **20**, 103–118 (2010). doi: 10.1517/13543770902762885; pmid: 20021287
3. W. Jelkmann, Developments in the therapeutic use of erythropoiesis stimulating agents. *Br. J. Haematol.* **141**, 287–297 (2008). doi: 10.1111/j.1365-2141.2007.06948.x; pmid: 18410567
4. BCC Research, *Global Markets for Bioengineered Protein Drugs* (BCC Research, 2014); www.bccresearch.com/market-research/biotechnology/bioengineered-protein-drugs-report-bio009f.html.
5. W. R. Strohl, D. M. Knight, Discovery and development of biopharmaceuticals: Current issues. *Curr. Opin. Biotechnol.* **20**, 668–672 (2009). doi: 10.1016/j.copbio.2009.10.012; pmid: 19896824
6. S. Mitragotri, P. A. Burke, R. Langer, Overcoming the challenges in administering biopharmaceuticals: Formulation and delivery strategies. *Nat. Rev. Drug Discov.* **13**, 655–672 (2014). doi: 10.1038/nrd4363; pmid: 25103255
7. R. Vaishya, V. Khurana, S. Patel, A. K. Mitra, Long-term delivery of protein therapeutics. *Expert Opin. Drug Deliv.* **12**, 415–440 (2015). doi: 10.1517/17425247.2015.961420; pmid: 25251334
8. F. Wu, T. Jin, Polymer-based sustained-release dosage forms for protein drugs, challenges, and recent advances. *AAPS PharmSciTech* **9**, 1218–1229 (2008). doi: 10.1208/s12249-008-9148-3; pmid: 19085110
9. K. Vulic, M. S. Shoichet, Affinity-based drug delivery systems for tissue repair and regeneration. *Biomacromolecules* **15**, 3867–3880 (2014). doi: 10.1021/bm501084u; pmid: 25230248
10. A. S. Fu, T. R. Thatiparti, G. M. Saidel, H. A. von Recum, Experimental studies and modeling of drug release from a tunable affinity-based drug delivery platform. *Ann. Biomed. Eng.* **39**, 2466–2475 (2011). doi: 10.1007/s10439-011-0336-z; pmid: 21678091
11. C.-C. Lin, A. T. Metters, Metal-chelating affinity hydrogels for sustained protein release. *J. Biomed. Mater. Res. A* **83A**,

954–964 (2007). doi: 10.1002/jbm.a.31282; pmid: 17580324
12. K. Vulic, M. M. Pakulska, R. Sonthalia, A. Ramachandran, M. S. Shoichet, Mathematical model accurately predicts protein release from an affinity-based delivery system. *J. Control. Release* **197**, 69–77 (2015). doi: 10.1016/j.jconrel.2014.10.032; pmid: 25449806
13. P. L. Kastritis, A. M. J. J. Bonvin, On the binding affinity of macromolecular interactions: Daring to ask why proteins interact. *J. R. Soc. Interface* **10**, 20120835 (2013). pmid: 23235262
14. K. Vuignier, J. Schappler, J.-L. Veuthey, P.-A. Carrupt, S. Martel, Drug-protein binding: A critical review of analytical tools. *Anal. Bioanal. Chem.* **398**, 53–66 (2010). doi: 10.1007/s00216-010-3737-1; pmid: 20454782
15. J. E. Ladbury, B. Z. Chowdhry, Sensing the heat: The application of isothermal titration calorimetry to thermodynamic studies of biomolecular interactions. *Chem. Biol.* **3**, 791–801 (1996). doi: 10.1016/S1074-5521(96)90063-0; pmid: 8939696
16. M. Willander, S. Al-Hilli, *Micro and Nano Technologies in Bioanalysis*, vol. 544 of *Methods in Molecular Biology* (Humana, 2009).
17. M. C. Dixon, Quartz crystal microbalance with dissipation monitoring: Enabling real-time characterization of biological materials and their interactions. *J. Biomol. Tech.* **19**, 151–158 (2008).pmid: 19137101
18. R. Karlsson, A. Larsson, Affinity measurement using surface plasmon resonance. *Methods Mol. Biol.* **248**, 389–415 (2004).pmid: 14970510
19. P. Schwille, F. J. Meyer-Almes, R. Rigler, Dual-color fluorescence cross-correlation spectroscopy for multicomponent diffusional analysis in solution. *Biophys. J.* **72**, 1878–1886 (1997). doi: 10.1016/S0006-3495(97)78833-7; pmid: 9083691
20. T. Heyduk, Y. Ma, H. Tang, R. H. Ebright, *RNA Polymerase and Associated Factors*, vol. 274 of *Methods in Enzymology Part B* (Elsevier, 1996).
21. T. Heyduk, J. C. Lee, Application of fluorescence energy transfer and polarization to monitor *Escherichia coli* cAMP receptor protein and lac promoter interaction. *Proc. Natl. Acad. Sci. U.S.A.* **87**, 1744–1748 (1990). doi: 10.1073/pnas.87.5.1744; pmid: 2155424
22. Y. Song, V. Madahar, J. Liao, Development of FRET assay into quantitative and high-throughput screening technology platforms for protein-protein interactions. *Ann. Biomed. Eng.* **39**, 1224–1234 (2011). doi: 10.1007/s10439-010-0225-x; pmid: 21174150
23. F. E. Torres, M. I. Recht, J. E. Coyle, R. H. Bruce, G. Williams, Higher throughput calorimetry: Opportunities, approaches and challenges. *Curr. Opin. Struct. Biol.* **20**, 598–605 (2010). doi: 10.1016/j.sbi.2010.09.001; pmid: 20888754
24. C. T. Campbell, G. Kim, SPR microscopy and its applications to high-throughput analyses of biomolecular binding events and their kinetics. *Biomaterials* **28**, 2380–2392 (2007). doi: 10.1016/j.biomaterials.2007.01.047; pmid: 17337300
25. W. Wang *et al*., Label-free measuring and mapping of binding kinetics of membrane proteins in single living cells. *Nat. Chem.* **4**, 846–853 (2012). doi: 10.1038/nchem.1434; pmid: 23000999
26. E. Ouellet *et al*., Parallel microfluidic surface plasmon resonance imaging arrays. *Lab Chip* **10**, 581–588 (2010). doi: 10.1039/b920589f; pmid: 20162233
27. G. S. Huang, M.-T. Wang, M.-Y. Hong, A versatile QCM matrix system for online and high-throughput bio-sensing. *Analyst* **131**, 382–387 (2006). doi: 10.1039/b515722f; pmid: 16496046
28. M. Geertz, D. Shore, S. J. Maerkl, Massively parallel measurements of molecular interaction kinetics on a microfluidic platform. *Proc. Natl. Acad. Sci. U.S.A.* **109**, 16540–16545 (2012). doi: 10.1073/pnas.1206011109; pmid: 23012409
29. S. J. Maerkl, S. R. Quake, A systems approach to measuring the binding energy landscapes of transcription factors. *Science* **315**, 233–237 (2007). doi: 10.1126/science.1131007; pmid: 17218526
30. R. I. Osmond, W. C. Kett, S. E. Skett, D. R. Coombe, Protein–heparin interactions measured by BIAcore 2000 are affected by the method of heparin immobilization. *Anal. Biochem.* **310**, 199–207 (2002). doi: 10.1016/S0003-2697(02)00396-2; pmid: 12423639
31. H. F. EL-Sharif, D. M. Hawkins, D. Stevenson, S. M. Reddy, Determination of protein binding affinities within hydrogel-based molecularly imprinted polymers (HydroMIPs). *Phys. Chem. Chem. Phys.* **16**, 15483–15489 (2014). doi: 10.1039/c4cp01798f; pmid: 24950144
32. Y. Wei, P. J. Wesson, I. Kourkine, B. A. Grzybowski, Measurement of protein-ligand binding constants from reaction-diffusion concentration profiles. *Anal. Chem.* **82**, 8780–8784 (2010). doi: 10.1021/ac102055a; pmid: 20923152
33. J. M. Carothers, S. C. Oestreich, J. W. Szostak, Aptamers selected for higher-affinity binding are not more specific for the target ligand. *J. Am. Chem. Soc.* **128**, 7929–7937 (2006). doi: 10.1021/ja060952q; pmid: 16771507
34. S. J. Davis, E. A. Davies, M. G. Tucknott, E. Y. Jones, P. A. van der Merwe, The role of charged residues mediating low affinity protein-protein recognition at the cell surface by CD2. *Proc. Natl. Acad. Sci. U.S.A.* **95**, 5490–5494 (1998). doi: 10.1073/pnas.95.10.5490 pmid: 9576909
35. D. Szwajkajzer, J. Carey, Molecular and biological constraints on ligand-binding affinity and specificity. *Biopolymers* **44**, 181–198 (1997). doi: 10.1002/(SICI)1097-0282(1997)44:2<181::AID-BIP5>3.0.CO;2-R; pmid: 9354760
36. S. E. Sakiyama-Elbert, Incorporation of heparin into biomaterials. *Acta Biomater.* **10**, 1581–1587 (2014). doi: 10.1016/j.actbio.2013.08.045; pmid: 24021232
37. H. F. M. Cremers *et al*., Albumin-heparin microspheres as carriers for cytostatic agents. *J. Control. Release* **11**, 167–179 (1990). doi: 10.1016/0168-3659(90)90130-L
38. E. R. Edelman, M. A. Nugent, L. T. Smith, M. J. Karnovsky, Basic fibroblast growth factor enhances the coupling of intimal hyperplasia and proliferation of vasa vasorum in injured rat arteries. *J. Clin. Invest.* **89**, 465–473 (1992). doi: 10.1172/JCI115607; pmid: 1371124
39. E. R. Edelman, E. Mathiowitz, R. Langer, M. Klagsbrun, Controlled and modulated release of basic fibroblast growth factor. *Biomaterials* **12**, 619–626 (1991). doi: 10.1016/0142-9612(91)90107-L; pmid: 1742404
40. J. J. Yoon, H. J. Chung, H. J. Lee, T. G. Park, Heparin-immobilized biodegradable scaffolds for local and sustained release of angiogenic growth factor. *J. Biomed. Mater. Res. A* **79A**, 934–942 (2006). doi: 10.1002/jbm.a.30843; pmid: 16941589
41. D. B. Pike *et al*., Heparin-regulated release of growth factors in vitro and angiogenic response in vivo to implanted hyaluronan hydrogels containing VEGF and bFGF. *Biomaterials* **27**, 5242–5251 (2006). doi: 10.1016/j.biomaterials.2006.05.018; pmid: 16806456
42. G. Tae, M. Scatena, P. S. Stayton, A. S. Hoffman, PEG-cross-linked heparin is an affinity hydrogel for sustained release of vascular endothelial growth factor. *J. Biomater. Sci. Polym. Ed.* **17**, 187–197 (2006). doi: 10.1163/156856206774879090; pmid: 16411608
43. S. E. Sakiyama-Elbert, J. A. Hubbell, Controlled release of nerve growth factor from a heparin-containing fibrin-based cell ingrowth matrix. *J. Control. Release* **69**, 149–158 (2000). doi: 10.1016/S0168-3659(00)00296-0; pmid: 11018553
44. S. J. Taylor, J. W. McDonald 3rd, S. E. Sakiyama-Elbert, Controlled release of neurotrophin-3 from fibrin gels for spinal cord injury. *J. Control. Release* **98**, 281–294 (2004). doi: 10.1016/j.jconrel.2004.05.003; pmid: 15262419
45. O. Jeon, C. Powell, L. D. Solorio, M. D. Krebs, E. Alsberg, Affinity-based growth factor delivery using biodegradable, photocrosslinked heparin-alginate hydrogels. *J. Control. Release* **154**, 258–266 (2011). doi: 10.1016/j.jconrel.2011.06.027; pmid: 21745508
46. I. Freeman, S. Cohen, The influence of the sequential delivery of angiogenic factors from affinity-binding alginate scaffolds on vascularization. *Biomaterials* **30**, 2122–2131 (2009). doi: 10.1016/j.biomaterials.2008.12.057; pmid: 19152972
47. I. Freeman, A. Kedem, S. Cohen, The effect of sulfation of alginate hydrogels on the specific binding and controlled release of heparin-binding proteins. *Biomaterials* **29**, 3260–3268 (2008). doi: 10.1016/j.biomaterials.2008.04.025; pmid: 18462788
48. S. Young, M. Wong, Y. Tabata, A. G. Mikos, Gelatin as a delivery vehicle for the controlled release of bioactive molecules. *J. Control. Release* **109**, 256–274 (2005). doi: 10.1016/j.jconrel.2005.09.023; pmid: 16266768
49. M. Sutter, J. Siepmann, W. E. Hennink, W. Jiskoot, Recombinant gelatin hydrogels for the sustained release of proteins. *J. Control. Release* **119**, 301–312 (2007). doi: 10.1016/j.jconrel.2007.03.003; pmid: 17467099
50. D. Olsen *et al*., Recombinant collagen and gelatin for drug delivery. *Adv. Drug Deliv. Rev.* **55**, 1547–1567 (2003). doi: 10.1016/j.addr.2003.08.008; pmid: 14623401
51. N. X. Wang, H. A. von Recum, Affinity-based drug delivery. *Macromol. Biosci.* **11**, 321–332 (2011). doi: 10.1002/mabi.201000206; pmid: 21108454
52. A. Bossi, F. Bonini, A. P. F. Turner, S. A. Piletsky, Molecularly imprinted polymers for the recognition of proteins: The state of the art. *Biosens. Bioelectron.* **22**, 1131–1137 (2007). doi: 10.1016/j.bios.2006.06.023; pmid: 16891110
53. L. Oss-Ronen, D. Seliktar, Photopolymerizable hydrogels made from polymer-conjugated albumin for affinity-based drug delivery. *Adv. Eng. Mater.* **12**, B45–B52 (2010). doi: 10.1002/adem.200980005
54. Y. Zhao *et al*., The osteogenic effect of bone morphogenetic protein-2 on the collagen scaffold conjugated with antibodies. *J. Control. Release* **141**, 30–37 (2010). doi: 10.1016/j.jconrel.2009.06.032; pmid: 19580831
55. E. Jeon, Y.-R. Yun, H.-W. Kim, J.-H. Jang, Engineering and application of collagen-binding fibroblast growth factor 2 for sustained release. *J. Biomed. Mater. Res. A* **102**, 1–7 (2014). doi: 10.1002/jbm.a.34689; pmid: 23468239
56. K. Vulic, M. S. Shoichet, Tunable growth factor delivery from injectable hydrogels for tissue engineering. *J. Am. Chem. Soc.* **134**, 882–885 (2012). doi: 10.1021/ja210638x; pmid: 22201513
57. M. M. Pakulska, K. Vulic, M. S. Shoichet, Affinity-based release of chondroitinase ABC from a modified methylcellulose hydrogel. *J. Control. Release* **171**, 11–16 (2013). doi: 10.1016/j.jconrel.2013.06.029; pmid: 23831055
58. J. Parker, N. Mitrousis, M. S. Shoichet, Hydrogel for simultaneous tunable growth factor delivery and enhanced viability of encapsulated cells in vitro. *Biomacromolecules* **17**, 476–484 (2015). pmid: 26762290
59. J. Huang *et al*., MimoDB 2.0: A mimotope database and beyond. *Nucleic Acids Res.* **40**, D271–D277 (2012). doi: 10.1093/nar/gkr922; pmid: 22053087
60. E. T. Boder, K. S. Midelfort, K. D. Wittrup, Directed evolution of antibody fragments with monovalent femtomolar antigen-binding affinity. *Proc. Natl. Acad. Sci. U.S.A.* **97**, 10701–10705 (2000). doi: 10.1073/pnas.170297297; pmid: 10984501
61. B. P. Yates, M. A. Peck, P. B. Berget, Directed evolution of a fluorogen-activating single chain antibody for function and enhanced brightness in the cytoplasm. *Mol. Biotechnol.* **54**, 829–841 (2013). doi: 10.1007/s12033-012-9631-7; pmid: 23242633
62. H. K. Binz, P. Amstutz, A. Plückthun, Engineering novel binding proteins from nonimmunoglobulin domains. *Nat. Biotechnol.* **23**, 1257–1268 (2005). doi: 10.1038/nbt1127; pmid: 16211069
63. A. Skerra, Alternative non-antibody scaffolds for molecular recognition. *Curr. Opin. Biotechnol.* **18**, 295–304 (2007). doi: 10.1016/j.copbio.2007.04.010; pmid: 17643280
64. K. Hida, J. Hanes, M. Ostermeier, Directed evolution for drug and nucleic acid delivery. *Adv. Drug Deliv. Rev.* **59**, 1562–1578 (2007). doi: 10.1016/j.addr.2007.08.022; pmid: 17933418
65. A. Furka, F. Sebestyén, M. Asgedom, G. Dibó, General method for rapid synthesis of multicomponent peptide mixtures. *Int. J. Pept. Protein Res.* **37**, 487–493 (1991). doi: 10.1111/j.1399-3011.1991.tb00765.x; pmid: 1917305
66. H. D. Maynard, J. A. Hubbell, Discovery of a sulfated tetrapeptide that binds to vascular endothelial growth factor. *Acta Biomater.* **1**, 451–459 (2005). doi: 10.1016/j.actbio.2005.04.004; pmid: 16701826
67. F. A. Fellouse, G. Pal, in *Phage Display in Biotechnology and Drug Discovery*, S. S. Sidhu, C. R. Geyer, Eds. (CRC Press, ed. 2, 2015), pp. 111–142.
68. A. Ono, A. Matsuda, J. Zhao, D. V. Santi, The synthesis of blocked triplet-phosphoramidites and their use in mutagenesis. *Nucleic Acids Res.* **23**, 4677–4682 (1995). doi: 10.1093/nar/23.22.4677; pmid: 8524660
69. B. Virnekäs *et al*., Trinucleotide phosphoramidites: Ideal reagents for the synthesis of mixed oligonucleotides for random mutagenesis. *Nucleic Acids Res.* **22**, 5600–5607 (1994). doi: 10.1093/nar/22.25.5600; pmid: 7838712
70. P. Neuner, R. Cortese, P. Monaci, Codon-based mutagenesis using dimer-phosphoramidites. *Nucleic Acids Res.* **26**, 1223–1227 (1998). doi: 10.1093/nar/26.5.1223; pmid: 9469829
71. W. P. Stemmer, DNA shuffling by random fragmentation and reassembly: In vitro recombination for molecular evolution. *Proc. Natl. Acad. Sci. U.S.A.* **91**, 10747–10751 (1994). doi: 10.1073/pnas.91.22.10747; pmid: 7938023

72. M. Baker, Protein engineering: Navigating between chance and reason. *Nat. Methods* **8**, 623–626 (2011). doi: 10.1038/nmeth.1654; pmid: 21799494
73. C. Zahnd *et al*., Directed in vitro evolution and crystallographic analysis of a peptide-binding single chain antibody fragment (scFv) with low picomolar affinity. *J. Biol. Chem.* **279**, 18870–18877 (2004). doi: 10.1074/jbc.M309169200; pmid: 14754898
74. C. Neylon, Chemical and biochemical strategies for the randomization of protein encoding DNA sequences: Library construction methods for directed evolution. *Nucleic Acids Res.* **32**, 1448–1459 (2004). doi: 10.1093/nar/gkh315; pmid: 14990750
75. C. G. Acevedo-Rocha, M. T. Reetz, Y. Nov, Economical analysis of saturation mutagenesis experiments. *Sci. Rep.* **5**, 10654 (2015). doi: 10.1038/srep10654; pmid: 26190439
76. S. Kille *et al*., Reducing codon redundancy and screening effort of combinatorial protein libraries created by saturation mutagenesis. *ACS Synth. Biol.* **2**, 83–92 (2013). doi: 10.1021/sb300037w; pmid: 23656371
77. L. Tang *et al*., Construction of "small-intelligent" focused mutagenesis libraries using well-designed combinatorial degenerate primers. *Biotechniques* **52**, 149–158 (2012). pmid: 22401547
78. G. Béhar *et al*., Tolerance of the archaeal Sac7d scaffold protein to alternative library designs: Characterization of anti-immunoglobulin G Affitins. *Protein Eng. Des. Sel.* **26**, 267–275 (2013). doi: 10.1093/protein/gzs106; pmid: 23315487
79. D. Schönfeld *et al*., An engineered lipocalin specific for CTLA-4 reveals a combining site with structural and conformational features similar to antibodies. *Proc. Natl. Acad. Sci. U.S.A.* **106**, 8198–8203 (2009). doi: 10.1073/pnas.0813399106; pmid: 19416843
80. R. Vazquez-Lombardi *et al*., Challenges and opportunities for non-antibody scaffold drugs. *Drug Discov. Today* **20**, 1271–1283 (2015). doi: 10.1016/j.drudis.2015.09.004; pmid: 26360055
81. A. Koide, J. Wojcik, R. N. Gilbreth, R. J. Hoey, S. Koide, Teaching an old scaffold new tricks: Monobodies constructed using alternative surfaces of the FN3 scaffold. *J. Mol. Biol.* **415**, 393–405 (2012). pmid: 22198408
82. Y. S. Choi *et al*., Computational design of binding proteins to EGFR domain II. *PLOS ONE* **9**, e92513 (2014). doi: 10.1371/journal.pone.0092513; pmid: 24710267
83. K. Mross *et al*., First-in-human phase I study of PRS-050 (Angiocal), an Anticalin targeting and antagonizing VEGF-A, in patients with advanced solid tumors. *PLOS ONE* **8**, e83232 (2013). doi: 10.1371/journal.pone.0083232; pmid: 24349470
84. Z. Taimeh, J. Loughran, E. J. Birks, R. Bolli, Vascular endothelial growth factor in heart failure. *Nat. Rev. Cardiol.* **10**, 519–530 (2013). doi: 10.1038/nrcardio.2013.94; pmid: 23856679
85. J. Rakonjac, N. J. Bennett, J. Spagnuolo, D. Gagic, M. Russel, Filamentous bacteriophage: Biology, phage display and nanotechnology applications. *Curr. Issues Mol. Biol.* **13**, 51–76 (2011). pmid: 21502666
86. S. Miersch, S. S. Sidhu, Synthetic antibodies: Concepts, potential and practical considerations. *Methods* **57**, 486–498 (2012). doi: 10.1016/j.ymeth.2012.06.012; pmid: 22750306
87. G. Fuh *et al*., Analysis of PDZ domain-ligand interactions using carboxyl-terminal phage display. *J. Biol. Chem.* **275**, 21486–21491 (2000).pmid: 10887205
88. L. Burch, H. Shimizu, A. Smith, C. Patterson, T. R. Hupp, Expansion of protein interaction maps by phage peptide display using MDM2 as a prototypical conformationally flexible target protein. *J. Mol. Biol.* **337**, 129–145 (2004). doi: 10.1016/j.jmb.2004.01.017; pmid: 15001357
89. K. Nord *et al*., Binding proteins selected from combinatorial libraries of an alpha-helical bacterial receptor domain. *Nat. Biotechnol.* **15**, 772–777 (1997). doi: 10.1038/nbt0897-772; pmid: 9255793
90. J. Feldwisch *et al*., Design of an optimized scaffold for affibody molecules. *J. Mol. Biol.* **398**, 232–247 (2010). doi: 10.1016/j.jmb.2010.03.002; pmid: 20226194
91. D. J. Maxwell, B. C. Hicks, S. Parsons, S. E. Sakiyama-Elbert, Development of rationally designed affinity-based drug delivery systems. *Acta Biomater.* **1**, 101–113 (2005). doi: 10.1016/j.actbio.2004.09.002; pmid: 16701784
92. S. M. Willerth *et al*., Rationally designed peptides for controlled release of nerve growth factor from fibrin matrices. *J. Biomed. Mater. Res. A* **80A**, 13–23 (2007). doi: 10.1002/jbm.a.30844; pmid: 16958043
93. J. A. Francisco, R. Campbell, B. L. Iverson, G. Georgiou, Production and fluorescence-activated cell sorting of *Escherichia coli* expressing a functional antibody fragment on the external surface. *Proc. Natl. Acad. Sci. U.S.A.* **90**, 10444–10448 (1993). doi: 10.1073/pnas.90.22.10444; pmid: 8248129
94. P. H. Bessette, J. J. Rice, P. S. Daugherty, Rapid isolation of high-affinity protein binding peptides using bacterial display. *Protein Eng. Des. Sel.* **17**, 731–739 (2004). doi: 10.1093/protein/gzh084; pmid: 15531628
95. A. Christmann, K. Walter, A. Wentzel, R. Krätzner, H. Kolmar, The cystine knot of a squash-type protease inhibitor as a structural scaffold for *Escherichia coli* cell surface display of conformationally constrained peptides. *Protein Eng.* **12**, 797–806 (1999). doi: 10.1093/protein/12.9.797; pmid: 10506290
96. J. J. Rice, A. Schohn, P. H. Bessette, K. T. Boulware, P. S. Daugherty, Bacterial display using circularly permuted outer membrane protein OmpX yields high affinity peptide ligands. *Protein Sci.* **15**, 825–836 (2006). doi: 10.1110/ps.051897806; pmid: 16600968
97. P. S. Daugherty, G. Chen, M. J. Olsen, B. L. Iverson, G. Georgiou, Antibody affinity maturation using bacterial surface display. *Protein Eng.* **11**, 825–832 (1998). doi: 10.1093/protein/11.9.825; pmid: 9796833
98. J. M. Van der Vaart *et al*., Comparison of cell wall proteins of *Saccharomyces cerevisiae* as anchors for cell surface expression of heterologous proteins. *Appl. Environ. Microbiol.* **63**, 615–620 (1997).pmid: 9023939
99. L. R. Pepper, Y. K. Cho, E. T. Boder, E. V. Shusta, A decade of yeast surface display technology: Where are we now? *Comb. Chem. High Throughput Screen.* **11**, 127–134 (2008). doi: 10.2174/138620708783744516; pmid: 18336206
100. A. Angelini *et al*., in *Yeast Surface Display*, B. Liu, Ed., vol. 1319 of *Methods in Molecular Biology* (Humana, 2015), pp. 3–36.
101. E. T. Boder, K. D. Wittrup, Yeast surface display for screening combinatorial polypeptide libraries. *Nat. Biotechnol.* **15**, 553–557 (1997). doi: 10.1038/nbt0697-553; pmid: 9181578
102. S. A. Gai, K. D. Wittrup, Yeast surface display for protein engineering and characterization. *Curr. Opin. Struct. Biol.* **17**, 467–473 (2007). doi: 10.1016/j.sbi.2007.08.012; pmid: 17870469
103. M. J. Feldhaus *et al*., Flow-cytometric isolation of human antibodies from a nonimmune *Saccharomyces cerevisiae* surface display library. *Nat. Biotechnol.* **21**, 163–170 (2003). doi: 10.1038/nbt785; pmid: 12536217
104. K. S. Weber, D. L. Donermeyer, P. M. Allen, D. M. Kranz, Class II-restricted T cell receptor engineered in vitro for higher affinity retains peptide specificity and function. *Proc. Natl. Acad. Sci. U.S.A.* **102**, 19033–19038 (2005). doi: 10.1073/pnas.0507554102; pmid: 16365315
105. D. Lipovsek, A. Plückthun, In-vitro protein evolution by ribosome display and mRNA display. *J. Immunol. Methods* **290**, 51–67 (2004). doi: 10.1016/j.jim.2004.04.008; pmid: 15261571
106. S. W. Millward, S. Fiacco, R. J. Austin, R. W. Roberts, Design of cyclic peptides that bind protein surfaces with antibody-like affinity. *ACS Chem. Biol.* **2**, 625–634 (2007). doi: 10.1021/cb7001126; pmid: 17894440
107. S. M. Howell *et al*., Serum stable natural peptides designed by mRNA display. *Sci. Rep.* **4**, 6008 (2014). doi: 10.1038/srep06008; pmid: 25234472
108. S. L. Emanuel *et al*., A fibronectin scaffold approach to bispecific inhibitors of epidermal growth factor receptor and insulin-like growth factor-I receptor. *MAbs* **3**, 38–48 (2011). doi: 10.4161/mabs.3.1.14168; pmid: 21099371
109. A. A. Stoop, C. S. Craik, Engineering of a macromolecular scaffold to develop specific protease inhibitors. *Nat. Biotechnol.* **21**, 1063–1068 (2003). doi: 10.1038/nbt860; pmid: 12923547
110. J. Nilvebrant *et al*., Engineering of bispecific affinity proteins with high affinity for ERBB2 and adaptable binding to albumin. *PLOS ONE* **9**, e103094 (2014). doi: 10.1371/journal.pone.0103094; pmid: 25089830
111. C. Tuerk, L. Gold, Systematic evolution of ligands by exponential enrichment: RNA ligands to bacteriophage T4 DNA polymerase. *Science* **249**, 505–510 (1990). doi: 10.1126/science.2200121; pmid: 2200121
112. A. D. Ellington, J. W. Szostak, In vitro selection of RNA molecules that bind specific ligands. *Nature* **346**, 818–822 (1990). doi: 10.1038/346818a0; pmid: 1697402
113. S. D. Jayasena, Aptamers: An emerging class of molecules that rival antibodies in diagnostics. *Clin. Chem.* **45**, 1628–1650 (1999). pmid: 10471678
114. R. R. White, B. A. Sullenger, C. P. Rusconi, Developing aptamers into therapeutics. *J. Clin. Invest.* **106**, 929–934 (2000). doi: 10.1172/JCI11325; pmid: 11032851
115. E. N. Brody, L. Gold, Aptamers as therapeutic and diagnostic agents. *J. Biotechnol.* **74**, 5–13 (2000). pmid: 10943568
116. K. B. Jensen, B. L. Atkinson, M. C. Willis, T. H. Koch, L. Gold, Using in vitro selection to direct the covalent attachment of human immunodeficiency virus type 1 Rev protein to high-affinity RNA ligands. *Proc. Natl. Acad. Sci. U.S.A.* **92**, 12220–12224 (1995). doi: 10.1073/pnas.92.26.12220; pmid: 8618873
117. M. C. Golden, B. D. Collins, M. C. Willis, T. H. Koch, Diagnostic potential of PhotoSELEX-evolved ssDNA aptamers. *J. Biotechnol.* **81**, 167–178 (2000). doi: 10.1016/S0168-1656(00)00290-X; pmid: 10989176
118. E. W. M. Ng *et al*., Pegaptanib, a targeted anti-VEGF aptamer for ocular vascular disease. *Nat. Rev. Drug Discov.* **5**, 123–132 (2006). doi: 10.1038/nrd1955; pmid: 16518379
119. V. Bagalkot, O. C. Farokhzad, R. Langer, S. Jon, An aptamer-doxorubicin physical conjugate as a novel targeted drug-delivery platform. *Angew. Chem. Int. Ed. Engl.* **45**, 8149–8152 (2006). doi: 10.1002/anie.200602251; pmid: 17099918
120. O. C. Farokhzad, J. M. Karp, R. Langer, Nanoparticle-aptamer bioconjugates for cancer chemotherapy in vivo. *Expert Opin. Drug Deliv.* **3**, 311–324 (2006). doi: 10.1517/17425247.3.3.311; pmid: 16640493
121. O. C. Farokhzad *et al*., Targeted nanoparticle-aptamer bioconjugates for cancer chemotherapy in vivo. *Proc. Natl. Acad. Sci. U.S.A.* **103**, 6315–6320 (2006). doi: 10.1073/pnas.0601755103; pmid: 16606824
122. B. Soontornworajit, J. Zhou, M. T. Shaw, T.-H. Fan, Y. Wang, Hydrogel functionalization with DNA aptamers for sustained PDGF-BB release. *Chem. Commun. (Camb.)* **46**, 1857–1859 (2010). doi: 10.1039/b924909e; pmid: 20198232
123. M. R. Battig, Y. Huang, N. Chen, Y. Wang, Aptamer-functionalized superporous hydrogels for sequestration and release of growth factors regulated via molecular recognition. *Biomaterials* **35**, 8040–8048 (2014). doi: 10.1016/j.biomaterials.2014.06.001; pmid: 24954732
124. M. Cho *et al*., Quantitative selection and parallel characterization of aptamers. *Proc. Natl. Acad. Sci. U.S.A.* **110**, 18460–18465 (2013). doi: 10.1073/pnas.1315866110; pmid: 24167271
125. X. Zhang, B. Soontornworajit, Z. Zhang, N. Chen, Y. Wang, Enhanced loading and controlled release of antibiotics using nucleic acids as an antibiotic-binding effector in hydrogels. *Biomacromolecules* **13**, 2202–2210 (2012). doi: 10.1021/bm3006227; pmid: 22658064
126. S. S. Oh, K. Plakos, Y. Xiao, M. Eisenstein, H. T. Soh, In vitro selection of shape-changing DNA nanostructures capable of binding-induced cargo release. *ACS Nano* **7**, 9675–9683 (2013). doi: 10.1021/nn404079v; pmid: 24168267
127. B. Kuhlman *et al*., Design of a novel globular protein fold with atomic-level accuracy. *Science* **302**, 1364–1368 (2003). doi: 10.1126/science.1089427; pmid: 14631033
128. D. Röthlisberger *et al*., Kemp elimination catalysts by computational enzyme design. *Nature* **453**, 190–195 (2008). doi: 10.1038/nature06879; pmid: 18354394
129. J. Reina *et al*., Computer-aided design of a PDZ domain to recognize new target sequences. *Nat. Struct. Biol.* **9**, 621–627 (2002). pmid: 12080331
130. C. E. Tinberg *et al*., Computational design of ligand-binding proteins with high affinity and selectivity. *Nature* **501**, 212–216 (2013). doi: 10.1038/nature12443; pmid: 24005320
131. E. Procko *et al*., Computational design of a protein-based enzyme inhibitor. *J. Mol. Biol.* **425**, 3563–3575 (2013). doi: 10.1016/j.jmb.2013.06.035; pmid: 23827138
132. A. Morin, J. Meiler, L. S. Mizoue, Computational design of protein-ligand interfaces: Potential in therapeutic development. *Trends Biotechnol.* **29**, 159–166 (2011). doi: 10.1016/j.tibtech.2011.01.002; pmid: 21295366
133. T. Kortemme, D. Baker, Computational design of protein-protein interactions. *Curr. Opin. Chem. Biol.* **8**, 91–97 (2004). doi: 10.1016/j.cbpa.2003.12.008; pmid: 15036162
134. J. Karanicolas *et al*., A de novo protein binding pair by computational design and directed evolution. *Mol. Cell* **42**, 250–260 (2011). doi: 10.1016/j.molcel.2011.03.010; pmid: 21458342
135. N. London *et al*., Covalent docking predicts substrates for haloalkanoate dehalogenase superfamily phosphatases.

*Biochemistry* **54**, 528–537 (2015). doi: 10.1021/bi501140k; pmid: 25513739
136. J. Desmet, M. De Maeyer, B. Hazes, I. Lasters, The dead-end elimination theorem and its use in protein side-chain positioning. *Nature* **356**, 539–542 (1992). doi: 10.1038/356539a0; pmid: 21488406
137. Digitalis Investigation Group, The effect of digoxin on mortality and morbidity in patients with heart failure. *N. Engl. J. Med.* **336**, 525–533 (1997). doi: 10.1056/NEJM199702203360801; pmid: 9036306
138. E.-M. Strauch, S. J. Fleishman, D. Baker, Computational design of a pH-sensitive IgG binding protein. *Proc. Natl. Acad. Sci. U.S.A.* **111**, 675–680 (2014). doi: 10.1073/pnas.1313605111; pmid: 24381156
139. J. L. Wike-Hooley, J. Haveman, H. S. Reinhold, The relevance of tumour pH to the treatment of malignant disease. *Radiother. Oncol.* **2**, 343–366 (1984). doi: 10.1016/S0167-8140(84)80077-8; pmid: 6097949
140. S. Ganta, H. Devalapally, A. Shahiwala, M. Amiji, A review of stimuli-responsive nanocarriers for drug and gene delivery. *J. Control. Release* **126**, 187–204 (2008). doi: 10.1016/j.jconrel.2007.12.017; pmid: 18261822
141. L. E. Gerweck, K. Seetharaman, Cellular pH gradient in tumor versus normal tissue: Potential exploitation for the treatment of cancer. *Cancer Res.* **56**, 1194–1198 (1996). pmid: 8640796
142. M. Fischer, R. G. Coleman, J. S. Fraser, B. K. Shoichet, Incorporation of protein flexibility and conformational energy penalties in docking screens to improve ligand discovery. *Nat. Chem.* **6**, 575–583 (2014). doi: 10.1038/nchem.1954; pmid: 24950326
143. L. Jiang *et al.*, De novo computational design of retro-aldol enzymes. *Science* **319**, 1387–1391 (2008). pmid: 18323453
144. M. Levitt, Growth of novel protein structural data. *Proc. Natl. Acad. Sci. U.S.A.* **104**, 3183–3188 (2007). doi: 10.1073/pnas.0611678104; pmid: 17360626
145. A. Fiser, A. Sali, Modeller: Generation and refinement of homology-based protein structure models. *Methods Enzymol.* **374**, 461–491 (2003). doi: 10.1016/S0076-6879(03)74020-8; pmid: 14696385
146. Attana, "Frequently Asked Questions" (2016); www.attana.com/about-us/faq/.

## ACKNOWLEDGMENTS

We are grateful to B. Shoichet (University of California–San Francisco) for his thoughtful review of this manuscript. We thank the Natural Sciences and Engineering Research Council (Discovery grant to M.S.S. and Vanier Scholarship to M.M.P.) and the Canadian Institutes of Health Research (operating grant to M.S.S.) for funding our research in affinity-controlled release.

10.1126/science.aac4750

RESEARCH ARTICLE SUMMARY

PLANETARY SCIENCE

# The atmosphere of Pluto as observed by New Horizons

**G. Randall Gladstone,* S. Alan Stern, Kimberly Ennico, Catherine B. Olkin, Harold A. Weaver, Leslie A. Young, Michael E. Summers, Darrell F. Strobel, David P. Hinson, Joshua A. Kammer, Alex H. Parker, Andrew J. Steffl, Ivan R. Linscott, Joel Wm. Parker, Andrew F. Cheng, David C. Slater,† Maarten H. Versteeg, Thomas K. Greathouse, Kurt D. Retherford, Henry Throop, Nathaniel J. Cunningham, William W. Woods, Kelsi N. Singer, Constantine C. C. Tsang, Eric Schindhelm, Carey M. Lisse, Michael L. Wong, Yuk L. Yung, Xun Zhu, Werner Curdt, Panayotis Lavvas, Eliot F. Young, G. Leonard Tyler, the New Horizons Science Team**

**INTRODUCTION:** For several decades, telescopic observations have shown that Pluto has a complex and intriguing atmosphere. But too little has been known to allow a complete understanding of its global structure and evolution. Major goals of the New Horizons mission included the characterization of the structure and composition of Pluto's atmosphere, as well as its escape rate, and to determine whether Charon has a measurable atmosphere.

ON OUR WEB SITE

Read the full article at http://dx.doi.org/10.1126/science.aad8866

**RATIONALE:** The New Horizons spacecraft included several instruments that observed Pluto's atmosphere, primarily (i) the Radio Experiment (REX) instrument, which produced near-surface pressure and temperature profiles; (ii) the Alice ultraviolet spectrograph, which gave information on atmospheric composition; and (iii) the Long Range Reconnaissance Imager (LORRI) and Multispectral Visible Imaging Camera (MVIC), which provided images of Pluto's hazes. Together, these instruments have provided data that allow an understanding of the current state of Pluto's atmosphere and its evolution.

**RESULTS:** The REX radio occultation determined Pluto's surface pressure and found a strong temperature inversion, both of which are generally consistent with atmospheric profiles retrieved from Earth-based stellar occultation measurements. The REX data showed near-symmetry between the structure at ingress and egress, as expected from sublimation driven dynamics, so horizontal winds are expected to be weak. The shallow near-surface boundary layer observed at ingress may arise directly from sublimation.

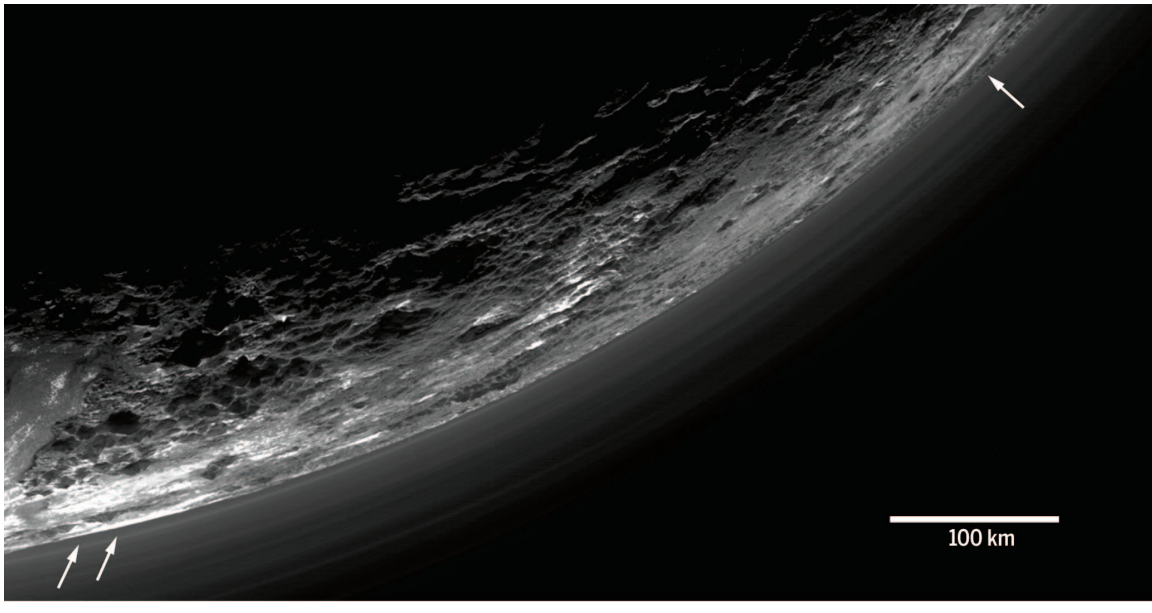
The Alice solar occultation showed absorption by methane and nitrogen and revealed the presence of the photochemical products acetylene and ethylene. The observed nitrogen opacity at high altitudes was lower than expected, which is consistent with a cold upper atmosphere. Such low temperatures imply an additional, but as yet unidentified, cooling agent.

A globally extensive haze extending to high altitudes, and with numerous embedded thin layers, is seen in the New Horizons images. The haze has a bluish color, suggesting a composition of very small particles. The observed scattering properties of the haze are consistent with a tholin-like composition. Buoyancy waves generated by winds flowing over orography can produce vertically propagating compression and rarefaction waves that may be related to the narrow haze layers.

Pluto's cold upper atmosphere means atmospheric escape must occur via slow thermal Jeans' escape. The inferred escape rate of nitrogen is ~10,000 times slower than predicted, whereas that of methane is about the same as predicted. The low nitrogen loss rate is consistent with an undetected Charon atmosphere but possibly inconsistent with sublimation/erosional features seen on Pluto's surface, so that past escape rates may have been much larger at times. Capture of escaping methane and photochemical products by Charon, and subsequent surface chemical reactions, may contribute to the reddish color of its north pole.

**CONCLUSION:** New Horizons observations have revolutionized our understanding of Pluto's atmosphere. The observations revealed major surprises, such as the unexpectedly cold upper atmosphere and the globally extensive haze layers. The cold upper atmosphere implies much lower escape rates of volatiles from Pluto than predicted and so has important implications for the volatile recycling and the long-term evolution of Pluto's atmosphere. ■

The list of author affiliations is available in the full article online.
*Corresponding author. E-mail: rgladstone@swri.edu
†Deceased.
Cite this article as G. R. Gladstone *et al.*, *Science* **351**, aad8866 (2016). DOI: 10.1126/science.aad8866




**MVIC image of haze layers above Pluto's limb.** About 20 haze layers are seen from a phase angle of 147°. The layers typically extend horizontally over hundreds of kilometers but are not exactly horizontal. For example, white arrows on the left indicate a layer ~5 km above the surface, which has descended to the surface at the right.

Downloaded from on March 17, 2016

RESEARCH ARTICLE

PLANETARY SCIENCE

# The atmosphere of Pluto as observed by New Horizons

G. Randall Gladstone,[1,2]* S. Alan Stern,[3] Kimberly Ennico,[4] Catherine B. Olkin,[3] Harold A. Weaver,[5] Leslie A. Young,[3] Michael E. Summers,[6] Darrell F. Strobel,[7] David P. Hinson,[8] Joshua A. Kammer,[3] Alex H. Parker,[3] Andrew J. Steffl,[3] Ivan R. Linscott,[9] Joel Wm. Parker,[3] Andrew F. Cheng,[5] David C. Slater,[1]† Maarten H. Versteeg,[1] Thomas K. Greathouse,[1] Kurt D. Retherford,[1,2] Henry Throop,[7] Nathaniel J. Cunningham,[10] William W. Woods,[9] Kelsi N. Singer,[3] Constantine C. C. Tsang,[3] Eric Schindhelm,[3] Carey M. Lisse,[5] Michael L. Wong,[11] Yuk L. Yung,[11] Xun Zhu,[5] Werner Curdt,[12] Panayotis Lavvas,[13] Eliot F. Young,[3] G. Leonard Tyler,[9] the New Horizons Science Team‡

**Observations made during the New Horizons flyby provide a detailed snapshot of the current state of Pluto's atmosphere. Whereas the lower atmosphere (at altitudes of less than 200 kilometers) is consistent with ground-based stellar occultations, the upper atmosphere is much colder and more compact than indicated by pre-encounter models. Molecular nitrogen ($N_2$) dominates the atmosphere (at altitudes of less than 1800 kilometers or so), whereas methane ($CH_4$), acetylene ($C_2H_2$), ethylene ($C_2H_4$), and ethane ($C_2H_6$) are abundant minor species and likely feed the production of an extensive haze that encompasses Pluto. The cold upper atmosphere shuts off the anticipated enhanced-Jeans, hydrodynamic-like escape of Pluto's atmosphere to space. It is unclear whether the current state of Pluto's atmosphere is representative of its average state—over seasonal or geologic time scales.**

Major goals of the New Horizons mission were to explore and characterize the structure and composition of Pluto's atmosphere and to determine whether Charon has a measurable atmosphere of its own (*1*). Several instruments contribute to these goals, primarily (i) the Radio Experiment (REX) instrument (*2*), through uplink X-band radio occultations; (ii) the Alice instrument (*3*), through extreme- and far-ultraviolet solar occultations; and (iii) the Long Range Reconnaissance Imager (LORRI) and Multispectral Visible Imaging Camera (MVIC) (*4*, *5*), through high-phase-angle imaging. The associated data sets were obtained within a few hours of the closest approach of New Horizons to Pluto at 11:48 UT on 14 July 2015. Pressure and temperature profiles of the lower atmosphere are derived from the REX data, the composition and structure of the extended atmosphere are derived from the Alice data (supported by approach observations of reflected ultraviolet sunlight), and the distribution and properties of Pluto's hazes are derived from LORRI and MVIC images. This Research Article provides an overview of atmosphere science results.

A suggested atmosphere around Pluto (*6*–*11*) was confirmed by means of ground-based stellar occultation in 1988 (*12*, *13*) and subsequently studied with later occultations (*14*–*16*) and spectra at near-infrared and microwave wavelengths (*17*, *18*) and with models of increasing sophistication. These results revealed a primarily $N_2$ atmosphere with trace amounts of $CH_4$, CO, and HCN with complex surface interaction, an uncertain surface pressure of ~3 to 60 μbar, and a warm stratosphere at ~100 K above a much colder surface (38 to 55 K). On the eve of the New Horizons flyby, critical questions remained about the atmospheric temperature and pressure profiles, dynamics, the presence and nature of possible clouds or hazes, the escape of Pluto's atmosphere, and possible interactions with its large moon, Charon. The New Horizons flyby (*19*) enabled us to address these questions using radio occultations, ultraviolet occultations, and imaging at several phase angles between 15° and 165°.

## Pressure and temperature

The New Horizons trajectory was designed to permit nearly simultaneous radio and solar occultations (*20*). The radio occultation was implemented in an uplink configuration by using 4.2-cm-wavelength signals transmitted by antennas of the NASA Deep Space Network and received by the REX instrument onboard New Horizons (*2*). The spacecraft passed almost diametrically behind Pluto as viewed from Earth, with ingress at sunset near the center of the anti-Charon hemisphere and egress at sunrise near the center of the Charon-facing hemisphere. Other characteristics of the REX observation are listed in table S1.

The location of Pluto's surface is indicated by a characteristic diffraction pattern in the REX

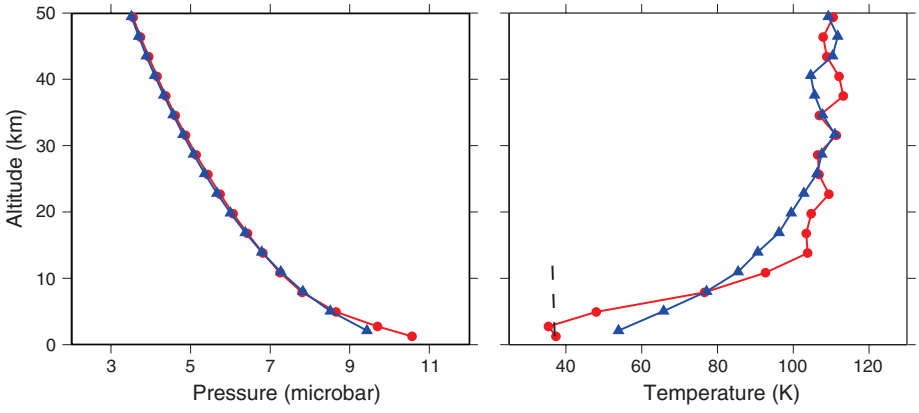



**Fig. 1. Pressure and temperature in Pluto's lower atmosphere.** (**Left**) Pressure. (**Right**) Temperature. These profiles were retrieved from radio occultation data recorded by the REX instrument onboard New Horizons. Diffraction effects were removed from the data (*53*), which greatly improves the accuracy of the results, and the conventional "Abel-transform" retrieval algorithm (*2*, *54*, *55*) was applied to the diffraction-corrected phase measurements. Each graph shows results at both entry (red line with circles) and exit (blue line with triangles), situated on opposite sides of Pluto. The profiles are most accurate at the surface, where the uncertainties in pressure and temperature are ~1 μbar and 3 K, respectively. Temperature fluctuations at altitudes of >20 km are caused by noise; no gravity waves were detected at the sensitivity of these measurements. The dashed line indicates the saturation temperature of $N_2$ (*29*).

[1]Southwest Research Institute, San Antonio, TX 78238, USA. [2]University of Texas at San Antonio, San Antonio, TX 78249, USA. [3]Southwest Research Institute, Boulder, CO 80302, USA. [4]National Aeronautics and Space Administration, Ames Research Center, Space Science Division, Moffett Field, CA 94035, USA. [5]The Johns Hopkins University Applied Physics Laboratory, Laurel, MD 20723, USA. [6]George Mason University, Fairfax, VA 22030, USA. [7]The Johns Hopkins University, Baltimore, MD 21218, USA. [8]Search for Extraterrestrial Intelligence Institute, Mountain View, CA 94043, USA. [9]Stanford University, Stanford, CA 94305, USA. [10]Nebraska Wesleyan University, Lincoln, NE 68504, USA. [11]California Institute of Technology, Pasadena, CA 91125, USA. [12]Max-Planck-Institut für Sonnensystemforschung, 37191 Katlenburg-Lindau, Germany. [13]Groupe de Spectroscopie Moléculaire et Atmosphérique, Université Reims Champagne-Ardenne, 51687 Reims, France.
***Corresponding author. E-mail: rgladstone@swri.edu**
†Deceased. ‡New Horizons Science Team authors and affiliations are listed in the supplementary materials.

amplitude measurements (*2*). According to scalar diffraction theory (*21*), the limb of Pluto is aligned with the location where the amplitude is reduced by 50% from its "free space" value, as determined from data recorded well before or well after the occultation by Pluto. (The change in amplitude from refractive bending in Pluto's atmosphere is negligible, in contrast to what occurs in stellar occultations observed from Earth.) At both entry and exit, the amplitude drops from 80 to 20% of its free-space value in a radial span of ~1.5 km. We used the solutions for the location of the surface at entry and exit to anchor the REX atmospheric profiles (Fig. 1), yielding an altitude scale with a relative uncertainty of ±~0.4 km.

The absolute radii at entry and exit are much less certain, owing to limitations on the accuracy of the reconstructed spacecraft trajectory. Because the occultation was nearly diametric, the main concern is with any systematic bias in the position of the spacecraft along its flight path. This sort of error causes an underestimate in the radius on one side of Pluto and an overestimate on the other side. However, the magnitude of the errors is nearly the same so that the mean radius is largely unaffected; its value is $R_P$ = 1189.9 ± 0.4 km. This result is consistent with the global radius derived from images, 1187 ± 4 km (*19*). The difference, if real, could be a consequence of local topography or global flattening.

The atmospheric structure at altitudes of 0 to 50 km was retrieved from REX measurements of the Doppler-shifted frequency (or, equivalently, the phase) of the uplink radio signal (Fig. 1). We found that there is a strong temperature inversion at both ingress and egress for altitudes below ~20 km, which is qualitatively consistent with profiles retrieved from Earth-based stellar occultation measurements (*16*, *22*, *23*). However, there are two notable differences between the REX profiles at entry and exit, which indicate the presence of horizontal variations in temperature that had not been identified previously. First, the temperature inversion at entry is much stronger than its counterpart at exit; the derived mean vertical gradient in the lowest 10 km of the inversion is 6.4 ± 0.9 K km$^{-1}$ at entry but only 3.4 ± 0.9 K km$^{-1}$ at exit. Second, the temperature inversion at entry ends abruptly at an altitude of ~4 km, marking the top of a distinctive boundary layer. In contrast, the temperature inversion at exit appears to extend all the way to the surface, and we find no evidence for a boundary layer at that location. Because the radiative time constant of Pluto's atmosphere is 10 to 15 Earth years (*24*), equivalent to ~700 Pluto days, these differences in temperature structure cannot be attributed to nighttime radiative cooling or daytime solar heating within the atmosphere. A boundary layer had been discussed on energetic grounds or as a way to connect stellar occultation profiles to conditions at an unknown surface radius (*23*, *25*–*28*). REX results indicate that the boundary layer is not uniform across Pluto.

We estimated the surface pressure through downward extrapolation of the REX pressure profiles (Fig. 1), obtaining values of 11 ± 1 μbar at entry and 10 ± 1 μbar at exit. Analysis of stellar occultation data from 2012 and 2013 has yielded essentially the same result, a pressure of 11 μbar at 1190 km radius (*16*). Hence, the mass of Pluto's atmosphere has not changed dramatically in recent years.

Downward extrapolation of the REX exit profile yields a temperature adjacent to the surface of 45 ± 3 K. For comparison, a surface covered in $N_2$ ice would have a temperature of 37.0 K to remain in vapor pressure equilibrium with the measured value of surface pressure (*29*). This may be indicative of a surface material less volatile than $N_2$ ice. Occultation exit was closer than entry to the subsolar latitude—52°N at the time of the observation—which would contribute to a warmer surface temperature in the absence of $N_2$ ice. [Where $N_2$ ice is present, any increase in insolation is balanced largely by latent heating, with only a small change in the ice temperature (*30*).]

At occultation entry, the mean temperature in the lowest 4 km above the surface is 37 ± 3 K, which is close to the saturation temperature of $N_2$ (*29*). This layer of cold air could arise directly from sublimation, and the close proximity of occultation entry to the region known informally as Sputnik Planum (SP)—with its large reservoirs of $N_2$, CO, and $CH_4$ ices (*19*, *31*)—supports this interpretation. Moreover, Earth-based observations of Pluto imply that there is a strong zonal asymmetry in the distribution of $N_2$ ice (*32*); the abundance is largest near the REX entry longitude and smallest near the REX exit longitude. This raises the possibility that a scarcity of nearby sublimation sources could prevent the formation of a cold boundary layer at REX exit.

The cold boundary layer in the entry profile is steadily warmed by downward heat conduction in the overlying temperature inversion (*33*). We used a formula for the thermal conductivity of $N_2$ vapor (*34*) along with the measured temperature gradient to estimate the heating rate. The results indicate that it takes ~2 Earth years for this process to establish an inversion that extends to the ground. Without resupply of cold $N_2$, the boundary layer will vanish on this time scale. Hence, our interpretation implies that SP is an active sublimation source.

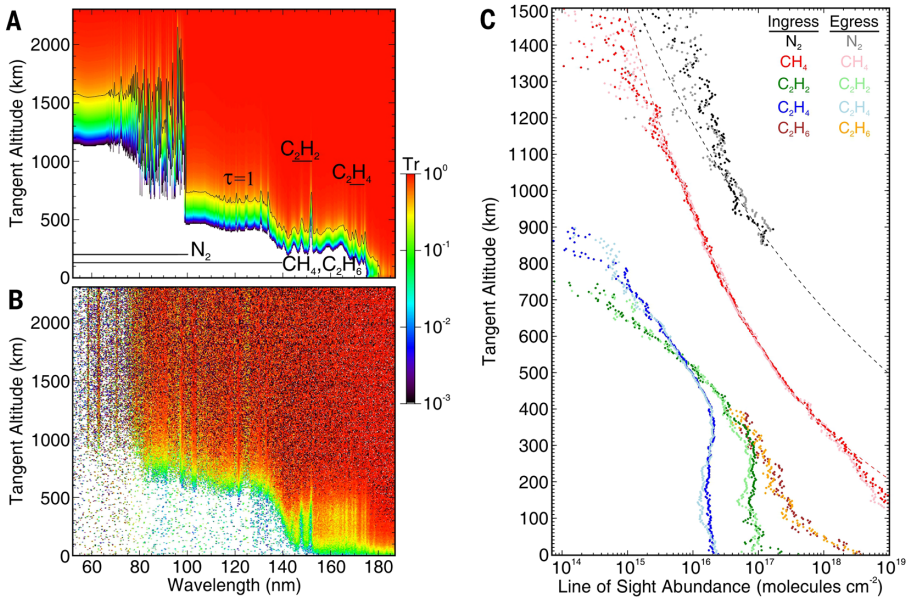



**Fig. 2. Ultraviolet transmission of Pluto's atmosphere.** (**A**) Line-of-sight (LOS) transmission as a function of ultraviolet wavelength and tangent altitude for the M2 model Pluto atmosphere (*37*), with the τ =1 line indicated along with the regions where $N_2$, $CH_4$, $C_2H_2$, $C_2H_4$, and $C_2H_6$ contribute to the opacity. $N_2$ absorbs in discrete bands for wavelengths 80 to 100 nm, with bands and an underlying continuum at wavelengths 65 to 80 nm and an ionization continuum at wavelengths of <65 nm. $CH_4$ dominates the opacity at wavelengths of <140 nm. $C_2H_6$ has a similar cross section to $CH_4$ but absorbs to 145 nm, where it contributes to the opacity. $C_2H_2$ has strong absorption bands at 144, 148, and 152 nm. $C_2H_4$ dominates the opacity at 155 to 175 nm. The model also contains $C_4H_2$, which accounts for much of the opacity at wavelengths 155 to 165 nm. (**B**) LOS transmission of Pluto's atmosphere determined from the Alice solar occultation data. The Alice data are normalized (at each ultraviolet wavelength) to unabsorbed levels at high altitude. In comparison with the model transmission, $N_2$ opacity begins at much lower altitudes (~500 km lower), whereas $CH_4$ opacity begins ~100 km higher than in the model. Pluto's atmosphere has somewhat less $C_2H_2$ and $C_2H_4$ than the model. Continuum absorption by Pluto's haze (not included in the model) is important at wavelengths >175 nm. (**C**) LOS column density profiles retrieved from the observed transmission data of (B) using known absorption cross sections for the indicated species. The quality of the data can be judged by the overlap of ingress and egress profiles (because the atmosphere is expected to be nearly spherically symmetric away from the surface) and by the amount of scatter in the data points. The dashed lines are LOS column densities computed by using the $N_2$ and $CH_4$ number density profiles in Fig. 3.

Last, the vertical resolution of the entry profile in Fig. 1 is not sufficient to determine the temperature lapse rate in the boundary layer. The results to date cannot distinguish an isothermal layer from one with a wet or dry adiabatic gradient.

## Composition and chemistry

Models indicate that photochemistry in Pluto's upper atmosphere is similar to that of Titan and Triton (*35*–*38*). Methane ($CH_4$) is processed by far-ultraviolet sunlight into heavier hydrocarbons, and at Pluto's distance from the Sun, interplanetary hydrogen scattering of solar Lyman α photons provides a comparable secondary source of $CH_4$ photolysis, which is also effective at night and in winter (*39*). Extreme-ultraviolet sunlight photolyzes molecular nitrogen ($N_2$), leading to nitrile production in conjunction with $CH_4$ (*37*), and also ionizes $N_2$ to initiate the formation of large ions, which may lead to the production of high-altitude haze nuclei (*40*). Establishing Pluto's atmospheric composition as a function of altitude is important for understanding its atmospheric chemistry, and the solar occultations by the New Horizons Alice ultraviolet spectrograph (*3*) provide an excellent data set for this purpose. The circumstances of the solar occultations by Pluto and Charon are presented in tables S2 and S3, respectively. The transmission of Pluto's atmosphere is directly derived from the Alice ingress and egress data (Fig. 2; the full solar occultation light curve is presented in fig. S1). The transmission profile clearly indicates the altitude at which the tangent line-of-sight opacity reaches unity for a given wavelength and also provides a useful scale height at that level.

The Pluto solar occultation results are surprising in that the expected upper atmospheric opacity of $N_2$ at wavelengths ~65 to 100 nm is largely absent, and the opacity is mostly due to $CH_4$. At wavelengths longward of 100 nm, $CH_4$, $C_2H_2$, $C_2H_4$, $C_2H_6$, and haze account for a majority of the observed opacity. A model consistent with the observed transmission requires a much colder upper atmosphere than in pre-encounter models (Fig. 3). The absorption of sunlight in the 57- to 64-nm-wavelength range by $N_2$ at high altitudes (~850 to 1400 km) constrains the temperature of the upper atmosphere to be ~70 K. Such low temperatures are potentially achievable through cooling by $C_2H_2$ $\nu_5$ band emission and HCN rotational line emission (if HCN is supersaturated, not in vapor pressure equilibrium at these cold temperatures). However, recent Earth-based observations by using the Atacama Large Millimeter/submillimeter Array (ALMA) suggest that the HCN abundances in Pluto's upper atmosphere are many times less than would be required (*16*, *18*). Currently, the details of exactly how Pluto's upper atmosphere is being cooled are poorly understood. Also, the ALMA data provide a definitive observation of CO on Pluto, which has not been detected in the Alice solar occultation data.

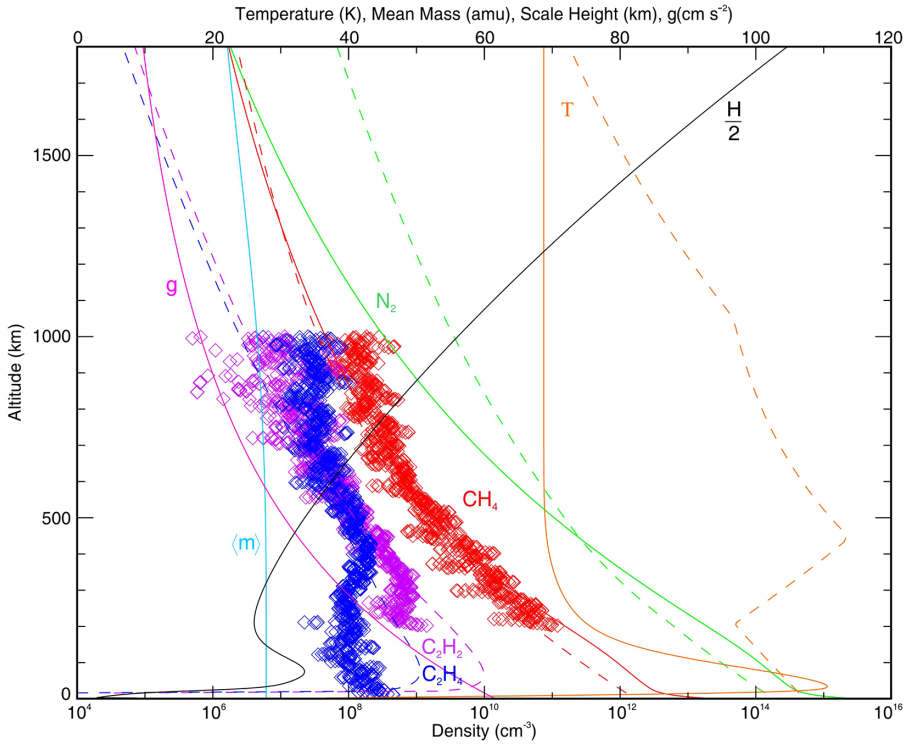



**Fig. 3. Pluto's atmospheric composition and structure.** Model profiles of temperatures, densities, and other relevant quantities (such as gravity $g$, mean mass $\langle m \rangle$, and $N_2$ density scale height $H$—plotted as $H/2$ in order to facilitate a common $x$ axis range) in the atmosphere of Pluto are shown, which are consistent with the transmission results of Fig. 2. Methane, acetylene, and ethylene densities retrieved from the solar occultation data are indicated (diamonds). Pre-encounter model values (*37*) are given by dashed lines. Pluto's upper atmosphere is very cold ($T$ ~ 70 K), resulting in a very low escape rate.

## Hazes

Extensive, optically thin hazes are seen in New Horizons images of Pluto (Fig. 4), extending to altitudes of >200 km, with typical brightness scale heights of ~50 km. Distinct layers are present, which vary with altitude but are contiguous over distances of >1000 km. Separated by ~10 km, the layers merge, separate (divide into thinner layers), or appear and disappear when traced around the limb. Using radial brightness profiles at various points around the limb, prominent haze layers are found in LORRI images at altitudes of ~10, 30, 90, and 190 km, but in the highest-resolution MVIC images (<1 km/pixel), about 20 haze layers are resolved. The haze scale height decreases to ~30 km at altitudes of 100 to 200 km, which is consistent with the decreasing atmospheric scale height (Fig. 3). Although most obvious at high phase angles (Θ ~ 165° to 169°) with $I/F$ values (observed intensity times π and divided by the incident solar flux) of ~0.2 to 0.3 at red wavelengths (in MVIC red, 540 to 700 nm, and LORRI images, 350 to 850 nm) and $I/F$ values up to 0.7 to 0.8 at blue wavelengths (in MVIC blue images, 400 to 550 nm), the hazes are also seen at moderate scattering angles (for example, at $I/F$ ~ 0.02 at Θ ~ 38°, in MVIC red and blue images) and are just barely detectable at low phase angles (for example, at $I/F$ ~ 0.003 at Θ ~ 20°, in LORRI images) but are undetected at the lowest phase angles (Θ ~ 15°) on approach. Although the blue haze color is consistent with very small (radii $r$ ~ 10 nm) particles (Rayleigh scatterers), their large high- to low-phase brightness ratio suggests much larger particles (with $r$ > 0.1 μm); it is possible that they are aggregate particles (randomly shaped particles of a fraction of a micrometer in radius, composed of ~10-nm spheres), which could satisfy both of these constraints. The MVIC blue/red ratio increases with altitude, which is consistent with smaller particles at higher altitudes. As seen in Fig. 4, the haze is brightest just above the limb, and from this and other images, the haze is brightest around the limb near the direction of Pluto north.

Haze optical properties can be roughly estimated as a function of particle size by using Mie theory—for example, with optical constants of $n$ = 1.69 and $k$ = 0.018 (where $n$ and $k$ are the real and imaginary parts of the complex refractive index, respectively), which are appropriate for tholin-like particles (*41*) at the LORRI pivot wavelength of 607.6 nm (although over the LORRI bandpass, $n$ varies between 1.63 and 1.72, whereas $k$ varies between 0.11 and 0.0024). For optically thin conditions, $I/F$ ~ $P(\Theta)$ $\tau_{LOS}/4$, where $P$ is the scattering phase function at phase angle Θ and $\tau_{LOS}$ is the line-of-sight opacity. On the basis of their large forward/backward scattering ratio, which is met by Mie-scattering particles with radii no smaller than ~0.2 μm, $P$(165°) ~ 5, leading to $\tau_{LOS}$ ~ 0.16, or a vertical haze scattering optical depth of ~0.013. For particles of $r$ ~ 0.2 μm, the scattering cross section of a single particle is

$\pi r^2 Q_S$ or ~3.4 × $10^{-9}$ $cm^2$ (with $Q_S$ ~ 2.7 from Mie theory). Using $\tau \sim \pi r^2 Q_S n_{HAZE} H_{HAZE}$, where $H_{HAZE}$ is the low-altitude haze scale height of 50 km, the haze density near Pluto's surface is $n_{HAZE}$ ~ 0.8 particles/$cm^3$, or a column mass of 8 × $10^{-8}$ g $cm^{-2}$ (assuming a particle density of 0.65 g $cm^{-3}$) (*42*).

If the haze particles are photochemically produced in a manner similar to Titan's hazes (*40*), an upper limit to their mass production rate is given by the photolysis loss rate of methane; from photochemical models (*37*, *38*), we estimate this at ~1 × $10^{-14}$ g $cm^{-2}$ $s^{-1}$. In steady state, this is also the loss rate, so (dividing the column mass by the production rate) the haze residence time is calculated to be $t_{HAZE}$ ~ 90 Earth days. By comparison, the time expected for 10-nm particles to settle through the lowest 10 km of the atmosphere is ~400 Earth days (fig. S2), whereas 0.2-μm particles would be expected to traverse this region much faster, in ~10 Earth days.

## Dynamics

Pluto's atmospheric pressure and composition is buffered by sublimation equilibrium with surface ices (principally $N_2$, with minor amounts of $CH_4$ and CO ices). Solar-induced sublimation of these ices drives transport to colder surface regions. Subsequent condensation constrains pressure variations in the atmosphere above the first ½-scale height to $\Delta p/p < 0.002$ for a surface pressure ~10 μbar (*43*, *44*) and for ice $\Delta T/T < 0.002$ (*44*). For pressures <5 μbar, the radio occultation data exhibits global symmetry, as expected from sublimation-driven dynamics. Previously, ground-based stellar occultations also yielded symmetry within the error bars about the occultation midpoint (for example, as shown for the 2006 Siding Spring light curve) (*45*). With very little pressure variation in the current atmosphere on a global scale, horizontal winds are expected to be weak (no more than ~10 m $s^{-1}$). Radiative time constants ($\alpha_{RAD}$) for Pluto's atmosphere above its planetary boundary layer are on the order of 10 to 15 Earth years (*24*), or $\alpha_{RAD}$ ~ 2.5 × $10^{-9}$ Hz. Diurnally driven dynamics with frequency of $\Omega = 2\pi/6.39$ $days^{-1}$ = 1.14 × $10^{-5}$ Hz will be damped in amplitude by a factor ~$\alpha_{RAD}^2/(\alpha_{RAD}^2 + \Omega^2)$ ~ 5.6 × $10^{-8}$. Although the surface likely has a short thermal response time constant, surface radiative exchange with the atmosphere is very weak, and the very steep positive temperature gradient in the near-surface layer as seen both in REX occultation data (Fig. 1) and ground-based stellar occultation data (*15*) should suppress convection and inhibit the formation of a deep global troposphere.

Gravity waves have previously been investigated as a source for scintillations seen in Earth-based stellar occultation data (*46*, *47*). Pluto's atmospheric dynamics can generate internal gravity (buoyancy) waves driven by sublimation forcing (*48*) and orographic forcing (wind blowing over topography). Mountains and mountain ranges with heights of 2 to 3 km have been detected with New Horizons imagery (*19*, *49*), and the distinct haze layers in Pluto's atmosphere are possibly a result of orographic forcing. For example, a

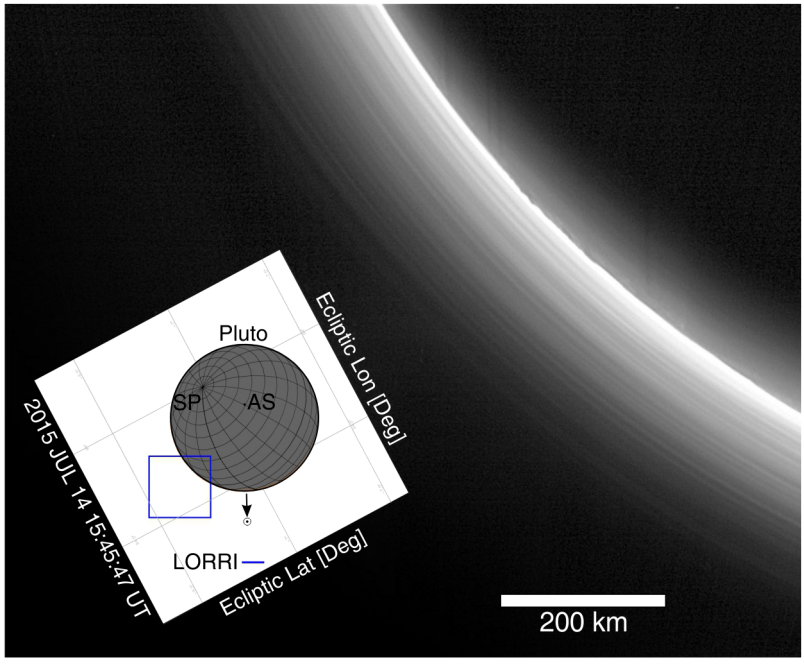



**Fig. 4. Pluto hazes.** LORRI two-image stack at 0.95 km $pixel^{-1}$ resolution, showing many haze layers up to an altitude of ~200 km, as well as night-side surface illumination. Acquired on 14 July 2015 starting at 15:45:43 UTC (observation 5 of P_MULTI_DEP_LONG_1 at MET 299194661-299194671; 0.3 s total exposure time), at a range from Pluto of 196,586 km and a phase angle of 169°. The raw images have been background-subtracted and sharpened and have a square root stretch. (Inset) The orientation of the image, with Pluto's south pole (SP) indicated, along with the direction to the Sun (11° from Pluto), and the latitude and longitude of the sub–anti-Sun (AS) position.

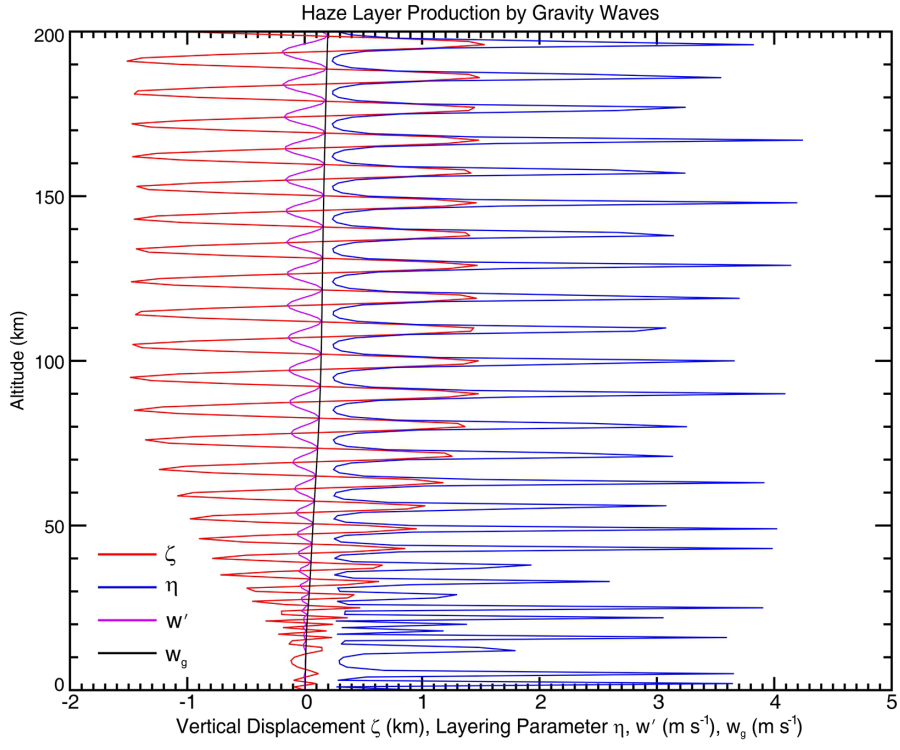



**Fig. 5. Haze layer production.** Haze particles undergo vertical displacements ζ by vertical gravity wave parcel velocity $w'$, which at saturation equals $w_g$, the vertical group velocity. Because $w'$ is much larger than the sedimentation velocity, compression and rarefaction of haze particle densities are associated with gravity wave displacements. The quantity $\eta = (½\lambda_Z + 2\zeta)/(½\lambda_Z - 2\zeta)$ is a measure of compaction and layering.

$u_0$ = 1 m s$^{-1}$ wind blowing over topography with height amplitude of $h_0$ = 1.5 km, horizontal wavelength $\lambda_x$ ~ 120 km (zonal wavenumber $k_x = 2\pi/\lambda_x$ ~ $60/R_P$), meridional wavelength $\lambda_y$ ~ 3600 km, and period $\tau = 2\pi/k_x u_0$ ~ 1.4 Earth days yields a vertical forcing velocity $w_0 \sim u_0 h_0 k_x$ ~ 0.08 m s$^{-1}$. Because of the small adiabatic lapse rate (~0.62 K km$^{-1}$ at the surface and decreasing with altitude), the gravity wave reaches saturation amplitudes by an altitude of 10 km. Saturation occurs when the buoyancy-restoring force vanishes—when the sum of the wave and mean temperature gradients render the atmosphere adiabatic, and the vertical parcel velocity $w'$ is equal to $w_g$, the vertical group velocity (*50*). At 10 km altitude, with any surface vertical forcing velocity $w_0 > 0.008$ m s$^{-1}$, the solution to the gravity wave equation yields saturated amplitudes for the wave temperature of $T'$ ~ 0.7 K and for the vertical parcel velocity of $w'$ ~ 0.01 m s$^{-1}$ (with $w' = w_g$). These perturbation temperatures are consistent with the temperature profile, at the current level of analysis. The prime influence of horizontal winds, $u$, is on the vertical wavelength $\lambda_z \sim 2\pi u/N$, where $N$ is the buoyancy frequency (~0.01 Hz at the surface and decreasing to ~0.001 Hz above 50 km), and the layering of the haze provides important constraints on this quantity. Shown in Fig. 5 is the vertical displacement, $\zeta = D^{-1}w' = w'/ik_x u$, of haze particles by gravity waves, with Lagrangian derivative $D$ and $i = \sqrt{-1}$. Because $w'$ is much larger than the sedimentation velocity (fig. S2), there is compression and rarefaction of haze particles associated with gravity wave displacements. If $\frac{1}{2}\lambda_z$ ~ 5 km and $\zeta$ ~ 1.5 km, compression leads to ~2 km separation and rarefaction to ~8 km separation between wave amplitude negative and positive peaks and could thus account for haze layering. Forcing by zonal winds would vanish at the poles, and variations of orography would affect the predictions as well, but gravity waves provide a viable mechanism for producing haze layers on Pluto.

## Escape

Before the New Horizons flyby, the escape rate to space of $N_2$ from Pluto was expected (*33*) to be 0.7 × 10$^{27}$ to 4 × 10$^{27}$ molecules s$^{-1}$, with a preferred value of 2.8 × 10$^{27}$ molecules s$^{-1}$ based on estimates of Pluto's surface pressure and radius, as well as $CH_4$ and CO mixing ratios (*17*). This escape rate is fundamentally limited by solar extreme ultraviolet and far-ultraviolet net heating rates and by the effective area of Pluto's extended atmosphere. However, these pre-encounter calculations neglected cooling by photochemically produced HCN (*16*) and $C_2H_2$, which might reduce the net heating and hence the escape rate. On the basis of fits to the solar occultation transmission (Fig. 2), our calculated current escape rates of nitrogen and methane from Pluto's upper atmosphere are 1 × 10$^{23}$ and 5 × 10$^{25}$ molecules s$^{-1}$, respectively (with the exobase located at $r$ ~ 2750 to 2850 km, where the $N_2$ and $CH_4$ densities are 4 × 10$^6$ to 7 × 10$^6$ cm$^{-3}$ and 3 × 10$^6$ to 5 × 10$^6$ cm$^{-3}$, respectively). These are the Jeans escape rates—Pluto's atmosphere is not currently undergoing hydrodynamic escape—and they are low enough to strongly reduce the altitude of any interaction region between Pluto's upper atmosphere/ionosphere and the solar wind (*51*). If these rates are stable over a single Pluto orbit, the equivalent thickness of nitrogen and methane surface ice lost to space would be ~3 nm and 1.5 μm, respectively. If these rates were stable over the age of the solar system, the equivalent thickness of nitrogen and methane surface ice lost to space would be ~6 cm and 28 m, respectively. The relatively small amount of nitrogen loss is consistent with an undetected Charon atmosphere (of less than a pre-encounter prediction of ~8 pbar) (*52*) but appears to be inconsistent with the primarily erosional features seen on Pluto's surface (*49*), so that past $N_2$ escape rates may have occasionally been much larger. The loss of methane is much closer to predicted values (*37*), and a suggested origin for Charon's north polar red color (involving "varnishing" of the winter poles over millions of years through cold-trapping and polymerization of escaping hydrocarbons from Pluto) remains viable (*19*, *31*).

## Conclusions

Observations made from New Horizons have already greatly altered our understanding of how Pluto's atmosphere works, even with many data remaining to be reduced and analyzed. LORRI, MVIC, and Linear Etalon Imaging Spectral Array (LEISA) imaging clearly reveal optically thin hazes extending to altitudes of at least 200 km. Photochemical models have long predicted the formation of higher hydrocarbons, and species such as acetylene ($C_2H_2$) and ethylene ($C_2H_4$) are clearly detected in the Alice solar occultation data (ultraviolet reflectance spectra also show the absorption signatures of $C_2H_2$ and $C_2H_4$). Last, the escape rate of Pluto's atmosphere is found to be much less than expected, although over time it may have left its signature on Charon (*19*, *31*).

Although most of the results obtained to date agree with each other, there are several problem areas: Is cooling by HCN self-limited because of condensation? Are the haze layers consistent with transport by winds? Does the escape of much more methane than nitrogen agree with geologic evidence? The data obtained by the New Horizons mission are likely to provide the answers and allow the development of a fully self-consistent description of Pluto's atmosphere.

## REFERENCES AND NOTES


1. L. A. Young *et al.*, New Horizons: Anticipated scientific investigations at the Pluto system. *Space Sci. Rev.* **140**, 93–127 (2008). doi: 10.1007/s11214-008-9462-9
2. G. L. Tyler *et al.*, The New Horizons radio science experiment (REX). *Space Sci. Rev.* **140**, 217–259 (2008). doi: 10.1007/s11214-007-9302-3
3. S. A. Stern *et al.*, Alice: The ultraviolet imaging spectrograph aboard the New Horizons Pluto-Kuiper Belt mission. *Space Sci. Rev.* **140**, 155–187 (2008). doi: 10.1007/s11214-008-9407-3
4. A. F. Cheng *et al.*, Long-Range Reconnaissance Imager on New Horizons. *Space Sci. Rev.* **140**, 189–215 (2008). doi: 10.1007/s11214-007-9271-6
5. D. C. Reuter *et al.*, Ralph: A Visible/Infrared Imager for the New Horizons Pluto/Kuiper Belt Mission. *Space Sci. Rev.* **140**, 129–154 (2008). doi: 10.1007/s11214-008-9375-7
6. M. H. Hart, A possible atmosphere for Pluto. *Icarus* **21**, 242–247 (1974). doi: 10.1016/0019-1035(74)90039-6
7. G. S. Golitsyn, A possible atmosphere on Pluto. *Sov. Astron. Lett.* **1**, 19 (1975).
8. D. P. Cruikshank, P. M. Silvaggio, The surface and atmosphere of Pluto. *Icarus* **41**, 96–102 (1980). doi: 10.1016/0019-1035(80)90162-1
9. U. Fink *et al.*, Detection of a $CH_4$ atmosphere on Pluto. *Icarus* **44**, 62–71 (1980). doi: 10.1016/0019-1035(80)90055-X
10. L. Trafton, S. A. Stern, On the global distribution of Pluto's atmosphere. *Astrophys. J.* **267**, 872 (1983). doi: 10.1086/160921
11. N. Brosch, The 1985 stellar occultation by Pluto. *Mon. Not. R. Astron. Soc.* **276**, 571–578 (1995). doi: 10.1093/mnras/276.2.571
12. W. B. Hubbard, D. M. Hunten, S. W. Dieters, K. M. Hill, R. D. Watson, Occultation evidence for an atmosphere on Pluto. *Nature* **336**, 452–454 (1988). doi: 10.1038/336452a0
13. J. L. Elliot *et al.*, Pluto's atmosphere. *Icarus* **77**, 148–170 (1989). doi: 10.1016/0019-1035(89)90014-6
14. A. S. Bosh *et al.*, The state of Pluto's atmosphere in 2012-2013. *Icarus* **246**, 237–246 (2015). doi: 10.1016/j.icarus.2014.03.048
15. C. B. Olkin *et al.*, Pluto's atmospheric structure from the July 2007 stellar occultation. *Icarus* **239**, 15–22 (2014). doi: 10.1016/j.icarus.2014.05.018
16. A. Dias-Oliveira *et al.*, Pluto's atmosphere from stellar occultations in 2012 and 2013. *Astrophys. J.* **811**, 53 (2015). doi: 10.1088/0004-637X/811/1/53
17. E. Lellouch *et al.*, Exploring the spatial, temporal, and vertical distribution of methane in Pluto's atmosphere. *Icarus* **246**, 268–278 (2015). doi: 10.1016/j.icarus.2014.03.027
18. E. Lellouch *et al.*, (134340) Pluto. *IAU Circular* **9273**, 1 (2015).
19. S. A. Stern *et al.*, The Pluto system: Initial results from its exploration by New Horizons, *Science* **350**, aad1815 (2015).
20. Y. Guo, R. W. Farquhar, New Horizons mission design. *Space Sci. Rev.* **140**, 49–74 (2007). doi: 10.1007/s11214-007-9242-y
21. M. Born, E. Wolf, *Principles of Optics* (Cambridge Univ. Press, ed. 7, 1999).
22. B. Sicardy *et al.*, Large changes in Pluto's atmosphere as revealed by recent stellar occultations. *Nature* **424**, 168–170 (2003). pmid: 12853950
23. J. L. Elliot *et al.*, Changes in Pluto's atmosphere: 1988–2006. *Astron. J.* **134**, 1–13 (2007). doi: 10.1086/517998
24. D. F. Strobel, X. Zhu, M. E. Summers, M. H. Stevens, On the vertical thermal structure of Pluto's atmosphere. *Icarus* **120**, 266–289 (1996). doi: 10.1006/icar.1996.0050
25. J. A. Stansberry, J. L. Lunine, W. B. Hubbard, R. V. Yelle, D. M. Hunten, *Icarus* **111**, 503–513 (1994).
26. L. A. Young, "Bulk properties and atmospheric structure of Pluto and Charon," thesis, Massachusetts Institute of Technology, 1994.
27. E. F. Young *et al.*, Vertical structure in Pluto's atmosphere from the 2006 June 12 stellar occultation. *Astron. J.* **136**, 1757–1769 (2008). doi: 10.1088/0004-6256/136/5/1757
28. E. Lellouch *et al.*, Pluto's lower atmosphere structure and methane abundance from high-resolution spectroscopy and stellar occultations. *Astron. Astrophys.* **495**, L17–L21 (2009). doi: 10.1051/0004-6361/200911633
29. G. N. Brown Jr., W. T. Ziegler, Vapor pressure and heats of vaporization and sublimation of liquids and solids of interest in cryogenics below 1-atm pressure. *Adv. Cryog. Eng.* **25**, 662 (1980).
30. J. R. Spencer *et al.*, "Volatile transport, seasonal cycles, and atmospheric dynamics on Pluto," in *Pluto and Charon*, S. A. Stern, D. J. Tholen, Eds. (Univ. of Arizona Press, 1997), pp. 435–473.
31. W. M. Grundy *et al.*, Surface compositions across Pluto and Charon. *Science* **351**, aad9189-1 (2016).
32. W. M. Grundy, C. B. Olkin, L. A. Young, M. W. Buie, E. F. Young, Near-infrared spectral monitoring of Pluto's ices: Spatial distribution and secular evolution. *Icarus* **223**, 710–721 (2013). doi: 10.1016/j.icarus.2013.01.019
33. X. Zhu, D. F. Strobel, J. T. Erwin, The density and thermal structure of Pluto's atmosphere and associated escape processes and rates. *Icarus* **228**, 301–314 (2014). doi: 10.1016/j.icarus.2013.10.011
34. W. B. Hubbard, R. V. Yelle, J. I. Lunine, Nonisothermal Pluto atmosphere models. *Icarus* **84**, 1–11 (1990). doi: 10.1016/0019-1035(90)90154-2
35. M. E. Summers, D. F. Strobel, G. R. Gladstone, "Chemical models of Pluto's atmosphere," in *Pluto and Charon*, S. A. Stern, D. J. Tholen, Eds. (Univ. of Arizona Press, 1997), pp. 391–434.

36. L. M. Lara, W.-H. Ip, R. Rodrigo, Photochemical models of Pluto's atmosphere. *Icarus* **130**, 16–35 (1997). doi: 10.1006/icar.1997.5798
37. V. A. Krasnopolsky, D. P. Cruikshank, Photochemistry of Pluto's atmosphere and ionosphere near perihelion. *J. Geophys. Res.* **104** (E9), 21,979–21996 (1999). doi: 10.1029/1999JE001038
38. M. L. Wong, Y. L. Yung, G. R. Gladstone, Pluto's implications for a snowball Titan. *Icarus* **246**, 192–196 (2015). doi: 10.1016/j.icarus.2014.05.019
39. G. R. Gladstone, W. R. Pryor, S. A. Stern, Lyα@Pluto. *Icarus* **246**, 279 (2015). doi: 10.1016/j.icarus.2014.04.016
40. P. Lavvas *et al*., Aerosol growth in Titan's ionosphere. *Proc. Natl. Acad. Sci. U.S.A.* **110**, 2729–2734 (2013). doi: 10.1073/pnas.1217059110; pmid: 23382231
41. B. N. Khare *et al*., Optical constants of organic tholins produced in a simulated Titanian atmosphere—From soft x-ray to microwave frequencies. *Icarus* **60**, 127–137 (1984). doi: 10.1016/0019-1035(84)90142-8
42. S. M. Hörst, M. A. Tolbert, In situ measurements of the size and density of Titan aerosol analogs. *Astrophys. J.* **770**, L10 (2013). doi: 10.1088/2041-8205/770/1/L10
43. A. P. Ingersoll, M. E. Summers, S. G. Schlipf, Supersonic meteorology of Io—Sublimation-driven flow of $SO_2$. *Icarus* **64**, 375–390 (1985). doi: 10.1016/0019-1035(85)90062-4
44. L. A. Young, Volatile transport on inhomogeneous surfaces: I—Analytic expressions, with application to Pluto's day. *Icarus* **221**, 80–88 (2012). doi: 10.1016/j.icarus.2012.06.032
45. A. M. Zalucha, A. A. S. Gulbis, X. Zhu, D. F. Strobel, J. L. Elliot, An analysis of Pluto occultation light curves using an atmospheric radiative-conductive model. *Icarus* **211**, 804–818 (2011). doi: 10.1016/j.icarus.2010.08.018
46. M. J. Person *et al*., Waves in Pluto's upper atmosphere. *Astrophys. J.* **136**, 1510 (2008).
47. W. B. Hubbard *et al*., Buoyancy waves in Pluto's high atmosphere: Implications for stellar occultations. *Icarus* **204**, 284–289 (2009). doi: 10.1016/j.icarus.2009.06.022
48. A. D. Toigo, P. J. Gierasch, B. Sicardy, E. Lellouch, Thermal tides on Pluto. *Icarus* **208**, 402–411 (2010). doi: 10.1016/j.icarus.2010.01.027
49. J. M. Moore *et al*., The geology of Pluto and Charon through the eyes of New Horizons. *Science* **351**, 1284–1293 (2016).
50. D. C. Fritts, Gravity wave saturation in the middle atmosphere - A review of theory and observations. *Rev. Geophys. Space Phys.* **22**, 275 (1984). doi: 10.1029/RG022i003p00275
51. F. Bagenal *et al*., Pluto's interaction with its space environment: Solar wind, energetic particles, and dust. *Science* **351**, aad9045 (2016).
52. O. J. Tucker, R. E. Johnson, L. A. Young, Gas transfer in the Pluto-Charon system: A Charon atmosphere. *Icarus* **246**, 291–297 (2015). doi: 10.1016/j.icarus.2014.05.002
53. E. A. Marouf, G. L. Tyler, P. A. Rosen, Profiling Saturn's rings by radio occultation. *Icarus* **68**, 120–166 (1986). doi: 10.1016/0019-1035(86)90078-3
54. G. F. Lindal *et al*., The atmosphere of Titan—An analysis of the Voyager 1 radio occultation measurements. *Icarus* **53**, 348–363 (1983). doi: 10.1016/0019-1035(83)90155-0
55. D. P. Hinson, R. A. Simpson, J. D. Twicken, G. L. Tyler, F. M. Flasar, Initial results from radio occultation measurements with Mars Global Surveyor. *J. Geophys. Res.* **104** (E11), 26,997–27012 (1999). doi: 10.1029/1999JE001069



## ACKNOWLEDGMENTS

We thank the NASA's New Horizons project for their excellent and long-term support. We thank our colleagues B. Bézard, J. Erwin, F. Forget, M. Gurwell, S. Gusewich, C. Hansen, A. Heays, K. L. Jessup, V. Krasnopolsky, E. Lellouch, B. Lewis, B. Sicardy, G. Stark, K. Stothoff, A. Toigo, R. Vervack, and R. Yelle for excellent advice, data, and useful comments. We thank the reviewers for their very useful comments. S.A.S. is also affiliated with Florida Space Institute, Uwingu, Golden Spike Co., and World View Enterprises. N.J.C. was a paid consultant to Southwest Research Institute. As contractually agreed to with NASA, fully calibrated New Horizons Pluto system data will be released via the NASA Planetary Data System at https://pds.nasa.gov in a series of stages in 2016 and 2017 owing to the time required to fully downlink and calibrate the data set.


## SUPPLEMENTARY MATERIALS

www.sciencemag.org/content/351/6279/aad8866/suppl/DC1
Materials and Methods
Figs. S1 and S2
Tables S1 to S3
New Horizons Science Team Author List
References (*56*–*63*)

16 November 2015; accepted 17 February 2016
10.1126/science.aad8866

RESEARCH ARTICLE SUMMARY

PLANETARY SCIENCE

# The small satellites of Pluto as observed by New Horizons

H. A. Weaver,* M. W. Buie, B. J. Buratti, W. M. Grundy, T. R. Lauer, C. B. Olkin, A. H. Parker, S. B. Porter, M. R. Showalter, J. R. Spencer, S. A. Stern, A. J. Verbiscer, W. B. McKinnon, J. M. Moore, S. J. Robbins, P. Schenk, K. N. Singer, O. S. Barnouin, A. F. Cheng, C. M. Ernst, C. M. Lisse, D. E. Jennings, A. W. Lunsford, D. C. Reuter, D. P. Hamilton, D. E. Kaufmann, K. Ennico, L. A. Young, R. A. Beyer, R. P. Binzel, V. J. Bray, A. L. Chaikin, J. C. Cook, D. P. Cruikshank, C. M. Dalle Ore, A. M. Earle, G. R. Gladstone, C. J. A. Howett, I. R. Linscott, F. Nimmo, J. Wm. Parker, S. Philippe, S. Protopapa, H. J. Reitsema, B. Schmitt, T. Stryk, M. E. Summers, C. C. C. Tsang, H. H. B. Throop, O. L. White, A. M. Zangari

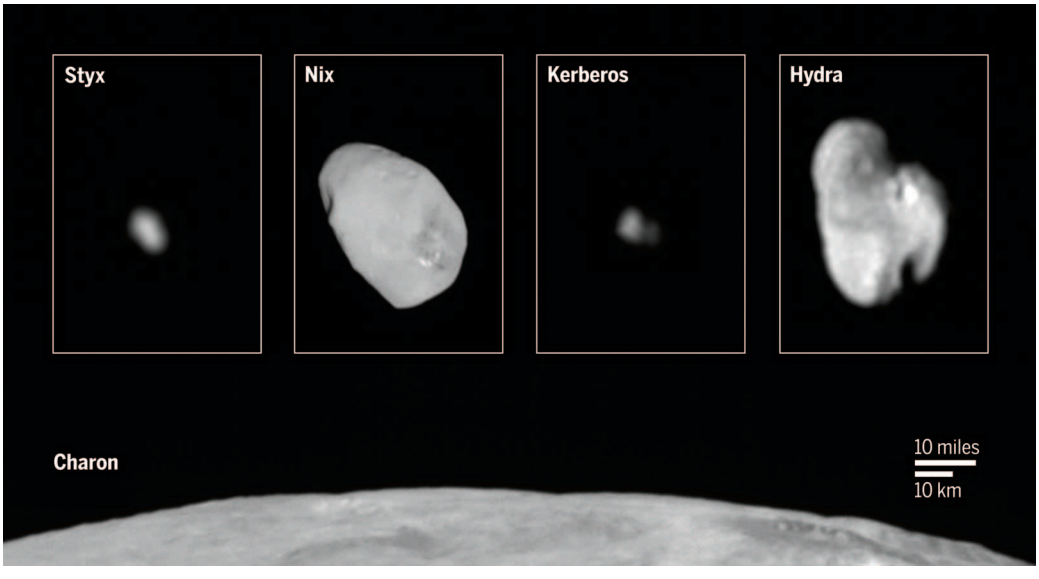
**INTRODUCTION:** The Pluto system is surprisingly complex, comprising six objects that orbit their common center of mass in approximately a single plane and in nearly circular orbits. When the New Horizons mission was selected for flight by NASA in 2001, only the two largest objects were known: the binary dwarf planets Pluto and Charon. Two much smaller moons, Nix and Hydra, were discovered in May 2005, just 8 months before the launch of the New Horizons spacecraft, and two even smaller moons, Kerberos and Styx, were discovered in 2011 and 2012, respectively. The entire Pluto system was likely produced in the aftermath of a giant impact between two Pluto-sized bodies approximately 4 to 4.5 billion years ago, with the small moons forming within the resulting debris disk. But many details remain unconfirmed, and the New Horizons results on Pluto's small moons help to elucidate the conditions under which the Pluto system formed and evolved.

**RATIONALE:** Pluto's small moons are difficult to observe from Earth-based facilities, with only the most basic visible and near-infrared photometric measurements possible to date. The New Horizons flyby enabled a whole new category of measurements of Pluto's small moons. The Long Range Reconnaissance Imager (LORRI) provided high–spatial resolution panchromatic imaging, with thousands of pixels across the surfaces of Nix and Hydra and the first resolved images of Kerberos and Styx. In addition, LORRI was used to conduct systematic monitoring of the brightness of all four small moons over several months, from which the detailed rotational properties could be deduced. The Multispectral Visible Imaging Camera (MVIC) provided resolved color measurements of the surfaces of Nix and Hydra. The Linear Etalon Imaging Spectral Array (LEISA) captured near-infrared spectra (in the wavelength range 1.25 to 2.5 μm) of all the small moons for compositional studies, but those data have not yet been sent to Earth.

**RESULTS:** All four of Pluto's small moons are highly elongated objects with surprisingly high surface reflectances (albedos) suggestive of a water-ice surface composition. Kerberos appears to have a double-lobed shape, possibly formed by the merger of two smaller bodies. Crater counts for Nix and Hydra imply surface ages of at least 4 billion years. Nix and Hydra have mostly neutral (i.e., gray) colors, but an apparent crater on Nix's surface is redder than the rest of the surface; this finding suggests either that the impacting body had a different composition or that material with a different composition was excavated from below Nix's surface. All four small moons have rotational periods much shorter than their orbital periods, and their rotational poles are clustered nearly orthogonal to the direction of the common rotational poles of Pluto and Charon.

ON OUR WEB SITE

Read the full article at http://dx.doi.org/10.1126/science.aae0030




**Pluto's family of satellites.** NASA's New Horizons mission has resolved Pluto's four small moons, shown in order of their orbital distance from Pluto (from left to right). Nix and Hydra have comparable sizes (with equivalent spherical diameters of ~40 km) and are much larger than Styx and Kerberos (both of which have equivalent spherical diameters of ~10 km). All four of these moons are highly elongated and are dwarfed in size by Charon, which is nearly spherical with a diameter of 1210 km. The scale bars apply to all images.

**CONCLUSION:** Pluto's small moons exhibit rapid rotation and large rotational obliquities, indicating that tidal despinning has not played the dominant role in their rotational evolution. Collisional processes are implicated in determining the shapes of the small moons, but collisional evolution was probably limited to the first several hundred million years after the system's formation. The bright surfaces of Pluto's small moons suggest that if the Pluto-Charon binary was produced during a giant collision, the two precursor bodies were at least partially differentiated with icy surface layers. ■

The list of author affiliations is available in the full article online.
*Corresponding author. E-mail: hal.weaver@jhuapl.edu
Cite this article as H. A. Weaver *et al.*, *Science* 351, aae0030 (2016). DOI: 10.1126/science.aae0030

Downloaded from on March 17, 2016

RESEARCH ARTICLE

PLANETARY SCIENCE

# The small satellites of Pluto as observed by New Horizons

H. A. Weaver,[1]* M. W. Buie,[2] B. J. Buratti,[3] W. M. Grundy,[4] T. R. Lauer,[5] C. B. Olkin,[2] A. H. Parker,[2] S. B. Porter,[2] M. R. Showalter,[6] J. R. Spencer,[2] S. A. Stern,[2] A. J. Verbiscer,[7] W. B. McKinnon,[8] J. M. Moore,[9] S. J. Robbins,[2] P. Schenk,[10] K. N. Singer,[2] O. S. Barnouin,[1] A. F. Cheng,[1] C. M. Ernst,[1] C. M. Lisse,[1] D. E. Jennings,[11] A. W. Lunsford,[11] D. C. Reuter,[11] D. P. Hamilton,[12] D. E. Kaufmann,[2] K. Ennico,[9] L. A. Young,[2] R. A. Beyer,[6,9] R. P. Binzel,[13] V. J. Bray,[14] A. L. Chaikin,[15] J. C. Cook,[2] D. P. Cruikshank,[9] C. M. Dalle Ore,[9] A. M. Earle,[14] G. R. Gladstone,[16] C. J. A. Howett,[2] I. R. Linscott,[17] F. Nimmo,[18] J. Wm. Parker,[2] S. Philippe,[19] S. Protopapa,[12] H. J. Reitsema,[2] B. Schmitt,[19] T. Stryk,[20] M. E. Summers,[21] C. C. C. Tsang,[2] H. H. B. Throop,[22] O. L. White,[9] A. M. Zangari[2]

**The New Horizons mission has provided resolved measurements of Pluto's moons Styx, Nix, Kerberos, and Hydra. All four are small, with equivalent spherical diameters of ~40 kilometers for Nix and Hydra and ~10 kilometers for Styx and Kerberos. They are also highly elongated, with maximum to minimum axis ratios of ~2. All four moons have high albedos (~50 to 90%) suggestive of a water-ice surface composition. Crater densities on Nix and Hydra imply surface ages of at least 4 billion years. The small moons rotate much faster than synchronous, with rotational poles clustered nearly orthogonal to the common pole directions of Pluto and Charon. These results reinforce the hypothesis that the small moons formed in the aftermath of a collision that produced the Pluto-Charon binary.**

Pluto's four small moons Styx, Nix, Kerberos, and Hydra (in order of increasing distance from Pluto; hereafter we refer to this sequence as SNKH) were discovered using the Hubble Space Telescope (HST): Nix and Hydra in 2005 (*1*), Kerberos in 2011 (*2*), and Styx in 2012 (*3*). SNKH orbit the Pluto system barycenter in essentially the same plane (coincident with the Pluto-Charon orbital plane) and in nearly circular orbits with orbital semimajor axes of 42,656, 48,694, 57,783, and 64,738 km, and orbital periods of 20.2, 24.9, 32.2, and 38.2 days, respectively (*4*, *5*). These orbital periods are nearly integer multiples of Charon's 6.4-day orbital period, with ratios of 3:4:5:6 for SNKH, respectively (*4*, *5*). Sensitive searches for other moons with New Horizons were unsuccessful (*6*), demonstrating that no other moons larger than ~1.7 km in diameter (assuming the geometric albedo is ~0.5) are present at orbital radii between 5000 and 80,000 km, with less stringent limits at larger radii.

The long-term dynamical stability of Kerberos places severe constraints on the allowable masses and surface reflectances (i.e., albedos) of Nix and Hydra (*7*). These latter constraints, together with the disk-integrated brightness measurements of Nix and Hydra (brightness is proportional to the product of the object's cross-sectional area and its albedo), suggested that Nix and Hydra are relatively small, icy satellites (*7*). Adopting the hypothesis that impact-generated debris from the small moons produced a regolith covering Charon's surface (*8*, *9*), so that all of Pluto's moons would have similar visible-light albedos (the visible-light albedo of Charon is ~0.38), the average spherical-equivalent spherical diameters of Styx, Nix, Kerberos, and Hydra would be approximately 7, 40, 10, and 45 km, respectively. However, the observed brightness of Kerberos, together with dynamical constraints on its mass (*4*), suggested (*5*) that it has a much lower albedo and a much larger size (e.g., diameter of 25 km for an albedo of 0.06). On the basis of an extensive set of HST brightness measurements over time, it was argued that Nix is highly elongated, with a maximum to minimum axial ratio of ~2 (*5*). Similar measurements suggested that Hydra was also elongated, but less so than Nix (*5*). No stable rotational period could be found for either Nix or Hydra, perhaps suggesting that both bodies were tumbling chaotically as a result of the large and regular torques exerted on them by the Pluto-Charon binary (*5*).

The New Horizons mission provided an opportunity to make spatially resolved observations of Pluto's small moons, thereby testing the findings from Earth-based observations (*4*, *5*) and various theoretical predictions (*7*–*9*) by giving direct measurements of their sizes, shapes, surface albedo, and color variations, along with snapshots of their rotational states. In addition, an extensive and systematic set of unresolved panchromatic brightness measurements of the small moons over several months (early April to early July 2015) was obtained by New Horizons during the approach to Pluto, which provides further information on their shapes and more precise information on their rotational states. Here, we report on the results from the New Horizons observations of Pluto's small moons using data received on Earth by mid-December 2015. All the data discussed here were obtained by either the Long Range Reconnaissance Imager (LORRI), a panchromatic camera (*10*), or the Multispectral Visible Imaging Camera (MVIC), a color camera (*11*). Infrared spectral measurements from the Linear Etalon Imaging Spectral Array (LEISA) (*11*) will provide detailed compositional information, but those data will not be sent to Earth until March or April 2016.

## Physical properties

Table 1 presents a log of all the resolved measurements of Pluto's small moons. Some examples of the resolved images are shown in Fig. 1 (see also fig. S1 and figs. S7 to S14). Systematic measurements of the brightness variations of Pluto's moons between May and early July 2015 were used together with the resolved measurements to constrain the sizes, shapes, rotation periods, and rotation poles of all four moons (*12*) (Table 2). Figure 2 shows the observed brightness variations after phasing by the best-fit rotational periods (see also figs. S2 and S3). Unlike the case for Pluto and Charon—each of which synchronously rotates with a period of 6.3872 days, equal to their mutual orbital period around their common barycenter—Pluto's small moons rotate surprisingly rapidly (Hydra has the fastest rotational period, ~10 hours) and all are far from synchronous. The rotational poles (Table 2 and table S4) are clustered nearly orthogonal to the direction of the common rotational poles of Pluto and Charon: The inclination angles relative to the Pluto-Charon pole direction are 91°, 123°, 96°, and 110° for SNKH, respectively. Nominally, all the small moons have retrograde rotation, but Nix is the only one significantly so (i.e., retrograde with greater than 1σ confidence). This collection of inclinations is inconsistent

[1]Johns Hopkins University Applied Physics Laboratory, Laurel, MD 20723, USA. [2]Southwest Research Institute, Boulder, CO 80302, USA. [3]NASA Jet Propulsion Laboratory, California Institute of Technology, Pasadena, CA 91109, USA. [4]Lowell Observatory, Flagstaff, AZ 86001, USA. [5]National Optical Astronomy Observatory, Tucson, AZ 26732, USA. [6]SETI Institute, Mountain View, CA 94043, USA. [7]Department of Astronomy, University of Virginia, Charlottesville, VA 22904, USA. [8]Department of Earth and Planetary Sciences, Washington University, St. Louis, MO 63130, USA. [9]Space Science Division, NASA Ames Research Center, Moffett Field, CA 94035, USA. [10]Lunar and Planetary Institute, Houston, TX 77058, USA. [11]NASA Goddard Space Flight Center, Greenbelt, MD 20771, USA. [12]Department of Astronomy, University of Maryland, College Park, MD 20742, USA. [13]Massachusetts Institute of Technology, Cambridge, MA 02139, USA. [14]University of Arizona, Tucson, AZ 85721, USA. [15]Independent science writer, Arlington, VT, USA. [16]Southwest Research Institute, San Antonio, TX 78238, USA. [17]Stanford University, Stanford, CA 94305, USA. [18]University of California, Santa Cruz, CA 95064, USA. [19]Université Grenoble Alpes, CNRS, IPAG, F-38000 Grenoble, France. [20]Roane State Community College, Oak Ridge, TN 37830, USA. [21]George Mason University, Fairfax, VA 22030, USA. [22]Planetary Science Institute, Tucson, AZ 85719, USA.
*Corresponding author. E-mail: hal.weaver@jhuapl.edu

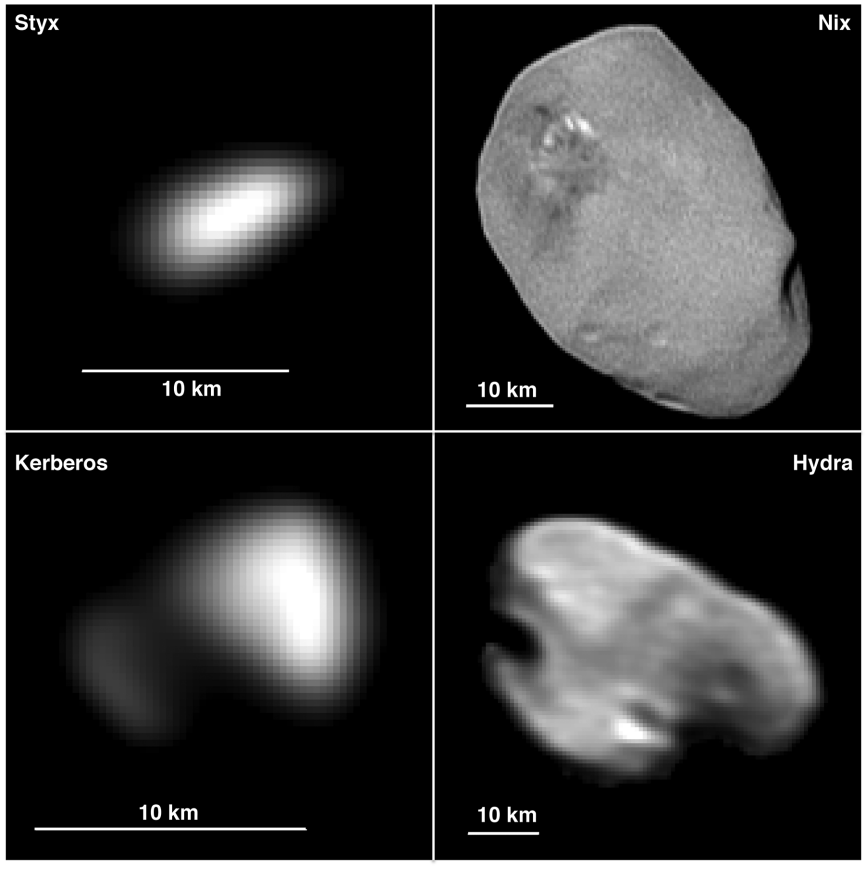



**Fig. 1. Best-resolved images of Pluto's four small moons.** Celestial north is up; east is to the left. The Styx image is a deconvolved (*12*) composite of six images from U_TBD_1_02 (Table 1) that has been resampled with pixels one-eighth of the native pixel scale for cosmetic purposes. The Nix image is a deconvolved single image from N_LEISA_LORRI_BEST and is displayed with the native pixels. The Kerberos image is a deconvolved composite of four images from U_TBD_2 and has been resampled with pixels one-eighth of the native pixel scale for cosmetic purposes (*12*) (fig. S1). The Hydra image is a deconvolved composite of two images from H_LORRI_BEST with pixels one-half of the native scale. Some surface features on Nix and Hydra appear to be impact craters (*12*).

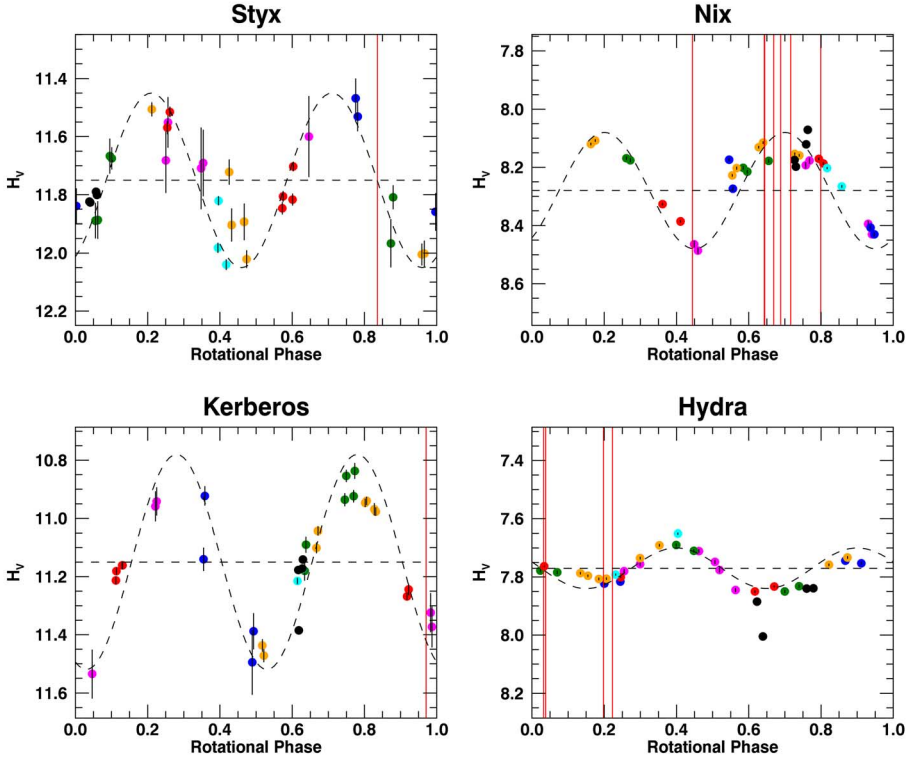



**Fig. 2. Rotational light curves for Pluto's small moons.** Systematic measurements of the brightnesses of Pluto's small satellites were obtained by LORRI during the approach to Pluto from May through early July 2015. $H_v$ refers to the total (i.e., integrated over the entire target) visible magnitude (V band) referenced to a heliocentric distance of 1 AU, a spacecraft-to-target distance of 1 AU, and a solar phase angle of 0° (using a phase law of 0.04 mag/deg). Different colors are used for the seven different observing epochs (*12*) (table S4); ±1σ error bars are shown for each measurement (some error bars are smaller than the symbols). Three different algorithms were used to search for periodic variations in the data (*12*). The rotational periods derived from that analysis (Table 2) were then used to phase the brightness data, producing the light curves displayed above. These double-peaked light curves presumably result from the rotation of elongated bodies, with the light-curve amplitude determined by the variation in the cross-sectional area presented to the observer, which depends on the body's shape and the angle between the rotational pole and the line of sight to the body. The rotational phases for all the resolved observations of the small satellites (Table 1) are indicated by the vertical red lines, although the angle between the observer and the rotational pole may be different for these observations relative to the earlier ones. The dashed curves are sinusoids with the best-matched periods. The amplitudes for Styx, Nix, Kerberos, and Hydra, respectively, are 0.30, 0.20, 0.37, and 0.07 mag. The dashed horizontal lines are the mean $H_v$ values, which are 11.75, 8.28, 11.15, and 7.77 mag for Styx, Nix, Kerberos, and Hydra, respectively.

with an isotropic distribution; even with only four points, a Kolmogorov-Smirnov test shows a less than 1% probability that this is a uniform distribution in inclination (i.e., the pole inclinations are nonuniform to a 2σ to 3σ confidence level). These results on the rotational properties have not been seen in other regular satellite systems in the solar system. Rapid rotations and large obliquities imply that tidal despinning has not played a major role in the moons' rotational histories. The moons have probably never reached the state of near synchronicity where chaotic perturbations by Charon have been predicted to dominate (*5*); determining whether chaos plays a role in the moons' current rotational dynamics is deferred to a future study.

Pluto's small moons have highly elongated shapes with maximum to minimum axial ratios of ~1.5 to 2 (Table 2). Highly asymmetrical shapes are typical of many other small bodies in the solar system and presumably reflect a growth process by agglomeration of small objects into loosely bound, macroporous bodies whose gravity was insufficient to pull them into more spherical shapes. Kerberos, in particular, has a double-lobed shape, suggesting the merger of two smaller bodies. Hydra also has a highly asymmetrical shape that may also indicate the merger of smaller bodies, but the divots in Hydra's surface may plausibly have been produced by impacts from the local Kuiper Belt population. The nonspherical shapes of Pluto's small satellites are consistent with their formation in the remnant disk produced by the collision of two large Kuiper Belt objects (KBOs) that formed the Pluto-Charon binary (*13*–*15*).

Large uncertainties in the masses of the small moons (up to ~100%), as well as large uncertainties in their volumes, preclude determining accurate values for their densities at this time (densities of 0 are within the current error estimates). However, the New Horizons results on Kerberos (see below) clearly demonstrate that the current dynamical estimate for its mass (*4*) is an overestimate, possibly by a factor of ~100.

**Table 1. Log of available resolved observations of Pluto's small moons.** All observations of Pluto's small satellites with a resolution better than 15 km per pixel and downlinked to Earth before 15 December 2015 are listed. The dates are the mid-observation times at the New Horizons spacecraft. Resolution refers to the projected distance at the object subtended by a single instrument pixel. The phase angle is the Sun–object–New Horizons angle. All observations were taken with the LORRI panchromatic camera (*10*), except "N_COLOR_2" and "N_MPAN_CA," which were taken with the MVIC color camera (*11*).

| Object | Observation name | Date in 2015 (UTC) | No. of images containing object | Resolution (km/pixel) | Phase angle (degrees) |
|---|---|---|---|---|---|
| Styx | U_TBD_1_02 | 07-13 23:44:56 | 6 | 3.13 | 17.3 |
| Nix | N_LORRI_APPR_1D2 | 07-13 23:19:29 | 2 | 2.92 | 13.4 |
| | N_COLOR_2 | 07-14 08:03:29 | 1 | 3.10 | 8.45 |
| | N_LORRI_BACKUP | 07-14 08:06:58 | 4 | 0.76 | 8.34 |
| | N_COLOR_BEST | 07-14 09:12:59 | 1 | 1.99 | 6.13 |
| | N_LEISA_LORRI_BEST | 07-14 10:03:10 | 1 | 0.30 | 9.45 |
| | N_MPAN_CA | 07-14 11:16:35 | 1 | 0.45 | 85.9 |
| | N_DEP_SOONEST | 07-14 14:56:57 | 16 | 0.93 | 158 |
| Kerberos | U_TBD_2 | 07-14 04:24:17 | 4 | 1.97 | 24.7 |
| Hydra | H_LORRI_APPR_1D2 | 07-13 23:16:23 | 2 | 3.18 | 21.5 |
| | H_COLOR_1 | 07-14 04:54:09 | 1 | 7.17 | 26.7 |
| | H_COLOR_BEST | 07-14 07:37:00 | 1 | 4.59 | 33.5 |
| | H_LORRI_BEST | 07-14 07:40:28 | 8 | 1.14 | 33.9 |

## Albedos and surface features

The New Horizons spacecraft trajectory was designed to maximize the scientific return on Pluto and Charon, and observations of those bodies were given priority during the flyby. Nonetheless, Nix and Hydra were imaged with sufficient resolution to investigate brightness variations, color variations, and topographical features across their surfaces. Direct surface reflectance (I/F, the ratio of reflected intensity to incident flux from the Sun) measurements are also available for Kerberos and Styx. Contour maps of raw I/F values for the best-resolved images of SNKH are shown in figs. S8 to S11.

All four small satellites have high albedos, similar to those of some of Saturn's small, icy moons (*16*). Even at a phase angle of 34°, I/F on Hydra reaches 0.56 ± 0.03 (the quoted error is the estimated ±1σ uncertainty in the LORRI absolute calibration). Peak values of I/F for Styx, Nix, and Kerberos are 0.40 ± 0.02, 0.57 ± 0.03, and 0.45 ± 0.02 at phase angles of 17.3°, 9.5°, and 24.7°, respectively. Converting these reflectances into geometric albedos (by definition, the geometric albedo is the I/F at a phase angle of 0°) requires knowledge of the phase function, including any brightness increase that might occur near 0° as a result of coherent backscattering. We used the total light integrated over the best image of Nix to constrain its geometric albedo, and then we used the relative albedos derived from the unresolved brightness measurements of all the small moons (when the phase angle was identical for all the small moons; we also accounted for rotational light-curve variations among the small moons) to estimate the geometric albedos of Styx, Kerberos, and Hydra.

We derive a visible-band apparent magnitude $V = -0.79 \pm 0.05$ for the best image of Nix, which was taken at a moderate phase angle of 9.5°. For a phase law with a linear phase coefficient of 0.04 mag/deg, which we favor, the geometric

**Table 2. Properties of Pluto's small satellites.** The sizes (diameters) are three-dimensional ellipsoidal best fits to the resolved and unresolved (light curve) measurements (*12*). Uncertainties are ±3 km (±1σ) for Styx, Kerberos, and Nix and ±10 km (±1σ) for Hydra. Kerberos has a dual-lobed shape that is not fit well by a single ellipsoid. The orbital periods are from (*5*). The rotation rates are determined from analyses of light-curve data taken over several months (*12*). Rotational pole directions are determined from a model that attempts to match both the light-curve measurements and the resolved measurements (*12*). The pole positions listed below are accurate to ±10° (±1σ, see also fig. S4); the rotational poles of Pluto and Charon both point at [RA, DEC] = [132.993°, −6.163°]. The geometric albedos listed here may not fully account for any potential rapid increase in brightness near 0° phase angle (see text for further details). On the basis of a recent (November 2015) analysis of stellar calibration data, we have reduced LORRI's sensitivity by 20% relative to the preflight value, which raises the derived geometric albedo values (tabulated below) by 20% relative to the values based on the original calibration. LORRI's sensitivity has been stable at the ~1% level since launch, and a more definitive absolute calibration is expected from stellar observations planned in July 2016.

| Object | Size (km) | Orbital period (days) | Rotation rate (days) | Rotation pole [RA, DEC] | Geometric albedo |
|---|---|---|---|---|---|
| Styx | 16 × 9 × 8 | 20.16155 ± 0.00027 | 3.24 ± 0.07 | [196°, 61°] | 0.65 ± 0.07 |
| Nix | 50 × 35 × 33 | 24.85463 ± 0.00003 | 1.829 ± 0.009 | [350°, 42°] | 0.56 ± 0.05 |
| Kerberos | 19 × 10 × 9 | 32.16756 ± 0.00014 | 5.31 ± 0.10 | [222°, 72°] | 0.56 ± 0.05 |
| Hydra | 65 × 45 × 25 | 38.20177 ± 0.00003 | 0.4295 ± 0.0008 | [257°, −24°] | 0.83 ± 0.08 |

albedo is 0.61. For a phase law of 0.02 mag/deg, which is near the extreme of what is observed for asteroids and other planetary satellites, the geometric albedo would be 0.51. Thus, for Nix we adopt a geometric albedo of 0.56 ± 0.05. Using the relative albedo measurements derived from the extensive set of observations taken during May to July 2015 (Fig. 2), we derive the geometric albedos for Styx, Kerberos, and Hydra listed in Table 2. None of these geometric albedo values account for potential rapid brightness increases near 0° phase angle, where observations from New Horizons were not possible.

The vast majority of KBOs that are considered small (although most of their diameters exceed 100 km) have visible-band geometric albedos of less than 20%, with typical values of ~10% (*17*, *18*). Thus, these new measurements provide further evidence that Pluto's small moons were not captured from the general Kuiper Belt population, but instead formed by agglomeration in a disk of material produced in the aftermath of the Charon-forming collision (*13*–*15*). The geometric albedos of the small moons appear to be larger than the value for Charon (~0.38), contrary to the prediction that regolith transfer from the small moons to Charon would result in approximately equal geometric albedos for all of Pluto's moons (*8*, *9*). The high albedo and small size for Kerberos directly contradict the prediction (*5*) that Kerberos should be large and dark. However, our observational results from New Horizons support the predictions from two theoretical studies (*7*, *15*), which argued for high albedos for the small moons on the basis of dynamical considerations.

Although diagnostic compositional spectra on Pluto's small moons have not yet been received from the New Horizons spacecraft, the combination of high surface albedo and their residence at large heliocentric distances strongly suggests that all the moons are covered with icy material. By analogy with Charon, which is covered in $H_2O$ ice but not massive enough to retain more volatile ices (e.g., $N_2$, $CH_4$, CO, etc.) over the age of the solar system (*19*, *20*), we propose that the surfaces of Pluto's small moons are likely also covered with $H_2O$ ice. We further note that if the Pluto-Charon binary was produced by a giant collision in which both precursor bodies were at least partially differentiated with icy surface layers, any small moons formed in the resulting debris disk are predicted to be rich in water ice (*14*, *15*).

Both Nix and Hydra have surface features that we attribute to impact craters caused by bombardment from small bodies in the local Kuiper Belt population. We identify 11 craterlike features on Nix and 3 craterlike features on Hydra (*12*) (figs. S12 to S14). We calculate crater densities of $1 \times 10^{-3}$ to $3 \times 10^{-3}$ km$^{-2}$ for crater diameters of ≥4 km, which match or exceed the values found (*21*) on the older regions of Pluto and Charon after accounting for the much lower gravities of Nix and Hydra (Fig. 3) (*22*). Given the resolution and phase angle limitations of the images (Table 1) and the difference in impact speeds for the small moons relative to Pluto, these cumulative counts should be considered minimum values. Assuming that our identification of craters on Nix and Hydra is correct, the high crater densities suggest (*21*, *22*) that the surfaces of Nix and Hydra date back to at least 4 billion years ago, when the population density of the Kuiper Belt was perhaps 100 times the present-day value (*23*). Catastrophic disruption since that time is not predicted for Nix and Hydra (*22*), which is consistent with their ancient surface ages.

Nix and Hydra have mostly neutral (i.e., gray) colors, but Hydra is somewhat bluer than Nix (Fig. 4). Perhaps Hydra's surface is icier than Nix's, which might explain both its higher albedo and bluer color. The largest crater on Nix's surface is redder than the rest of its surface (Fig. 5). Possible explanations are that the impacting body had a composition different from that of Nix or that the impact exposed material with a different composition from below Nix's surface. No color variation is detected for the other impact craters identified on Nix's or Hydra's surfaces.

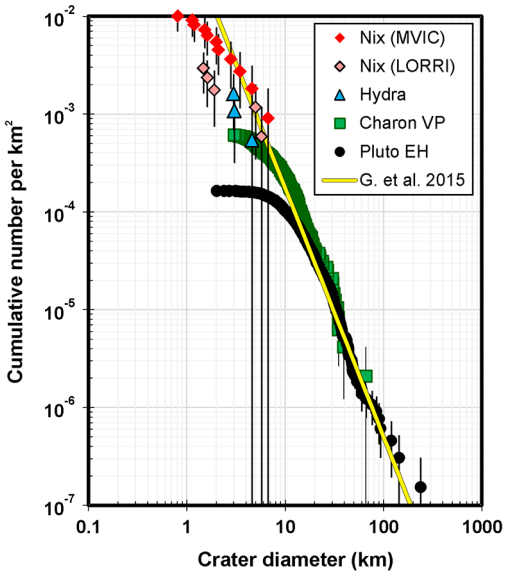



**Fig. 3. Cumulative crater size-frequency distributions for Nix, Hydra, Pluto's encounter hemisphere (EH), and Charon's Vulcan Planum (VP).** The curves for Pluto and Charon are from Moore *et al*. (*21*). Nix and Hydra crater sizes (table S2) are scaled downward by a factor of 2.1 (appropriate for porous regolith-type material) to account for the difference in gravity between these small moons and Pluto (*12*). Standard Poisson statistical errors ($\sqrt{N}$) are displayed. The phase angle for the "Nix (LORRI)" data (N_LEISA_LORRI_BEST; phase angle 9.45°) was less ideal for topographic feature identification than the phase angle for the "Nix (MVIC)" observation (N_MPAN_CA; phase angle 85.9°). Thus, the lower crater density for Nix (LORRI) versus Nix (MVIC) may be an artifact of the viewing and lighting geometry. The yellow line indicates the Greenstreet *et al*. (*22*) prediction for the cumulative density of craters on Pluto's surface over a span of 4 billion years for their "knee" model. Although not saturated in appearance, Nix and Hydra both exhibit slightly higher crater densities than Pluto and Charon, implying a surface age of at least 4 billion years (see text).

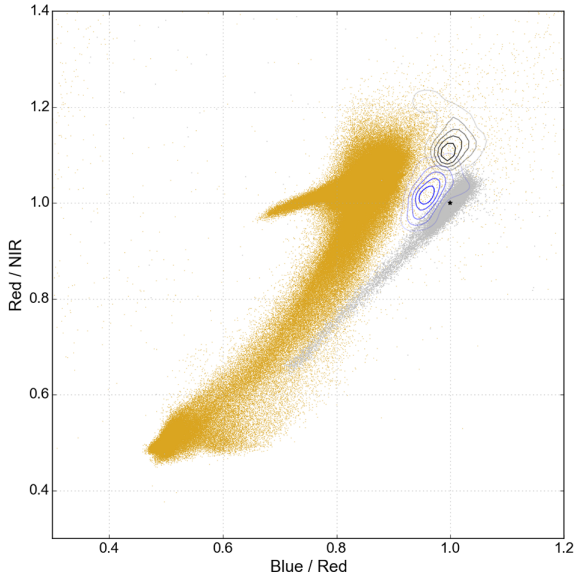



**Fig. 4. Color ratios for the surfaces of Pluto, Charon, Nix, and Hydra.** Blue/Red and Red/NIR color ratios derived from MVIC images are displayed (Blue = 400 to 550 nm, Red = 540 to 700 nm, NIR = 780 to 975 nm). Gold points are from Pluto's surface; silver points are from Charon's surface. Blue contours show the distribution of colors on Nix's surface; black contours show the distribution of colors on Hydra's surface. The normalized solar color is denoted by the star (at coordinate [1,1] in the plot); surfaces redder than solar are at the lower left of the star, and regions bluer than solar appear at the upper right. Pluto exhibits a diversity of colors over its surface (*24*). Charon has less color diversity than Pluto, and the range of its colors follows a mixing line (*24*). Nix and Hydra have nearly solar colors (i.e., gray color) that are distinct from either Pluto or Charon, with Hydra being slightly bluer than Nix.

## Implications

The New Horizons observations of Pluto's small satellites have produced a number of results:

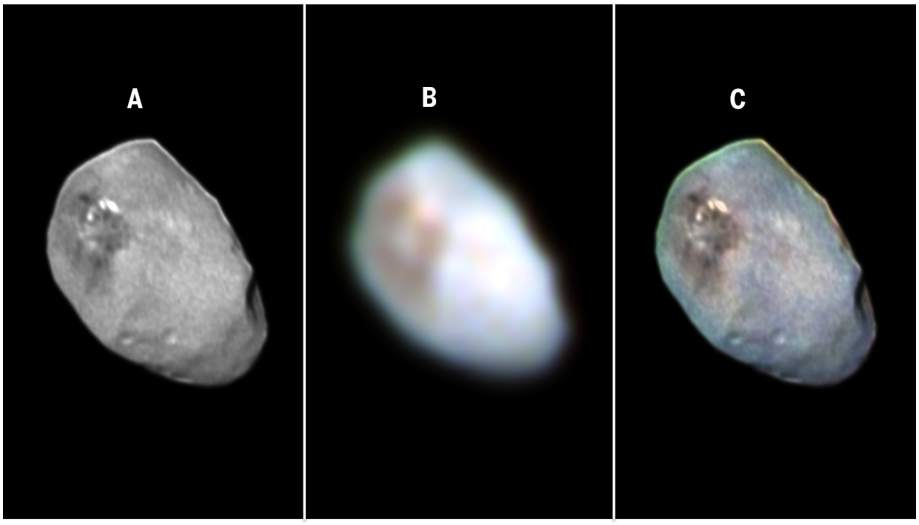



**Fig. 5. Color of Nix's surface.** (**A**) Panchromatic LORRI image of Nix taken from N_LEISA_LORRI_BEST (Table 1). (**B**) Enhanced MVIC color image of Nix taken from N_COLOR_BEST. (**C**) The LORRI image of Nix was colored using the data derived from the MVIC image. Most of Nix's surface is neutral (i.e., gray) in color, but the region near the largest impact crater is slightly redder than the rest of the surface. Celestial north is up and east is to the left for all images.

rapid rotation rates and unusual pole orientations; bright, icy surfaces with albedos and colors distinctly different from those of Pluto and Charon; evidence of merged bodies; and surface ages of at least 4 billion years. Perhaps the rotational properties of the small moons are affected by stochastic collisional processes, which could both spin up the moons and reorient their rotational axes, more strongly than had been appreciated. The presence of a distinctly different layer of material uncovered and/or deposited by an impact on Nix demonstrates that these bodies possess regoliths. The New Horizons measurements suggest that regolith sharing between the small moons and Charon is less extensive than previously thought (*8*, *9*). Collisions are also implicated in determining the shapes of the small moons: Kerberos appears to record the slow merger of two separate bodies, and Hydra has large surface indentations that might reflect mass loss by impacting bodies. However, the major collisional evolution of the small moons was probably limited to the first several hundred million years after the solar system's formation, because the surface crater retention ages of Nix and Hydra exceed 4 billion years.

## REFERENCES AND NOTES


1. H. A. Weaver *et al*., Discovery of two new satellites of Pluto. *Nature* **439**, 943–945 (2006). doi: 10.1038/nature04547; pmid: 16495991
2. M. R. Showalter *et al*., New satellite of (134340) Pluto: S/2011 (134340). *IAU Circ. 9221* (2011).
3. M. R. Showalter *et al*., New satellite of (134340) Pluto: S/2012 (134340). *IAU Circ. 9253* (2012).
4. M. Brozović, M. R. Showalter, R. A. Jacobson, M. W. Buie, The orbits and masses of satellites of Pluto. *Icarus* **246**, 317–329 (2015). doi: 10.1016/j.icarus.2014.03.015
5. M. R. Showalter, D. P. Hamilton, Resonant interactions and chaotic rotation of Pluto's small moons. *Nature* **522**, 45–49 (2015). doi: 10.1038/nature14469; pmid: 26040889
6. S. A. Stern *et al*., The Pluto system: Initial results from its exploration by New Horizons. *Science* **350**, aad1815 (2015). doi: 10.1126/science.aad1815; pmid: 26472913
7. A. N. Youdin, K. M. Kratter, S. J. Kenyon, Circumbinary chaos: Using Pluto's newest moon to constrain the masses of Nix and Hydra. *Astrophys. J.* **755**, 17 (2012). doi: 10.1088/0004-637X/755/1/17
8. S. A. Stern, Ejecta exchange and satellite color evolution in the Pluto system, with implications for KBOs and asteroids with satellites. *Icarus* **199**, 571–573 (2009). doi: 10.1016/j.icarus.2008.10.006
9. S. B. Porter, W. M. Grundy, Ejecta transfer in the Pluto system. *Icarus* **246**, 360–368 (2015). doi: 10.1016/j.icarus.2014.03.031
10. A. F. Cheng *et al*., Long-Range Reconnaissance Imager on New Horizons. *Space Sci. Rev.* **140**, 189–215 (2008). doi: 10.1007/s11214-007-9271-6
11. D. C. Reuter *et al*., Ralph: A visible/infrared imager for the New Horizons Pluto/Kuiper Belt mission. *Space Sci. Rev.* **140**, 129–154 (2008). doi: 10.1007/s11214-008-9375-7
12. See supplementary materials on *Science* Online.
13. S. A. Stern *et al*., A giant impact origin for Pluto's small moons and satellite multiplicity in the Kuiper belt. *Nature* **439**, 946–948 (2006). doi: 10.1038/nature04548; pmid: 16495992
14. R. Canup, On a giant impact origin of Charon, Nix, and Hydra. *Astron. J.* **141**, 35 (2011). doi: 10.1088/0004-6256/141/2/35
15. S. J. Kenyon, B. C. Bromley, The formation of Pluto's low-mass satellites. *Astron. J.* **147**, 8–24 (2014). doi: 10.1088/0004-6256/147/1/8
16. A. Verbiscer, R. French, M. Showalter, P. Helfenstein, Enceladus: Cosmic graffiti artist caught in the act. *Science* **315**, 815 (2007). doi: 10.1126/science.1134681; pmid: 17289992
17. E. Vilenius *et al*., "TNOs are cool": A survey of the trans-Neptunian region VI. Herschel_/PACS observations and thermal modeling of 19 classical Kuiper belt objects. *Astron. Astrophys.* **541**, A94 (2012). doi: 10.1051/0004-6361/201118743
18. E. Lellouch *et al*., "TNOs are cool": A survey of the trans-Neptunian region IX. Thermal properties of Kuiper belt objects and Centaurs from combined Herschel and Spitzer observations. *Astron. Astrophys.* **557**, A60 (2013). doi: 10.1051/0004-6361/201322047
19. E. L. Schaller, M. E. Brown, Volatile loss and retention on Kuiper belt objects. *Astrophys. J.* **659**, L61–L64 (2007). doi: 10.1086/516709
20. R. E. Johnson, A. Oza, L. A. Young, A. N. Volkov, C. Schmidt, Volatile loss and classification of Kuiper belt objects. *Astrophys. J.* **809**, 43 (2015). doi: 10.1088/0004-637X/809/1/43
21. J. M. Moore *et al*., The geology of Pluto and Charon through the eyes of New Horizons. *Science* **351**, 1284–1293 (2016).
22. S. Greenstreet, B. Gladman, W. B. McKinnon, Impact and cratering rates onto Pluto. *Icarus* **258**, 267–288 (2015). doi: 10.1016/j.icarus.2015.05.026
23. R. Gomes, H. F. Levison, K. Tsiganis, A. Morbidelli, Origin of the cataclysmic Late Heavy Bombardment period of the terrestrial planets. *Nature* **435**, 466–469 (2005). doi: 10.1038/nature03676; pmid: 15917802
24. W. M. Grundy *et al*., Surface compositions across Pluto and Charon. *Science* **351**, aad9189 (2016).


## ACKNOWLEDGMENTS

We thank the many dedicated engineers who contributed to the success of the New Horizons mission and NASA's Deep Space Network for a decade of excellent support to New Horizons. This work was supported by NASA's New Horizons project. As contractually agreed to with NASA, fully calibrated New Horizons Pluto system data will be released via the NASA Planetary Data System at https://pds.nasa.gov/ in a series of stages in 2016 and 2017 because of the time required to fully downlink and calibrate the data set. Also supported by NASA's Origins research program (D.P.H.) and Centre National d'Etudes Spatiales, France (S. Philippe and B.S.). S.A.S. is affiliated with Florida Space Institute, Uwingu LLC, Golden Spike Co., and World View Enterprises.

## SUPPLEMENTARY MATERIALS

www.sciencemag.org/content/351/6279/aae0030/suppl/DC1
Materials and Methods
Supplementary Text
Tables S1 to S4
Figs. S1 to S14
Movie S1
References (*25*–*30*)

5 December 2015; accepted 22 February 2016
10.1126/science.aae0030

RESEARCH ARTICLE SUMMARY

PLANETARY SCIENCE

# Pluto's interaction with its space environment: Solar wind, energetic particles, and dust

F. Bagenal,* M. Horányi, D. J. McComas, R. L. McNutt Jr., H. A. Elliott, M. E. Hill, L. E. Brown, P. A. Delamere, P. Kollmann, S. M. Krimigis, M. Kusterer, C. M. Lisse, D. G. Mitchell, M. Piquette, A. R. Poppe, D. F. Strobel, J. R. Szalay, P. Valek, J. Vandegriff, S. Weidner, E. J. Zirnstein, S. A. Stern, K. Ennico, C. B. Olkin, H. A. Weaver, L. A. Young, New Horizons Science Team†

**INTRODUCTION:** The scientific objectives of NASA's New Horizons mission include quantifying the rate at which atmospheric gases are escaping Pluto and describing its interaction with the surrounding space environment. The two New Horizons instruments that measure charged particles are the Solar Wind Around Pluto (SWAP) instrument and the Pluto Energetic Particle Spectrometer Science Investigation (PEPSSI) instrument. The Venetia Burney Student Dust Counter (SDC) counts the micrometer-sized dust grains that hit the detectors mounted on the ram direction of the spacecraft. This paper describes preliminary results from these three instruments when New Horizons flew past Pluto in July 2015 at a distance of 32.9 astronomical units (AU) from the Sun.

ON OUR WEB SITE

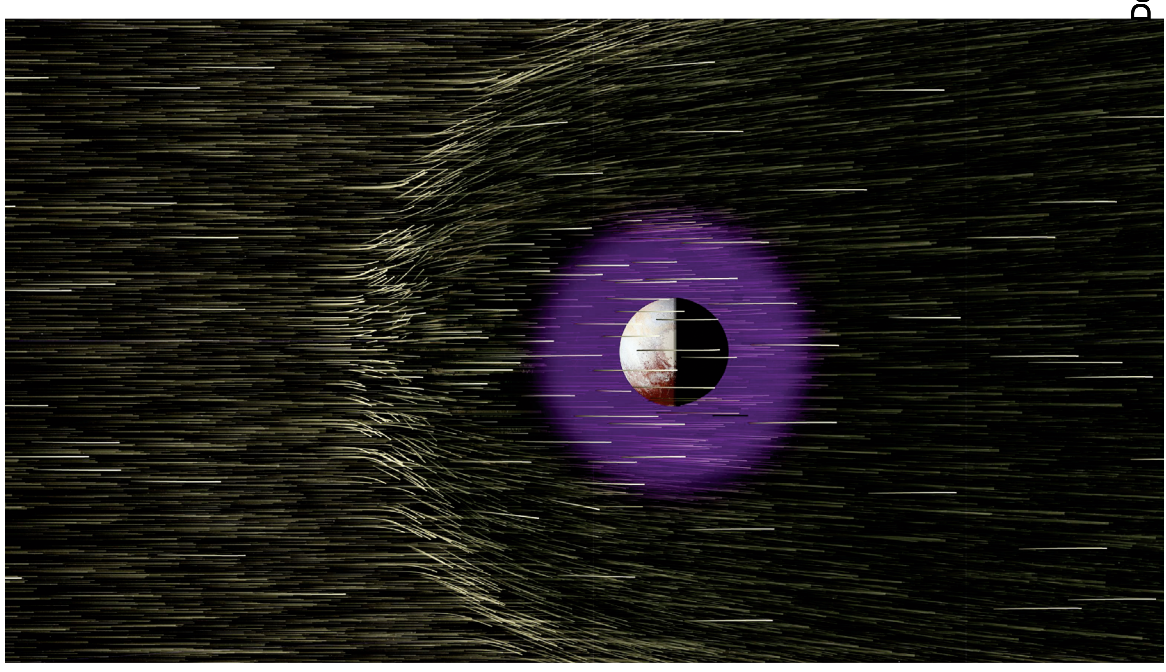
Read the full article at http://dx.doi.org/10.1126/science.aad9045

**RATIONALE:** Initial studies of the solar wind interaction with Pluto's atmosphere suggested that the extent of the interaction depends on whether the atmospheric escape flux is strong (producing a comet-like interaction, where the interaction region is dominated by ion pick-up and is many times larger than the object) or weak (producing a Mars-like interaction dominated by ionospheric currents with limited upstream pick-up and where the scale size is comparable to the object). Before the New Horizons flyby, the estimates of the atmospheric escape rate ranged from as low as $1.5 \times 10^{25}$ molecules $s^{-1}$ to as high as $2 \times 10^{28}$ molecules $s^{-1}$. Combining these wide-ranging predictions of atmospheric escape rates with Voyager and New Horizons observations of extensive variability of the solar wind at 33 AU produced estimates of the scale of the interaction region that spanned all the way from 7 to 1000 Pluto radii ($R_P$).

**RESULTS:** At the time of the flyby, SWAP measured the solar wind conditions near Pluto to be nearly constant and stronger than usual. The abnormally high solar wind density and associated pressures for this distance are likely due to a relatively strong traveling interplanetary shock that passed over the spacecraft 5 days earlier. Heavy ions picked up sunward from Pluto should mass-load and slow the solar wind. However, there is no evidence of such solar wind slowing in the SWAP data taken as near as ~20 $R_P$ inbound, which suggests that very few atmospheric molecules are escaping upstream and becoming ionized. The reorientation of the spacecraft to enable imaging of the Pluto system meant that both the SWAP and PEPSSI instruments were turned away from the solar direction, thus complicating our analysis of the particle data. Nevertheless, when the spacecraft was ~10 $R_P$ from Pluto, SWAP data indicated that the solar wind had slowed by ~20%. We use these measurements to estimate a distance of ~6 $R_P$ for the 20% slowing location directly upstream of Pluto. At this time, PEPSSI detected an enhancement of ions with energies in the kilo–electron volt range. The SDC, which measures grains with radii >1.4 μm, detected one candidate impact in ±5 days around its closest approach, indicating a dust density estimate of $n = 1.2$ $km^{-3}$, with a 90% confidence level range of $0.6 < n < 4.6$ $km^{-3}$.

**CONCLUSION:** New Horizons's particle instruments revealed an interaction region confined sunward of Pluto to within ~6 $R_P$. The surprisingly small size is consistent with a reduced atmospheric escape rate of $6 \times 10^{25}$ $CH_4$ molecules $s^{-1}$, as well as a particularly high solar wind flux due to a passing compression region. This region is similar in scale to the solar wind interaction with Mars's escaping atmosphere. Beyond Pluto, the disturbance persists to distances greater than 400 $R_P$ downstream. ■

The list of author affiliations is available in the full article online.
*Corresponding author E-mail: bagenal@colorado.edu
†New Horizons Science Team authors and affiliations are listed in the supplementary materials.
Cite this article as F. Bagenal *et al.*, *Science* **351**, aad9045 (2016). DOI: 10.1126/science.aad9045



CREDIT: STEVE BARTLETT AND NASA'S SCIENTIFIC VISUALIZATION STUDIO

**Interaction of the solar wind with Pluto's extended atmosphere.** Protons and electrons streaming from the Sun at ~400 km $s^{-1}$ are slowed and deflected around Pluto because of a combination of ionization of Pluto's atmosphere and electrical currents induced in Pluto's ionosphere.

Downloaded from on March 17, 2016

RESEARCH ARTICLE

PLANETARY SCIENCE

# Pluto's interaction with its space environment: Solar wind, energetic particles, and dust

F. Bagenal,[1]* M. Horányi,[1] D. J. McComas,[2,3] R. L. McNutt Jr.,[4] H. A. Elliott,[2] M. E. Hill,[4] L. E. Brown,[4] P. A. Delamere,[5] P. Kollmann,[4] S. M. Krimigis,[4,6] M. Kusterer,[4] C. M. Lisse,[4] D. G. Mitchell,[4] M. Piquette,[1] A. R. Poppe,[7] D. F. Strobel,[8] J. R. Szalay,[1,9] P. Valek,[2] J. Vandegriff,[4] S. Weidner,[2] E. J. Zirnstein,[2] S. A. Stern,[9] K. Ennico,[10] C. B. Olkin,[9] H. A. Weaver,[4] L. A. Young,[9] New Horizons Science Team†

**The New Horizons spacecraft carried three instruments that measured the space environment near Pluto as it flew by on 14 July 2015. The Solar Wind Around Pluto (SWAP) instrument revealed an interaction region confined sunward of Pluto to within about 6 Pluto radii. The region's surprisingly small size is consistent with a reduced atmospheric escape rate, as well as a particularly high solar wind flux. Observations from the Pluto Energetic Particle Spectrometer Science Investigation (PEPSSI) instrument suggest that ions are accelerated and/or deflected around Pluto. In the wake of the interaction region, PEPSSI observed suprathermal particle fluxes equal to about 1/10 of the flux in the interplanetary medium and increasing with distance downstream. The Venetia Burney Student Dust Counter, which measures grains with radii larger than 1.4 micrometers, detected one candidate impact in ±5 days around New Horizons' closest approach, indicating an upper limit of <4.6 kilometers$^{-3}$ for the dust density in the Pluto system.**

After a journey of more than 9 years, NASA's New Horizons spacecraft flew past Pluto on 14 July 2015 (*1*). Scientific objectives of the New Horizons mission include quantifying the rate at which atmospheric gases are escaping Pluto (*2*) and describing its interaction with the surrounding space environment. The two New Horizons instruments that measure charged particles are the Solar Wind Around Pluto (SWAP) instrument (*3*) and the Pluto Energetic Particle Spectrometer Science Investigation (PEPSSI) instrument (*4*). The Venetia Burney Student Dust Counter (SDC) counts the micrometer-sized dust grains that hit the detectors mounted on the ram direction of the spacecraft (*5*). This paper describes preliminary results measured by these three instruments during the Pluto encounter period (the geometry of which is illustrated in Fig. 1). New Horizons reached its closest approach distance of 11.54 $R_P$, where a Pluto radius is $R_P$ = 1187 km (*1*), on day of year (DOY) 195 at 11:49 universal time coordinated (UTC).

Initial studies of the solar wind interaction with Pluto's atmosphere (*6*–*15*), all assuming the absence of an intrinsic magnetic field, suggested that the extent of the interaction depends on whether the atmospheric escape flux is strong or weak: Strong escape flux produces a comet-like interaction, where the interaction region is dominated by ion pick-up and is many times larger than the object. Conversely, weak flux results in a Mars-like interaction dominated by ionospheric currents with limited upstream pick-up and where the scale size is comparable to that of the object. Before the New Horizons flyby, estimates of the atmospheric escape rate ranged from as low as $1.5 \times 10^{25}$ molecules s$^{-1}$ to as high as $2 \times 10^{28}$ molecules s$^{-1}$ (*16*–*23*). Combining these atmospheric escape rates with Voyager and New Horizons observations of the solar wind at 33 astronomical

[1]Laboratory of Atmospheric and Space Physics, University of Colorado, Boulder, CO 80600, USA. [2]Southwest Research Institute, San Antonio, TX 78228, USA. [3]University of Texas at San Antonio, San Antonio, TX 78249, USA. [4]Johns Hopkins University Applied Physics Laboratory, Laurel, MD 20723, USA. [5]University of Alaska, Fairbanks, AK 99775, USA. [6]Academy of Athens, 28 Panapistimiou, 10679 Athens, Greece. [7]Space Sciences Laboratory, University of California, Berkeley, CA 94720, USA. [8]Johns Hopkins University, Baltimore, MD 21218, USA. [9]Southwest Research Institute, Boulder, CO 80302, USA. [10]NASA Ames Research Center, Moffett Field, CA 94035, USA.
***Corresponding author E-mail: bagenal@colorado.edu** †New Horizons Science Team authors and affiliations are listed in the supplementary materials.

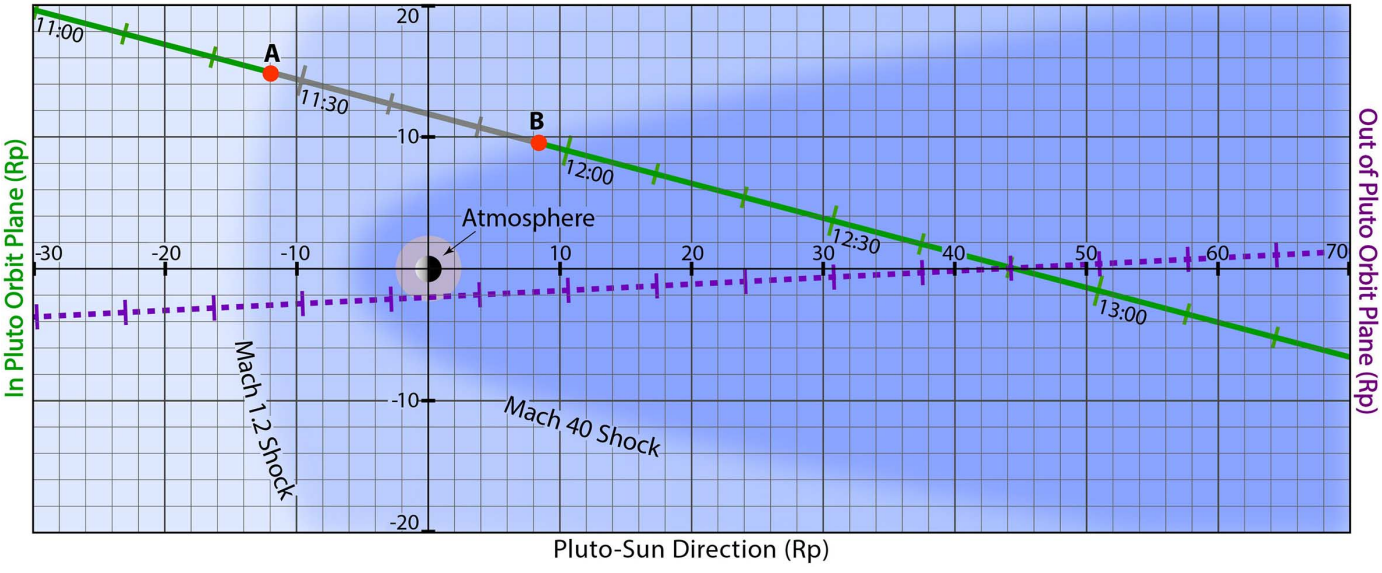



**Fig. 1. Geometry of the New Horizons trajectory through the solar wind interaction with Pluto's atmosphere on DOY 195.** Along the gray section of the trajectory between points A and B, the New Horizons spacecraft pointed the SWAP instrument's field of view away from the solar direction. The pink circle shows the extent of Pluto's atmosphere (*2*).

units (AU) produced estimates of the scale of the interaction region that ranged from 7 to 1000 $R_P$ (*24*).

New Horizons flew past Pluto at a distance of 32.9 AU from the Sun. At the time of encounter, Pluto was 1.9° above the ecliptic plane on its eccentric orbit. The flyby occurred as the Sun was in the descending phase of the solar cycle. In Table 1, we compare the interplanetary plasma

**Table 1. Solar wind conditions at 33 AU.** Predictions are based on Voyager 2 plasma data obtained from 1988 to 1992 between 25 and 39 AU (*24*) and observed by the New Horizons SWAP instrument. γ, adiabatic index; $m_i$, ion mass.

| Plasma property | Formula [units] | Predicted 10th percentile | Predicted mean | Predicted 90th percentile | Observed by SWAP |
|---|---|---|---|---|---|
| Solar wind speed | $V_{SW}$ [km/s] | 380 | 430 | 480 | 403 |
| Proton density | $n$ [cm$^{-3}$] | 0.0020 | 0.0058 | 0.014 | 0.025 |
| Proton flux | $nV$ [km s$^{-1}$ cm$^{-3}$] | 0.84 | 2.4 | 7.0 | 10 |
| Proton temperature | $T$ [K] | 3040 | 6650 | 16800 | 7700 |
| | $T$ [eV] | 0.26 | 0.57 | 1.5 | 0.66 |
| Proton thermal pressure (IPUI pressure*) | $P = nkT$ [fPa] | 0.12 | 0.53 (20 ± 8*) | 2.1 | 2.5 |
| Proton ram pressure | $P = \rho V^2$ [pPa] | 0.55 | 1.7 | 4.0 | 6.0 |
| Sound speed (with IPUIs*) | $V_s = (\gamma kT/m_i)^{1/2}$ [km/s] | 6.3 | 9.4 (58*) | 15 | 10 (28*) |
| Sonic Mach number (with IPUIs) | $M_S = V_{SW}/V_s$ | 60 | 46 (7.5*) | 32 | 40 (14*) |
| Magnetic field strength | $B$ [nT] | 0.08 | 0.15 | 0.28 | 0.3† |
| Pickup $CH_4^+$ gyroradius | $R_{gyro}$ [$R_P$] | 670 | 400 | 240 | 190† |
| Alfvén speed | $V_A = B/(\mu_0\rho)^{1/2}$ [km/s] | 22 | 45 | 96 | 41† |
| Alfvén Mach number | $M_A = V_{SW}/V_A$ | 4.6 | 9.5 | 20 | 9.8† |
| Magnetosonic Mach no. (with IPUIs*) | $M_{MS} = V_{SW}/(V_A^2 + V_s^2)^{1/2}$ | 17 | 9 (6*) | 5 | 9.5† (8*†) |

*Including the thermal pressure of IPUIs from (*31*, *32*, *56*). †For the Pluto flyby, we take an interplanetary magnetic field strength of ~0.3 nT.

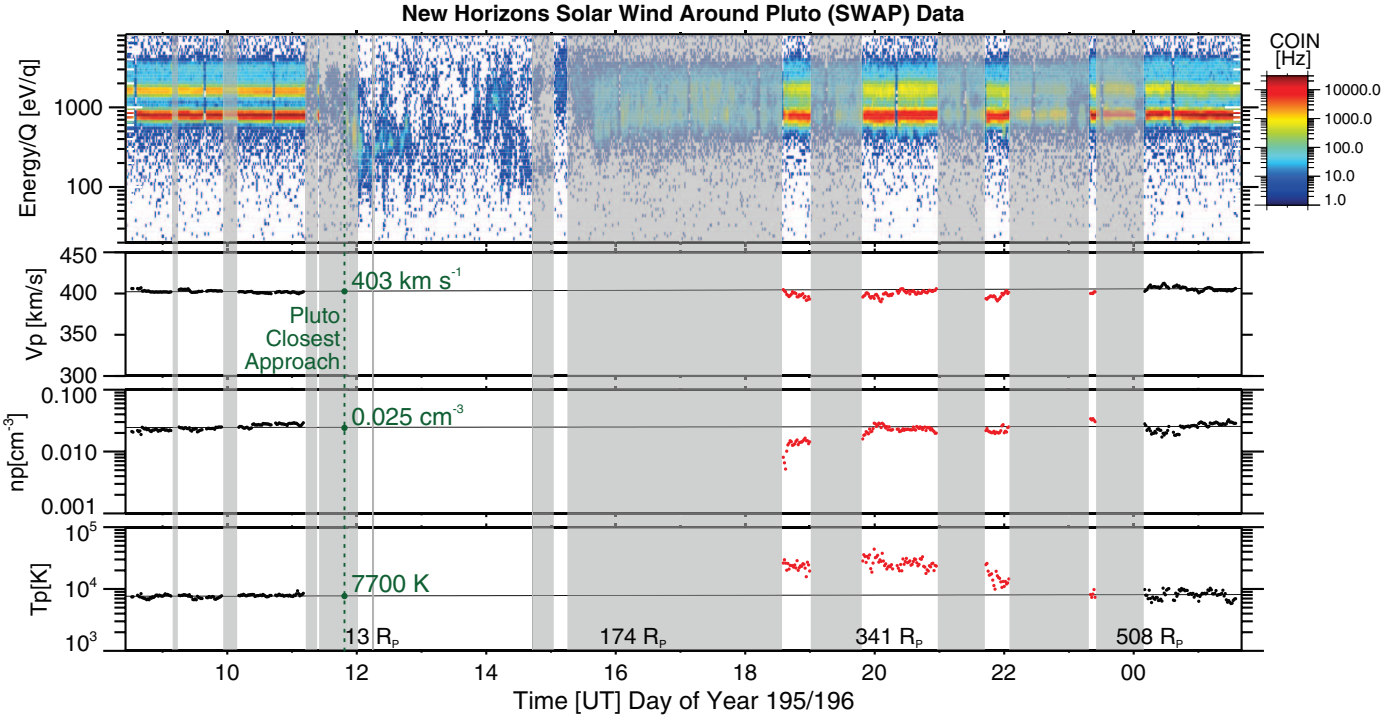



**Fig. 2. Overview of SWAP data.** Color spectrogram of coincidence count rate (COIN) as a function of $E/q$ and derived proton flow speed, density, and temperature values for the interval surrounding the Pluto flyby. The vertical dashed green line shows the time of closest approach. Unshaded regions indicate times during which some portion of SWAP's very broad field of view was pointed within 5° of the Sun direction, and thus SWAP would be able to observe a radially outflowing solar wind. Moments are derived for these times when solar wind–like distributions were observed. Black data points at the start and end of this interval allow linear least-squares fits to these samples of essentially pristine solar wind (nearly horizontal lines), whereas disturbed, higher-temperature solar wind (red points) is evident in the interaction region several hundred $R_P$ behind Pluto.

conditions predicted based on Voyager data for 33 AU (*24*) with the observations made by the New Horizons SWAP instrument. In the absence of a direct measurement of the local magnetic field, we assume an interplanetary magnetic field (IMF) of 0.3 nT, at the upper end of the range observed by Voyager (as discussed further below).

## Solar Wind Around Pluto

### *The SWAP instrument*

The SWAP instrument was specifically designed and optimized for the New Horizons mission, with the primary design drivers being (i) a large aperture and geometric factor to accurately measure the tenuous solar wind at ~33 AU, (ii) minimum use of spacecraft resources such as mass and power, and (iii) its position mounted on a spacecraft that would rotate over a very wide range of spacecraft-pointing directions throughout the flyby. Early in the mission development phase, the flyby-pointing directions were not well known, but the best information available at that time was that most spacecraft pointing would involve rotation around a single spacecraft axis: the $z$ axis. Thus, SWAP was designed to have an extremely broad acceptance angle (~276°) in the plane perpendicular to this axis, which requires an electrostatic top-hat style analyzer with its axis of symmetry aligned with the spacecraft's $z$ axis. Ions are bent through the electrostatic analyzer, pass through a nearly field-free conical region, and are focused into a coincidence detector section, which provides very high signal-to-noise ratio measurements for solar wind ions. Details of the SWAP instrument design are provided by McComas *et al.* (*3*), and SWAP data has already been used to examine the Jovian magnetosphere and distant magnetotail (*25*–*29*).

### *The solar wind at the time of the Pluto flyby*

At the time of the flyby, the solar wind conditions near Pluto (measured by SWAP) were nearly constant, which is advantageous for interpreting the solar wind–Pluto interaction. The top panel of Fig. 2 shows a color spectrogram of SWAP coincidence counts as a function of energy per charge ($E/q$) and time. On the left and right sides of the plot, away from the Pluto interaction, the red and yellow bands located slightly under 1 and 2 keV/$q$ are solar wind protons and alpha particles, respectively. We calculate the solar wind proton parameters for these intervals (*30*) and find a strong consistency between the values before ~11:20 UTC on DOY 195 and again on DOY 196 (black points). These intervals represent the unperturbed solar wind ahead of and beyond Pluto along the New Horizons trajectory, respectively. Interpolating between these points (black line), we infer—at the time of the New Horizons's closest approach (11:48 UTC; green vertical dashed line)—a solar wind speed of ~403 km s$^{-1}$, a proton density of ~0.025 cm$^{-3}$, a proton temperature of ~7700 K (0.7 eV), a proton dynamic pressure of ~6.0 pPa, and a core solar wind proton thermal pressure of ~2.5 × 10$^{-3}$ pPa (Table 1). From the properties of just the thermal solar wind, we calculate a sonic Mach number of ~40. The sonic Mach number is substantially reduced to 14 if we include the interstellar pick-up ions (IPUIs), which provide thermal pressure that is roughly an order of magnitude greater than the aforementioned value at these heliocentric distances (*31*, *32*). The measured unusually high solar wind density and associated pressures for this distance are probably due to a relatively strong traveling interplanetary shock that passed over the spacecraft 5 days earlier on DOY 190.

New Horizons was not equipped with a magnetometer, so the interplanetary magnetic field strength at the time of the flyby is not known. In Table 1, we list typical values of the IMF magnitude ($|B|$) of 0.08 to 0.3 nT at 33 AU in the solar wind (*24*, *33*). If we assume the interplanetary shock that passed New Horizons on DOY 190 also increased $|B|$ to the top of this range, we calculate an Alfvén speed [$V_A = B/(\mu_0\rho)^{1/2}$, where $\mu_0$ is the vacuum permeability and $\rho$ is the total mass density of the charged plasma particles] of 41 km s$^{-1}$; an Alfvén Mach number ($M_A = V_{SW}/V_A$; where $V_{SW}$ is the solar wind speed) of 9.8; and a magnetosonic Mach number [$M_{MS} = V_{SW}/(V_A^2 + V_s^2)^{1/2}$; where $V_s$ is the speed of sound] of 9.5, which is reduced to 8 if we include the IPUIs. The ratio of proton thermal pressure to magnetic pressure [$\beta = nkT/(B^2/2\mu_0)$; where $n$ is the proton density, $k$ is Boltzmann's constant, and $T$ is temperature] is just 0.07, which appears to suggest that the IMF dominates the dynamics. But if we include the substantial pressure of the IPUIs, β becomes greater than unity, emphasizing the importance of IPUIs for the dynamics of the outer heliosphere. We stress that all of these values are based

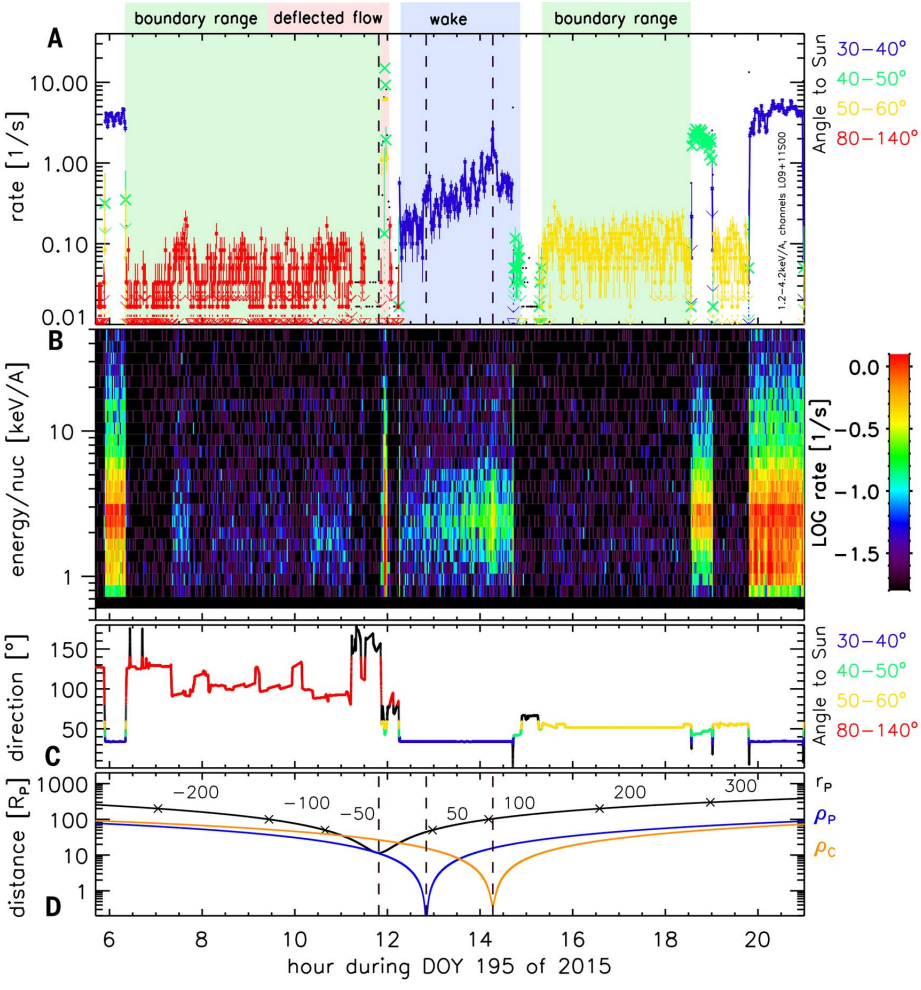



**Fig. 3. Overview of PEPSSI data taken near Pluto.** (**A**) Measurement of ions with Poisson error bars based on TOF data. Ion speeds inside the instrument correspond to 1 to 4 keV/amu. The colors of the symbols identify the viewing angles relative to the Sun direction (D). Background colors refer to time periods discussed in the text. Dashed lines denote locations where New Horizons had its closest approach to Pluto and was directly antisunward of Pluto and Charon. (**B**) Energy spectrogram of TOF data, assuming that ions have not been accelerated by the potential but not accounting for energy losses in the foils. (**C**) Angle of PEPSSI's sector S0 to the Sun direction, with colors corresponding to those used in (A). (**D**) Location of New Horizons relative to Pluto and Charon. Black, radial distance to Pluto; blue, distance along the Pluto-Sun line; red, distance to the Pluto-Sun line; orange, distance to the Charon-Sun line.

on assumed field strengths and not measured values.

### Upstream interaction confined close to Pluto

Heavy ions picked up sunward from Pluto should mass-load and slow the solar wind ahead of it. However, there is no evidence of such solar wind slowing and hence no evidence of the addition of Pluto pick-up ions (PPUIs) in the SWAP data as close as ~20 $R_P$ inbound (point A in Fig. 1 at 11:25 UTC). The calculated speed value at that location is 405 km $s^{-1}$, but if we take an upper bound of 1% slowing at this point, or 399 km $s^{-1}$ compared with the interpolated value at Pluto of 403 km $s^{-1}$, we can use conservation of momentum to calculate an upper bound on the density of a fully picked up heavy ion [$CH_4$ (*2*)] at this distance. We note that if the pick-up ions are $N_2$ instead of $CH_4$, densities would be smaller by the mass ratio of the ions [28 atomic mass units (amu)/16 amu = 1.75]. For a solar wind proton density of 0.025 $cm^{-3}$, we obtain

$$403\ \text{km s}^{-1} \times 0.025\ \text{cm}^{-3} = 399\ \text{km s}^{-1} \times 0.025\ \text{cm}^{-3}\ (1 + 16N_{CH4}/N_p)$$

providing an upper bound on the $N_{CH4}/N_p$ ratio (number of CH4 molecules/number of protons) of ~$6 \times 10^{-4}$ and upper bound on the fully picked up $CH_4$ density of $2 \times 10^{-5}$ $cm^{-3}$ at 20 $R_P$ along the New Horizons trajectory.

Between 11:25 and 11:56 UTC, the New Horizons spacecraft was pointed in directions that did not allow SWAP to view back toward the Sun and into the solar wind. However, from 11:56 to 11:58 UTC (point B in Fig. 1), the spacecraft rotated through directions sufficiently close to the sunward direction such that SWAP was able to take three contiguous energy-per-charge scans of what appears to be solar wind plasma. For each sample, we made Gaussian fits around the peak of the coincidence counts, including errors, and calculated speeds of 314, 343, and 315 km $s^{-1}$, for an average of 324 km $s^{-1}$. Therefore, we conclude that the solar wind had slowed by ~20% at this location. Repeating the conservation of momentum calculation as above

$$403\ \text{km s}^{-1} \times 0.025\ \text{cm}^{-3} = 324\ \text{km s}^{-1} \times 0.025\ \text{cm}^{-3}\ (1 + 16N_{CH4}/N_p)$$

produces an approximate $N_{CH4}/N_p$ ratio of ~$2 \times 10^{-2}$ and a fully picked up $CH_4$ density of ~$4 \times 10^{-4}$ $cm^{-3}$ at this location along Pluto's dawn flank. This very small amount of mass loading so close to Pluto demonstrates that Pluto cannot have a strong comet-like interaction as was generally thought before the flyby.

### Extended interaction behind Pluto

For roughly 3 hours after its closest approach to Pluto, SWAP observed much lower levels of coincidence counts and no obvious beamlike distribution characteristic of the solar wind. From

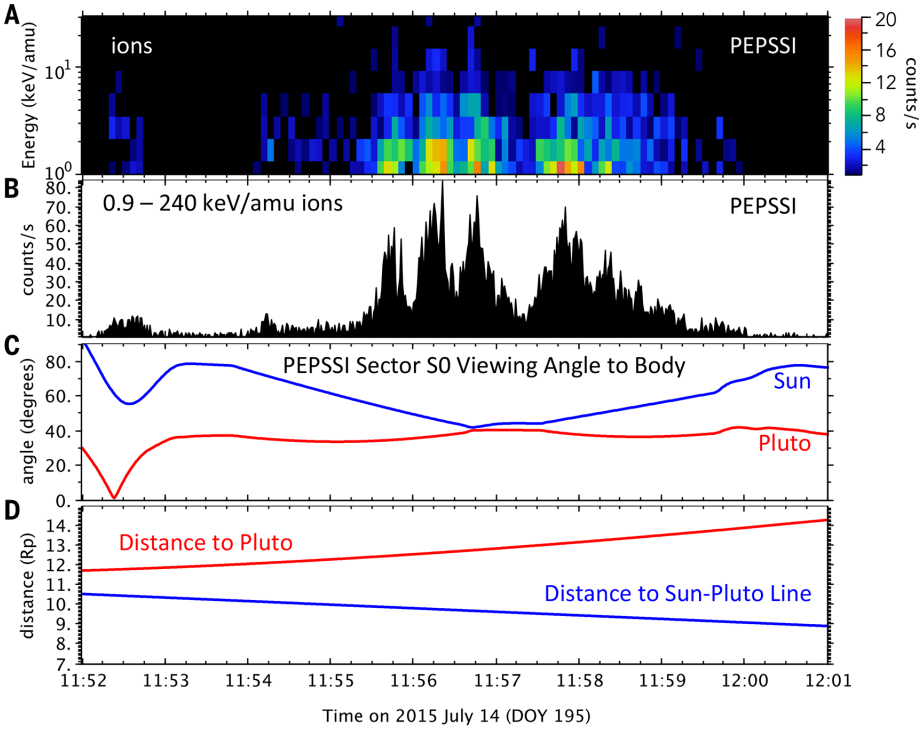



**Fig. 4. Burst of energetic ions.** Zooming in to the interval shaded pink in Fig. 3A, we show PEPSSI TOF observations from 11:52 to 12:01 UTC on 14 July 2015. (**A**) Color spectrogram of 6625 single TOF events returned during this period from all PEPSSI sectors. Raw data are acquired once every second and have been binned into 5-s average rates and logarithmically spaced bins in energy per mass. (**B**) Corresponding total counts per second integrated across all energies. (**C**) Angle between the direction to the Sun and the normal to the S0 sector. (**D**) Distance of New Horizons to Pluto and to the Sun-Pluto line during this period.

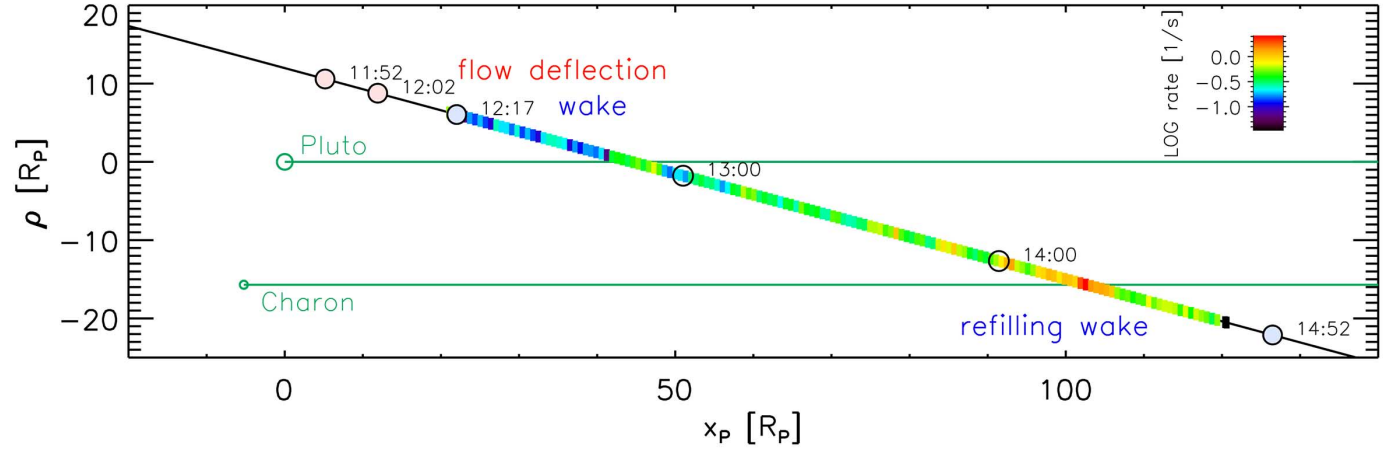



**Fig. 5. Energetic particles along the trajectory of New Horizons.** The $x_P$ axis points away from the Sun. The vertical axis shows $\rho_P$, the distance from the $x_P$ axis in a plane containing Pluto and the trajectory. Green circles show the locations of Pluto and Charon. Open circles show times in UTC. Pink-filled circles mark the range of the ion enhancement; blue-filled circles delimit the wake. Color along the trajectory shows a PEPSSI count rate (same as in Fig. 3A).

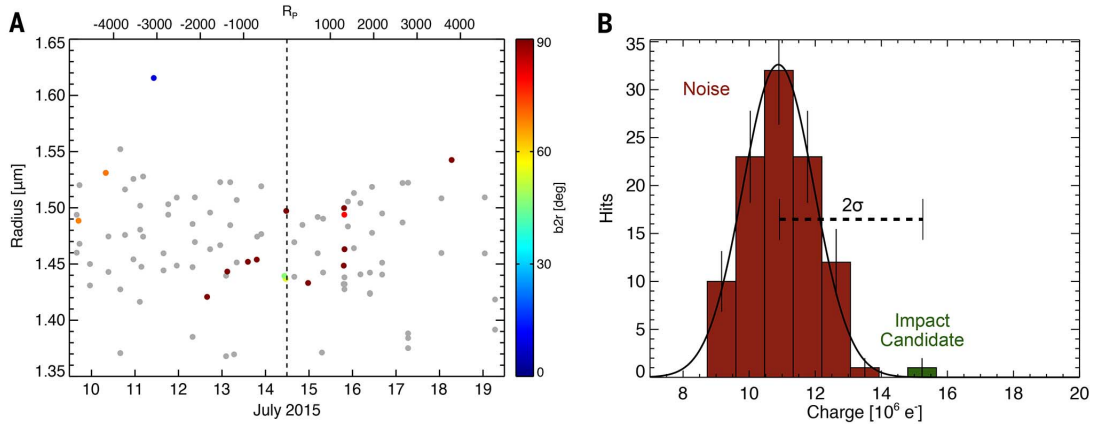



**Fig. 6. Events around Pluto.** (**A**) The events recorded during ±5 days of the closest approach to Pluto. Gray colored dots indicate noise events identified to be coincident dust hits or a single event coincident with thruster firings. The color code represents the boresight-to-ram angle (b2r), measured between the SDC surface normal and the velocity vector of the spacecraft. SDC's sensitivity rapidly drops to zero for impact angles >45°; hence, events marked by red and green dots are also noise events. A single detection at a distance of ~3000 $R_P$ (11 July 2015), before the closest encounter remains, the only candidate for detecting a Pluto-system dust particle. (**B**) The amplitude distribution of all the noise events during this period is well fit to a Gaussian curve with an average of 1.1 × $10^7$ *e* and a 1σ error = 1.5 × $10^6$ *e*, indicating that our candidate impact event generated a charge that had an amplitude with a 2σ error above the average.

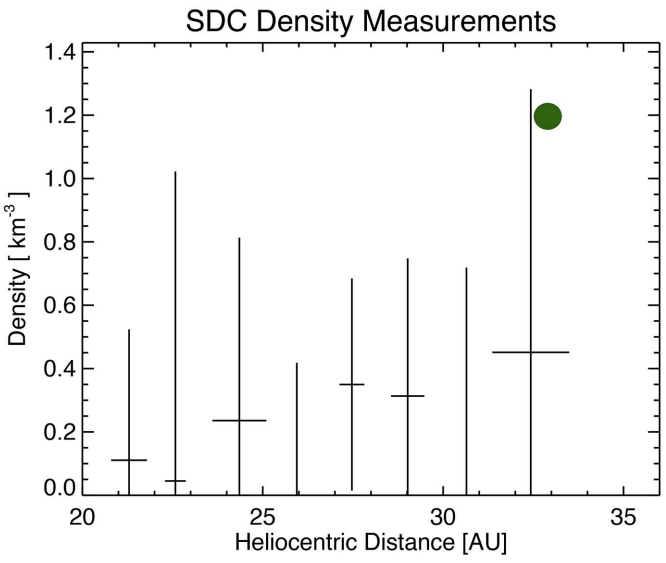



**Fig. 7. Dust in the outer solar system.** The image shows dust density or particles with radii >1.4 μm, as measured by SDC in the outer solar system. The last data point with an error bar shows the data collected since 1 January 2015. The green dot indicates the most likely dust density of 1.2 $km^{-3}$, on the basis of a single candidate dust event.

~12:00 to 14:40 UTC and again from ~15:00 to 15:15 UTC (unshaded regions in Fig. 2), SWAP was viewing close enough to the sunward direction to see such a beam. However, because (i) a relatively narrow, solar wind–like distribution could have been deflected in this region, and (ii) sufficiently slow-flowing solar wind plasma would drop below the energy range sampled by SWAP, it is not possible to determine from these coincidence data whether the solar wind was somehow excluded from all or part of the sampled region and/or whether it was simply flowing in a way that SWAP was not able to observe. More detailed analysis of the SWAP data, including identification of the light (solar wind) versus heavy (Pluto) ions will be required to understand the plasma distributions observed behind Pluto.

Starting at ~18:30 UTC, New Horizons was turned several times to observe the solar wind direction, and SWAP measured disturbed solar wind with somewhat variable speed and density and proton temperatures up to ~40,000 K (3.4 eV), much higher than the ~7700 K (0.7 eV) of the surrounding solar wind. As seen in Fig. 2 (red points), the temperature shows elevated values that generally drop off with distances greater than 400 $R_P$ and return to the essentially unperturbed values by around the start of DOY 196. These SWAP observations suggest substantial heating by the Pluto interaction. Finally, by the time that New Horizons next viewed the solar wind at the start of DOY 196, the plasma conditions had essentially returned to those observed before the flyby, indicating the end of any noteworthy interaction with Pluto.

## Particle measurements

### *The PEPSSI instrument*

The PEPSSI instrument measures the time of flight (TOF) of energetic ions and electrons by detecting their passage between start and stop foils. For particles with sufficiently high energy, the energy deposited in a given solid-state detector is measured (*4*). PEPSSI has six angular sectors labeled S0 to S5, and we concentrate on the measurements in S0, which observes particles close to the Sun direction during the time of the Pluto encounter. We report on TOF-only ion measurements corresponding to an energy per mass of ~0.5 to 50 keV/amu, for which PEPSSI observed the highest counting rates at Pluto. The PEPSSI TOF range nominally extends from 3 to 168 ns (*34*) for time intervals reported for ions traversing a 6.00-cm path internal to the instrument.

Ions are accelerated into PEPPSI by a potential of –2.63 kV by a negatively biased grid at the entrance apertures. This potential is with respect to the spacecraft, which we assume to be close to that of the ambient plasma. The reported energy/mass range given above is measured inside the instrument. Without knowledge of an ion's mass, there is ambiguity about what ion species are being measured. The likely composition of ions in the solar wind in the outer heliosphere includes $H^+$, $He^{++}$, $He^+$, and $O^{n+}$, either from the ions originating in the solar corona (*35*) or from IPUIs originating in the interstellar medium (*36*).

### *PEPSSI observations of the Pluto environment*

Pluto has a substantial effect on the interstellar pickup and suprathermal ions, as illustrated in Fig. 3. We have found no decisive evidence for plutogenic heavy ions in the PEPPSI energy range in the immediate vicinity of Pluto (within 500 $R_P$ of Pluto). There were also no detections near Pluto of >25-keV electrons above a background consistent with the expected galactic cosmic ray fluxes.

Figure 3 shows an overview of the PEPSSI measurements obtained during the Pluto flyby. New Horizons entered the region of Pluto's interaction, as seen in the energetic particles sometime between 06:20 and 11:52 UTC on the flyby day. PEPSSI data suggest that New Horizons left the

Pluto interaction region sometime between 15:20 and 18:33 UTC, equivalent to a downstream distance of 120 to 270 $R_P$. These periods are marked by green background shading in Fig. 3. The energetic particles return to a normal state after 18:33 UTC. The earliest and latest times delimit periods using two criteria: when PEPSSI was close to its nominal attitude (sector S0 of the instrument pointed ~35° from the Sun direction) and when measured fluxes and spectra were characteristic of those observed in the interplanetary medium.

Around 11:57 UTC (point B in Fig. 1) and 50° from the solar direction, PEPSSI detected intensities >10 times larger than those typically observed for that attitude. At that time, New Horizons was ~10 $R_P$ to the side of Pluto. Figure 4 shows a close-up of this time period. The envelope of the measured intensities is modulated by the change in PEPSSI's look direction, and there is a superimposed fine structure on the time scale of several seconds (corresponding to ~0.1 $R_P$). This fine structure, together with the higher-than-normal intensities for this look direction, suggests that New Horizons entered a new region. One hypothesis is that PEPSSI detects particles accelerated from lower energies at a compressive shock near Pluto. Such a shock might be similar to the exotic shock observed at Titan in the solar wind (*37*). Moreover, the TOF spectrum at that time is too similar to measurements in the interplanetary medium (compare to Fig. 3) to make this scenario likely. Another hypothesis is that the intensity enhancements result from the flow being deflected closer to the PEPSSI field of view, and that the fine structure reflects rapid changes associated with the flow being turbulent about this mean deflection. This interpretation has the virtue of simultaneously explaining the similarity of the spectra and difference in the direction relative to the Sun, as well as the position of the enhancement relative to Pluto.

From at least 12:15 to 14:42 UTC (to at least 100 $R_P$ downstream; compare with Fig. 3), New Horizons was in a region very different from that observed in the interplanetary medium, which we assume to be a wake downstream of Pluto. Although PEPSSI was in its nominal attitude favorable for measuring pick-up ions, the intensities at TOFs equivalent to ~1 to 4 keV/amu were ~10 times lower than in the surrounding interplanetary medium. We note that the intensity but not the spectral shape appear to be changing over time. The color scale along the trajectory curve in Fig. 5 shows a gradual increase in count rate during this period as the spacecraft departs from Pluto. It is the distance from Pluto, not the distance away from the Sun-Pluto line, that organizes the intensification trend. The TOF observations show a break in the energy spectrum, at an energy similar to comparable instances in the interplanetary medium.

The ion intensity throughout the wake exhibits 20-min quasi-periodic enhancements superposed on the overall trend. These might be a result of turbulent flow within the wake, similar to the possible deflected flow interpretation of observations closer to Pluto, but the scale is much larger in the wake. Two of these enhancements are broader, with sharp peaks in their center, and coincide with New Horizons passing the geometric wakes of Pluto and Charon. Figures 3 and 5 show these enhancements at 12:50 UTC, when New Horizons was 44 $R_P$ downstream of Pluto, and at 14:17 UTC, when it was 97 $R_P$ downstream of Charon. These enhancements are reminiscent of measurements at 12 to 25 lunar radii downstream of Earth's Moon, immersed in the solar wind and magnetosheath (*38*). At the Moon, there is a density enhancement on the central axis of the wake where protons refilling the wake parallel and antiparallel to the magnetic field merge together.

PEPSSI data reveal an interaction between Pluto and the solar wind, with a scale of at least 11 $R_P$ on the flank of Pluto and extending at least 84 $R_P$ downstream in the solar wind when the spacecraft attitude changed to an unfavorable orientation for PEPSSI observations before completely exiting the Pluto interaction region.

## Dust measurements at Pluto

### *The SDC*

The SDC is an impact dust detector onboard the New Horizons spacecraft. SDC measures the mass of dust grains in the range of $10^{-12} < m < 10^{-9}$ g, covering an approximate size range of 0.5 to 10 μm in particle radius (*5*). Since April 2006, SDC has been taking near-continuous measurements across the solar system (*39*, *40*) and has already provided estimates for the dust production rate and initial size distribution of dust in the Edgeworth-Kuiper belt (*41*, *42*). SDC is the first dedicated dust instrument to reach beyond 18 AU.

To optimize its observations during the Pluto encounter, New Horizons executed a complicated sequence of attitude changes by firing its thrusters. To avoid recording excessive noise during the encounter, on 1 January 2015 we set our charge threshold to $Q \sim 10^7\ e$ (where $e$ is the electron charge), corresponding to a smallest detectable particle radius of 1.4 μm. This charge threshold is above the level of the majority of SDC-recorded thruster events throughout the mission. The thresholds were reset to their pre-encounter values on DOY 211 in 2015.

### *Dust measurements during the encounter*

A period of ±5 days centered on New Horizons's closest approach, corresponding to approximately ±5000 $R_P$, is used to calculate the dust density distribution of the Pluto system. SDC recorded a total of 102 events in this time period. Throughout the mission, due to the expected low dust fluxes, coincident events between multiple channels or events coincident with thruster firings were identified as noise events for both the exposed and the reference detectors. Figure 6 shows all of the recorded events throughout the encounter.

After identifying the coincident events as noise, 16 events remained as candidate dust hits. None of these events occurred on the two reference detectors. New Horizons passed through the Pluto system with a speed of $v_{s/c} \sim 14$ km/s relative to Pluto. Dust grains in the Pluto system are expected to have speeds $<<v_{s/c}$; hence, to a good approximation, $v_{s/c}$ becomes the impact speed. Due to the sequence of observations executed by New Horizons, the orientation of the spacecraft changed almost continuously during the encounter, pointing SDC only intermittently in the ram direction. Because of the impact angle dependence of SDC's sensitivity, the detection probability of dust particles with impact angles >45° approaches 0, and these events are also identified as noise. Throughout the entire period of the close encounter, SDC recorded only a single large amplitude event that could be attributable to a dust impact. To assess to probability that this event was not noise, we examined the amplitude distribution of the recorded noise events and estimated that the detection is outside the 2σ error of the average amplitude of the noise events. Hence, the probability that this event is a dust particle is ~95%. We use this single detection as an upper limit to estimate the dust density near Pluto (see supplementary materials), indicating that the density is most likely 1.2 $km^{-3}$ and the 90% confidence level for the density is in the range of $0.6 < n < 4.6$ $km^{-3}$.

Figure 7 compares this density estimate with dust measurements in the outer solar system, indicating that the dust density of particles with radii >1.4 μm remained within a 1σ error of our last data point representing the SDC measurements since 1 January 2015.

The plasma wave instruments on Voyager 1 and 2 also showed a roughly flat dust density of ~0.2 $km^{-3}$, though in that case the size of the detected particles remained poorly determined (*43*). This match can now be used to estimate that the Voyager dust detection threshold is similar to that of SDC during the Pluto flyby.

The dust density distribution perhaps indicates a slight increase with distance. This could be the result of the inner edge of the Kuiper belt dust disk extending inward and engulfing the outer solar system. Alternatively, the dust density increase could be local to the Pluto system. As SDC will map the dust density distribution for years to come, we will learn how the trend continues deep into the Kuiper belt.

## Discussion

### *The obstacle Pluto presents to the solar wind*

Pluto presents an unusual obstacle to the solar wind, and any theory that seeks to explain it has to account simultaneously for a challenging range of observations provided by New Horizons. In particular, the SWAP observations of limited (<1%) slowing of the solar wind at ~20 $R_P$ upstream of Pluto (point A in Fig. 1) suggest that very few atmospheric molecules are escaping, becoming ionized, and mass-loading the solar wind. When the spacecraft was 8.8 $R_P$ tailward and at a transverse distance of 9.6 $R_P$ from Pluto (point B in Fig. 1), the solar wind

had slowed by ~20%. At this time, PEPSSI detected an enhancement of ions with energies in the kilo–electron volt range. Although there is no current consensus on the nature of the interaction boundary, we can still estimate its size. We can make a zero-order calculation of the size of the Pluto obstacle to the solar wind by assuming the same transverse distance applies at Pluto's terminator and multiplying by two-thirds (on the basis of experience at terrestrial planets) to get a very approximate distance of ~6 $R_P$ for the 20% slowing location directly upstream of Pluto. This distance is about twice as large (scaled to the planet) as the maximum observed bow shock distance in the terminator plane for Mars and Venus (*44*). The interaction at Pluto is therefore consistent with a Mars-like interaction, given the current uncertainties in its bow shock location.

The solar wind interaction with Pluto's atmosphere is expected to depend on (i) the solar wind flux at Pluto, which varies by a factor of 10 on time scales of a few days and by $1/a^2$ with Pluto's heliocentric distance $a$; (ii) the escape rate of Pluto's neutral atmosphere; and (iii) the ionization rate of Pluto's atmosphere, which, for both photoionization and charge-exchange, also varies by $1/a^2$. The enhanced solar wind pressure (due to recent passage of a interplanetary compression region) at the time of the Pluto encounter suggests that the interaction region was in a compressed state at the time of the New Horizons flyby.

If the obstacle is mass-loading the solar wind via ionization of an escaping atmosphere, then we would expect the size of the obstacle to be inversely proportional to the upstream solar wind momentum flux. Comparing the observed solar wind flux with typical Voyager 2 values (Table 1), the factor of ~4 enhancement at the time of the New Horizons flyby suggests that more typical size range for the obstacle (for the same atmospheric escape rate) would be ~25 $R_P$.

On the other hand, if the solar wind does not suffer substantial mass loading due to ionization of an escaping neutral atmosphere well upstream of the object, the solar wind will be slowed by ion pick-up (and subsequent mass-loading) in the outer atmosphere and diverted by electrical currents induced in Pluto's ionosphere. The size of such an interaction, similar in nature to Mars and Venus, is set by the altitude of the peak ionospheric electron density and how sharply the atmospheric density drops with altitude. This Mars-type interaction of the solar wind with an exosphere or ionosphere would be less compressible and would fluctuate less in size with solar wind flux.

Whereas the small size of the interaction region relative to the Pluto is reminiscent of Mars and Venus, recent observations of the solar wind interaction with the relatively weakly outgassing comet 67P Churyumov-Gerasimenko by instruments on ESA's Rosetta spacecraft (*45*–*47*) show deflection of the solar wind with a relatively modest decrease in speed. We anticipate productive discussions of the relative roles of atmospheric escape rate, solar wind flux, and IMF strength at Mars, comet 67P, and Pluto as the data from the MAVEN (Mars Atmosphere and Volatile Evolution), Rosetta, and New Horizons spacecraft are further analyzed.

### Atmospheric escape

Pluto's atmosphere was first detected in 1988 during stellar occultation (*48*) and was later determined to be primarily composed of $N_2$ with minor abundances of $CH_4$ and CO, with surface pressures of ~17 μbar (*49*, *50*). Pluto's low gravity implies that a large flux of atmospheric neutrals can escape. Estimates of escape rates range from as low as $1.5 \times 10^{25}$ molecules $s^{-1}$ to as high as $2 \times 10^{28}$ molecules $s^{-1}$. The most recent (pre–New Horizons) atmospheric model (*23*) indicates a denser and more expanded atmosphere with an escape rate of ~$3.5 \times 10^{27}$ $N_2$ molecules $s^{-1}$ and an exobase at 8 $R_P$ ~ 9600 km. These are the conditions that were anticipated on arrival at Pluto.

The New Horizons trajectory was designed to provide solar and Earth occultations of Pluto's atmosphere by the ultraviolet spectrometer (Alice) and Radio Science Experiment (REX) instruments, respectively (*51*, *52*). These occultation measurements revealed Pluto's upper atmosphere to be colder and less extended than predicted (*2*). Matching the Zhu *et al.* (*8*, *23*) model to the New Horizons data suggests a cooler upper atmosphere, composed primarily of methane (rather than nitrogen), with an exobase height of 2.5 $R_P$ and an escape rate of only $6 \times 10^{25}$ molecules $s^{-1}$. This limited atmospheric escape drastically reduces the neutral material upstream of Pluto available for ionization and mass-loading the solar wind.

### Ionosphere

New Horizons did not make a direct measurement of Pluto's ionosphere. Adapting a pre-encounter model of the atmosphere to the density, temperature, and composition measurements from New Horizons (*2*), we find a peak electron density of ≤1300 $cm^{-3}$ at a distance of 1900 km = 1.6 $R_P$. The density drops above this peak with a scale height of ~330 km. The main ions are $H_2CN^+$ (mass = 28 amu) and $C_2H_5^+$ (mass = 29 amu). Preliminary estimates of the electrical conductivity of such an ionosphere suggest that it is sufficient to sustain currents that would divert the solar wind.

### Bow shock

In modeling interactions (cometary or Mars-like) it is often assumed that the planet's atmosphere and ionosphere and the solar wind can be considered as fluids. For many solar system bodies, fluid descriptions of a plasma-obstacle interaction are often good starting points. Global-scale magnetohydrodynamic (MHD) models have been successful in capturing the basic structure of many plasma interactions. The fast, cold flow of the solar wind in the heliosphere is highly supersonic (Table 1). We illustrate the shape of a Mach 40 shock in Fig. 1 to show how bent such a shock could be behind Pluto. We also show a low Mach number shock to illustrate how including a high density of IPUIs and/or substantial upstream ionization of plutogenic PPUIs would move the shock farther upstream and reduce the shock angle.

With the IMF being very weak at Pluto's orbital distance, the length scales on which the plasma reacts are large compared with the size of the interaction region. For instance, at 33 AU the gyroradius of solar wind protons is ~23 $R_P$ and the pick-up ion gyroradius of $CH_4^+$ ions is ~200 to 800 $R_P$ (*7*, *9*).

There is no direct evidence of a sharp bow shock in Figs. 2 and 3. This may be because the spacecraft attitude was unfavorable during the passage of the shock (see the gray shading in Fig. 2 and the large angles in Fig. 3) so that it could not be observed well. However, it is important to consider the expected shock thickness. Two thicknesses that have been used in the past are the proton "turn-around" distance and the ion inertial length. For relatively strong magnetic fields, the turn-around distance is approximated by $V_{SW}/\Omega_{ci}$ (where $\Omega_{ci}$ is gyrofrequency), which is proportional to $V_{SW}/B$ (*53*). High Mach number shocks observed by Voyager at Uranus (*54*) and Neptune (*55*), as well as by Cassini at Titan (*37*), indicate that this is a reasonable approximation, with observed shock widths being ~30 to 70% of this quantity calculated from upstream conditions. For the observed upstream solar wind speed and |B| of 0.3 nT, we obtain ~50 $R_P$ for a solar wind proton turn-around distance. Perhaps a better scaling for the weak IMF conditions and small obstacle size at Pluto—for which the interaction may be mediated by whistler waves rather than shock-forming MHD modes—is the ion inertial length (*53*). Again using the measured upstream density of ~0.025 $cm^{-3}$, we get an ion inertial length of ~1.2 $R_P$. Because the derived 20% slowing interaction distance of ~6 $R_P$ is intermediate between the scaled turn-around and ion inertial lengths, we conclude that an ionospheric obstacle could produce the derived dayside size scale of the solar wind slowing ahead of Pluto.

## Conclusions

Pluto continues to deliver surprises. The New Horizons instruments that measure plasma and particles revealed an interaction region unlike any other body in the solar system and considerably smaller than predicted. This reduced interaction region is possibly due to the combination of a much-smaller-than-expected atmospheric escape rate, as indicated by the New Horizons atmospheric measurements (*2*), and the flyby occurring during a time of particularly high solar wind flux.

1) Observations indicated enhanced upstream solar wind flux detected by the SWAP instrument. The lack of any slowing until New Horizons was within 20 $R_P$ indicates that almost no heavy ions were ionized within the several thousand $R_P$ upstream of Pluto. The SWAP data revealed a surprisingly small interaction region, confined on its upwind side to within ~6 $R_P$ of Pluto. The interaction persists to a distance of more than 400 $R_P$ behind Pluto.

2) PEPSSI has not detected evidence of plutogenic pick-up ions or energetic electrons in its

energy range within 500 $R_P$ of Pluto, but the interplanetary energetic particle intensities are considerably perturbed by the interaction. Changes in PEPSSI measurements near Pluto's terminator suggest that <10-keV ions are accelerated and/or deflected away from the direction radially from the Sun. PEPSSI observed decreased suprathermal particles in the wake of the interaction region. The particle intensities near Pluto decreased by a factor of ~10 below the heliospheric value and increased with distance downstream.

3) During the encounter, SDC could detect grains with an effective radius greater than ~1.4 μm. Eliminating spurious events, such as thruster firings (leading to events that are not dust impacts), SDC detected one candidate impact in ±5 days around closest approach. In this time period, the effective volume carved out by SDC was 0.83 $km^{-3}$, leading to a dust density estimate of 1.2 $km^{-3}$, with a 90% confidence level range of $0.6 < n < 4.6$ $km^{-3}$.

## REFERENCES AND NOTES


1. S. A. Stern *et al*., The Pluto system: Initial results from its exploration by New Horizons. *Science* **350**, aad1815 (2015). doi: 10.1126/science.aad1815; pmid: 26472913
2. G. R. Gladstone *et al*.New Horizons Science Team, The atmosphere of Pluto as observed by New Horizons. *Science* **351**, aad8866 (2016).
3. D. J. McComas *et al*., The Solar Wind Around Pluto (SWAP) instrument aboard New Horizons. *Space Sci. Rev.* **140**, 261–313 (2008). doi: 10.1007/s11214-007-9205-3
4. R. L. McNutt Jr. *et al*., The Pluto Energetic Particle Spectrometer Science Investigation (PEPSSI) on the New Horizons Mission. *Space Sci. Rev.* **140**, 315–385 (2008). doi: 10.1007/s11214-008-9436-y
5. M. Horányi *et al*., The Student Dust Counter on the New Horizons mission. *Space Sci. Rev.* **140**, 387–402 (2008). doi: 10.1007/s11214-007-9250-y
6. F. Bagenal, R. L. McNutt Jr., Pluto's interaction with the solar wind. *Geophys. Res. Lett.* **16**, 1229–1232 (1989). doi: 10.1029/GL016i011p01229
7. K. Kecskeméty, T. E. Cravens, Pick-up ions at Pluto. *Geophys. Res. Lett.* **20**, 543–546 (1993). doi: 10.1029/93GL00487
8. F. Bagenal, T. E. Cravens, J. G. Luhmann, R. L. McNutt, A. F. Cheng, in *Pluto and Charon*, S. A. Stern, D. J. Tholan, Eds. (Univ. of Arizona Press, 1997), pp. 523–555.
9. K. Sauer, A. Lipatov, K. Baumgartel, E. Dubinin, Solar wind-Pluto interaction revised. *Adv. Space Res.* **20**, 295–299 (1997). doi: 10.1016/S0273-1177(97)00551-6
10. V. I. Shevchenko, S. K. Ride, M. Baine, Wave activity near Pluto. *Geophys. Res. Lett.* **24**, 101–104 (1997). doi: 10.1029/96GL03696
11. W.-H. Ip, A. Kopp, L. M. Lara, R. Rodrigo, Pluto's ionospheric models and solar wind interaction. *Adv. Space Res.* **26**, 1559–1563 (2000). doi: 10.1016/S0273-1177(00)00098-3
12. P. A. Delamere, F. Bagenal, Pluto's kinetic interaction with the solar wind. *Geophys. Res. Lett.* **31**, L04807 (2004). doi: 10.1029/2003GL018122
13. E. M. Harnett, R. M. Winglee, P. A. Delamere, Three-dimensional multi-fluid simulations of Pluto's magnetosphere: A comparison to 3D hybrid simulations. *Geophys. Res. Lett.* **32**, L19104 (2005). doi: 10.1029/2005GL023178
14. P. A. Delamere, Hybrid code simulations of the solar wind interaction with Pluto. *J. Geophys. Res.* **114**, A03220 (2009). doi: 10.1029/2008JA013756
15. T. E. Cravens, D. F. Strobel, Pluto's solar wind interaction: Collisional effects. *Icarus* **246**, 303–309 (2015). doi: 10.1016/j.icarus.2014.04.011
16. D. M. Hunten, A. J. Watson, Stability of Pluto's atmosphere. *Icarus* **51**, 665–667 (1982). doi: 10.1016/0019-1035(82)90155-5
17. R. L. McNutt Jr., Models of Pluto's upper atmosphere. *Geophys. Res. Lett.* **16**, 1225–1228 (1989). doi: 10.1029/GL016i011p01225
18. V. A. Krasnopolsky, Hydrodynamic flow of $N_2$ from Pluto. *J. Geophys. Res.* **104**, 5955–5962 (1999). doi: 10.1029/1998JE900052
19. F. Tian, O. B. Toon, Hydrodynamic escape of nitrogen from Pluto. *Geophys. Res. Lett.* **32**, L18201 (2005). doi: 10.1029/2005GL023510
20. D. F. Strobel, $N_2$ escape rates from Pluto's atmosphere. *Icarus* **193**, 612–619 (2008). doi: 10.1016/j.icarus.2007.08.021
21. O. J. Tucker, J. T. Erwin, J. I. Deighan, A. N. Volkov, R. E. Johnson, Thermally driven escape from Pluto's atmosphere: A combined fluid/kinetic model. *Icarus* **217**, 408–415 (2012). doi: 10.1016/j.icarus.2011.11.017
22. O. J. Tucker, R. E. Johnson, L. A. Young, Gas transfer in the Pluto-Charon system: Charon atmosphere. *Icarus* **246**, 291–297 (2015). doi: 10.1016/j.icarus.2014.05.002
23. X. Zhu, D. F. Strobel, J. T. Erwin, The density and thermal structure of Pluto's atmosphere and associated escape processes and rates. *Icarus* **228**, 301–314 (2014). doi: 10.1016/j.icarus.2013.10.011
24. F. Bagenal *et al*., Solar wind at 33 AU: Setting bounds on the Pluto interaction for New Horizons. *J. Geophys. Res.* **120**, 1497–1511 (2015). doi: 10.1002/2015JE004880
25. D. J. McComas *et al*., Diverse plasma populations and structures in Jupiter's magnetotail. *Science* **318**, 217–220 (2007). doi: 10.1126/science.1147393; pmid: 17932282
26. R. W. Ebert, D. J. McComas, F. Bagenal, H. A. Elliott, Location, structure, and motion of Jupiter's dusk magnetospheric boundary from ~1625 to 2550 $R_J$. *J. Geophys. Res.* **115**, A12223 (2010). doi: 10.1029/2010JA015938
27. G. Nicolaou, D. J. McComas, F. Bagenal, H. A. Elliott, Properties of plasma ions in the distant Jovian magnetosheath using Solar Wind Around Pluto (SWAP) data on New Horizons. *J. Geophys. Res.* **119**, 3463–3479 (2014).
28. G. Nicolaou, D. J. McComas, F. Bagenal, H. A. Elliott, R. W. Ebert, Jupiter's deep magnetotail boundary layer. *Planet. Space Sci.* **111**, 116–125 (2015). doi: 10.1016/j.pss.2015.03.020
29. G. Nicolaou, D. J. McComas, F. Bagenal, H. A. Elliott, R. J. Wilson, Plasma properties in the deep Jovian magnetotail. *Planet. Space Sci.* **119**, 222–232 (2015). doi: 10.1016/j.pss.2015.10.001
30. H. A. Elliott *et al*., http://arxiv.org/abs/1601.07156 (2016).
31. B. M. Randol, H. A. Elliott, J. T. Gosling, D. J. McComas, N. A. Schwadron, Observations of isotropic interstellar pick-up ions at 11 and 17 AU from New Horizons. *Astrophys. J.* **755**, 75–82 (2012). doi: 10.1088/0004-637X/755/1/75
32. B. M. Randol, D. J. McComas, N. A. Schwadron, Interstellar pick-up ions observed between 11 and 22 AU by New Horizons. *Astrophys. J.* **768**, 120–128 (2013). doi: 10.1088/0004-637X/768/2/120
33. J. D. Richardson, C. Wang, L. F. Burlaga, Correlated solar wind speed, density, and magnetic field changes at Voyager 2. *Geophys. Res. Lett.* **30**, 2207 (2003). doi: 10.1029/2003GL018253
34. Note that these values are updated from (*4*).
35. L. Villanueva, R. L. McNutt Jr., A. J. Lazarus, J. T. Steinberg, Voyager observations of $O^{6+}$ and other minor ions in the solar wind. *J. Geophys. Res.* **99**, 2553–2565 (1994). doi: 10.1029/92JA02899
36. M. E. Hill, N. A. Schwadron, D. C. Hamilton, R. D. DiFabio, R. K. Squier, Interplanetary suprathermal $He^+$ and $He^{++}$ observations during quiet periods from 1 to 9 AU and implications for particle acceleration. *Astrophys. J.* **699**, L26–L30 (2009). doi: 10.1088/0004-637X/699/1/L26
37. C. Bertucci *et al*., Titan's interaction with the supersonic solar wind. *Geophys. Res. Lett.* **42**, 193–200 (2015). doi: 10.1002/2014GL062106
38. D. Clack, J. C. Kasper, A. J. Lazarus, J. T. Steinberg, W. M. Farrell, Wind observations of extreme ion temperature anisotropies in the lunar wake. *Geophys. Res. Lett.* **31**, L06812 (2004). doi: 10.1029/2003GL018298
39. A. R. Poppe, D. James, B. Jacobsmeyer, M. Horányi, First results from the Venetia Burney Student Dust Counter on the New Horizons mission. *Geophys. Res. Lett.* **37**, L11101 (2010). doi: 10.1029/2010GL043300
40. J. R. Szalay, M. Piquette, M. Horányi, The Student Dust Counter: Status report at 23 AU. *Earth Planets Space* **65**, 1145–1149 (2013). doi: 10.5047/eps.2013.02.005
41. D. Han, A. R. Poppe, M. Piquette, E. Grun, M. Horányi, Constraints on dust production in the Edgeworth-Kuiper Belt from Pioneer 10 and New Horizons measurements. *Geophys. Res. Lett.* **38**, L24102 (2011). doi: 10.1029/2011GL050136
42. A. R. Poppe, An improved model for interplanetary dust fluxes in the outer solar system. *Icarus* **264**, 369–386 (2016). doi: 10.1016/j.icarus.2015.10.001
43. D. A. Gurnett, J. A. Ansher, W. S. Kurth, L. J. Granroth, Micron-sized dust particles detected in the outer solar system by the Voyager 1 and 2 plasma wave instruments. *Geophys. Res. Lett.* **24**, 3125–3128 (1997). doi: 10.1029/97GL03228
44. N. J. T. Edberg *et al*., Magnetosonic Mach number effect of the position of the bow shock at Mars in comparison to Venus. *J. Geophys. Res.* **115**, A07203 (2010). doi: 10.1029/2009JA014998
45. H. Nilsson *et al*., Birth of a comet magnetosphere: A spring of water ions. *Science* **347**, aaa0571 (2015). doi: 10.1126/science.aaa0571; pmid: 25613894
46. H. Nilsson *et al*., Evolution of the ion environment of comet 67P/Churyumov- Gerasimenko - Observations between 3.6 and 2.0 AU. *Astron. Astrophys.* **583**, A20 (2015). doi: 10.1051/0004-6361/201526142
47. T. W. Broiles *et al*., Rosetta observations of solar wind interaction with the comet 67P/Churyumov-Gerasimenko. *Astron. Astrophys.* **583**, A21 (2015). doi: 10.1051/0004-6361/201526046
48. J. L. Elliot *et al*., Pluto's atmosphere. *Icarus* **77**, 148–170 (1989). doi: 10.1016/0019-1035(89)90014-6
49. L. A. Young, J. C. Cook, R. V. Yelle, E. F. Young, Upper limits on gaseous CO at Pluto and Triton from high-resolution near-IR spectroscopy. *Icarus* **153**, 148–156 (2001). doi: 10.1006/icar.2001.6662
50. E. Lellouch *et al*., Exploring the spatial, temporal, and vertical distribution of methane in Pluto's atmosphere. *Icarus* **246**, 268–278 (2015). doi: 10.1016/j.icarus.2014.03.027
51. S. A. Stern, The New Horizons Pluto Kuiper Belt mission: An overview with historical context. *Space Sci. Rev.* **140**, 3–21 (2008). doi: 10.1007/s11214-007-9295-y
52. L. A. Young *et al*., New Horizons: Anticipated scientific investigations at the Pluto system. *Space Sci. Rev.* **140**, 93–127 (2008). doi: 10.1007/s11214-008-9462-9
53. S. J. Schwartz, M. F. Thomsen, J. T. Gosling, Ions upstream of the Earth's bow shock: A theoretical comparison of alternative source populations. *J. Geophys. Res.* **88**, 2039–2047 (1983). doi: 10.1029/JA088iA03p02039
54. F. Bagenal, J. W. Belcher, E. C. Sittler Jr., R. P. Lepping Jr., The Uranian bow shock: Voyager 2 inbound observations of a high Mach number shock. *J. Geophys. Res.* **92**, 8603–8612 (1987). doi: 10.1029/JA092iA08p08603
55. A. Szabo, R. P. Lepping, Neptune inbound bow shock. *J. Geophys. Res.* **100**, 1723–1730 (1995). doi: 10.1029/94JA02491
56. D. J. McComas, H. A. Elliott, N. A. Schwadron, Pickup hydrogen distributions in the solar wind at ~11 AU: Do we understand pickup ions in the outer heliosphere? *J. Geophys. Res.* **115**, A03102 (2010). doi: 10.1029/2009JA014604


## ACKNOWLEDGMENTS

We thank the many contributors to the development of the SDC, SWAP, and PEPSSI instruments and acknowledge many useful discussions with colleagues. The New Horizons mission is supported by NASA's New Frontiers Program. S.A.S. is also affiliated with Florida Space Institute, Uwingu, Golden Spike, and World View Enterprises. A.R.P. acknowledges support from NASA's Planetary Atmospheres Program (grant NNX13AG55G). As contractually agreed to with NASA, fully calibrated New Horizons Pluto system data will be released via the NASA Planetary Data System (https://pds.nasa.gov/) in a series of stages in 2016 and 2017 as the data set is fully downlinked and calibrated.

## SUPPLEMENTARY MATERIALS

www.sciencemag.org/content/351/6279/aad9045/suppl/DC1
Materials and Methods
Supplementary Text
Figs. S1 and S2
References (*57*–*59*)
New Horizons Science Team Author List

18 November 2015; accepted 29 January 2016
10.1126/science.aad9045

RESEARCH ARTICLE SUMMARY

PLANETARY SCIENCE

# Surface compositions across Pluto and Charon

W. M. Grundy,* R. P. Binzel, B. J. Buratti, J. C. Cook, D. P. Cruikshank, C. M. Dalle Ore, A. M. Earle, K. Ennico, C. J. A. Howett, A. W. Lunsford, C. B. Olkin, A. H. Parker, S. Philippe, S. Protopapa, E. Quirico, D. C. Reuter, B. Schmitt, K. N. Singer, A. J. Verbiscer, R. A. Beyer, M. W. Buie, A. F. Cheng, D. E. Jennings, I. R. Linscott, J. Wm. Parker, P. M. Schenk, J. R. Spencer, J. A. Stansberry, S. A. Stern, H. B. Throop, C. C. C. Tsang, H. A. Weaver, G. E. Weigle II, L. A. Young, and the New Horizons Science Team

**INTRODUCTION:** The Kuiper Belt hosts a swarm of distant, icy objects ranging in size from small, primordial planetesimals to much larger, highly evolved objects, representing a whole new class of previously unexplored cryogenic worlds. Pluto, the largest among them, along with its system of five satellites, has been revealed by NASA's New Horizons spacecraft flight through the system in July 2015, nearly a decade after its launch.

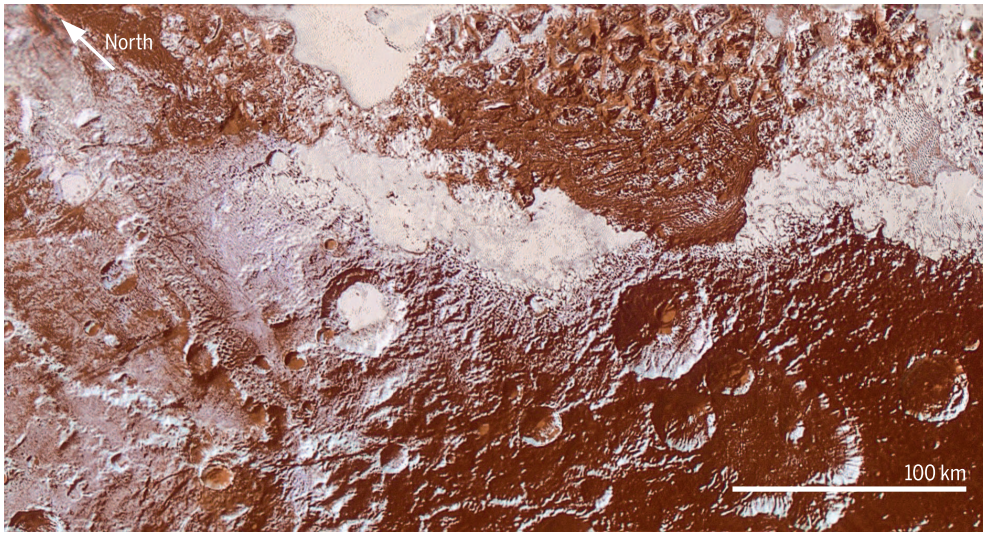
**RATIONALE:** Landforms expressed on the surface of a world are the product of the available materials and of the action of the suite of processes that are enabled by the local physical and chemical conditions. They provide observable clues about what processes have been at work over the course of time, the understanding of which is a prerequisite to reconstructing the world's history. Materials known to exist at Pluto's surface from ground-based spectroscopic observations include highly volatile cryogenic ices of $N_2$ and CO, along with somewhat less volatile $CH_4$ ice, as well as $H_2O$ and $C_2H_6$ ices and more complex tholins that are inert at Pluto surface temperatures. Ices of $H_2O$ and $NH_3$ are inert components known to exist on Pluto's large satellite Charon. New Horizons' Ralph instrument was designed to map colors and compositions in the Pluto system. It consists of a charge-coupled device camera with four color filters spanning wavelengths from 400 to 970 nm plus a near-infrared imaging spectrometer covering wavelengths from 1.25 to 2.5 μm, where the various cryogenic ices are distinguishable via their characteristic vibrational absorption features.

**RESULTS:** New Horizons made its closest approach to the system on 14 July 2015. Observations of Pluto and Charon obtained that day reveal regionally diverse colors and compositions. On Pluto, the color images show nonvolatile tholins coating an ancient, heavily cratered equatorial belt. A smooth, thousand-kilometer plain must be able to refresh its surface rapidly enough to erase all impact craters. Infrared observations of this region show volatile ices including $N_2$ and CO. $H_2O$ ice is not detected there, but it does appear in neighboring regions. $CH_4$ ice appears on crater rims and mountain ridges at low latitudes and is abundant at Pluto's high northern latitudes. Pluto's regional albedo contrasts are among the most extreme for solar system objects. Pluto's large moon Charon offers its own surprises. Its $H_2O$ ice–rich surface is unlike other outer solar system icy satellites in exhibiting distinctly reddish tholin coloration around its northern pole as well as a few highly localized patches rich in $NH_3$ ice.

ON OUR WEB SITE

Read the full article at http://dx.doi.org/10.1126/science.aad9189

**CONCLUSION:** Pluto exhibits evidence for a variety of processes that act to modify its surface over time scales ranging from seasonal to geological. Much of this activity is enabled by the existence of volatile ices such as $N_2$ and CO that are easily mobilized even at the extremely low temperatures prevalent on Pluto's surface, around 40 K. These ices sublimate and condense on seasonal time scales and flow glacially. As they move about Pluto's surface environment, they interact with materials such as $H_2O$ ice that are sufficiently rigid to support rugged topography. Although Pluto's durable $H_2O$ ice is probably not active on its own, it appears to be sculpted in a variety of ways through the action of volatile ices of $N_2$ and CO. $CH_4$ ice plays a distinct role of its own, enabled by its intermediate volatility. $CH_4$ ice condenses at high altitudes and on the winter hemisphere, contributing to the construction of some of Pluto's more unusual and distinctive landforms. The latitudinal distribution of Charon's polar reddening suggests a thermally controlled production process, and the existence of highly localized patches rich in $NH_3$ ice on its surface implies relatively recent emplacement. ■




**Enhanced color view of Pluto's surface diversity.** This mosaic was created by merging Multispectral Visible Imaging Camera color imagery (650 m per pixel) with Long Range Reconnaissance Imager panchromatic imagery (230 m per pixel). At lower right, ancient, heavily cratered terrain is coated with dark, reddish tholins. At upper right, volatile ices filling the informally named Sputnik Planum have modified the surface, creating a chaos-like array of blocky mountains. Volatile ice occupies a few nearby deep craters, and in some areas the volatile ice is pocked with arrays of small sublimation pits. At left, and across the bottom of the scene, gray-white $CH_4$ ice deposits modify tectonic ridges, the rims of craters, and north-facing slopes.

The list of author affiliations is available in the full article online.
*Corresponding author. E-mail: w.grundy@lowell.edu
Cite this article as W. M. Grundy *et al.*, Science 351, aad9189 (2016). DOI: 10.1126/science.aad9189

Downloaded from on March 17, 2016

RESEARCH ARTICLE

PLANETARY SCIENCE

# Surface compositions across Pluto and Charon

W. M. Grundy,[1]* R. P. Binzel,[2] B. J. Buratti,[3] J. C. Cook,[4] D. P. Cruikshank,[5] C. M. Dalle Ore,[5,6] A. M. Earle,[2] K. Ennico,[5] C. J. A. Howett,[4] A. W. Lunsford,[7] C. B. Olkin,[4] A. H. Parker,[4] S. Philippe,[8] S. Protopapa,[9] E. Quirico,[8] D. C. Reuter,[7] B. Schmitt,[8] K. N. Singer,[4] A. J. Verbiscer,[10] R. A. Beyer,[5,6] M. W. Buie,[4] A. F. Cheng,[11] D. E. Jennings,[7] I. R. Linscott,[12] J. Wm. Parker,[4] P. M. Schenk,[13] J. R. Spencer,[4] J. A. Stansberry,[14] S. A. Stern,[4] H. B. Throop,[15] C. C. C. Tsang,[4] H. A. Weaver,[11] G. E. Weigle II,[16] L. A. Young,[4] and the New Horizons Science Team

**The New Horizons spacecraft mapped colors and infrared spectra across the encounter hemispheres of Pluto and Charon. The volatile methane, carbon monoxide, and nitrogen ices that dominate Pluto's surface have complicated spatial distributions resulting from sublimation, condensation, and glacial flow acting over seasonal and geological time scales. Pluto's water ice "bedrock" was also mapped, with isolated outcrops occurring in a variety of settings. Pluto's surface exhibits complex regional color diversity associated with its distinct provinces. Charon's color pattern is simpler, dominated by neutral low latitudes and a reddish northern polar region. Charon's near-infrared spectra reveal highly localized areas with strong ammonia absorption tied to small craters with relatively fresh-appearing impact ejecta.**

NASA's New Horizons probe explored the Pluto system in July 2015, returning data from instruments sensitive to electromagnetic radiation from ultraviolet through radio wavelengths, as well as to charged particles and dust (*1*, *2*). Since the publication of initial results (*3*), more data have been transmitted to Earth. This paper focuses on the spectral and spatial dependence of sunlight reflected from Pluto and Charon in the wavelength range 400 to 2500 nm. These wavelengths are useful for investigating the cryogenic ices prevalent on their surfaces. We restrict our attention to the encounter hemispheres of both bodies because data for the non-encounter hemispheres are as yet incomplete and have lower spatial resolution. Accompanying papers in this issue present results on geology (*4*), atmospheres (*5*), the particle environment (*6*), and small satellites (*7*).

## Instrument overview

Data in this paper were chiefly obtained with New Horizons' Ralph instrument (*8*). Ralph consists of a single *f*/8.7 telescope with a 658-mm effective focal length that feeds light to two focal planes: (i) the Multispectral Visible Imaging Camera (MVIC), a visible/near-infrared (NIR) panchromatic and color imager, and (ii) the Linear Etalon Imaging Spectral Array (LEISA), a short-wavelength IR hyperspectral imager. A dichroic beamsplitter transmits IR wavelengths longer than 1.1 μm to LEISA and reflects shorter wavelengths to MVIC.

MVIC is composed of seven independent charge-coupled device (CCD) arrays on a single substrate. Six large-format (5024 × 32 pixel) CCD arrays operate in time delay integration (TDI) mode, providing two panchromatic (400 to 975 nm) channels and four color channels: BLUE (400 to 550 nm), RED (540 to 700 nm), NIR (780 to 975 nm), and narrow-band methane ("CH4," 860 to 910 nm; the 4 in the filter name is full-size to distinguish it from the chemical formula). Using TDI allows very-large-format images to be obtained as the spacecraft scans the field of view (FOV) rapidly across the scene. A single MVIC pixel is 20 μrad × 20 μrad, resulting in a total FOV of 5.7° in the direction orthogonal to the scan. This width is well matched to the size of Pluto as seen from New

[1]Lowell Observatory, Flagstaff, AZ 86001, USA. [2]Massachusetts Institute of Technology, Cambridge, MA 02139, USA. [3]NASA Jet Propulsion Laboratory, La Cañada Flintridge, CA 91011, USA. [4]Southwest Research Institute, Boulder, CO 80302, USA. [5]NASA Ames Research Center, Space Science Division, Moffett Field, CA 94035, USA. [6]Carl Sagan Center, SETI Institute, Mountain View, CA 94043, USA. [7]NASA Goddard Space Flight Center, Greenbelt, MD 20771, USA. [8]Université Grenoble Alpes, CNRS, IPAG, F-38000 Grenoble, France. [9]Department of Astronomy, University of Maryland, College Park, MD 20742, USA. [10]Department of Astronomy, University of Virginia, Charlottesville, VA 22904, USA. [11]Johns Hopkins University Applied Physics Laboratory, Laurel, MD 20723, USA. [12]Stanford University, Stanford, CA 94305, USA. [13]Lunar and Planetary Institute, Houston, TX 77058, USA. [14]Space Telescope Science Institute, Baltimore, MD, USA. [15]Planetary Science Institute, Mumbai, India. [16]Southwest Research Institute, San Antonio, TX 28510, USA.
*Corresponding author. E-mail: w.grundy@lowell.edu

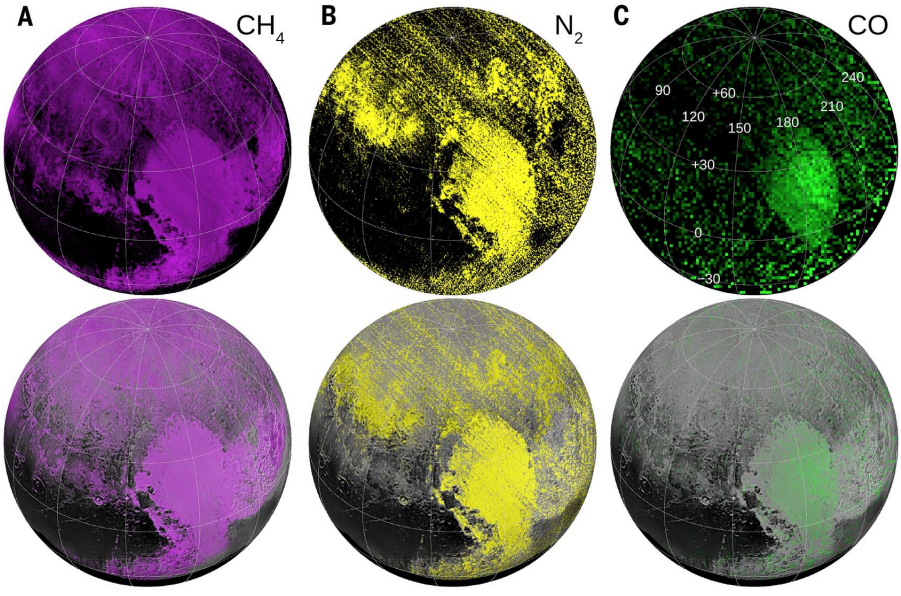



**Fig. 1. LEISA maps of Pluto's volatile ices $CH_4$, $N_2$, and CO.** For each species, the top panel shows the LEISA map, with brighter colors corresponding to greater absorption; the bottom panel shows the same data overlaid on a base map made from LORRI images reprojected to the geometry of the LEISA observation. (**A**) The $CH_4$ absorption map shows the equivalent width of the 1.3- to 1.4-μm band complex. (**B**) The $N_2$ absorption map is a ratio of the average over the band center (2.14 to 2.16 μm) to that of adjacent wavelengths (2.12 to 2.14 μm and 2.16 to 2.18 μm). (**C**) The CO absorption map is a ratio of the average over the band center (1.56 to 1.58 μm) to that of adjacent wavelengths (1.55 to 1.56 μm and 1.58 to 1.59 μm). Latitude and longitude grids at 30° intervals [shown in (C)] apply to all maps.

Horizons near closest approach. The seventh CCD is a 5024 × 128 element frame transfer panchromatic array operated in staring mode, with a FOV of 5.7° × 0.15°.

LEISA produces spectral maps in the compositionally important 1.25- to 2.5-μm IR spectral region by imaging a scene through a wedged etalon filter (*9*) mounted above a 256 × 256 pixel mercury cadmium telluride (HgCdTe) detector array with 62 μrad × 62 μrad pixels. LEISA forms a spectral map by scanning the 0.91° × 0.91° FOV across the scene in a push-broom fashion. The filter was fabricated such that the wavelength varies along the scan direction. It has two segments: (i) 1.25 to 2.5 μm with an average spectral resolving power of 240, and (ii) 2.1 to 2.25 μm with an average spectral resolving power of 560.

Supporting observations were obtained with the Long Range Reconnaissance Imager (LORRI) (*10*). LORRI's 1024 × 1024 pixel CCD detector has no filter, providing panchromatic response from 350- to 850-nm wavelengths, with a 608-nm pivot wavelength [a measure of effective wavelength independent of the source spectrum (*11*)]. It provides a narrow FOV (0.29°) and high spatial resolution (4.95-μrad pixels). In this paper, the LORRI images are used to provide high-resolution geological context imagery and to derive the absolute reflectance of the surface.

## Pluto

New Horizons scanned the LEISA imaging spectrometer across the planet several times on the closest approach date, 14 July 2015. We present two LEISA scans, obtained at 9:33 and 9:48 UTC from ranges of 114,000 km and 102,000 km (*12*). The resulting spatial scales are 7 km per pixel and 6 km per pixel, respectively. In combination, the two observations cover the visible disk of Pluto. The data are used to map absorption by various molecules across Pluto's surface, including methane ($CH_4$), nitrogen ($N_2$), carbon monoxide (CO), and water ($H_2O$) ices, revealing that these ices have complex and distinct spatial distributions as described below.

### *Pluto's volatile ices*

$N_2$, CO, and $CH_4$ ices are all volatile at Pluto's surface temperatures of 35 to 50 K (*13*, *14*). They support Pluto's atmosphere via vapor pressure equilibrium and participate in Pluto's seasonal cycles (*15*). Of the three, $N_2$ has the highest vapor pressure and thus dominates the lower atmosphere, while $CH_4$ is the least volatile, with a vapor pressure one-thousandth that of $N_2$ (*13*). $N_2$, CO, and $CH_4$ ices are all soluble in one another to varying degrees, so on Pluto's surface, the three ices are likely mixed to some extent at the molecular level (*16*–*18*). The volatility contrasts and complex thermodynamic behaviors of ice mixtures are expected to produce distinct spatial distributions of these ices across Pluto's surface as functions of season, heliocentric distance, latitude, altitude, local slope, substrate albedo, and thermal properties. The LEISA data reveal complex distributions of the volatile ices (Fig. 1). Brighter colors correspond to greater absorption by each ice, but the scale is arbitrary, so only relative variations are meaningful in this context. The geological context is shown by overlaying each colored absorption map on the higher-resolution LORRI base map (*4*) in the bottom part of each panel.

$CH_4$ ice's numerous absorption bands dominate Pluto's NIR spectrum. Figure 1A shows absorption by $CH_4$ ice at 1.3 to 1.4 μm to be widely distributed across the planet's surface. The $CH_4$ absorption is especially strong in the bright, heart-shaped region informally known (*19*) as Tombaugh Regio (TR), in Tartarus Dorsa to the east, in the high northern latitudes of Lowell Regio, and in the sliver of the southern winter hemisphere visible south of Cthulhu Regio. $CH_4$ absorption appears relatively uniform across the 1000-km-wide icy plain of Sputnik Planum (SP), the western half of TR. At northern mid-latitudes, the $CH_4$ distribution is much more patchy, evidently influenced by topographic features (see fig. S4). Many craters show strong $CH_4$ absorption on their rims but not on their floors, although there is some variability to this pattern. Figure 1A shows the floors of Burney and Kowal craters having some $CH_4$ absorption, whereas those of Giclas and Drake craters look more depleted (see also fig. S4). In eastern TR, the region around Pulfrich crater has conspicuously little $CH_4$ absorption. Other areas with weak $CH_4$ absorption include parts of al-Idrisi and Baré Montes west of SP and the low-albedo equatorial regions Cthulhu Regio and Krun Macula, although a few crater rims and the peaks of a mountainous ridge within Cthulhu Regio do show strong $CH_4$ absorption.

$N_2$ ice was first identified on Pluto from its weak absorption band at 2.15 μm (*20*). The absorption coefficient of this band is less than that of $CH_4$ at similar wavelengths by a factor of ~$10^5$, so the fact that it could be detected at all suggests that $N_2$ could be the dominant ice on the surface of the planet. Figure 1B shows a map of $N_2$ ice absorption from LEISA data. Relatively little absorption is seen at low latitudes, except for SP, where $N_2$ absorption is strong. As with the $CH_4$ absorption, $N_2$ absorption is patchy in northern mid-latitudes, but the spatial distribution is quite distinct from that of $CH_4$. $N_2$ absorption appears strongest on many crater floors, notably those of Burney, Safronov, Kowal, and Drake craters, consistent with topographic control (Fig. 1B and fig. S4). Little $N_2$ absorption is seen in Lowell Regio, possibly related to seasonal sublimation because high northern latitudes have been exposed to continuous sunlight since the late 1980s (*21*). However, substantial path lengths are required to produce observable $N_2$ absorption [e.g., (*20*, *22*)], so lack of absorption does not necessarily exclude its presence. A texture that produces short optical path lengths through the $N_2$ ice could also make it undetectable.

CO ice has absorption bands at 1.58 and 2.35 μm (*20*, *22*). Because the 2.35-μm CO band is entangled with adjacent strong $CH_4$ bands, we constructed a CO map using the more isolated 1.58-μm band. This band is very narrow and shallow, producing a noisy map; to help overcome the noise, it was spatially binned to 24 km × 24 km pixels. The most salient feature in the CO map (Fig. 1C) is greater absorption in SP, most prominently to the south of ~40°N latitude.

SP stands out as the one region of Pluto's encounter hemisphere where all three volatile ices coexist. This region has been interpreted as a cold trap where volatile ices have accumulated in a topographic low, possibly originating as an impact basin (*4*). The uncratered and therefore young surface of SP is apparently refreshed by glacial flow of volatile ices, possibly driven by convective overturning (*4*). The absorptions of Pluto's two most volatile ices, $N_2$ and CO, are especially prominent south and east of a line running roughly from Zheng-He Montes to the southern part of Cousteau Rupes. The greater absorption by $N_2$ and CO ices in the core of SP coincides with higher albedos and possibly elevations, perhaps indicating the area of most active or recent convective recycling.

### *Pluto's less volatile surface materials*

Water ice, heavier hydrocarbons, and other materials had long been sought on Pluto. Absorptions of $H_2O$ and $CO_2$ ices are readily apparent in the spectra of Neptune's largest moon Triton (*23*–*25*), considered an analog for Pluto. Pluto's stronger $CH_4$ absorptions frustrated the unambiguous detection of $H_2O$ from Earth-based observations [e.g., (*26*)]. $CO_2$ ice's narrow absorptions have never been reported in remote observations of Pluto, and New Horizons LEISA observations have produced no unambiguous detection of exposed $CO_2$ ice.

LORRI images of Pluto show mountain ranges bordering SP (*3*, *4*). These mountains, some as high as several kilometers, could not be constructed of the volatile ices $N_2$, $CH_4$, and CO and still endure for geological time scales (*27*, *28*). $H_2O$ ice is the most cosmochemically abundant durable material consistent with Pluto's origins and likely internal structure [e.g., (*29*)].

The broad nature of $H_2O$ ice absorption bands and the plethora of strong $CH_4$ bands make mapping Pluto's $H_2O$ with simple ratios or equivalent widths difficult. Instead, we computed the linear correlation coefficient with an $H_2O$ ice template spectrum (Fig. 2). The highest correlations are in the vicinity of Pulfrich crater in east TR, and also along Virgil Fossa. In MVIC enhanced color images, the water-rich region in Virgil Fossa appears distinctly reddish-orange in color (see below). High $H_2O$ spectral correlations are seen in several regions in Viking Terra and Baré Montes, with similarly reddish-orange coloration in the enhanced MVIC color images. In contrast, the $H_2O$-rich region around Pulfrich crater looks more neutral in the color images. Other montes including al-Idrisi, Hillary, and Zheng-He have lower correlation values, but when their spectra are compared with more $CH_4$-dominated spectra such as "a" and "e," they show clear evidence for water ice via enhanced absorption at 1.5 and 2.0 μm (Fig. 3 and fig. S5). Localized $H_2O$-rich regions in these areas tend to correspond to valleys between individual mountain peaks or topographic lows, as in the core of al-Idrisi Montes, rather than the summits of the mountains.

Cthulhu Regio shows some correlation with the water ice template spectrum, especially toward the west and along the northern and southern flanks of the regio, but Cthulhu's $H_2O$ absorptions at 1.5 and 2.0 μm are relatively shallow. An absorption around 2.3 μm is probably indicative of hydrocarbons heavier than $CH_4$. The occurrence of heavier hydrocarbons in Cthulhu Regio is consistent with ground-based observations suggesting that ethane ice absorptions are most prominent at those longitudes (*30*), although additional hydrocarbons are also likely to be contributing to the absorption in that wavelength region. A region toward the east of Cthulhu, near the equator, shows little evidence of $H_2O$ absorption and could represent the spot richest in tholins across Pluto's encounter hemisphere.

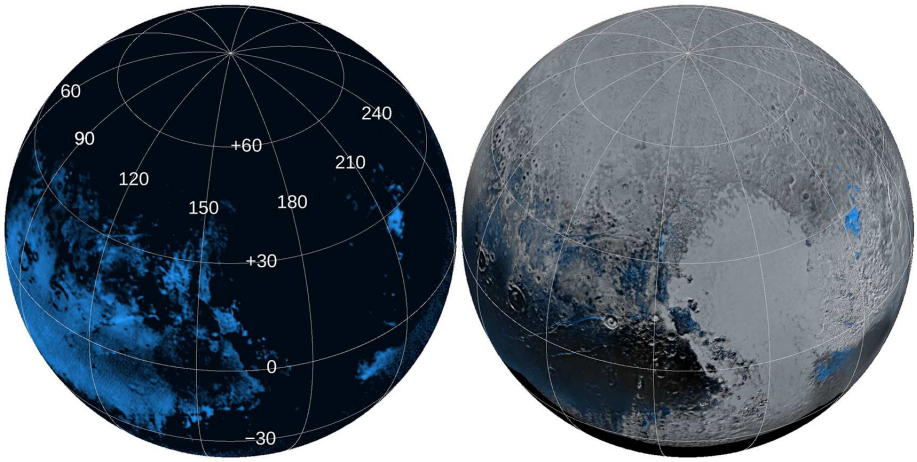



**Fig. 2. LEISA map of Pluto's nonvolatile $H_2O$ ice.** Left: Map showing the correlation coefficient between each LEISA spectrum and a template Charon-like $H_2O$ ice spectrum [e.g., (*47*, *49*)], highlighting where $H_2O$ absorption is least contaminated by other spectral features. Right: LEISA map superposed on the reprojected LORRI base map.

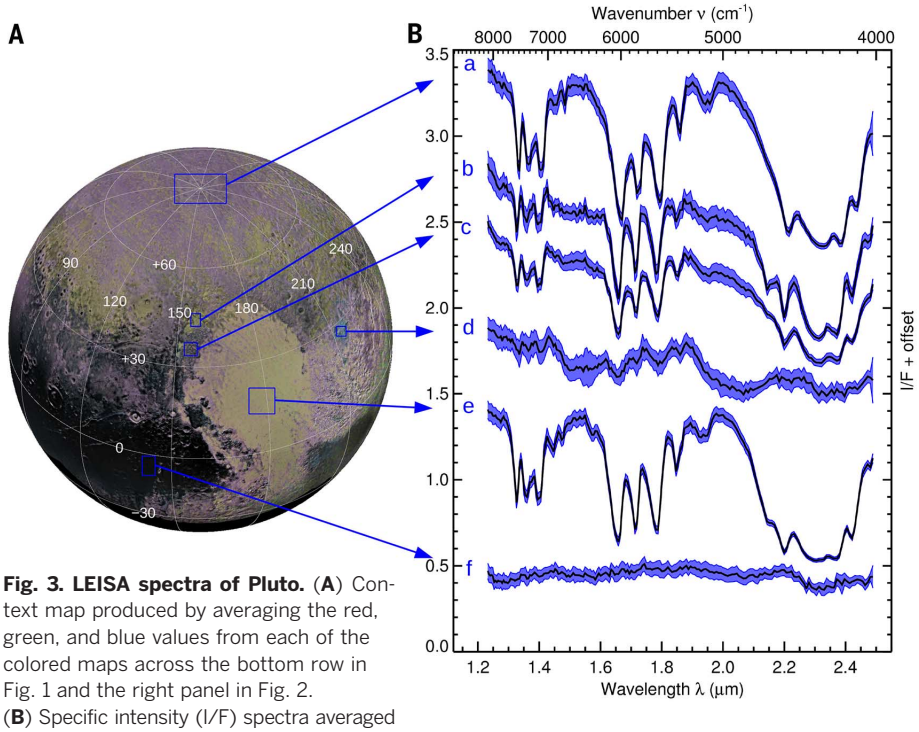



**Fig. 3. LEISA spectra of Pluto.** (**A**) Context map produced by averaging the red, green, and blue values from each of the colored maps across the bottom row in Fig. 1 and the right panel in Fig. 2. (**B**) Specific intensity (I/F) spectra averaged over regions in blue boxes, with envelopes indicating the standard deviations within the boxes. These regions were selected to highlight Pluto's spectral diversity. Vertical offsets for spectra "a" through "f" are +2.3, +1.7, +1.5, +1.2, +0.45, and 0, respectively. Pluto's north pole ("a") shows strong absorptions by $CH_4$ ice. Spectrum "b" is a region characterized by a strong $N_2$ ice absorption at 2.15 μm and weak $H_2O$ ice bands at 1.5 and 2 μm. Spectrum "c" is al-Idrisi Montes, very similar to "b" except without the $N_2$ absorption. The area around Pulfrich crater ("d") has $H_2O$ ice absorptions at 1.5, 1.65, and 2 μm and comparatively weak $CH_4$ ice absorptions. Spectrum "e" is the center of Sputnik Planum, with strong $CH_4$ bands, $N_2$ ice absorption at 2.15 μm, and CO ice absorption at 1.58 μm. Spectrum "f" is eastern Cthulhu Regio, with weak $H_2O$ ice absorptions at 1.5 and 2 μm and a feature attributed to heavier hydrocarbons at 2.3 μm.

### *Pluto colors*

MVIC obtained color images of Pluto on multiple epochs. We present an observation obtained on 14 July 2015, 11:11 UTC, about 40 min prior to closest approach, from a range of 35,000 km. The resulting spatial scale was 700 m per pixel, the best color spatial resolution returned to Earth thus far. Figure 4A shows an "extended" color view of this data set, in which MVIC's BLUE, RED, and NIR filter images are displayed in the blue, green, and red channels, respectively.

Color ratios remove illumination effects and highlight color variability, as shown in Fig. 4B. RED/BLUE and NIR/RED ratios both vary by more than a factor of 2 across Pluto's encounter hemisphere. Most of this variation is distributed along an axis from blue/neutral colors in the lower left to much redder colors in the upper right, but various clumps and deviations from this axis are indicative of additional subtleties.

Pluto's color diversity is further explored via principal components analysis (PCA), projecting brightnesses in the four MVIC filters into an orthogonal basis set where each dimension successively accounts for the maximum amount of remaining variance. The first principal component (PC1) corresponds to overall brightness across the scene. PC1 accounts for 98.8% of the variance of the MVIC color data, mostly due to illumination geometry and to Pluto's extreme albedo variations (see below). Principal components 2, 3, and 4 account for 1%, 0.12%, and 0.05% of the total variance in the full MVIC data set, respectively. The coherent spatial patterns seen in all three are indicative of distinctly colored provinces across Pluto's surface. Shown in Fig. 4, C to F, are the four principal component images along with the eigenvectors; Fig. 4G combines the principal component images, showing many distinct color units.

We used the narrow MVIC CH4 filter in conjunction with RED and NIR filters to compute a $CH_4$ equivalent-width map (Fig. 5) and a color slope map (fig. S3; details in supplementary text). A key distinction between this and the LEISA $CH_4$ map in Fig. 1 is that they probe two different $CH_4$ ice bands. The 0.89-μm band targeted by the MVIC CH4 filter has a peak absorption coefficient roughly an order of magnitude below that of the 1.3- to 1.4-μm band complex being mapped in Fig. 1 (*31*). Consequently, Fig. 5 is mapping greater path lengths in $CH_4$ ice, and thus areas that are especially rich in $CH_4$ ice and/or have especially large particle sizes. The distribution is broadly similar to the LEISA $CH_4$ map, but there are differences. Regions standing out for their strong 0.89-μm band absorption include the bladed terrain of Tartarus Dorsa and low-latitude bands flanking Cthulhu Regio. The much higher spatial resolution of the MVIC observation makes it

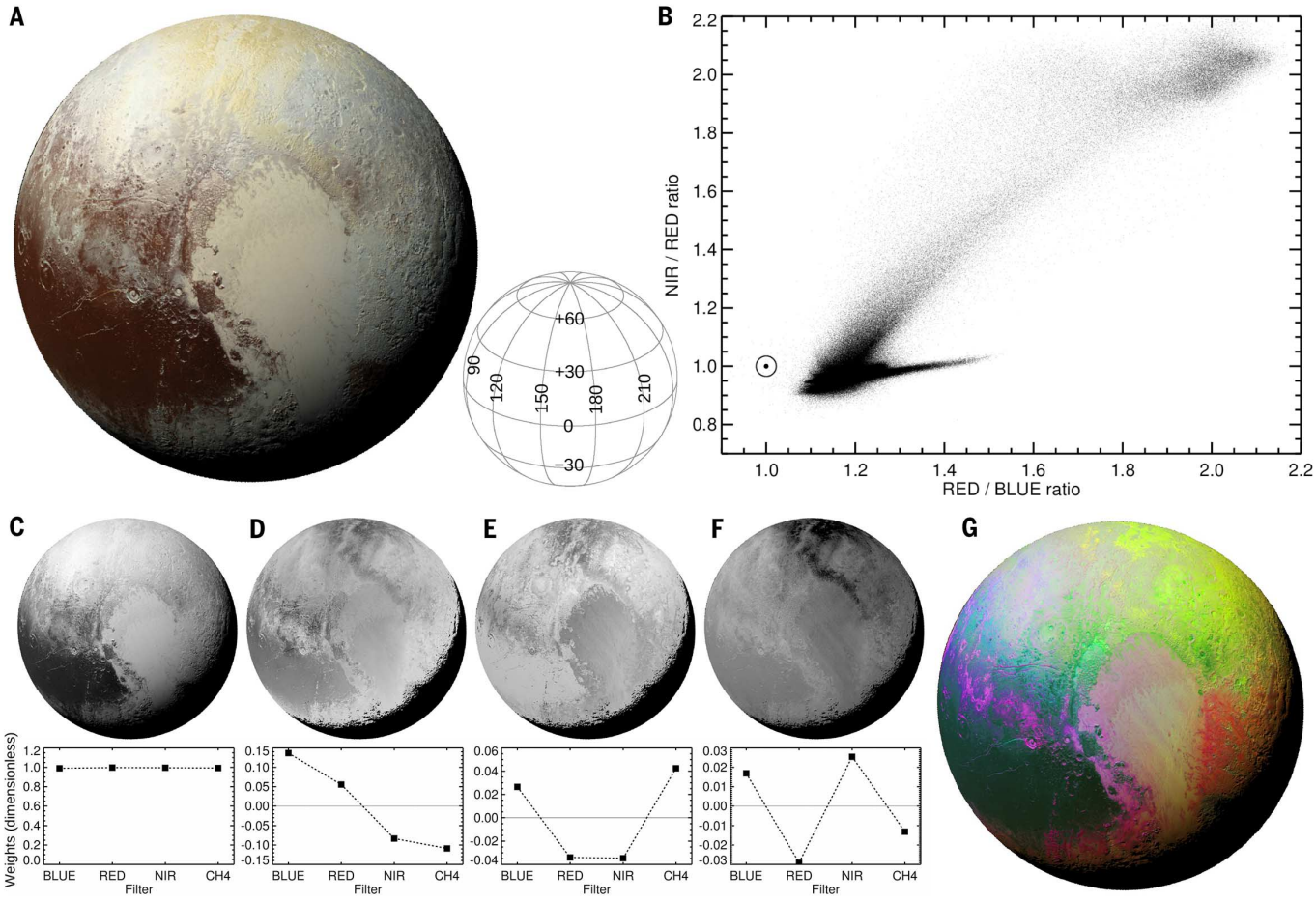



**Fig. 4. MVIC colors of Pluto.** (**A**) "Enhanced" color with MVIC's BLUE, RED, and NIR filter images displayed in blue, green, and red color channels, respectively. Geometry is indicated by the wire grid. (**B**) Distribution of NIR/RED and RED/BLUE color ratios, excluding regions where the incidence angle from the Sun or the emission angle to the spacecraft exceeds 70° from the zenith. The Sun symbol indicates neutral colors; redder colors extend up and to the right. (**C** to **F**) Principal component images and eigenvectors for PC1 to PC4, respectively. (**G**) False-color view with shading from PC1 and the hue set by PC2, PC3, and PC4 displayed in red, green, and blue channels, respectively.

possible to see subtle variations in $CH_4$ absorption within SP. The north, west, and southwest margins of SP show stronger $CH_4$ absorption. In the core of SP, where absorptions of the more volatile ices $N_2$ and CO are more prominent, the boundaries between the polygonal convection cells [described in (*1*, *4*)] show less $CH_4$ absorption.

When Pluto's known atmospheric gases ($N_2$, $CH_4$, and CO) are exposed to energetic photons or charged particles, chemical reactions produce more complex radicals and molecules that are generally nonvolatile at Pluto's surface temperatures (*32*–*34*). Similar photolytic and radiolytic processing occurs in these same molecules condensed as ices (*35*, *36*). Pluto's present-day atmosphere is opaque to Lyman-alpha (Ly-α) solar ultraviolet light (*21*), so photochemical products are mostly produced in the atmosphere, condense as haze particles, and eventually settle to the surface. Because in the present epoch Ly-α does not reach the surface, ices on the surface are currently primarily affected by interstellar pickup ions, galactic rays, and their spallation products from their interactions with the atmosphere. Cosmic rays can induce chemical changes at depths exceeding 1 m into the surface (*37*, *38*).

Laboratory simulations of radiolysis of a Pluto ice mixture at $T \approx 15$ K (*39*) yield refractory residues with colors resembling some of the colors on Pluto. Chemical analysis of this material shows atomic ratios N/C ≈ 0.9 and O/C ≈ 0.2, indicating that the 1.2-keV electrons used in the experiments dissociate the $N_2$ molecule, allowing the N atoms to react with other atoms and molecular fragments. The residue contains urea, alcohols, carboxylic acids, ketones, aldehydes, amines, and nitriles. A substantial aromatic component is found in two-step laser desorption mass spectroscopy, with mass peaks throughout the range ~50 to 250 daltons.

During any putative epoch when Pluto's atmosphere collapses, it would not shield the surface from ultraviolet photons and solar wind particles as it does now. These would then reach the surface and directly contribute to its chemical evolution. The production of the colored ice residue in the laboratory with low-energy electrons occurs in a matter of hours with an electron fluence of ~$10^{17}$/mm$^2$. Charged particles and scattered Ly-α can arrive from all directions, so in the absence of an atmosphere, coloration could arise as quickly as a few years, even on unilluminated surface regions, much faster than the ~40,000-year time scale for tholin haze deposition from Pluto's atmosphere (*5*).

### *Pluto albedos*

Four major global albedo units are evident in New Horizons Pluto images: low-albedo equatorial regions exemplified by Cthulhu Regio and Krun Macula, the northern summer polar region Lowell Regio, a sliver of southern winter hemisphere, and the high-albedo TR. TR's albedo is similar to that of Triton (*40*). Pluto's dark equatorial regions have albedos similar to some outer solar system moons that are rich in carbonaceous or organic material, such as the saturnian moons Hyperion and Phoebe and the uranian moon Umbriel, although they are not as dark as the low-albedo hemisphere of Iapetus (*41*).

In planetary surface images, intensity differences are mostly due to illumination and observing geometry. A photometric function is needed to obtain quantitative measurements of normal albedo (brightness for incident, emission, and

solar phase angles all equal to 0°). Figure 6A is a global map of normal albedo from LORRI images, using a photometric function in which 30% of the reflected photons obey Lambertian scattering while the rest follow a single-scattering lunar function (see supplementary text). This function is similar to those found for the icy moons of Saturn (*41*). We also accounted for the 0.04 magnitude opposition surge shown in Fig. 6C for phase angles below 0.10° (*42*, *43*).

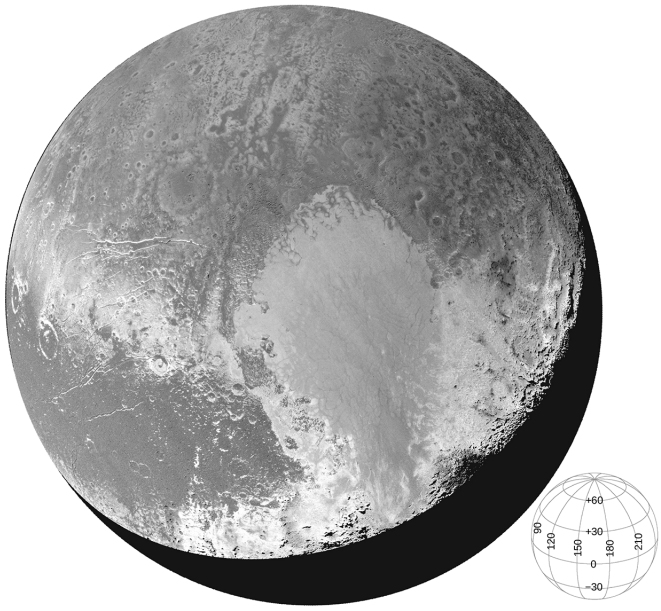



**Fig. 5. Pluto MVIC $CH_4$ absorption map.** The equivalent width of absorption in the MVIC CH4 filter is computed by comparison with the NIR and RED filter images (see supplementary text for details). This filter is centered on a weaker $CH_4$ ice absorption than the one mapped with LEISA data in Fig. 1. Brighter shades correspond to stronger $CH_4$ ice absorption. Differences between the maps are discussed in the text. Except for a sliver of poorly illuminated terrain along the terminator, where geometric effects become extreme, most of the contrast in this map corresponds to regional variations in $CH_4$ ice absorption.

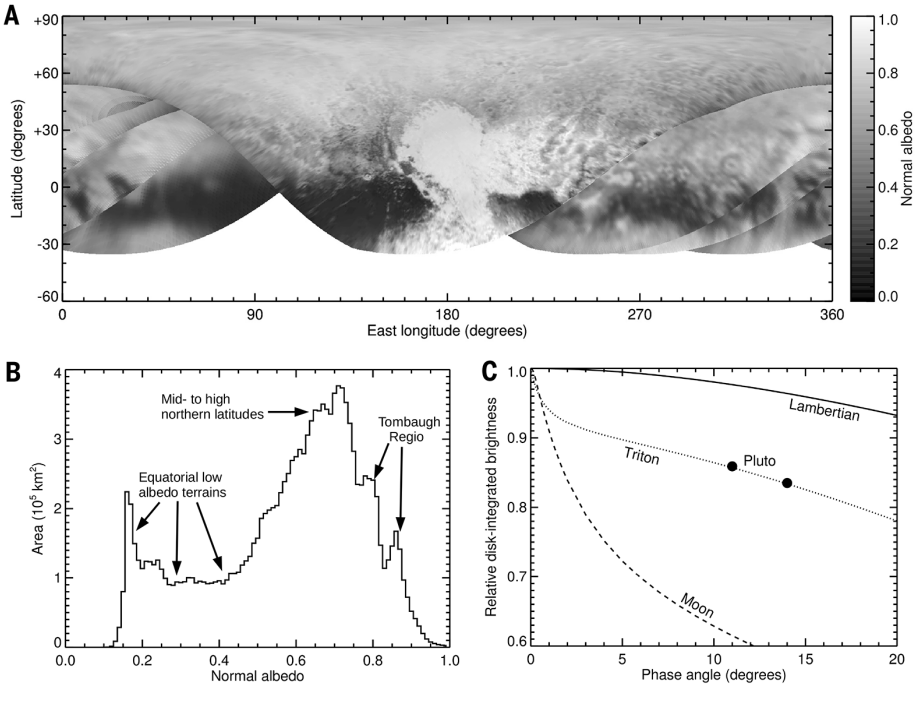



**Fig. 6. LORRI albedos on Pluto.** (**A**) Normal albedo across Pluto from LORRI panchromatic images sensitive to wavelengths from 350 to 850 nm (*10*). (**B**) Histogram of albedo values. (**C**) Decline of Pluto's disk-integrated brightness with phase angle, compared with the same data for a Lambertian sphere, the icy satellite Triton, and Earth's Moon. The Triton curve is based on Voyager green filter and ground-based observations with an effective wavelength of 550 nm (*40*). The lunar curve is for a Johnson V filter wavelength of 550 nm. The Pluto data points show LORRI brightness after correcting for light-curve variability, relative to zero-phase data from ground-based monitoring (*43*) (Bessel R filter, 630 nm).

This albedo map illustrates the quantitative differences in albedo for regions characterized by the distinct combinations of volatile ices and colors seen in the preceding figures. Albedo and composition can interact in complex ways: High-albedo regions that absorb less sunlight tend to become sites of volatile ice deposition, whereas low-albedo regions can absorb much more sunlight, driving sublimation of volatiles and reaching higher temperatures. Deposition of volatile ices can raise the albedos of regions if they are configured into textures that scatter light, and the texture of mixed volatile ices can change as a result of annealing, sintering, or temperature changes that lead to phase transitions or fracturing.

## Charon

### *Charon colors*

Figure 7A shows the highest–spatial resolution MVIC color observation of Charon from New Horizons, with a spatial scale of 1.5 km per pixel. The spacecraft recorded this scan on 14 July 2015, 10:42 UTC, about 70 min before closest approach, from a range of 74,000 km. As previously known from Earth-based observations, Charon's surface color is generally neutral (*44*, *45*). New Horizons data reveal a large-scale exception with Mordor Macula, the northern polar region, being distinctly red. The red coloration begins to appear northward of about 45°, as measured by NIR/BLUE and NIR/RED color ratios (Fig. 7B). In addition to this large-scale feature, there are a variety of local color variations. Craters and other features complicate or interrupt the trend toward redder coloration at high latitudes, such as Dorothy Gale crater, which is less red than the local latitude trend, and Vader crater, which is more red. Lower-latitude color variations include the ejecta of Nasreddin crater being bluer than surrounding terrain, and Gallifrey Macula redder. North and south of the tectonic belt extending across Charon's encounter hemisphere, colors are similar, but the smoother plains of Vulcan Planum show less color diversity.

Charon MVIC color ratios (Fig. 7C) show a simpler distribution of colors than seen on Pluto. The bulk of the surface is spectrally neutral, with a mixing trend toward the redder colors at high latitudes. Principal components analysis of the four colors corroborates this simple color distribution. As before, PC1 (Fig. 7D) maps brightness across the scene, controlled by albedo and illumination geometry, accounting for 97.3% of the observed variance. PC2 corresponds to the reddish polar coloration (Fig. 7E), albeit inverted so the pole looks dark. It accounts for 2.7% of the observed variance, greater than for Pluto's PC2. Charon's PC3 and PC4 show little coherent structure (Fig. 7, F and G), apparently responding primarily to noise. They account for only 0.03% and 0.02%, respectively, of the variance—much less than their counterparts on Pluto.

### *Charon spectral characteristics*

New Horizons observed Charon with LEISA from a range of 82,000 km on 14 July 2015, 10:30 UTC, at a spatial scale of 5 km per pixel. The data

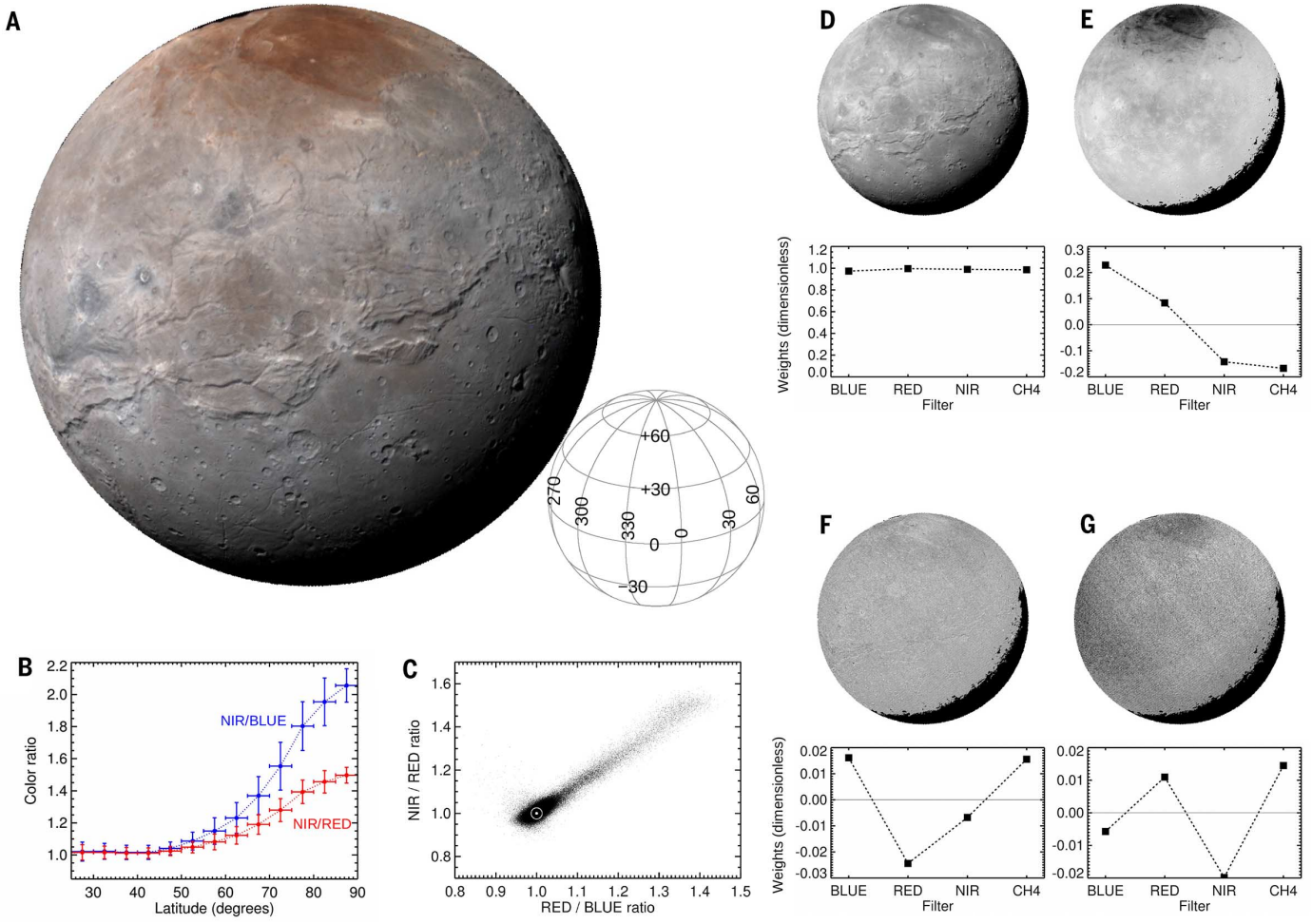



**Fig. 7. MVIC colors of Charon.** (**A**) Enhanced color, with MVIC's BLUE, RED, and NIR filter images displayed in blue, green, and red color channels, respectively. Geometry is indicated by the associated wire grid. (**B**) MVIC NIR/BLUE and NIR/RED color ratio means and standard deviations averaged over 5° latitude annuli, excluding points near the limb with emission angles greater than 75°. (**C**) Scatterplot of NIR/RED and RED/BLUE color ratios, excluding incidence and emission angles greater than 70°. Most pixels cluster near solar colors, with a mixing line extending toward redder colors at upper right. (**D** to **G**) Principal component images and eigenvectors for principal components 1, 2, 3, and 4, respectively.

confirm that Charon's encounter hemisphere is composed predominantly of water ice, as first identified in the mid-1980s (*46*). Earth-based observations had also shown that Charon's water ice was at least partially in the crystalline phase, as indicated by the 1.65-μm band, and that the water absorption was seen at all longitudes as Charon rotated (*47*–*49*). LEISA observations confirm that water ice is everywhere on Charon's encounter hemisphere, with the 1.5-, 1.65-, and 2-μm bands being evident in all of the example spectra in Fig. 8.

Spectral observations also revealed an absorption band around 2.22 μm, attributed to ammonia hydrates (*47*–*49*). Subsequent studies (*50*, *51*) showed that the band varies with sub-observer longitude as Charon rotates. LEISA observations now show that the ammonia absorption is distributed across Charon's encounter hemisphere at a low level, with local concentrations associated with a few of Charon's bright rayed craters. Organa crater in the northern hemisphere is the best example. The crater is about 5 km across and is thus not resolved by the LEISA pixels. The $NH_3$ signature appears to be associated with the crater plus some, but not all, of the ejecta blanket (see Fig. 8C and fig. S6). According to laboratory studies, ammonia ice is destroyed by ultraviolet photons and cosmic rays (*52*, *53*). From fluxes in Charon's environment (*38*), the time scale for radiolytic destruction of Charon's $NH_3$ was estimated to be on the order of $10^7$ years (*50*), implying that these deposits are relatively recent.

LEISA spectra of Mordor Macula do not reveal distinguishing spectral features coinciding with the red coloration, apart from subtle differences in continuum slope toward the shorter-wavelength end of LEISA's spectral range. The reddish colorant may be too thin to produce stronger features at NIR wavelengths, or may simply lack distinct absorption bands at LEISA wavelengths.

## Discussion

Various patterns emerge from the observations. Latitude-dependent distributions of materials were expected from seasonal volatile transport processes (*54*), and indeed, the LEISA and MVIC data confirm a number of distinct latitude zones, especially in the western half of the encounter hemisphere. Pluto's equatorial latitudes feature regions that are strikingly dark and red at visible wavelengths, typified on the encounter hemisphere by Cthulhu Regio and Krun Macula. These provinces are much less dark at IR wavelengths, and in many areas they show weak 1.5- and 2-μm features of $H_2O$ ice, along with absorptions by hydrocarbons around 2.3 μm (Fig. 3). A possible scenario is that these regions are ancient, heavily cratered landscapes where tholins and other inert materials have accumulated over geological time scales.

Flanking the dark equatorial belt to both the north and south are higher-albedo regions rich in $CH_4$ ice (Figs. 1A and 5). As the least volatile of Pluto's volatile ices, it should be the first to condense and the last to sublimate away, consistent with its proximity to the volatile-depleted maculae. The $CH_4$ is most prominent in topographically high regions such as ridges and crater rims, and $CH_4$ can even be found in a few isolated high-altitude regions within the maculae. The bladed

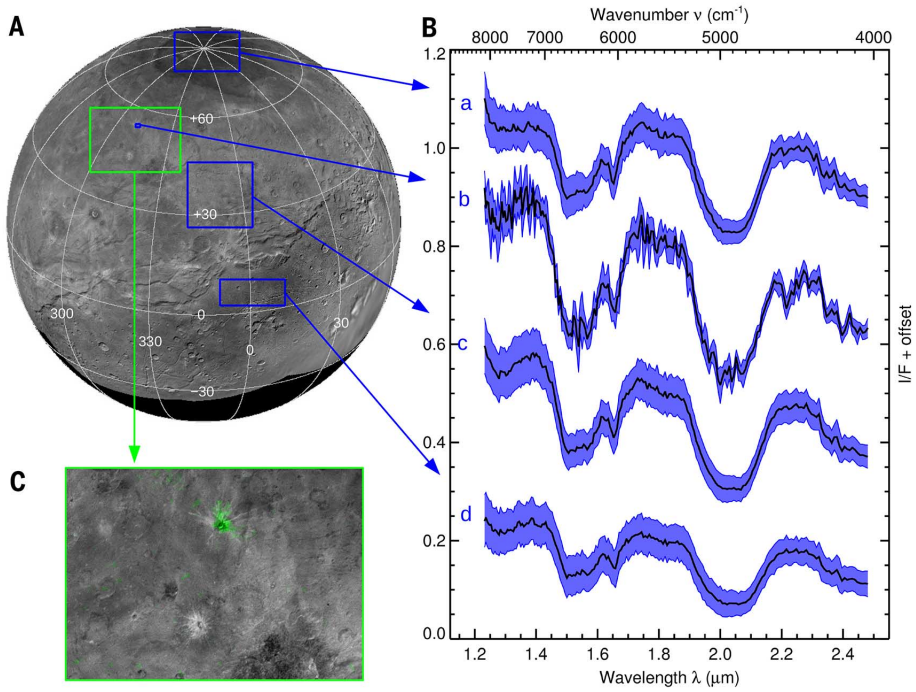



**Fig. 8. LEISA spectra of Charon.** (**A**) LORRI composite base map. Regions where I/F spectra were averaged for plotting in (B) are indicated by blue boxes. (**B**) Vertical offsets for spectra "a" through "d" are +0.7, +0.4, +0.2, and 0, respectively. All four spectra show the characteristic absorption bands of cold, crystalline $H_2O$ ice at 1.5, 1.65, and 2 μm. Charon's north pole ("a") shows a little more continuum absorption toward short wavelengths, but no other obvious differences, relative to spectra from lower latitudes on Charon. Spectrum "b" is a region around Organa crater showing $NH_3$ absorption at 2.22 μm. (**C**) Close-up of the region indicated by the green box in (A), with 2.22-μm absorption mapped in green to show the spatial distribution of $NH_3$-rich material (fig. S6 shows the full map). Spectra "c" and "d" compare plains units above and below the tectonic belt.

terrain of Tartarus Dorsa is especially $CH_4$-rich (Figs. 1A and 5), and this could be the result of many seasonal cycles of $CH_4$ accumulation on elevated low-latitude regions. At northern latitudes above ~35°N, more volatile $N_2$ ice begins to appear, favoring topographic lows where the surface pressure is higher (Fig. 1B). Still farther north, $N_2$ and CO absorptions are weak in Lowell Regio (Fig. 1, B and C), whereas $CH_4$ absorption continues right up to the pole (Figs. 1A and 5). This high-albedo region has been described as a "polar cap," although the lack of prominent $N_2$ and CO ice absorptions makes that term seem poorly suited to describing a summer pole comparatively depleted in Pluto's more volatile ices.

This latitude-dependent distribution of Pluto's surface materials is interrupted in TR. The western half of TR is SP, a deep basin hosting a unique, youthful surface morphology described in detail in (*4*). The spectral signatures of $N_2$, $CH_4$, and CO ices are all present in this region, with the absorptions of the more volatile $N_2$ and CO ices being especially prominent in the southeastern part of SP, below the southern limit for latitudes experiencing the "midnight sun" during the current epoch (*21*). But this pattern does not seem to be purely governed by climatic factors, because the boundary curves from around Zheng-He Montes in the southwest to Columbia Colles in the northeast. Another potential explanation could involve bulk glacial flow of ices to the northwest, with ablation of the more volatile $N_2$ and CO from the surface of the flow. Alternatively, the locus of most active convection could migrate around within SP, with less active regions showing less absorption by the volatile ices. It is also possible to interpret the reduced volatile ice absorption toward SP's northwest flank as being due to evolution of the surface texture alone, with no change in bulk composition. A reduction in particle size or an increase in scattering could account for the reduced absorption toward that flank. Eastern TR also does not fit easily into the latitude-dependent picture described above. There appears to be a connection between the two halves, with glacial flow from east TR down into SP (*4*), and also some shared color features with wisps of $CH_4$-rich material with colors similar to east TR extending westward into SP (see Fig. 4G). $CH_4$ ice has a low density and could perhaps be transported as a crust on glacially flowing $N_2$ and CO ice.

Water ice presents a number of puzzles on Pluto. Its IR spectral signature is associated with two very distinct shorter-wavelength color units. $H_2O$-rich outcrops in Virgil Fossa and Viking Terra (Fig. 2) show a distinct, reddish color in Fig. 4A, unlike the more neutral coloration of the $H_2O$-rich outcrops around Pulfrich crater. Rugged mountains such as Zheng-He and Norgay Montes, which had been expected to be composed of $H_2O$ ice, show comparatively weak $H_2O$ spectral signatures.

Charon presents its own mysteries. The reddish polar region of Mordor Macula is a unique and striking feature not seen on other icy satellites in the outer solar system. The latitudinal dependence of its distribution suggests a mechanism involving seasonal cold trapping of volatiles such as $CH_4$ that would not otherwise be stable at Charon's surface. During Charon's long winter, polar latitudes remain unilluminated for multiple Earth decades, during which time they can cool to temperatures below 20 K [e.g., (*55*)]. Potential sources of $CH_4$ briefly resident in Charon's surface environment could be outgassing from Charon's interior and Pluto's escaping atmosphere, as discussed in (*5*, *55*). Seasonally cold-trapped $CH_4$ would be rapidly photolyzed by solar Ly-α radiation, roughly half of which arrives at Charon's surface indirectly via scattering by interplanetary hydrogen. Resulting radicals would combine into heavier products that are sufficiently nonvolatile to remain after Charon's pole emerges back into the sunlight and warms to summer temperatures in the 50 to 60 K range. Further photolysis and radiolysis would lead to production of reddish tholins, as discussed above. This hypothesis predicts that Charon's southern hemisphere should exhibit a similar high-latitude reddish patch.

Charon's isolated ammonia-rich areas are also intriguing. $NH_3$ is a potentially important geochemical material in icy satellites that has heretofore mostly eluded detection via remote sensing techniques. A possible scenario for its appearance in just a few of Charon's craters is that these impacts dredged up the $NH_3$ from below Charon's surface too recently for it to have been destroyed by space weathering processes. It is also possible that $NH_3$-rich material is delivered by a subset of impactors, or that Charon's subsurface is heterogeneous, with local subsurface concentrations of $NH_3$ emplaced during an earlier era of cryovolcanic activity being subsequently exhumed by impacts.

## Conclusions

We have presented spatially resolved visible and near-infrared observations of the encounter hemispheres of Pluto and Charon, obtained by the New Horizons spacecraft on 14 July 2015. Data returned so far reveal complex spatial distributions of Pluto's $CH_4$, $N_2$, and CO ices as well as the local emergence of water-ice bedrock and broad expanses of accumulated tholins at low latitudes. The data point to atmospheric and geological processes having acted over a range of time scales to create the currently observed surface. On Charon, the presence and distribution of localized ammonia-ice outcrops and of reddish circumpolar material raise questions about the exogenous and endogenous processes acting on this large satellite.

Many of the data collected by New Horizons have yet to be transmitted back to Earth. They will enable us to quantitatively map the composition, state, and texture distributions of the system's inventory of materials in order to disentangle the

history of these icy bodies and understand their place in the broader context of the outer solar system.

## REFERENCES AND NOTES


1. H. A. Weaver, W. C. Gibson, M. B. Tapley, L. A. Young, S. A. Stern, Overview of the New Horizons science payload. *Space Sci. Rev.* **140**, 75–91 (2008). doi: 10.1007/s11214-008-9376-6
2. L. A. Young *et al*., New Horizons: Anticipated scientific investigations at the Pluto system. *Space Sci. Rev.* **140**, 93–127 (2008). doi: 10.1007/s11214-008-9462-9
3. S. A. Stern *et al*., The Pluto system: Initial results from its exploration by New Horizons. *Science* **350**, aad1815 (2015). doi: 10.1126/science.aad1815; pmid: 26472913
4. J. M. Moore *et al*., The geology of Pluto and Charon through the eyes of New Horizons. *Science* **351**, 1284–1293 (2016).
5. G. R. Gladstone *et al*., The atmosphere of Pluto as observed by New Horizons. *Science* **351**, aad8866 (2016). doi: 10.1126/science.aad8866
6. F. Bagenal *et al*., Pluto's interaction: Solar wind, energetic particles, dust. *Science* **351**, aad9045 (2016). doi: 10.1126/science.aad9045
7. H. A. Weaver *et al*., The small satellites of Pluto as observed by New Horizons. *Science* **351**, aae0030 (2016). doi: 10.1126/science.aae0030
8. D. C. Reuter *et al*., Ralph: A visible/infrared imager for the New Horizons Pluto/Kuiper belt mission. *Space Sci. Rev.* **140**, 129–154 (2008). doi: 10.1007/s11214-008-9375-7
9. K. P. Rosenberg, K. D. Hendrix, D. E. Jennings, D. C. Reuter, M. D. Jhabvala, A. T. La, Logarithmically variable infrared etalon filters. *Proc. SPIE 2262* (1994). doi: 10.1117/12.185804
10. A. F. Cheng *et al*., Long-Range Reconnaissance Imager on New Horizons. *Space Sci. Rev.* **140**, 189–215 (2008). doi: 10.1007/s11214-007-9271-6
11. A. Tokunaga, W. D. Vacca, The Mauna Kea Observatories near-infrared filter set. III. Isophotal wavelengths and absolute calibration. *Publ. Astron. Soc. Pac.* **117**, 421–426 (2005). doi: 10.1086/429382
12. All ranges reported in this paper are relative to target center.
13. N. Fray, B. Schmitt, Sublimation of ices of astrophysical interest: A bibliographic review. *Planet. Space Sci.* **57**, 2053–2080 (2009). doi: 10.1016/j.pss.2009.09.011
14. E. Lellouch, J. Stansberry, J. Emery, W. Grundy, D. P. Cruikshank, Thermal properties of Pluto's and Charon's surfaces from Spitzer observations. *Icarus* **214**, 701–716 (2011). doi: 10.1016/j.icarus.2011.05.035
15. S. A. Stern, L. M. Trafton, On the atmospheres of objects in the Kuiper belt. In *The Solar System Beyond Neptune*, A. Barucci, H. Boehnhardt, D. Cruikshank, A. Morbidelli, Eds. (Univ. of Arizona Press, Tucson, 2009), pp. 365–380.
16. E. Quirico, B. Schmitt, Near-infrared spectroscopy of simple hydrocarbons and carbon oxides diluted in solid $N_2$ and as pure ices: Implications for Triton and Pluto. *Icarus* **127**, 354–378 (1997). doi: 10.1006/icar.1996.5663
17. S. Douté *et al*., Evidence for methane segregation at the surface of Pluto. *Icarus* **142**, 421–444 (1999). doi: 10.1006/icar.1999.6226
18. L. A. Trafton, On the state of methane and nitrogen ice on Pluto and Triton: Implications of the binary phase diagram. *Icarus* **246**, 197–205 (2015). doi: 10.1016/j.icarus.2014.05.022
19. All place names used in this paper are informal designations at this time. Maps showing them are available as figs. S1 and S2.
20. T. C. Owen *et al*., Surface ices and the atmospheric composition of pluto. *Science* **261**, 745–748 (1993). doi: 10.1126/science.261.5122.745; pmid: 17757212
21. A. M. Earle, R. P. Binzel, Pluto's insolation history: Latitudinal variations and effects on atmospheric pressure. *Icarus* **250**, 405–412 (2015). doi: 10.1016/j.icarus.2014.12.028
22. W. M. Grundy, C. B. Olkin, L. A. Young, M. W. Buie, E. F. Young, Near-infrared spectral monitoring of Pluto's ices: Spatial distribution and secular evolution. *Icarus* **223**, 710–721 (2013). doi: 10.1016/j.icarus.2013.01.019
23. D. P. Cruikshank *et al*., Ices on the surface of Triton. *Science* **261**, 742–745 (1993). doi: 10.1126/science.261.5122.742; pmid: 17757211
24. D. P. Cruikshank *et al*., Water ice on Triton. *Icarus* **147**, 309–316 (2000). doi: 10.1006/icar.2000.6451
25. W. M. Grundy *et al*., Near-infrared spectral monitoring of Triton with IRTF/SpeX II: Spatial distribution and evolution of ices. *Icarus* **205**, 594–604 (2010). doi: 10.1016/j.icarus.2009.08.005
26. W. M. Grundy, M. W. Buie, Spatial and compositional constraints on non-ice components and $H_2O$ on Pluto's surface. *Icarus* **157**, 128–138 (2002). doi: 10.1006/icar.2002.6833
27. Y. Yamashita, M. Kato, M. Arakawa, Experimental study on the rheological properties of polycrystalline solid nitrogen and methane: Implications for tectonic processes on Triton. *Icarus* **207**, 972–977 (2010). doi: 10.1016/j.icarus.2009.11.032
28. S. A. Stern, S. B. Porter, A. M. Zangari, On the roles of escape erosion and the viscous relaxation of craters on Pluto. *Icarus* **250**, 287–293 (2015). doi: 10.1016/j.icarus.2014.12.006
29. W. B. McKinnon, D. Prialnik, S. A. Stern, A. Coradini, Structure and evolution of Kuiper belt objects and dwarf planets. In *The Solar System Beyond Neptune*, A. Barucci, H. Boehnhardt, D. Cruikshank, A. Morbidelli, Eds. (Univ. of Arizona Press, Tucson, 2009), pp. 213–241.
30. B. J. Holler, L. A. Young, W. M. Grundy, C. B. Olkin, J. C. Cook, Evidence for longitudinal variability of ethane ice on the surface of Pluto. *Icarus* **243**, 104–110 (2014). doi: 10.1016/j.icarus.2014.09.013
31. W. M. Grundy, B. Schmitt, E. Quirico, The temperature-dependent spectrum of methane ice I between 0.7 and 5 μm and opportunities for near-infrared remote thermometry. *Icarus* **155**, 486–496 (2002). doi: 10.1006/icar.2001.6726
32. Y.-J. Wu, H.-F. Chen, S.-J. Chuang, T.-P. Huang, Ultraviolet and infrared spectra of electron-bombarded solid nitrogen and methane diluted in solid nitrogen. *Astrophys. J.* **768**, 83 (2013). doi: 10.1088/0004-637X/768/1/83
33. Y.-J. Wu *et al*., Spectra and photolysis of pure nitrogen and methane dispersed in solid nitrogen with vacuum-ultraviolet light. *Astrophys. J.* **746**, 175 (2012). doi: 10.1088/0004-637X/746/2/175
34. Y. S. Kim, R. I. Kaiser, Electron irradiation of Kuiper belt surface ices: Ternary $N_2$-$CH_4$-CO mixtures as a case study. *Astrophys. J.* **758**, 37 (2012). doi: 10.1088/0004-637X/758/1/37
35. M. H. Moore, R. L. Hudson, Infrared study of ion-irradiated $N_2$-dominated ices relevant to Triton and Pluto: Formation of HCN and HNC. *Icarus* **161**, 486–500 (2003). doi: 10.1016/S0019-1035(02)00037-4
36. C. K. Materese *et al*., Ice chemistry on outer solar system bodies: Carboxylic acids, nitriles, and urea detected in refractory residues produced from the UV photolysis of $N_2$:$CH_4$:CO-containing ices. *Astrophys. J.* **788**, 111 (2014). doi: 10.1088/0004-637X/788/2/111
37. R. E. Johnson, Effect of irradiation on the surface of Pluto. *Geophys. Res. Lett.* **16**, 1233–1236 (1989). doi: 10.1029/GL016i011p01233
38. J. F. Cooper, E. R. Christian, J. D. Richardson, C. Wang, Proton irradiation of centaur, Kuiper belt, and Oort cloud objects at plasma to cosmic ray energy. *Earth Moon Planets* **92**, 261–277 (2003). doi: 10.1023/B:MOON.0000031944.41883.80
39. C. K. Materese, D. P. Cruikshank, S. A. Sandford, H. Imanaka, M. Nuevo, Ice chemistry on outer solar system bodies: Electron radiolysis of $N_2$-, $CH_4$-, and CO-containing ices. *Astrophys. J.* **812**, 150 (2015). doi: 10.1088/0004-637X/812/2/150
40. B. J. Buratti *et al*., Photometry of Triton 1992–2004: Surface volatile transport and discovery of a remarkable opposition surge. *Icarus* **212**, 835–846 (2011). doi: 10.1016/j.icarus.2011.01.012
41. B. J. Buratti, Voyager disk resolved photometry of the Saturnian satellites. *Icarus* **59**, 392–405 (1984). doi: 10.1016/0019-1035(84)90109-X
42. M. W. Buie, W. M. Grundy, E. F. Young, L. A. Young, S. A. Stern, Pluto and Charon with the Hubble Space Telescope II. Resolving changes on Pluto's surface and a map for Charon. *Astron. J.* **139**, 1128–1143 (2010). doi: 10.1088/0004-6256/139/3/1128
43. B.J. Buratti *et al*., Photometry of Pluto 2008-2014: Evidence of ongoing seasonal volatile transport and activity. *Astrophys. J.* **804**, L6 (2015). doi: 10.1088/2041-8205/804/1/L6
44. R. P. Binzel, Hemispherical color differences on Pluto and Charon. *Science* **241**, 1070–1072 (1988). doi: 10.1126/science.241.4869.1070; pmid: 17747488
45. U. Fink, M. A. DiSanti, The separate spectra of Pluto and its satellite Charon. *Astron. J.* **95**, 229–236 (1988). doi: 10.1086/114632
46. M. W. Buie, D. P. Cruikshank, L. A. Lebofsky, E. F. Tedesco, Water frost on Charon. *Nature* **329**, 522–523 (1987). doi: 10.1038/329522a0
47. M. E. Brown, W. M. Calvin, Evidence for crystalline water and ammonia ices on Pluto's satellite charon. *Science* **287**, 107–109 (2000). doi: 10.1126/science.287.5450.107; pmid: 10615040
48. M. W. Buie, W. M. Grundy, The distribution and physical state of $H_2O$ on Charon. *Icarus* **148**, 324–339 (2000). doi: 10.1006/icar.2000.6509
49. C. Dumas, R. J. Terrile, R. H. Brown, G. Schneider, B. A. Smith, Hubble Space Telescope NICMOS spectroscopy of Charon's leading and trailing hemispheres. *Astron. J.* **121**, 1163–1170 (2001). doi: 10.1086/318747
50. J. C. Cook, S. J. Desch, T. L. Roush, C. A. Trujillo, T. R. Geballe, Near-infrared spectroscopy of Charon: Possible evidence for cryovolcanism on Kuiper belt objects. *Astrophys. J.* **663**, 1406–1419 (2007). doi: 10.1086/518222
51. F. E. DeMeo *et al*., Spectral variability of Charon's 2.21-μm feature. *Icarus* **246**, 213–219 (2015). doi: 10.1016/j.icarus.2014.04.010
52. G. Strazzulla, M. E. Palumbo, Evolution of icy surfaces: An experimental approach. *Planet. Space Sci.* **46**, 1339–1348 (1998). doi: 10.1016/S0032-0633(97)00210-9
53. S. Pilling *et al*., Radiolysis of ammonia-containing ices by energetic, heavy, and highly charged ions inside dense astrophysical environments. *Astron. Astrophys.* **509**, A87 (2010). doi: 10.1051/0004-6361/200912274
54. C. J. Hansen, D. A. Paige, L. A. Young, Pluto's climate modeled with new observational constraints. *Icarus* **246**, 183–191 (2015). doi: 10.1016/j.icarus.2014.03.014
55. O. J. Tucker, R. E. Johnson, L. A. Young, Gas transfer in the Pluto-Charon system: A Charon atmosphere. *Icarus* **246**, 291–297 (2015). doi: 10.1016/j.icarus.2014.05.002


## ACKNOWLEDGMENTS

This work was supported by NASA's New Horizons Project. Additional support was provided by the Centre National d'Etudes Spatiales through its "Système Solaire" program (E.Q., S. Philippe, and B.S.). S.A.S. is also affiliated with Florida Space Institute, Uwingu LLC, Golden Spike Co., and World View Enterprises. As contractually agreed to with NASA, fully calibrated New Horizons Pluto system data will be released via the NASA Planetary Data System at https://pds.nasa.gov/ in a series of stages in 2016 and 2017 as the data set is fully downlinked and calibrated.

## SUPPLEMENTARY MATERIALS

www.sciencemag.org/content/351/6279/aad9189/suppl/DC1
Supplementary Text
Figs. S1 to S6
Reference (56)

21 November 2015; accepted 12 February 2016
10.1126/science.aad9189

RESEARCH ARTICLES

PLANETARY SCIENCE

# The geology of Pluto and Charon through the eyes of New Horizons

Jeffrey M. Moore,[1]* William B. McKinnon,[2] John R. Spencer,[3] Alan D. Howard,[4] Paul M. Schenk,[5] Ross A. Beyer,[6,1] Francis Nimmo,[7] Kelsi N. Singer,[3] Orkan M. Umurhan,[1] Oliver L. White,[1] S. Alan Stern,[3] Kimberly Ennico,[1] Cathy B. Olkin,[3] Harold A. Weaver,[8] Leslie A. Young,[3] Richard P. Binzel,[9] Marc W. Buie,[3] Bonnie J. Buratti,[10] Andrew F. Cheng,[8] Dale P. Cruikshank,[1] Will M. Grundy,[11] Ivan R. Linscott,[12] Harold J. Reitsema,[3] Dennis C. Reuter,[13] Mark R. Showalter,[6] Veronica J. Bray,[14] Carrie L. Chavez,[6,1] Carly J. A. Howett,[3] Tod R. Lauer,[15] Carey M. Lisse,[8] Alex Harrison Parker,[3] S. B. Porter,[3] Stuart J. Robbins,[3] Kirby Runyon,[8] Ted Stryk,[16] Henry B. Throop,[17] Constantine C. C. Tsang,[3] Anne J. Verbiscer,[18] Amanda M. Zangari,[3] Andrew L. Chaikin,[19] Don E. Wilhelms,[20] New Horizons Science Team

**NASA's New Horizons spacecraft has revealed the complex geology of Pluto and Charon. Pluto's encounter hemisphere shows ongoing surface geological activity centered on a vast basin containing a thick layer of volatile ices that appears to be involved in convection and advection, with a crater retention age no greater than ~10 million years. Surrounding terrains show active glacial flow, apparent transport and rotation of large buoyant water-ice crustal blocks, and pitting, the latter likely caused by sublimation erosion and/or collapse. More enigmatic features include tall mounds with central depressions that are conceivably cryovolcanic and ridges with complex bladed textures. Pluto also has ancient cratered terrains up to ~4 billion years old that are extensionally faulted and extensively mantled and perhaps eroded by glacial or other processes. Charon does not appear to be currently active, but experienced major extensional tectonism and resurfacing (probably cryovolcanic) nearly 4 billion years ago. Impact crater populations on Pluto and Charon are not consistent with the steepest impactor size-frequency distributions proposed for the Kuiper belt.**

We present a preliminary geological examination of Pluto and Charon based on images and other data collected by NASA's New Horizons spacecraft during its flyby of these worlds on 14 July 2015. The two camera systems pertinent to geological investigations are the wide-angle color Multispectral Visible Imaging Camera (MVIC) and the narrow-angle panchromatic Long Range Reconnaissance Imager (LORRI) (*1*). This paper focuses on the portions of the illuminated surfaces seen near closest approach at better than 1 km/pixel resolutions, centered on 180° longitude for Pluto and 0° longitude for Charon (*2*, *3*). All topographic measurements were obtained using stereo photogrammetric techniques, supplemented by preliminary photoclinometry and shadow and limb measurements (*4*). An acronym list is provided in the supplementary materials. All feature names used in this paper are informal, and the locations of named features on Pluto and Charon are shown in figs. S1 and S2, respectively; terrain locations are indicated in fig. S3.

[1]National Aeronautics and Space Administration (NASA) Ames Research Center, Space Science Division, Moffett Field, CA 94035, USA. [2]Department of Earth and Planetary Sciences, Washington University in St. Louis, St. Louis, MO 63130, USA. [3]Southwest Research Institute, Boulder, CO 80302, USA. [4]Department of Environmental Sciences, University of Virginia, Charlottesville, VA 22904, USA. [5]Lunar and Planetary Institute, Houston, TX 77058, USA. [6]The SETI Institute, Mountain View, CA 94043, USA. [7]University of California, Santa Cruz, CA 95064, USA. [8]Johns Hopkins University Applied Physics Laboratory, Laurel, MD 20723, USA. [9]Massachusetts Institute of Technology, Cambridge, MA 02139, USA. [10]NASA Jet Propulsion Laboratory, Pasadena, CA 91019, USA. [11]Lowell Observatory, Flagstaff, AZ 86001, USA. [12]Stanford University, Stanford, CA 94305, USA. [13]NASA Goddard Space Flight Center, Greenbelt, MD 20771, USA. [14]University of Arizona, Tucson, AZ 85721, USA. [15]National Optical Astronomy Observatory, Tucson, AZ 85719, USA. [16]Roane State Community College, Oak Ridge, TN 37830, USA. [17]Planetary Science Institute, Tucson, AZ 85719, USA. [18]Department of Astronomy, University of Virginia, Charlottesville, VA 22904, USA. [19]Independent Science Writer, Arlington, VT 05250, USA. [20]U.S. Geological Survey, Retired, Menlo Park, CA 94025, USA.
*Corresponding author. E-mail: jeff.moore@nasa.gov

## Pluto

Pluto's surface exhibits an astonishing variety of landscapes (Fig. 1A). Broadly, the encounter hemisphere (EH) contains several regional provinces: (i) the ~1000-km-wide uncratered plain, Sputnik Planum (SP), centered on the EH; (ii) arcuate, rugged-to-mountainous regions surrounding SP on three sides; (iii) mantled and eroded plains at higher latitudes; and (iv) a heterogeneous surface west of SP containing plains with various degrees of crater density and surface texture, scarps (both erosional and tectonic), troughs (graben), and patches of rugged cratered terrain.

### *Sputnik Planum and environs*

This ~870,000-km$^2$ oval-shaped unit of high-albedo plains, centered at ~20°N, 175°E, is likely a massive unit of volatile ices (solid $N_2$, CO, and $CH_4$) (*5*), the level of which is 3 to 4 km below the surrounding uplands. The central and northern regions of SP display a distinct cellular pattern (*5*), which varies in appearance across the planum. In the bright central portion (fig. S4A), the cells are bounded by shallow troughs up to 100 m deep (*5*); the centers of at least some cells are elevated by ~50 m relative to their edges, though some apparently have less relief. The southern region and eastern margin of SP do not display cellular morphology, instead showing featureless plains and dense concentrations of pits, themselves reaching a few kilometers across (fig. S4D). Details of the different morphologies encountered within SP are described in the supplementary materials.

No impact craters have been confirmed on SP in contiguous mapping coverage at 390 m/pixel scale. Following the arguments in (*5*), the crater retention age of SP is very young (≲10 million years old) and is discussed in the supplementary materials. Such geologically recent resurfacing and/or topographic relaxation is consistent with the weak rheology of $N_2$-dominated ices (*6*, *7*) and with the interpretation of cells as expressions of potentially active solid-state convection in a thick layer of such ices (supplementary materials).

A discontinuous chain of mountains, consisting of discrete angular blocks with apparently random orientations and sizes up to 40 km across and 5 km high, extends for hundreds of kilometers along the west margin of SP. Those in the south are often separated by embaying materials, whereas those in the north, particularly the northernmost al-Idrisi Montes (AIM, Fig. 2), have minimal separation. At AIM, blocks are closely packed, and many blocks have flat or gently sloping upper surfaces with linear textures similar to those of some of the surrounding highland terrain, suggesting breakup of a preexisting surface.

The northern interblock material has a distinctive reddish color (Fig. 2A), contains many smaller blocks, and is slightly elevated relative to SP; similar terrain surrounds some of the mountains to the south. The AIM region contains two depressions floored largely by this finer, interblock material and small blocks ("c" in Fig. 2), and another occupied by a small plain with similar texture and color to that of SP ("e" in Fig. 2). An inward-facing terrace surrounds this depression ("d" in Fig. 2), suggesting an earlier, higher level of plains material.

It was argued by (*5*) that the steep slopes and high elevations of the mountain blocks require a water-ice–based composition; this has now been confirmed spectroscopically (*8*). Like the angular blocks in europan chaos, Pluto's mountain blocks appear to consist of fragments of preexisting ice crust that have been detached by fracturing, transported, and rotated. The exclusive location of this

Downloaded from on March 17, 2016

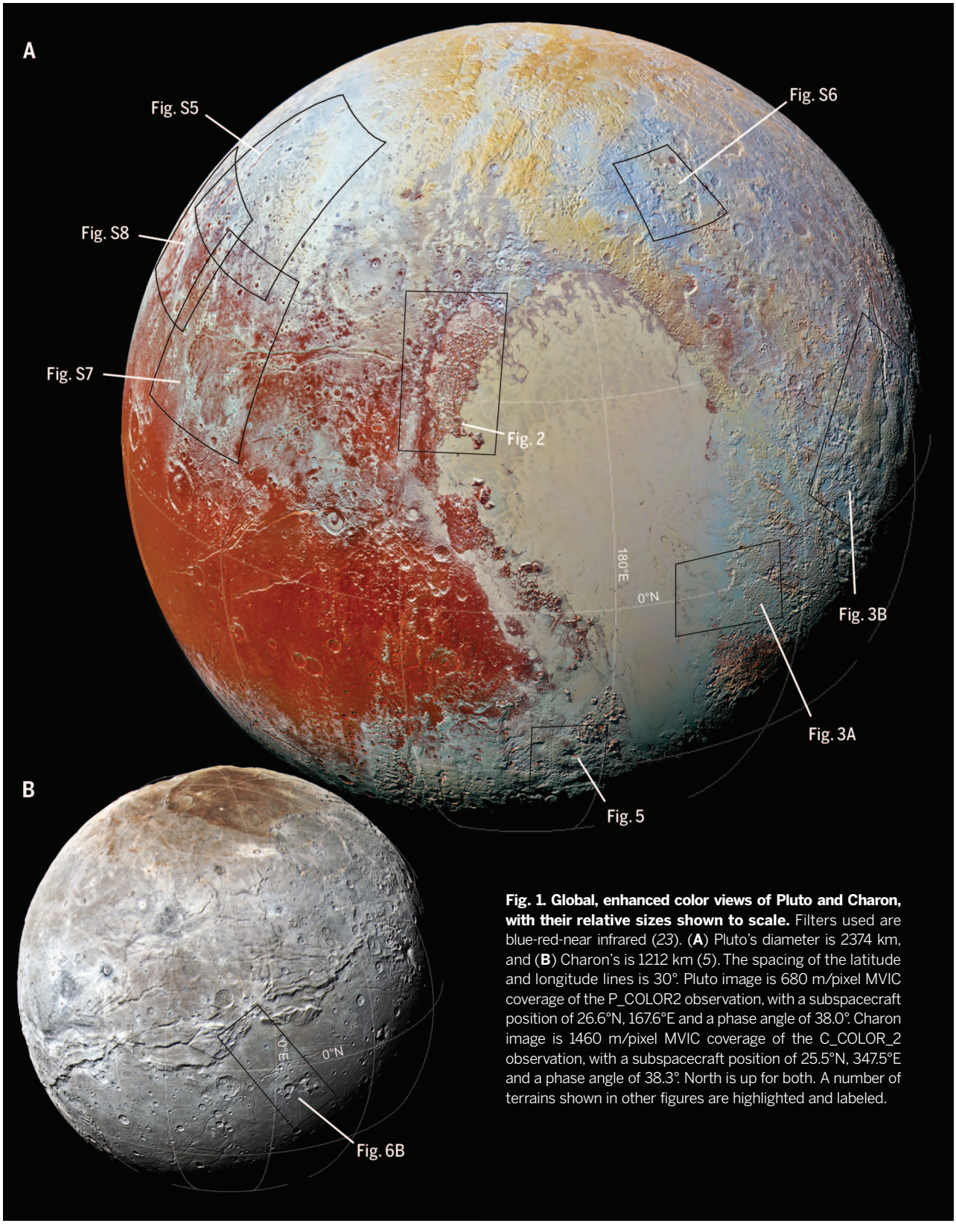



**Fig. 1. Global, enhanced color views of Pluto and Charon, with their relative sizes shown to scale.** Filters used are blue-red-near infrared (*23*). (**A**) Pluto's diameter is 2374 km, and (**B**) Charon's is 1212 km (*5*). The spacing of the latitude and longitude lines is 30°. Pluto image is 680 m/pixel MVIC coverage of the P_COLOR2 observation, with a subspacecraft position of 26.6°N, 167.6°E and a phase angle of 38.0°. Charon image is 1460 m/pixel MVIC coverage of the C_COLOR_2 observation, with a subspacecraft position of 25.5°N, 347.5°E and a phase angle of 38.3°. North is up for both. A number of terrains shown in other figures are highlighted and labeled.

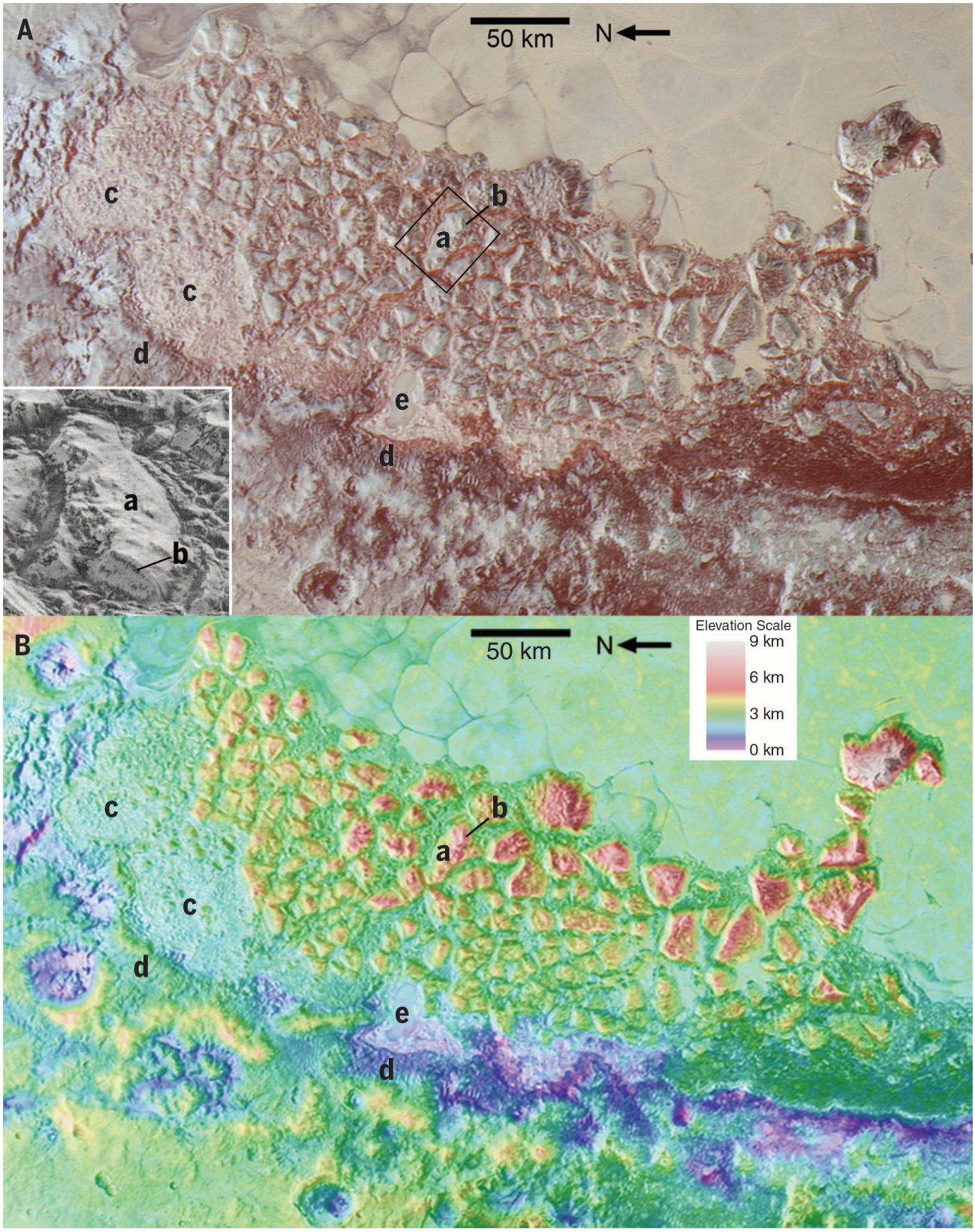



**Fig. 2. The chaotic mountains of al-Idrisi Montes on the northwest margin of SP.** (**A**) Image is 680 m/pixel, reprojected, MVIC enhanced color coverage of the P_COLOR2 observation, centered at 34.5°N, 155°E. The 30 by 40 km–wide inset shows a detail of one mountain in 79 m/pixel, LORRI coverage of the P_MVIC_LORRI_CA observation. (**B**) Colorized digital elevation model (DEM) overlain on the 680 m/pixel MVIC coverage. (a) Textured surface possibly predating block formation; (b) steep fracture surface with possible exposed layering; (c) chaos composed of small blocks; (d) inward-facing terraces; (e) small exposure of SP-like material.

chaotic, blocky mountainous terrain on the margins of SP (fig. S3), which evidently contains a substantial thickness of low-viscosity ices, makes it plausible that these latter ices play a role in the disruption of Pluto's crust.

$H_2O$ ice is buoyant with respect to $N_2$ and CO ice, but not $CH_4$ ice, and blocks of $H_2O$ ice embedded or buried in solid $N_2$ and/or CO will tend to rise isostatically. Small blocks can be carried along by convective or advective motions, essentially as icebergs, and large blocks may be undermined, shifted, and rotated. If the solid $N_2$/CO ice is sufficiently deep, then several of the smaller mountains may be floating within the plains, although the reliefs of the largest mountains (2 to 3 km), which skirt the western margin of SP, implies that their keels are likely "grounded" on the basement (supplementary materials). Why mountainous terrains within SP are limited to its western margin is unknown.

### Pits, blades, plains, and glaciers east of SP

An intricate, high-albedo, 500-km-wide landscape of pitted uplands and smooth plains, bordered by lower-albedo bladed terrain, forms most of the eastern portion of Tombaugh Regio (TR).

Pitted uplands: The dominant features are pits ("a" in Fig. 3A), most of which are a few kilometers across, but some exceed 25 km, locally intersecting to form long, linear troughs. Based upon preliminary topography, pits average ~1 km deep. The crests of the pits define an undulating upland surface 2 to 4 km above SP. In parts of the uplands, the pitting is organized into distinct northeast-southwest–trending ridge-and-trough terrain with ~5-km crest-to-crest spacing. The sidewalls of the pits typically slope up to 30°, suggesting that rigid material underlies the thin, bright surface layer.

Bladed terrain: The pitted uplands transition northeastward to several broad (~100-km-wide) swells named Tartarus Dorsa (TD), whose flanks and crests are covered with numerous roughly aligned blade-like ridges oriented approximately north-south (Fig. 3B). Individual ridges are typically several hundred meters high and are spaced 5 to 10 km crest to crest, separated by V-shaped valleys with slopes of ~20°. Many ridges merge at acute angles to form Y-shape junctions in plan view. Along the west flank of TD are a number of triangular-to-rectangular facets of the plains that ramp upward toward the east.

Smooth plains: Nearly level expanses of smooth plains up to 50 km across occur at relative low points in the pitted uplands as well as elevated terraces adjacent to SP ("b" in Fig. 3A). They are generally smooth at 300 m/pixel resolution, but locally collections of kilometer-scale hills extend above the plains, probably as protrusions or embedded fragments of the pitted terrain material. The smoothness of the level plains suggests that they are composed of deformable ices, probably similar in composition to SP.

Glaciers: At a few locations along the SP–pitted uplands boundary, smooth materials connect with SP along the floors of troughs 1.5 to 6 km wide ("b" in Fig. 3A). High-phase imaging of the southernmost of these systems reveals conspicuous medial flow lines within the troughs extending onto SP, with the ice in the troughs sloping 2° to 3° over more than 50 km (supplementary materials). This pattern implies glacial-like flow of the plains material into SP, perhaps analogous to ice streams at the margins of terrestrial ice sheets. At present, it is unresolved whether the flowing ice carved the troughs.

Origins of these terrains: Both the pitted uplands and bladed terrain may be remnants of a formerly continuous deposit degraded either by sublimation (forming features analogous to those of degraded terrestrial snow or ice fields —penitentes and sun-cups—but much larger), or through undermining and collapse, possibly through melting at depth. An additional possibility is growth of ridges through preferential deposition of volatiles on ridge crests, analogous to pinnacle formation on Callisto (*3*). The preferential orientation of troughs and ridges in both terrains suggests an origin influenced by solar illumination direction and/or atmospheric circulation. In the case of the bladed terrain, if the material forming it was exposed through upwarping and erosion, it may have been a once-buried layer. The high albedo of the pitted uplands suggests condensation of volatiles sublimated and transported from SP (the pits that are prevalent on south SP may form through sublimation of $N_2$ ice; see supplementary materials); these volatiles may accumulate to form the smooth plains.

### Upland terrains: Washboard and dissected terrains

The uplands north and northwest of SP contain a variety of morphologies, notably including expanses of parallel ridges and troughs that we call washboard terrain, and dissected terrain locally organized into valley networks. Fretted terrain and eroded mantles are discussed in the supplementary materials.

Washboard terrain: Many expanses in this region feature parallel ridges and grooves with a crest-to-crest wavelength of about 1 km (Fig. 4A). The ridges retain a consistent northeast-southwest orientation, even where developed on the interior floors of craters. The albedo of washboard surfaces matches that of nearby ungrooved terrain, and underlying terrain features remain visible where grooved. These observations suggest that washboarding is a superficial modification, either by erosion of the underlying surface or, alternatively, as part of a thin regional deposit. The grooving is superimposed on higher-relief topographic features such as ridges, craters, and dissected terrain. Occasional 1- to 2-km-diameter craters are superposed on the washboarding.

Dissected terrain: Terrains dissected by valleys are common on the EH, including fluted, dendritic, plateau, alpine, and mountainous variants (Fig. 4B). Two of these types occur widely. Fluted terrain containing troughs 15 to 20 km across with up to 2-km relative relief that are eroded into broad hills constitute one of these. The troughs or flutes are regularly spaced at 3 to 4 km and are oriented downhill with slopes up to 20°. The interior walls of some craters are similarly fluted. These troughs terminate abruptly in depressions or crater floors without obvious evidence of deposition. Similarly spaced dendritic valley networks are another type of dissected terrain. The networks generally terminate in broad depressions. Dissected terrain appears to postdate and modify the larger upland craters. The other, less common, styles of dissection are described in the supplementary materials.

Origins of these terrains: The mechanisms regulating the characteristic scale and groove orientation of washboarding remain uncertain. In the dissected terrain, both the fluted terrain and the dendritic valley networks probably result from advective processes, most likely flow of nitrogen-rich ice, possibly accompanied by basal melting (supplementary materials). The spatial variation in morphology of the valley networks is likely to be a response to local topographic setting, substrate properties, latitudinal variations in insolation, and variation in depths and durations of $N_2$ ice accumulation.

### Cthulhu Regio (CR)

CR is a large dark area that covers a swath from ~15°N to ~20°S (fig. S1), bordering TR at 160°E, and stretching westward almost halfway around the planet to 20°E. Eastern CR is not a distinct physiographic province, but instead a region of dark mantling thin enough to preserve underlying topography, superimposed upon various geological terrains, including dendritic valleys, craters, fossae (long, narrow troughs), and retreating scarps. The dark coating is likely the result of atmospheric tholin deposition (*8*). CR contains striking correlations between color/albedo and topography: Bright material is correlated with high elevations in some areas and with north-facing slopes in others. This may result in part from insolation-dependent deposition of the bright material on the dark landscape. Other western low-latitude terrains are discussed in the supplementary materials.

### Large mounds with central depressions

Southwest of Norgay Montes (figs. S1C and S3) are two broad quasicircular mounds (Fig. 5). The northernmost (Wright Mons, WM) is 3 to 4 km high and ~150 km across. At its summit is a central depression at least 5 km deep that has a rim showing concentric fabric. The mound surface has a hummocky, blocky surface texture and is very lightly cratered. A similar but even larger feature (Piccard Mons, PM) is seen in twilight stereo imaging 300 km to the south. This reaches ~6 km high and 225 km across. The general shapes of these edifices and associated structures appear to be constructional. Their origin could involve cryovolcanism (*3*), but entailing materials considerably stronger than $N_2$ ice.

### Tectonics

Pluto's EH shows numerous belts of aligned, often arcuate, troughs and scarps that can reach several hundred kilometers in length and several

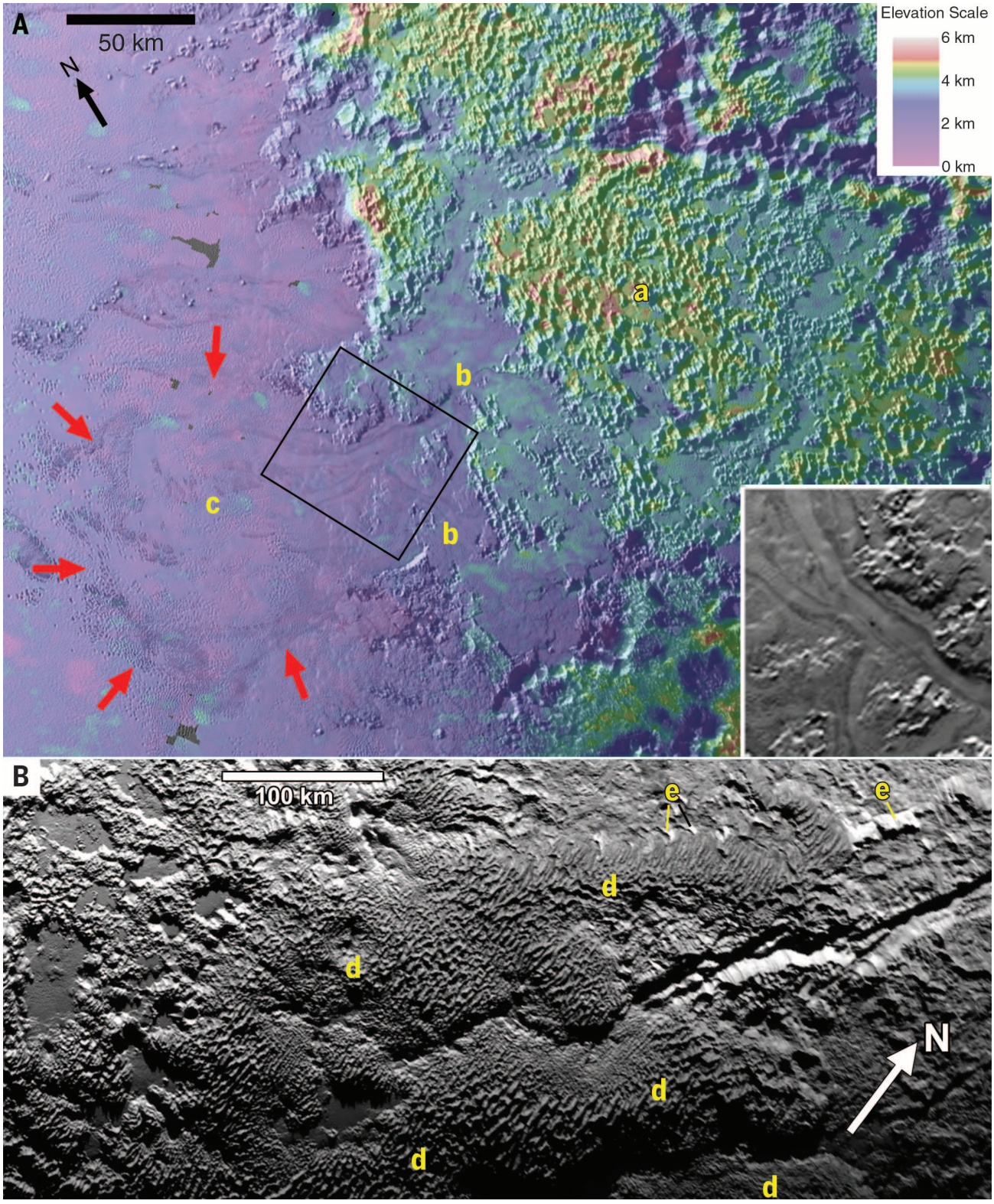



**Fig. 3. Pitted uplands, glaciers, and bladed terrain.** (**A**) Colorized DEM of pitted uplands and valley glaciers east of SP, overlain on 320 m/pixel, reprojected MVIC coverage of the P_MVIC_LORRI_CA observation, centered at 2°N, 195.5°E. (a) Densely pitted terrain, with smooth material covering the floors of the pits. (b) Smooth plains exhibiting glacial flow through notches in the pitted uplands toward SP. The 60 by 50 km–wide rotated inset enhances the contrast of the original MVIC image to emphasize flow lines. (c) Debouchment of a valley glacier into SP, where it assumes the lobate planform of a piedmont glacier. Possible outer flow edges are indicated by red arrows. (B) Bladed terrain outcropping on top of several broad swells (marked with "d") of Tartarus Dorsa. Image is 680 m/pixel, reprojected MVIC coverage of the P_COLOR2 observation, centered at 17.5°N, 227°E. (e) Triangular and rectangular facets of the plains ramping upwards onto the ridges.

kilometers high, and which are often observed to cut across preexisting landforms as well as branch into one another (fig. S9 and supplementary materials). We interpret these features to be extensional fractures (graben and normal faults) in varying stages of degradation. Notable is the single 3- to 4-km-deep V-shaped trough, Virgil Fossa (VF, fig. S9C), which has unbroken segments of at least 200 km and an asymmetric upward displacement on the south scarp of 1 to 2 km. Toward the trough's eastern end, it cuts through Elliot crater, and to the west links with a network of smaller, subparallel fractures. The high scarp has an anomalously red color and is associated with water ice (*8*). Other extensional fracture systems are shown in fig. S9.

Compressional features, if present, are less obvious. One candidate, TD (figs. S9F and 3B), consists of several elongated swells ~200 km wide, traversed by at least one long, prominent extensional feature (Sleipnir Fossa). TD could be due to compressional folding, but may also be analogous to a salt-cored anticline or arch, in which low-density core material contributes to the arching.

The differing fault trends and states of degradation suggest multiple deformation episodes and prolonged tectonic activity. We do not elaborate on their origin here, but note that equatorial normal faults would not arise from despinning stresses alone (*9*). The great length of individual faults on Pluto, their scarp steepness (>20°, from stereo), spectral evidence (*8*), and the absence of localized flank uplift strongly suggest a thick water-ice lithosphere (as opposed to a thin water-ice lithosphere, or one made of any of Pluto's volatile ices).

### *Impact craters*

Pluto displays a wide variety of crater sizes and morphologies (figs. S11 and S12; supplementary materials). Globally, recognizable crater diameters range from ~0.5 to 250 km, not including any possible ancient basin underlying SP. Crater densities

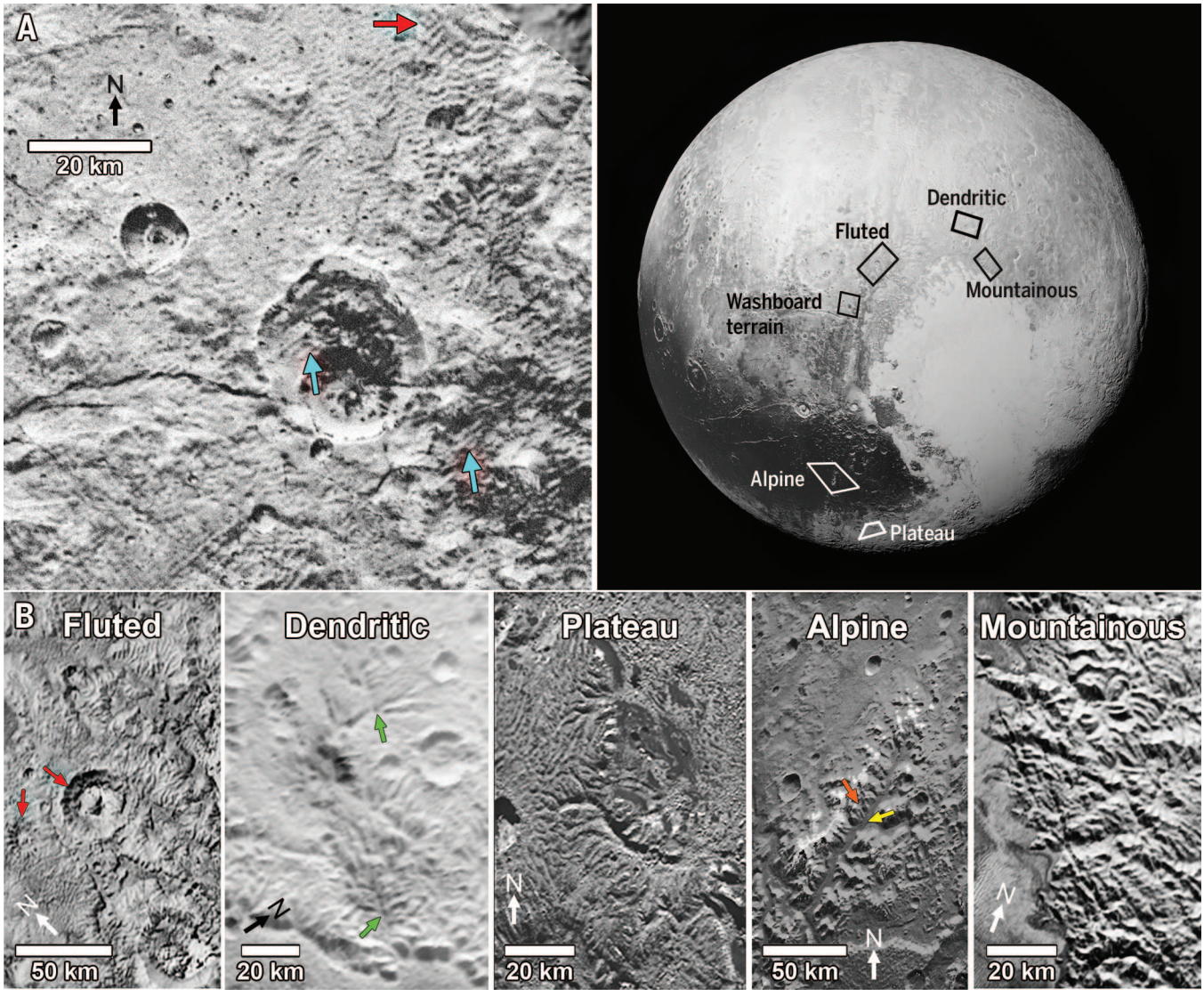



**Fig. 4. Washboard and dissected terrains on Pluto.** Locations of the terrains are highlighted at upper right. (**A**) Washboard terrain northwest of SP. Image is 125 m/pixel, reprojected, LORRI coverage from the P_MPAN_1 observation, centered at 38°N, 145.5°E. Blue arrows indicate washboard texture within craters, and the red arrow indicates where washboard terrain has modified fluted terrain. (**B**) The five types of dissected terrains with informal typology discussed in the text and supplementary materials. Fluted, dendritic, and mountainous terrain images are taken from 680 m/pixel, reprojected MVIC coverage of the P_COLOR2 observation; plateau and alpine terrain images are taken from 320 m/pixel MVIC coverage of the P_MVIC_LORRI_CA observation. The fluted terrain image is centered at 48.4°N, 153.4°E. Red arrows indicate incision of downslope-oriented grooves. The image of dendritic valley networks (green arrows) is centered at 54.8°N, 186.6°E. The dissected plateaus image is centered at 22.1°S, 155.6°E. Alpine valley systems show wide, dendritic trunk valleys (yellow arrow) that head on dissected mountainous slopes (orange arrow); image is centered at 5.2°S, 146.5°E. The mountainous dissection image is centered at 45.4°N, 188.9°E.

vary widely on Pluto, from the heavily cratered portions of CR, to SP, which has no identifiable impact craters. The total cumulative crater size–frequency distribution (SFD) on the EH is shown in fig. S13A. From this, we conclude that Pluto's surface as a whole dates back nearly to the time of the end of Late Heavy Bombardment (LHB), or in the context of the Kuiper belt, the proposed era of rearrangement of the outer solar system [perhaps 4 billion years ago; e.g., (*10*)]. On the EH, only the eastern portion of CR appears to approach the saturation crater densities (for large craters, compare fig. S13B) that would be expected of a terrain that survived from the LHB itself, when cratering rates were likely much higher than at present. In contrast, TD, eastern TR, the water-ice mountain ranges, the mounds (all very lightly cratered), and especially SP (no identified craters) are all very young (fig. S13C). No craters have been detected in SP down to 2-km diameter, which is a tighter size limit than reported previously (*5*) and implies a model crater retention age of no greater than ~10 million years, and possibly much less (*11*) (supplementary materials).

### *Geologic evolution*

Though complex and largely novel, landforms on Pluto present many clues to their origin and history. The basin in which SP is located is ancient, despite the youthfulness of its interior deposits. Its semicircular rim of elevated mountainous terrains suggests that it probably is a heavily modified impact basin. The larger visible craters in

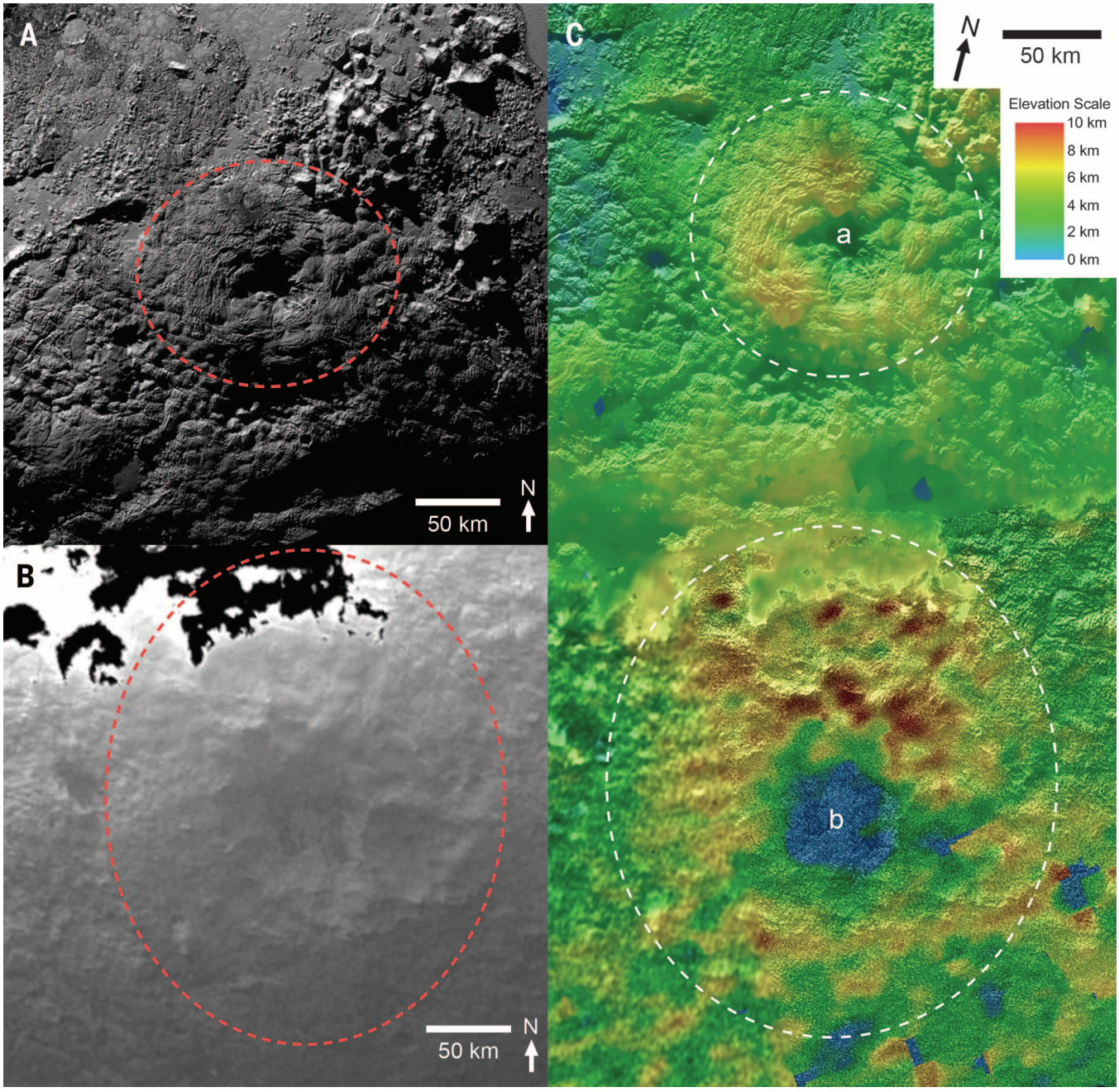



**Fig. 5. Quasicircular mounds south of SP, both with depressions at their summits, which may have a cryovolcanic contribution.** Dashed lines mark their approximate boundaries. Image is 320 m/pixel, reprojected MVIC coverage of the P_MVIC_LORRI_CA observation. (**A**) Wright Mons at 22°S, 173°E. (**B**) Piccard Mons at 35°S, 176°E, seen in twilight. (**C**) Colorized DEM overlain on the MVIC coverage of the mounds. "a" marks Wright Mons, "b" marks Piccard Mons.

these mountainous terrains probably postdate this SP basin.

Except in the west, the uplands surrounding SP have been blanketed with mantles of substantial thickness and various surface compositions (*8*), which have been partially stripped. The primary agents of upland modification probably include sublimation, frost deposition, and glacial erosion. We envision two end-member scenarios: In one, a formerly deep ice mantle (largely $N_2$) covered the uplands surrounding SP but was gradually lost to space. As ice levels dropped, glacial ice eroded the dissected terrains and, to the east of SP, flowed back into SP, leaving remnants in smooth-floored depressions. Alternatively, ices may have been cycled between SP and its surroundings, perhaps episodically, to form the glaciers and dissected terrains. In this case, loss to space of volatile ices need not have occurred (*12*). Nitrogen and other volatiles available to the surface environment may also be replenished episodically by sources within Pluto's interior (*13*).

The dark mantles of CR and other local regions conform to present topography, suggesting that they postdate the erosional sculpting of the landscape or are actively recycled. The cellular pattern imposed on SP ices is a relatively young feature, given the absence of craters, and the hectometer-scale pits and ridges on SP constitute the youngest widespread landforms on Pluto.

The relative youth of some extensional features is consistent with predicted recent extensional stresses associated with a late, possibly partial freezing of a subsurface ocean (*14*), though other explanations are also possible. Various lines of evidence, including the spectroscopic identification of water ice along the exposed walls of VF, as well as the steep, chaotic mountains bordering SP, suggest a cold, strong, water ice–based crust.

## Charon

Charon's EH (Fig. 1B) can be divided into two broad provinces separated by an assemblage of ridges and canyons, which span the EH from east to west. North of this tectonic belt is rugged, cratered terrain; south of it are smoother but geologically complex plains. The northern hemisphere is capped by the dark, reddish Mordor Macula (MM). Relief exceeding 20 km is seen in limb profiles and stereo topography (fig. S16), and is a testament to the bearing strength of cold water ice and Charon's modest surface gravity [0.29 m $s^{-2}$ (*15*)].

### *Cratered northern terrain*

Charon's northern terrain is exceptionally rugged, and contains both a network of polygonal troughs 3 to 6 km deep, and a possibly related irregular depression almost 10 km deep immediately south of the edge of MM near 270°E (fig. S14). A prominent, ~230-km-diameter, 6-km-deep crater (Dorothy Gale) at 58°N, 38°E (fig. S2) straddles the discrete edge of MM (*5*). The cumulative crater distribution for Charon's northern terrain is shown in fig. S14A. The crater density at large sizes, for which counts are reliable, implies a surface age older than ~4 billion years (Gy) (supplementary materials).

The overall dark deposit of MM does not correlate with any specific terrain boundary or geologic unit. A prominent, arcuate ridge ~5 km high ("a" in fig. S14) coincides with a prominent albedo and color boundary (compare fig. S14 with Fig. 1B) and may be an impact basin rim or an extension of the tectonic deformation seen more clearly to the south. Other morphological indicators of an impact origin, such as a well-defined ejecta blanket or secondary craters, have not been discerned.

### *Ridges, troughs, and canyons*

The structural belt that bisects Charon's EH consists of subparallel scarps, ridges, and troughs of variable extent, but over 200 km wide in places (Fig. 1B). Notable are two chasmata: (i) Serenity Chasma, which is >50 km wide and ~5 km deep, and exhibits a pronounced rift-flank uplift; and (ii) Mandjet Chasma, which appears to be fault bounded and reaches ~7-km depth (fig. S2). These chasmata resemble extensional rifts on several mid-sized icy satellites (*9*).

We interpret this assemblage as the structural expression of normal faults and graben that represent substantial, aligned, tectonic extension of Charon's icy crust. Several large craters superposed on the chasmata indicate that this extension is geologically old (see below and fig. S15). Given the horizontal and vertical scale of these structures, steeply dipping normal faults likely extend to depths of tens of kilometers. They represent global areal extension on the order of ~1%.

### *Southern plains*

The smoother southern half of Charon's EH forms an apparently continuous surface with low relief named Vulcan Planum (VP). Near the bounding scarps to the north, the planum slopes gently downward by ~1 km toward the scarps. Portions of the plains observed at higher resolution exhibit a distinctive, lineated texture of closely spaced grooves or furrows (fig. 6B). One possible origin for the southern plains is tectonic resurfacing like that seen on the icy satellites Ganymede and Enceladus (*3*). Morphologically distinct groups of deeper, rille-like narrow troughs and furrows that postdate the plains also occur. Although deep, these troughs are nonetheless superimposed by a number of impact craters, and thus are themselves relatively old. The en echelon nature of these troughs, and rough parallelism with the chasmata to the north, suggests a tectonic origin or structural control.

Fields of small hills (2 to 3 km across), areas of relatively low crater density, and at least one pancake-shaped unit are consistent with cryovolcanic resurfacing (fig. 6B) (*16*). Peaks surrounded by "moats" (Kubrick and Clarke Montes, KM and CM; see fig. S2 and "b" labels in Fig. 6A) were noted by (*5*). The peaks are up to 3 to 4 km high above the floors of the moats, and the moats 1 to 2 km deep below the surrounding plains. The moat at CM appears to expose a more rugged terrain ("j" label in Fig. 6B), with smooth plains embaying the margins, two of which are lobate. The moats are perhaps due to mountain loading and flexure of Charon's lithosphere. There are two additional depressions surrounded by rounded or lobate margins ("a" labels in Fig. 6A); thus alternatively, both the moats and depressions may be the expressions of the flow of, and incomplete enclosure by, viscous, cryovolcanic materials, such as proposed for the uranian moons Ariel and Miranda (*3*, *17*).

The SFD of impact craters on the southern plains lies below that for the north at large diameters (≥50 km, fig. S15A), yet model ages for the plains point to an age of ~4 Gy (supplementary materials), thus implying an older age for the northern terrain, and a similar or older age for those chasmata that predate (were resurfaced by) VP. In limited regions on VP, however, craters are sparse (Fig. 6B), implying that the resurfacing of VP may have acted over an extended time. The crater SFD of VP is also likely the truest expression of the Kuiper belt impact crater production function for the Pluto system (*5*), and one that appears to rule out certain classes of Kuiper belt object population size distributions (supplementary materials).

### *Geological evolution*

Charon's surface is dominated by impacts, tectonic deformation, and resurfacing, and as such fits broadly into the accepted picture of geologic evolution on icy satellites (*18*, *19*). That Charon is so geologically complex, however, would seem to require a heat source for reshaping what would have otherwise been a heavily cratered surface. If the ~4-Gy age of even the youngest of Charon's surfaces is correct, then this activity dates back to an early warmer epoch. The tectonic record is consistent with global expansion, and the smooth plains consistent with the mobilization of volatile ices from the interior. The spatial distribution of tectonic features is not readily reconciled with the kinds of patterns expected (indeed, predicted) from tidal or despinning stresses (*3*). Charon may have had an ancient subsurface ocean that subsequently froze, which would generate the global set of extensional features, and might permit eruption of cryovolcanic magmas (*20*).

## A divergent binary

Pluto and Charon are strikingly different in surface appearance, despite their similar densities and presumed bulk compositions (*5*). With the possible exception of MM, the dynamic remolding of landscapes by volatile transport seen on Pluto is not evident on Charon, whose surface is instead dominated spectrally by the signature of water ice (*8*). Whether this is because Charon's near-surface volatile ices have sublimated and have been totally lost to space owing to that body's lower gravity (*21*), or whether something more fundamental related to the origin of the binary and subsequent internal evolution (*22*) is responsible, remains to be determined.

Much of what we see on Pluto can be attributed to surface-atmosphere interactions and the mobilization of volatile ices by insolation. Other geological activity requires or required internal heating. The convection and advection of volatile ices in SP can be powered by present-day radiogenic heat

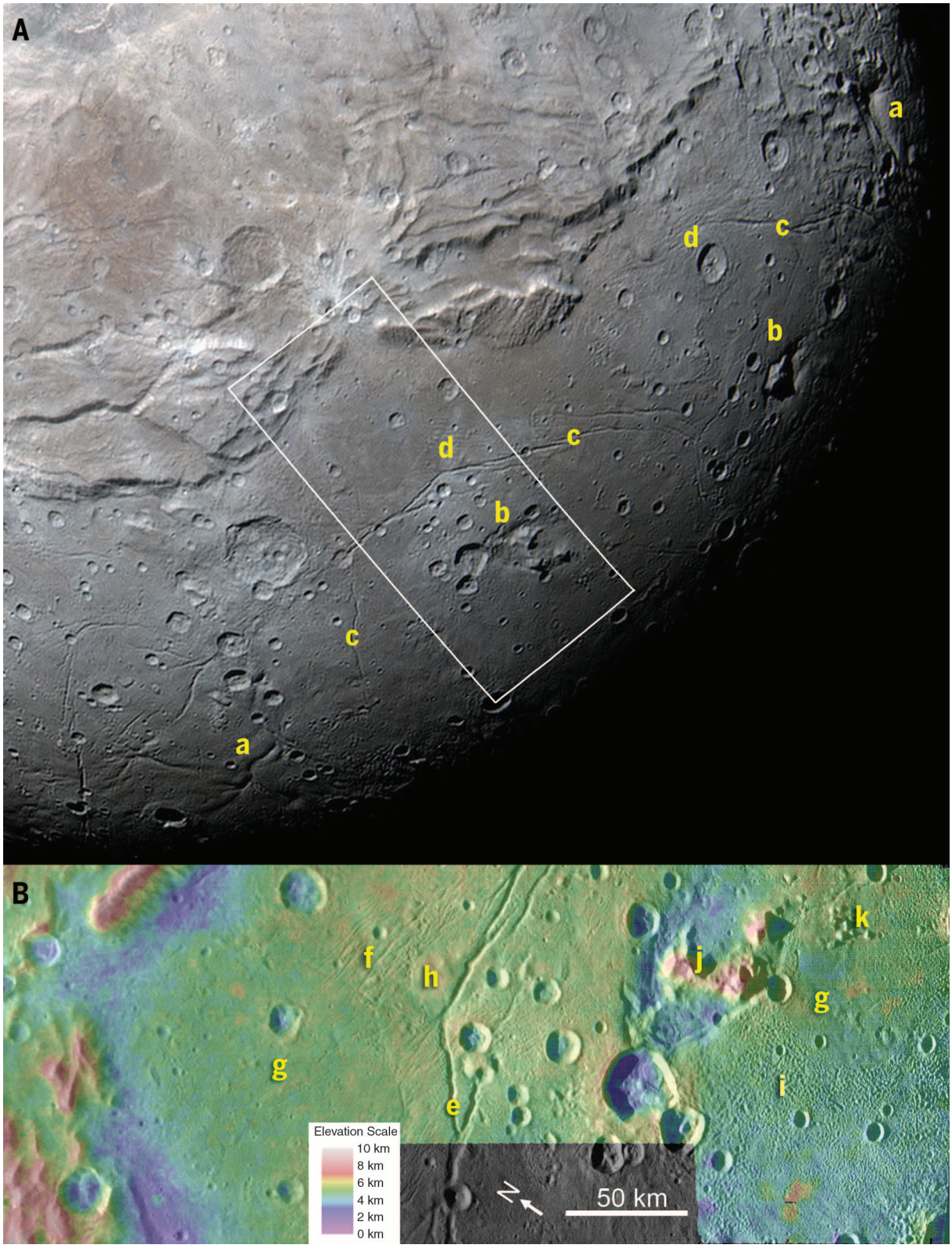



**Fig. 6. Enlargement of a portion of Fig. 1B showing details of Vulcan Planum on Charon.** (**A**) Image is 1460 m/pixel MVIC coverage from the C_COLOR_2 observation, centered at 5.5°N, 3°E, with north up. (a) Depressions with lobate margins; (b) mountains surrounded by moat-like depressions; (c) deep, rille-like troughs; and (d) shallow, finely spaced furrows. White outline indicates high-resolution image in (B). (**B**) High-resolution view of resurfacing on Vulcan Planum. Image is 160 m/pixel, reprojected LORRI coverage from the C_MVIC_LORRI_CA observation centered at 0°N, 0.5°E, with DEM color overlain. Seen in this LORRI view are rille-like troughs (e) and more finely spaced, shallow furrows (f), smoother regions of lower crater density (g), a pancake-shaped deposit (h), and unusual textured terrain (i). Clarke Mons (j) lies in a depression, which is itself bordered on two sides by distinctive lobate scarps. (k) A field of small hills.

loss (supplementary materials). However, the prominent mountains at the western margin of SP, and the strange, multikilometer-high mound features to the south are both young geologically and presumably composed of relatively strong, water-ice–based geological materials. Their origin, and what drove their formation so late in solar system history, remain uncertain. What is more certain is that all three major Kuiper belt bodies (past or present) visited by spacecraft so far—Pluto, Charon, and Triton—are more different than similar and bear witness to the potential diversity awaiting the future exploration of their realm.

## REFERENCES AND NOTES


1. H. A. Weaver, W. C. Gibson, M. B. Tapley, L. A. Young, S. A. Stern, *Space Sci. Rev.* **140**, 75–91 (2008).
2. L. A. Young *et al.*, *Space Sci. Rev.* **140**, 93–127 (2008).
3. J. M. Moore *et al.*, *Icarus* **246**, 65–81 (2015).
4. Materials and methods are available as supplementary materials on *Science* Online.
5. S. A. Stern *et al.*, *Science* **350**, aad1815 (2015).
6. J. Eluszkiewicz, D. J. Stevenson, *Geophys. Res. Lett.* **17**, 1753–1756 (1990).
7. Y. Yamashita, M. Kato, M. Arakawa, *Icarus* **207**, 972–977 (2010).
8. W. M. Grundy *et al.*, *Science* **351**, aad9189 (2016).
9. G. C. Collins *et al.*, in *Planetary Tectonics*, R. A. Schultz, T. R. Watters, Eds. (Cambridge Univ. Press, New York, 2010), pp. 264–350.
10. R. Gomes, H. F. Levison, K. Tsiganis, A. Morbidelli, *Nature* **435**, 466–469 (2005).
11. S. Greenstreet, B. Gladman, W. B. McKinnon, *Icarus* **258**, 267–288 (2015).
12. G. R. Gladstone *et al.*, *Science* **351**, aad8866 (2016).
13. K. N. Singer, S. A. Stern, *Astrophys. J.* **808**, L50 (2015).
14. G. Robuchon, F. Nimmo, *Icarus* **216**, 426–439 (2011).
15. M. Brozović, M. R. Showalter, R. A. Jacobson, M. W. Buie, *Icarus* **246**, 317–329 (2015).
16. P. M. Schenk, J. M. Moore, in *Solar System Ices*, B. Schmitt, C. de Bergh, M. Festou, Eds. (Kluwer Academic, Dordrecht, Netherlands, 1998), pp. 551–578.
17. D. G. Jankowski, S. W. Squyres, *Science* **241**, 1322–1325 (1988).
18. L. M. Prockter *et al.*, *Space Sci. Rev.* **153**, 63–111 (2010).
19. G. Schubert *et al.*, *Space Sci. Rev.* **153**, 447–484 (2010).
20. M. Manga, C.-Y. Wang, *Geophys. Res. Lett.* **34**, L07202 (2007).
21. E. L. Schaller, M. E. Brown, *Astrophys. J.* **659**, L61–L64 (2007).
22. W. B. McKinnon, in *Treatise on Geophysics*, G. Schubert, Ed. (Elsevier, Amsterdam, ed. 2, 2015), vol. 10, pp. 637–651.
23. D. C. Reuter *et al.*, *Space Sci. Rev.* **140**, 129–154 (2008).


## ACKNOWLEDGMENTS

We thank the many engineers who have contributed to the success of the New Horizons mission and NASA's Deep Space Network for a decade of excellent support to New Horizons. We thank the reviewers for close and meticulous reading, and P. Engebretson for contribution to figure production. S.A.S. is also affiliated with Florida Space Institute, Uwingu LLC, Golden Spike Co., and World View Enterprises. H.J.R. is also affiliated with B612 Foundation and Cornell Technical Service. Supporting imagery is available in the supplementary materials. As contractually agreed to with NASA, fully calibrated New Horizons Pluto system data will be released via the NASA Planetary Data System at https://pds.nasa.gov/ in a series of stages in 2016 and 2017 as the data set is fully downlinked and calibrated. This work was supported by NASA's New Horizons project.

## SUPPLEMENTARY MATERIALS

www.sciencemag.org/content/351/6279/1284/suppl/DC1
Materials and Methods
Supplementary Text
Figs. S1 to S15
Table S1
References (*24*–*83*)

16 November 2015; accepted 11 February 2016
10.1126/science.aad7055

FEEDING BEHAVIOR

# The nutrient sensor OGT in PVN neurons regulates feeding

**Olof Lagerlöf,[1,2] Julia E. Slocomb,[3] Ingie Hong,[1] Yeka Aponte,[1,4] Seth Blackshaw,[1] Gerald W. Hart,[2] Richard L. Huganir[1]***

**Maintaining energy homeostasis is crucial for the survival and health of organisms. The brain regulates feeding by responding to dietary factors and metabolic signals from peripheral organs. It is unclear how the brain interprets these signals. O-GlcNAc transferase (OGT) catalyzes the posttranslational modification of proteins by O-GlcNAc and is regulated by nutrient access. Here, we show that acute deletion of OGT from αCaMKII-positive neurons in adult mice caused obesity from overeating. The hyperphagia derived from the paraventricular nucleus (PVN) of the hypothalamus, where loss of OGT was associated with impaired satiety. These results identify O-GlcNAcylation in αCaMKII neurons of the PVN as an important molecular mechanism that regulates feeding behavior.**

Obesity is a major contributor to disease throughout the world (*1*). Currently, there is no successful and available treatment for the majority of obese patients. One of the genes most commonly linked to human obesity, *Gnpda2*, affects flux through the hexosamine biosynthesis pathway (HBP) (*2*–*4*). The HBP produces uridine-diphosphate: N-acetylglucosamine (UDP-GlcNAc), which is the donor substrate for the enzyme O-GlcNAc transferase (OGT). OGT cleaves UDP-GlcNAc and covalently attaches GlcNAc to the hydroxyl group of serine or threonine in nuclear and cytoplasmic proteins in β-linkage (O-GlcNAc). Nutrient access directly via the HBP, and metabolic hormones such as insulin regulate the activity of OGT (*5*, *6*). Although OGT has been shown to be important for neuronal development, the role of OGT for mature brain function is almost completely unknown (*7*–*9*). To study the function of OGT in normal behavior, we created conditional OGT knockout mice by crossing floxed OGT mice ($OGT^{Fl}$) with mice expressing a tamoxifen-inducible version of Cre recombinase under the αCaMKII promoter (αCaMKII-$CreER^{T2}$). This enables acute brain-specific deletion of OGT in αCaMKII-expressing neurons in adult mice, which we confirmed by means of immunohistochemistry, Western blotting, and polymerase chain reaction (fig. S1). Knockout of OGT in other tissues and cells has been shown to lead to decreases in cell number, probably because of impaired mitosis, and in fact, constitutive knockout of OGT leads to early embryonic lethality (*8*, *10*, *11*). In contrast, in post-mitotic neurons deletion of OGT did not affect cell number in vitro or in vivo (fig. S2, A and B).

Acute and brain-specific loss of OGT in adult mice caused rapid weight gain (Fig. 1, A and B, and fig. S3, A and B). Within 3 weeks, the amount of adipose tissue tripled, whereas the lean weight had not changed, as quantified with whole-body nuclear magnetic resonance (NMR) [fat mass, $n$ = 7 wild-type (WT) mice, 2.5 ± 0.21 g; $n$ = 6 OGT knockout mice, 8.3 ± 0.86 g] (fig. S3, C and D). The incorporation of fat was general and not particular to any specific body region (fig. S3, E to G). Obesity can result from either excessive caloric intake or insufficient energy expenditure. Daily food intake rapidly increased upon knockout of OGT and plateaued at a level more than twice as high (Fig. 1C). If access to food was restricted to the same amount consumed by WT mice, the OGT knockout mice retained normal body weight. When free access to food was reintroduced, the OGT knockout mice quickly approached the weight of OGT knockout littermates who had been fed ad libitum throughout the experiment (Fig. 1D). To quantify food intake and energy expenditure simultaneously in real time, we used comprehensive laboratory animal monitoring system (CLAMS). CLAMS confirmed that loss of OGT leads to hyperphagia (fig. S3H). Energy expenditure was actually increased (fig. S3I). The accelerated energy expenditure resulted from, at least in part, hyperactivity (fig. S3J). As expected from a combination of hyperphagia and hyperactivity, knocking out OGT caused higher $vO_2$ and $vCO_2$, leading to a respiratory exchange ratio (RER) above 1 ($n$ = 17 WT mouse days (6 mice), 0.94 ± 0.004; $n$ = 20 OGT knockout mouse days (6 mice), 1.04 ± 0.007) (fig. S3, K to M).

Daily food intake is a factor of both the size of each meal and meal frequency. A normal diurnal rhythm was preserved in OGT knockout mice (Fig. 1E and fig. S4, A and B). Although there was no difference in meal frequency, loss of OGT increased meal size as well as meal duration (meal size, $n$ = 268 WT mouse meals (6 mice),

[1]Solomon H. Snyder Department of Neuroscience, Kavli Neuroscience Discovery Institute, Johns Hopkins University School of Medicine, Baltimore, MD 21205, USA. [2]Department of Biological Chemistry, Johns Hopkins University School of Medicine, Baltimore, MD 21205, USA. [3]National Institute on Drug Abuse + National Institutes of Health/Johns Hopkins University Graduate Partnership Program, Baltimore, MD 21224, USA. [4]Intramural Research Program, Neuronal Circuits and Behavior Unit, National Institute on Drug Abuse, Baltimore, MD 21224, USA.
***Corresponding author. E-mail: rhuganir@jhmi.edu**

Downloaded from on March 17, 2016

0.25 ± 0.02 g; $n$ = 330 OGT knockout mouse meals (7 mice), 0.42 ± 0.02 g) (Fig. 1E and fig. S4, C to E). The point at which a meal is terminated depends on the total caloric content of the food but also noncaloric determinants of the food, mainly its volume and composition. When fed either regular carbohydrate-rich pellets or fat-based food paste with higher caloric density, the OGT knockout mice overate the same amount of calories (fig. S4F).

Immunohistochemistry for OGT showed that within the core feeding circuitry, the major loss of OGT in the knockout mice occurred in medial nuclei of the hypothalamus, most notably in the paraventricular nucleus (PVN) (Fig. 2A and fig. S5A). There was only minor loss of OGT from nuclei of the midbrain and the brainstem (Fig. 2A and fig. S5A). Using αCaMKII-CreER$^{+}$ × TdT$^{Fl}$ mice and immunohistochemistry, we noticed that some αCaMKII PVN cells expressed thyrotropin-releasing hormone (TRH) and some oxytocin (fig. S6A). Before any major weight gain, OGT deletion reduced the expression of TRH, as determined with in situ hybridization, in a subpopulation of cells in the PVN without affecting their viability, whereas several other known neuropeptides regulating feeding behavior were largely unaltered: proopiomelanocortin (POMC), cocaine- and amphetamine-regulated transcript (CART), orexin, agouti-related peptide (AgRP), neuropeptide Y (NPY), vasopressin (AVP), and oxytocin (TRH, $n$ = 4 WT mice, 40 ± 4.1 cells/150 × $10^3$ μm$^2$; $n$ = 4 OGT knockout mice, 23 ± 2.9 cells/150 × $10^3$ μm$^2$) (Fig. 2B and figs. S6, B to E, and S7A) (*12*, *13*). Next, we infected hypothalamic organotypic cultures with a virus that expresses green fluorescent protein (GFP) under the αCaMKII promoter and treated the explants with varying concentrations of glucose. The PVN retained its normal morphology and expression of neuropeptide during the extent of the experiment (~2.5 weeks) (fig. S8A). Immunohistochemistry for O-GlcNAc demonstrated that 1 hour of treatment with 5 mM glucose, simulating physiological and meal-derived fluctuations in glucose, increased O-GlcNAc in αCaMKII-positive cells [1 mM glucose, $n$ = 360 cells, 134 ± 10 intensity/cell (arbitrary units, a.u.); 5 mM glucose $n$ = 330 cells, 211 ± 12 intensity/cell (a.u.)] (Fig. 2C) (*14*–*16*). In contrast, there was no change in O-GlcNAc levels in neighboring αCaMKII-negative cells (fig. S8B). Incubation for 16 hours with 25 mM glucose raised the O-GlcNAc levels in αCaMKII cells to a larger extent [5 mM glucose, $n$ = 390 cells, 156 ± 9 intensity/cell (a.u.); 25 mM glucose, $n$ = 375 cells, 298 ± 14 intensity/cell (a.u.)] (fig. S8, C and D). Unlike cortex and the hippocampus, where O-GlcNAc levels mirror food intake, it has recently been reported that fasting increased O-GlcNAc in AgRP neurons, which has been proposed to be due to stimulation of OGT expression by ghrelin in these cells (*6*, *7*, *15*). In the PVN, fasting decreased O-GlcNAc, but only in αCaMKII-positive cells [αCaMKII-positive cells, fed mice $n$ = 455 cells, 158 ± 5 intensity/cell (a.u.); starved mice $n$ = 259 cells, 81 ± 6 intensity/cell (a.u.)] (fig. S8E). In addition, we compared the expression of the immediate early gene c-Fos in αCaMKII PVN cells in vivo in mice fed ad libitum or refed upon starvation. This enabled us to characterize cellular responses to food intake as mice start eating after a period of starvation. Food intake appeared to activate αCaMKII cells in the PVN, and loss of OGT blocked this activation completely (fig. S8, F and G).

O-GlcNAc is highly expressed in neuronal synapses in the brain (*17*). We crossed αCaMKII-CreER$^{+}$ × OGT$^{Fl/WT}$ × TdT$^{Fl}$ mice to assess whether OGT regulates excitatory synaptic input onto αCaMKII PVN cells. If deleting OGT attenuates excitatory input, it would explain, at least in part, how OGT regulates the activity of these cells. The mean capacitance of labeled cells averaged ~15 pF and did not differ between WT and knockout mice (fig. S9A). The mean miniature excitatory postsynaptic current (mEPSC) frequency decreased by 72% in OGT knockout cells ($n$ = 6 WT cells, 1.75 ± 0.11 Hz; $n$ = 6 OGT knockout cells, 0.50 ± 0.10 Hz) (Fig. 3, A and B). The sharp decrease in mEPSC frequency suggests that OGT is essential for maintaining the number of functional excitatory synapses onto αCaMKII PVN neurons.

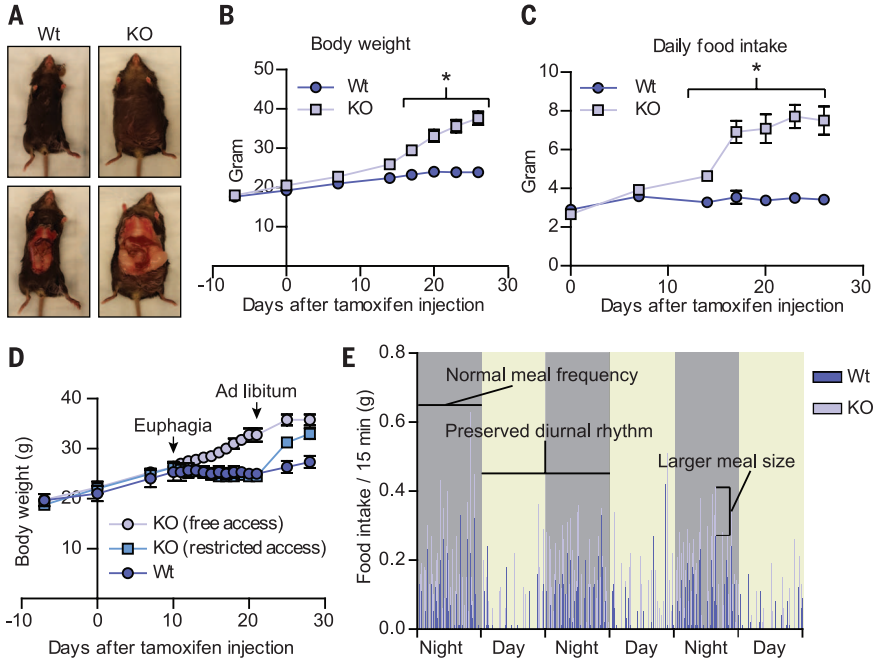



**Fig. 1. Acute deletion of OGT in αCaMKII-positive neurons causes hyperphagia-dependent obesity.** (**A**) Photo of mice 4 weeks after OGT deletion. (**B**) Body weight time course [$n$ = 8 WT mice, $n$ = 8 OGT knockout mice; repeated-measures two-way analysis of variance (ANOVA) with post hoc Bonferroni test, $P$ < 0.05]. (**C**) Daily food intake time course ($n$ = 6 WT mice, $n$ = 6 OGT knockout mice; repeated-measures two-way ANOVA with post hoc Bonferroni test, $P$ < 0.05). (**D**) Body weight time course upon pair-feeding ($n$ = 4 free mice, $n$ = 4 restricted mice, $n$ = 3 WT mice). (**E**) Food intake every 15 min from sample mice. Quantifications represent mean ± SEM.

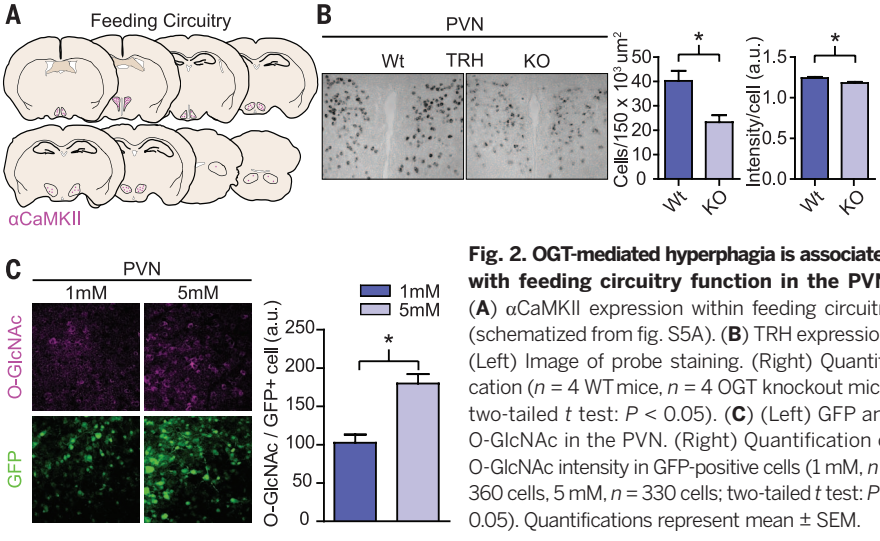



**Fig. 2. OGT-mediated hyperphagia is associated with feeding circuitry function in the PVN.** (**A**) αCaMKII expression within feeding circuitry (schematized from fig. S5A). (**B**) TRH expression. (Left) Image of probe staining. (Right) Quantification ($n$ = 4 WT mice, $n$ = 4 OGT knockout mice; two-tailed $t$ test: $P$ < 0.05). (**C**) (Left) GFP and O-GlcNAc in the PVN. (Right) Quantification of O-GlcNAc intensity in GFP-positive cells (1 mM, $n$ = 360 cells, 5 mM, $n$ = 330 cells; two-tailed $t$ test: $P$ < 0.05). Quantifications represent mean ± SEM.

The mean mEPSC amplitude was also decreased, but to a much smaller degree ($n$ = 6 WT cells 19.7 ± 1.2 pA; $n$ = 6 knockout cells, 15.6 ± 0.9 pA) (Fig. 3, A and C). Neither the rise time nor the decay time of the EPSCs changed upon deletion of OGT (fig. S9, B and C). Pharmacological inhibition of glutamatergic signaling in the PVN has previously been shown to elicit intense feeding (*18*).

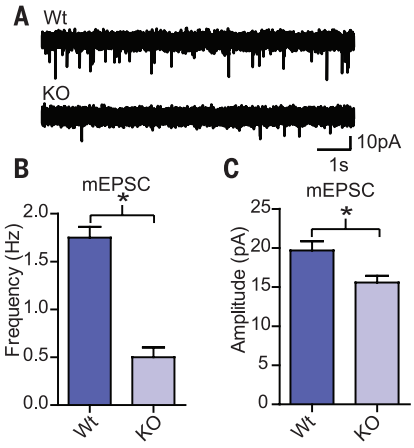



**Fig. 3. OGT regulates excitatory synaptic function in αCaMKII PVN neurons.** (**A**) Sample traces from WT and OGT knockout cells. (**B**) mEPSC frequency and (**C**) amplitude in αCaMKII-positive PVN neurons ($n$ = 6 WT cells, $n$ = 6 OGT knockout cells; two-tailed $t$ test, $P < 0.05$). Quantifications represent mean ± SEM.

Selectively deleting OGT in the αCaMKII cells of the PVN by means of stereotactic virus injection caused concurrent obesity and hyperphagia (Fig. 4, A to C, and fig. S9D). Because deletion of OGT in αCaMKII cells in the PVN prevents their feeding-induced activation and leads to hyperphagia, we predicted that stimulating those cells would decrease food intake. Activating αCaMKII PVN cells optogenetically decreased cumulative food consumption over 24 hours (baseline, $n$ = 11 experiments (5 mice), 3.6 ± 0.14 g; 50 Hz, $n$ = 11 experiments (5 mice), 2.6 ± 0.33 g) (Fig. 4, D and E) (*19*). The amount of food ingested per meal was smaller, whereas there was no significant effect on meal frequency (meal size, baseline, $n$ = 125 meals, 0.25 ± 0.014 g; 50 Hz, $n$ = 110 meals, 0.20 ± 0.014 g) (Fig. 4F and fig. S9E). In a second experiment, we started the stimulation at the onset of darkness after fasting the mice during the light phase. Fasting increased food intake, and 20 Hz optogenetic stimulation for 4 hours produced a significant decrease in food intake, whereas 50 Hz stimulation for 1 or 4 hours produced large, significant drops in feeding (fig. S9F). The decrease in meal size with 50 Hz stimulation was evident in the first meal, without any change in latency to initiation of feeding (fig. S9, G and H).

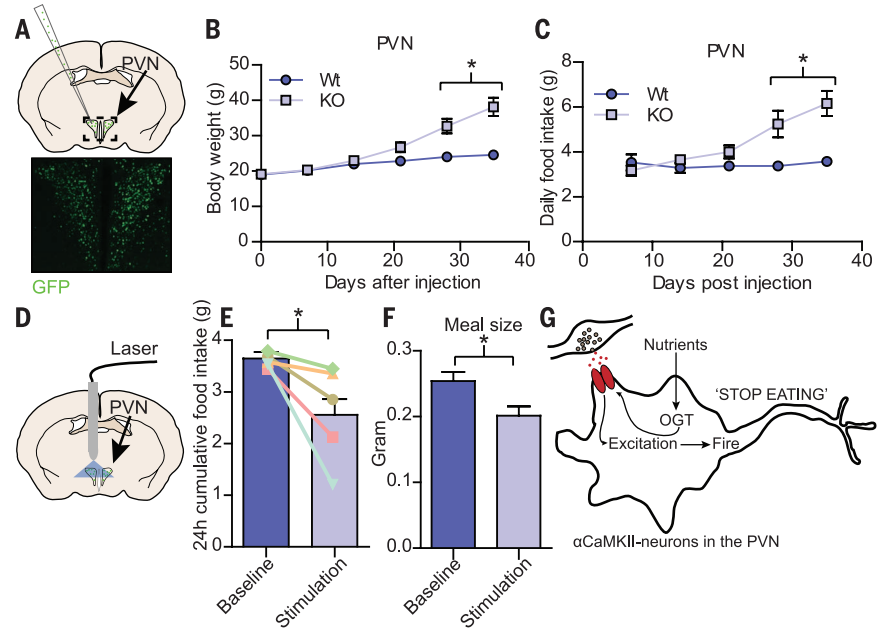



**Fig. 4. OGT regulates feeding behavior in αCaMKII neurons of the PVN.** (**A**) (Top) Schematic of stereotactic PVN injection. (Bottom) GFP expression in the PVN after stereotactic injection. (**B**) Body weight and (**C**) daily food intake time course ($n$ = 5 WT mice, $n$ = 7 OGT knockout mice; repeated-measures two-way ANOVA with post hoc Bonferroni test, $P < 0.05$). (**D**) Schematic of optogenetic setup with αCaMKII-driven expression of channelrhodopsin-2 in the PVN with the abutting laser. (**E** and **F**) Food intake after optogenetic stimulation. (E) 24 hours cumulative food intake. Bars represent average intake over all mice, and lines represent average intake per individual mouse (baseline, $n$ = 11 experiments (5 mice); stimulation, $n$ = 11 experiments (5 mice); two-tailed $t$ test, $P < 0.05$). (F) Average meal size (baseline, $n$ = 125 meals (5 mice); stimulation, $n$ = 110 meals (5 mice); two-tailed $t$ test, $P < 0.05$). (**G**) Model of OGT-dependent hyperphagia. Quantifications represent mean ± SEM.

Together, our data favor a model in which the function of OGT is to couple energy intake with energy need, at least in part, by regulating the excitatory synaptic input in αCaMKII PVN cells (Fig. 4G). The select effect on meal termination suggests that OGT regulates satiation. αCaMKII neurons are often excitatory. Although vGlut2-positive excitatory neurons in the PVN decrease food intake, there appears to be only partial overlap between αCaMKII and vGlut2 expression in the PVN (*20*, *21*). Because glucose remains elevated in the cerebrospinal fluid more than 1 hour upon eating, the feeding-related changes in O-GlcNAc integrates nutrient availability on a time scale longer than a single meal (*14*, *22*, *23*). The brain promotes satiation by coordinating adipokines, reflecting body energy depots, and acute food-derived signals into circuits that turn off feeding. Rather than constituting a link in meal-to-meal satiety feedback loops, our observations suggest that OGT controls the threshold of such loops through its regulation of excitatory synaptic transmission onto αCaMKII PVN neurons. The observation that OGT knockout mice quickly reached a plateau in daily food intake supports this idea. Thresholding satiation between meals confers the behavioral advantage of stabilizing caloric intake over time so that the previous meal informs on the caloric need of the next. These data do not exclude additional, faster regulation of OGT activity and levels via metabolic hormones. These findings identify the regulation of excitatory synapses onto αCaMKII PVN neurons by OGT as an important mechanism underlying satiation, representing a potential medicinal target for human obesity.

## REFERENCES AND NOTES


1. C. E. Lewis *et al.*, *Circulation* **119**, 3263–3271 (2009).
2. E. K. Speliotes *et al.*, *Nat. Genet.* **42**, 937–948 (2010).
3. R. Gutierrez-Aguilar, D. H. Kim, S. C. Woods, R. J. Seeley, *Obesity (Silver Spring)* **20**, 306–312 (2012).
4. H. Wolosker *et al.*, *FASEB J.* **12**, 91–99 (1998).
5. G. W. Hart, C. Slawson, G. Ramirez-Correa, O. Lagerlöf, *Annu. Rev. Biochem.* **80**, 825–858 (2011).
6. X. Li, F. Lu, J. Z. Wang, C. X. Gong, *Eur. J. Neurosci.* **23**, 2078–2086 (2006).
7. H. B. Ruan *et al.*, *Cell* **159**, 306–317 (2014).
8. N. O'Donnell, N. E. Zachara, G. W. Hart, J. D. Marth, *Mol. Cell. Biol.* **24**, 1680–1690 (2004).
9. J. E. Rexach *et al.*, *Nat. Chem. Biol.* **8**, 253–261 (2012).
10. C. Slawson *et al.*, *J. Biol. Chem.* **280**, 32944–32956 (2005).
11. R. Shafi *et al.*, *Proc. Natl. Acad. Sci. U.S.A.* **97**, 5735–5739 (2000).
12. E. Vijayan, S. M. McCann, *Endocrinology* **100**, 1727–1730 (1977).
13. J. W. Sohn, J. K. Elmquist, K. W. Williams, *Trends Neurosci.* **36**, 504–512 (2013).
14. A. B. Steffens, A. J. Scheurink, D. Porte Jr., S. C. Woods, *Am. J. Physiol.* **255**, R200–R204 (1988).
15. G. Pekkurnaz, J. C. Trinidad, X. Wang, D. Kong, T. L. Schwarz, *Cell* **158**, 54–68 (2014).
16. M. Karnani, D. Burdakov, *Am. J. Physiol. Regul. Integr. Comp. Physiol.* **300**, R47–R55 (2011).
17. J. C. Trinidad *et al.*, *Mol. Cell. Proteomics* **11**, 215–229 (2012).
18. S. R. Hettes *et al.*, *Brain Res.* **992**, 167–178 (2003).
19. A. K. Sutton *et al.*, *J. Neurosci.* **34**, 15306–15318 (2014).
20. Y. Xu *et al.*, *Cell Metab.* **18**, 860–870 (2013).
21. A. Wallén-Mackenzie *et al.*, *J. Neurosci.* **29**, 2238–2251 (2009).

22. American Diabetes Association, *Diabetes Care* **24**, 775–778 (2001).
23. S. Marshall, O. Nadeau, K. Yamasaki, *J. Biol. Chem.* **279**, 35313–35319 (2004).

**ACKNOWLEDGMENTS**

O.L., G.W.H., and R.L.H. designed all experiments; the optogenetics experiments were also designed by Y.A. and J.E.S., and the elecotrophysiological experiments were also designed by I.H. O.L. performed all experiments and analyzed all data but the electrophysiology (I.H.) and the optogenetics (J.E.S.). The optogenetics data were analyzed by J.E.S., Y.A., and O.L. O.L., G.W.H., and R.L.H. wrote the manuscript. We thank G. Schütz for providing the αCaMKII-CreER$^{T2}$ mice, J. L. Bedont for help with in situ hybridization experiments, and R. H. White for assistance with mating and genotyping. All data necessary to understand and assess the conclusions of the manuscript are in the body of the paper and in the supplementary materials. All primary data are archived on a secure server located in the Department of Neuroscience at Johns Hopkins University (JHU). All data will be made available upon request. G.W.H. receives a share of royalty received by the university on sales of the CTD 110.6 antibody, which are managed by JHU. The research was supported by NIH (grant R01NS036715 to R.L.H. and grants R01DK6167, N01-HV-00240, and P01HL107153 to G.W.H.) and the National Institute on Drug Abuse Intramural Research Program (Y.A.).

**SUPPLEMENTARY MATERIALS**

www.sciencemag.org/content/351/6279/1293/suppl/DC1
Materials and Methods
Figs. S1 to S9
References (*24*–*29*)

29 September 2015; accepted 5 February 2016
10.1126/science.aad5494

MICROBIOTA

# The maternal microbiota drives early postnatal innate immune development

**Mercedes Gomez de Agüero,[1]* Stephanie C. Ganal-Vonarburg,[1]* Tobias Fuhrer,[2] Sandra Rupp,[1] Yasuhiro Uchimura,[1] Hai Li,[1] Anna Steinert,[1] Mathias Heikenwalder,[3] Siegfried Hapfelmeier,[4] Uwe Sauer,[2] Kathy D. McCoy,[1]* Andrew J. Macpherson[1]*†**

**Postnatal colonization of the body with microbes is assumed to be the main stimulus to postnatal immune development. By transiently colonizing pregnant female mice, we show that the maternal microbiota shapes the immune system of the offspring. Gestational colonization increases intestinal group 3 innate lymphoid cells and F4/80$^+$CD11c$^+$ mononuclear cells in the pups. Maternal colonization reprograms intestinal transcriptional profiles of the offspring, including increased expression of genes encoding epithelial antibacterial peptides and metabolism of microbial molecules. Some of these effects are dependent on maternal antibodies that potentially retain microbial molecules and transmit them to the offspring during pregnancy and in milk. Pups born to mothers transiently colonized in pregnancy are better able to avoid inflammatory responses to microbial molecules and penetration of intestinal microbes.**

During pregnancy, the eutherian fetus inhabits a largely sterile environment in utero, protected from infections by maternal immunity. Rejection of the allogeneic fetus is avoided through maternal and fetal vascular separation, the immune privileged status of the placental trophoblast, and gestational maternal tolerance mechanisms (*1*). At birth, the situation changes dramatically as body surfaces become progressively colonized with microbes, directly exposing the immature neonatal immune system to potential pathogens (*2*, *3*). Despite continued protection from the immunoglobulins and antibacterial peptides in milk, the consequence of this transition for human health is that most of the worldwide mortality in children up to 5 years old is due to infectious disease (*4*–*6*).

Immune system development is both preprogrammed in neonatal tissues and driven later by exposure to pathogenic and nonpathogenic microbes (*3*). Germ-free mice have low immunoglobulin concentrations; lymphopenia of lymphoid structures; reduced bone marrow leukocyte pools; and aberrant innate and adaptive immune functions (*7*, *8*). It has been widely assumed that most microbiota-driven immune alterations are postnatal effects induced by the neonate's own microbiota (*2*, *9*, *10*). Here, we challenge this assumption by asking how the maternal microbiota in pregnancy alone affects the early postnatal immune system of the offspring.

To achieve gestation-only colonization under conditions where the mice deliver their pups spontaneously at term, we used a system in which pregnant dams are transiently colonized with genetically engineered *Escherichia coli* HA107 (*11*). Because this strain does not persist in the intestine, pregnant dams become germ-free again before term and naturally deliver germ-free pups (fig. S1A). Although *E. coli* is a minor component of the adult human microbiota, it is commoner in the neonatal intestine (*12*) and a frequent cause of human neonatal sepsis (*13*).

## Gestation-only colonization shapes the intestinal mucosal innate immune composition

Gestation-only colonization with *E. coli* HA107 altered the numbers of early postnatal intestinal innate leukocytes in wild-type C57BL/6 mice. At postnatal day 14, there was an increase in small intestinal innate lymphoid cell (ILC) proportions and total numbers compared with germ-free controls, particularly the NKp46$^+$RORγt$^+$ ILC3 subset (Fig. 1, A and B, and fig. S1B). Small intestinal NKp46$^+$RORγt$^+$ ILC3 are described in germ-free mice (*14*), but persistently increased following transient gestational colonization, reaching a maximum in 14- to 21-day-old pups: This increase persisted even after weaning (Fig. 1C and fig. S1C), consistent with increased small intestinal ILC3 content of colonized compared with germ-free mice (*15*) and the microbiota-dependent modulation of RORγt expression in this subset (*16*). Increases in the expression of the cytokine interleukin-22 (IL-22) in this population have been observed following permanent colonization or the introduction of segmented filamentous bacteria to the microbiota (*17*, *18*). Total numbers of IL-22–expressing cells increased in line with the increased NKp46$^+$RORγt$^+$ ILC3 numbers as a result of gestational colonization, although individual IL-22 expression levels did not change, likely because the pups were born and raised germ-free (fig. S1, D to F).

There was also an increase in the small and large intestinal F4/80$^+$CD11c$^+$ mononuclear cells (iMNCs) in day 14 (d14) pups born to gestation-only colonized dams (Fig. 1, D and E, and fig. S2, A to C), whereas the F4/80$^+$CD11c$^-$ macrophages, F4/80$^{lo}$CD11c$^+$ dendritic cells (DCs), and the CD103$^+$ or CD11b$^+$ DC subpopulations were not significantly affected (Fig. 1, D and E, and fig. S2, B to E). The gestational effects on increased F4/80$^+$CD11c$^+$ iMNCs were also maximal between postnatal days 14 to 21, and they persisted until at least 8 weeks of age in the colon (Fig. 1F). Gestational colonization caused no significant changes in small intestinal ILC2 numbers (fig. S3, A and B) or in other early postnatal innate leukocyte populations in either systemic or intestinal tissues (table S1). These results showed that temporary colonization of a pregnant dam has long-term consequences for certain populations of innate lymphoid and mononuclear cells in the intestines of her offspring.

We next sought to verify that the effects of gestational *E. coli* on early postnatal innate leukocytes would also be seen with animals stably colonized by a different microbiota both in the mother and after birth. We compared C57BL/6 animals carrying the defined altered Schaedler flora (ASF) of eight microbes with germ-free controls. Both small intestinal NKp46$^+$ ILC3 and intestinal F4/80$^+$CD11c$^+$ MNC populations were increased in pups born to stably colonized ASF

[1]Maurice Müller Laboratories (DKF), Universitätsklinik für Viszerale Chirurgie und Medizin Inselspital, Murtenstrasse 35, University of Bern, 3010 Bern, Switzerland. [2]Institute of Molecular Systems Biology, Swiss Federal Institute of Technology (ETH) Zürich, 8093 Zürich, Switzerland. [3]Division of Chronic Inflammation and Cancer, German Cancer Research Center (DKFZ), Heidelberg, Germany. [4]Institute for Infectious Diseases, University of Bern, 3010 Bern, Switzerland.
*These authors contributed equally to this work. †Corresponding author: E-mail: andrew.macpherson@insel.ch

Downloaded from on March 17, 2016

mothers compared with germ-free controls (fig. S4, A and B). Colonization of adult germ-free C57BL/6 animals with an ASF microbiota for 21 days also selectively increased intestinal NKp46$^+$ ILC3 and F4/80$^+$CD11c$^+$ iMNC populations (fig. S4, C and D, and table S2). Given that the ASF microbiota does not contain Proteobacteria, we concluded that the innate leukocyte alterations seen through gestation-only colonization with *E. coli* are also present in mice colonized with a defined microbiota, dominated by *Bacteroides distasonis* (*19*). Nevertheless, given the alterations in adaptive immunity when germ-free mice are permanently colonized with a microbiota (*8*), we next assessed the extent of adaptive immune changes after gestation-only colonization.

### Maternal gestational colonization does not affect adaptive immune composition of pups

We found that gestation-only colonization did not alter relative or absolute populations of B or T cells during development in the bone marrow, spleen, or thymus (fig. S5, A and B). Intestinal and systemic CD4 or CD8 T cell numbers, T cell activation status (table S3), CD4 subpopulations (fig. S5, C to G), and intestinal microarchitecture (fig. S6) were also generally unaffected. Because all the neonatal mice in these experiments were germ-free, we concluded that the well-known microbiota-driven effects of amplification of B and T cell numbers and resulting reorganization of lymphoid structures result from postnatal colonization with an endogenous microbiota (*19*–*21*).

### Maternal microbiota induces intestinal transcriptional reprogramming in offspring

Many functions of the neonatal intestine are developmentally regulated, including transport of nutrients, salts, and water; barrier function; and secretion of antibacterial peptides and mucus (*22*). Because different aspects of intestinal development determine the ability of the neonate to tolerate an incoming microbiota, we questioned whether the changes in innate leukocytes after gestational colonization were part of a much wider range of adaptations triggered by maternal exposure to intestinal microbes. We carried out RNA sequencing (RNA-Seq) analysis of whole small intestinal mucosal RNA from neonates at day 14. Unsupervised analysis showed a series of consistent transcriptional changes in the pups born to gestation-only colonized dams compared with controls (Fig. 2A). The genetic and protein interactions inferred from differentially expressed transcripts (*23*) included up-regulated gene networks for cell division and differentiation, mucus and ion channels, and the polymeric immunoglobulin receptor and mononuclear recruitment, as well as for metabolism of xenobiotics, bile acids, complex lipids, and sugars (Fig. 2B). These differentially expressed genes included significantly increased overall expression of signature genes for the different Paneth cell, goblet cell, and early/late enterocyte precursor epithelial lineages (*24*, *25*) (fig. S7, A to C). Transcripts for the C-lectin Reg family and antibacterial defensin peptides were also significantly increased in the pups of gestation-only colonized dams compared with controls (Fig. 2C and fig. S7D).

These results show that the maternal microbiota drives wide-ranging mucosal transcriptional

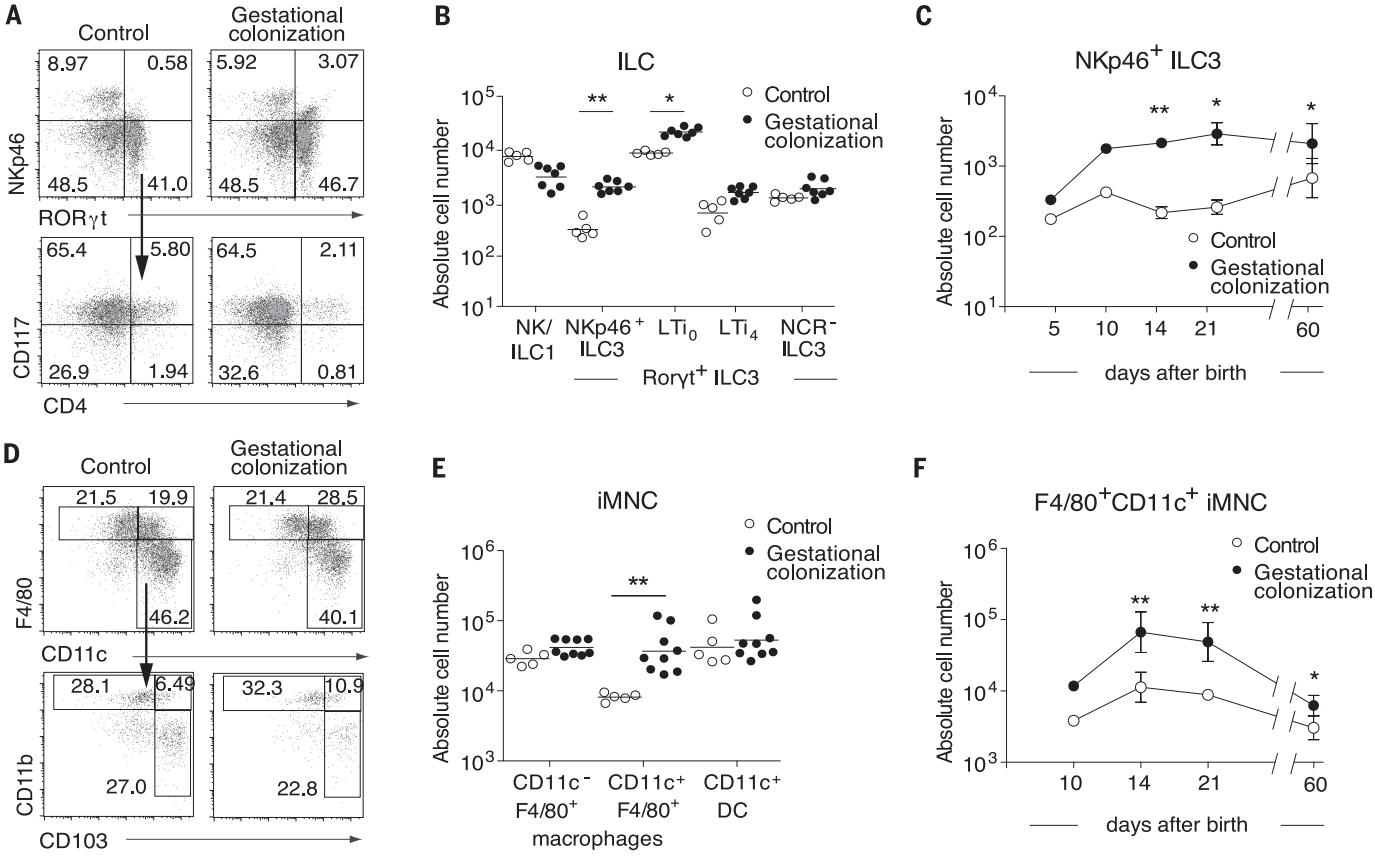



**Fig. 1. Maternal microbial exposure during pregnancy shapes the frequency of intestinal innate lymphoid and mononuclear cell populations in the offspring.** Germ-free C57BL/6 dams were transiently colonized with *E. coli* HA107 (gestational colonization) or kept germ-free throughout (controls). All offspring were analyzed by flow cytometry at day 14 after birth unless indicated. (**A**) Representative dot plots showing Lin$^-$ (CD19$^-$CD3$^-$) small intestinal lamina propria lymphocytes (upper row) and Lin$^-$RORγt$^+$NKp46$^-$ ILC3 (lower row). (**B**) Absolute numbers (geometric mean, sample number $n \geq 5$) of the indicated Lin$^-$ small intestinal ILC populations. (**C**) Absolute numbers of small intestinal Lin$^-$NKp46$^+$RORγt$^+$ ILC3 at indicated time points after birth. Data represent geometric mean ± SD, $n = 3$ to 10 per time point. (**D**) Representative dot plots showing Lin$^-$MHC-II$^+$ colon lamina propria intestinal mononuclear cells (iMNCs) (upper row) and Lin$^-$MHC-II$^+$CD11c$^+$F4/80$^{lo}$ iMNCs (lower row). (**E**) Absolute numbers (geometric mean, $n \geq 5$) of indicated Lin$^-$MHC-II$^+$ iMNC populations in the colon. (**F**) Absolute numbers (geometric mean ± SD, $n = 3$ to 10 per time point) of colon Lin$^-$MHC-II$^+$CD11c$^+$F4/80$^+$ iMNCs at different time points after birth. Data are each representative of four independent experiments or show pooled data from four experiments. *$P \leq 0.05$; **$P \leq 0.01$.

signatures that are consistent with adapting early postnatal immunity and intestinal function generally to postnatal microbial colonization and the metabolic consequences of inevitable bile salt and dietary xenobiotic exposure, even in pups born germ-free. Thus, many aspects of what might have been thought of as canonical host epithelial development and innate immunity are likely shaped through maternal microbial colonization.

### Gestational colonization effects depend on maternal antibodies

Live intestinal microbes, including *E. coli* HA107, generally do not penetrate the body further than the lymph nodes draining the intestinal mesentery (*26*, *27*), and we found no culturable organisms in the placenta after treatment in our gestational colonization experiments. It was therefore likely that the effects of maternal gestational microbes on early postnatal innate immunity resulted from penetration of microbial molecular products, first to maternal tissues, and subsequently to the fetus or neonate. Supporting this hypothesis, we found that serum transfer from gestation-only colonized females to unexposed pregnant dams was sufficient to shape intestinal NKp46$^{+}$ ILC3 populations in the neonates (Fig. 3A and fig. S8, A and B), but not when immunoglobulin G (IgG) was depleted from the serum before transfer, nor when the serum was derived from gestationally colonized $J_H^{-/-}$ antibody-deficient dams (fig. S8, A and B). Given the sufficiency of serum IgG transfer, antibody transfer from the mother to her offspring was likely important to realize some features of early postnatal immune development, because the gestation-only induction of small intestinal NKp46$^{+}$ ILC3 by the maternal microbiota was lost in the antibody-deficient $J_H^{-/-}$ strain (Fig. 3, B and C). We confirmed that this effect was due to the lack of maternal antibodies using a heterozygous strain combination approach (fig. S8C). Nevertheless, not all aspects of maternal microbiota-driven early postnatal immune system development are antibody dependent, because induction of F4/80$^{+}$CD11c$^{+}$ iMNCs was preserved despite the lack of neonatal and/or maternal antibodies (fig. S8, D and E).

Because NKp46$^{+}$ ILC3 but not CD11c$^{+}$F4/80$^{+}$ iMNC increases are mediated through maternal antibody-dependent mechanisms after transient gestational colonization, we predicted that only a subset of the many transcriptional responses attributable to epithelial and other intestinal cells would be maternal antibody-dependent. RNA-Seq analysis was carried out in d14 ileum to compare the responses of C57BL/6 wild-type and $J_H^{-/-}$ groups, each of which was compared to germ-free controls. Only a subset of up-regulated genes in all networks were maternal antibody-dependent (Fig. 3D and fig. S9, A to C). For example, although *RegIIIa* transcript numbers were elevated in the pups of antibody-deficient mothers, maximal up-regulation of *RegIIIb* and *RegIIIg* was antibody dependent (Fig. 3E and fig. S9D).

### Maternal microbial molecular transfer to the offspring

Maternal microbiota effects on the pups were only seen when the mother was transiently colonized during pregnancy itself (fig. S10, A

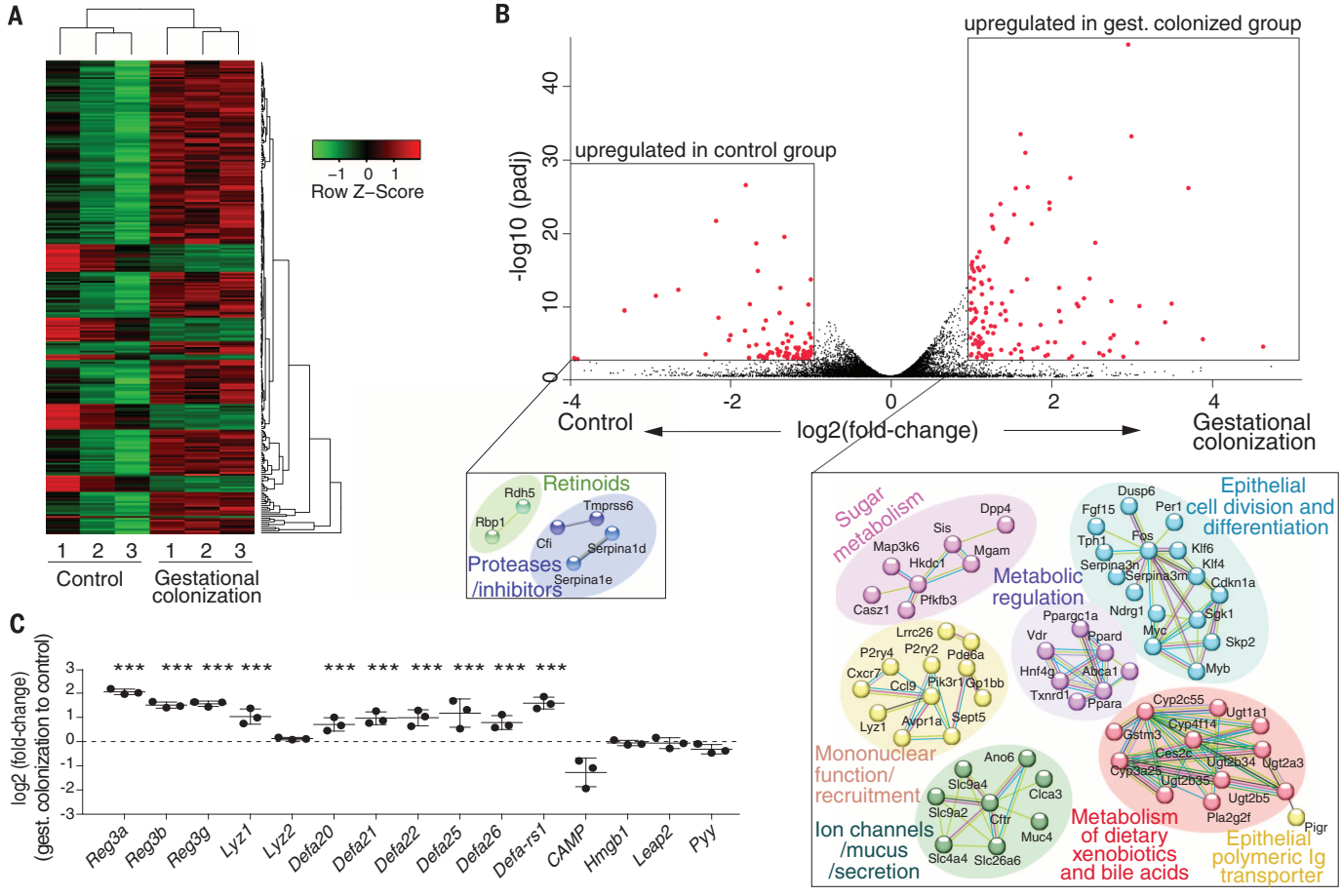



**Fig. 2. Maternal microbial exposure during pregnancy causes extensive changes in the intestinal gene expression profile in neonates.** Germ-free C57BL/6 dams were transiently colonized with *E. coli* HA107 during pregnancy (gestational colonization) or kept germ-free throughout (controls). Whole-tissue RNA from the small intestine was isolated from the offspring on day 14 after birth and used for RNA-Seq ($n$ = 3 per group). (**A**) Heat map of genes differentially expressed (fold-change ≥ 2; adjusted $P$ value padj < 0.001). The color scale shows the relative expression profiles. (**B**) Upper: Volcano plot showing fold-change of gene expression in offspring born to gestationally colonized mothers compared to offspring born to control mothers. Genes with significantly different expression between the two groups (fold-change ≥ 2; padj < 0.01) are highlighted in red; lower: STRING analyses for significantly altered transcripts in each case. (**C**) Fold-change of selected transcripts for antimicrobial peptides between the gestationally colonized and control pups (***padj < 0.001; see also data file S1).

and B). In mice, maternal IgG is transferred across the placenta and through intestinal uptake from the milk (*28*), so we used litter-swap experiments to distinguish between antenatal and postnatal effects of the maternal microbiota. Although there was a nonsignificant trend toward increased small intestinal NKp46$^{+}$ ILC3 in neonates born to an unmanipulated mother and nursed by a gestation-only colonized mother, both in utero gestation and postnatal nursing by dams that had been colonized during pregnancy were necessary for significant ILC3 induction (Fig. 4A).

These results imply that maternal microbiota-derived compounds are transferred from the mother to the offspring and that this process is increased in the presence of maternal antibodies. We next considered antibody-enhanced retention of bacterial products in the mother and antibody-mediated transfer of bacterial products. The first of these effects was demonstrated by following $^{14}$C elimination from metabolically labeled *E. coli* HA107 in wild-type and antibody-deficient mice. The presence of antibodies significantly increased retention of $^{14}$C-labeled molecules in the mesenteric lymph nodes, spleen, liver, and serum for at least 36 hours compared with antibody-deficient controls (Fig. 4, B and C, and fig. S11, A to D): Microbial molecular exposure of the placenta and the fetus was also enhanced at embryonic day 16 (E16) (Fig. 4, D and E). We also found significantly increased radioactivity originating from maternal microbial molecules in the milk, and from postnatal intestinal mucosa and liver of wild-type pups (Fig. 4, F to I). This shows that maternal antibodies enhance the retention and transmission of microbial molecules, although effects other than direct microbial molecular binding cannot be excluded. To verify that these compounds are really of microbial origin rather than the products of secondary metabolism in the mother, we grew HA107 on [$^{13}$C]glucose so that bacterial compounds became fully labeled with $^{13}$C, as judged by mass spectrometry–shift data. Intestinal $^{13}$C-labeled metabolite levels were equivalent whether or not the mother expressed antibodies (fig. S12); however, after intestinal administration of $^{13}$C-labeled HA107 in C57BL/6 intravenously (i.v.) primed mice, serum contained bacterial metabolites comigrating with IgG that were absent from the serum of antibody-deficient mice (fig. S13 and data file S5). Even if HA107 was only delivered through the intestinal route, which does not induce high-affinity serum IgG (*11*), there was evidence of low-affinity IgG coating of *E. coli* that was absent from serum of untreated germ-free controls or from HA107-treated J$_H$-deficient mice (fig. S14). We therefore concluded that either sterile bacterial fragments or small molecules can potentially be bound to maternal IgG after intestinal exposure.

Given that increases in NKp46$^{+}$ ILC3 and components of the mucosal transcriptome were antibody dependent, whereas F4/80$^{+}$CD11c$^{+}$ iMNCs were induced by gestational colonization even in pups of antibody-deficient dams, we assumed that a number of molecular ligand–receptor systems are driving different aspects of neonatal adaptation in response to the maternal microbiota. Toll-like receptor ligand signaling was not essential for the effect (fig. S15, A and B). There was an extensive range of bacterial-derived ($^{13}$C-labeled) molecules passed from the mother to the offspring (Fig. 5A and fig. S16), some of which also reached neonatal tissues (fig. S16). These

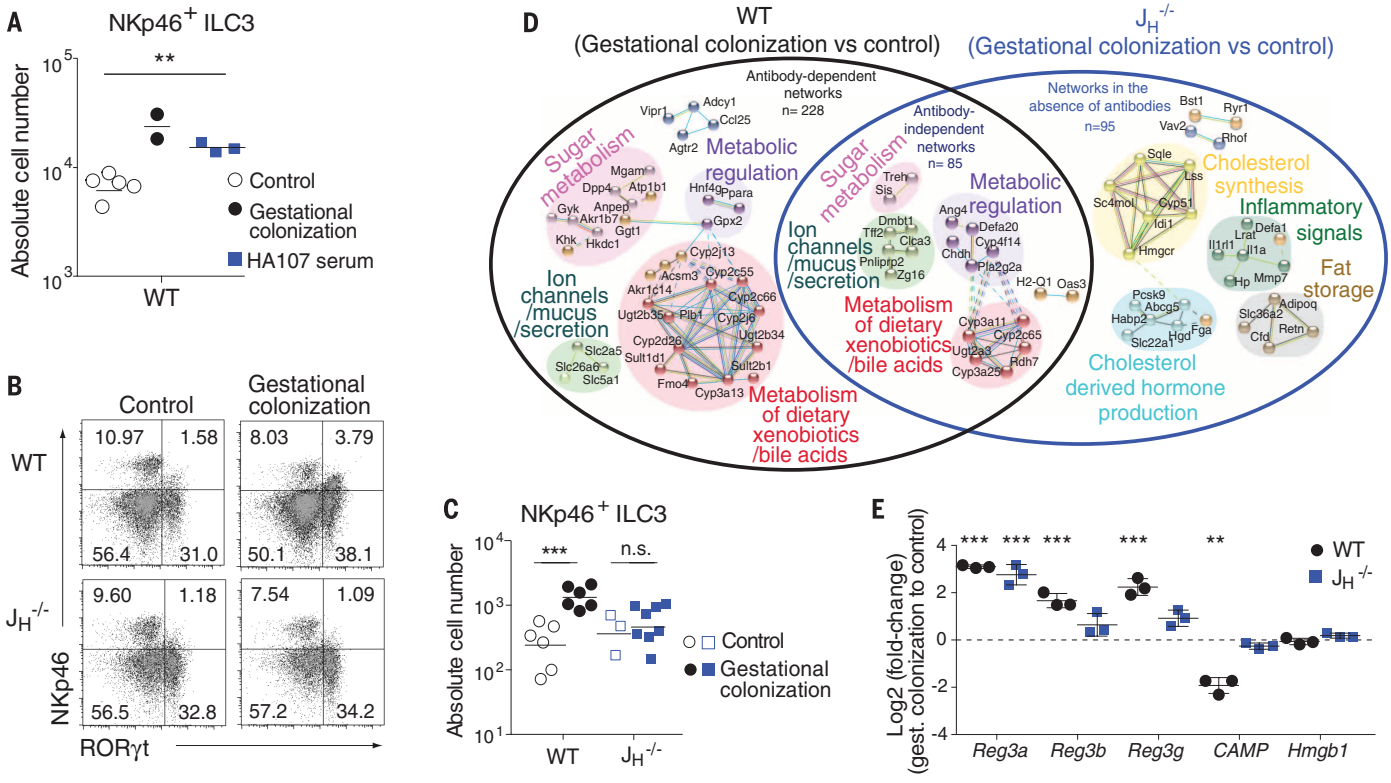



**Fig. 3. Sufficiency of serum transfer and requirement for maternal antibodies for gestational colonization effects.** (**A**) Pregnant germ-free C57BL/6 dams were transiently colonized (gestational colonization), left germ-free (control), or injected i.v. with serum from a germ-free donor previously gavaged with *E. coli* HA107 (HA107 serum). Total Lin$^{-}$RORγt$^{+}$NKp46$^{+}$ ILC3 (geometric mean, $n \geq 2$) in d14 offspring small intestine. (**B** to **E**) Germ-free C57BL/6 (WT, wild type) or J$_H^{-/-}$ dams were colonized with *E. coli* HA107 during pregnancy (gestational colonization) or kept germ-free (control). (B) Representative flow cytometry dot plots showing Lin$^{-}$RORγt$^{+}$NKp46$^{+}$ ILC3 in d14 small intestine. (C) Total numbers (geometric mean, $n \geq 3$) of Lin$^{-}$RORγt$^{+}$NKp46$^{+}$ ILC3 in d14 small intestine. (D and E) RNA-Seq of d14 distal small intestinal RNA in offspring of J$_H^{-/-}$ and wild-type dams ($n = 3$ per group). (D) STRING analysis comparing genes significantly enriched after gestational colonization versus germ-free in either WT (black circle) or J$_H^{-/-}$ (blue circle) strains. Total number of differentially regulated genes are shown. (E) Fold-change of expression of indicated genes in offspring from gestationally colonized compared to control mothers in WT or J$_H^{-/-}$ strains (***padj < 0.001, see also data files S2 and S3). Data are representative of two (A) and three (B and C) independent experiments. (A and C) $^{**}P \leq 0.01$; $^{***}P \leq 0.001$.

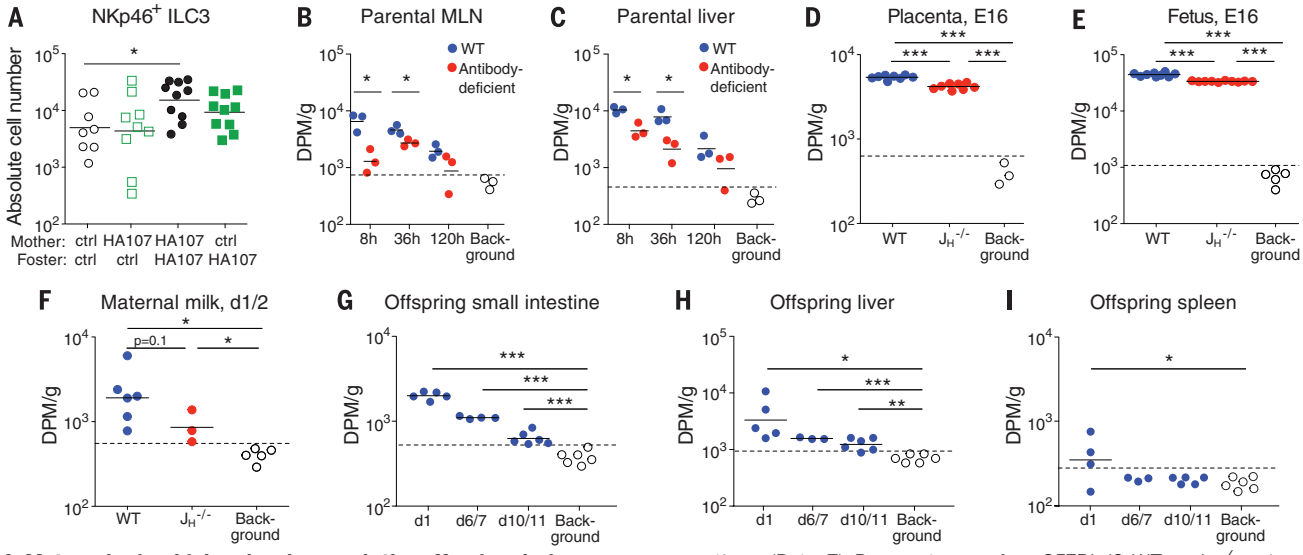
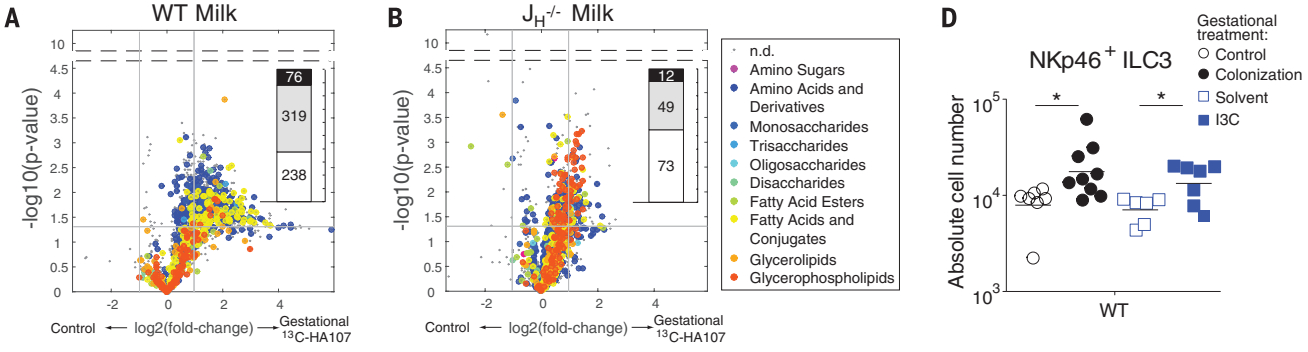



**Fig. 4. Maternal microbial molecules reach the offspring during pregnancy and after birth.** (**A**) Pregnant germ-free C57BL/6 mice were colonized with *E. coli* HA107 or germ-free (ctrl). Half of each litter was swapped to another group for fostering at birth. Total numbers (geometric mean, $n \geq 8$) of Lin$^-$RORγt$^+$NKp46$^+$ ILC3 in the offspring small intestine on postnatal day 14. (**B** and **C**) Adult germ-free WT or *Rag1*$^{-/-}$ (antibody-deficient) mice received three gavages of $10^{10}$ colony-forming units (CFU) of unlabeled *E. coli* HA107 and one gavage of $10^{10}$ CFU of $^{14}$C-labeled *E. coli* HA107. Radioactivity in the indicated tissues of WT and *Rag1*$^{-/-}$ adults was monitored over time. (**D** to **F**) Pregnant germ-free C57BL/6 WT or $J_H^{-/-}$ mice were gavaged with $10^{10}$ CFU of $^{14}$C-labeled *E. coli* HA107 on E14. Placental or fetal tissues at E16 (D and E) or milk at d1/2 after birth (F) from WT or $J_H^{-/-}$ mice was analyzed for radioactivity. (**G** to **I**) Postnatal tissues from WT offspring were analyzed for persistence of transferred radioactive maternal microbial products. Geometric means are shown. Open circles show background scintillation in offspring from nongavaged mice (B to I). Results are representative of three (A) or two (D to I) independent experiments. *$P \leq 0.05$; **$P \leq 0.01$; ***$P \leq 0.001$.




**C**

| Tissue | Compound | Sum formula | WT | | $J_H^{-/-}$ | |
|---|---|---|---|---|---|---|
| | | | fold-change | p-value | fold-change | p-value |
| Milk | Kynurenine | [+10] C10H12N2O3 | 7.807 | 0.0325 | 2.529 | > 0.05 |
| | Indolelactic acid | [+11] C11H11NO3 | 6.790 | 0.0341 | n.d. | |
| | 5-Hydroxy-L-tryptophan | [+11] C11H12N2O3 | 5.248 | 0.0308 | 1.791 | > 0.05 |
| | Hydroxykynurenamine | [+9] C9H12N2O2 | 4.973 | 0.0278 | 0.974 | > 0.05 |
| | Hydroxykynurenine | [+10] C10H12N2O4 | 4.539 | 0.0406 | 1.457 | > 0.05 |
| | 5-Methoxytryptamine | [+11] C11H14N2O | 4.181 | 0.0380 | 1.190 | > 0.05 |
| | 5-Methoxytryptophol | [+11] C11H13NO2 | 3.808 | 0.0109 | 1.235 | > 0.05 |
| | Indole-5,6-quinone | [+8] C8H5NO2 | 2.024 | 0.0019 | 1.307 | 0.0057 |
| Neonatal liver | Hydroxykynurenine | [+10] C10H12N2O4 | 2.394 | < 0.0001 | 1.679 | 0.0015 |
| Neonatal spleen | Hydroxykynurenine | [+10] C10H12N2O4 | 2.754 | < 0.0001 | 1.656 | 0.0015 |

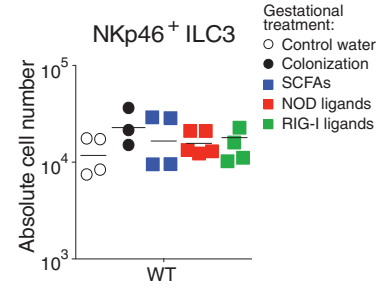



**Fig. 5. Profiles of maternal microbial molecules shaping the neonatal immune system.** (**A** to **C**) Pregnant germ-free wild-type or $J_H^{-/-}$ mice were gavaged on E10 and E12 with unlabeled *E. coli* HA107, and on E15 and E16 with $^{13}$C-labeled *E. coli* HA107. Maternal milk (gestationally colonized, $n = 6$ to 8; germ-free control, $n = 2$) was analyzed by mass spectrometry. (A and B) Volcano plots of fold-change analysis between milk from treated and untreated WT (A) and $J_H^{-/-}$ (B) dams. Metabolite compound classes are color-coded. Inset histogram: percentage $^{13}$C labeling for each significantly altered compound (fold-change ≥ 2; $P \leq 0.05$): unlabeled (white), ≥25% labeled (gray), 100% labeled (black). A total of 395 potentially $^{13}$C-labeled compounds were significantly enriched in the milk of WT dams. (C) Fully labeled metabolites of the AhR ligand class present in d1 to d3 milk of WT and $J_H^{-/-}$ females gestationally exposed to $^{13}$C-HA107. See also data file S4. (**D**) Pregnant germ-free C57BL/6 mice were gavaged with indole-3-carbinol (I3C) or solvent, or gestationally colonized. Total numbers of Lin$^-$RORγt$^+$NKp46$^+$ ILC3 in the d14 offspring small intestine (geometric mean, $n \geq 6$). (**E**) Pregnant germ-free C57BL/6 mice were exposed to short-chain fatty acids (SCFAs), NOD1/2 ligands, or RIG-I ligand or gestationally colonized. Total numbers of Lin$^-$RORγt$^+$NKp46$^+$ ILC3 in d14 offspring small intestine (geometric mean, $n \geq 3$). Data are representative of three (D) independent experiments. *$P \leq 0.05$.

bacterial-derived metabolites present in milk or offspring tissues from gestationally colonized mice included natural microbial ligands for the aryl hydrocarbon receptor (AhR) or their precursors (Fig. 5, A to C, and table S4) (*29*). Most of these bacterial metabolites, including the fully labeled AhR ligands (Fig. 5C), were not enriched in the milk of treated $J_H^{-/-}$ mice (Fig. 5, B and C), although these data do not prove that these molecules are necessarily bound to the antibodies for transfer. Because AhR-deficient mice have a compound phenotype (*30*), and strain combination experiments reveal globally nonredundant signaling pathways, we took the approach of treating pregnant germ-free mice with authentic ligands for AhR, short-chain fatty acids, nucleotide-binding oligomerization domain (NOD) ligands and the retinoic acid–inducible gene I (RIG-I) ligand. Of these, only the AhR ligand (indole-3-carbinol, I3C) increased $NKp46^+$ ILC3 in the offspring of the treated mothers (Fig. 5, D and E). This occurred even in the absence of antibodies, although to a significantly lower extent (fig. S17, A and B). Although this shows that early postnatal $NKp46^+$ ILC3 numbers are increased in response to aryl hydrocarbons, antibodies are not essential for the effect provided that a sufficient dose of

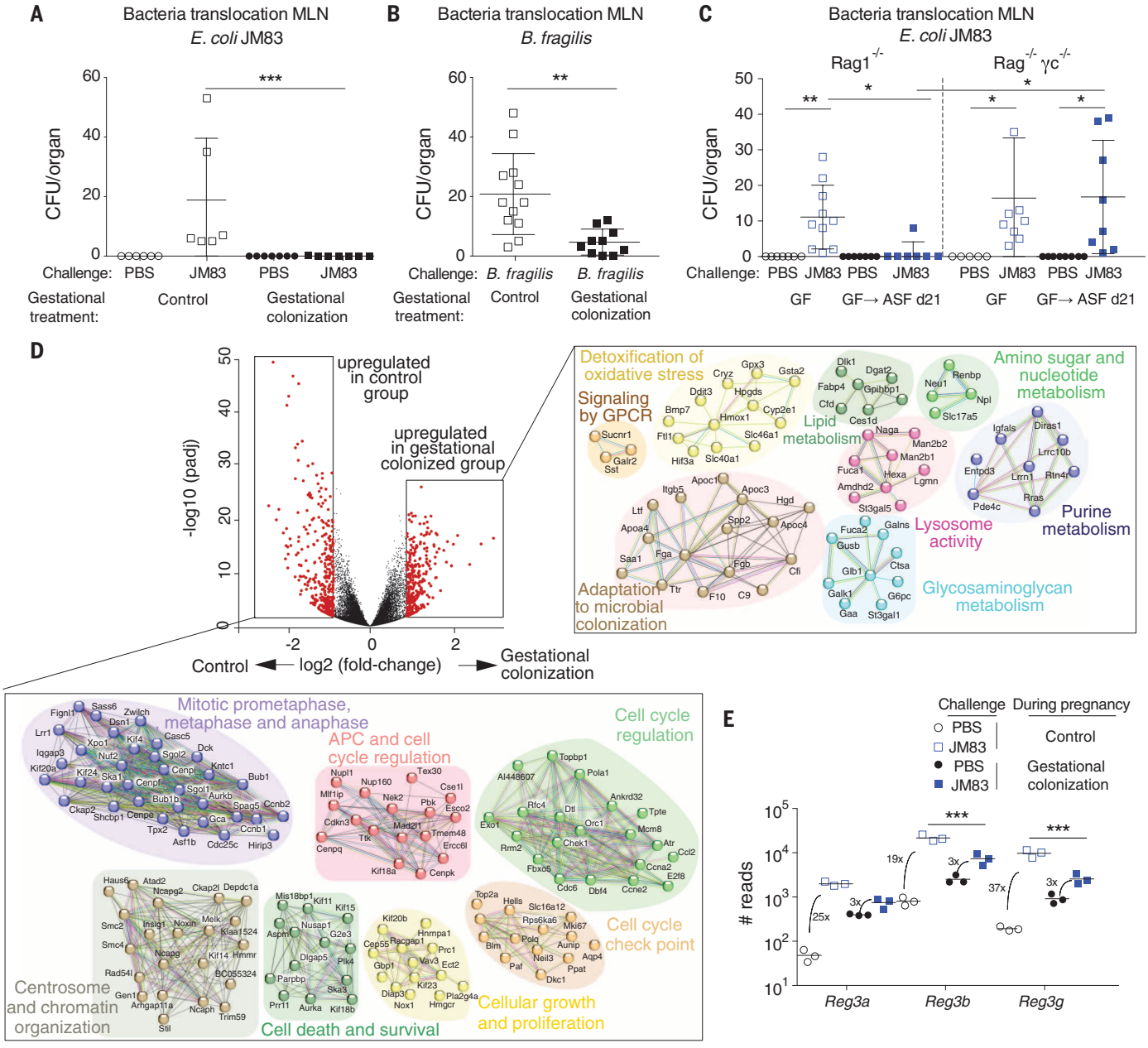



**Fig. 6. Microbial exposure during pregnancy functionally protects the offspring.** (**A**, **B**, **D**, and **E**) Germ-free C57BL/6 dams were gestationally colonized or kept germ-free. (A) Day 14 pups were challenged with $10^5$ CFU of *E. coli* JM83 or phosphate-buffered saline (PBS). Bacterial titers in mesenteric lymph nodes (MLN) were determined at 18 hours ($\bar{x}$ ± SD, $n \geq 5$). (B) Day 14 pups were challenged with $10^{10}$ CFU of *B. fragilis* or PBS. Bacterial titers in MLNs were determined at 18 hours ($\bar{x}$ ± SD, $n \geq 10$). (**C**) Adult germ-free C57BL/6 *Rag1*$^{-/-}$ or *Rag2*$^{-/-}$γc$^{-/-}$ were colonized for 21 days with ASF or kept germ-free before challenge with $10^7$ CFU of *E. coli* JM83 or PBS. Bacterial titers at 18 hours in MLNs are shown ($\bar{x}$ ± SD, $n \geq 5$). (D and E) Day 14 pups were challenged with $10^5$ CFU of *E. coli* JM83 or PBS ($n = 3$ per group) before small intestinal RNA-Seq. 18 hours later. STRING analyses for differentially expressed transcripts (fold-change ≥ 2; padj < 0.01, data file S6) compare challenged pups born to germ-free or gestationally colonized mothers. (E) Read number of indicated genes in *E. coli*– or PBS-challenged offspring (geometric mean, $n = 3$, ***padj < 0.001; see also data files S7 and S8). Data are representative of three (A and C) or two (B) independent experiments. (A to C) *$P \leq 0.05$; **$P \leq 0.01$; ***$P \leq 0.001$.

AhR ligand is transmitted from the mother to her offspring. Indeed, we found that ILC3 increases induced by an endogenous ASF microbiota in adult mice were also antibody independent, presumably because endogenous colonization provides a sufficient dose of bacterial ligands (fig. S17C). We concluded that maternal antibodies assist the transfer of microbial compounds to the offspring, but are not independently required to increase ILC3 numbers. Given the diversity of maternal microbial molecular transfer, it remains probable that other microbial molecular species can also drive early postnatal adaptation.

### Gestational colonization effects on innate immune precursors

The elevated number of intestinal NKp46$^+$ ILC3 and F4/80$^+$CD11c$^+$ iMNCs in the offspring born to gestation-only colonized dams may result from amplified precursor populations or increased proliferation of the mature intestinal population. Neonatal ILC3 precursors (*14*, *31*) were not increased in the liver or intestine of E17 fetuses from gestationally HA107-colonized mice (fig. S18, A to D). We did detect increased proliferative capacity of small intestinal NKp46$^+$ ILC3 isolated from 14-day-old pups born to gestation-only colonized dams (fig. S18, E and F). F4/80$^+$CD11c$^+$ iMNCs stem from CD11b$^+$CX3CR1$^{int}$Ly6C$^+$ monocytes (*32*, *33*), which were significantly increased in the colon lamina propria of 14-day-old pups from gestationally colonized dams (fig. S18, G and H).

### Functional impact of gestational colonization on the early postnatal immune system

To test whether the integrity of the early postnatal intestine to live microbial challenge was improved by gestational colonization, we challenged pups with the replication-competent parent strain of HA107, *E. coli* JM83. Despite equal *E. coli* cecal colonization at 18 hours, only the pups of gestationally colonized mothers or dams treated with the AhR ligand I3C could avoid translocation of JM83 to the mesenteric lymph nodes (Fig. 6A and fig. S19, A and B). Because presence of HA107-specific antibodies might contribute to *E. coli*–primed protection, we confirmed these results by challenge with *Bacteroides fragilis*, where HA107-induced antibodies do not cross-react (Fig. 6B and fig. S19C).

To verify the role of ILC3 in intestinal integrity (*34*), we exploited the fact that ILC3 can be induced in adults independently of B cells and antibodies (fig. S17C and table S5). Comparison of Rag$^{-/-}$ and Rag$^{-/-}\gamma_c^{-/-}$ mice (which lack ILCs as well as B and T cells) showed that ILCs were required to mediate the microbiota-driven protection from bacterial translocation during challenge with JM83 (Fig. 6C).

Systemic immune responsiveness is also likely shaped by gestational colonization, as tumor necrosis factor–α and IL-6 proinflammatory cytokine production was reduced in the pups' splenocytes after intraperitoneal lipopolysaccharide (fig. S20). Because ILC3 are a very minor population in the spleen, the mechanism is likely to be quite distinct from the gestational effects on intestinal function.

These functional readouts of gestational colonization only show some of the potential benefits of maternal microbial molecular exposure in the pups. After challenge with replication-competent *E. coli*, small intestinal RNA-Seq analysis showed expression of antioxidant and lysosomal enzyme networks in the pups of gestation-only colonized dams, whereas control pups had wide-ranging expression signatures for cellular proliferation, cytoskeletal organization, and ribosome biosynthesis (Fig. 6D and fig. S21A). Expression of some genes for antimicrobial peptides induced by gestational colonization also increased further after intestinal bacterial challenge (Fig. 6E and fig. S21B).

## Conclusion

The maternal microbiota prepares the newborn for host-microbial mutualism. This results from microbial molecular transfer because in our experimental system, live microbes are no longer present at birth; we do not detect live microbes in the placenta or the neonate; and the result can be recapitulated with sterile serum transfer. In other words, maternal antibodies not only protect the neonate through pathogen neutralization (*4*, *5*), but also have a more general effect promoting microbial molecular transfer. Short-chain fatty acids from microbes are known to shape the adult immune system (*35*, *36*). We show here that ligands for the AhR, known to drive ILC3 expansion (*37*) and limit adult bacterial translocation (*38*), can be derived from the maternal microbiota and shape the composition and function of early postnatal immunity. Nevertheless, AhR ligands are unlikely to be the only molecular mechanism involved in gestational microbial shaping.

Secretory antibodies in the milk are known to delay the maturation of the early postnatal immune system and determine long-term intestinal microbiota composition (*39*–*41*). Here we show that maternal antibodies also enhance microbial molecular levels in the fetus and the neonate. The molecular constituents of the maternal microbiota are able to ready neonatal innate immunity in time for the tsunami of microbes that successively colonize the intestine (*42*, *43*). Although these studies were focused on benign microbes, the immune morphogenesis driven by the maternal microbiota is likely also to benefit young mammals when they encounter pathogens. Postnatal microbial colonization is a pivotal early event in autonomous host-microbial mutualism. Fortunately, the maternal microbiota and maternal immunity prepare the neonate for its inevitable challenges.

### REFERENCES AND NOTES


1. R. M. Samstein, S. Z. Josefowicz, A. Arvey, P. M. Treuting, A. Y. Rudensky, *Cell* **150**, 29–38 (2012).
2. M. Fulde, M. W. Hornef, *Immunol. Rev.* **260**, 21–34 (2014).
3. H. Renz, P. Brandtzaeg, M. Hornef, *Nat. Rev. Immunol.* **12**, 9–23 (2012).
4. P. Brandtzaeg, *Vaccine* **21**, 3382–3388 (2003).
5. R. M. Zinkernagel, *N. Engl. J. Med.* **345**, 1331–1335 (2001).
6. GBD 2013 Mortality and Causes of Death Collaborators, *Lancet* **385**, 117–171 (2015).
7. T. Olszak *et al.*, *Science* **336**, 489–493 (2012).
8. L. V. Hooper, D. R. Littman, A. J. Macpherson, *Science* **336**, 1268–1273 (2012).
9. A. M. Kabat, N. Srinivasan, K. J. Maloy, *Trends Immunol.* **35**, 507–517 (2014).
10. S. Rakoff-Nahoum *et al.*, *Proc. Natl. Acad. Sci. U.S.A.* **112**, 1929–1936 (2015).
11. S. Hapfelmeier *et al.*, *Science* **328**, 1705–1709 (2010).
12. F. Bäckhed *et al.*, *Cell Host Microbe* **17**, 690–703 (2015).
13. M. J. Bizzarro *et al.*, *J. Pediatr.* **166**, 1193–1199 (2015).
14. S. Sawa *et al.*, *Science* **330**, 665–669 (2010).
15. S. L. Sanos *et al.*, *Nat. Immunol.* **10**, 83–91 (2009).
16. C. Vonarbourg *et al.*, *Immunity* **33**, 736–751 (2010).
17. T. Sano *et al.*, *Cell* **163**, 381–393 (2015).
18. K. Atarashi *et al.*, *Cell* **163**, 367–380 (2015).
19. M. B. Geuking *et al.*, *Immunity* **34**, 794–806 (2011).
20. A. J. Macpherson, N. L. Harris, *Nat. Rev. Immunol.* **4**, 478–485 (2004).
21. K. Smith, K. D. McCoy, A. J. Macpherson, *Semin. Immunol.* **19**, 59–69 (2007).
22. J. Pácha, *Physiol. Rev.* **80**, 1633–1667 (2000).
23. D. Szklarczyk *et al.*, *Nucleic Acids Res.* **43**, D447–D452 (2015).
24. D. Grün *et al.*, *Nature* **525**, 251–255 (2015).
25. M. L. Robinette *et al.*, *Nat. Immunol.* **16**, 306–317 (2015).
26. A. J. Macpherson, T. Uhr, *Science* **303**, 1662–1665 (2004).
27. M. L. Balmer *et al.*, *Sci. Transl. Med.* **6**, 237ra66 (2014).
28. V. Ghetie, E. S. Ward, *Immunol. Today* **18**, 592–598 (1997).
29. C. Esser, A. Rannug, *Pharmacol. Rev.* **67**, 259–279 (2015).
30. B. Stockinger, P. Di Meglio, M. Gialitakis, J. H. Duarte, *Annu. Rev. Immunol.* **32**, 403–432 (2014).
31. M. Cherrier, S. Sawa, G. Eberl, *J. Exp. Med.* **209**, 729–740 (2012).
32. S. Tamoutounour *et al.*, *Eur. J. Immunol.* **42**, 3150–3166 (2012).
33. C. C. Bain *et al.*, *Nat. Immunol.* **15**, 929–937 (2014).
34. G. F. Sonnenberg *et al.*, *Science* **336**, 1321–1325 (2012).
35. N. Arpaia *et al.*, *Nature* **504**, 451–455 (2013).
36. Y. Furusawa *et al.*, *Nature* **504**, 446–450 (2013).
37. E. A. Kiss *et al.*, *Science* **334**, 1561–1565 (2011).
38. G. F. Sonnenberg, D. Artis, *Nat. Med.* **21**, 698–708 (2015).
39. D. R. Kramer, J. J. Cebra, *J. Immunol.* **154**, 2051–2062 (1995).
40. N. L. Harris *et al.*, *J. Immunol.* **177**, 6256–6262 (2006).
41. E. W. Rogier *et al.*, *Proc. Natl. Acad. Sci. U.S.A.* **111**, 3074–3079 (2014).
42. R. I. Mackie, A. Sghir, H. R. Gaskins, *Am. J. Clin. Nutr.* **69**, 1035S–1045S (1999).
43. Y. R. Nobel *et al.*, *Nat. Commun.* **6**, 7486 (2015).



### ACKNOWLEDGEMENTS

We thank W.-D. Hardt, C. Mueller, and D. Candinas for critical input and support. J. Limenitakis and I. Keller helped with bioinformatic analyses. The data presented in this manuscript are tabulated in the main paper and in the supplementary materials; sequencing data are available via www.ebi.ac.uk/ena/data/view/PRJEB12398. *E. coli* HA107 is available from A.J.M. under a material transfer agreement with the University of Bern. The Clean Mouse Facility is supported by the Genaxen Foundation, Inselspital and the University of Bern. This work was funded by the Swiss National Science Foundation (SNSF 310030B_160262, SNF Sinergia CRSII3_136286, and SNSF Sinergia CRSII3_154414) to A.J.M. K.D.M is supported by a grant from the SNSF (SNSF310030_134902) and the European Research Council (ERC, FP/2007-2013) Agreement no. 281785. S.C.G.-V. was funded by a Marie Curie Intra-European Fellowship (FP7-PEOPLE-2013-IEF Project No. 627206). S.H. was funded by SNSF grant 310030_138452 and the ERC (FP/2007-2013) Agreement no. 281904. The authors have no conflicts of interest.


### SUPPLEMENTARY MATERIALS

www.sciencemag.org/content/351/6279/1296/suppl/DC1
Materials and Methods
Figs. S1 to S21
Tables S1 to S5
References (*44*–*53*)
Data Files S1 to S8

28 August 2015; accepted 22 January 2016
10.1126/science.aad2571

REPORTS

SUPERCONDUCTIVITY

# Observation of superconductivity in hydrogen sulfide from nuclear resonant scattering

Ivan Troyan,[1,2]*† Alexander Gavriliuk,[2,3]† Rudolf Rüffer,[4] Alexander Chumakov,[4,5] Anna Mironovich,[3] Igor Lyubutin,[2] Dmitry Perekalin,[6] Alexander P. Drozdov,[1] Mikhail I. Eremets[1]

**High-temperature superconductivity remains a focus of experimental and theoretical research. Hydrogen sulfide ($H_2S$) has been reported to be superconducting at high pressures and with a high transition temperature. We report on the direct observation of the expulsion of the magnetic field in $H_2S$ compressed to 153 gigapascals. A thin $^{119}Sn$ film placed inside the $H_2S$ sample was used as a sensor of the magnetic field. The magnetic field on the $^{119}Sn$ sensor was monitored by nuclear resonance scattering of synchrotron radiation. Our results demonstrate that an external static magnetic field of about 0.7 tesla is expelled from the volume of $^{119}Sn$ foil as a result of the shielding by the $H_2S$ sample at temperatures between 4.7 K and approximately 140 K, revealing a superconducting state of $H_2S$.**

High-temperature superconductivity at high pressures has been predicted for numerous hydrides (*1*–*7*), including $H_2S$ (*8*, *9*). Recent resistivity and magnetic susceptibility measurements indicate that a superconducting transition occurs in $H_2S$ compressed to between 150 and 190 GPa with a high onset temperature of 203 K (*10*). For an unambiguous identification of the superconducting state, a direct observation of the Meissner effect in an external magnetic field is desirable. However, measurements of the Meissner effect using a superconducting quantum interference device (SQUID) or inductor methods at pressures above 130 GPa are difficult, and experimental results do not allow for a clear interpretation.

Historically, the Meissner effect was defined as the expulsion of the external magnetic field from a superconducting sample as the sample enters the superconducting state with decreasing temperature—that is, upon field cooling (FC) conditions. In our experiment, the sample was first transformed into the superconducting state upon zero field cooling (ZFC), and then the external magnetic field was applied. Upon warming the sample, we monitored the expulsion of the magnetic flux in the diamagnetic shielding mode. Relative to the FC option, the ZFC protocol is a better choice for high-temperature superconductors because this method provides a larger contrast in measurements of the expulsion of the magnetic field (*11*). To detect the expulsion of the magnetic field, we used a magnetic field sensor immersed into the $H_2S$ specimen (Fig. 1). A 2.6-μm-thick foil of tin enriched with the $^{119}Sn$ isotope to 95% was used as the sensor. It was placed in the gasket hole of the diamond anvil cell (DAC) before loading $H_2S$. The sensor monitored the magnetic field via the magnetic interaction at the $^{119}Sn$ nucleus, as detected by nuclear resonance scattering (NRS) of synchrotron radiation (*12*, *13*). The presence of the magnetic field at tin nuclei was identified by quantum beats in the time spectra of NRS (*14*). The resonant character of NRS ensured that we acquired data only from the $^{119}Sn$ sensor, with zero background from the sample environment.

[1]Max-Planck-Institut für Chemie, 55020 Mainz, Germany. [2]Shubnikov Institute of Crystallography, Russian Academy of Sciences, Moscow 119333, Russia. [3]Institute for Nuclear Research, Russian Academy of Sciences, Troitsk, Moscow 142190, Russia. [4]European Synchrotron Radiation Facility, CS40220, F-38043 Grenoble Cedex 9, France. [5]National Research Center "Kurchatov Institute," 123182 Moscow, Russia. [6]A. N. Nesmeyanov Institute of Organoelement Compounds, Russian Academy of Sciences, Moscow 119991, Russia.
*Corresponding author. E-mail: itrojan64@gmail.com
†These authors contributed equally to this work.

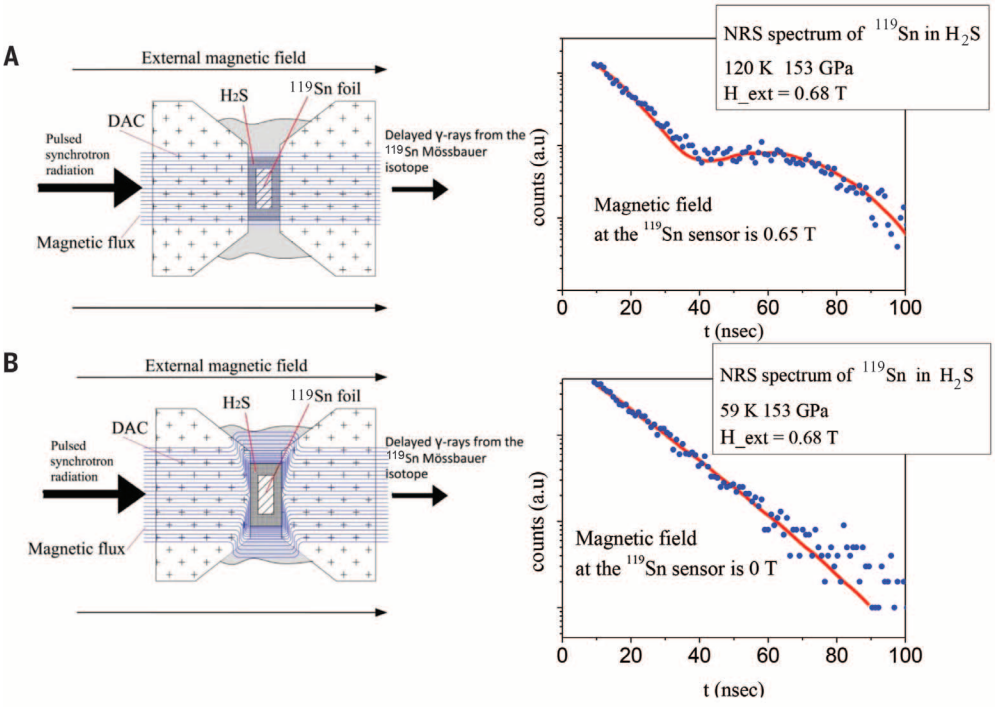



**Fig. 1. Layout of the experiment.** The tin foil, surrounded by compressed hydrogen sulfide, is located in a diamond anvil cell (DAC) at a pressure of about 153 GPa. Pulsed synchrotron radiation excites the nuclei of the tin Mössbauer isotope $^{119}Sn$. The detection system measures the time evolution of radiation emitted by the tin nuclei in the forward direction. (**A**) At $T > T_c$, in the external magnetic field directed along the x-ray beam, the time spectra show quantum beats due to magnetic splitting of tin nuclear levels. (**B**) At $T < T_c$, the tin foil is screened from the external magnetic field by the superconducting hydrogen sulfide, and consequently no splitting of nuclear levels occurs and no magnetic quantum beats are seen in the time spectra. The blue dots are experimental data; the red lines were obtained from fits using the MOTIF software (*17*).

Downloaded from on March 17, 2016

For sample preparation, we followed the procedure described in (*10*). The gaseous $H_2S$ was filled into the DAC through a capillary system in an optical cryostat that enabled in situ pressure changes in the DAC. The filling started after the temperature had been decreased to 197 K. The $^{119}$Sn foil was immersed in liquid $H_2S$ in the hole inside the gasket of the DAC (Fig. 2A). The $H_2S$ sample was identified by Raman scattering (Fig. 2A, bottom). The value of the pressure was measured by Raman scattering from the diamond anvils (*15*, *16*).

The DAC was installed into the cryo-magnet system with exchange gas cooling. To verify that superconductivity occurred in the studied $H_2S$ sample and not in the sensor $^{119}$Sn foil, we conducted the measurements simultaneously with two DACs. One DAC contained the $H_2S$ sample and the $^{119}$Sn sensor foil, and the other contained the reference $^{119}$Sn foil loaded with hydrogen ($H_2$) as a pressure-transmitting medium (Fig. 2C and fig. S1). The samples in both DACs were maintained under the same magnetic field and temperature conditions. The alternating position of each DAC relative to the x-ray beam spot was performed by vertical motion of the sample insert (fig. S1). For a cross-check of data reliability, the measurements were performed using two cryomagnet systems with different directions of the external magnetic field: one for the horizontal field directed along the x-ray beam, and another for the vertical field perpendicular to the x-ray beam. The measuring procedure was as follows: First, the sample was cooled in zero magnetic field down to the lowest temperature of 5 K. Then, a magnetic field of about 0.7 T was applied. The exact values of the external field were derived from the measurements with the reference foil (*11*) as 0.68 T and 0.65 T for the magnetic field perpendicular and parallel to the sample plane, respectively. After that, the NRS spectra were recorded at each temperature point while the temperature was increased.

In the superconducting state of $H_2S$, an external magnetic field applied perpendicular to the sample did not penetrate to the $^{119}$Sn foil (fig. S6). Therefore, the $^{119}$Sn nuclear ground (nuclear spin $I_g$ = 1/2) and excited ($I_{ex}$ = 3/2) levels are not split. The corresponding time spectra show an exponential decay (Fig. 1B). When the superconducting state is partially destroyed, the magnetic field penetrates into the sample volume, and the nuclear levels of $^{119}$Sn become split by the external magnetic field. For split levels, NRS (*14*) involves several radiation components with different energies. Their interference leads to the quantum beats in the time dependence of nuclear decay, and the beat period is inversely proportional to the splitting of the nuclear levels. In the time window available in our measurements, the quantum beats are observed by the appearance of the first beat minimum (Fig. 1A), with the position inversely proportional to the value of magnetic field at the $^{119}$Sn nuclei. The exact data of the observed magnetic fields at tin nuclei were obtained by the theoretical fit to the experimental data points [red line in Fig. 1A; see (*11*, *17*) for details].

Figure 3, A and B, shows the results obtained with an external magnetic field of 0.68 T applied along the x-ray beam (i.e., perpendicular to the sample plane). In the range of 4.7 to 59 K, the NRS spectra show an exponential decay, which demonstrates that the magnetic field is completely expelled from the sensor. The screening of the magnetic field at the $^{119}$Sn sensor is due to the expulsion of the field in a superconducting $H_2S$. At and above 100 K, quantum beats appear, indicating that the external magnetic field starts penetrating into the sensor foil. The penetration of the magnetic field inside the $^{119}$Sn foil increases gradually above 100 K. However, even for the data point at 120 K, the magnetic field on the sensor still does not reach the value of the external magnetic field (Figs. 3A and 4A). This demonstrates that the partial screening still remains up to at least 120 K. The sample is in the mixed superconducting state, and the amount of the samples in the normal state increases with temperature.

The distributions of magnetic flux at different magnetic field directions for a finite-size superconducting sample have been carefully investigated theoretically (*18*–*20*). The calculations show that the effect of strong expulsion of perpendicular magnetic field from the central part of a finite-size type II superconductor could be observed even if the first critical field is lower than the external magnetic field.

In contrast to the case of the $H_2S$ sample, the measurements of the reference sample showed the quantum beats even at the lowest temperatures (Fig. 3B). This confirmed that the reference $^{119}$Sn foil is not in a superconducting state; therefore, the observed expulsion of the magnetic field is associated only with the superconducting $H_2S$.

A similar trend was observed when an external magnetic field of 0.65 T was applied vertically (i.e., parallel to the sample plane) (Fig. 3, C and D), although this case is more complicated because of the less favorable conditions of screening (*11*). For all temperatures, the fit of the NRS spectra for the $H_2S$ sample (Fig. 3C) reveals a superposition of states with the zero and finite

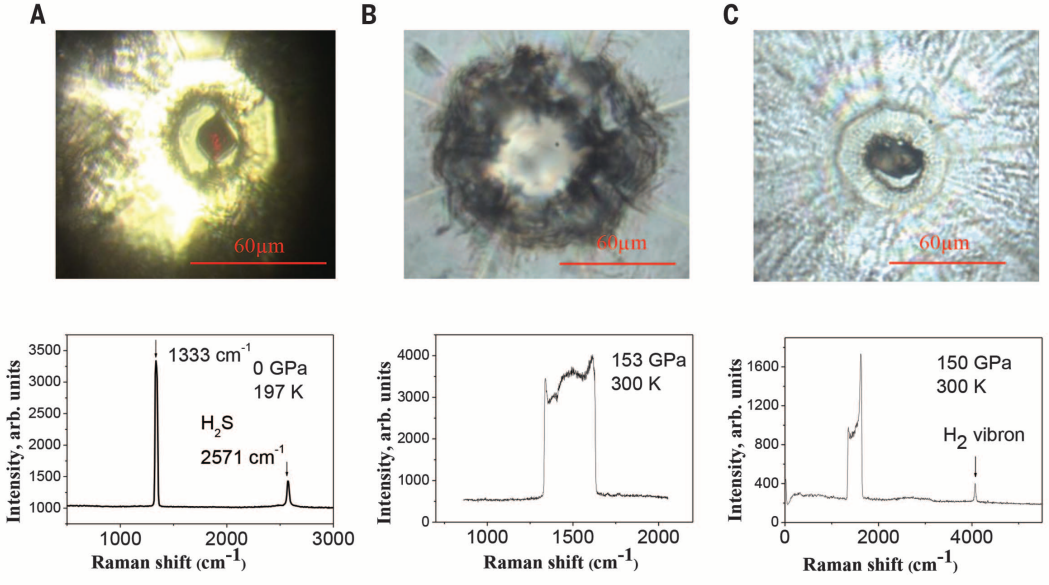



**Fig. 2. Experimental mounts.** (**A**) Top: Tin foil sensor (seen as a black square) immersed in liquefied hydrogen sulfide in the just-clamped DAC at pressures near ambient. The photo in transmitted light was taken in a special cryostat designed for the cryogenic filling DAC. The $H_2S$ sample size is approximately 30 μm. Bottom: The Raman spectrum measured when filling liquefied hydrogen sulfide into DAC. The Raman line of diamond (1333 cm$^{-1}$) and the hydrogen sulfide vibron (2571 cm$^{-1}$) are clearly visible in the spectrum. (**B**) Top: Hydrogen sulfide at pressure of 153 GPa. The central well-reflecting part is the superconducting phase of $H_2S$. The tin foil is located inside the superconducting sample. Bottom: The Raman spectrum from the surface of the diamond anvil taken over the central part is broadened by the pressure in the chamber. The right sharp edge of the spectrum indicates good hydrostatic conditions in the sample. This spectrum was used to measure pressure during the experiment. (**C**) Top: The reference DAC. The central dark object is the tin foil in hydrogen at a pressure of 150 GPa. The $^{119}$Sn sample size is about 20 to 35 μm. Bottom: The Raman spectrum contains the broadened line of the diamond anvils and the hydrogen vibron.

magnetic field. This suggests that the field can partially penetrate into the sensor. In addition, this effect can appear if the $H_2S$ sample is mixed with the material of the gasket at the boundary of the gasket hole, and the sample $H_2S$ is a type II superconductor. This allows the magnetic field parallel to the surface of the anvil to penetrate into the $^{119}Sn$ foil. The value of the average magnetic field inside $H_2S$ as a function of temperature is shown in Fig. 4B. The increase of penetration of the external magnetic field into the sensor foil occurred at about 100 K. This is the same temperature near which the transition was observed with a perpendicular magnetic field (Fig. 4A). Above 100 K, the fraction of the samples in the normal state increased with temperature. However, even for the data point at 145 K, the magnetic field on the sensor still did not reach the value of the external magnetic field (Figs. 3C and 4B). This shows that the partial screening still remains at least up to 145 K. In contrast, the NRS spectra measured for the reference $^{119}Sn$ foil reveal the absence of the superconducting state for all temperatures (Fig. 3D). Additionally, this

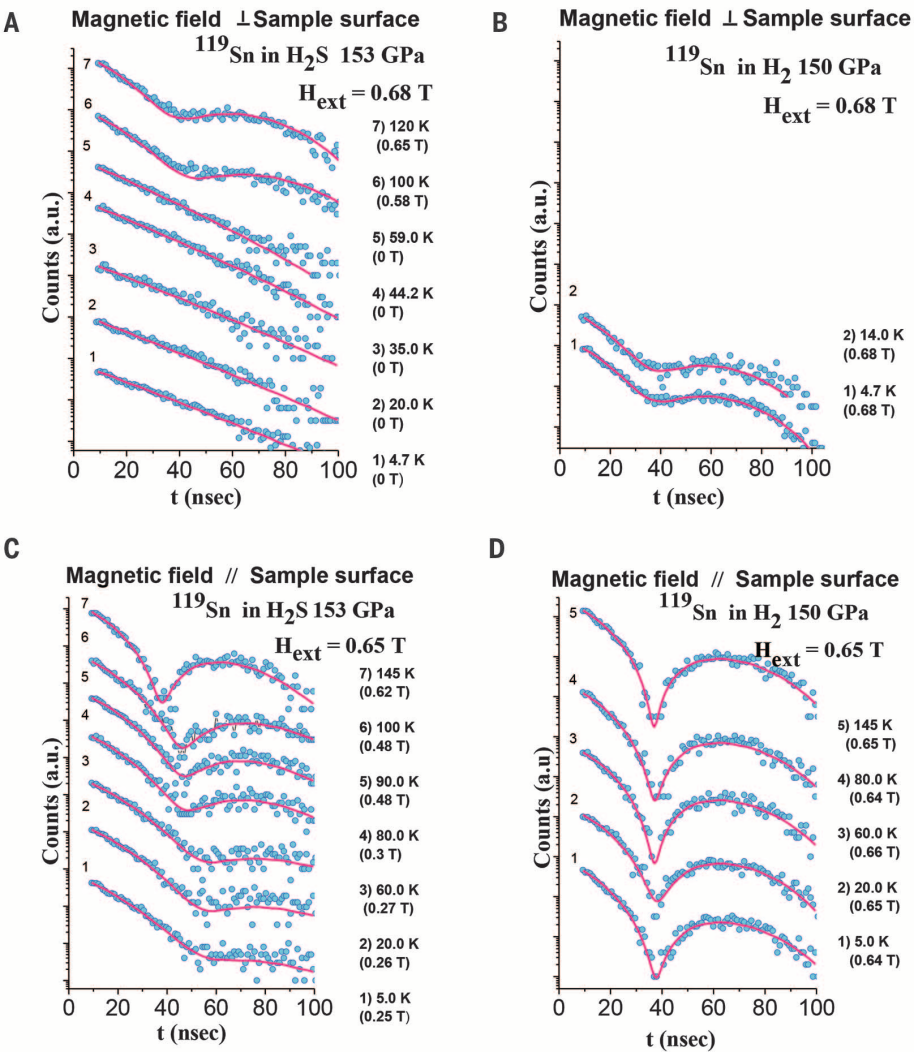



**Fig. 3. Experimental NRS spectra.** The time NRS spectra from $^{119}Sn$ in $H_2S$ at 153 GPa (left panels) and in $H_2$ at 150 GPa (right panels) in an external magnetic field in the horizontal (top) and vertical (bottom) field geometry. Dots (blue) are the experimental data; solid lines (red) are the fits by the MOTIF software (*17*). Temperatures of the samples and the values of magnetic fields at the $^{119}Sn$ nuclear site obtained from the fits are shown to the right of the corresponding NRS spectra. (**A**) Temperature evolution of the NRS spectra from $^{119}Sn$ in $H_2S$ at pressure of 153 GPa and magnetic field of 0.68 T (horizontal) between 4.7 and 120 K. The pure exponential decay shown in curves 1 to 5 indicates that no magnetic field is present at the $^{119}Sn$ nuclear sites. This proves that the external magnetic field cannot penetrate through $H_2S$, hence it is a superconductor (expulsion of the magnetic field). At 100 K, pronounced oscillations (quantum beats) start to develop, revealing the occurrence of a magnetic field at the sensor. (**B**) Temperature evolution of the NRS spectra in the reference sample $^{119}Sn$ in $H_2$ at 150 GPa and magnetic field of 0.68 T (horizontal) at 4.7 and 14 K. The quantum beats reveal the presence of a magnetic field at the sensor. (**C**) Temperature evolution of the NRS spectra of $^{119}Sn$ in $H_2S$ at 153 GPa and magnetic field of 0.65 T (vertical) between 5 and 145 K. As temperature increases, the slowly developing quantum beats indicate the decreasing screening of the external magnetic field by the superconductor. (**D**) Temperature evolution of the NRS spectra of the reference sample $^{119}Sn$ in $H_2$ at 150 GPa and magnetic field of 0.65 T (vertical) between 5 and 145 K. The quantum beats reveal the presence of a magnetic field.

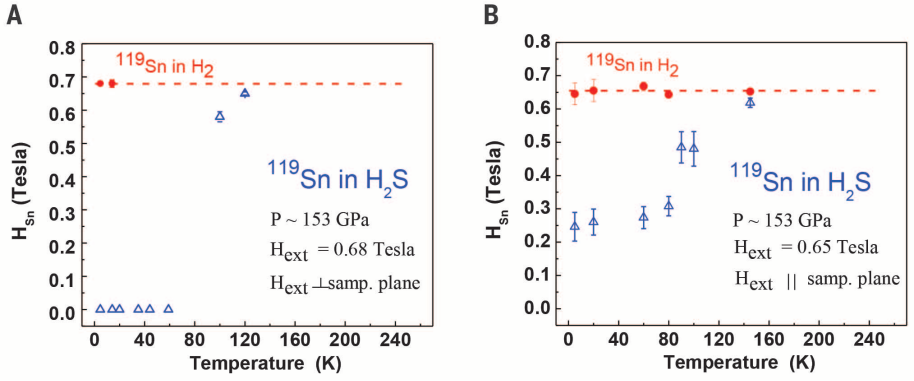



**Fig. 4. Influence of temperature on magnetic field inside $H_2S$.** The temperature dependence of the magnetic field was determined from the NRS spectra of the $^{119}Sn$ sensor inside $H_2S$ at 153 GPa (blue triangles) and the field at the reference sample $^{119}Sn$ in $H_2$ at 150 GPa (red dots). (**A** and **B**) Measurements in the horizontal and vertical geometry of the external magnetic field, respectively. Dashed lines are guides to the eye. Some error bars are smaller than the size of the symbols.

confirms that the observed superconductivity of the studied sample is related entirely to $H_2S$.

Our results demonstrate that the superconducting $H_2S$ sample effectively shields the strong magnetic field of about 0.7 T up to temperatures of 90 to 100 K. The partial shielding of the magnetic field persists up to about 140 K. This confirms that $H_2S$ compressed to 150 GPa is the superconductor with the very high critical parameters. Referring to data given in (*10*), it should be noted that the resistivity measurements rely on the very onset of the current percolation, whereas the magnetic measurements require a somewhat larger amount of the sample to be transformed to the superconducting phase.

## REFERENCES AND NOTES


1. N. W. Ashcroft, *Phys. Rev. Lett.* **92**, 187002 (2004).
2. J. Feng *et al.*, *Phys. Rev. Lett.* **96**, 017006 (2006).
3. G. Gao *et al.*, *Phys. Rev. Lett.* **101**, 107002 (2008).
4. D. Y. Kim, R. H. Scheicher, H. K. Mao, T. W. Kang, R. Ahuja, *Proc. Natl. Acad. Sci. U.S.A.* **107**, 2793–2796 (2010).
5. G. Gao *et al.*, *Proc. Natl. Acad. Sci. U.S.A.* **107**, 1317–1320 (2010).
6. D. Y. Kim, R. H. Scheicher, C. J. Pickard, R. J. Needs, R. Ahuja, *Phys. Rev. Lett.* **107**, 117002 (2011).
7. H. Wang, J. S. Tse, K. Tanaka, T. Iitaka, Y. Ma, *Proc. Natl. Acad. Sci. U.S.A.* **109**, 6463–6466 (2012).
8. D. Duan *et al.*, *Sci. Rep.* **4**, 6968 (2014).
9. Y. Li, J. Hao, H. Liu, Y. Li, Y. Ma, *J. Chem. Phys.* **140**, 174712 (2014).
10. A. P. Drozdov, M. I. Eremets, I. A. Troyan, V. Ksenofontov, S. I. Shylin, *Nature* **525**, 73–76 (2015).
11. See supplementary materials on *Science* Online.
12. I. S. Lyubutin, T. V. Dmitrieva, *JETP Lett.* **21**, 59 (1975).
13. E. Gerdau, H. de Waard, *Nuclear Resonant Scattering of Synchrotron Radiation*, vol. 123–124 of *Hyperfine Interactions* (Springer, 1999), pp. 1–2.
14. J. B. Hastings, D. P. Siddons, U. van Bürck, R. Hollatz, U. Bergmann, *Phys. Rev. Lett.* **66**, 770–773 (1991).
15. N. Dubrovinskaia, L. Dubrovinsky, R. Caracas, M. Hanfland, *Appl. Phys. Lett.* **97**, 251903 (2010).
16. Y. Akahama, H. Kawamura, *J. Phys. Conf. Ser.* **215**, 012195 (2010).
17. Y. V. Shvyd'ko, *Phys. Rev. B* **59**, 9132–9143 (1999).
18. E. H. Brandt, *Phys. Rev. B* **54**, 4246–4264 (1996).
19. E. H. Brandt, *Phys. Rev. B* **58**, 6506–6522 (1998).
20. G. P. Mikitik, E. H. Brandt, M. V. Indenbom, *Phys. Rev. B* **70**, 014520 (2004).


## ACKNOWLEDGMENTS

The high-pressure samples of hydrogen sulfide and hydrogen investigated in this study have been prepared using the techniques and equipment designed and built by M.I.E. and A.P.D. Funding was provided by the European Research Council (ERC Advanced Grant 267777 of M.I.E.) and the Max Planck Institute for Chemistry, Mainz. This work was also supported by Russian Science Foundation grant 14-12-00848 (I.T., A.G., and I.L.), Russian Foundation for Basic Research grant 14-02-00483-a (A.G.), and the Russian Academy of Sciences program "Physics of elementary particles, fundamental nuclear physics and nuclear technologies."

## SUPPLEMENTARY MATERIALS

www.sciencemag.org/content/351/6279/1303/suppl/DC1
Materials and Methods
Supplementary Text
Figs. S1 to S6
References (*21*–*24*)

17 June 2015; accepted 4 January 2016
10.1126/science.aac8176

NANOMATERIALS

# Formation of pseudomorphic nanocages from $Cu_2O$ nanocrystals through anion exchange reactions

**Hsin-Lun Wu, Ryota Sato, Atsushi Yamaguchi, Masato Kimura, Mitsutaka Haruta, Hiroki Kurata, Toshiharu Teranishi***

**The crystal structure of ionic nanocrystals (NCs) is usually controlled through reaction temperature, according to their phase diagram. We show that when ionic NCs with different shapes, but identical crystal structures, were subjected to anion exchange reactions under ambient conditions, pseudomorphic products with different crystal systems were obtained. The shape-dependent anionic framework (surface anion sublattice and stacking pattern) of $Cu_2O$ NCs determined the crystal system of anion-exchanged products of $Cu_xS$ nanocages. This method enabled us to convert a body-centered cubic lattice into either a face-centered cubic or a hexagonally close-packed lattice to form crystallographically unusual, multiply twinned structures. Subsequent cation exchange reactions produced CdS nanocages while preserving the multiply-twinned structures. A high-temperature stable phase such as wurtzite ZnS was also obtained with this method at ambient conditions.**

Chemical conversion of semiconductor nanocrystals (NCs) via ion-exchange reactions can overcome the difficulties associated with controlling the size, shape, chemical composition, and crystal structure in conventional syntheses (*1*–*7*). However, the crystal structure transformation in ion-exchange reactions is still not well understood. When the entire crystal is in a structurally nonequilibrium state in ion-exchange reactions, both the cations and anions are mobile and can induce morphological changes to the thermodynamically more stable shape before reaching the final equilibrium state. For ionic NCs above a critical size, the anion framework remains intact, and the original shape of the parent NCs is retained throughout the cation-exchange reaction (*8*). The retained shape of the parent NCs in ion exchange provides an opportunity to obtain nonequilibrium distinct structures and even new structures of ionic NCs (*9*)—these final structures being known as "pseudomorphs."

We show, using $Cu_2O$ NCs with well-defined shapes as parent NCs (*10*, *11*), a distinctive shape-dependent anionic frameworks–induced crystal phase transition in anion-exchange reaction at ambient conditions. Regular hexahedral (RH) $Cu_2O$ NCs with a cubic phase were converted into RH $Cu_{1.8}S$ nanocages with a cubic phase, whereas rhombic dodecahedral (RD) $Cu_2O$ NCs with a cubic phase were converted into RD $Cu_{1.75}S$ nanocages with a triclinic phase (*12*) after partial anion-exchange reaction. The $Cu_2O$ NCs have a body-centered cubic (bcc) anion sublattice, but they were converted into the $Cu_xS$ nanocages with either a face-centered cubic (fcc) or a hexagonally close-packed (hcp) anion sublattice.

Institute for Chemical Research, Kyoto University, Gokasho, Uji, Kyoto 611-0011, Japan.
*Corresponding author. E-mail: teranisi@scl.kyoto-u.ac.jp

Furthermore, shape retention of the $Cu_xS$ pseudomorphic nanocages after the $Cu_2O$ NCs provided new multiply twinned structures consisting of unusual connections between crystallographically independent walls. Subsequent cation-exchange reactions performed on RH and RD $Cu_xS$ nanocages produced RH and RD CdS nanocages with a zincblende and a wurtzite phase, respectively, and preserved the pseudomorphic structures. The wurtzite ZnS nanocages, which formed under ambient conditions, are much more desirable for their optical properties than are the zincblende phases (*13*, *14*), which are usually synthesized at ~600°C (*15*).

Scanning electron microscopy (SEM) images, x-ray diffraction (XRD), and ultraviolet–visible–near infrared (UV-Vis-NIR) spectra of the $Cu_2O$ NCs and the $Cu_xS$ and CdS pseudomorphic nanocages are shown in Fig. 1. All reactions were performed under ambient conditions (*16*). Partial anion-exchange reactions of the RH and RD $Cu_2O$ NCs (Fig. 1, A to C) with $Na_2S$ gave cubic RH $Cu_{1.8}S$ and triclinic RD $Cu_{1.75}S$ nanocages (Fig. 1, D and E). The characteristic UV-Vis-NIR spectra of the products (Fig. 1F) confirmed that they were indeed $Cu_xS$ nanocages (*17*). Subsequent cation exchange of RH $Cu_{1.8}S$ nanocages with $Cd^{2+}$ generated the zincblende RH CdS as majority (Fig. 1, G and H). More accurately, the XRD pattern (Fig. 1H) reflects the large amount of twinning in the RH nanocages, and heavily twinned fcc shows up as hcp. On the other hand, the cation exchange of RD $Cu_{1.75}S$ nanocages with $Cd^{2+}$ generated the wurtzite RD CdS nanocages. The UV-Vis-NIR spectra displayed the characteristic semiconducting CdS phase (Fig. 1I). Low-magnification SEM images of the $Cu_xS$ and CdS nanocages are presented in fig. S1.

The overall phase transitions starting from the RH and RD $Cu_2O$ NCs are illustrated schematically in Fig. 2. The RH $Cu_2O$ NCs, which were

Downloaded from on March 17, 2016

enclosed by six {100} facets (anionic framework: $C_4$ symmetry, AB stacking), were converted into RH $Cu_{1.8}S$ nanocages with a cubic phase ($C_4$ symmetry, AB stacking), whereas the RD $Cu_2O$ NCs, which were enclosed by twelve {110} facets ($C_2$ symmetry, AB stacking), were converted into RD $Cu_{1.75}S$ nanocages with a triclinic phase ($C_2$ symmetry, ABA′B′ stacking) (*12*). Subsequent cation-exchange reactions, in which the $Cu^+$ was replaced with $Cd^{2+}$, predominantly conserved the anionic frameworks (*5*, *6*, *18*); that is, the RH $Cu_{1.8}S$ nanocages produced RH CdS nanocages with a cubic zincblende phase ($C_4$ symmetry, AB stacking), and the $Cu_{1.75}S$ nanocages produced RD CdS nanocages with a hexagonal wurtzite phase ($C_2$ symmetry, AB stacking).

A detailed examination of the nanocage crystal structures by means of transmission electron microscopy (TEM) revealed that the walls consisted of lattice structures with unusual directions and distinctive interwall crystallographic connections. Images of RH $Cu_{1.8}S$ and CdS nanocages are shown in Fig. 3, A and G, respectively, and the corresponding nanobeam diffraction (NBD) patterns from the center of single RH $Cu_{1.8}S$ and CdS nanocages are shown in Fig. 3, B and H, respectively. The high-resolution TEM (HR-TEM) image (Fig. 3A, white square region) shown in Fig. 3C revealed lattice fringe spacing of 0.28 and 0.19 nm, corresponding to the (200) and (220) lattice planes of a cubic phase, respectively, indicating that the faces of the walls were the (001) planes. The HR-TEM image of the walls of the $Cu_{1.8}S$ nanocages revealed a cubic phase with a [110] direction to the edge and a [100] direction to the corner (Fig. 3A, yellow arrow). Crystal planes in RH nanostructures with a cubic phase normally displayed a [110] direction parallel to the diagonal line and a [100] direction parallel to the edge line.

Because of the pseudomorphic transformation in anion exchange reaction, the walls in our RH $Cu_{1.8}S$ nanocages are inclined 45° to commonly observed lattice planes (*19*). The crystal structure of the walls of the nanostructures viewed over the faces and the sides is shown in Fig. 4. The anion sublattice viewed over the face of the RH $Cu_2O$ NC (Fig. 4A) has a bcc structure, whereas the anion sublattice of the RH $Cu_{1.8}S$ nanocage (Fig. 4B) has an fcc structure. Both unit cells displayed a similar anionic framework, but the $Cu_{1.8}S$ unit cell was rotated 45° with respect to the $Cu_2O$ unit cell. The rotation observed in the unit cell of the RH $Cu_{1.8}S$ nanocages was caused by the similarity of the surface anion sublattice symmetry and stacking way to those of the RH $Cu_2O$ NCs.

To understand the crystallographic relation between the neighboring walls of the nanocages, we took the fast Fourier transform (FFT) patterns from the face and side of the wall (Fig. 4B). As discussed previously, the face of the RH $Cu_{1.8}S$ nanocage was assigned to the (001) plane, and

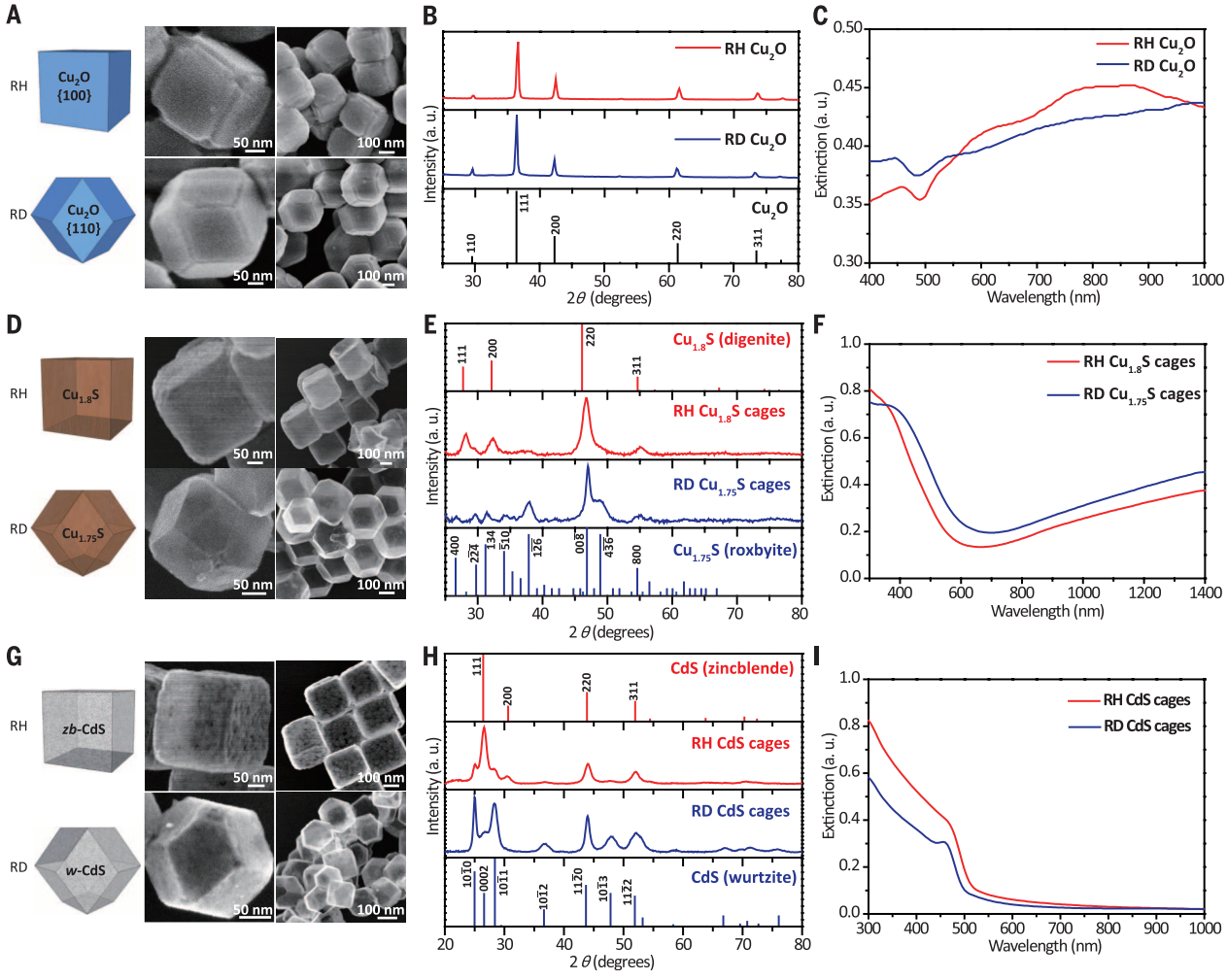



**Fig. 1. Characterization and optical properties of the nanostructures.** (**A**) SEM images, (**B**) XRD patterns, and (**C**) UV-Vis-NIR spectra of the RH and RD $Cu_2O$ NCs. The UV-Vis-NIR spectra show the characteristic extinction feature of $Cu_2O$ NCs, in which a band-gap absorption band was observed at ~450 nm (*10*). (**D**) SEM images, (**E**) XRD patterns, and (**F**) UV-Vis-NIR spectra of the $Cu_xS$ pseudomorphic nanocages obtained through partially sulfiding $Cu_2O$ NCs with $Na_2S$ solution to form $Cu_2O$-$Cu_xS$ core-shell ($Cu_2O$@$Cu_xS$) NCs, followed by etching the interior $Cu_2O$ cores with HCl solution. (**G**) SEM images, (**H**) XRD patterns, and (**I**) UV-Vis-NIR spectra of the CdS pseudomorphic nanocages obtained through further cation exchange of the $Cu_xS$ nanocages with $Cd^{2+}$ (*8*). The UV-Vis-NIR spectra show the clear band-gap absorption bands characteristic of CdS nanocages at ~460 nm (*22*).

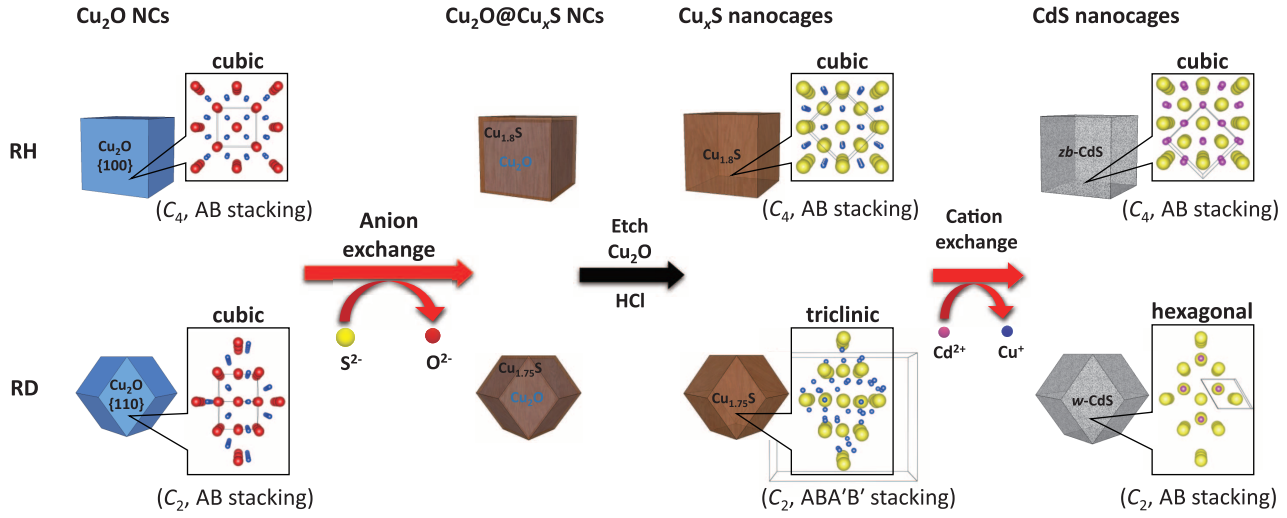



**Fig. 2. Schematic illustration for phase transitions induced by the shape-dependent anionic frameworks in anion-exchange reactions and the subsequent cation-exchange reactions.** The crystal structures are projections of the crystal lattice on the faces. Information in parentheses below each structure stands for the symmetry and the stacking way of surface anion sublattices.

the [100] and [110] directions were parallel to the diagonal and edge lines, respectively. The FFT pattern of the side revealed that the wall was formed by stacking the (100) planes in the [100] direction and that the wall sides were composed of stacked (110) planes in the [110] direction. Thus, the (001) face of a single wall was parallel to the (011) side of the neighboring wall, meaning that each wall was crystallographically independent. Thus, single-crystal $Cu_2O$ was converted into multiply twinned $Cu_{1.8}S$ through the anion-exchange reaction. The speculated connections between the neighboring walls are depicted schematically in fig. S2A, in which the (001) and (011) faces are connected through a coherent junction with similarly arranged anions. Subsequent cation exchange reaction, in which $Cd^{2+}$ replaced $Cu^{+}$, preserved the unusual directions and distinctive interwall crystallographic connections. The HR-TEM image of the RH CdS nanocage revealed lattice fringe spacing of 0.28 and 0.22 nm, corresponding to (200) and (220) lattice planes of zincblende CdS, respectively (Fig. 3I). The FFT patterns of the face and side of the walls of the RH CdS nanocage (Fig. 4C) were similar to those of the RH $Cu_{1.8}S$ nanocage. The unusual rotation of the unit cell was maintained, suggesting that the RH CdS nanocages had a similar interwall connection (fig. S2A). Moreover, the sides of the walls displayed a similar lattice stacking way (AB) after the ion-exchange reactions (Fig. 4, A to C).

Details of the structural transformations that occurred to the RD $Cu_2O$ NCs after the ion exchange were revealed through TEM images; those for RD $Cu_{1.75}S$ and CdS nanocages are shown in Fig. 3, D and J, respectively. The corresponding NBD patterns from the center of single RD $Cu_{1.75}S$ and CdS nanocages are shown in Fig. 3, E and K, respectively. The HR-TEM image (Fig. 3D, square region) shown in Fig. 3F revealed lattice fringe spacing of 0.33 and 0.19 nm, corresponding to the (400) and $(00\bar{8})$ lattice planes of a triclinic

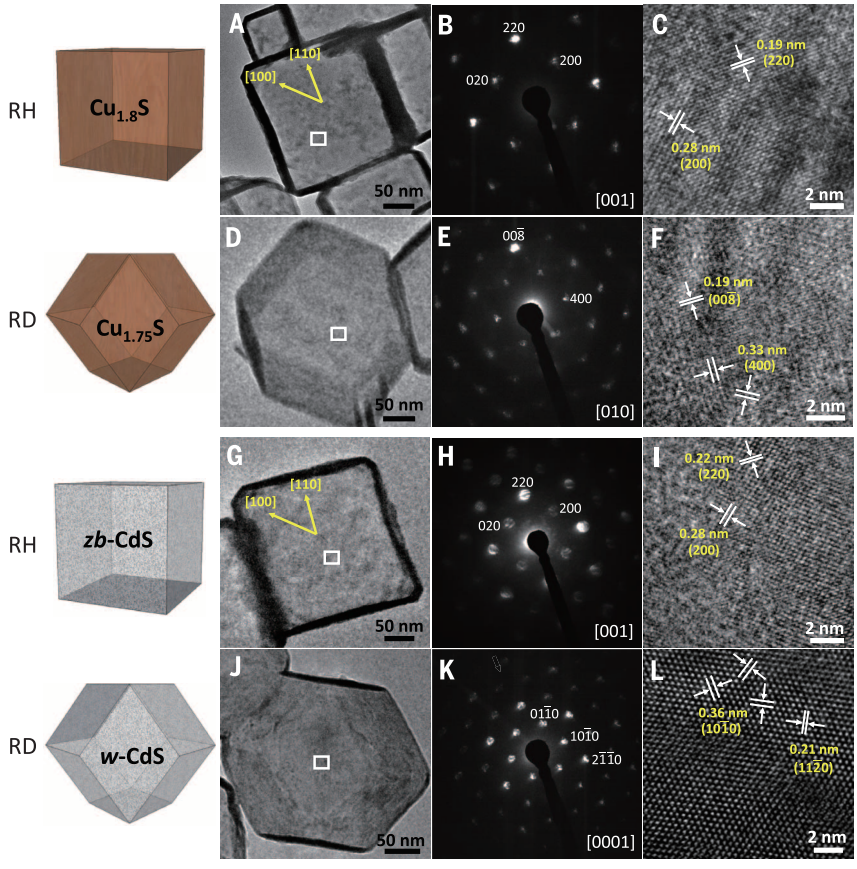



**Fig. 3. Crystal structure analyses of the walls of nanocages.** (**A** and **G**) TEM images and (**B** and **H**) the corresponding NBD patterns viewed over the {200} facets of a single-RH $Cu_{1.8}S$ and CdS nanocages, respectively. The NBD spot patterns indicate that the walls of the nanocages are single-crystalline. (**C** and **I**) HR-TEM images of the square regions of the RH $Cu_{1.8}S$ nanocage in (A) and the RH CdS nanocage in (G). (**D** and **J**) TEM images and (**E** and **K**) the corresponding NBD patterns viewed over the {040} and {0002} facets of a single-RD $Cu_{1.75}S$ and CdS nanocages, respectively. The NBD spot patterns also indicate that the walls of the nanocages are single-crystalline, as observed in RH nanocages. (**F** and **L**) HR-TEM images of the square regions of the RD $Cu_{1.8}S$ nanocage in (D) and the RD CdS nanocage in (J).

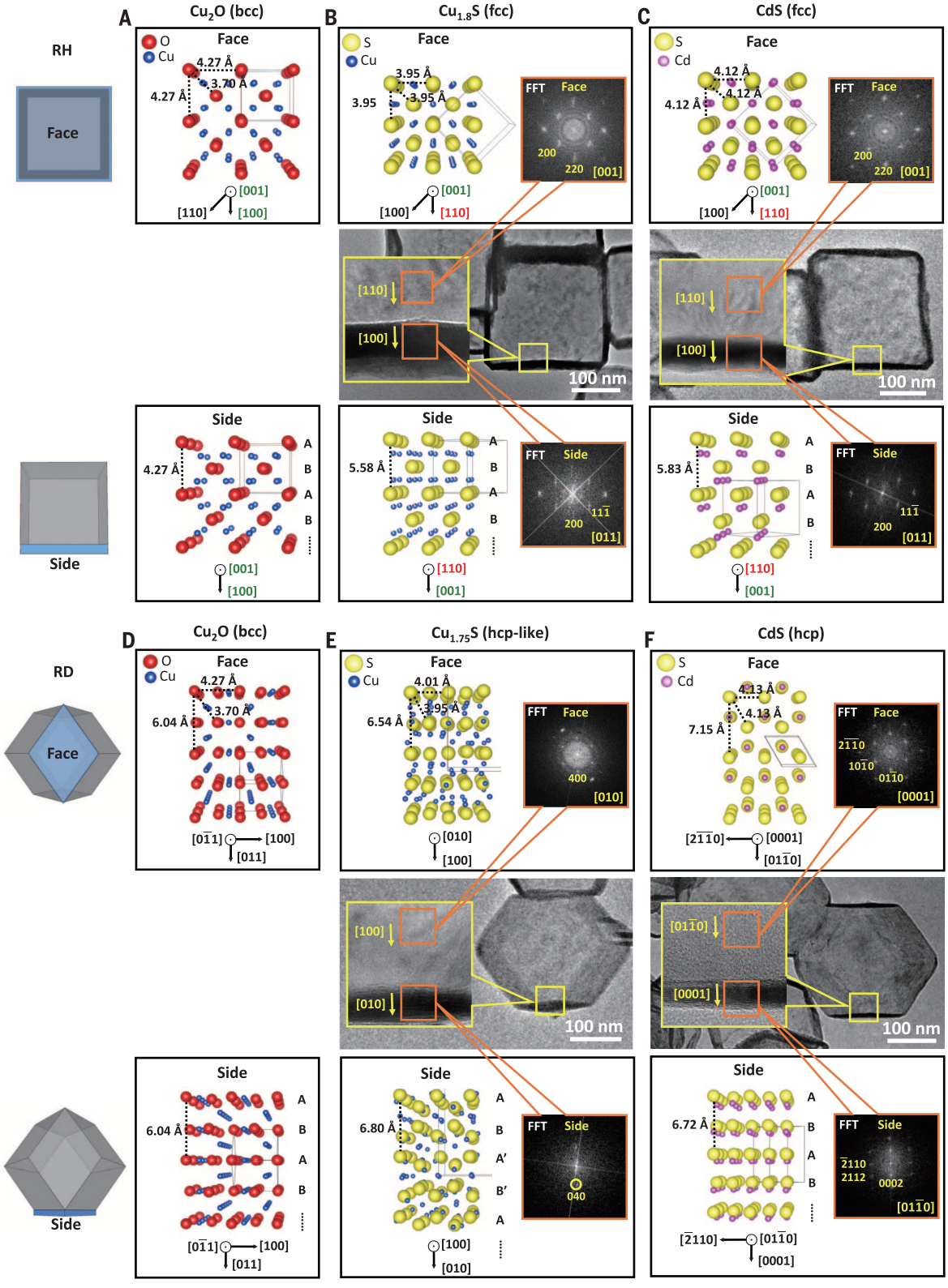



**Fig. 4. Comparison of surface anion sublattice symmetry and stacking way of nanostructures.** (**A** to **C**) The anion sublattices viewed over the faces of (A) the RH $Cu_2O$ NC (bcc structure), with a [100] direction to the edge and a [110] direction to the corner of the wall; (B) the RH $Cu_{1.8}S$ nanocage (fcc structure), with a [110] direction to the edge and a [100] direction to the corner of the wall; and (C) the RH CdS nanocage (fcc structure), with a [110] direction to the edge and a [100] direction to the corner of the wall. The sides of the walls showed the similar lattice stacking way (AB) after a sequence of the ion-exchange reactions. (**D** to **F**) The anion sublattices viewed over the faces of (D) the RD $Cu_2O$ NC (bcc structure), with [011] direction to a (011) plane; (E) the RD $Cu_{1.75}S$ nanocage (hcp-like structure), with [100] direction to a (010) plane; and (F) the RD CdS nanocage (hcp structure), with $[01\bar{1}0]$ direction to a (0001) plane. The lattice stacking way (AB) of the walls is also unchanged after a sequence of the ion-exchange reactions.

phase, respectively (*12*), indicating that the faces of the walls were the (010) planes. The anion sublattice viewed over the face of the RD $Cu_2O$ NC displayed a twofold symmetry (AB stacking), with a bcc structure (Fig. 4D). The anion sublattice of the (010) face of the RD $Cu_{1.75}S$ nanocage displayed a superimposed pseudohexagonal symmetry—more precisely, $C_2$ symmetry (ABA′B′ stacking), with an hcp-like structure (Fig. 4E).

The similarities between the surface anion sublattice symmetries and stacking way indicated that it was possible to transform the crystal structure from a cubic $Cu_2O$ to triclinic $Cu_{1.75}S$ structure via anion-exchange reaction while maintaining the shape. The pseudohexagonal symmetry of the anion sublattice in $Cu_{1.75}S$ was similar to that of a hexagonally symmetrical (0001) plane (AB stacking) of a wurtzite structure. Thus, RD CdS nanocages with a wurtzite structure could be formed by further cation-exchange reaction of the RD $Cu_{1.75}S$ nanocages even at ambient temperature (Fig. 4F). The HR-TEM image of the RD CdS nanocage (Fig. 3L) displayed lattice fringe spacing of 0.36 and 0.21 nm, corresponding to $(10\bar{1}0)$ and $(11\bar{2}0)$ lattice planes of a wurtzite CdS nanocage, respectively. The crystallographic relation between the neighboring walls of the RD nanocages was determined from the FFT patterns of the faces and sides of the walls (Fig. 4, E and F). Similar to the RH nanocages, the RD nanocages were also composed of crystallographically independent or polycrystalline walls, induced by the pseudomorphic transformation in anion-exchange reaction. The connection between neighboring walls is depicted schematically in fig. S2B. The lattice stacking way (AB) of the walls was also unchanged after the ion-exchange reactions (Fig. 4, D to F). Although the anion sublattices of the $Cu_{1.75}S$ nanocage in layer A′ and B′ are slightly distorted (fig. S3), the symmetry of the anion sublattices still closely resembles the layers A and B. In addition, the volumes of the ion-exchanged products expanded because of the larger radii of $S^{2-}$ and $Cd^{2+}$ (table S1) (*20*).

One of the advantages of this phase-transition method is to selectively obtain polymorphic crystal phases at ambient conditions. The phase transition from a zincblende to wurtzite structure of ZnS takes place at 1020°C. With this phase transition method, ZnS with a zincblende and a wurtzite phase could both be obtained, even at room temperature. We conducted the pseudomorphic transformation of the RH and RD $Cu_2O$ to $Cu_xS$ and further to ZnS under ambient conditions. The SEM and TEM images of the resulting ZnS nanocages are shown in fig. S4A. Similar to the case of the CdS nanocages, subsequent cation exchange reactions of RH $Cu_{1.8}S$ and RD $Cu_{1.75}S$ nanocages with $Zn^{2+}$ are likely to give the zincblende RH ZnS and the wurtzite RD ZnS nanocages, respectively (fig. S4B). The UV-Vis-NIR spectra displayed the characteristic semiconducting ZnS phase (fig. S4C) but showed weakly localized surface plasmon resonance peaks in both ZnS nanocages, indicating that small amounts of the $Cu_xS$ phases were present (*21*). The complete cation exchange did not proceed, but we could demonstrate the potential of our method to produce the unobtainable crystal phases under ambient conditions.

We emphasize that the validity of our observation is strongly supported by the previous report (*4*) that demonstrated an anion exchange of the hexagonal pyramid–shaped ZnO NCs with a wurtzite phase to the ZnS hollow NCs with a wurtzite phase. We envisage that this pseudomorphic transformation method could be applicable to a number of other ionic NCs at ambient temperatures, even if they are high-temperature stable phases such as wurtzite ZnS.

## REFERENCES AND NOTES


1. G. D. Moon *et al.*, *Nano Today* **6**, 186–203 (2011).
2. M. Saruyama *et al.*, *J. Am. Chem. Soc.* **133**, 17598–17601 (2011).
3. T. Teranishi, M. Sakamoto, *J. Phys. Chem. Lett.* **4**, 2867–2873 (2013).
4. J. Park, H. Zheng, Y. W. Jun, A. P. Alivisatos, *J. Am. Chem. Soc.* **131**, 13943–13945 (2009).
5. P. K. Jain, L. Amirav, S. Aloni, A. P. Alivisatos, *J. Am. Chem. Soc.* **132**, 9997–9999 (2010).
6. H. Li *et al.*, *Nano Lett.* **11**, 4964–4970 (2011).
7. D. Zhang *et al.*, *J. Am. Chem. Soc.* **136**, 17430–17433 (2014).
8. D. H. Son, S. M. Hughes, Y. Yin, A. Paul Alivisatos, *Science* **306**, 1009–1012 (2004).
9. R. D. Robinson *et al.*, *Science* **317**, 355–358 (2007).
10. W. C. Huang, L. M. Lyu, Y. C. Yang, M. H. Huang, *J. Am. Chem. Soc.* **134**, 1261–1267 (2012).
11. C. H. Kuo, M. H. Huang, *J. Phys. Chem. C* **112**, 18355–18360 (2008).
12. W. G. Mumme, R. W. Gable, V. Petricek, *Can. Mineral.* **50**, 423–430 (2012).
13. S. B. Qadri *et al.*, *J. Appl. Phys.* **89**, 115–119 (2001).
14. Z. Wang *et al.*, *Nat. Mater.* **4**, 922–927 (2005).
15. S. B. Qadri *et al.*, *Phys. Rev. B* **60**, 9191–9193 (1999).
16. Materials and methods are available as supplementary materials on *Science* Online.
17. C. H. Kuo, Y. T. Chu, Y. F. Song, M. H. Huang, *Adv. Funct. Mater.* **21**, 792–797 (2011).
18. M. Kanehara, H. Arakawa, T. Honda, M. Saruyama, T. Teranishi, *Chem. Eur. J.* **18**, 9230–9238 (2012).
19. C. H. Kuo, C. H. Chen, M. H. Huang, *Adv. Funct. Mater.* **17**, 3773–3780 (2007).
20. J. B. Rivest, P. K. Jain, *Chem. Soc. Rev.* **42**, 89–96 (2013).
21. D. H. Ha *et al.*, *Nano Lett.* **14**, 7090–7099 (2014).
22. W. W. Yu, X. Peng, *Angew. Chem. Int. Ed. Engl.* **41**, 2368–2371 (2002).


## ACKNOWLEDGMENTS

This work was partly supported by the Artificial Photosynthesis Project (ARPChem) of the New Energy and Industrial Technology Development Organization (NEDO) of Japan.

## SUPPLEMENTARY MATERIALS

www.sciencemag.org/content/351/6279/1306/suppl/DC1
Materials and Methods
Figs. S1 to S4
Table S1

29 September 2015; accepted 1 February 2016
10.1126/science.aad5520

Downloaded from on March 17, 2016

HYDROGEN BONDING

# Concerted hydrogen-bond breaking by quantum tunneling in the water hexamer prism

**Jeremy O. Richardson,[1,2]* Cristóbal Pérez,[3]† Simon Lobsiger,[3] Adam A. Reid,[1]‡ Berhane Temelso,[4] George C. Shields,[4] Zbigniew Kisiel,[5] David J. Wales,[1] Brooks H. Pate,[3]* Stuart C. Althorpe[1]***

**The nature of the intermolecular forces between water molecules is the same in small hydrogen-bonded clusters as in the bulk. The rotational spectra of the clusters therefore give insight into the intermolecular forces present in liquid water and ice. The water hexamer is the smallest water cluster to support low-energy structures with branched three-dimensional hydrogen-bond networks, rather than cyclic two-dimensional topologies. Here we report measurements of splitting patterns in rotational transitions of the water hexamer prism, and we used quantum simulations to show that they result from geared and antigeared rotations of a pair of water molecules. Unlike previously reported tunneling motions in water clusters, the geared motion involves the concerted breaking of two hydrogen bonds. Similar types of motion may be feasible in interfacial and confined water.**

In addition to its bulk phases, water can form small gas-phase clusters $(H_2O)_n$, in which the molecules are held together by a network of hydrogen bonds. The cluster dynamics can be probed by high-resolution rovibrational spectroscopy (*1–9*) and interpreted by theoretical simulations (*10–27*). The nature of the interactions between the water molecules is the same in the clusters as in the bulk (many-body forces beyond the three-body term are relatively weak) (*28*), and hence the cluster spectra can be used to test universal models (*25, 29–32*) of the water intermolecular potential energy surface, giving insight into hydrogen bonding in all phases of water. At low temperatures, the molecules are frozen into a network and can only rearrange by quantum tunneling, which causes splittings in the spectrum ranging from megahertz to terahertz (*33*). Quantum simulations (*10–27*) have identified rearrangements that involve free hydrogen flips that break no

hydrogen bonds, and bifurcations that break one bond (*2*).

Here we report observation of a tunneling motion that concertedly breaks two hydrogen bonds in a water cluster. The hexamer is the smallest cluster with a branched three-dimensional equilibrium geometry (*5*) and has thus been dubbed the smallest droplet of water. It has a variety of isomers (*12–14*, *21*, *34–36*), of which the spectrum of the lowest-energy prism isomer, PR1 of Fig. 1 (see the supplementary materials for a discussion of other prism isomers), was recently found to show a splitting pattern, which was attributed to tunneling (*6*). Here we report new measurements and quantum simulations on PR1 that uncover the dynamics responsible for the splittings.

Tunneling in water clusters occurs when the molecules in their equilibrium geometry rearrange to produce an equivalent structure, by permuting equivalent atoms or inverting the structure through its center of mass. These geometrically identical structures (which can be distinguished only by labeling the atoms and specifying the chirality) are termed versions. The number of versions is equal to the size of the group of all nuclear permutations and inversions (*37*), which for PR1 gives an enormous total of $2 \times 6! \times 12! \simeq 10^{12}$. However, only versions linked by short and energetically accessible tunneling pathways produce observable splittings. We therefore need to consider only pathways that rotate the water molecules within the structure, because these avoid breaking covalent bonds. For smaller clusters, these rules are sufficient to assign tunneling splittings (*2*, *15*, *16*, *20*, *27*). However, for PR1, the size of the space left to explore is still vast.

To narrow down further the number of likely tunneling pathways, we measured the rotational spectra of all 64 isotopologs of the hexamer PR1 prism with the formula $(H_2{}^{18}O)_n(H_2{}^{16}O)_{6-n}$ ($n = 0 \ldots 6$); these are presented in tables S5 to S68. Figure 2A shows the tunneling patterns for three *a*-type rotational transitions of the $(H_2{}^{16}O)_6$ cluster. These spectra show the characteristic splitting pattern previously observed (*6*). Isotopic substitution destroys this pattern, except in $(H_2{}^{18}O)_6$ and in the six doubly substituted isotopologs shown in Fig. 2B. This tells us immediately that the tunneling paths must rearrange two separate water molecules in the structure, ruling out motions such as the flip and bifurcation observed in other water clusters (*2*, *15*, *16*, *20*, *27*). Closer inspection shows that the observed splitting is slightly reduced when the A+D dimer is substituted with the heavier isotope; the composition of the remaining tetramer portion of the cluster does not affect the splitting. The tunneling motion must therefore involve rearrangements of molecules A and D, and the dynamics are probably localized in this part of the cluster.

To elucidate the dynamics further, it was necessary to carry out quantum simulations on an accurate potential energy surface. Full quantum calculations are impossible for this 48-degrees-of-freedom problem, so we used the ring-polymer instanton (RPI) method (*27*, *38*, *39*). This method assumes that the tunneling can be approximated by fluctuations around the minimum-action or instanton paths connecting different versions (*40*). The instanton path is found by minimizing the potential energy of a fictitious polymer formed by linking replicas of the system by harmonic springs. Previous studies on other water clusters (*27*, *39*) have shown that this method correctly predicts the pattern and order of magnitude of the tunneling splittings and that the instanton paths give a useful representation of the tunneling dynamics. Further details of the RPI method are given in the supplementary materials. The potential energy surface used was the HBB2-pol surface (*31*); we also made comparisons with the MB-pol surface (*32*) and found no major qualitative differences in the results (table S1).

Because the space of possible tunneling paths is vast, it is necessary to have an idea of the starting path, which can then be refined using the RPI method. Initially, we considered paths that resemble the flip motions observed in other water clusters, which involve the wag of a non–hydrogen-bonded H atom. No single flip connects versions in the hexamer prism, but a double flip corresponding to the permutation $P_a = (AD)(BF)(CE)(1\,7)(2\,8)(3\,11)(4\,12)(5\,9)(6\,10)$ (using the labeling in Fig. 1) does. The resulting instanton path is shown in Fig. 3A (and the corresponding transition state is shown in fig. S1A). Unlike single flips, this double flip breaks one hydrogen bond. We call this the antigeared path because the H-1 atom rotates out of its hydrogen bond in the opposite sense to H-7 (which rotates in to form a hydrogen bond with O-A).

Because $P_a^2 = E$ (the identity), it follows that the antigeared path gives a simple doublet splitting pattern. Now, $P_a$ is the only permutation that breaks no more than one hydrogen bond. Hence the observed pattern (Fig. 2A), in which the doublet is split further into six lines, implies that, unlike other water clusters, the PR1 hexamer supports tunneling paths that break two or more hydrogen bonds. In other water clusters, the next most feasible tunneling pathways after the flips are bifurcations, in which an H atom rotates away from its hydrogen bond and is replaced by the other H atom on the same water molecule (*15*). This mechanism breaks only one hydrogen bond in the trimer, but in PR1, owing to its three-dimensional structure, such a bifurcation rearrangement must break at least two hydrogen bonds. We located a variety of single-bifurcation tunneling pathways but found that, as in the water octamer (*39*), the resulting instanton tunneling splittings were tiny, indicating that these paths are unfeasible. However, we found that there exists a single feasible pathway that combines a double flip with a bifurcation, corresponding to the permutation $P_g = (AD)(BF)(CE)(1\,8\,2\,7)(3\,11)(4\,12)(5\,9)(6\,10)$. This path also breaks two hydrogen bonds, but surprisingly, the resulting instanton pathway (Fig. 3B) gives a small but observable tunneling splitting. This is because it describes a geared pathway, in which atoms H-1 and H-7 rotate in the same sense, resulting in a reduction in energy, which offsets the increase in energy required to break the additional H-2···O-B hydrogen bond.

The combination of both the geared and antigeared pathways explains the doublet-of-triplets splitting observed in the spectrum. $P_a$ and $P_g$ generate a group of permutations (described in the supplementary materials), which link together eight versions of the prism; Fig. 4A shows the graph that represents the connections between versions associated with these two tunneling pathways. To predict the splitting pattern, we must first obtain the energy levels by diagonalizing the tunneling matrix $\mathbf{h}$ (Fig. 4B), in which every connection in the graph is represented by a matrix element $h_{ij}$ (where $i,j = 1, \ldots, 8$ label the versions). These elements were calculated using a normal-mode analysis of the ring-polymer instantons (*27*, *38*). Elements corresponding to a direct link by a single instanton path gave the values $h_a = -0.88$ MHz (antigeared) and $h_g = -0.15$ MHz (geared); all other permutations in the group were found to give negligibly small values of $h_{ij}$, which were thus set to zero. The resulting energy-level splitting obtained by diagonalizing the tunneling matrix is given in Fig. 4C. A symmetry analysis of the nonrigid cluster (*37*) shows that the eigenfunctions of the tunneling matrix transform as irreducible representations of a group isomorphic to the $D_{2d}$ point group. We can therefore assign symmetry labels to the levels (Fig. 4C).

In the hexamer prism, the energy-level splittings caused by tunneling (on the order of megahertz) are significantly smaller than the energy separation for the rotational energy levels (several gigahertz). Therefore, it is appropriate to consider a tunneling energy level pattern for each different

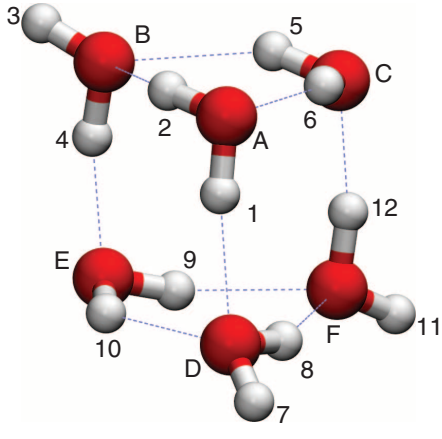



**Fig. 1. Minimum-energy structure of the PR1 prism isomer of the water hexamer.** The labels define one version (i.e., arrangement of the atoms), which can tunnel to other versions by permuting identical atomic nuclei within the structure.

[1]Department of Chemistry, University of Cambridge, Lensfield Road, Cambridge CB2 1EW, UK. [2]Department of Chemistry, Durham University, South Road, Durham DH1 3LE, UK. [3]Department of Chemistry, University of Virginia, McCormick Road, Charlottesville, VA 22903, USA. [4]Dean's Office, College of Arts and Sciences, and Department of Chemistry, Bucknell University, Lewisburg, PA 17837, USA. [5]Institute of Physics, Polish Academy of Sciences, Aleja Lotników 32/46, 02-668 Warszawa, Poland.
***Corresponding author. E-mail: jeremy.richardson@durham.ac.uk (J.O.R.); brookspate@virginia.edu (B.H.P.); sca10@cam.ac.uk (S.C.A.)** †Present address: Max Planck Institute for the Structure and Dynamics of Matter, Luruper Chausse 149, D-22761 Hamburg, Germany. ‡Present address: Department of Mathematics, Tonbridge School, High Street, Tonbridge, TN9 1JP, UK.

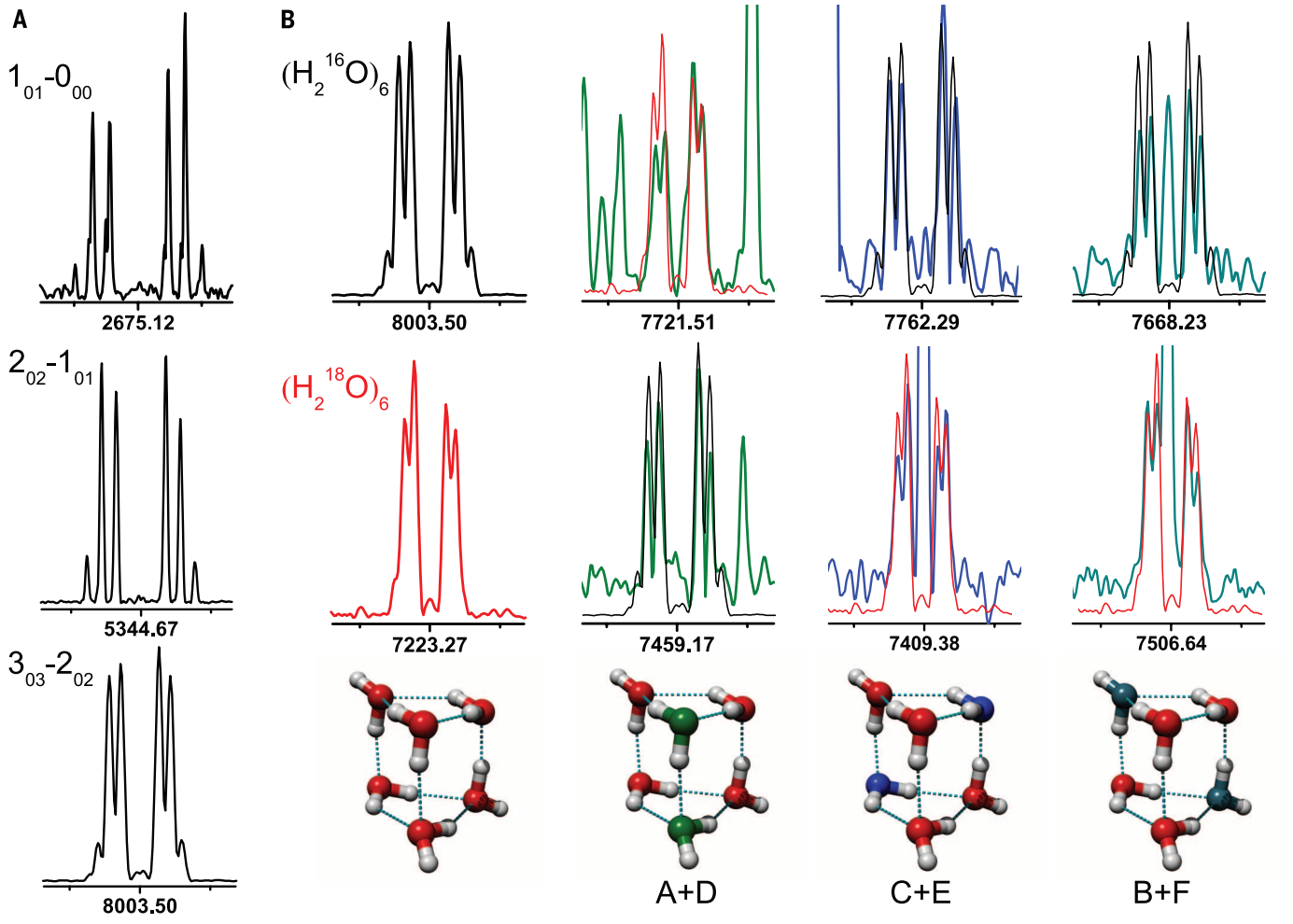



**Fig. 2. Rotational spectral evidence for tunneling.** (**A**) Three spectra for the $(H_2{}^{16}O)_6$ PR1 prism, showing the doublet-of-triplets splitting pattern attributed to tunneling. The rotational levels involved in each transition are denoted using the standard asymmetric top notation, $J_{K_aK_c}$. The labeled frequency is the asymmetric-top rotational transition frequency, and the tunneling pattern is symmetric around this frequency. (**B**) The $3_{03}$–$2_{02}$ spectra for the eight isotopologs (of 64 possible) that display tunneling. Tunneling is observed for both the $(H_2{}^{16}O)_6$ transition centered at 8003.50 MHz (black trace) and the $(H_2{}^{18}O)_6$ transition centered at 7223.27 MHz (red trace), and the width of the splitting pattern is reduced for the heavier isotopolog. The other isotopologs that show tunneling have either two $H_2{}^{18}O$ substitutions in the $(H_2{}^{16}O)_6$ structure (top row) or two $H_2{}^{16}O$ substitutions in the $(H_2{}^{18}O)_6$ cluster (bottom row). The substituted positions are depicted by the molecular structures at the bottom. All six of the doubly substituted clusters have a tunneling splitting (green and blue traces) that matches either the $(H_2{}^{16}O)_6$ or $(H_2{}^{18}O)_6$ clusters, as shown by the overlay of these spectra. All four spectra where water molecules A+D are $H_2{}^{16}O$ have the same, larger splitting (black trace), whereas all four clusters where A+D are $H_2{}^{18}O$ have the reduced tunneling splitting (red trace). The additional transitions observed in the doubly substituted spectra come from rotational transitions of other water cluster isotopologs and are not part of the tunneling-splitting pattern. The tick marks in all panels have 1-MHz spacing.

rotational level; these patterns can have a slight dependence on the rotational quantum numbers, as suggested by Fig. 2A. To obtain the splitting pattern in the rotational spectrum that consists of transitions between the tunneling states for different rotational levels, we note that $\mu_a$ transforms as $B_2$ and only allows strong transitions between the tunneling states $A_1 \leftrightarrow B_2$, $A_2 \leftrightarrow B_1$, and $E_{(1)} \leftrightarrow E_{(2)}$. These transitions give the doublet-of-triplet splitting pattern shown in Fig. 4D, and the amplitudes of the pattern are obtained from the nuclear-spin statistics. As explained in the supplementary materials, there are also some pure rotational transitions, which are not rigorously forbidden by symmetry but contribute only weakly to a small central peak, and evidence of these nominally forbidden transitions appears in Fig. 2. As shown in Fig. 4D, the theoretical splitting pattern qualitatively reproduces the experimentally observed splitting pattern but is about twice as wide. An analysis of the *J*-dependent geared and antigeared tunneling matrix elements, presented in the supplementary materials, gives the values of $h_a = -0.382$ MHz and $h_g = -0.073$ MHz for the ground state, which can be compared directly to the theoretical values given above. The ratio of the theoretical matrix elements $h_g : h_a$ is 1 : 5.8 and in excellent agreement with the experimental value of 1 : 5.2. Furthermore, full isotopic substitution of $^{16}O$ with $^{18}O$ is found to reduce the predicted tunneling matrix elements to 85% of their value, indicating a slight participation of the heavy oxygen-atom framework during tunneling. This is confirmed by the experimental tunneling splittings (Fig. 2B), which are proportional to the tunneling matrix elements, where the observed reduction is 84%. This level of agreement is good for an instanton calculation and is consistent with previous applications to other water clusters (*27*, *39*), where the main errors in the instanton calculation were attributed to neglect of anharmonicity in the fluctuations around the instanton, along with rotation-tunneling coupling. This implies that the potential energy surfaces give an excellent description of the intermolecular forces, and we can be confident that the geared and antigeared tunneling pathways in Fig. 3 correctly describe the tunneling responsible for the observed splittings.

Plots of the potential energy along the tunneling paths (Fig. 3) show striking differences between

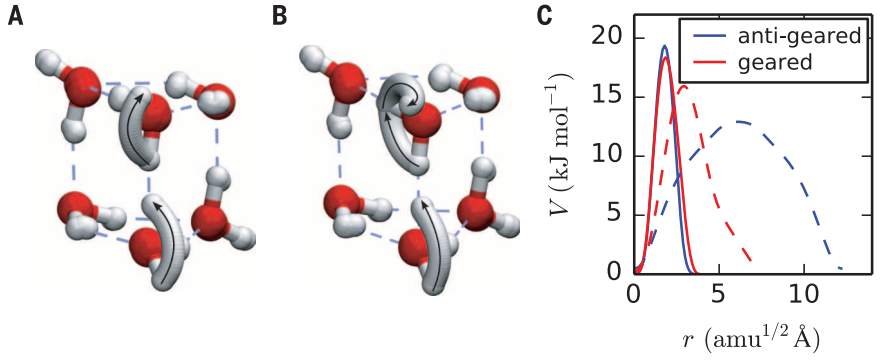



**Fig. 3. Instanton tunneling pathways in the water hexamer prism.** (**A**) Antigeared and (**B**) geared variations. The pathways are shown as conflated snapshots of replicas of the system obtained from ring-polymer representations of the instantons. The geared pathway involves the concerted breaking of two hydrogen bonds. (**C**) Variation of the potential energy along the instanton paths (solid lines) and minimum-energy paths (dashed lines), where $r$ is the integrated mass-weighted path length and $V$ is the potential energy along the path.

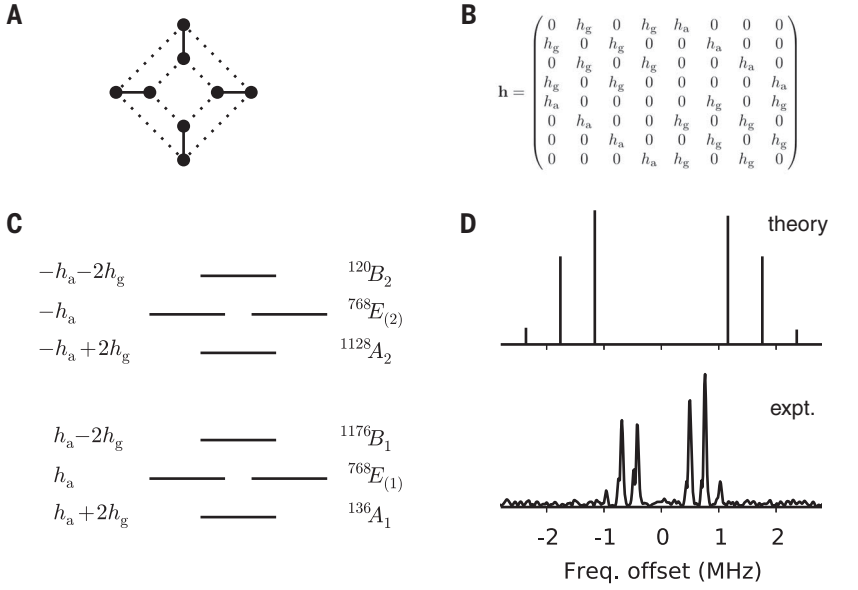



**Fig. 4. Origin of the splitting pattern.** (**A**) Graph showing how the versions (vertices) are connected by the tunneling paths (antigeared, solid lines; geared, dotted lines). Diagonalization of the associated tunneling matrix, $\mathbf{h}$, defined in (**B**) splits the ground-state energy level as shown in (**C**), where the symmetry is also given with its nuclear-spin degeneracy as a superscript. The states labeled $E_{(1)}$ and $E_{(2)}$ both have symmetry $E$. The rotational spectrum involves transitions between the tunneling-level patterns for different rotational energy levels. The resulting tunneling-splitting pattern centered on the expected rotational transition frequency is $2h_a + 4h_g$, $2h_a$, $2h_a-4h_g$, $-2h_a + 4h_g$, $-2h_a$, $-2h_a-4h_g$, where $h_a$ and $h_g$ are the average values of the antigeared and geared tunneling matrix elements in the rotational energy levels for the spectroscopic transition. This spectral pattern is plotted in (**D**) using the theoretical matrix elements as the average values in the rotational levels and is compared with the measured $1_{01}$–$0_{00}$ transition (represented to scale). This explains the observed doublet-of-triplets splitting pattern, where the outermost lines are considerably smaller.

the instanton and minimum-energy paths. The mass-weighted length of the minimum-energy path is four times that of the instanton path for the antigeared pathway and twice that for the geared. A naïve one-dimensional analysis using the minimum-energy paths might conclude that the geared tunneling is more facile than the antigeared (because the effective barrier is much thinner), and that in either case the splitting pattern is probably too small to be observed on account of the long tunneling pathways. That the splittings are observable and that the ratio is the other way around are the result of corner-cutting by the instanton pathway (*40*). Unlike the minimum-energy path, it bypasses the transition state in order to avoid the penalty in the action associated with moving the heavy oxygen atoms.

It is likely that other prism clusters, such as the pentagonal prism decamer, could exhibit similar pathways. These results also raise the possibility that the rearrangement dynamics of water in interfacial (*41*, *42*) or confined environments might also involve similar concerted breaking of two (or more) hydrogen bonds.

## REFERENCES AND NOTES


1. A. C. Legon, D. J. Millen, *Chem. Soc. Rev.* **21**, 71 (1992).
2. N. Pugliano, R. J. Saykally, *Science* **257**, 1937–1940 (1992).
3. R. J. Saykally, G. A. Blake, *Science* **259**, 1570–1575 (1993).
4. K. Liu, J. D. Cruzan, R. J. Saykally, *Science* **271**, 929–933 (1996).
5. F. N. Keutsch, R. J. Saykally, *Proc. Natl. Acad. Sci. U.S.A.* **98**, 10533–10540 (2001).
6. C. Pérez *et al.*, *Science* **336**, 897–901 (2012).
7. R. J. Saykally, D. J. Wales, *Science* **336**, 814–815 (2012).
8. C. Pérez *et al.*, *Chem. Phys. Lett.* **571**, 1–15 (2013).
9. C. Pérez *et al.*, *Angew. Chem. Int. Ed.* **53**, 14368–14372 (2014).
10. S. C. Althorpe, D. C. Clary, *J. Chem. Phys.* **101**, 3603 (1994).
11. D. Sabo, Z. Bačić, T. Bürgi, S. Leutwyler, *Chem. Phys. Lett.* **244**, 283–294 (1995).
12. K. Liu *et al.*, *Nature* **381**, 501–503 (1996).
13. K. Liu, M. G. Brown, R. J. Saykally, *J. Phys. Chem. A* **101**, 8995–9010 (1997).
14. D. J. Wales, *Theory of Atomic and Molecular Clusters: With a Glimpse at Experiments*, J. Jellinek, Ed. (Springer-Verlag, Berlin, 1999), pp. 86–110.
15. D. J. Wales, *J. Am. Chem. Soc.* **115**, 11180–11190 (1993).
16. T. R. Walsh, D. J. Wales, *J. Chem. Soc., Faraday Trans.* **92**, 2505 (1996).
17. D. J. Wales, T. R. Walsh, *J. Chem. Phys.* **105**, 6957 (1996).
18. D. J. Wales, T. R. Walsh, *J. Chem. Phys.* **106**, 7193 (1997).
19. J. K. Gregory, D. C. Clary, *J. Chem. Phys.* **103**, 8924 (1995).
20. J. K. Gregory, D. C. Clary, *J. Chem. Phys.* **102**, 7817 (1995).
21. J. K. Gregory, D. C. Clary, *J. Phys. Chem. A* **101**, 6813–6819 (1997).
22. E. H. T. Olthof, A. van der Avoird, P. E. S. Wormer, K. Liu, R. J. Saykally, *J. Chem. Phys.* **105**, 8051 (1996).
23. C. Leforestier, L. B. Braly, K. Liu, M. J. Elrod, R. J. Saykally, *J. Chem. Phys.* **106**, 8527 (1997).
24. R. S. Fellers, L. B. Braly, R. J. Saykally, C. Leforestier, *J. Chem. Phys.* **110**, 6306 (1999).
25. R. Bukowski, K. Szalewicz, G. C. Groenenboom, A. van der Avoird, *Science* **315**, 1249–1252 (2007).
26. X. Huang *et al.*, *J. Chem. Phys.* **128**, 034312 (2008).
27. J. O. Richardson, S. C. Althorpe, D. J. Wales, *J. Chem. Phys.* **135**, 124109 (2011).
28. U. Góra, R. Podeszwa, W. Cencek, K. Szalewicz, *J. Chem. Phys.* **135**, 224102 (2011).
29. Y. Wang, B. C. Shepler, B. J. Braams, J. M. Bowman, *J. Chem. Phys.* **131**, 054511 (2009).
30. Y. Wang, X. Huang, B. C. Shepler, B. J. Braams, J. M. Bowman, *J. Chem. Phys.* **134**, 094509 (2011).
31. V. Babin, G. R. Medders, F. Paesani, *J. Phys. Chem. Lett.* **3**, 3765–3769 (2012).
32. V. Babin, G. R. Medders, F. Paesani, *J. Chem. Theory Comput.* **10**, 1599–1607 (2014).
33. F. N. Keutsch, J. D. Cruzan, R. J. Saykally, *Chem. Rev.* **103**, 2533–2578 (2003).
34. B. Temelso, K. A. Archer, G. C. Shields, *J. Phys. Chem. A* **115**, 12034–12046 (2011).
35. Y. Wang, V. Babin, J. M. Bowman, F. Paesani, *J. Am. Chem. Soc.* **134**, 11116–11119 (2012).
36. V. Babin, F. Paesani, *Chem. Phys. Lett.* **580**, 1–8 (2013).
37. H. C. Longuet-Higgins, *Mol. Phys.* **6**, 445–460 (1963).
38. J. O. Richardson, S. C. Althorpe, *J. Chem. Phys.* **134**, 054109 (2011).
39. J. O. Richardson *et al.*, *J. Phys. Chem. A* **117**, 6960–6966 (2013).
40. S. Chapman, B. C. Garrett, W. H. Miller, *J. Chem. Phys.* **63**, 2710 (1975).
41. T. Mitsui, M. K. Rose, E. Fomin, D. F. Ogletree, M. Salmeron, *Science* **297**, 1850–1852 (2002).
42. V. A. Ranea *et al.*, *Phys. Rev. Lett.* **92**, 136104 (2004).


## ACKNOWLEDGMENTS


The authors acknowledge financial support from a European Union COFUND/Durham Junior Research Fellowship (J.O.R.), a Research Fellowship from the Alexander von Humboldt Foundation (C.P.), U.S. National Science Foundation grants CHE-0960074 (C.P. and B.H.P.) and CHE-1213521 and CHE-1229354 (B.T. and G.C.S.), Swiss National Science Foundation grant PBBEP2-144907 (S.L.), the UK Engineering and Physical Sciences Research Council (J.O.R., A.A.R., D.J.W., and S.C.A.), and a grant from the Polish National Science Centre, decision number DEC/2011/02/A/ST2/00298 (Z.K.).


## SUPPLEMENTARY MATERIALS

www.sciencemag.org/content/351/6279/1310/suppl/DC1
Materials and Methods
Figs. S1 to S9
Tables S1 to S74
References (*43*–*66*)


6 December 2015; accepted 2 February 2016
10.1126/science.aae0012

IONIC MATERIALS

# Pure $H^-$ conduction in oxyhydrides

Genki Kobayashi,[1,2]* Yoyo Hinuma,[3] Shinji Matsuoka,[4] Akihiro Watanabe,[1,4] Muhammad Iqbal,[4] Masaaki Hirayama,[4] Masao Yonemura,[5] Takashi Kamiyama,[5] Isao Tanaka,[3] Ryoji Kanno[4]*

**A variety of proton ($H^+$)–conducting oxides are known, including those used in electrochemical devices such as fuel cells. In contrast, pure $H^-$ conduction, not mixed with electron conduction, has not been demonstrated for oxide-based materials. Considering that hydride ions have an ionic size appropriate for fast transport and also a strong reducing ability suitable for high-energy storage and conversion devices, we prepared a series of $K_2NiF_4$-type oxyhydrides, $La_{2-x-y}Sr_{x+y}LiH_{1-x+y}O_{3-y}$, in the hope of observing such $H^-$ conductors. The performance of an all-solid-state $TiH_2$/*o*-$La_2LiHO_3$ ($x = y = 0$, *o*: orthorhombic)/Ti cell provided conclusive evidence of pure $H^-$ conduction.**

Electric conduction is generally classified into two categories, electronic and ionic, which are attributed to the transport of electrons and ions in materials, respectively. Ionic charge carriers include a variety of species, such as $Li^+$, $H^+$, $Ag^+$, $Cu^+$, $F^-$, and $O^{2-}$, and their conductors have found applications in energy devices such as fuel cells and batteries (*1*–*5*), for example. The conduction of hydride ions, $H^-$, is also attractive. These are similar in size to oxide and fluoride ions (*6*) and show strong reducing properties with a standard redox potential of $H^-/H_2$ (−2.3 V), which is close to that of $Mg/Mg^{2+}$ (−2.4 V). Hydride ion conductors may therefore be applied in energy storage and conversion devices with high energy densities.

In contrast to proton conduction that takes place widely in oxides (*7*) and other systems, pure $H^-$ conduction has been verified only for a few hydrides of alkaline earth metals such as $BaH_2$ (*8*–*13*). Unfortunately, utilization of the hydrides is difficult because of their structural inflexibility, which makes control of the lattice structure to create smooth transport pathways and control of the conducting hydride ion content difficult. We have considered oxyhydrides, where hydride ions and oxide ions share the anion sublattices, as candidate hydride conductors equipped with flexible anion sublattices. Known oxyhydrides include $A_2BH_xO_{4-x}$ ($K_2NiF_4$ structure; A: La, Ce, Nd, Pr, Sr; B: Co, V, Li; $0 < x \leq 1$), $Sr_3Co_2O_{4.33}H_{0.84}$ (Ruddlesden-Popper structure), $ATiO_{3-x}H_x$ (perovskite structure; A: Ba, Sr, Ca) (*14*–*19*), and $[Ca_{24}Al_{28}O_{64}]^{4+}\cdot 4H^-$ (mayenite structure) (*20*–*22*). However, none of these displays pure $H^-$ conductivity.

Hydride ions have been reported to act as electron donors in oxide-based materials (*20*–*24*), transferring electrons from hydride ions to the lattice. This causes conduction of electrons accompanied by a characteristic change in the hydrogen charge from $H^-$ to $H^+$. Indeed, the perovskite and mayenite-type oxyhydrides are dominated by electron conduction caused by the dissociation of hydride ions into electrons and protons (*16*, *20*–*22*, *25*). Taking this into consideration, preventing electron donation from hydride ions in the crystal lattice may be important for achieving pure $H^-$ conduction in the oxide framework structure. In this study, we attempted to prepare a series of $K_2NiF_4$-type oxyhydrides, $La_{2-x-y}Sr_{x+y}LiH_{1-x+y}O_{3-y}$ ($0 \leq x \leq 1$, $0 \leq y \leq 2$, $0 \leq x + y \leq 2$), which are equipped with cation sublattices featuring cations more electron-donating than $H^-$ and anion sublattices that exhibit flexibility in the storage of $H^-$, $O^{2-}$, and vacancies.

To aid in the understanding of the compositional and structural features of the present system, a few representative examples are shown below: $La_2LiHO_3$ ($x = y = 0$), $Sr_2LiH_3O$ ($x = 0$, $y = 2$), $La_{2-x}Sr_xLiH_{1-x}O_3$ ($0 \leq x \leq 1$, $y = 0$), and $La_{1-x}Sr_{1+x}LiH_{2-x}O_2$ ($0 \leq x \leq 1$, $y = 1$). Solid solutions between $La_2LiHO_3$ and $Sr_2LiH_3O$ are represented as $La_{2-y}Sr_yLiH_{1+y}O_{3-y}$ ($x = 0$, $0 \leq y \leq 2$). Here, the H:O ratio changes accordingly as La is substituted with Sr, maintaining the simple $A_2BX_4$ composition (A: La, Sr; B: Li; X: O, H). In $La_{2-x}Sr_xLiH_{1-x}O_3$ and $La_{1-x}Sr_{1+x}LiH_{2-x}O_2$, by contrast, the anion sublattice contains vacancies. Several starting compositions (see table S1) contained in the colored compositional range in Fig. 1A were synthesized by treating the appropriate starting materials in sealed Au capsules at high pressure and high temperature (*26*).

The x-ray diffraction (XRD) pattern of $La_2LiHO_3$ ($x = y = 0$) could be assigned to the $K_2NiF_4$-type structure, but the lattice symmetry was found to change between tetragonal (*I*4/*mmm*, *t*-$La_2LiHO_3$) and orthorhombic (*Immm*, *o*-$La_2LiHO_3$), depending on certain experimental factors, including the LiH/$La_2O_3$ ratio of the starting materials (1/1 and 2/1 for *t*- and *o*-$La_2LiHO_3$, respectively), heating temperature, and pressure (fig. S1). All other samples were prepared under the same conditions as outlined for *o*-$La_2LiHO_3$. Regarding the Sr-substituted series of $La_{2-y}Sr_yLiH_{1+y}O_{3-y}$, the diffraction peaks continuously shifted to lower angles with increasing $y$ (Fig. 1B) and the lattice symmetry changed from *Immm* ($y < 1$) to *I*4/*mmm* ($y \geq 1$) (Fig. 1C).

The compositions and structures of $La_{2-y}Sr_yLiH_{1+y}O_{3-y}$ ($y = 0$, 1, 2) were determined by x-ray and neutron Rietveld analyses. Details of the analyses are given in figs. S2 and S3, in tables S2 and S3, and in the supplementary text. In $La_2LiHO_3$, the two apical sites of the $LiX_6$ octahedra are occupied only by $O^{2-}$, as illustrated schematically in Fig. 2, whereas the four in-plane apexes are occupied by $O^{2-}$ and $H^-$. These results indicate that the highly charged cations (i.e., $La^{3+}$ and $Sr^{2+}$) require highly charged anions around them. $LaSrLiH_2O_2$ is composed of tetragonal $(LiH_2)^-$ and $(LaSrO_2)^+$ layers alternately stacked along the *c* axis. The further increase in hydride content up to $Sr_2LiH_3O$ results in the formation of $(Sr_2HO)^+$ layers. In the series of compositions, we note here that there exists a $K_2NiF_4$-type, $H^-$–free oxide, $La_2LiO_{3.5}$, in which the anion vacancies are randomly distributed in the basal $(LiO_{0.75})^{0.5-}$ layers (*27*).

It is notable that *t*-$La_2LiHO_3$ contains anion vacancies ($V_{(H,O)}$) with the chemical formula $La_2Li(H_{0.53}O_{1.21}V_{(H,O)0.26})O_2$, exhibiting $H^-$, $O^{2-}$, and $V_{(H,O)}$ disorder at the axial sites of the $LiX_6$ octahedra. In contrast, the orthorhombic phase, *o*-$La_2LiHO_3$, is stoichiometric, and $H^-$ and $O^{2-}$ are ordered on the axial anion sites. The symmetry change can be attributed to the order-disorder transition of $H^-$ and $O^{2-}$ in the axial sites, both with and without vacancies. The XRD results for a pair of anion-deficient series, $La_{2-x}Sr_xLiH_{1-x}O_3$ and $La_{1-x}Sr_{1+x}LiH_{2-x}O_2$, are shown in figs. S4 and S5. The occupancy parameters determined by a neutron Rietveld analysis for $La_{0.7}Sr_{1.3}LiH_{1.7}O_2$ ($x = 0.3$, $y = 1$) of $g_{H1} = 0.938(2)$, $g_{H2} = 0.118(3)$, and $g_{O1} = 0.882(3)$ lead to a composition of $La_{0.7}Sr_{1.3}Li(H_{1.88}V_{(H)0.12})H_{0.24}O_{1.76}$ (fig. S6 and table S4). A vacancy was introduced with $x$ at the $LiH_4$ plane together with $H^-/O^{2-}$ anion mixing at the apical sites.

The valence state of each constituent atom was estimated for $La_2LiHO_3$, $LaSrLiH_2O_2$, and $Sr_2LiH_3O$ by means of valence charge integration over its Voronoi cell (table S5). The valences of hydrogen and oxygen in all materials were estimated as approximately −0.8 to −1.0 and −1.3 to −1.6, respectively, which indicates that these elements exist as $H^-$ and $O^{2-}$. Electronic density of states calculations also corroborate the presence of hydride ions, as can be seen in fig. S7, where these ions have localized electrons between approximately 0 and −5 eV below the Fermi level. The Li–$H^-$ bond was confirmed to be ionic in nature.

The conductivities of the oxyhydrides were estimated from the impedance plots, which are characteristic of typical ionic conductors, as shown in fig. S8. Figure 3, A to C, shows Arrhenius plots of the conductivity of $La_{2-x-y}Sr_{x+y}LiH_{1-x+y}O_{3-y}$. The conductivity and activation energy values (see table S6) demonstrate that the ionic conductivity varies with the compositions of both $x$ and $y$ in

[1]Research Center of Integrative Molecular Systems (CIMoS), Institute for Molecular Science, 38 Nishigonaka, Myodaiji, Okazaki, Aichi 444-8585, Japan. [2]Japan Science and Technology Agency (JST), Precursory Research for Embryonic Science and Technology (PRESTO), 4-1-8 Honcho, Kawaguchi, Saitama 332-0012, Japan. [3]Department of Materials Science and Engineering, Kyoto University, Sakyo, Kyoto 606-8501, Japan. [4]Department of Electronic Chemistry, Interdisciplinary Graduate School of Science and Engineering, Tokyo Institute of Technology, 4259 Nagatsuta, Midori, Yokohama 226-8502, Japan. [5]Neutron Science Laboratory (KENS), Institute of Materials Structure Science, High Energy Accelerator Research Organization (KEK), 203-1, Shirakata, Tokai, Ibaraki 319-1106, Japan.
*Corresponding author. E-mail: gkobayashi@ims.ac.jp (G.K.); kanno@echem.titech.ac.jp (R.K.).

Downloaded from on March 17, 2016

$La_{2-x-y}Sr_{x+y}H_{1-x+y}O_{3-y}$. Figure 3A shows the temperature dependence of the conductivity for *o*-$La_2LiHO_3$ ($x = 0, y = 0$), $LaSrLiH_2O_2$ ($x = 0, y = 1$), and $Sr_2LiH_3O$ ($x = 0$, $y = 2$). The conductivity increases with increasing $y$, with the highest conductivity of $3.2 \times 10^{-5}$ S cm$^{-1}$ at 573 K being observed for $Sr_2LiH_3O$ ($y = 2$). The introduction of hydride ions into the anion sites of the $K_2NiF_4$ structure improved the ionic conductivity, suggesting that the primary charge carriers seem to be these hydride ions. The conduction is further facilitated by the introduction of vacancies, as can be seen both for $La_{2-x}Sr_xLiH_{1-x}O_3$ ($0 \le x \le 0.2$, $y = 0$, Fig. 3B) and $La_{1-x}Sr_{1+x}LiH_{2-x}O_2$ ($0 \le x \le 0.4$, $y = 1$, Fig. 3C), up to $2.1 \times 10^{-4}$ S cm$^{-1}$ for $La_{0.6}Sr_{1.4}LiH_{1.6}O_2$ at 590 K (activation energy ~68.4 kJ mol$^{-1}$). This increase in conductivity with the introduction of vacancies indicates that the structural defects can affect the ionic diffusion. To further identify the nature of charge carriers, we measured the electrical conductivity of $La_{0.6}Sr_{1.4}LiH_{1.6}O_2$ ($x = 0.4$, $y = 1.0$) by the Hebb–Wagner polarization method (*28*) using an asymmetric (–) Pd/$La_{0.6}Sr_{1.4}LiH_{1.6}O_2$/Mo (+) cell at 480 and 590 K. The total electrical conductivities (electrons + holes) at the irreversible Mo-electrolyte interface of the cell at 480 and 590 K were $2.9 \times 10^{-8}$ and

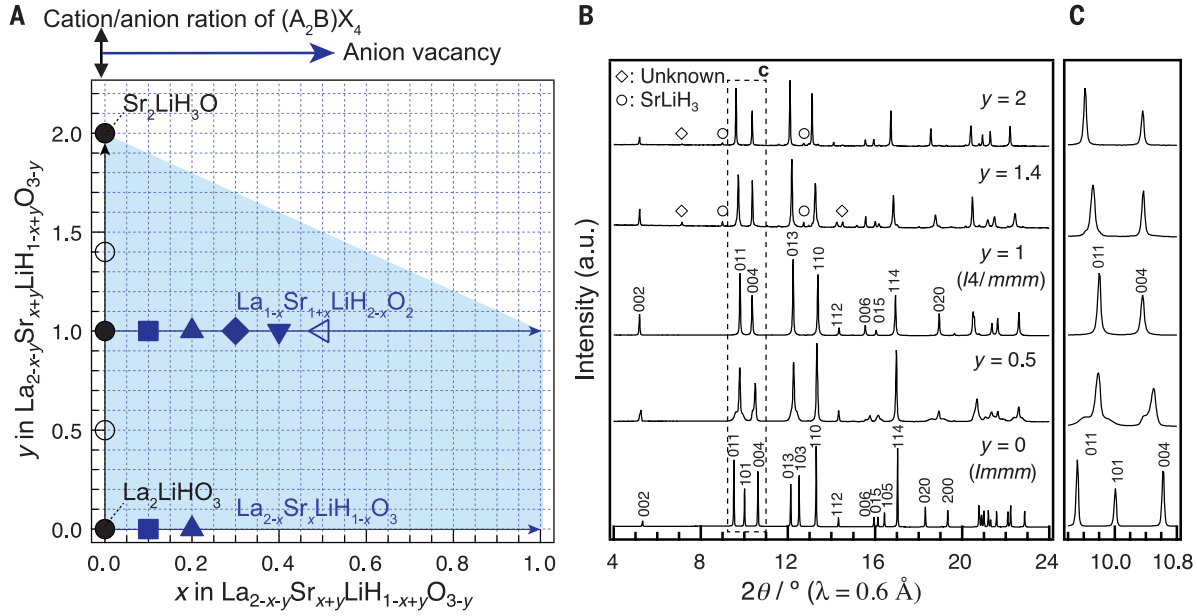



**Fig. 1. $La_{2-x-y}Sr_{x+y}LiH_{1-x+y}O_{3-y}$ ($0 \le x < 1, 0 \le y \le 2$) oxyhydride system.** (**A**) Compositional range of the oxyhydride. The compositions for the standard (maintaining $A_2BX_4$) and anion-deficient samples are represented by black and blue markers, respectively. Filled markers indicate that ionic conductivities were measured for these compositions. (**B**) Comparison of the synchrotron XRD profiles for $La_{2-y}Sr_yLiH_{1+y}O_{3-y}$ ($x = 0$, $0 \le y \le 2$). (**C**) Magnified view of typical peaks.

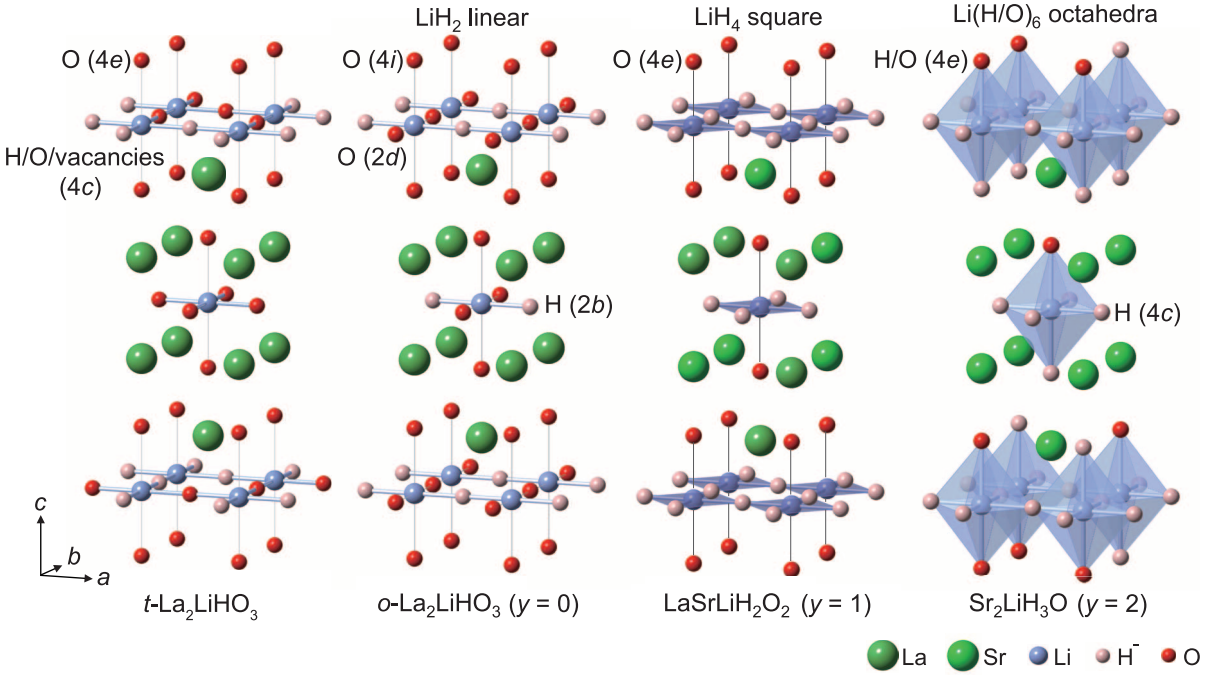



**Fig. 2. Crystal structures of *t*-$La_2LiHO_3$ and $La_{2-y}Sr_yLiH_{1+y}O_{3-y}$ ($y = 0, 1, 2$).** (**A**) A unit cell of the prepared oxyhydrides. Lanthanum (and strontium) ions occupy the A sites of the $K_2NiF_4$-type structure that are 12-fold coordinated with anions. Lithium occupies the B sites that are octahedrally coordinated with anions. The structure is composed of perovskite and rock-salt structure blocks stacked along the *c* axis. The perovskite-type layers are separated by rock-salt layers.

$4.1 \times 10^{-7}$ S $cm^{-1}$, respectively. It is evident that $La_{0.6}Sr_{1.4}LiH_{1.6}O_2$ is a pure ionic conductor (fig. S9 and table S7).

An all-solid-state cell was then constructed with *o*-$La_2LiHO_3$ as the solid electrolyte. The electrode configuration—namely, a powdered mixture of the electrode and electrolyte materials—was similar to those used for the all-solid-state lithium battery (*1*). Figure 4A shows the discharge curve of the Ti/*o*-$La_2LiHO_3$/$TiH_2$ cell, displaying a constant discharge current of 0.5 μA at 300°C. The cell showed an initial open circuit voltage of 0.28 V, which is consistent with the theoretical value calculated from the standard Gibbs energy of formation of $TiH_2$ (*29*). During the electrochemical reaction, the cell voltage dropped rapidly from 0.28 to 0.06 V and then decreased gradually to 0.0 V. This steep drop-off in the first reaction step corresponds to an increase in hydride ion content at the anode, according to the constant current discharge reaction:

$$Ti + xH^- \rightarrow TiH_x + xe^-$$

where the reaction at the cathode is as follows:

$$TiH_2 + xe^- \rightarrow TiH_{2-x} + xH^-$$

These discharge reactions were confirmed by observation of the phases that appeared following the reaction. Figure 4B shows the synchrotron XRD patterns for the cathode, electrolyte, and anode, both before and after the reaction. The absence of any variation in the diffraction patterns of the electrolyte indicates that the $La_2LiHO_3$ electrolyte is stable when in contact with the Ti and $TiH_2$ electrodes during the reaction. Phase changes detected for the cathode and anode materials are consistent with those expected from the Ti-H phase diagram (*29*), where the δ-$TiH_2$ ($Fm\bar{3}m$) phase releases hydrogen and is transformed into α-Ti ($P6_3/mmc$) through a two-phase (α-$TiH_b$ + δ-$TiH_{2-a}$) coexistence region, which is found below ~573 K (fig. S10). In the case of the cathode, additional diffraction peaks corresponding to $P6_3/mmc$ symmetry were detected. In addition, the signals corresponded to a shift of $TiH_2$ to a higher angle, thus indicating that lattice shrinkage takes place with the release of hydrogen from $TiH_2$. In the case of the anode, peaks corresponding to ($Fm\bar{3}m$) symmetry were detected. These results indicate that during the electrochemical reaction, hydride ions are released from the $TiH_2$ cathode and diffuse into the Ti anode through the *o*-$La_2LiHO_3$ (fig. S11).

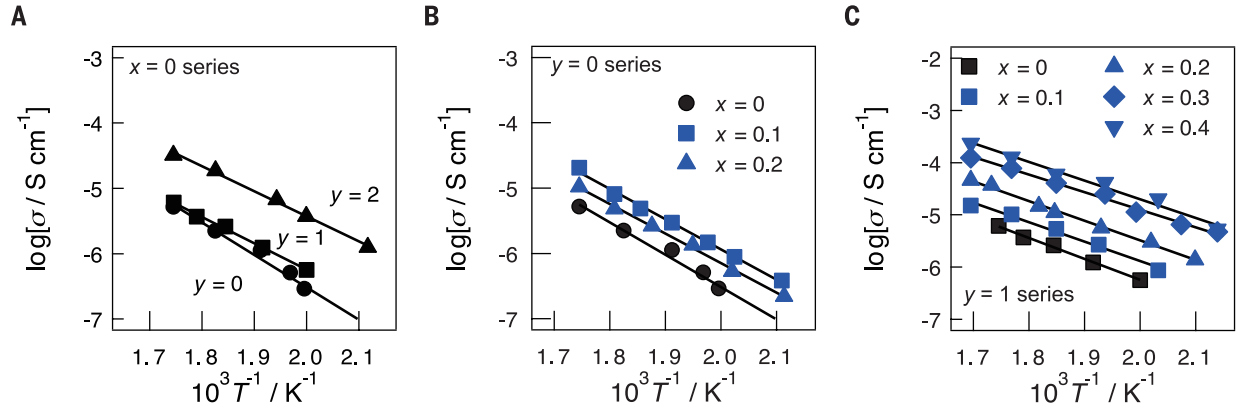



**Fig. 3. Temperature dependence of the ionic conductivities of $La_{2-x-y}Sr_{x+y}LiH_{1-x+y}O_{3-y}$.** (**A**) Compositions for $La_{2-y}Sr_yLiH_{1+y}O_{3-y}$ ($x = 0$, $y = 0$, 1, and 2) with a fixed cation/anion ratio of $(A_2B)/X_4$, where A, B, and X are La(Sr), Li, and O(H), respectively. Anion-deficient series, (**B**) $La_{2-x}Sr_xLiH_{1-x}O_3$ ($y = 0$, $0 \le x \le 0.2$) and (**C**) $La_{1-x}Sr_{1+x}LiH_{2-x}O_2$ ($y = 1$, $0 \le x \le 0.4$).

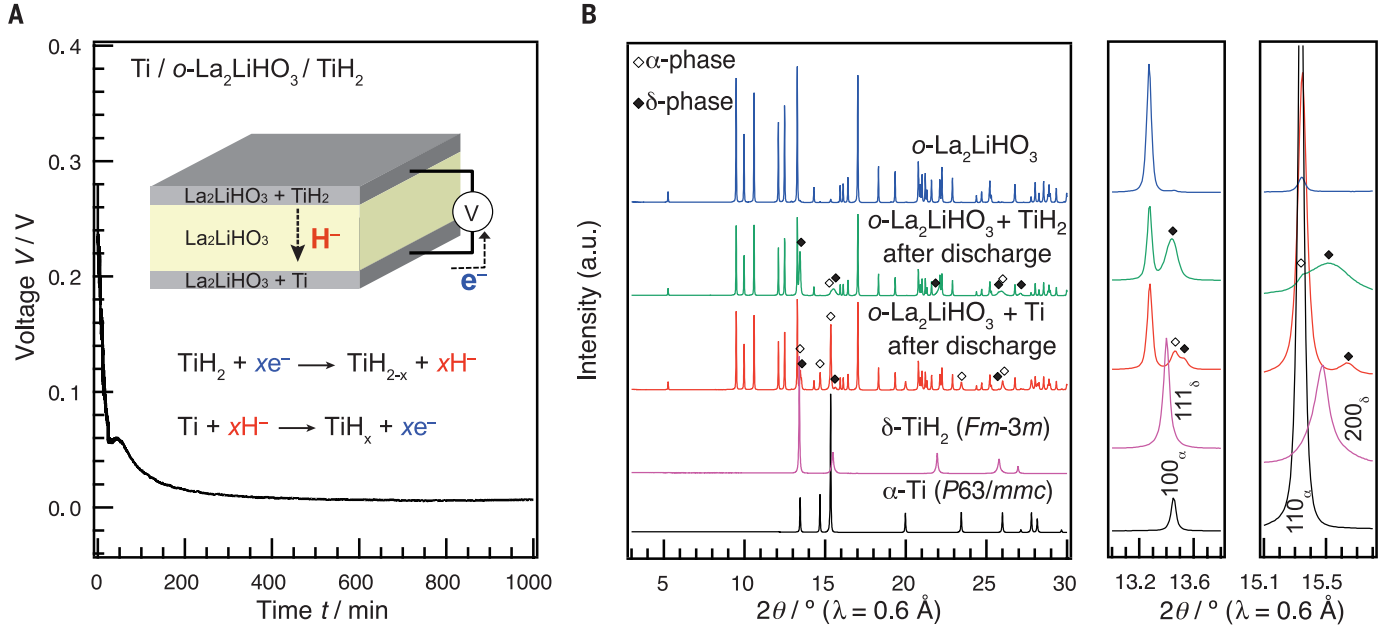



**Fig. 4. All-solid-state hydride cell.** (**A**) Discharge curve for a solid-state battery with the Ti/*o*-$La_2LiHO_3$/$TiH_2$ structure. The inset shows an illustration of the cell and the proposed electrochemical reaction. (**B**) X-ray diffraction patterns for the electrolyte (*o*-$La_2LiHO_3$), cathode ($TiH_2$ + *o*-$La_2LiHO_3$), and anode (Ti + *o*-$La_2LiHO_3$) materials after the reaction. Magnifications are supplied for ranges 13° to 13.8° and 15.1° to 15.8°.

In conclusion, pure $H^-$ conduction was realized in the $La_{2-x-y}Sr_{x+y}LiH_{1-x+y}O_{3-y}$ system. The present success in the construction of an all-solid-state electrochemical cell exhibiting $H^-$ diffusion confirms not only the capability of the oxyhydride to act as an $H^-$ solid electrolyte but also the possibility of developing electrochemical solid devices based on $H^-$ conduction.

## REFERENCES AND NOTES


1. N. Kamaya *et al.*, *Nat. Mater.* **10**, 682–686 (2011).
2. L. Malavasi, C. A. J. Fisher, M. S. Islam, *Chem. Soc. Rev.* **39**, 4370–4387 (2010).
3. S. Hull, *Rep. Prog. Phys.* **67**, 1233–1314 (2004).
4. R. Kanno, Y. Takeda, Y. Oda, H. Ikeda, O. Yamamoto, *Solid State Ion.* **18–19**, 1068–1072 (1986).
5. G. Dénès, G. Milova, M. C. Madamba, M. Perfiliev, *Solid State Ion.* **86–88**, 77–82 (1996).
6. P. F. Lang, B. C. Smith, *Dalton Trans.* **39**, 7786–7791 (2010).
7. H. Iwahara, H. Uchida, K. One, K. Ogaki, *J. Electrochem. Soc.* **135**, 529–533 (1988).
8. A. F. Andresen, A. J. Maeland, D. Slotfeldt-Ellingsen, *J. Solid State Chem.* **20**, 93–101 (1977).
9. B. Wegner, R. Essmann, J. Bock, H. Jacobs, *Eur. J. Solid State Inorg. Chem.* **29**, 1217–1227 (1992).
10. F. Altorfer *et al.*, *Solid State Ion.* **70–71**, 272–277 (1994).
11. B. Zhu, X. Liu, *Electrochem. Commun.* **2**, 10–14 (2000).
12. M. C. Verbraeken, E. Suard, J. T. S. Irvine, *J. Mater. Chem.* **19**, 2766–2770 (2009).
13. M. C. Verbraeken, C. Cheung, E. Suard, J. T. S. Irvine, *Nat. Mater.* **14**, 95–100 (2015).
14. M. A. Hayward *et al.*, *Science* **295**, 1882–1884 (2002).
15. R. M. Helps, N. H. Rees, M. A. Hayward, *Inorg. Chem.* **49**, 11062–11068 (2010).
16. Y. Kobayashi *et al.*, *Nat. Mater.* **11**, 507–511 (2012).
17. T. Sakaguchi *et al.*, *Inorg. Chem.* **51**, 11371–11376 (2012).
18. H. Schwarz, thesis, Univ. Karlsrühe (1991).
19. J. Bang *et al.*, *J. Am. Chem. Soc.* **136**, 7221–7224 (2014).
20. K. Hayashi, S. Matsuishi, T. Kamiya, M. Hirano, H. Hosono, *Nature* **419**, 462–465 (2002).
21. K. Hayashi, P. V. Sushko, A. L. Shluger, M. Hirano, H. Hosono, *J. Phys. Chem. B* **109**, 23836–23842 (2005).
22. S. Matsuishi, K. Hayashi, M. Hirano, H. Hosono, *J. Am. Chem. Soc.* **127**, 12454–12455 (2005).
23. C. G. Van de Walle, *Phys. Rev. Lett.* **85**, 1012–1015 (2000).
24. G. Chris, *Nature* **423**, 626–628 (2003).
25. J. Zhang, G. Gou, B. Pan, *J. Phys. Chem. C* **118**, 17254–17259 (2014).
26. Details of synthesis condition for the oxyhydrides are described in supplementary materials.
27. J. P. Attfield, G. Ferey, *J. Solid State Chem.* **80**, 112–119 (1989).
28. B. J. Neudecker, W. Weppner, *J. Electrochem. Soc.* **143**, 2198–2203 (1996).
29. A. San-Martin, F. D. Manchester, *Bull. Alloy Phase Diagrams* **8**, 30–42 (1987).


## ACKNOWLEDGMENTS

This research was supported by JST, PRESTO, and Grant-in-Aid for Young Scientists (A) no. 15H05497 and (B) no. 24750209; Grant-in-Aid for Challenging Exploratory Research nos. 15K13803, 23655191, and 25620180; and Grant-in-Aid for Scientific Research on Innovative Areas nos. 25106005 and 25106009, from the Japan Society for the Promotion of Science. Synchrotron and neutron radiation experiments were carried out as four projects approved by the Japan Synchrotron Radiation Research Institute (JASRI) (Proposal no. 2013A1704), the Japan Proton Accelerator Research Complex (J-PARC) (Proposal no. 2010A0058), the Spallation Neutron Source (SNS) in the Oakridge National Laboratory (Proposal no. IPTS5808), and the Neutron Scattering Program Advisory Committee of IMSS, KEK (Proposal no. 2014S10). A part of neutron experiments (Proposal no. 2014S10) was performed at BL09 Special environment neutron powder diffractometer (SPICA) developed by the Research and Development Initiative for Scientific Innovation of New Generation Batteries (RISING) project of the New Energy and Industrial Technology Development Organization (NEDO). Supercomputing time on the Academic Center for Computing and Media Studies (ACCMS) at Kyoto University is gratefully acknowledged. Further information regarding the materials and methods is included in the supplementary materials. G.K., A.W., M.H., and R.K. have filed for a patent application with the Japan Patent Office under no. JP2015-22868 on the $H^-$ conductive oxyhydride system and its manufacture.

## SUPPLEMENTARY MATERIALS

www.sciencemag.org/content/351/6279/1314/suppl/DC1
Materials and Methods
Supplemental Text
Figs. S1 to S11
Tables S1 to S7
References (*30*–*39*)

29 June 2015; accepted 20 January 2016
10.1126/science.aac9185

GAS INFRASTRUCTURE

# Methane emissions from the 2015 Aliso Canyon blowout in Los Angeles, CA

**S. Conley,[1,2]*† G. Franco,[3] I. Faloona,[2] D. R. Blake,[4] J. Peischl,[5,6] T. B. Ryerson[6]†**

**Single-point failures of natural gas infrastructure can hamper methane emission control strategies designed to mitigate climate change. The 23 October 2015 blowout of a well connected to the Aliso Canyon underground storage facility in California resulted in a massive release of natural gas. Analysis of methane and ethane data from dozens of plume transects, collected during 13 research-aircraft flights between 7 November 2015 and 13 February 2016, shows atmospheric leak rates of up to 60 metric tons of methane and 4.5 metric tons of ethane per hour. At its peak, this blowout effectively doubled the methane emission rate of the entire Los Angeles basin and, in total, released 97,100 metric tons of methane to the atmosphere.**

Large volumes of processed natural gas are stored underground to accommodate variability in energy demand on diurnal to seasonal time scales. Underground storage facilities constitute strategic gas reserves in many countries worldwide, with a volume equal to 10% of global annual consumption (*1*). Roughly 86% of stockpiled natural gas in the United States is stored at high pressure in depleted subsurface oil reservoirs (*2*). The Aliso Canyon storage facility, a depleted subsurface oil reservoir in the San Fernando Valley 40 km northwest of Los Angeles, CA, has a total capacity of 168 billion standard cubic feet (SCF) ($4.79 \times 10^9$ $m^3$) at standard temperature and pressure, of which only 86 billion SCF ($2.5 \times 10^9$ $m^3$; the "working capacity") is routinely accessed for commercial use (*2*). It is the fourth largest facility of its kind in the United States, accounting for 2.1% of the total U.S. natural gas storage in 2014 (*2*). Processed natural gas is composed primarily of methane ($CH_4$), a powerful greenhouse gas, and ethane ($C_2H_6$), both of which can lead to background tropospheric ozone production; at sufficiently high concentrations, natural gas leaks pose an explosion hazard and, if inhaled, can induce nausea, headaches, and impaired coordination. Exposure to odorants that are added to natural gas, which are typically sulfur-containing compounds such as tetrahydrothiophene [$(CH_2)_4S$] and 2-methylpropane-2-thiol [*t*-butyl mercaptan; $(CH_3)_3CSH$] can cause short-term loss of the sense of smell, headaches, and respiratory tract irritation. Major natural gas leaks therefore can have adverse impacts on climate, air quality, and human health.

On 23 October 2015, a major natural gas leak of indeterminate size was reported in the Aliso Canyon area and was later identified as originating from SS-25, one of 115 wells connected to the subsurface storage reservoir. The SS-25 well began oil production in 1954 and was converted to a gas storage well in 1973 (*3*). Seven unsuccessful attempts to close the leak have been reported. A relief well intercepted the leaking pipe at a depth of ~2600 m, below the subsurface breach; heavy fluid injection (a "bottom kill") temporarily halted the leak on 11 February 2016, and cement injection sealed the well on 18 February 2016 (*4*).

We deployed a chemically instrumented Mooney aircraft in 13 flights from 7 November 2015 to 13 February 2016. We measured $CH_4$ and $C_2H_6$ to quantify the atmospheric leak rate and to assess air quality downwind of the leaking well (*5*). Ground-based whole-air sampling (WAS) with stainless steel canisters on 23 December 2015, followed by laboratory analysis, provided information on the chemical speciation of the leaking hydrocarbon mixture. We used the continuous airborne data and the ground-based WAS canister

[1]Scientific Aviation, 3335 Airport Road, Boulder, CO 80301, USA. [2]Department of Land, Air, and Water Resources, University of California–Davis, Davis, CA 95616, USA. [3]Research and Development Division, California Energy Commission, Sacramento, CA 95814, USA. [4]Department of Chemistry, University of California–Irvine, Irvine, CA 92617, USA. [5]Cooperative Institute for Research in Environmental Sciences, University of Colorado–Boulder, Boulder, CO, 80309, USA. [6]Earth System Research Laboratory, National Oceanic and Atmospheric Administration (NOAA), Boulder, CO, 80305, USA.
***Corresponding author. E-mail: sconley@scientificaviation.com** †These authors contributed equally to this work.

Downloaded from on March 17, 2016

data to fingerprint the plume's chemical composition, quantify the atmospheric leak rate, and document trends in the leak rate over time.

The airborne chemical data showed the continuing transport on northerly winds of exceptionally high concentrations of $CH_4$ and $C_2H_6$ into the densely populated San Fernando Valley, a few kilometers south of the leaking well (Fig. 1). The plume $C_2H_6$-to-$CH_4$ enhancement ratio (ER) derived from linear least-squares regression fits to the 23 December 2015 continuous airborne data is identical, within total uncertainties propagated by quadrature addition of errors (*6*), to the plume ER derived from WAS canister data taken at the surface on the same day (Fig. 2A).

The hydrocarbon composition of WAS canister samples taken at surface locations in the San Fernando Valley (Fig. 1) on 23 December 2015 (*5*) is consistent with a leak of pipeline-quality processed natural gas with a hydrocarbon composition of ~95% $CH_4$, ~4% $C_2H_6$, and ~0.3% propane ($C_3H_8$) (table S1). Plume enhancements of natural gas liquids (ethane, propane, and butanes) and condensates (pentanes and longer-chain hydrocarbons that are liquid at ambient temperature and pressure) were detected (table S1) and were probably responsible for reports of oily deposits on surfaces in downwind residential areas. Trace enhancements of benzene, toluene, ethylbenzene, and xylene isomers (the so-called BTEX compounds) were also detected at ratios of 0.001% or lower relative to $CH_4$ (table S1).

Benzene is a known human carcinogen (*7*); thus, population exposure to benzene from the Aliso Canyon leak has received particular attention. Composition data from the WAS canisters indicate a benzene-to-$CH_4$ enhancement ratio of $(5.2 \pm 0.1) \times 10^{-6}$ (uncertainties throughout are ±1 SEM), which is broadly consistent with an ER of ~$7 \times 10^{-6}$ found in highly concentrated samples that were collected ~3 m downwind of the SS-25 well site (*8*). Together, these samples suggest minimal variation over time in the benzene composition of the leaking gas. Publicly available benzene data, reported in near-daily 12-hour air samples (*9*), were often below the detection limit of 1 nmol/mol [or 1 part per billion (ppb)] of the contract laboratories used for the analyses, but these data also show a relatively constant ER over time. Plume benzene enhancements can be estimated from the abundant $CH_4$ data by multiplying plume $CH_4$ enhancements by the benzene-to-$CH_4$ ER determined using the research-grade WAS canister samples. Sulfur-containing odorants were not measured, but concentrations above the odor threshold can be estimated similarly (Fig. 1) from observed $CH_4$ enhancements by assuming an industry-standard value of ~5 parts per million (ppm) of total odorant in processed natural gas (*10*).

Continuous airborne $CH_4$ and $C_2H_6$ data were taken on each flight between 11 AM and 3:30 PM (local time) with a resolution of 30 m along-track during repeated crosswind transects at multiple altitudes from 60 to 1400 m above ground. These data define the horizontal and vertical extent of the leaking natural gas plume on each flight (Fig. 1 and fig. S1). The flights provided highly spatially resolved data from which an atmospheric mass flux can be accurately calculated (*11*) within well-defined uncertainties (*12*). Plumes from nearby landfills have low concentrations of $CH_4$, are easily identified by their lack of co-emitted $C_2H_6$, and were eliminated from further analysis. Background levels of $CH_4$ and $C_2H_6$ were measured during aircraft transects on multiple flights immediately upwind, confirming the SS-25 well as the dominant source of enhanced natural gas to the region. Operational restrictions on aircraft flight patterns were imposed by the elevated terrain at the leak site, the highly controlled airspace of the San Fernando Valley, and the proximity to approach corridors of the nearby Van Nuys Airport (Fig. 1). These restrictions were overcome by performing crosswind transects at multiple altitudes immediately downwind of the leak site,

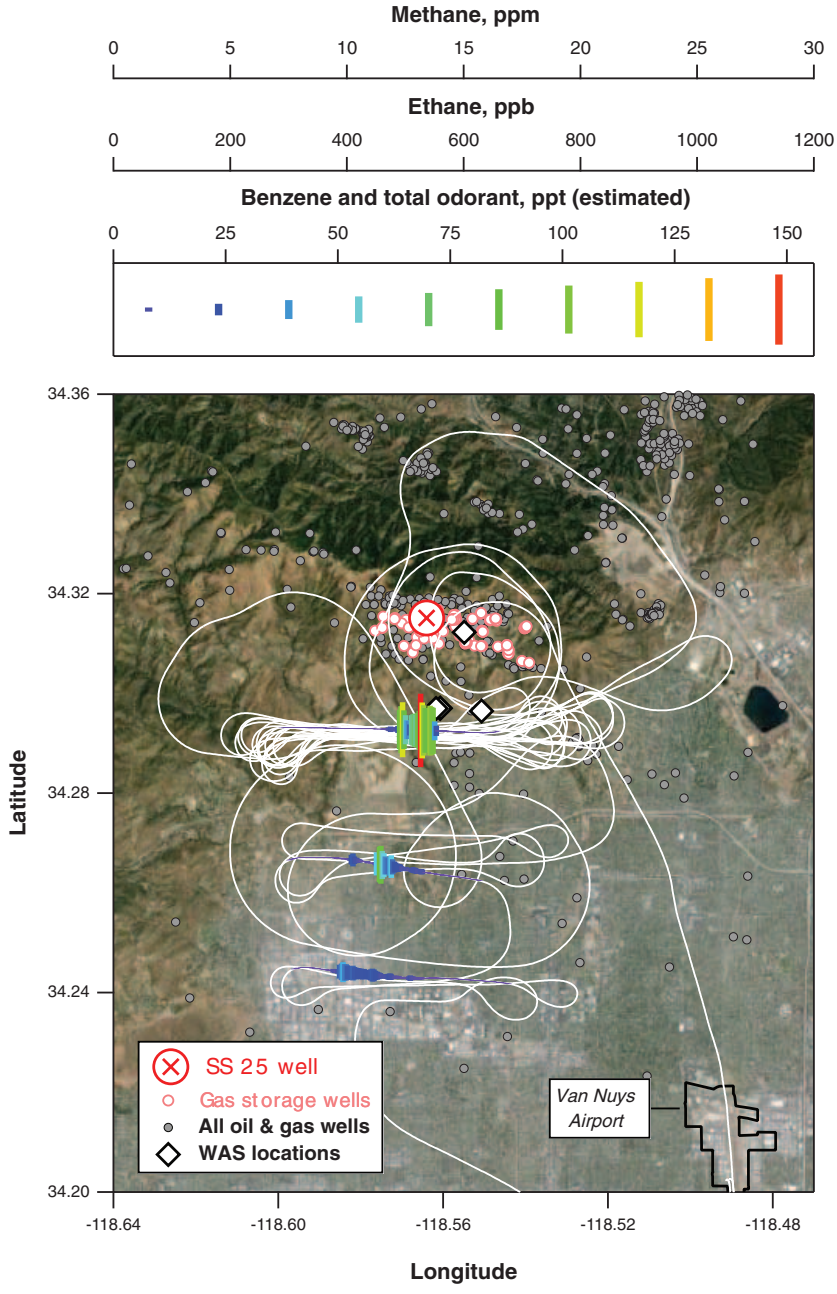



**Fig. 1. Aliso Canyon gas plume transport into populated areas.** Airborne chemical data illustrate plume transport into the San Fernando Valley; data from 10 November 2015 are shown. Plume enhancements above the local background (colored markers) from example transects are plotted along the flight track (white line) and can be scaled using the legends at top to yield measured $CH_4$, measured $C_2H_6$, estimated benzene based on the WAS benzene-to-$CH_4$ ER, and estimated total odorant (assuming 5 ppm in the leaking gas). Benzene and total odorant are in parts per trillion by volume (ppt).

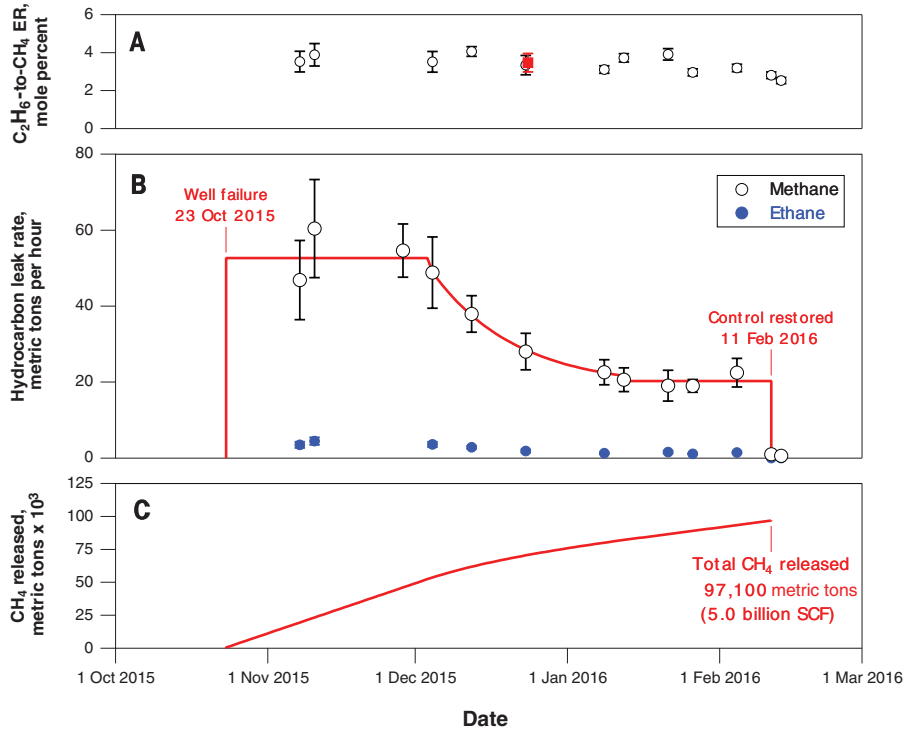



**Fig. 2. Time series of the Aliso Canyon natural gas leak.** (**A**) Plume $C_2H_6$-to-$CH_4$ ERs from airborne measurements (open circles) and ground-based WAS measurements (red square). (**B**) Leak rates (in metric tons per hour) of $CH_4$ (open circles) and $C_2H_6$ (blue circles), determined from airborne measurements. The red line is a fit to the airborne $CH_4$ data, assuming an average leak rate from the blowout (day 0) to day 43, an exponential decrease between days 43 and 80, and an average leak rate thereafter to day 112, when control was restored. (**C**) The total amount of $CH_4$ released (in metric tons), calculated from the fit in (B). Error bars indicate ±1 SEM.

which enabled accurate reconstruction of a vertical concentration profile, even before the plume had completely mixed throughout the full vertical extent of the atmospheric boundary layer (*5*).

The chemical data show that the airborne sampling captured the full vertical extent of the lofted plumes on each flight day (fig. S1). Atmospheric mass fluxes calculated from the chemical data from each transect collected downwind (*5*) suggest an average leak rate of 53 ± 3 metric tons of $CH_4$ and 3.9 ± 0.3 metric tons of $C_2H_6$ per hour for the first six weeks of the leak, decreasing thereafter (Fig. 2B and table S2). The decreasing trend, which began around the first week of December 2015 (Fig. 2B and table S2), is consistent with decreasing reservoir pressure in response to the withdrawal of gas through other storage wells connected to the subsurface reservoir, which was done in a deliberate effort to slow the leak (*13*). The lack of a decrease in the leak rate after the first week of January 2016 is consistent with the cessation of withdrawals to maintain a minimum working pressure in the reservoir, which supplied natural gas to customers in the greater Los Angeles basin throughout the leak duration.

These data demonstrate that the blowout of a single well in Aliso Canyon temporarily created the largest known anthropogenic point source of $CH_4$ in the United States (*14*), effectively doubling the leak rate of all other sources in the Los Angeles basin combined (*15, 16*). Further, at its peak, this leak rate exceeded that of the next largest point source in the United States—an underground coal mine in Alabama—by over a factor of 2 (*14*) and was a factor of 10 larger than the $CH_4$ leak rate reported from the Total *Elgin* rig blowout in the North Sea in 2012 (*17*). The Aliso Canyon $CH_4$ leak rates were comparable to the total $CH_4$ emission rates of entire oil and gas production regions in the United States [e.g., the Barnett shale, 76 metric tons per hour (*18*); the Haynesville shale, 80 metric tons per hour (*19*); the Fayetteville shale, 39 metric tons per hour (*19*); and the northeastern Marcellus shale, 15 metric tons per hour (*19*)].

Our aircraft flights after the "bottom kill" confirmed the cessation of flow from the SS-25 well on 11 February 2016 and revealed a residual leak rate of <1 metric ton of $CH_4$ per hour (Fig. 2B and table S2), consistent with nonzero leak rates observed at other natural gas, oil, and petrochemical facilities nationwide (*16*, *18*–*24*). These data show that over its 112-day duration, the Aliso Canyon natural gas leak released a total of 97,100 metric tons (5.0 billion SCF) of $CH_4$ (Fig. 2C) and 7300 metric tons (0.2 billion SCF) of $C_2H_6$ to the atmosphere, which is equal to 24% of the $CH_4$ and 56% of the $C_2H_6$ emitted each year from all other sources in the Los Angeles basin combined (*16*).

This $CH_4$ release is the second largest of its kind recorded in the United States, exceeded only by the 6 billion SCF (115,000 metric tons) of natural gas released in the 2004 collapse of an underground storage facility in Moss Bluff, TX, and greatly surpassing the 0.1 billion SCF (1900 metric tons) of natural gas leaked from an underground storage facility near Hutchinson, KS, in 2001 (*25*). Aliso Canyon will have the largest climate impact by far, however, given that an explosion and subsequent fire during the Moss Bluff release combusted most of the leaked $CH_4$, immediately forming $CO_2$. The total release from Aliso Canyon will substantially affect the State of California greenhouse gas (GHG) emission targets for the year (*26*) and is equivalent to the annual energy sector $CH_4$ emissions from medium-sized European Union nations (*27*). The radiative forcing from this amount of $CH_4$, integrated over the next 100 years, is equal to that from the annual GHG emissions of 572,000 passenger cars in the United States (*28*). The volume of $CH_4$ released represents only 3% of the total capacity of the Aliso Canyon storage facility, raising the possibility of substantial additional emissions if the leaking SS-25 well had not been sealed, or if the remaining natural gas had not been withdrawn through other wells, before the reservoir was completely exhausted to the atmosphere.

The agreement reached at the 21st Conference of the Parties (COP21) to the UN Framework Convention on Climate Change (*29*) includes specific requirements for the Parties to account for anthropogenic GHG emissions with accuracy and completeness. In the post-COP21 world, rapid evaluation of episodic GHG release events, such as the Aliso Canyon blowout, will be an essential contribution to meeting these requirements.

Our analysis quantifies a massive $CH_4$ release using a rapid, direct, and repeatable method with known accuracy. As such, results from this method serve as reference values for less direct and timely estimates that use retrievals of surface (*30, 31*), airborne (*32*), and/or satellite remote sensing observations (*33*). For example, our airborne method offers a priori estimates of the Aliso Canyon leak rates that can be used for inverse modeling analysis of continuous in situ $CH_4$ monitoring data from fixed ground sites (*15, 34*). This incident highlights the utility of rapid-response airborne chemical sampling in providing an independent, time-critical, accurate, and spatially and temporally resolved leak rate, as well as in ascertaining the source location and plume chemical composition. Such information can help to document human exposure, formulate optimal well-control intervention strategies, quantify the efficacy of deliberate control measures, and assess the climate and air quality impacts of major unanticipated chemical releases to the atmosphere (*35, 36*).

## REFERENCES AND NOTES

1. S. Cornot-Gandolphe, *Underground Gas Storage in the World 2013: Executive Summary* (Centre International d'Information sur le Gaz Naturel et tous Hydrocarbures Gazeux, Rueil-Malmaison, France, 2013).

2. Natural Gas Annual Respondent Query System (U.S. Energy Information Administration, 2015); www.eia.gov/cfapps/ngqs/ngqs.cfm?f_report=RP7.
3. State of California Department of Conservation, Division of Oil and Gas, *Report on Proposed Change of Well Designation* (1991); ftp://ftp.consrv.ca.gov/pub/oil/Standard_Sesnon_25_API_037-00776_Well_File/03700776_DATA_03-19-2008.pdf.
4. SoCalGas, press release (18 February 2016); www.alisoupdates.com/1443738511730/press-release-doggr-confirms-en.pdf.
5. Materials and methods are available as supplementary materials on *Science* Online.
6. P. R. Bevington, D. K. Robinson, *Data Reduction and Error Analysis in the Physical Sciences* (McGraw-Hill, ed. 3, 2003).
7. U.S. Environmental Protection Agency (EPA), "Benzene" (2014); http://cfpub.epa.gov/ncea/iris2/chemicalLanding.cfm?substance_nmbr=276.
8. South Coast Air Quality Management District, "Laboratory results" (2016); srvwww.aqmd.gov/home/regulations/compliance/aliso-canyon-update/gas-sample-near-leaking-well/laboratory-results [accessed 13 February 2016].
9. SoCalGas, "Aliso Canyon air sample results" (2016); www.socalgas.com/newsroom/aliso-canyon-updates/aliso-canyon-air-sample-results.
10. Pacific Gas and Electric Company, "Gas system sulfur survey results" (2015); www.pge.com/pipeline/operations/sulfur/sulfur_info_values/index.page.
11. W. H. White *et al.*, *Science* **194**, 187–189 (1976).
12. T. B. Ryerson *et al.*, *Science* **292**, 719–723 (2001).
13. SoCalGas, press release (11 February 2016); www.alisoupdates.com/1443738468372/SoCalGas-Temporarily-Controls-Flow-of-Gas-021116-2.pdf.
14. U.S. EPA (2014); http://ghgdata.epa.gov/ghgp/service/html/2014?id=1010328&et=undefined.
15. S. Jeong *et al.*, *J. Geophys. Res.* **117**, D11306 (2012).
16. J. Peischl *et al.*, *J. Geophys. Res. D Atmospheres* **118**, 4974–4990 (2013).
17. Total, press release (11 March 2013); www.elgin.total.com/elgin/pressrelease.aspx.
18. A. Karion *et al.*, *Environ. Sci. Technol.* **49**, 8124–8131 (2015).
19. J. Peischl *et al.*, *J. Geophys. Res.* **120**, 2119–2139 (2015).
20. A. R. Brandt *et al.*, *Science* **343**, 733–735 (2014).
21. A. Karion *et al.*, *Geophys. Res. Lett.* **40**, 4393–4397 (2013).
22. E. A. Kort *et al.*, *Geophys. Res. Lett.* **41**, 6898–6903 (2014).
23. G. Pétron *et al.*, *J. Geophys. Res.* **119**, 6836–6852 (2014).
24. T. B. Ryerson *et al.*, *J. Geophys. Res.* **108**, 4249 (2003).
25. B. Miyazaki, in *Underground Gas Storage: Worldwide Experiences and Future Development in the UK and Europe*, D. J. Evans, R. A. Chadwick, Eds. (Geological Society, vol. 313, London, 2009), pp. 163–172.
26. California Environmental Protection Agency Air Resource Board, "Assembly Bill 32 overview" (2014); www.arb.ca.gov/cc/ab32/ab32.htm.
27. EDGAR - Emission Database for Global Atmospheric Research (European Commission Joint Research Centre, 2016); http://edgar.jrc.ec.europa.eu/datasets_grid_list42FT2010.php?v=42FT2010&edgar_compound=CH4.
28. U.S. EPA, *Greenhouse Gas Emissions from a Typical Passenger Vehicle* (2014).
29. UN Framework Convention on Climate Change, *Adoption of the Paris Agreement* (2015); http://unfccc.int/resource/docs/2015/cop21/eng/l09r01.pdf.
30. R. A. Washenfelder, P. O. Wennberg, G. C. Toon, *Geophys. Res. Lett.* **30**, 2226 (2003).
31. K. W. Wong *et al.*, *Atmos. Chem. Phys.* **15**, 241–252 (2015).
32. R. O. Green *et al.*, *Remote Sens. Environ.* **65**, 227–248 (1998).
33. A. Butz *et al.*, *Geophys. Res. Lett.* **38**, L14812 (2011).
34. S. M. Miller *et al.*, *Proc. Natl. Acad. Sci. U.S.A.* **110**, 20018–20022 (2013).
35. M. K. McNutt *et al.*, *Proc. Natl. Acad. Sci. U.S.A.* **109**, 20260–20267 (2012).
36. T. B. Ryerson *et al.*, *Proc. Natl. Acad. Sci. U.S.A.* **109**, 20246–20253 (2012).



**ACKNOWLEDGMENTS**

The first two Scientific Aviation flights were funded by the California Energy Commission through University of California–Davis project #201401201. Subsequent flights were funded by the Southern California Gas Company, the operator of the Aliso Canyon storage facility. I.F. was supported in part by the California Agricultural Experiment Station (Hatch project CA-D-LAW-2229-H). J.P. and T.R. were supported in part by the NOAA Climate Program Office and the NOAA Atmospheric Chemistry, Carbon Cycle, and Climate program. We acknowledge the contributions of M. Trainer for scientific input and K. Aikin and S. Wolter for time-critical technical support. The views expressed here are those of the authors and do not constitute endorsement by their funding agencies. Data used in this report are posted at esrl.noaa.gov/csd/scientificaviation.


**SUPPLEMENTARY MATERIALS**

www.sciencemag.org/content/351/6279/1317/suppl/DC1
Materials and Methods
Figs. S1 and S2
Tables S1 and S2
References (*37*–*44*)


11 January 2016; accepted 17 February 2016
Published online 25 February 2016
10.1126/science.aaf2348


BIOCHEMISTRY

# Fine-tuning of a radical-based reaction by radical *S*-adenosyl-L-methionine tryptophan lyase


**Giuseppe Sicoli,[1,2] Jean-Marie Mouesca,[1,2] Laura Zeppieri,[3] Patricia Amara,[3] Lydie Martin,[3] Anne–Laure Barra,[4] Juan C. Fontecilla-Camps,[3] Serge Gambarelli,[1,2]* Yvain Nicolet[3]***



**The radical *S*-adenosyl-L-methionine tryptophan lyase NosL converts L-tryptophan into 3-methylindolic acid, which is a precursor in the synthesis of the thiopeptide antibiotic nosiheptide. Using electron paramagnetic resonance spectroscopy and multiple L-tryptophan isotopologues, we trapped and characterized radical intermediates that indicate a carboxyl fragment migration mechanism for NosL. This is in contrast to a proposed fragmentation-recombination mechanism that implied Cα–Cβ bond cleavage of L-tryptophan. Although NosL resembles related tyrosine lyases, subtle substrate motions in its active site are responsible for a fine-tuned radical chemistry, which selects the Cα–C bond for disruption. This mechanism highlights evolutionary adaptation to structural constraints in proteins as a route to alternative enzyme function.**


Nosiheptide, produced by *Streptomyces actuosus*, is a highly modified, sulfur-rich, polythiazolyl macrocyclic peptide antibiotic (*1*). This compound exhibits highly potent activity against multidrug-resistant strains of several gram-positive pathogens (*2*–*5*). Originating from a 13-residue-long, ribosomally synthesized peptide, nosiheptide contains a central tetra-substituted pyridine ring, five thiazole rings, and an unusual indolic acid (*6*, *7*). The latter is produced by the tryptophan lyase (NosL) enzyme, which converts L-tryptophan to the methylindolic acid (MIA) precursor that is subsequently inserted into the thiopeptide (*8*, *9*). NosL belongs to the radical *S*-adenosyl-L-methionine (SAM) protein superfamily, which uses a reduced $[Fe_4S_4]^+$ cluster and SAM to initiate a 5′-deoxyadenosyl radical (5′-dA•)–based reaction (*10*). Homologous tyrosine lyases (CofH, ThiH, and HydG) cleave the Cα–Cβ bond of tyrosine, producing a *p*-cresyl radical and dehydroglycine (DHG) (*11*–*15*).

Because of the prevalence of tyrosyl and tryptophanyl radicals in proteins, it was initially proposed that the H-atom abstraction from L-tyrosine and L-tryptophan by the highly reactive 5′-dA• should take place at the L-tyrosine phenol group and at the L-tryptophan indole nitrogen, respectively (*9*, *12*, *14*). However, a recent NosL structure in complex with L-tryptophan (*16*) indicates that the H-atom abstraction takes place at the amino nitrogen atom (Fig. 1A). Biochemical studies confirmed that this abstraction in NosL is the first step in the conversion of L-tryptophan into MIA. NosL can perform β-scissions from the amino-centered radical intermediate at either Cα–Cβ or Cα–C when using L-tryptophan analogs (*17*, *18*). These observations suggest a relative propensity of NosL for substrate promiscuity that, combined with slight differences in


[1]Université Grenoble–Alpes, Institut Nanosciences et Cryogénie (INAC)–Service de Chimie Inorganique et Biologique (SCIB)/Laboratoire de Résonance Magnétique (LRM), F-38000 Grenoble, France. [2]Commissariat à l'Energie Atomique et aux Energies Alternatives (CEA), INAC-SCIB/LRM, F-38000 Grenoble, France. [3]Metalloproteins Unit, Institut de Biologie Structurale, CEA, CNRS, Université Grenoble-Alpes, 71, Avenue des Martyrs, 38044 Grenoble Cedex 9, France. [4]Laboratoire National des Champs Magnétiques Intenses, UPR CNRS 3228, F-38048 Grenoble, France.
***Corresponding author. E-mail: yvain.nicolet@ibs.fr (Y.N.); serge.gambarelli@cea.fr (S.G.)**


Downloaded from on March 17, 2016

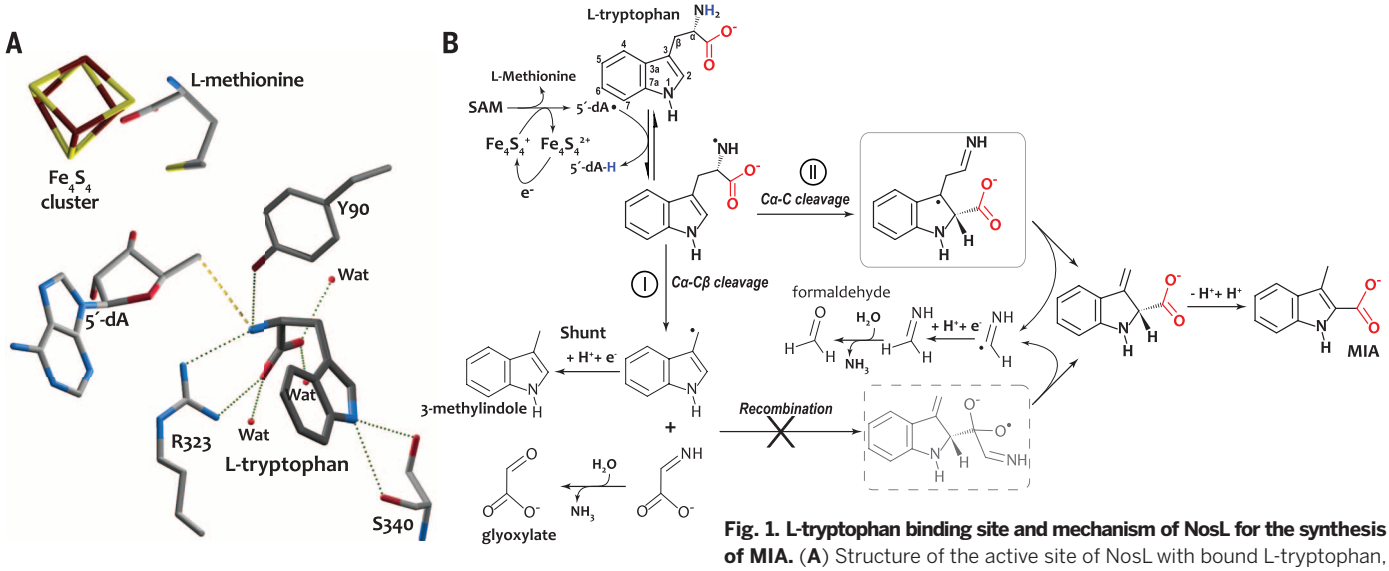



**Fig. 1. L-tryptophan binding site and mechanism of NosL for the synthesis of MIA.** (**A**) Structure of the active site of NosL with bound L-tryptophan, L-methionine, and 5′-dA (*16*). Only L-tryptophan (in dark gray), 5′-dA, L-methionine, the $Fe_4S_4$ cluster, and the residues interacting with substrate are depicted. (**B**) After H-atom abstraction from the amino nitrogen atom by the radical SAM enzyme, path **I** corresponds to the previously proposed fragmentation-recombination mechanism based on the in vitro observation of "shunt" reaction products (3-methylindole and glyoxylate) (*9*, *17*, *18*). In path **II**, our proposed productive mechanism differs from the shunt reaction and leads to MIA, without involving recombination but including two successive β-scissions. The first β-scission involves an unanticipated carboxyl fragment migration, leading to an unprecedented C3-centered radical intermediate (solid-line box).

the orientation of these different substrates in the active site cavity, fine-tunes the β-scission selection.

Through homology to radical SAM tyrosine lyases, it was proposed that productive β-scission in NosL should correspond to the Cα–Cβ bond disruption of L-tryptophan, leading to a 3-methylindolyl radical and DHG intermediates (Fig. 1B, path **I**) (*9*, *14*, *18*). MIA formation would then require a complex recombination step through a radical aromatic addition reaction, leading to an oxygen-centered radical intermediate (Fig. 1B, dashed-line box). A subsequent β-scission would lead to MIA and most probably a methyleneimine by-product subsequently hydrolyzed to formaldehyde (*9*). Apart from the shunt and by-products (Fig. 1B, path **I**), no intermediate has been observed for this complex radical-based reaction, and the mechanism for the proposed recombination step has remained elusive. To understand the enzymatic mechanism in this reaction, we used electron paramagnetic resonance (EPR) spectroscopy to examine NosL from *S. actuosus*. Using multiple isotopologues of L-tryptophan combined with quantum mechanical calculations, we characterized several free-radical intermediates of the reaction.

We initially sought to trap and characterize the previously proposed 3-methylindolyl radical (Fig. 1B, path **I**) equivalent to the *p*-cresyl radical reported for HydG (*14*). When we conducted EPR experiments on sodium dithionite (DTH)–reduced NosL in the presence of SAM and L-tryptophan, we observed at 20 K an X-band continuous wave (CW) EPR rhombic signal with *g* tensor values 1.88, 1.91, and 2.04 that we attributed to the spin 1/2 reduced $[Fe_4S_4]^+$ cluster (fig. S1). In addition to this signal, we observed an unusually broad and complex X-band CW EPR signal centered at $g = 2.00402$, most likely corresponding to an organic radical species (Fig. 2A and fig. S1). Repeating the experiment with samples cryo-trapped at different times *t* indicated that this species is transient with a maximum intensity at about $t = 45$ s (fig. S2C). Other than the broader signal resulting from the reduced $[Fe_4S_4]^+$ cluster, this $g \approx 2.0$–centered signal was the only one observed between 5 s and 10 min. As expected, when the temperature was increased above 40 K, the signal from the $[Fe_4S_4]^+$ cluster rapidly decayed, whereas the organic radical signal remains even at 100 K. However, when comparing spectra recorded at 80 and 60 K, some lines exhibited partial saturation, suggesting that they correspond to the superposition of signals from at least two different organic radical species (Fig. 2 and fig. S2). Using these differential saturation properties, we distinguished two species with respective spectral widths of 9.0 and 6.2 mT, here named "broad" and "narrow" signals, respectively. The relative abundance of these species remained the same in all our experiments.

To better distinguish the two radical species, we performed Q-band (33.6 GHz) EPR measurements and obtained no detectable shifting of line positions (fig. S3). Even very high-field (345 GHz) EPR measurements did not show splitting between the two species, indicating that their *g* values are nearly the same (fig. S4). The extremely small anisotropy of the *g*-factor favors a carbon-centered radical and excludes oxygen- or nitrogen-centered radicals. In order to determine the identity of these two radical species, we used different L-tryptophan isotopologues as reaction substrates (fig. S5) and recorded X-band EPR spectra under the same conditions (fig. S6). All the tested isotopic substitutions alter the broad and narrow signals in the same manner (Fig. 2 and table S1). These results, and the fact that their *g* values are indistinguishable, suggest very similar chemical structures for these two species.

A more detailed analysis of these spectra and comparison with density functional theory (DFT) calculations excludes several otherwise plausible radical intermediate structures (*9*, *18*) (tables S1 to S14 and fig. S7). First, a strong reduction in the width of both species' spectra by using 2,4,5,6,7-$^2H_5$–labeled L-tryptophan (Fig. 2B, "*c*" and "*d*"), confirmed that they both derive from L-tryptophan and could correspond to different intermediates in the time course of the reaction. This observation also indicates that the radical is located either close to or directly on the indole ring. This excludes (i) an amino-centered tryptophanyl radical, (ii) a putative glycyl radical, and (iii) the proposed final methyleneiminyl radical as one of these trapped intermediates (Fig. 1B). 1-$^{15}$N–labeling had no detectable effect on any of the CW-EPR spectra (Fig. 2B, "*b*," and fig. S8), thus excluding an unpaired electron located at the N1 position, as would be the case for the conventional tryptophanyl radical. Furthermore, the hyperfine couplings (3.0 to 6.0 MHz) measured from two-dimensional EPR experiments (fig. S8) were not compatible with a nitrogen-centered radical. Conversely, $^{13}$C-labeled L-tryptophan either at C2 or at the C(OOH) carbon atoms altered spectra of both species with the appearance of an additional large hyperfine coupling (Fig. 2B, "*f*" and "*g*," and figs. S9 and S10). This unexpected result (i) excludes the 3-methylindolyl radical as one of the two intermediates and (ii) supports a structure with the C(OOH) and C2 atoms in close proximity to the radical. No effect was observed in any of the spectra when substituting $H_2O$ with $D_2O$ (Fig. 2B, "*d*" and

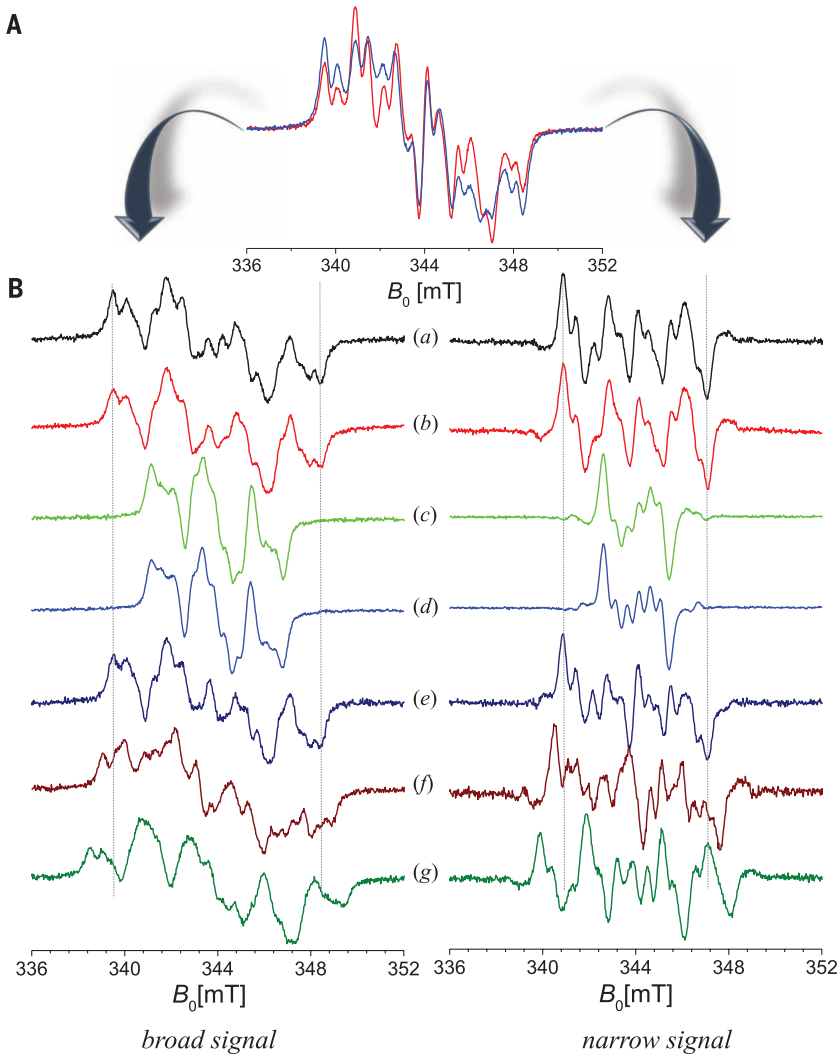



**Fig. 2. CW EPR spectra recorded at different temperature values.** (**A**) NosL containing unlabeled L-tryptophan (Trp) in $H_2O$ (quenching time of the reaction, 45 s) at 80 K (red line) and 60 K (blue line). Spectra were recorded at 9.65 GHz, 1 mW. (**B**) Broad and narrow components obtained upon deconvolution of CW spectra recorded at 80 and 60 K. The deconvolution is based on the different relaxation properties of single species. Unlabeled Trp in $H_2O$ (*a*, black), $^{15}$N-Trp (*b*, indole N-1, red), 2,4,5,6,7-$^{2}H_5$-Trp in $H_2O$ (*c*, light green), 2,4,5,6,7-$^{2}H_5$-Trp in $D_2O$ (*d*, blue), unlabeled Trp in $D_2O$ (*e*, navy), $^{13}$C-Trp (*f*, indole C-2, brown), and $^{13}$C-Trp (*g*, carboxyl, dark green).

"*e*"), ruling out substantial spin density located on any atom carrying an exchangeable proton. This excludes the oxygen-centered radical presented in path **I** of Fig. 1B because it exhibits a strong coupling at the Nα-H exchangeable proton (table S14, **13**).

Only one C3-centered radical species satisfies all the above conditions (Fig. 3). A complete simultaneous simulation of all spectra is possible with parameters compatible with those obtained from DFT calculations (Fig. 3, figs. S11 and S12, and tables S15 and S16). Rotation around the C3–Cβ bond produces sets of rotamers that explain both broad or narrow spectra because the hyperfine couplings transferred to Cβ are large and generally nonequivalent, as already reported for tyrosyl radicals (Fig. 3) (*19*). The presence of an intact Cα–Cβ bond is strongly supported by the fact that a methyl at Cβ would bear undistinguishable protons (table S13). Furthermore, whereas the third proton of the methyl group in MIA comes from solvent (*9*), no effect was observed when substituting $H_2O$ with $D_2O$. The aldehyde (–Cα=O) and aldimine (–Cα=NH) radical species are spectroscopically indistinguishable because there is no spin density on either the O- or N-heteroatoms. Hydrolysis of the aldimine may occur either before or after the second scission. Thus, our species may either correspond to two conformers of the same radical or to a mixture of the aldehyde- and aldimine-bearing radical species.

This unanticipated radical intermediate between L-tryptophan and MIA invalidates the previously proposed Cα–Cβ fragmentation-recombination mechanism (Fig. 1B, path **I**). Instead, NosL operates through a •COO(H) fragment transfer from Cα to C2 (Fig. 1B, path II) and is therefore different from its next-of-kin tyrosine lyases. Despite sharing similar active sites and 5′-dA• abstraction of a hydrogen atom from the amino nitrogen of their respective substrate, NosL and HydG likely diverged by subsequently selecting alternative C–C bond cleavage. When in silico scanning the C2–C3–Cβ–Cα dihedral of the amino-centered tryptophanyl radical (*20*), which results from the H-atom abstraction by 5′-dA•, we found two thermally accessible stable conformations in the protein (Fig. 4). One of them resembles the x-ray structure of L-tryptophan–bound NosL complex, and its corresponding spin density indicates depletion at the Cα–Cβ bond (Fig. 4, **1**). In the alternative orientation, the spin density shows depletion at the Cα–C bond (Fig. 4, **2**). This rotation around the C3–Cβ is potentially responsible for the fine-tuning of the C–C bond cleavage selection (fig. S13) in NosL, distinguishing it from tyrosine lyases. However, although NosL produces MIA through this Cα–C bond cleavage, it also concurrently catalyzes the Cα–Cβ bond cleavage shunt in vitro, producing methylindole and glyoxylate (Fig. 1B). This in vitro NosL promiscuity is modulated by the amount and the nature of the reductant used (*9*, *18*), which supposes a tighter control in vivo.

The propensity to allow for alternative cleavages is likely a vestige from evolution, during which selection transformed a molecular architecture initially suited for Cα–Cβ bond cleavage and compatible with the conformation of L-tryptophan in our crystallographic structure to satisfy the needs of Cα–C cleavage for MIA synthesis. Indeed, multiple deuteron incorporation

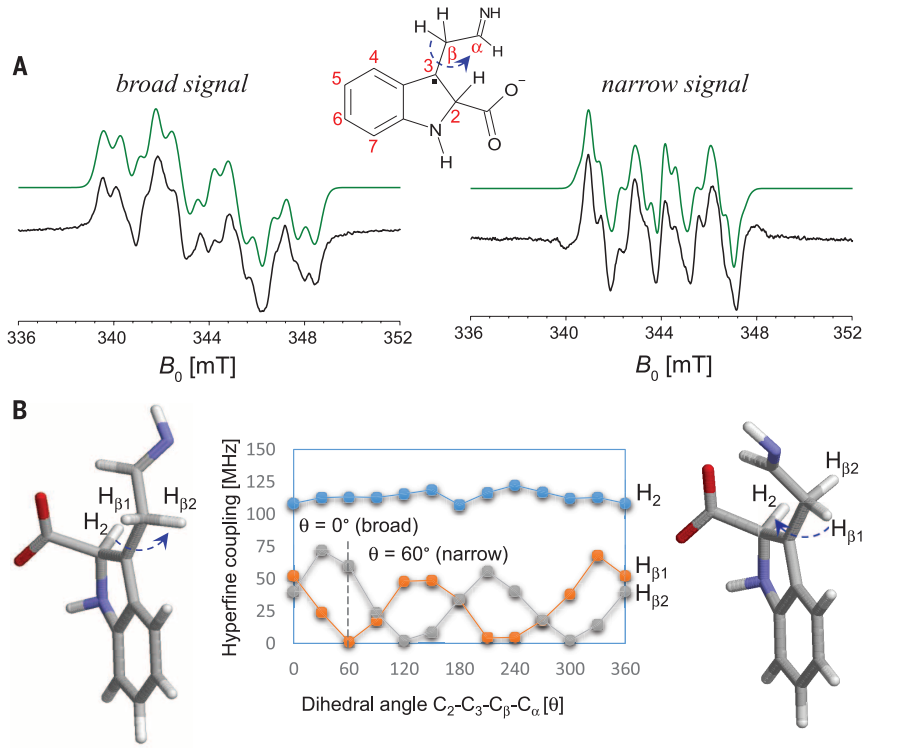



**Fig. 3. Proposed C3-centered radical intermediates.** The structure of the C3-centered radical is depicted at the top of the figure. (**A**) The HN=Cα–Cβ fragment is still attached to the C3 of the indole ring. Broad and narrow signals obtained upon deconvolution (black lines) and their corresponding best fit (green lines). (**B**) Hyperfine couplings of H2, $H\beta_1$, and $H\beta_2$ (in blue, orange, and gray, respectively) with respect to the dihedral angle [C2–C3–Cβ–Cα]. Negligible variations are observed for the H2 proton coupling, whereas substantial changes affect $H\beta_1$ and $H\beta_2$. Structures corresponding to θ = 0° and θ = 60° are depicted on the left and right side, respectively. For the selected C3-centered radical, the C2–C3–Cβ–Cα dihedral angle has been constrained to fixed values from 0° to 330° by steps of 30° during geometry optimization.

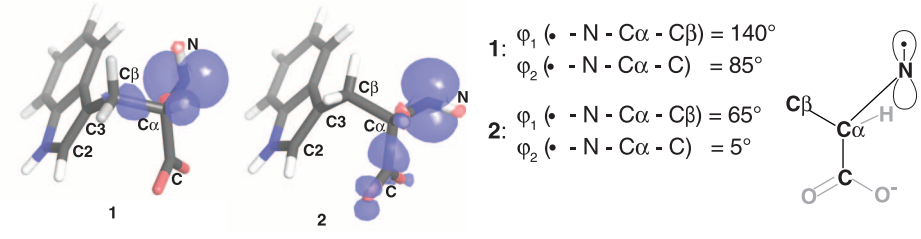



**Fig. 4. Changes in spin density are responsible for fine-tuning radical-based chemistry.** The depicted spin density of the amino-centered tryptophanyl radical is a direct visualization of the electron hole resulting from H• abstraction. Two stable conformers were obtained for this radical from a calculation including the protein matrix (*20*). In **1**, the Cα–C σ bond lies in the nodal plane of the radical p orbital ($\varphi 2 = 85°$), which prevents radical delocalization/electron depletion at this bond. In contrast, the Cα–Cβ σ bond is weakened through electron hole delocalization ($\varphi_1 = 140°$). In **2**, the situation is almost reversed, and the Cα–C σ bond is now the one being weakened. (Right) A representation of the discussed dihedral angles.

in 5′-dA was observed in solution in the homologous HydG (*21*), suggesting a reversible H-atom abstraction step. Furthermore, L-tryptophan was not processed in our crystals upon SAM cleavage to 5′-dA (*16*). These observations indicate that L-tyrosine and L-tryptophan in HydG and NosL are probably not ideally oriented for a fast β-scission after H-atom abstraction. In NosL, this limiting step would allow for the tryptophanyl radical conformational change that is responsible for MIA synthesis. In addition, accumulation of our EPR-trapped intermediate in two conformations suggests that the subsequent β-scission, converting the radical intermediate we observed into MIA, is also a slow process. The penultimate step (Fig. 1B), reminiscent of the first β-scission, requires similar orbital matches afforded by the rotation around the C3–Cβ bond. The absence of an EPR signal for the •COO(H) fragment suggests that its migration is either fast or concerted with Cα–C bond cleavage.

## REFERENCES AND NOTES


1. M. C. Bagley, J. W. Dale, E. A. Merritt, X. Xiong, *Chem. Rev.* **105**, 685–714 (2005).
2. F. Benazet *et al.*, *Experientia* **36**, 414–416 (1980).
3. B. N. Naidu *et al.*, *Bioorg. Med. Chem. Lett.* **14**, 5573–5577 (2004).
4. M. J. Pucci *et al.*, *Antimicrob. Agents Chemother.* **48**, 3697–3701 (2004).
5. W. Li *et al.*, *J. Antibiot. (Tokyo)* **56**, 226–231 (2003).
6. T. Prange, A. Ducruix, C. Pascard, J. Lunel, *Nature* **265**, 189–190 (1977).
7. C. Pascard, A. Ducruix, J. Lunel, T. Prangé, *J. Am. Chem. Soc.* **99**, 6418–6423 (1977).
8. Y. Yu *et al.*, *ACS Chem. Biol.* **4**, 855–864 (2009).
9. Q. Zhang *et al.*, *Nat. Chem. Biol.* **7**, 154–160 (2011).
10. J. B. Broderick, B. R. Duffus, K. S. Duschene, E. M. Shepard, *Chem. Rev.* **114**, 4229–4317 (2014).
11. L. Decamps *et al.*, *J. Am. Chem. Soc.* **134**, 18173–18176 (2012).
12. M. Kriek, F. Martins, M. R. Challand, A. Croft, P. L. Roach, *Angew. Chem. Int. Ed. Engl.* **46**, 9223–9226 (2007).
13. Y. Nicolet, J. C. Fontecilla-Camps, *J. Biol. Chem.* **287**, 13532–13540 (2012).
14. J. M. Kuchenreuther *et al.*, *Science* **342**, 472–475 (2013).
15. B. Philmus, L. Decamps, O. Berteau, T. P. Begley, *J. Am. Chem. Soc.* **137**, 5406–5413 (2015).
16. Y. Nicolet, L. Zeppieri, P. Amara, J. C. Fontecilla-Camps, *Angew. Chem. Int. Ed. Engl.* **53**, 11840–11844 (2014).
17. X. Ji, Y. Li, W. Ding, Q. Zhang, *Angew. Chem. Int. Ed. Engl.* **54**, 9021–9024 (2015).
18. D. M. Bhandari, H. Xu, Y. Nicolet, J. C. Fontecilla-Camps, T. P. Begley, *Biochemistry* **54**, 4767–4769 (2015).
19. K. Warncke, M. S. Perry, *Biochim. Biophys. Acta* **1545**, 1–5 (2001).
20. Materials and methods are available as supplementary materials on *Science* Online.
21. B. R. Duffus, S. Ghose, J. W. Peters, J. B. Broderick, *J. Am. Chem. Soc.* **136**, 13086–13089 (2014).


## ACKNOWLEDGMENTS


The authors thank the Commissariat à l'Energie Atomique et aux Energies Alternatives (CEA), the Centre National de la Recherche Scientifique (CNRS), and the Université Grenoble–Alpes for institutional support. G.S. was the recipient of an Enhanced Eurotalents fellowship (FP7 framework program, N. 600382). We appreciate the help from the staff of the computing facility provided by CEA (CEA/Direction des Sciences du Vivant/Groupe Informatique pour les Scientifiques d'Ile-de-France), Saclay, and Centre de Calcul Recherche et Technologie, Bruyères-le-Châtel. This work was supported by contract ANR-12-BSV8-0013 from the French Agence Nationale pour la Recherche and used the platforms of the Grenoble Instruct center (Integrated Structural Biology Grenoble; UMS 3518 CNRS-CEA–University Joseph Fourier–European Molecular Biology Laboratory) with support from the French Infrastructure for Integrated Structural Biology (ANR-10-INSB-05-02) within the Grenoble Partnership for Structural Biology (PSB). Data are available in the supplementary materials.


## SUPPLEMENTARY MATERIALS

www.sciencemag.org/content/351/6279/1320/suppl/DC1
Materials and Methods
Figs. S1 to S13
Tables S1 to S16
References (*22–30*)


18 November 2015; accepted 16 February 2016
10.1126/science.aad8995

NEUROINFLAMMATION

# *C9orf72* is required for proper macrophage and microglial function in mice

J. G. O'Rourke,[1] L. Bogdanik,[2] A. Yáñez,[1] D. Lall,[1] A. J. Wolf,[3] A. K. M. G. Muhammad,[1] R. Ho,[1] S. Carmona,[1] J.P. Vit,[3] J. Zarrow,[1] K. J. Kim,[1] S. Bell,[1] M. B. Harms,[5] T. M. Miller,[5] C. A. Dangler,[2] D. M. Underhill,[3] H. S. Goodridge,[1] C. M. Lutz,[2] R. H. Baloh[1,4]*

**Expansions of a hexanucleotide repeat (GGGGCC) in the noncoding region of the *C9orf72* gene are the most common genetic cause of amyotrophic lateral sclerosis (ALS) and frontotemporal dementia. Decreased expression of *C9orf72* is seen in expansion carriers, suggesting that loss of function may play a role in disease. We found that two independent mouse lines lacking the *C9orf72* ortholog (*3110043O21Rik*) in all tissues developed normally and aged without motor neuron disease. Instead, *C9orf72* null mice developed progressive splenomegaly and lymphadenopathy with accumulation of engorged macrophage-like cells. *C9orf72* expression was highest in myeloid cells, and the loss of *C9orf72* led to lysosomal accumulation and altered immune responses in macrophages and microglia, with age-related neuroinflammation similar to *C9orf72* ALS but not sporadic ALS human patient tissue. Thus, *C9orf72* is required for the normal function of myeloid cells, and altered microglial function may contribute to neurodegeneration in *C9orf72* expansion carriers.**

Amyotrophic lateral sclerosis (ALS) and frontotemporal dementia (FTD) are neurodegenerative disorders with overlapping clinical presentations, pathology, and genetic origins (*1*, *2*). Expansions of a GGGGCC hexanucleotide repeat in the first intron/promoter of the *C9orf72* gene are the most commonly identified genetic cause of ALS/FTD (*3*, *4*) and are found in other neurodegenerative diseases (*5*). Microglial dysfunction is strongly tied to ALS/FTD pathogenesis (*6*), with mutations in progranulin causing FTD (*7*, *8*) and variants in the microglial expressed genes *TREM2* and *TBK1* implicated in ALS (*9*–*11*). However, no connection has been made between microglial function and *C9orf72*, where focus instead has been on its role in neurons (*12*, *13*). Although the repeat expansion leads to decreased *C9orf72* expression in human patient tissues, most research has focused on gain-of-function toxicity as the primary mechanism in disease rather than loss of function (*14*–*18*).

To investigate the function of the mouse ortholog of *C9orf72* (*3110043O21Rik*, referred to as *C9orf72* below), we analyzed two independent loss-of-function alleles in mice (figs. S1 and S2). *C9orf72*$^{+/-}$ and *C9orf72*$^{-/-}$ mice showed normal weight gain and life span; had normal sensorimotor coordination, limb strength, femoral motor and sensory axon counts, and muscle electrophysiology; and showed no evidence of neurodegeneration on histology through advanced age (17 months) (figs. S1 to S3). The only histologic abnormalities in the nervous system were rare chromatolytic structures seen with hemotoxylin and eosin (H&E) staining, found in both gray and white matter of the spinal cord, that did not increase with age or show reactive gliosis (fig. S3). All studies were performed using the Knockout Mouse Project line except where specified.

*C9orf72*$^{-/-}$ mice from both lines developed visibly enlarged cervical lymph nodes and spleens (Fig. 1, A and B), detectable as early as 1 month after birth, that slowly enlarged with age (Fig. 1C and fig. S2). No gross or histological defects were observed in other organs at 5 months of age. Histology of lymph nodes and the white pulp of the spleen showed disruption of the normal follicular structure by enlarged debris-filled cells (Fig. 1D) that expressed CD11b and contained ubiquitin- and p62-positive vacuoles consistent with macrophages (Fig. 2A and fig. S4). Immunoblotting confirmed increased amounts of p62 and LC3 proteins, indicating an increase in components of the autophagy machinery in homozygote spleens (Fig. 2B). Massive up-regulation of *Trem2* expression was observed in *C9orf72*$^{-/-}$ spleens, a cell surface receptor expressed by macrophages and monocytes, as were inflammatory cytokines, including IL-1β, IL-6, and IL-10 (Fig. 2C). Despite the altered follicular architecture, there were no differences in the proportions of B cells, T cells, or CD11b$^{+}$ myeloid cells (Fig. 2D and fig. S2J). However, flow cytometry revealed changes in myeloid subsets, including the emergence of a CD11b$^{+}$Ly6C$^{-}$Ly6G$^{int}$ population unique to *C9orf72*$^{-/-}$ mice, and a decrease in F4/80$^{+}$ red pulp macrophages, indicating that *C9orf72* deficiency has a selective effect on myeloid populations in the spleen (Fig. 2, E to G). Complete blood counts and flow cytometry of bone marrow were normal in *C9orf72*$^{-/-}$ mice at 5 months (fig. S5), supporting the idea that splenic enlargement was not related to deficient hematopoiesis in bone marrow.

Given the progressive splenomegaly with altered myeloid cells, and the buildup of engorged macrophages with accumulations of LC3 and p62 in the spleens of *C9orf72*$^{-/-}$ mice, we hypothesized that C9orf72 protein is important for endosomal trafficking in macrophages. We first examined the expression of *C9orf72* by fluorescence-activated cell sorting (FACS) of different populations from wild-type mouse spleens and found that *C9orf72* was expressed at high levels in CD11b$^{+}$ (myeloid cell), as compared to CD3$^{+}$ (T cell) and CD19$^{+}$ (B cell) populations (Fig. 3A). Query of the immunological genome project (www.immgen.org) confirmed that the expression of *C9orf72* was highest in macrophages and dendritic cells as compared to other immune cells (fig. S6, A and B). Pathway analysis (*19*) of the 35 genes in the *C9orf72* constellation was significant for only one pathway, lysosomal function (Bonferroni $P = 2.32^{-6}$) (fig. S6C). To examine whether *C9orf72* is necessary for macrophage function, we differentiated bone marrow–derived macrophages (BMDMs) from *C9orf72*$^{-/-}$ mice and stained them for endosomal markers. BMDMs from *C9orf72*$^{-/-}$ mice showed marked accumulation of LysoTracker- and Lamp1-positive vesicles, indicating a defect in late endosome/lysosomal trafficking (Fig. 3, B and C). No changes in the early or late endosomal markers Rab5 or Rab7 were observed (figs. S7 and S8). The accumulation of LysoTracker- and Lamp1-positive vesicles was rescued by viral expression of human *C9orf72*, indicating that this defect was due to the loss of *C9orf72* (Fig. 3, D and E). *C9orf72*$^{-/-}$ BMDMs showed normal initial phagocytosis of zymosan particles (Fig. 3F); however, BMDMs from both *C9orf72*$^{-/-}$ and to a lesser extent *C9orf72*$^{+/-}$ mice showed enhanced production of phagocyte oxidase-derived reactive oxygen species (ROS) after feeding with zymosan particles (Fig. 3G), which has been reported in cells with defective fusion of phagosomes to lysosomes (*20*). BMDMs from *C9orf72*$^{-/-}$ and *C9orf72*$^{+/-}$ mice also showed enhanced cytokine production in response to several immune stimuli, including those sensed in endosomal/lysosomal compartments such as peptidoglycan, CpG, and silica (Fig. 3, H and I). Thus, *C9orf72* is critical for the proper function of macrophages, and the loss of *C9orf72* leads to a pro-inflammatory state that probably drives the splenic and lymph node hyperplasia. Although hemizygous mice did not have a phenotype at the tissue level, haploinsufficiency of *C9orf72* led to altered inflammatory responses in macrophages at the cellular level, which could lead to a physiological phenotype when the system is stressed.

[1]Board of Governors Regenerative Medicine Institute, Cedars-Sinai Medical Center, 8700 Beverly Boulevard, Los Angeles, CA 90048, USA. [2]The Jackson Laboratory, Bar Harbor, ME, USA. [3]Division of Biomedical Sciences, Cedars-Sinai Medical Center, 8700 Beverly Boulevard, Los Angeles, CA 90048, USA. [4]Department of Neurology, Cedars-Sinai Medical Center, 8700 Beverly Boulevard, Los Angeles, CA 90048, USA. [5]Department of Neurology, Washington University School of Medicine, 660 South Euclid Avenue, St. Louis, MO 63110, USA.
*Corresponding author. E-mail: robert.baloh@csmc.edu

Downloaded from on March 17, 2016

The defects in *C9orf72*$^{-/-}$ BMDMs raised the possibility that other myeloid cells, including resident microglia in the brain, also require *C9orf72* for normal function. Although an earlier report suggested that microglia express low levels of *C9orf72* (*12*), we observed that microglia showed the highest levels of *C9orf72* expression of any cell type in the brain in published data sets (*21*–*23*) (Fig. 3J) and in quantitative reverse transcription polymerase chain reaction (qRT-PCR) of cells isolated from adult mouse brains (Fig. 3K). Microglia from *C9orf72*$^{-/-}$ mice showed accumulation of LysoTracker- and Lamp1-positive structures, similar to BMDMs (Fig. 3, L and M), whereas primary cortical neurons did not (fig. S9). To probe the functional state of microglia lacking *C9orf72*, we performed qRT-PCR on spinal cord microglia isolated from *C9orf72*$^{-/-}$ mice and found increased levels of cytokines IL-6 and IL-1b, supporting the idea that the altered lysosomal function leads to a proinflammatory state (Fig. 4A) similar to that observed in BMDMs.

Although we did not see overt neurodegeneration in *C9orf72*$^{-/-}$ mice, given the pro-inflammatory phenotype in isolated microglia, we used transcriptional profiling to investigate *C9orf72*-deficient nervous tissue in greater detail. Gene set enrichment analysis (GSEA) on RNA sequencing (RNA-seq) of spinal cords from young animals (3 months) showed little difference between genotypes. In contrast, in aged animals (17 months), a large number of pathways were altered in *C9orf72*$^{-/-}$ versus *C9orf72*$^{+/-}$ or wild-type animals [false discovery rate (FDR) < 0.05] (Fig. 4B). We focused on the 19 pathways that were up-regulated in *C9orf72*$^{-/-}$ versus *C9orf72*$^{+/-}$ and control animals for further analysis (fig. S10). Of these 19 pathways, almost a third [6 out of 19 (6/19)] were related to inflammation (Fig. 4C). To determine whether similar changes are observed in *C9orf72* ALS (C9-ALS) tissue, we analyzed a recent RNA-seq data set that includes normal controls, sporadic ALS (sALS), and C9-ALS cases (*24*). Of the 19 up-regulated pathways in *C9orf72*$^{-/-}$ mice, there was little overlap (1/19) with pathways up-regulated in sporadic ALS brain tissue (frontal cortex or cerebellum; Fig. 4D). In contrast, the majority (10/19) of pathways up-regulated in *C9orf72*$^{-/-}$ mice were also up-regulated in C9-ALS human patient brains, including nearly all of the immune pathways (5/6). A direct comparison showed a significant increase in inflammatory pathways in C9-ALS versus sALS cases (fig. S11). Finally, we performed immunostaining for Iba1 and Lamp1 on motor cortex and spinal cord tissue from C9-ALS ($n$ = 3) and sALS ($n$ = 3) cases. Although frequent reactive microglia were present in all ALS cases, microglia containing large accumulations of Lamp1-positive material were only observed in the C9-ALS cases (Fig. 4E and fig. S11). Thus, both transcriptome and histologic analyses of C9-ALS patient tissue are consistent with the idea that the decreased *C9orf72* expression in C9-ALS leads to altered microglial function and neuroinflammation.

In summary, the loss of *C9orf72* in mice led to age-related inflammation in the spleen and

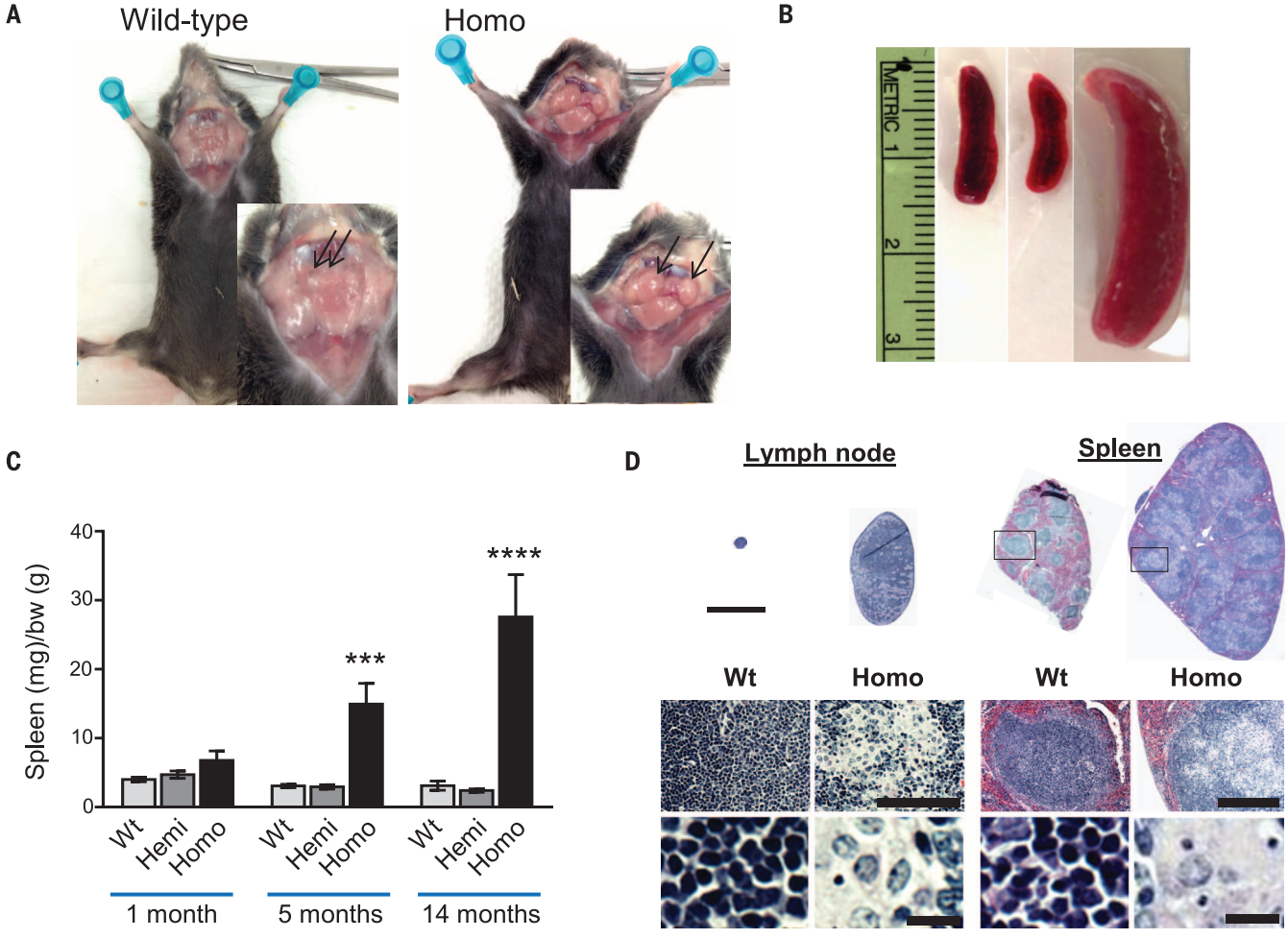



**Fig. 1. Generation of *C9orf72* (*3110043O21Rik*) null mice.** (**A**) Gross images of cervical lymphadenopathy (arrows) in *C9orf72*$^{-/-}$ mice (9 months of age). Wt, wild-type; homo, homozygote. (**B**) Gross images of splenomegaly (12 months of age). (**C**) Spleen weights (in milligrams) normalized to body weight (in grams) at indicated ages [***$P$ = 0.0008, ****$P$ < 0.0001, two-way analysis of variance (ANOVA)]. (**D**) H&E staining of wild-type and homozygote lymph nodes and spleens at 5 months (top; scale bar = 3 mm) showing disruption of follicular architecture in null mice by large cells with swollen cytoplasm. Higher-magnification images shown in bottom panels; scale bars = 100 μm and 10 μm (lymph node) and 300 μm and 10 μm (spleen).

nervous system, with defects in lysosomal trafficking and immune responses in macrophages and microglia. The disruption of lysosomal function in macrophages is consistent with the idea that *C9orf72* is a member of the DENN family of Rab-GEFs involved in late endosomal trafficking and autophagy (*25*–*27*). Our data support a model where *C9orf72* regulates the maturation of phagosomes to lysosomes in macrophages, because we observed both altered responses to immune stimuli, including those sensed in endosomal/lysosomal compartments (PGN, CpG, and silica) in BMDMs lacking *C9orf72*. Furthermore, loss of *C9orf72* function could affect neurodegeneration in C9-ALS and FTD by diminishing the ability of microglia to clear aggregated proteins and/or altering their immune responses. Our findings of altered immune responses in haploinsufficient macrophages indicate that even this partial decrease in *C9orf72* levels could affect microglial function (*3*, *28*–*30*). These data raise the possibility of a dual-effect mechanism for the pathogenesis of a single gene defect: that gain-of-function manifestations of *C9orf72* expansion (RNA foci and RAN dipeptides) in neurons are coupled with "primed" and dysfunctional microglia, which ultimately results in neurodegeneration (*31*). Given that many ALS genes are involved in late endosomal trafficking and lysosome function (*TBK1*, *TMEM106B*, *OPTN*, *SQSTM1*, *UBQLN2*, *VCP*, *CHMP2B*, and *PGRN*) (*32*) and are expressed in both neurons and microglia, the concept of a dual-effect mechanism may generalize to other forms of inherited ALS.

Finally, our findings raise important considerations about therapeutic knockdown of *C9orf72* in the nervous system. Although these approaches effectively target gain-of-function manifestations in neurons, they could exacerbate microglial dysfunction by further suppressing *C9orf72*, unless they specifically target repeat-containing transcripts (*33*). An initial report of *C9orf72* knockdown in

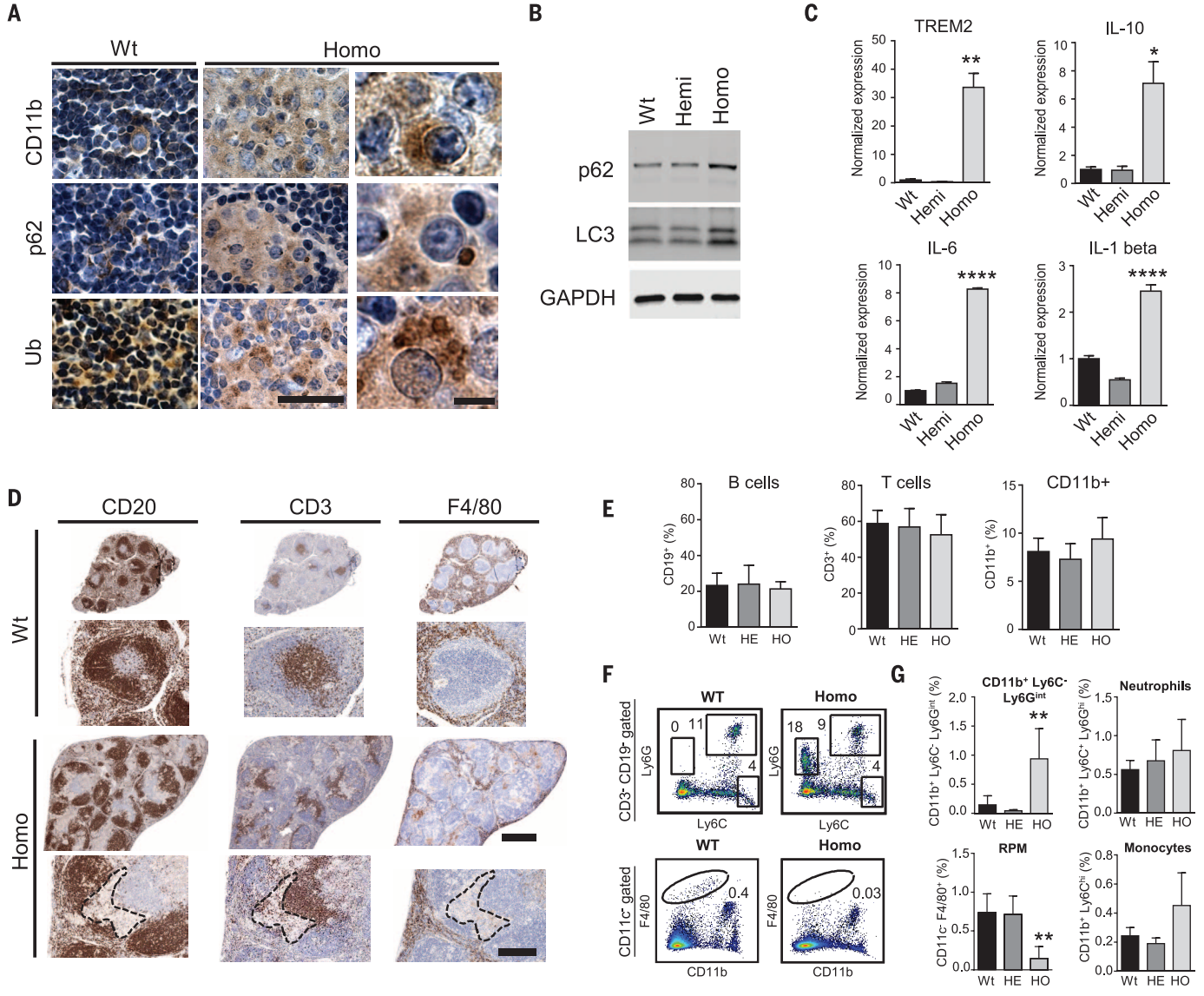



**Fig. 2. *C9orf72* null mice develop progressive splenomegaly with engorged macrophages, altered monocyte populations, and inflammation.** (**A**) Enlarged cells in homozygote spleens (5 months) stained for CD11b and containing p62 and ubiquitin (Ub) accumulations. Scale bars = 100 μm and 20 μm. (**B**) Immunoblot of spleen lysates showed an increase in p62 and LC3 in *C9orf72*$^{-/-}$ mice ($n$ = 3; 14 months). (**C**) qRT-PCR analysis of spleens (14 months) showed an increase in macrophage marker *Trem2* (**$P$ = 0.008), and cytokines IL-10 (*$P$ = 0.035), IL-6 (****$P$ < 0.0001), and IL-1β (****$P$ < 0.0001; one-way ANOVA). (**D**) Immunostains of wild-type and *C9orf72*$^{-/-}$ spleens (5 months) for CD20 (B cells), CD3 (T cells), and F4/80 (red pulp macrophages). The dashed outline highlights the region of abnormal CD11b$^{+}$ cells in the *C9orf72*$^{-/-}$ spleens. Scale bars = 1 mm and 300 μm. (**E**) FACS analysis of spleens (5 months). (**F**) Dot plots and (**G**) bar graphs showed a unique population of CD11b$^{+}$ Ly6C$^{-}$Ly6G$^{int}$ cells in *C9orf72*$^{-/-}$ spleens and a decrease in F4/80$^{+}$ red pulp macrophages as compared to wild-type mice or hemizygotes ($n$ = 4; 5 months) (**$P$ = 0.01, one-way ANOVA).

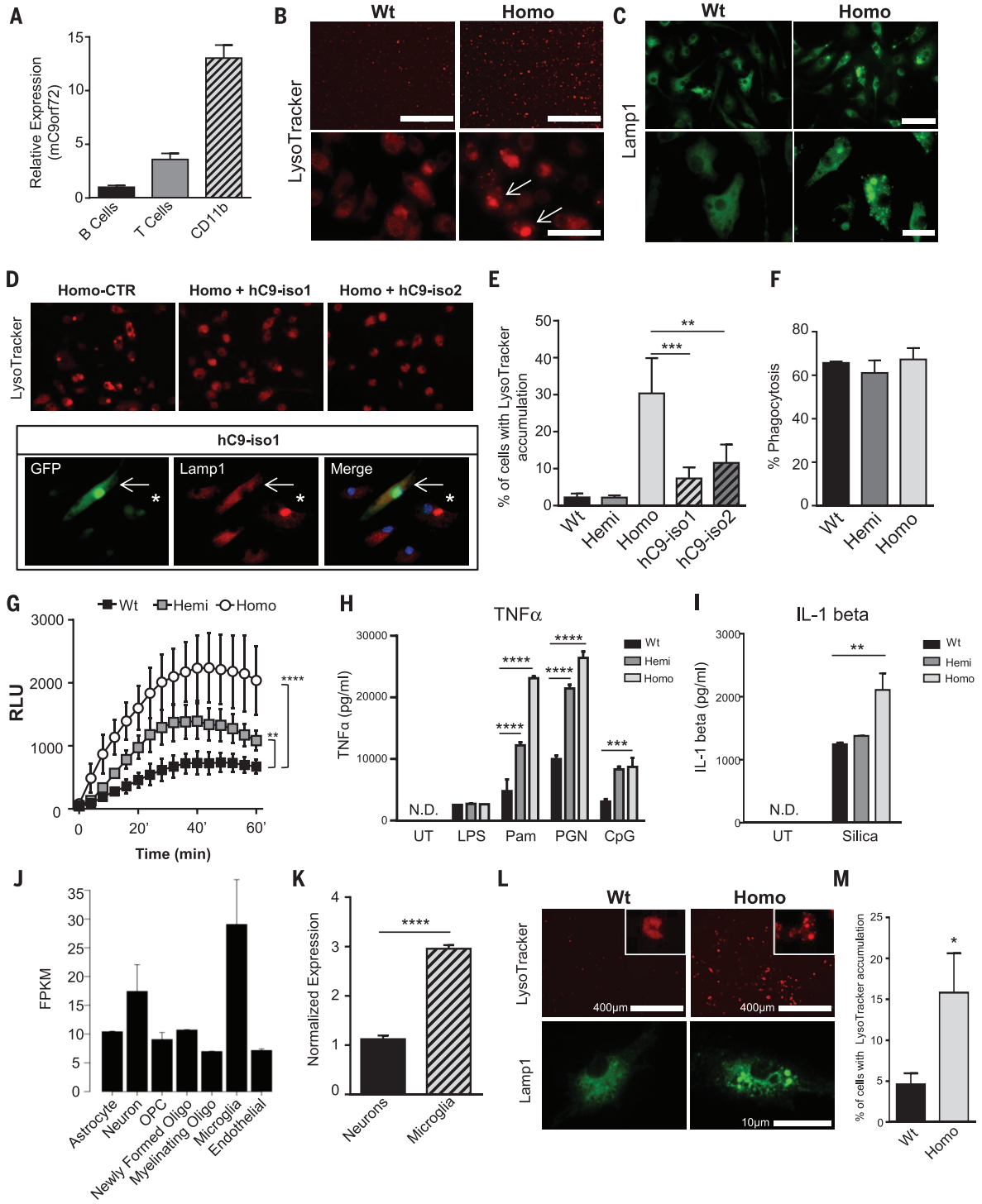
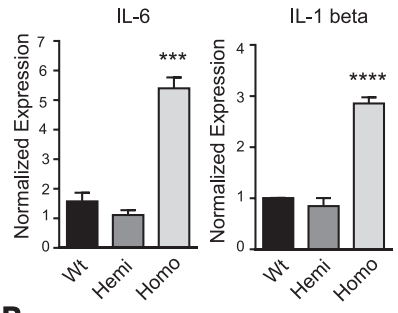



**Fig. 3. Analysis of macrophages and microglia from *C9orf72*-deficient mice.** (**A**) qRT-PCR analysis from B cells, T cells, and CD11b$^{+}$ cells FAC-sorted from wild-type mouse spleens ($n$ = 2). (**B** and **C**) BMDMs from *C9orf72*$^{-/-}$ mice showed accumulation of LysoTracker- and Lamp1-stained vesicles as compared to wild-type mice. Scale bars = 50 μm and 20 μm. (**D**) *C9orf72*$^{-/-}$ BMDMs treated with lentivirus encoding either human C9orf72 isoform 1-IRES-GFP (hC9-iso1) or isoform 2-IRES-GFP (hC9-iso2). LysoTracker (top panel) or Lamp1 (bottom panel) accumulation was rescued by either hC9-iso1 or hC9-iso2 (top panel). Arrow, hC9-iso1 infected cell; asterisk, uninfected cell. (**E**) Quantitation of LysoTracker accumulation in BMDMs of the indicated genotype or homozygotes treated with hC9-iso1 and hC9-iso2 lentivirus (***$P$ = 0.0002, **$P$ = 0.0018, one-way ANOVA). (**F**) BMDMs fed with fluorescent zymosan particles for 15 min and then analyzed by FACS analysis. (**G**) ROS production by BMDMs after zymosan ingestion in indicated genotypes (****$P$ = <0.0001, two-way ANOVA). (**H**) *C9orf72*$^{+/-}$ and *C9orf72*$^{-/-}$ BMDMs showed increased TNF-α production after stimulation with $Pam_3CSK_4$ (Pam), peptidoglycan (PGN), and CpG, but not lipopolysaccharide (LPS) (****$P$ < 0.0001, ***$P$ = 0.0002, two-way ANOVA; N.D., not detected). (**I**) IL-1β production after stimulation with silica (*$P$ < 0.05, two-way ANOVA). (**J**) RNA-seq of *C9orf72* in indicated cell types from the cerebral cortex (*21*). (**K**) qRT-PCR of *C9orf72* from neurons and microglia isolated from the adult mouse brain. (**L**) Microglia purified from *C9orf72*$^{-/-}$ mice showed accumulation of LysoTracker- and Lamp1-positive enlarged vesicles. (**M**) Quantification of percentage of microglia with enlarged LysoTracker-positive vesicles (*$P$ = 0.027, one-tailed $t$ test).

**A**




**B**

UP
DOWN

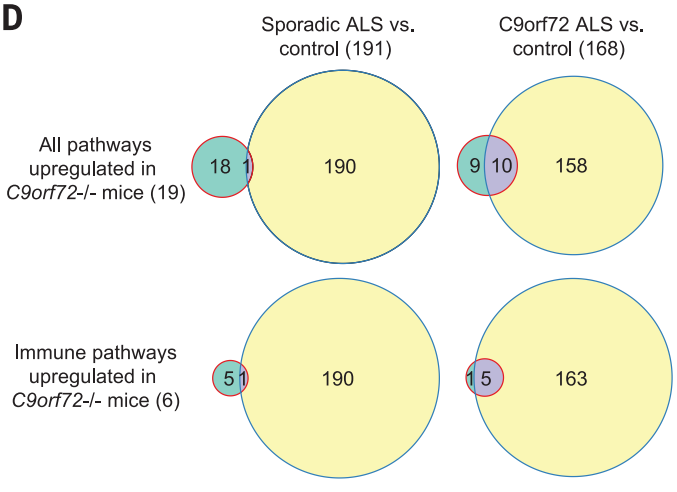
| 3 months | Wt | Hemi | Homo |
|---|---|---|---|
| Wt | | 0 | 7 |
| Hemi | 0 | | 9 |
| Homo | 0 | 1 | |

| 17 months | Wt | Hemi | Homo |
|---|---|---|---|
| Wt | | 0 | 28 |
| Hemi | 9 | | 103 |
| Homo | 13 | 38 | |

**C**

| | Pathway | FDR q-value (Homo vs Wt) |
|---|---|---|
| **Inflammation** | | |
| 1 | REACTOME_INTERFERON_GAMMA_SIGNALING | 0.013555 |
| 2 | REACTOME_ER_PHAGOSOME_PATHWAY | 0.019014 |
| 3 | REACTOME_INTERFERON_ALPHA_BETA_SIGNALING | 0.020657 |
| 4 | KEGG_COMPLEMENT_AND_COAGULATION_CASCADES | 0.021579 |
| 5 | REACTOME_ANTIGEN_PROCESSING_CROSS_PRESENTATION | 0.022685 |
| 6 | REACTOME_CELL_SURFACE_INTERACTIONS_AT_THE_VASCULAR_WALL | 0.044707 |
| **Ribosome and amino acid metabolism** | | |
| 7 | REACTOME_REGULATION_OF_ORNITHINE_DECARBOXYLASE_ODC | 0.018841 |
| 8 | REACTOME_AMINO_ACID_AND_OLIGOPEPTIDE_SLC_TRANSPORTERS | 0.019372 |
| 9 | REACTOME_SRP_DEPENDENT_COTRANSLATIONAL_PROTEIN_TARGETING_TO_MEMBRANE | 0.023572 |
| 10 | KEGG_RIBOSOME | 0.025481 |
| 11 | STRUCTURAL_CONSTITUENT_OF_RIBOSOME | 0.02626 |
| 12 | REACTOME_METABOLISM_OF_AMINO_ACIDS_AND_DERIVATIVES | 0.027797 |
| **Cell cycle** | | |
| 13 | REACTOME_CYCLIN_E_ASSOCIATED_EVENTS_DURING_G1_S_TRANSITION | 0.019978 |
| 14 | REACTOME_SCFSKP2_MEDIATED_DEGRADATION_OF_P27_P21 | 0.038089 |
| **Cytochrome P450 metabolism** | | |
| 15 | KEGG_METABOLISM_OF_XENOBIOTICS_BY_CYTOCHROME_P450 | 0.023326 |
| 16 | KEGG_DRUG_METABOLISM_CYTOCHROME_P450 | 0.025163 |
| **Glycoprotein biosynthesis** | | |
| 17 | KEGG_N_GLYCAN_BIOSYNTHESIS | 0.023445 |
| 18 | NABA_ECM_GLYCOPROTEINS | 0.028687 |
| 19 | REACTOME_BIOSYNTHESIS_OF_THE_N_GLYCAN_PRECURSOR_DOLICHOL_LIPID_LINKED_OLIGOSACCHARIDE_LLO_AND_TRANSFER_TO_A_NASCENT_PROTEIN | 0.029621 |

**D**




**E**

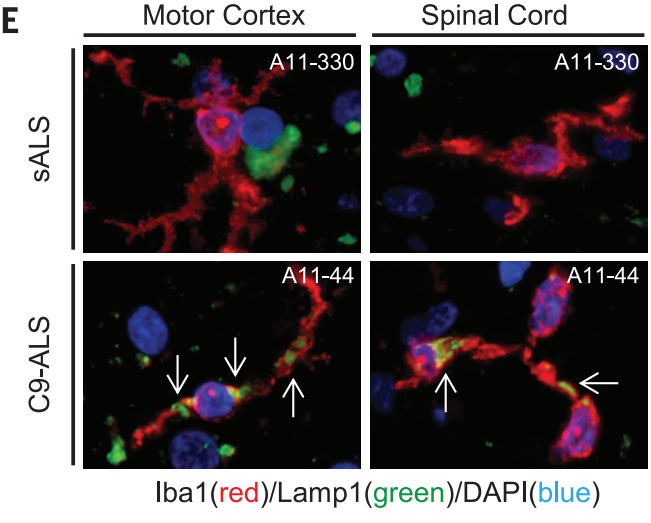



**Fig. 4. Neuroinflammation in *C9orf72*$^{-/-}$ mice and *C9orf72* expansion human patient tissue.** (**A**) qRT-PCR of inflammatory cytokines (IL-6 and IL-1β) in microglia isolated from *C9orf72*$^{-/-}$ mice (***$P$ = 0.0007; **** $P$ = <0.0001, one-way ANOVA). (**B**) Tables showing the number of up- and down-regulated pathways on GSEA (FDR < 0.05) of RNA-seq from 3- and 17-month-old lumbar spinal cords. (**C**) Table of up-regulated pathways in *C9orf72*$^{-/-}$ versus *C9orf72*$^{+/-}$ and wild-type mouse spinal cords (FDR < 0.05) at 17 months. Pathways up-regulated in both *C9orf72*$^{-/-}$ mice and human C9-ALS brain tissue are highlighted in red. (**D**) (Top) Venn diagrams showing overlap between the 19 up-regulated pathways in *C9orf72*$^{-/-}$ mice from (C) and those up-regulated in the cortex or cerebellum of sporadic ALS (left) or *C9orf72* ALS (right). (Bottom) Venn diagrams for the immune pathways from (C). (**E**) Human motor cortex and spinal cord tissue from C9-ALS and sALS cases double-labeled with Iba1 (red) to identify microglia and Lamp1 (green). Large accumulations of Lamp1 immunoreactivity (white arrows) were detected in activated microglia of C9-ALS but not sALS tissue.

mice using ASOs revealed up-regulation of immune markers in the nervous system, including *Trem2* and *Tyrobp* (*34*), suggesting that innate immune function should be monitored when performing *C9orf72* knockdown strategies in humans.

## REFERENCES AND NOTES


1. C. Lomen-Hoerth, T. Anderson, B. Miller, *Neurology* **59**, 1077–1079 (2002).
2. A. S. Chen-Plotkin, V. M. Lee, J. Q. Trojanowski, *Nat Rev Neurol* **6**, 211–220 (2010).
3. M. DeJesus-Hernandez *et al.*, *Neuron* **72**, 245–256 (2011).
4. A. E. Renton *et al.*, *Neuron* **72**, 257–268 (2011).
5. J. Cooper-Knock, P. J. Shaw, J. Kirby, *Acta Neuropathol.* **127**, 333–345 (2014).
6. K. G. Hooten, D. R. Beers, W. Zhao, S. H. Appel, *Neurotherapeutics* **12**, 364–375 (2015).
7. M. Baker *et al.*, *Nature* **442**, 916–919 (2006).
8. M. Cruts *et al.*, *Nature* **442**, 920–924 (2006).

9. J. Cady *et al.*, *J. Am. Med. Assoc. Neurol.* **71**, 449 (2014).
10. E. T. Cirulli *et al.*, *Science* **347**, 1436–1441 (2015).
11. A. Freischmidt *et al.*, *Nat. Neurosci.* **18**, 631–636 (2015).
12. N. Suzuki *et al.*, *Nat. Neurosci.* **16**, 1725–1727 (2013).
13. M. Koppers *et al.*, *Ann. Neurol.* **78**, 426–438 (2015).
14. P. Fratta *et al.*, *Acta Neuropathol.* **126**, 401–409 (2013).
15. S. Mizielinska, A. M. Isaacs, *Curr. Opin. Neurol.* **27**, 515–523 (2014).
16. K. Zhang *et al.*, *Nature* **525**, 56–61 (2015).
17. B. D. Freibaum *et al.*, *Nature* **525**, 129–133 (2015).
18. A. Jovičić *et al.*, *Nat. Neurosci.* **18**, 1226–1229 (2015).
19. W. Huang, B. T. Sherman, R. A. Lempicki, *Nat. Protoc.* **4**, 44–57 (2009).
20. J. Ma, C. Becker, C. Reyes, D. M. Underhill, *J. Immunol.* **192**, 1356–1360 (2014).
21. Y. Zhang *et al.*, *J. Neurosci.* **34**, 11929–11947 (2014).
22. K. Sharma *et al.*, *Nat. Neurosci.* **18**, 1819–1831 (2015).
23. O. Butovsky *et al.*, *Nat. Neurosci.* **17**, 131–143 (2014).
24. M. Prudencio *et al.*, *Nat. Neurosci.* **18**, 1175–1182 (2015).
25. D. Zhang, L. M. Iyer, F. He, L. Aravind, *Front. Genet.* **3**, 283 (2012).
26. T. P. Levine, R. D. Daniels, A. T. Gatta, L. H. Wong, M. J. Hayes, *Bioinformatics* **29**, 499–503 (2013).
27. M. A. Farg *et al.*, *Hum. Mol. Genet.* **23**, 3579–3595 (2014).
28. Z. Xi *et al.*, *Am. J. Hum. Genet.* **92**, 981–989 (2013).
29. V. V. Belzil *et al.*, *Acta Neuropathol.* **126**, 895–905 (2013).
30. J. Russ *et al.*, *Acta Neuropathol.* **129**, 39–52 (2015).
31. V. H. Perry, C. Holmes, *Nat. Rev. Neurol.* **10**, 217–224 (2014).
32. O. M. Peters, M. Ghasemi, R. H. Brown Jr., *J. Clin. Invest.* **125**, 2548 (2015).
33. D. Sareen *et al.*, *Sci. Transl. Med.* **5**, 208ra149 (2013).
34. C. Lagier-Tourenne *et al.*, *Proc. Natl. Acad. Sci. U.S.A.* **110**, E4530–E4539 (2013).

**ACKNOWLEDGMENTS**

We thank V. Funari for assistance with RNA sequencing, A. Cammack for assisting with patient tissue, and A. Koehne for assisting with pathology evaluation. This work was supported by NIH grants NS069669 (R.H.B), NS087351 (C.M.L), GM085796 (D.M.U.), NS078398 (T.M.M.), and UL1TR000124; the Robert and Louise Schwab family; the Cedars-Sinai ALS Research Fund (R.H.B.); and the Cedars-Sinai Board of Governors Regenerative Medicine Institute. T.M.M. has served on medical advisory boards for Ionis Pharmaceuticals and Biogen Idec. Mouse line F12 is available through the Jackson Repository, no. 27068, C57BL/6J-3110043021Rik<em5Lutzy>/J. RNA-seq data are located in the Gene Expression Omnibus, accession number GSE77681.

**SUPPLEMENTARY MATERIALS**

www.sciencemag.org/content/351/6279/1324/suppl/DC1
Materials and Methods
Supplementary Text
Figs. S1 to S11
Data Tables S1 and S2

20 December 2015; accepted 9 February 2016
10.1126/science.aaf1064

MUCOSAL IMMUNITY

# Tuft cells, taste-chemosensory cells, orchestrate parasite type 2 immunity in the gut

**Michael R. Howitt,[1] Sydney Lavoie,[1] Monia Michaud,[1] Arthur M. Blum,[2] Sara V. Tran,[3] Joel V. Weinstock,[2] Carey Ann Gallini,[1] Kevin Redding,[3] Robert F. Margolskee,[3] Lisa C. Osborne,[4]* David Artis,[4] Wendy S. Garrett[1,5,6]†**

**The intestinal epithelium forms an essential barrier between a host and its microbiota. Protozoa and helminths are members of the gut microbiota of mammals, including humans, yet the many ways that gut epithelial cells orchestrate responses to these eukaryotes remain unclear. Here we show that tuft cells, which are taste-chemosensory epithelial cells, accumulate during parasite colonization and infection. Disruption of chemosensory signaling through the loss of TRMP5 abrogates the expansion of tuft cells, goblet cells, eosinophils, and type 2 innate lymphoid cells during parasite colonization. Tuft cells are the primary source of the parasite-induced cytokine interleukin-25, which indirectly induces tuft cell expansion by promoting interleukin-13 production by innate lymphoid cells. Our results identify intestinal tuft cells as critical sentinels in the gut epithelium that promote type 2 immunity in response to intestinal parasites.**

The mammalian gut microbiota is a collective of bacteria, archaea, viruses, fungi, and parasites that reside in the lumen and mucosal surface of the intestine. These microbes are sequestered from interior tissues by a single layer of epithelial cells lining the gut that acts as a barrier and sensor. Intestinal epithelial cells (IECs) express pattern recognition receptors that detect microbial components and thus are critical sensors for and orchestrators of mucosal immunity (*1*–*4*).

Beyond pattern recognition receptors, hosts monitor and respond to the microbiota via heterotrimeric guanine nucleotide–binding protein (G protein)–coupled receptors (GPCRs). For example, microbially produced short-chain fatty acids are sensed via GPR41 and GPR43 (*5*, *6*), and sinonasal epithelial cells can detect the pathogen *Pseudomonas aeruginosa* via a taste-chemosensory GPCR (*7*–*12*). Many taste-chemosensory GPCRs require the taste-specific G protein subunit gustducin and the cation channel TRPM5 to transduce their signals (*7*, *9*). The disruption of either gustducin or TRPM5 can perturb physiological responses to *P. aeruginosa* (*13*–*15*). In the gut, TRPM5 and other canonical taste-chemosensory components are predominantly expressed by an intestinal epithelial subset called tuft cells (*16*). Tuft cells, which are identified by the expression of doublecortin-like kinase 1 (DCLK1), comprise a minor fraction of small intestinal epithelial cells (*17*–*19*) and are putative quiescent stem cells (*20*). Although tuft cells express taste-chemosensory machinery, it is unknown whether tuft cells sense the gut microbiota by means of taste chemosensation or transduce signals to the mucosal immune system (*21*).

We began by evaluating the frequency of DCLK1$^+$ tuft cells in the distal small intestine of wild-type (WT) specific-pathogen-free mice that were bred in-house (BIH). We found markedly more intestinal DCLK1$^+$ tuft cells (7.2%) (Fig. 1A) than previous reports (0.4%) (*19*, *22*) and confirmed this discrepancy with an alternative tuft cell marker, GFI1B (fig. S1) (*23*). As interinstitutional differences in microbiota can contribute to substantial variation among mucosal immune cell populations (*24*), we compared tuft cell abundance in mice obtained from The Jackson Laboratory (JAX) with BIH mice. Similar to previous reports (*19*, *25*), tuft cells constituted 1.0% of the total IEC population of JAX mice (Fig. 1A). Feeding the cecal contents from BIH mice to JAX mice was sufficient to increase tuft cell populations to BIH levels (fig. S2), suggesting that transmissible components of the BIH microbiota may drive tuft cell expansion when introduced to JAX mice. In support of this idea, intestinal histology revealed numerous single-celled protozoa in BIH but not in JAX mice (Fig. 1B). To identify these protozoa, we purified and imaged them by means of scanning electron microscopy (SEM); we identified them as tritrichomonads (Fig. 1C) (*26*–*28*). Quantitative polymerase chain reaction (qPCR) confirmed that they were *Tritrichomonas muris* (Tm), a common but understudied member of the rodent microbiota (Fig. 1D).

To eradicate Tm from BIH mice, we added metronidazole (2.5 g/liter) to their drinking water for 1 week. This eliminated Tm and concomitantly reduced tuft cell abundance (fig. S3). Because this treatment does not exclude the possibility that other metronidazole-sensitive organisms may contribute to tuft cell expansion, we cultured Tm (*28*, *29*) and colonized unexposed mice. Tm colonization significantly elevated tuft cell numbers in

[1]Departments of Immunology and Infectious Diseases and Genetics and Complex Diseases, Harvard T. H. Chan School of Public Health, Boston, MA 02115, USA. [2]Division of Gastroenterology, Tufts Medical Center, Boston, MA 02111, USA. [3]Monell Chemical Senses Center, Philadelphia, PA 19104, USA. [4]Jill Roberts Institute for Research in Inflammatory Bowel Disease, Weill Cornell Medical College, Cornell University, New York, NY 10021, USA. [5]Broad Institute of Harvard and Massachusetts Institute of Technology, Cambridge, MA 02142, USA. [6]Department of Medical Oncology, Dana-Farber Cancer Institute, Boston, MA 02215, USA.
*Present address: Department of Microbiology and Immunology, University of British Columbia, Vancouver, British Columbia V6T 1Z3, Canada. **†Corresponding author. E-mail: wgarrett@hsph.harvard.edu**

Downloaded from on March 17, 2016

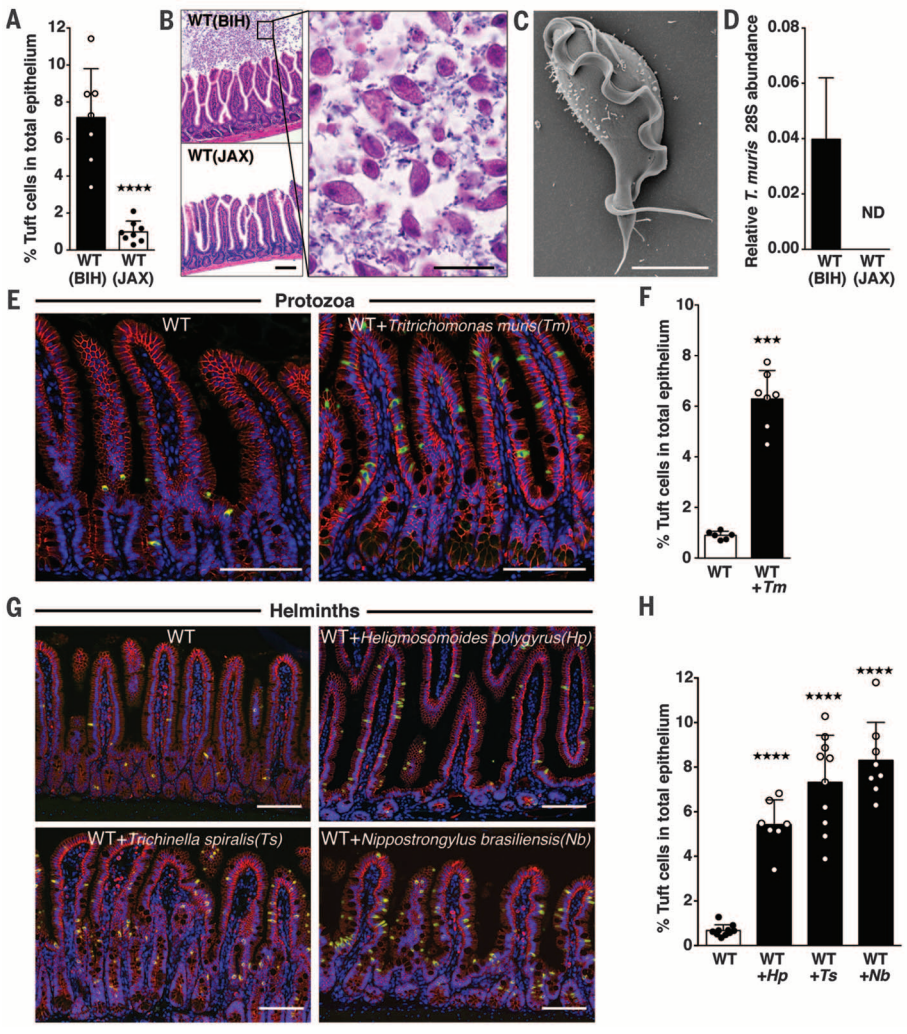



**Fig. 1. Symbiotic protozoa or helminths increase intestinal tuft cell abundance.** (**A**) DCLK1$^{+}$ tuft cell frequency in the small intestine (SI) of WT BIH and WT JAX mice. (**B**) Hemtoxylin and eosin–stained SI sections from WT BIH and WT JAX mice (scale bar, 50 μm) (left). A higher magnification of the WT BIH section is shown on the right (scale bar, 20 μm). (**C**) SEM micrograph of protozoa isolated from WT BIH mice (scale bar, 4 μm). (**D**) Tm abundance in stool DNA (Tm 28S rRNA relative to Eubacteria 16S rRNA), determined by qPCR (ND, not detectable). (**E**) Representative SI images from uninfected and Tm-colonized mice and (**F**) tuft cell frequency. (**G**) Representative SI images from uninfected and helminth-colonized mice and (**H**) tuft cell frequency. DCLK1 is shown in green, E-cadherin in red, and DAPI (4′,6-diamidino-2-phenylindole) in blue [scale bars in (E) and (G), 100 μm]. Each symbol represents an individual mouse, and all data are representative of two [(D), (F), and (H)] or three (A) independent experiments. Tm infection was 17 days in (E) and (F). In (G) and (H), Hp infection was 21 days, Ts infection was 15 days, and Nb infection was 8 days. Data are plotted as means with SD. Four stars, $P < 0.0001$; three stars, $P = 0.0001$; one-way analysis of variance (ANOVA) or Mann-Whitney test.

conventional (Fig. 1, E and F) and germ-free mice (fig. S4), suggesting that this symbiotic protozoa is sufficient to increase tuft cell frequency.

Helminths are common eukaryotic inhabitants of the mammalian intestine, but they are evolutionarily distinct from protozoa. These parasites inflict a substantial global health burden, yet worms may also provide therapeutic benefits (*8*). To investigate the effect of helminth infection on tuft cell abundance, we infected mice with a diverse set of parasitic worms including *Heligmosomoides polygyrus* (Hp), *Trichinella spiralis* (Ts), and *Nippostrongylus brasiliensis* (Nb). Similar to our results with Tm, infections with all three helminths increased tuft cell abundance, indicating that expansion of tuft cells is a broadly conserved feature of parasite colonization (Fig. 1, G and H).

Because tuft cells are postulated to be chemosensory cells (*30*), we considered whether perturbations to tuft chemosensory pathways may affect their expansion in response to parasites and/or to the type 2 immune response typically initiated by parasites. Multiple taste-chemosensory GPCRs sense sweet, bitter, and umami compounds; engagement of these different receptors activates a common signal transduction pathway involving gustducin, PLCβ2, and TRPM5 (Fig. S5) (*7*, *9*). We confirmed that GFI1B$^{+}$ tuft cells are the primary IEC subset expressing the canonical taste-associated components gustducin, PLCβ2, and TRPM5 (Fig. 2A) (*16*, *23*, *31*).

We compared tuft cell abundance in WT and gustducin-deficient (*gustducin*$^{-/-}$) mice colonized with Tm and found significantly fewer tuft cells in *gustducin*$^{-/-}$ animals (Fig. 2B). Using *Trpm5*$^{eGFP}$ (eGFP, enhanced green fluorescent protein) reporter mice, we validated that TRPM5 is restricted to the epithelium and expressed by DCLK1$^{+}$ tuft cells in the distal small intestine (Fig. 2C and fig. S6). Given the multiplicity of taste-chemosensory GPCRs, the established role of TRPM5 in taste chemosensation (*7*, *32*), and the predominant intestinal TRPM5 expression by tuft cells, we used TRPM5-deficient mice to evaluate whether these pathways affect tuft cell parasite responses. Similar to *gustducin*$^{-/-}$ mice, tuft cells failed to expand in *Trpm5*$^{-/-}$ mice during Tm colonization (Fig. 2, D to F). To determine whether the blunted response was due to reduced parasite colonization, we measured Tm in the distal small intestine (fig. S7A). We found slightly more parasites in both *gustducin*$^{-/-}$ and *Trpm5*$^{-/-}$ mice than in WT mice (fig. S7B), indicating that the lack of tuft cell response was not due to decreased Tm colonization. Because Tm is a stable component of the microbiota, we tested how the loss of TRPM5 would affect clearance of a pathogenic helminth such as Hp. Thirty-six days after infection, we determined that *Trpm5*$^{-/-}$ mice had a significantly higher worm burden than WT mice (fig. S7C). Collectively, these data suggest that pathways initiated upstream of TRPM5 may mediate tuft cell responses to intestinal parasites.

If tuft cell responses represent an early step in parasite recognition, we hypothesized that other antiparasitic responses may be altered in parasite-burdened *Trpm5*$^{-/-}$ mice. Consistent with helminth infections (*33*), Tm colonization also induced goblet cell hyperplasia in WT ($P < 0.0001$) but not in *Trpm5*$^{-/-}$ mice (Fig. 2, G and H). Similarly, we observed eosinophilia in WT but not in *Trpm5*$^{-/-}$ mice colonized with Tm (Fig. 2I).

Because epithelial cells are a key source of the parasite-induced cytokines thymic stromal lymphopoietin (TSLP) and interleukin-33 (IL-33) and -25 (*17*), we isolated tuft cells and the remaining epithelial fraction to determine TSLP, IL-33, and IL-25 expression patterns. Consistent with recent reports, we found that tuft cells expressed less

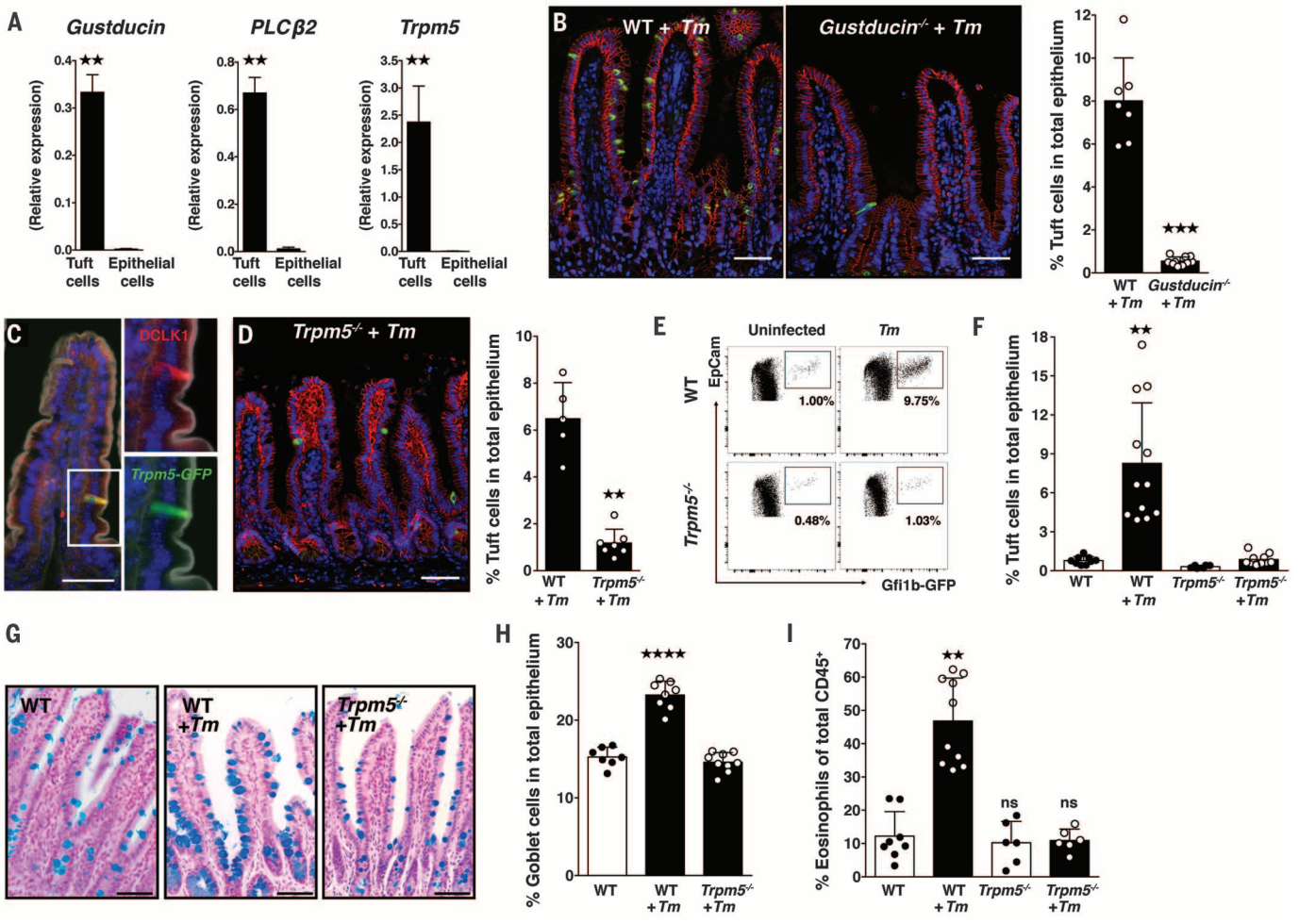



**Fig. 2. Tuft cells influence type 2 immunity through TRPM5.** (**A**) Gustducin, PLCβ2, and TRPM5 expression in sorted tuft cells, compared with the non–tuft cell epithelium. (**B**) Representative images of Tm-colonized WT and *gustducin*$^{-/-}$ mice and tuft cell frequencies. (**C**) Representative image from *Trpm5*$^{eGFP}$ mice. GFP is shown in green), DCLK1 in red), DAPI in blue, and phalloidin in white. (**D**) Representative image of Tm-colonized *Trpm5*$^{-/-}$ mice and tuft cell frequencies. Scale bars in (B), (C), and (D), 50 μm. (**E**) Representative flow cytometry plots of IECs from uninfected (left) or Tm-colonized (right) WT (*Gfi1b*$^{eGFP/+}$, top) and *Trpm5*$^{-/-}$ (*Gfi1b*$^{eGFP/+}$ *Trpm5*$^{-/-}$, bottom) mice and (**F**) tuft cell frequency. (**G**) Goblet cells in SI sections stained with Alcian blue and nuclear red in uninfected WT and Tm-colonized WT and *Trpm5*$^{-/-}$ mice and (**H**) goblet cell frequency. (**I**) Eosinophil frequency in the distal SI lamina propria (LP) of uninfected and Tm-colonized WT and *Trpm5*$^{-/-}$ mice. Scale bars, 50 μm. Each symbol represents an individual mouse, and all data are representative of at least three independent experiments. Data are plotted as means with SD. Four stars, $P < 0.0001$; three stars, $P = 0.0001$; two stars, $P < 0.01$; ns, not significant; one-way ANOVA, Kruskal-Wallis, or Mann-Whitney tests.

TSLP and IL-33 than other epithelial cells and are the main source of epithelial IL-25 (Fig. 3A and fig. S8A) (*34*, *35*). To determine whether TRPM5 affects parasite-induced IL-25 expression, we infected WT and *Trpm5*$^{-/-}$ mice with Tm and measured both parasite colonization and the corresponding epithelial IL-25 expression over time. Tm rapidly colonized both WT and *Trpm5*$^{-/-}$ mice, but *Trpm5*$^{-/-}$ mice had significantly reduced IL-25 expression 12 days after infection ($P = 0.0006$) (Fig. 3B).

IL-25 promotes proliferation and activation of type 2 innate lymphoid cells (ILC2s) via the receptor subunit IL17RB (*11*, *36*, *37*). Accordingly, the frequency of intestinal lamina propria IL17RB$^+$ ILC2s significantly increased in WT but not *Trpm5*$^{-/-}$ mice after 12 days of Tm infection (Fig. 3C). To determine whether the parasite response in *Trpm5*$^{-/-}$ mice could be complemented by exogenous IL-25, we injected IL-25 intraperitoneally into *Trpm5*$^{-/-}$ mice; we observed restoration of distal small intestinal eosinophilia and tuft cell abundance (Fig. 3, D to F), suggesting that tuft cells may influence their own abundance.

Epithelial cells are not only a crucial source of IL-25 but also signal in an autocrine manner via IL17RB (*22*). Therefore, we examined tuft cell IL17RB expression and found that it was significantly higher ($P = 0.0043$) than for other epithelial cells (fig. S8B). This raised the question of whether IL-25 induces tuft cell expansion via autocrine signaling or indirectly through recruitment of ILC2s. To evaluate factors that affect tuft cell abundance independently of the microbiota or immune system, we used an in vitro primary intestinal organoid system (*38*, *39*). Small intestinal organoids reconstitute all the epithelial subsets from IEC stem cells. By generating organoids from *Gfi1b*$^{eGFP/+}$ mice, we detected GFP$^+$ tuft cells (Fig. 4A and fig. S9A). Both WT and *Trpm5*$^{-/-}$ organoids contained ~0.3% tuft cells, but IL-25 did not increase tuft cell numbers (Fig. 4B and fig. S9A), suggesting that IL-25 does not act in an autocrine manner to expand tuft cell abundance. Because IL-25 promotes expansion of ILC2s, which are critical sources of IL-13 (*11*, *36*, *40*), a cytokine previously shown to increase goblet cell numbers (*25*), we considered that IL-13 may also increase tuft cell abundance. IL-13 significantly expanded tuft cells from 0.3% of total organoid cells to 11.9% and 10.9% (WT and *Trpm5*$^{-/-}$, respectively) (Fig. 4B and fig. S9A). In agreement with these results, expression of DCLK1 and TRPM5 also increased in IL-13–treated organoids (fig. S9, B and C).

To determine whether type 2 cytokine production by ILC2s may contribute to tuft cell expansion in vivo, we colonized WT, *Stat6*$^{-/-}$, *Rag2*$^{-/-}$,

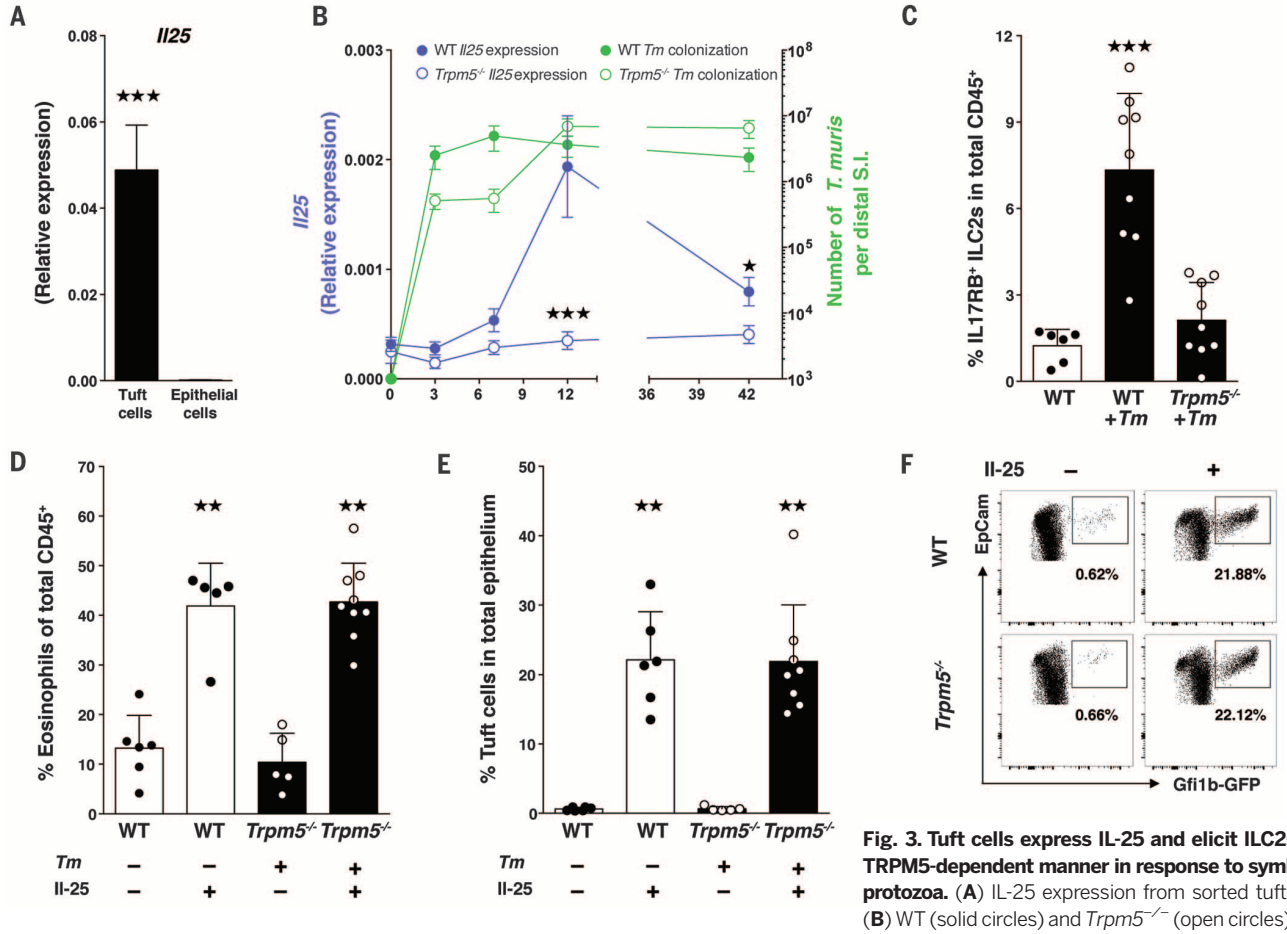



**Fig. 3. Tuft cells express IL-25 and elicit ILC2s in a TRPM5-dependent manner in response to symbiotic protozoa.** (**A**) IL-25 expression from sorted tuft cells. (**B**) WT (solid circles) and *Trpm5*$^{-/-}$ (open circles) mice were colonized with Tm for 3, 7, 12, and 42 days. At each time point, epithelial cell IL-25 expression was measured (purple line) and Tm colonization was quantified (green line). (**C**) Frequency of IL17RB$^{+}$ (IL-25R) ILC2s in the distal SI LP of uninfected WT mice and WT and *Trpm5*$^{-/-}$ mice colonized with Tm for 12 days. (**D**) Eosinophil frequency in the distal SI LP of uninfected WT or Tm-colonized *Trpm5*$^{-/-}$ mice intraperitoneally injected with IL-25 or phosphate-buffered saline (PBS) control. (**E**) Tuft cell frequencies and (**F**) flow plots of epithelial cells isolated from *Trpm5*$^{-/-}$ mice intraperitoneally injected with IL-25 or PBS. Each symbol in (C), (D), and (E) represents an individual mouse, and all data are representative of three independent experiments. Data are plotted as means with SD. Three stars, $P < 0.001$; two stars, $P < 0.01$; Kruskal-Wallis or Mann-Whitney tests.

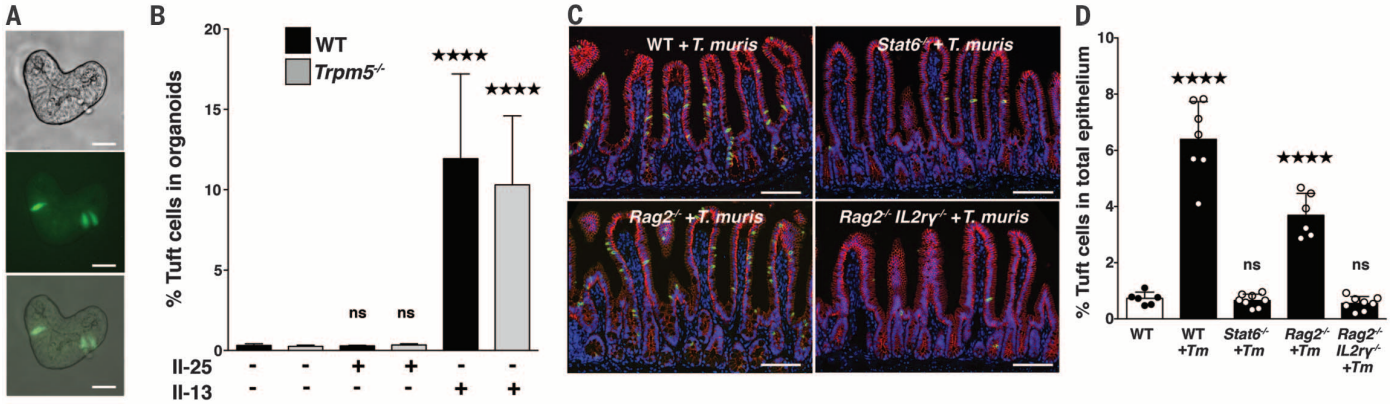



**Fig. 4. Innate lymphoid cells and IL-13 increase tuft cells in organoids and the small intestine.** (**A**) Differential interference contrast, fluorescent, and merged images of small intestinal organoids generated from *Gfi1b*$^{eGFP/+}$ mice (scale bars, 25 μm). (**B**) GFP$^{+}$ tuft cell abundance by flow cytometry of WT and *Trpm5*$^{-/-}$ organoids treated with recombinant IL-13 or IL-25. (**C**) Representative images of SI from WT, *Stat6*$^{-/-}$, *Rag2*$^{-/-}$, and *Rag2*$^{-/-}$*Il2rγ*$^{-/-}$ mice colonized with Tm and (**D**) tuft cell frequency. DCLK1 is shown in green, E-cadherin in red, and DAPI in blue (scale bars, 100 μm). Each symbol in (D) represents an individual mouse, and all data are representative of (D) two or (B) three independent experiments. Data are plotted as means with SD. Four stars, $P < 0.0001$; one-way ANOVA or Mann-Whitney tests.

and *Rag2*$^{-/-}$*Il2rγ*$^{-/-}$ mice with Tm (fig. S10). STAT6 is activated by the type 2 cytokines IL-4 and IL-13 and is required for intestinal helminth expulsion (*26*). Consistent with our organoid data demonstrating that IL-13 potently induces tuft cell expansion, tuft cells did not expand when Tm colonized *Stat6*$^{-/-}$ mice (Fig. 4, C and D). Although both T helper 2 ($T_H2$) and ILC2 cells can produce IL-13 in mucosal tissue (*41*), parasite-induced IL-25 potently activates IL-13 expression in ILCs (*11*, *36*, *42*). We compared tuft cell abundance in *Rag2*$^{-/-}$ mice that lack $T_H2$ cells but contain ILC2s versus *Rag2*$^{-/-}$*Il2rγ*$^{-/-}$ mice that lack both $T_H2$ and ILC2s cells (*8*, *11*, *12*). Infected *Rag2*$^{-/-}$ mice had elevated tuft cell abundance compared with uninfected WT mice; however, similar to both *Trpm5*$^{-/-}$ and *Stat6*$^{-/-}$ mice, *Rag2*$^{-/-}$*Il2rγ*$^{-/-}$ mice showed no tuft cell increase during Tm infection (Fig. 4, C and D). Collectively, these data suggest that tuft cells may detect Tm through TRPM5 taste chemosensation to elicit ILCs, which in turn produce IL-13 to expand tuft cell abundance (fig. S11).

IECs are positioned for direct contact with lumenal microbes and microbial products, and they function as sensory nodes to promote homeostasis with symbiotic microbes and initiate immunity against pathogens. Eukaryota, including helminths and protozoa, are common members of the gut microbiota (*43*, *44*) that profoundly modulate the host immune system (*45*, *46*). Many of the pattern recognition receptor systems that recognize bacterial members of the microbiota do not contribute to recognition of parasites (*47*, *48*). Here we show that tuft cells orchestrate type 2 immunity, in agreement with two recent studies (*34*, *35*). Taste receptors respond to a panoply of ingested agonists (*18*), and we speculate that tuft cells and taste chemosensation within the gut provide similarly broad recognition of parasitic signals.

## REFERENCES AND NOTES


1. K. S. Kobayashi *et al.*, *Science* **307**, 731–734 (2005).
2. S. Rakoff-Nahoum, J. Paglino, F. Eslami-Varzaneh, S. Edberg, R. Medzhitov, *Cell* **118**, 229–241 (2004).
3. S. Vaishnava, C. L. Behrendt, A. S. Ismail, L. Eckmann, L. V. Hooper, *Proc. Natl. Acad. Sci. U.S.A.* **105**, 20858–20863 (2008).
4. S. Vaishnava *et al.*, *Science* **334**, 255–258 (2011).
5. P. M. Smith *et al.*, *Science* **341**, 569–573 (2013).
6. M. H. Kim, S. G. Kang, J. H. Park, M. Yanagisawa, C. H. Kim, *Gastroenterology* **145**, 396–406.e10 (2013).
7. Y. Zhang *et al.*, *Cell* **112**, 293–301 (2003).
8. P. K. Mishra, M. Palma, D. Bleich, P. Loke, W. C. Gause, *Mucosal Immunol.* **7**, 753–762 (2014).
9. G. T. Wong, K. S. Gannon, R. F. Margolskee, *Nature* **381**, 796–800 (1996).
10. R. J. Lee *et al.*, *J. Clin. Invest.* **122**, 4145–4159 (2012).
11. Y. Huang *et al.*, *Nat. Immunol.* **16**, 161–169 (2015).
12. S. D. Hurst *et al.*, *J. Immunol.* **169**, 443–453 (2002).
13. M. Tizzano *et al.*, *Proc. Natl. Acad. Sci. U.S.A.* **107**, 3210–3215 (2010).
14. R. J. Lee *et al.*, *J. Clin. Invest.* **124**, 1393–1405 (2014).
15. C. J. Saunders, M. Christensen, T. E. Finger, M. Tizzano, *Proc. Natl. Acad. Sci. U.S.A.* **111**, 6075–6080 (2014).
16. C. Bezençon *et al.*, *J. Comp. Neurol.* **509**, 514–525 (2008).
17. L. W. Peterson, D. Artis, *Nat. Rev. Immunol.* **14**, 141–153 (2014).
18. W. Meyerhof *et al.*, *Chem. Senses* **35**, 157–170 (2010).
19. F. Gerbe *et al.*, *J. Cell Biol.* **192**, 767–780 (2011).
20. C. B. Westphalen *et al.*, *J. Clin. Invest.* **124**, 1283–1295 (2014).
21. F. Gerbe, C. Legraverend, P. Jay, *Cell. Mol. Life Sci.* **69**, 2907–2917 (2012).
22. Z. Kang *et al.*, *Immunity* **36**, 821–833 (2012).
23. M. Bjerknes *et al.*, *Dev. Biol.* **362**, 194–218 (2012).
24. I. I. Ivanov *et al.*, *Cell* **139**, 485–498 (2009).
25. G. J. McKenzie, A. Bancroft, R. K. Grencis, A. N. J. McKenzie, *Curr. Biol.* **8**, 339–342 (1998).
26. J. F. Urban Jr. *et al.*, *Immunity* **8**, 255–264 (1998).
27. D. G. Baker, in *Flynn's Parasites of Laboratory Animals*, D. G. Baker, Ed. (Blackwell Publishing, 2008), pp. 303–397.
28. Materials and methods are available as supplementary materials on *Science* Online.
29. H. Saeki, M. Togo, S. Imai, T. Ishii, *Japan. J. Vet. Sci.* **45**, 151–156 (1983).
30. B. Schütz *et al.*, *Front. Physiol.* **6**, 87 (2015).
31. S. Kusumakshi *et al.*, *Chem. Senses* **40**, 413–425 (2015).
32. C. A. Pérez *et al.*, *Nat. Neurosci.* **5**, 1169–1176 (2002).
33. W. I. Khan, P. Blennerhasset, C. Ma, K. I. Matthaei, S. M. Collins, *Parasite Immunol.* **23**, 39–42 (2001).
34. J. von Moltke, M. Ji, H. E. Liang, R. M. Locksley, *Nature* **529**, 221–225 (2016).
35. F. Gerbe *et al.*, *Nature* **529**, 226–230 (2016).
36. D. R. Neill *et al.*, *Nature* **464**, 1367–1370 (2010).
37. S. A. Saenz *et al.*, *Nature* **464**, 1362–1366 (2010).
38. H. Miyoshi, T. S. Stappenbeck, *Nat. Protoc.* **8**, 2471–2482 (2013).
39. T. Sato *et al.*, *Nature* **459**, 262–265 (2009).
40. P. G. Fallon *et al.*, *J. Exp. Med.* **203**, 1105–1116 (2006).
41. H.-E. Liang *et al.*, *Nat. Immunol.* **13**, 58–66 (2012).
42. A. E. Price *et al.*, *Proc. Natl. Acad. Sci. U.S.A.* **107**, 11489–11494 (2010).
43. L. W. Parfrey *et al.*, *Front. Microbiol.* **5**, 298 (2014).
44. P. J. Hotez *et al.*, *J. Clin. Invest.* **118**, 1311–1321 (2008).
45. L. C. Osborne *et al.*, *Science* **345**, 578–582 (2014).
46. T. A. Reese *et al.*, *Science* **345**, 573–577 (2014).
47. H. Helmby, R. K. Grencis, *Eur. J. Immunol.* **33**, 2974–2979 (2003).
48. L. A. Reynolds *et al.*, *J. Immunol.* **193**, 2984–2993 (2014).


## ACKNOWLEDGMENTS

We thank members of the Garrett Lab for helpful discussion, T. Stappenbeck for supplying L-WRN cells, R. Montgomery for help with organoid imaging, and W. Fowle for help with SEM. The data from this study are tabulated in the main paper and in the supplementary materials. *Trpm5*$^{eGFP}$, *Trpm5*$^{-/-}$, and *gustducin*$^{-/-}$ mice are available from Monell Chemical Senses Center under a material transfer agreement. This work was supported by NIH National Research Service Award (NRSA) F32DK098826 to M.R.H.; NIH NRSA F31DK105653 to S.L.; and NIH grants R01 CA154426 and R01 GM099531, a Burroughs Wellcome Career in Medical Sciences Award, and a Searle Scholars Award to W.S.G. The authors declare no competing financial interests.

## SUPPLEMENTARY MATERIALS

www.sciencemag.org/content/351/6279/1329/suppl/DC1
Materials and Methods
Figs. S1 to S13
References (*49*–*53*)

24 September 2015; accepted 27 January 2016
Published online 4 February 2016
10.1126/science.aaf1648

Downloaded from on March 17, 2016

INFLAMMATION

# Prostaglandin $E_2$ constrains systemic inflammation through an innate lymphoid cell–IL-22 axis

**Rodger Duffin,[1] Richard A. O'Connor,[1] Siobhan Crittenden,[1] Thorsten Forster,[2] Cunjing Yu,[1] Xiaozhong Zheng,[1] Danielle Smyth,[3]* Calum T. Robb,[1] Fiona Rossi,[4] Christos Skouras,[1] Shaohui Tang,[5] James Richards,[1] Antonella Pellicoro,[1] Richard B. Weller,[1] Richard M. Breyer,[6,7] Damian J. Mole,[1] John P. Iredale,[1] Stephen M. Anderton,[1] Shuh Narumiya,[8,9] Rick M. Maizels,[3]* Peter Ghazal,[2,10] Sarah E. Howie,[1] Adriano G. Rossi,[1] Chengcan Yao[1]†**

**Systemic inflammation, which results from the massive release of proinflammatory molecules into the circulatory system, is a major risk factor for severe illness, but the precise mechanisms underlying its control are not fully understood. We observed that prostaglandin $E_2$ ($PGE_2$), through its receptor EP4, is down-regulated in human systemic inflammatory disease. Mice with reduced $PGE_2$ synthesis develop systemic inflammation, associated with translocation of gut bacteria, which can be prevented by treatment with EP4 agonists. Mechanistically, we demonstrate that $PGE_2$-EP4 signaling acts directly on type 3 innate lymphoid cells (ILCs), promoting their homeostasis and driving them to produce interleukin-22 (IL-22). Disruption of the ILC–IL-22 axis impairs $PGE_2$-mediated inhibition of systemic inflammation. Hence, the ILC–IL-22 axis is essential in protecting against gut barrier dysfunction, enabling $PGE_2$-EP4 signaling to impede systemic inflammation.**

Systemic inflammation commonly develops from locally invasive infection, is characterized by dysregulation of the innate immune system and overproduction of proinflammatory cytokines, and can result in severe critical illness (e.g., bacteremia, sepsis, and septic shock) (*1*, *2*). Despite much research on systemic inflammation, our understanding of the precise mechanisms for its control remains incomplete and represents an unmet clinical need (*1*–*3*). Prostaglandins (PGs) are bioactive lipid mediators generated from arachidonic acid via the enzymatic activity of cyclooxygenases (COXs) (*4*). PGs participate in the pathogenesis of inflammatory

[1]Medical Research Council (MRC) Centre for Inflammation Research, Queen's Medical Research Institute, The University of Edinburgh, Edinburgh EH16 4TJ, UK. [2]Division of Pathway Medicine, Edinburgh Infectious Diseases, The University of Edinburgh, Edinburgh EH16 4SB, UK. [3]Institute for Immunology and Infection Research, The University of Edinburgh, Edinburgh EH9 3JT, UK. [4]MRC Centre for Regenerative Medicine, The University of Edinburgh, Edinburgh EH16 4UU, UK. [5]Department of Gastroenterology, First Affiliated Hospital of Jinan University, Guangzhou 510630, China. [6]Department of Veterans Affairs, Tennessee Valley Health Authority, Nashville, TN 37212, USA. [7]Department of Medicine, Vanderbilt University Medical Center, Nashville, TN 37232, USA. [8]Center for Innovation in Immunoregulative Technology and Therapeutics (AK Project), Kyoto University Graduate School of Medicine, Kyoto 606-8501, Japan. [9]Core Research for Evolutional Science and Technology (CREST), Japan Science and Technology Agency (JST), Tokyo 102-0075, Japan. [10]Centre for Synthetic and Systems Biology (SynthSys), The University of Edinburgh, Edinburgh EH9 3JD, UK. *Present address: Institute of Infection, Immunity and Inflammation, College of Medical, Veterinary and Life Sciences, University of Glasgow, Glasgow G12 8TA, UK. †Corresponding author. E-mail: chengcan.yao@ed.ac.uk

disease (*4*, *5*), and many inflammatory conditions are treated using nonsteroidal anti-inflammatory drugs (NSAIDs) that inhibit PG synthesis by blocking COXs (*6*). NSAID therapy is also thought to confer similar beneficial effects in treating severe inflammation, but large randomized and controlled clinical trials have shown that NSAIDs failed to reduce mortality in severe systemic inflammation (*7*, *8*). More importantly, the use of NSAIDs during evolving bacterial infection is associated with more severe critical illness (*9*–*13*). Therefore, it is imperative to define the paradoxical regulatory role of PGs in systemic inflammation (*14*).

Prostaglandin $E_2$ ($PGE_2$) is one of the most abundantly produced PGs and modulates immune and inflammatory responses through its receptors (EP1 to EP4) (*4*). We performed a genome-wide gene expression analysis of whole-blood samples from human neonates with sepsis (*15*) and found that expression levels of *PTGES2* (encoding membrane-associated PGE synthase-2) and *PTGER4* (encoding EP4) were significantly diminished in the sepsis group compared with noninfected controls (Fig. 1A). The reduced expression of *PTGES2* and *PTGER4* was associated with increased neutrophil blood count as a marker of inflammation (Fig. 1B). Down-regulation of *PTGER4* and *PTGS2* (encoding COX2) was similarly observed in patients suffering from systemic inflammatory response syndrome, sepsis, septic shock, or severe blunt trauma. In contrast, expression of *HPGD* (encoding 15-PGDH, which mediates $PGE_2$ degradation) in these patients was up-regulated compared with noninfected controls (fig. S1). Consistent with this finding, blood monocytes from patients with sepsis and septic shock produced less $PGE_2$ (*16*). Thus, the $PGE_2$-EP4 pathway is

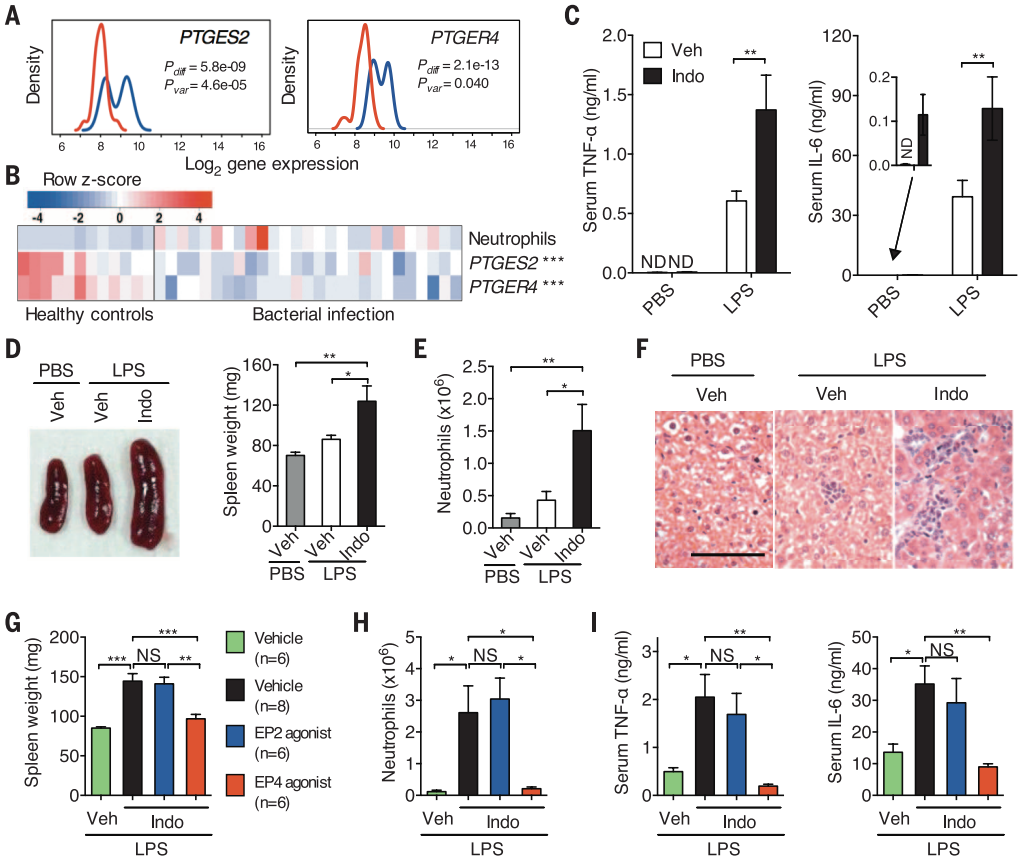



**Fig. 1. $PGE_2$-EP4 signaling controls LPS-induced systemic inflammation.** (**A**) Gene expression of *PTGES2* and *PTGER4* in whole-blood samples of neonates suffering from sepsis with confirmed bacterial infection (red, $n = 27$) and matched noninfected controls (blue, $n = 35$). Line graphs display gene expression ($log_2$ scale) as probability density plots for both group samples. Nonparametric Wilcoxon-Rank-Sum tests ($P_{diff}$) were used to test for differential expression of a gene between infected and control neonates. Fligner-Killeen tests ($P_{var}$) were used to evaluate whether sepsis and control groups have substantively different intersubject variation in gene expression levels. (**B**) Supervised heat map of clinical neutrophil counts and expression levels for *PTGES2* and *PTGER4* genes for noninfected healthy controls ($n = 12$) and bacterially infected neonates ($n = 27$). A colored scale bar is shown for neutrophil count or gene expression *z*-score transformed values, respectively. ***$P < 0.001$ by nonparametric Spearman correlation test performed to analyze the negative association between *PTGES2* (correlation coefficient $r_s = -0.6111$) or *PTGER4* ($r_s = -0.6323$) gene expression and blood neutrophil counts. (**C** to **F**) Serum TNF-α and IL-6 levels (C), spleen size and weight (D), neutrophil counts in peritoneal cavity lavage (E), and liver histology (F) of WT C57BL/6 mice treated with indomethacin (Indo) or vehicle control (Veh) for 5 days, followed by LPS challenge injection for another 2 hours [(C), $n = 6$ mice per group] or 24 hours [(D) to (F), $n = 8$ per group]. (**G** to **I**) Spleen weight (G), neutrophils (H), and serum TNF-α and IL-6 levels (I) of WT C57BL/6 mice treated with indomethacin and agonists for EP2 or EP4, followed by LPS challenge for 24 hours [(G) and (H)] or 2 hours (I). Data shown as means ± SEM (error bars) are pooled from two independent experiments. Scale bar in (F), 50 μm. *$P < 0.05$, **$P < 0.01$ by one-way analysis of variance (ANOVA). NS, not significant; ND, not detected; PBS, phosphate-buffered saline.

down-regulated in human severe systemic inflammatory disease.

To understand the mechanism(s) whereby $PGE_2$ regulates systemic inflammation, we challenged wild-type (WT) C57BL/6 mice with lipopolysaccharide (LPS) to induce systemic inflammation after pretreatment with indomethacin, which effectively suppresses $PGE_2$ production (*17*, *18*). Mice pretreated with indomethacin developed an enhanced cytokine storm [e.g., tumor necrosis factor–α (TNF-α) and interleukin-6 (IL-6)] (Fig. 1C), as well as other inflammatory signs such as splenomegaly (Fig. 1D), peritonitis characterized by accumulation of $CD11b^+Ly\text{-}6G^+$ neutrophils (Fig. 1E), and low-grade hepatic inflammation, as indicated by sinusoidal lymphocytosis and necrosis or inflammatory foci in the parenchyma (Fig. 1F). Furthermore, coadministration of an EP4 agonist almost completely diminished indomethacin-augmented systemic inflammation (Fig. 1, G to I). Thus, $PGE_2$-EP4 signaling constrains LPS-induced systemic inflammation.

In addition to the inflammatory markers described above, we also detected dissemination of gut bacteria into normally sterile tissues (e.g., liver) of indomethacin-treated mice but not controls (Fig. 2A). The coadministration of an EP4 agonist blocked the dissemination of bacteria to sterile tissues (Fig. 2B). Although pathogenic bacteria spread via the bloodstream usually cause severe systemic inflammation, gut leakage of commensal bacteria, especially in patients with damaged gut epithelium or endothelium, may also trigger systemic inflammation. Therefore, to test whether these disseminated bacteria contribute to indomethacin-augmented systemic inflammation, we treated mice with indomethacin and antibiotics, which are known to effectively deplete gut bacteria (*19*). Antibiotic therapy reduced indomethacin-facilitated systemic inflammation (Fig. 2, C to F). Indomethacin-dependent systemic inflammation was also observed in *Rag1*$^{-/-}$ mice (fig. S2) and was again diminished by EP4 agonism (Fig. 2, G to I). Hence, $PGE_2$-EP4 signaling prevents systemic inflammation independently of adaptive immune cells.

Given that IL-22 has recently been shown to inhibit inflammatory responses, particularly in the intestine (*19*–*22*), we hypothesized that IL-22 may mediate $PGE_2$ control of systemic inflammation. To test this hypothesis, we first examined the effect of $PGE_2$ on IL-22 production. Mice treated with indomethacin exhibited a decrease in LPS-induced IL-22 production (Fig. 3A), which was mimicked by an EP4 antagonist (Fig. 3B). Thus, $PGE_2$-EP4 signaling promotes IL-22 production in vivo. Whereas LPS-induced systemic inflammation in WT mice was exacerbated or prevented by indomethacin or an EP4 agonist, respectively (Fig. 1, G to I), both had negligible effects on LPS-induced inflammation in IL-22–deficient mice (*23*) (fig. S3). IL-22 is therefore required for coupling $PGE_2$-EP4 signaling–dependent control of systemic inflammation. Furthermore, coadministration of recombinant IL-22 (rIL-22) prompted a decrease in bacterial dissemination induced by indomethacin, which positively correlated with reduced systemic inflammation (Fig. 3, C to E), implying that IL-22 mediates $PGE_2$ suppression of gut bacterial dissemination and subsequent systemic inflammation.

As both $PGE_2$ and IL-22 can potentially protect the gut epithelial barrier (*17*–*22*), we reasoned that inhibition of bacterial dissemination by $PGE_2$ may proceed through augmentation of IL-22 action on gut epithelial cells. We therefore examined gene expression related to barrier function in intestinal tissues. Indomethacin suppressed expression of IL-22 as well as its receptors [i.e., *Il22ra1* (encoding IL-22Rα1) and *Il10rb* (encoding IL-10Rβ)], and their suppression was prevented by rIL-22 (Fig. 3F), which suggests that $PGE_2$ may strengthen IL-22–IL-22R signaling in intestinal epithelial cells. Indeed, IL-22R–target genes [such as *Reg3b*, *Reg3g*, and *Fut2* (*24*)], mucins, and tight junctions were similarly down-regulated by indomethacin but rescued by rIL-22 (Fig. 3G and fig. S4). Expression of genes related to IL-22R signaling and

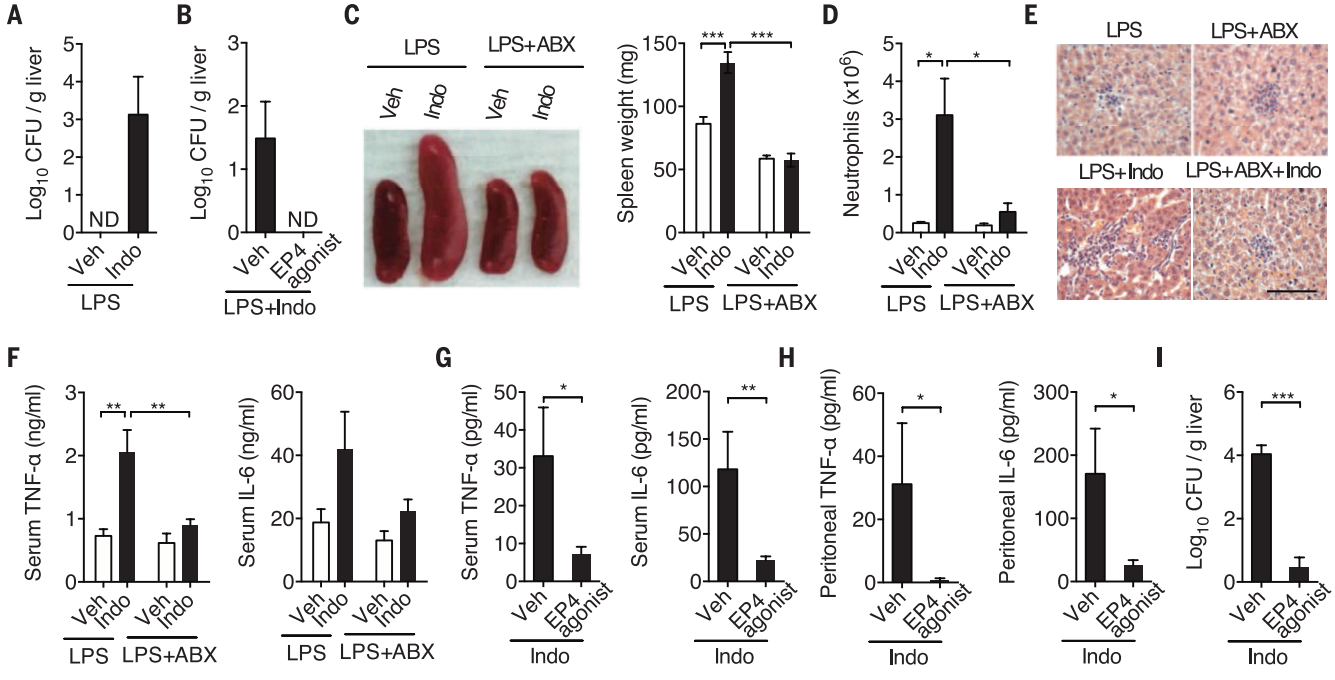



**Fig. 2. $PGE_2$ control of systemic inflammation involves gut bacterial dissemination and acts independently of adaptive immune cells.** (**A**) Colony forming units (CFU) present in liver homogenates from WT C57BL/6 mice ($n$ = 6) treated with indomethacin for 5 days, followed by LPS challenge for another 24 hours. (**B**) CFU present in liver homogenates from WT C57BL/6 mice treated with indomethacin plus an EP4 agonist ($n$ = 6) or vehicle ($n$ = 8) for 5 days, followed by LPS challenge for another 24 hours. (**C** to **F**) Spleen size and weight (C), neutrophils (D), liver histology (E), and serum TNF-α and IL-6 levels (F) of WT C57BL/6 mice ($n$ = 6 per group) treated with indomethacin and antibiotics (ABX) for 5 days, followed by LPS challenge for another 24 hours [(C) to (E)] or 2 hours (F). (**G** to **I**) TNF-α and IL-6 levels in serum (G) and peritoneal cavity lavage (H) and CFU present in liver homogenates (I) from *Rag1*$^{-/-}$ mice treated with indomethacin plus an EP4 agonist or vehicle control ($n$ = 8 per group) for 4 days. Data shown as means ± SEM (error bars) are pooled from two independent experiments. Scale bar in (E), 50 μm. *$P$ < 0.05, **$P$ < 0.01, ***$P$ < 0.001 by two-way ANOVA [(C), (D), and (F)] or Mann-Whitney test [(G) to (I)]. ND, not detected.

barrier function inversely correlated with gut bacterial dissemination (Fig. 3E). Given the protective role of $PGE_2$ in acute colonic mucosal injury (*17*), we proposed that this protection is mediated by IL-22. Indomethacin exacerbated colitis induced by dextran sulfate sodium (DSS), but rIL-22 had the reverse effect, producing significantly lower values of the colitis disease activity index, as measured by weight loss, diarrhea, and rectal bleeding (Fig. 3, H to J). Our results indicate an important role of $PGE_2$ in regulating the intestinal epithelial barrier function through innate IL-22 signaling.

Flow cytometric analysis showed that IL-22–producing cells were $CD45^{Low}$Lineage(Lin)$^-$ $CD90.2^+RORγt^+CCR6^+$ type 3 innate lymphoid cells (ILC3s) (*22*) in the gut and $CD45^+Lin^-CD90.2^+CD4^+$ ILC3s in the spleen (fig. S5). We wondered whether these cells are involved in EP4-dependent control of systemic inflammation. Although *Rag1*$^{-/-}$ mice cotreated with indomethacin and an EP4 agonist (i.e., lacking PG signaling except through EP4) did not develop systemic inflammation (Fig. 2, G to I), depletion of $CD90.2^+$ ILCs restored indomethacin-induced systemic inflammation in these mice (Fig. 4A). To address whether $PGE_2$-EP4 signaling specifically in ILCs controls

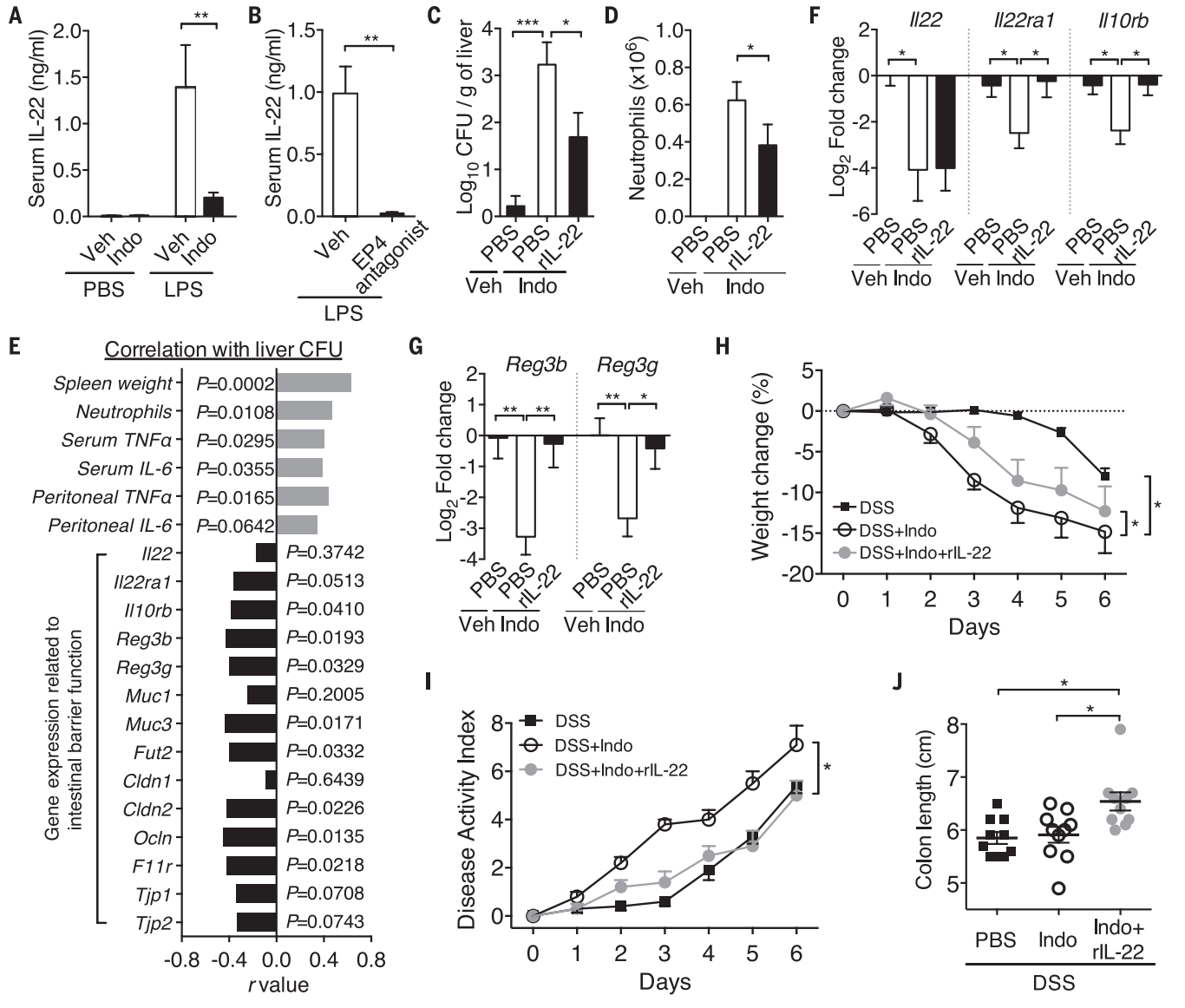



**Fig. 3. IL-22 mediates $PGE_2$ protection against systemic inflammation and intestinal barrier injury.** (**A**) Serum IL-22 levels of WT C57BL6 mice treated with indomethacin ( $n = 6$) or vehicle control ($n = 6$) for 5 days, followed by challenge with LPS or PBS for 2 hours. (**B**) Serum IL-22 levels in WT C57BL/6 mice treated with an EP4 antagonist or vehicle ($n = 4$ per group) in drinking water for 5 days, followed by LPS challenge for another 2 hours. (**C** to **G**) *Rag1*$^{-/-}$ mice were treated with vehicle ($n = 9$) or indomethacin plus rIL-22 ($n = 10$) or vehicle-control PBS ($n = 10$) for 4 days. (C) CFUs present in liver homogenates, (D) neutrophil counts, (E) correlation of liver CFU with systemic inflammation profile and expression profile of genes related to intestinal barrier function, and [(F) and (G)] gene expression of IL-22 and its receptors (F) and antimicrobial peptides (G) in the terminal ileum. Expression was measured by real-time PCR, normalized to the *Gapdh* gene and presented as relative expression (in $\log_2$ fold change) to the vehicle-control group. (**H** to **J**) Change in body weight (H), disease activity index (I), and colon length (J) of WT C57BL/6 mice ($n = 10$ per group) treated with 2% DSS and indomethacin or vehicle control in drinking water plus rIL-22 or vehicle-control PBS for 6 days. Data shown as means ± SEM (error bars) are pooled from two [(A) and (H) to (J)] or three [(C) to (G)] independent experiments or represent one experiment (B). $^*P < 0.05$, $^{**}P < 0.01$, $^{***}P < 0.001$ by Mann-Whitney test [(A), (B), and (D)], one-way ANOVA [(C) and (F) to (J)], or two-tailed Pearson correlation test (E).

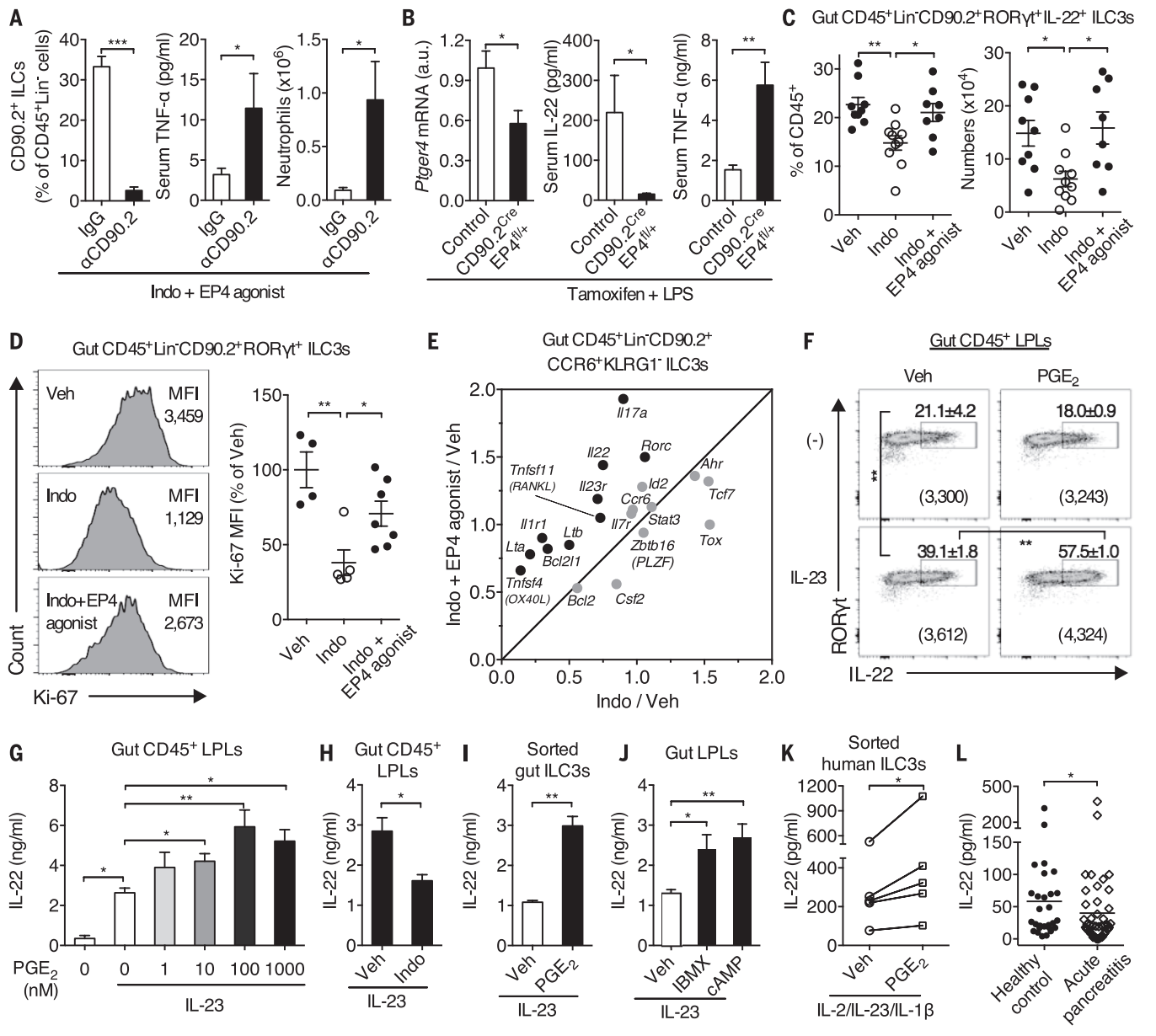



**Fig. 4. $PGE_2$-EP4 signaling potentiates ILC3 homeostasis and function that contributes to control of the systemic inflammatory response.** (**A**) Splenic CD90.2$^+$ ILCs, serum TNF-α levels, and neutrophil counts in *Rag1*$^{-/-}$ mice cotreated with indomethacin and an EP4 agonist plus anti-CD90.2 (αCD90.2) or control immunoglobulin G (IgG) antibodies ($n$ = 8 per group) for 4 days. (**B**) Expression of *Ptger4* mRNA in splenic CD90.2$^+$ cells and serum levels of IL-22 and TNF-α in tamoxifen-treated CD90.2$^{Cre}$EP4$^{fl/+}$ mice ($n$ = 7) and control C57BL/6 mice ($n$ = 5) at 1.5 hours after LPS challenge. (**C** to **E**) *Rag1*$^{-/-}$ [(C) and (D)] or C57BL/6 (E) mice were treated with indomethacin with or without an EP4 agonist for 4 to 5 days. (C) Percentages and numbers of ILC3s in small intestines. Cells were stimulated ex vivo with IL-23 for 3 hours. Each point represents an individual mouse. (D) $K_i$-67 expression in gut ILC3s. Each point represents an individual mouse. (E) Gene expression profile in gut ILC3s presented as relative expression to the vehicle-control group. Data are the summary of two independent experiments with eight mice per group. (**F**) Expression of RORγt and IL-22 by *Rag1*$^{-/-}$ gut CD45$^+$ lamina propria leukocytes (LPLs) stimulated with IL-23 and $PGE_2$ for 4 hours. Numbers in brackets represent IL-22 geometric mean fluorescence intensities of the RORγt$^+$IL-22$^+$ populations. (**G** to **J**) IL-22 production in supernatants by LPLs or ILC3s isolated from small intestines of *Rag1*$^{-/-}$ mice and then cultured with indicated conditions overnight [(G), (H), and (J)] or for 3 days (I). (**K**) IL-22 production by human ILC3s cultured with IL-2, IL-23, IL-1β, and $PGE_2$ for 4 days ($n$ = 5 donors). (**L**) Plasma IL-22 levels in individuals with acute pancreatitis (AP) at the time of hospital admission ($n$ = 48) or healthy individual donors ($n$ = 28). The vertical line represents the mean for each group. Data shown as means ± SEM (error bars) are pooled from two or more independent experiments [(A), (C) to (E), (G), (J), and (K)] or represent one (B) or two [(F), (H), and (I)] independent experiments. *$P$ < 0.05, **$P$ < 0.01, ***$P$ < 0.001 by unpaired Student's $t$ test [(A), (B), (H), and (I)], one-way ANOVA [(C), (D), (F), (G), and (J)], ratio paired $t$ test (K), or Mann Whitney test (L).

systemic inflammation, we crossed CD90.2-Cre mice (*25*) with EP4-floxed mice (*26*) to generate tamoxifen-induced selective down-regulation of EP4 in CD90.2$^+$ cells (including T cells and ILCs) in heterozygous CD90.2$^{Cre}$EP4$^{fl/+}$ mice (Fig. 4B). CD90.2$^{Cre}$EP4$^{fl/+}$ mice produced lower levels of IL-22 in response to LPS, which was associated with augmentation of systemic inflammatory response [e.g., TNF-α production (Fig. 4B)], whereas down-regulation of EP4 in T cells (*27*) did not affect IL-22 or TNF-α production (fig. S6). These data demonstrate that $PGE_2$-EP4 signaling controls systemic inflammation, at least in part, through the regulation of ILC3s.

Next, we investigated the effect of $PGE_2$ on ILC3 maintenance. Indomethacin significantly reduced ILC3 numbers in the gut and spleen in the steady state (Fig. 4C and fig. S7, A to C). This reduction was prevented by an EP4 agonist and was mimicked by an EP4 antagonist (Fig. 4C and fig. S7). Consistently, ILC3s express $PGE_2$ receptors with particularly high expression levels of EP4 (fig. S8). Furthermore, indomethacin down-regulated $K_i$-67 expression, and an EP4 agonist prevented this reduction in ILC3s (Fig. 4D), suggesting that $PGE_2$-EP4 signaling potentiates ILC3 proliferation. $PGE_2$-EP4 signaling also prevented ILC3 apoptosis in vitro but had little effect on ILC3 apoptosis in vivo (fig. S9, A and B). Moreover, down-regulation of EP4 in CD90.2$^+$ ILCs not only decreased RORγt$^+$ ILC3s but also weakened IL-7 responsiveness [e.g., Bcl-2 expression] in ILC3s (fig. S9C). To further understand the effect of $PGE_2$ on ILC3s, we measured gene expression by quantitative polymerase chain reaction (PCR) in Lin$^-$CD45$^{low}$CD90.2$^{hi}$KLRG1$^-$CCR6$^+$ ILC3s sorted from the small intestines of mice treated with indomethacin and an EP4 agonist. $PGE_2$-EP4 signaling up-regulates many ILC3 signature genes, including *Rorc*, *Il23r*, *Il1r1*, *Il22*, *Il17a*, *Lta*, *Ltb*, *Tnfsf11*, *Tnfsf4*, and *Bcl2l1* (Fig. 4E).

We next asked whether and how $PGE_2$ regulates ILC3 function. $PGE_2$ promoted IL-23–driven IL-22 production by gut lamina propria leukocytes isolated from *Rag1*$^{-/-}$ mice in vitro (Fig. 4, F and G), and this was inhibited by indomethacin (Fig. 4H). $PGE_2$ also promoted IL-22 production from splenic CD4$^+$ ILC3s, which was mediated by EP2 and EP4 (fig. S10, A to C). More importantly, $PGE_2$ increased IL-23–driven IL-22 production from highly purified CD45$^+$Lin$^-$CD90.2$^+$KLRG1$^-$CCR6$^+$ ILC3s from intestines and CD3$^-$CD11b$^-$CD11c$^-$CD4$^+$ ILC3s from spleen or bone marrow (Fig. 4I and fig. S10D), suggesting that $PGE_2$ acts directly on ILC3s. Additionally, $PGE_2$ increased IL-22 production from ILC3s in response to IL-1β and IL-7 (fig. S11). $PGE_2$ activated cyclic adenosine monophosphate signaling in ILC3s and, in turn, enhanced IL-22 production (Fig. 4J and fig. S12, A and B). Moreover, $PGE_2$-augmented IL-22 production was dependent on the transcription factor STAT3 (signal transducer and activator of transcription 3), which is critical for IL-22 production by ILC3s (*28*), but not RORγt or Ahr (fig. S12, C to E). Together, these data demonstrate that $PGE_2$-EP4 signaling promotes ILC3 homeostasis and IL-22 production by stimulating ILC3 proliferation and enhancing cytokine (e.g., IL-7, IL-23, and IL-1) responsiveness.

Finally, we sought to determine whether $PGE_2$ promotes IL-22 production from human ILC3s. To answer this question, we sorted human Lin$^-$CD161$^+$CD127$^+$CD117$^+$CRTH2$^-$ ILC3s from peripheral blood of healthy donors and cultured them with IL-2, IL-23, and IL-1β to induce IL-22 production. Addition of $PGE_2$ similarly up-regulated IL-22 production from sorted human ILC3s (Fig. 4K). Moreover, expression of the human *IL22* gene in healthy individuals infused with a bacterial endotoxin (*29*) positively correlated with expression of *PTGS2* and *PTGES* (encoding mPGES-1) (fig. S13), two inducible enzymes that mediate $PGE_2$ synthesis (*4*). Acute pancreatitis (AP) is a sterile initiator of systemic inflammation that results in multiple organ dysfunction where gut barrier injury is central to the pathogenesis (*30*). Given that IL-22 was protective in an animal model of AP (*31*), we measured IL-22 levels in patients with AP. IL-22 concentrations in plasma were lower in patients with AP compared with healthy controls at the time of hospital admission (Fig. 4L), further confirming that the reduction of IL-22 signaling is associated with development of systemic inflammation.

Here we identify a physiological role of endogenous $PGE_2$-EP4 signaling in activation of the ILC3–IL-22 axis, which functionally contributes to cross-talk between the innate immune system, gut epithelium, and microflora and subsequently constrains systemic inflammation (fig. S14). These findings provide valuable insight toward understanding how inactivation of COXs may be harmful in severe bacterial infection and inflammation (*32*–*34*). In addition, our results advance a crucial cellular and molecular mechanism for a scenario in which maintaining or augmenting $PGE_2$ signaling—e.g., by inhibiting the $PGE_2$-degrading enzyme 15-PGDH—protects against intestinal barrier injury and potentiates its repair and control of systemic inflammation (*35*, *36*).

## REFERENCES AND NOTES


1. R. S. Hotchkiss, I. E. Karl, *N. Engl. J. Med.* **348**, 138–150 (2003).
2. S. P. LaRosa, S. M. Opal, *Curr. Infect. Dis. Rep.* **14**, 474–483 (2012).
3. J. Cohen, S. Opal, T. Calandra, *Lancet Infect. Dis.* **12**, 503–505 (2012).
4. T. Hirata, S. Narumiya, *Adv. Immunol.* **116**, 143–174 (2012).
5. E. Ricciotti, G. A. FitzGerald, *Arterioscler. Thromb. Vasc. Biol.* **31**, 986–1000 (2011).
6. R. O. Day, G. G. Graham, *BMJ* **346**, f3195 (2013).
7. G. R. Bernard *et al.*, *N. Engl. J. Med.* **336**, 912–918 (1997).
8. M. T. Haupt, M. S. Jastremski, T. P. Clemmer, C. A. Metz, G. B. Goris, *Crit. Care Med.* **19**, 1339–1347 (1991).
9. D. M. Aronoff, *Mediators Inflamm.* **2012**, 696897 (2012).
10. D. P. Eisen, *Intensive Care Med.* **38**, 1249–1257 (2012).
11. D. L. Stevens, *Clin. Infect. Dis.* **21**, 977–980 (1995).
12. A. Legras *et al.*, *Crit. Care* **13**, R43 (2009).
13. B. H. Lee *et al.*, *Crit. Care* **16**, R33 (2012).
14. J. N. Fullerton, A. J. O'Brien, D. W. Gilroy, *Trends Immunol.* **35**, 12–21 (2014).
15. C. L. Smith *et al.*, *Nat. Commun.* **5**, 4649 (2014).
16. M. Bruegel *et al.*, *Crit. Care Med.* **40**, 1478–1486 (2012).
17. K. Kabashima *et al.*, *J. Clin. Invest.* **109**, 883–893 (2002).
18. T. Chinen *et al.*, *Nat. Commun.* **2**, 190 (2011).
19. G. F. Sonnenberg *et al.*, *Science* **336**, 1321–1325 (2012).
20. R. Sabat, W. Ouyang, K. Wolk, *Nat. Rev. Drug Discov.* **13**, 21–38 (2014).
21. G. F. Sonnenberg, L. A. Fouser, D. Artis, *Nat. Immunol.* **12**, 383–390 (2011).
22. G. Eberl, M. Colonna, J. P. Di Santo, A. N. McKenzie, *Science* **348**, aaa6566 (2015).
23. K. Kreymborg *et al.*, *J. Immunol.* **179**, 8098–8104 (2007).
24. Y. Goto *et al.*, *Science* **345**, 1254009 (2014).
25. B. Zonta *et al.*, *Neuron* **69**, 945–956 (2011).
26. A. Schneider *et al.*, *Genesis* **40**, 7–14 (2004).
27. C. Yao *et al.*, *Nat. Commun.* **4**, 1685 (2013).
28. X. Guo *et al.*, *Immunity* **40**, 25–39 (2014).
29. S. E. Calvano *et al.*, *Nature* **437**, 1032–1037 (2005).
30. J. E. Fishman *et al.*, *Shock* **42**, 264–270 (2014).
31. D. Feng *et al.*, *Int. J. Biol. Sci.* **8**, 249–257 (2012).
32. B. Xiang *et al.*, *Nat. Commun.* **4**, 2657 (2013).
33. L. E. Fredenburgh *et al.*, *J. Immunol.* **187**, 5255–5267 (2011).
34. S. M. Hamilton, C. R. Bayer, D. L. Stevens, A. E. Bryant, *J. Infect. Dis.* **209**, 1429–1435 (2014).
35. Y. Zhang *et al.*, *Science* **348**, aaa2340 (2015).
36. K. Németh *et al.*, *Nat. Med.* **15**, 42–49 (2009).


## ACKNOWLEDGMENTS


We thank J. Allen for critically reading and editing the manuscript; P. J. Brophy and D. Mahad for CD90.2(Thy1.2)-Cre mice; J.-C. Renauld for IL-22–deficient mice; J. Pollard, P. J. Spence, and J. Thompson for *Rag1*$^{-/-}$ mice; T. Walsh and J. Rennie for human blood samples; Y. X. Fu, X. G. Guo, D. Ruckerl, T. Kendall, J. Hu, Q. Huang, and G. T. Ho for advice, technical assistance, and/or discussion; and S. Johnston and W. Ramsay for cell sorting and analysis. We also thank the Wellcome Trust Clinical Research Facility staff and the Department of Surgery, NHS Lothian. Mice deficient in IL-22 are available from the Jean-Ludwig Institute For Cancer Research under a material transfer agreement with J.-C. Renauld. This work was supported in part by the University of Edinburgh start-up funding (Ch.Y.), the Wellcome Trust Institutional Strategic Support Fund (Ch.Y., J.P.I., S.M.A), MRC UK (J.P.I., S.M.A., R.D., A.G.R.), NIH (grant DK37097 to R.M.B.), a VA Merit Award (1BX000616 to R.M.B.), Health Foundation/Academy of Medical Sciences (D.J.M.), University of Edinburgh and GlaxoSmithKline Discovery Partnerships with Academia (DPAC) collaboration (D.J.M.), a Wellcome Trust Investigator Award (106122 to R.M.M.), the Rainin Trust (Award 13H6 to R.M.M.), CREST of JST (S.N.), European Union FP7 Industry Academia Partnerships and Pathways project ClouDx-I, Chief Scientists Office (grant ETM202 to P.G.), and Biotechnology and Biological Sciences Research Council (grant BB/K091121/1 to P.G.). The data presented in this manuscript are tabulated in the main paper and the supplementary materials. We declare no financial conflicts of interest.


## SUPPLEMENTARY MATERIALS

www.sciencemag.org/content/351/6279/1333/suppl/DC1
Materials and Methods
Figs. S1 to S14
References (*37*–*55*)


3 September 2015; accepted 3 February 2016
10.1126/science.aad9903

EBOLA VIRUS

# Protective monotherapy against lethal Ebola virus infection by a potently neutralizing antibody

Davide Corti,[1,2]* John Misasi,[3]* Sabue Mulangu,[3] Daphne A. Stanley,[3] Masaru Kanekiyo,[3] Suzanne Wollen,[4] Aurélie Ploquin,[3] Nicole A. Doria-Rose,[3] Ryan P. Staupe,[3] Michael Bailey,[3] Wei Shi,[3] Misook Choe,[3] Hadar Marcus,[3] Emily A. Thompson,[3] Alberto Cagigi,[3] Chiara Silacci,[1] Blanca Fernandez-Rodriguez,[1] Laurent Perez,[1] Federica Sallusto,[1] Fabrizia Vanzetta,[2] Gloria Agatic,[2] Elisabetta Cameroni,[2] Neville Kisalu,[5]† Ingelise Gordon,[3] Julie E. Ledgerwood,[3] John R. Mascola,[3] Barney S. Graham,[3] Jean-Jacques Muyembe-Tamfun,[5] John C. Trefry,[4]‡ Antonio Lanzavecchia,[1,6]‡ Nancy J. Sullivan[3]‡§

**Ebola virus disease in humans is highly lethal, with case fatality rates ranging from 25 to 90%. There is no licensed treatment or vaccine against the virus, underscoring the need for efficacious countermeasures. We ascertained that a human survivor of the 1995 Kikwit Ebola virus disease outbreak maintained circulating antibodies against the Ebola virus surface glycoprotein for more than a decade after infection. From this survivor we isolated monoclonal antibodies (mAbs) that neutralize recent and previous outbreak variants of Ebola virus and mediate antibody-dependent cell-mediated cytotoxicity in vitro. Strikingly, monotherapy with mAb114 protected macaques when given as late as 5 days after challenge. Treatment with a single human mAb suggests that a simplified therapeutic strategy for human Ebola infection may be possible.**

Ebola virus disease (EVD) causes severe illness characterized by rapid onset of fever, vomiting, diarrhea, and bleeding diathesis (*1*, *2*). The challenges of a large outbreak and the failure of traditional quarantine and contact-tracing measures (*3*, *4*) to control the 2014 West Africa outbreak highlight the urgent need for therapies. The success in nonhuman primates (NHP) of ZMapp—a cocktail of three chimeric monoclonal antibodies (mAbs) derived from immunized mice (*5*–*7*)—illustrated the potential of mAb therapies against EVD, and ZMapp is currently being evaluated in human trials. To date, efforts in NHP to simplify the ZMapp regimen to contain fewer mAbs have not been successful (*7*). We sought to isolate mAbs from human EVD survivors, with the goal of identifying antibodies that confer clinical protection either as single or dual-combination agents.

We obtained blood from two survivors of the 1995 EVD outbreak in Kikwit, Democratic Republic of the Congo (*8*), 11 years after infection. To determine whether the subjects retained circulating antibodies against Ebola virus (EBOV) glycoprotein (GP), we assessed GP-specific antibodies by enzyme-linked immunosorbent assay (ELISA) (Fig. 1A) (*9*). The reciprocal 10% maximal binding $EC_{90}$ titer (the reciprocal dilution at which there is a 90% decrease in antigen binding) for subject 1 (S1) was 2326, higher than control sera by more than a factor of 10. Moreover, serum from the more severely ill subject, S1, displayed potent virus-neutralizing activity (Fig. 1B); this finding indicates that S1 maintained serologic memory against EBOV GP more than a decade after infection and suggested the potential for cloning immunoglobulins with potent neutralizing activity from S1's memory B cells.

Therefore, we sorted memory B cells from S1's peripheral blood mononuclear cells and immortalized individual clones with Epstein-Barr virus (*10*). Forty clone supernatants displayed a range of GP binding (Fig. 1C); two of them, 100 and 114,

[1]Institute for Research in Biomedicine, Università della Svizzera Italiana, CH-6500 Bellinzona, Switzerland. [2]Humabs BioMed SA, 6500 Bellinzona, Switzerland. [3]Vaccine Research Center, National Institute of Allergy and Infectious Diseases, Bethesda, MD 20892, USA. [4]U.S. Army Medical Research Institute of Infectious Diseases, Fort Detrick, MD 21702, USA. [5]National Institute for Biomedical Research, National Laboratory of Public Health, Kinshasa B.P. 1197, Democratic Republic of the Congo. [6]Institute of Microbiology, ETH Zürich, CH-8093 Zürich, Switzerland.
*These authors contributed equally to this work. †Present address: Vaccine Research Center, National Institute of Allergy and Infectious Diseases, Bethesda, MD 20892, USA. ‡These authors contributed equally to this work. §Corresponding author. E-mail: njsull@mail.nih.gov

Downloaded from on March 17, 2016

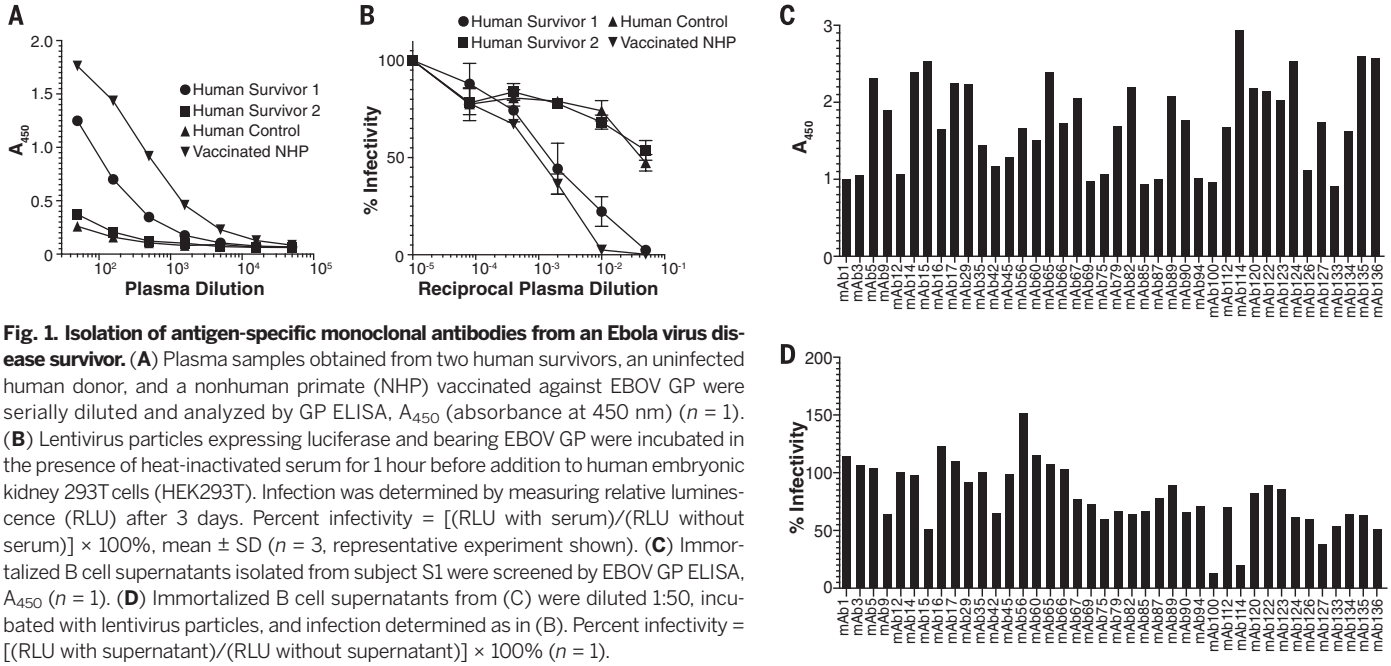



**Fig. 1. Isolation of antigen-specific monoclonal antibodies from an Ebola virus disease survivor.** (**A**) Plasma samples obtained from two human survivors, an uninfected human donor, and a nonhuman primate (NHP) vaccinated against EBOV GP were serially diluted and analyzed by GP ELISA, $A_{450}$ (absorbance at 450 nm) ($n$ = 1). (**B**) Lentivirus particles expressing luciferase and bearing EBOV GP were incubated in the presence of heat-inactivated serum for 1 hour before addition to human embryonic kidney 293T cells (HEK293T). Infection was determined by measuring relative luminescence (RLU) after 3 days. Percent infectivity = [(RLU with serum)/(RLU without serum)] × 100%, mean ± SD ($n$ = 3, representative experiment shown). (**C**) Immortalized B cell supernatants isolated from subject S1 were screened by EBOV GP ELISA, $A_{450}$ ($n$ = 1). (**D**) Immortalized B cell supernatants from (C) were diluted 1:50, incubated with lentivirus particles, and infection determined as in (B). Percent infectivity = [(RLU with supernatant)/(RLU without supernatant)] × 100% ($n$ = 1).

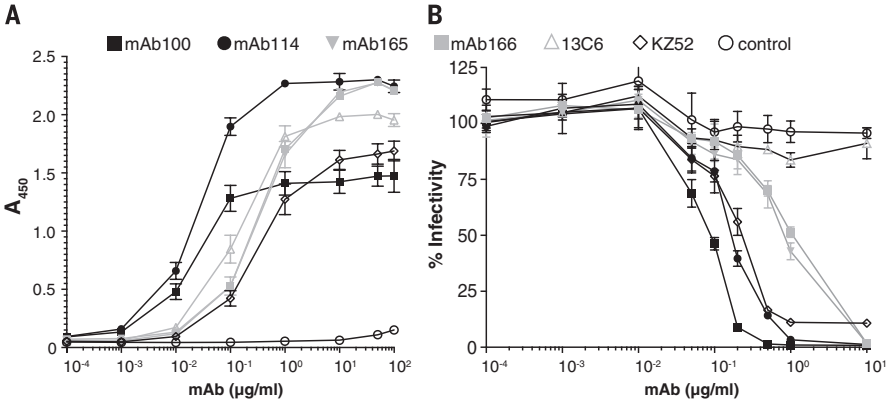
expressed antibodies with markedly higher neutralizing activity than all others (Fig. 1D). A second immortalization yielded 21 clones, from which the GP-specific clones 165 and 166 were rescued (fig. S1).

mAb100, mAb114, mAb165, and mAb166 sequences were amplified by polymerase chain reaction (PCR) and antibodies produced by transient transfection. We assessed ELISA binding to EBOV GP and observed that mAb114, mAb165, and mAb166 displayed maximal binding nearly 50% higher than that of KZ52, a prototypic EBOV GP–specific human mAb (*11*), and 25% higher than that of 13C6, a component of the ZMapp cocktail (*6*, *7*) (Fig. 2A). The binding curve of mAb100 had a plateau similar to that of KZ52 (Fig. 2A). mAb100 and mAb114 achieved half-maximal binding ($EC_{50}$) at a concentration of 0.02 μg/ml, which is lower than the other mAbs by a factor of 7 to 19. The binding profiles of mAb165 and mAb166 were similar to each other, with $EC_{50}$ values of 0.38 μg/ml and 0.35 μg/ml, respectively; EBOV control mAbs KZ52 and 13C6 had $EC_{50}$ values of 0.33 μg/ml and 0.14 μg/ml, respectively (Fig. 2A).

To evaluate the four S1 mAbs' capacity for neutralization, we used lentiviral particles pseudotyped with EBOV GP, a method that has been demonstrated to recapitulate wild-type EBOV results without the need for high-level biocontainment procedures (*12*) (Fig. 2B and fig. S2A). mAb165 and mAb166 exhibited similar half-maximal inhibition ($IC_{50}$) concentrations of 1.77 and 0.86 μg/ml, respectively. mAb100 and mAb114 were the most potent, with $IC_{50}$ values about one log unit lower (0.06 and 0.09 μg/ml, respectively) than those of mAb165 and mAb166. Notably, all four of the isolated mAbs inhibited 100% of the virus, unlike KZ52, which consistently displayed only 80 to 90% maximum inhibition, and 13C6, which neutralized <20% at 10 μg/ml. The S1 mAbs also potently neutralized the 2014 West African Makona variant (fig. S2B). Neutralization of wild-type EBOV particles by each of the isolated antibodies was confirmed by plaque reduction assay (fig. S3).

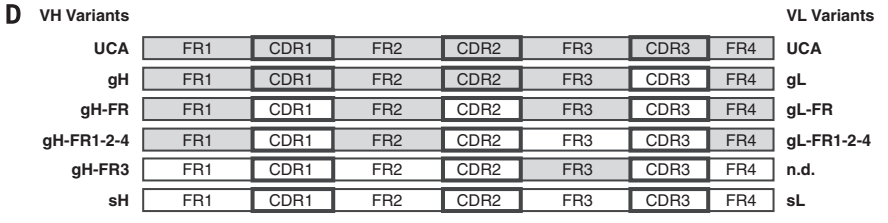
Sequence analysis revealed that the S1 mAbs displayed 85 to 95% germline identity for heavy chains and 89 to 97% germline identity for light chains (Fig. 2C). Analyses of germline gene usage and V(D)J recombination indicate that they originated from different B cell lineages. We analyzed the role of somatic hypermutations for the two most potent antibodies, mAb100 and mAb114, with the use of variants that were partially or completely reverted to the unmutated common ancestors (UCAs) (Fig. 2D and fig. S4, A and B). The fully reverted mAb100 (UCA/UCA), as well as a variant with a single change from the UCA VL (UCA/gL, $Ala^{89}$ → Thr), recognized cells expressing GP, with binding weaker than that of the fully matured antibody by a factor of 2 to 4 (Fig. 2E and fig. S4, A and B). When three HCDR3 (heavy chain complementarity-determining region 3) mutations—$Ala^{96}$ → Val, $Val^{103}$ → Tyr, and $Tyr^{114}$ → Ser—were introduced in the reverted germline antibody (gH/UCA), binding was comparable to the fully matured mAb100 (sH/sL); this result suggests that three mutations are sufficient to confer the binding observed for the fully matured mAb100.

In the case of mAb114, the fully reverted version (UCA/UCA) demonstrated negligible binding




C

| | VH | Identity % | D | JH | VL | Identity % | JL | HCDR3 length | IgG subclass |
|---|---|---|---|---|---|---|---|---|---|
| **mAb100** | V4-59*01 | 94.74% | D3-16*02 | J4*02 | VL3-1*01 | 92.11% | J2*01 | 19 | IgG3 |
| **mAb114** | V3-13*01 | 87.37% | D6-19*01 | J4*02 | VK1-27*01 | 92.83% | J4*01 | 13 | IgG1 |
| **mAb165** | V3-7*01 | 89.93% | D2-2*02 | J4*02 | VK1-39*01 | 89.96% | J1*01 | 21 | IgG1 |
| **mAb166** | V1-69*04 | 92.01% | D3-22*01 | J6*03 | VK3-20*01 | 97.16% | J3*01 | 16 | IgG3 |



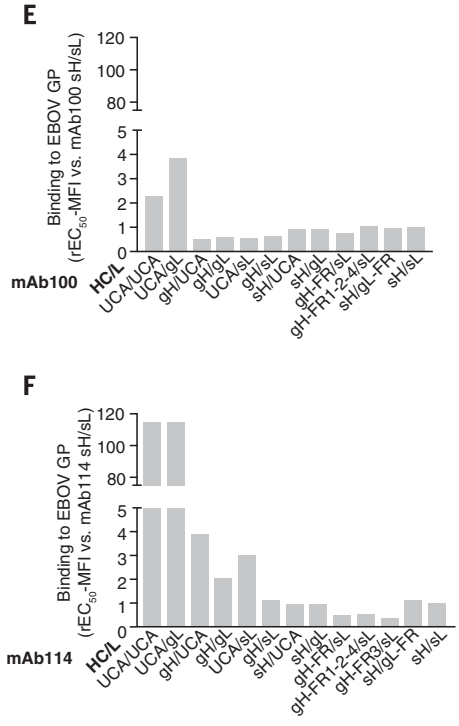




**Fig. 2. Characterization of purified EBOV GP monoclonal antibodies.** (**A**) EBOV GP ELISA in the presence of purified mAbs as indicated: $A_{450}$, mean ± SD ($n$ = 3, representative experiment shown). (**B**) Pseudotyped EBOV GP lentivirus particles were incubated with increasing amounts of purified mAbs and infection of HEK293T cells determined as in Fig. 1B. Percent infectivity = [(RLU with antibody)/(RLU without antibody)] × 100%, mean ± SD ($n$ = 3, representative experiment shown). (**C**) V-gene usage, sequence analysis, and immunoglobulin G (IgG) subclass of antibodies from S1. (**D**) Schematic of mAb100 and mAb114 unmutated common ancestor (UCA) and variants created for investigation of the binding requirements of these mAbs. Shaded areas represent sequence from UCA; light regions are from the somatic, mature antibody. Wild-type, somatically mutated heavy (sH), or somatically mutated light (sL) chains; gH or gL, germline V-gene revertants of sH or sL in which the HCDR or LCDR3 (light chain complementarity-determining region 3) are mature; gH-FR or gL-FR, germline V-gene revertants of sH or sL in which the HCDRs or LCDRs are mature; gH-FR1-2-4, germline V-gene revertants of sH in which the HCDRs and HFR3 (framework region 3 of heavy chain) are mature; gH-FR3, germline V-gene revertants of sH in which the HCDRs and HFR1, HFR2, and HFR4 are mature. (**E** and **F**) Binding to EBOV GP expressed on the surface of Madin-Darby canine kidney-2,6-sialtransferase (MDCK-SIAT) cells by versions of mAb100 (E) and mAb114 (F) in which all or subsets of somatic mutations were reverted to the germline sequence. Shown is the ratio between the $EC_{50}$ values of the variants and the wild type (sH/sL). Ratio values above 100 indicate a lack of detectable binding ($n$ = 1).

to GP (Fig. 2F and fig. S4, C and D). Introduction of two mutations (Ala$^{96}$ → Val and Tyr$^{108}$ → Ser) in the HCDR3 of the mAb114 germline (gH/UCA) was sufficient to confer an increase in binding, although still not to the degree seen with the fully matured mAb. Because these mutations are located at the base of the HCDR3 loop, they likely do not make direct contact with GP and thus may have a stabilizing effect on the whole HCDR3. The fully matured light chain and the two HCDR3 mutations (gH/sL) were sufficient to confer binding equivalent to the fully matured mAb (sH/sL). The fully mutated light chain gene (UCA/sL) could partially compensate for a lack of somatic mutation in the heavy chain (Fig. 2F and fig. S4, C and D). The presence of additional mutations on either VH or VL is required to achieve the level of the fully matured mAb114 binding. These results suggest a rapid pathway of mAb114 affinity maturation through one or two somatic mutations, which became redundant as further mutations accumulated—a finding that is reminiscent of what was recently observed for the generation of broadly neutralizing influenza antibodies (*13*).

Because mAb100 and mAb114 were the most potently neutralizing antibodies, they were considered optimal candidates for further evaluation in NHP. To assess the potential for combination therapy, we first sought to rule out antagonistic binding to GP. We found that each antibody bound to GP in the presence of the other, which suggests that they recognize distinct regions on GP (Fig. 3A) and therefore could be used as combination immunotherapy to maximize efficacy (*14*). To define the regions targeted by mAb100 and mAb114, we used biolayer interferometry to assess GP binding in competition with mAbs KZ52 and 13C6, which have epitopes in the GP base and glycan cap, respectively (*15*, *16*). We found that mAb100 competes with KZ52 for binding at the base of GP, whereas mAb114 recognizes (at least in part) the glycan cap region, as demonstrated by competition with 13C6 (Fig. 3, B and C).

Because some EBOV GP antibodies have been suggested to mediate antibody-dependent cell-mediated cytotoxicity (ADCC) (*17*), we determined the ADCC activity of mAb100 and mAb114 in a flow cytometric assay (Fig. 3D). We found that mAb100 and mAb114 mediated ADCC, with maximal activity observed at a mAb concentration of 0.03 μg/ml. Target cell killing was mediated through Fc receptors, because mAbs containing Fc LALA mutations [Leu$^{234}$ → Ala, Leu$^{235}$ → Ala (*18*)] abrogated ADCC activity. Therefore, these mAbs have the potential to induce direct killing of infected cells in vivo, a key viral clearance mechanism.

The presence of potent neutralizing and ADCC activity and the absence of cross-competition supported testing whether mAb100 and mAb114 offered in vivo protective efficacy. We challenged four rhesus macaques with a lethal dose of EBOV. One day after challenge, the treatment group ($n$ = 3) received an intravenous injection with a mixture of mAb100 and mAb114 at a combined dose of 50 mg/kg, and the treatment was repeated twice at 24-hour intervals. Circulating GP-specific antibody titers in mAb recipients peaked after the second injection, and reciprocal ELISA titers remained above 10$^5$ throughout the study, suggesting minimal clearance of the mAbs (Fig. 4A). The untreated macaque succumbed to EVD on day 10 with a circulating viral load exceeding 10$^8$ genome equivalents per milliliter (ge/ml) (Fig. 4, B and C). In contrast, all three mAb-treated macaques survived challenge without detectable viremia. Consistent with historical controls, the untreated animal displayed hallmark indicators of EVD including thrombocytopenia and elevations in alanine transaminase and creatinine from day 6 through the time of death (Fig. 4D and figs. S5 to S8). In contrast, the treatment group remained within normal ranges for these parameters and remained free of all EVD symptoms.

We next asked whether monotherapy is sufficient for protection, focusing on mAb114 because it showed higher maximal binding than mAb100. We exposed four macaques to a lethal dose of EBOV and administered mAb114 (50 mg/kg; $n$ = 3) to the treatment group after a 1-day delay, followed by two doses at 24-hour intervals. All treated macaques survived, whereas the control animal succumbed to EVD on day 6 with a peak viral load of 10$^{10}$ ge/ml (Fig. 4, E to G). In contrast to the previous experiment, transient viremia was observed in the treated animals (Fig. 4F) but

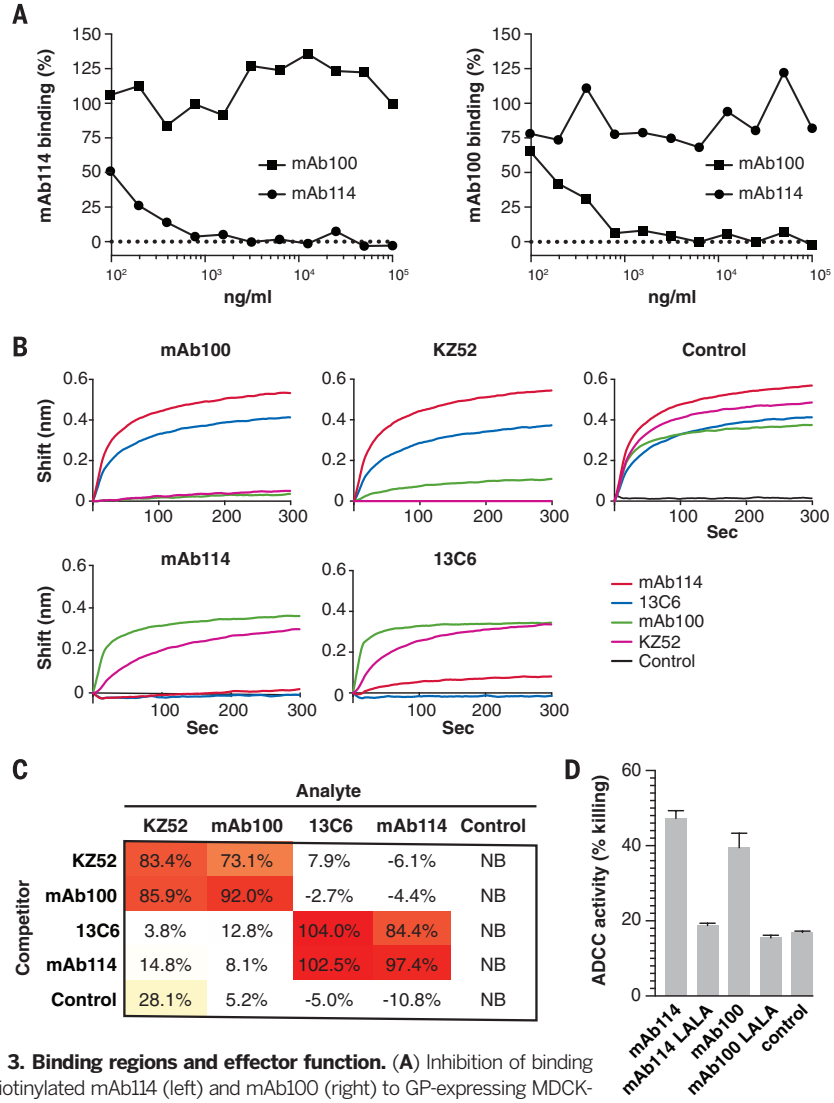



**Fig. 3. Binding regions and effector function.** (**A**) Inhibition of binding of biotinylated mAb114 (left) and mAb100 (right) to GP-expressing MDCK-SIAT cells by pre-incubation with increasing amounts of homologous or heterologous unlabeled antibodies. Shown is the percentage binding of biotinylated antibody ($n$ = 1). (**B** and **C**) Biolayer interferometry competitive binding assay to soluble EBOV GP using mAb100, mAb114, KZ52, 13C6, and isotype negative control. Biosensors were preloaded with GP followed by the competitor and analyte antibodies as indicated. Analyte binding curves (B) and quantitated percent inhibition (C) are reported ($n$ = 3, representative experiment shown). (**D**) Antibody-dependent cell-mediated cytotoxicity (ADCC) assay was determined for mAb100, mAb114 ($n$ = 3, representative experiment shown), control antibody, or derivative antibodies with LALA mutations that abrogate Fc-mediated killing of HEK293T cells ($n$ = 1), all at 31.6 ng/ml. ADCC activity is shown as mean ± SD.

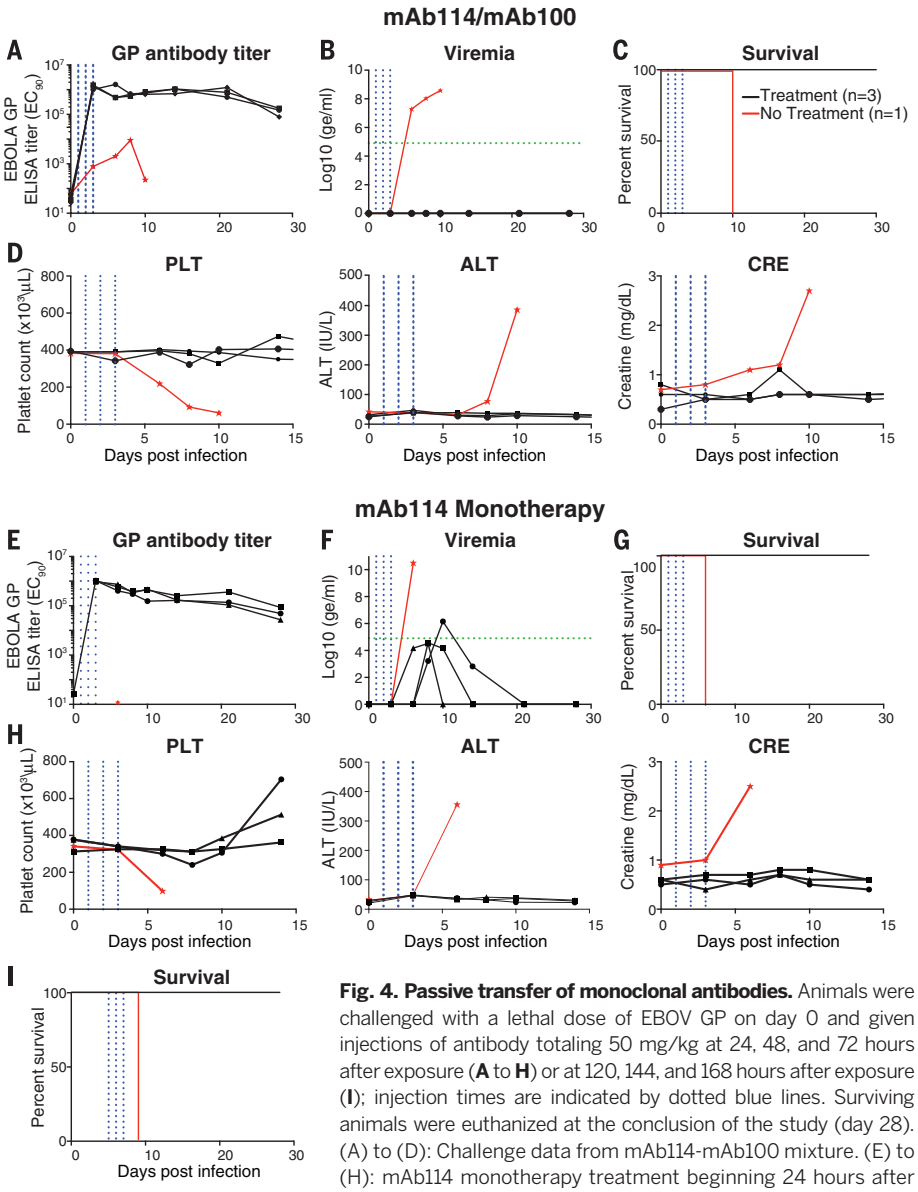



**Fig. 4. Passive transfer of monoclonal antibodies.** Animals were challenged with a lethal dose of EBOV GP on day 0 and given injections of antibody totaling 50 mg/kg at 24, 48, and 72 hours after exposure (**A** to **H**) or at 120, 144, and 168 hours after exposure (**I**); injection times are indicated by dotted blue lines. Surviving animals were euthanized at the conclusion of the study (day 28). (A) to (D): Challenge data from mAb114-mAb100 mixture. (E) to (H): mAb114 monotherapy treatment beginning 24 hours after exposure. (I): The same treatment beginning 120 hours after exposure. Black, treatment animals; red, untreated controls. (A) and (E): Ebola GP–specific ELISA titer (reciprocal $EC_{90}$). (B) and (F): Viremia in blood, as assessed by quantitative reverse transcription PCR (qRT-PCR). The dotted green lines denote the lower limit of quantitation of the qRT-PCR assay. (C), (G), and (I): Survival. (D) and (H): Selected hematologic and chemistry data. PLT, platelets; ALT, alanine transaminase; CRE, creatinine.

remained at levels less than 0.1% of the untreated control animal. Despite transient viremia, treated animals remained free of clinical and laboratory abnormalities (Fig. 4H and figs. S9 to S12).

Because a delay in treatment is a distinct possibility in an outbreak setting, we evaluated the therapeutic potential for mAb114 when treatment was delayed until 5 days after lethal EBOV challenge. All three animals in the treatment group survived, while the control animal succumbed to EVD on day 9. Moreover, animals in the treatment group remained symptom-free and protected against thrombocytopenia, transaminitis, and renal dysfunction (Fig. 4I and figs. S13 to S16).

mAb114 has several characteristics that may contribute to protection as a monotherapy when compared to KZ52 and 13C6, which were nonprotective in NHPs (*7*, *19*). First, although KZ52 and mAb114 potently neutralize EBOV in vitro, only mAb114 completely neutralizes input virus. Second, mAb114 does not require complement for neutralizing activity (Fig. 2B), in contrast to 13C6 (*6*). One hypothesis that might be derived from these observations is that protective monotherapy may require both potent binding and complete complement-independent neutralization. In addition, mAb114's specific mechanism of neutralization [which targets an essential step in virus entry (*20*)] and observed in vitro ADCC activity may contribute to mAb114's ability to protect against lethal EVD in macaques.

Our results show that antibodies as well as memory B cells specific to EBOV are maintained in a survivor more than a decade after infection. For the mAbs isolated from this survivor, a potential role for antibody-dependent killing is suggested by in vitro ADCC activity that in vivo may be mediated by multiple effector cells such as natural killer cells, macrophages, or neutrophils. In addition, these mAbs showed potent neutralizing activity against Ebola GP variants that have evolved over a 40-year period. Together, these data demonstrate the therapeutic potential of these mAbs as dual-combination therapy and/or monotherapy and contribute to understanding the mechanisms of antibody-mediated protection against Ebola virus disease.

## REFERENCES AND NOTES


1. WHO Ebola Response Team, *N. Engl. J. Med.* **371**, 1481–1495 (2014).
2. J. Burke, R. Declerq, G. Ghysebrechts, *Bull. World Health Organ.* **56**, 271–293 (1978).
3. A. Gulland, *BMJ* **350**, h1619 (2015).
4. J. J. Muyembe-Tamfum *et al.*, *Onderstepoort J. Vet. Res.* **79**, 451 (2012).
5. X. Qiu *et al.*, *Clin. Immunol.* **141**, 218–227 (2011).
6. J. A. Wilson *et al.*, *Science* **287**, 1664–1666 (2000).
7. X. Qiu *et al.*, *Nature* **514**, 47–53 (2014).
8. J. J. Muyembe-Tamfun, M. Kipasa, C. Kiyungu, R. Colebunders, *J. Infect. Dis.* **179** (suppl. 1), S259–S262 (1999).
9. See supplementary materials on *Science* Online.
10. E. Traggiai *et al.*, *Nat. Med.* **10**, 871–875 (2004).
11. T. Maruyama *et al.*, *J. Virol.* **73**, 6024–6030 (1999).
12. M. Côté *et al.*, *Nature* **477**, 344–348 (2011).
13. L. Pappas *et al.*, *Nature* **516**, 418–422 (2014).
14. D. H. Barouch *et al.*, *Nature* **503**, 224–228 (2013).
15. J. E. Lee *et al.*, *Nature* **454**, 177–182 (2008).
16. C. D. Murin *et al.*, *Proc. Natl. Acad. Sci. U.S.A.* **111**, 17182–17187 (2014).
17. G. G. Olinger Jr. *et al.*, *Proc. Natl. Acad. Sci. U.S.A.* **109**, 18030–18035 (2012).
18. M. Hezareh, A. J. Hessell, R. C. Jensen, J. G. van de Winkel, P. W. Parren, *J. Virol.* **75**, 12161–12168 (2001).
19. W. B. Oswald *et al.*, *PLOS Pathog.* **3**, e9 (2007).
20. J. Misasi *et al.*, *Science* **351**, 1343–1346 (2016).


## ACKNOWLEDGMENTS

We thank M. Cichanowski for graphics, B. Hartman for manuscript preparation, A. Tislerics and J. McLellan for critical reading of the manuscript, A. R. Townsend for providing EBOV-GP–expressing MDCK-SIAT cells, and the study volunteers for the donation of blood for these investigations. The data reported in this manuscript are tabulated in the main paper and in the supplementary materials. Antibody sequences have been deposited in GenBank with accession numbers KU594601, KU594602, KU594603, and KU594604. Supported by the Intramural Research Program of the Vaccine Research Center, National Institute of Allergy and Infectious Diseases. N.J.S., S.M., B.S.G., J.E.L., D.A.S., J.-J.M.-T., J.C.T., D.C., and A.L. are listed as inventors on patent applications related to anti-Ebola virus antibodies and their use. Opinions, interpretations, conclusions, and recommendations are those of the authors and are not necessarily endorsed by the U.S. Department of Defense or the U.S. Department of the Army.

## SUPPLEMENTARY MATERIALS

www.sciencemag.org/content/351/6279/1339/suppl/DC1
Materials and Methods
Figs. S1 to S16
References (*21*–*25*)

18 October 2015; accepted 17 February 2016
Published online 25 February 2016
10.1126/science.aad5224

EBOLA VIRUS

# Structural and molecular basis for Ebola virus neutralization by protective human antibodies

John Misasi,[1,5,8]* Morgan S. A. Gilman,[2]* Masaru Kanekiyo,[1]* Miao Gui,[4]* Alberto Cagigi,[1] Sabue Mulangu,[1] Davide Corti,[6] Julie E. Ledgerwood,[1] Antonio Lanzavecchia,[6,9] James Cunningham,[5] Jean Jacques Muyembe-Tamfun,[7] Ulrich Baxa,[3] Barney S. Graham,[1] Ye Xiang,[4]†‡ Nancy J. Sullivan,[1]†‡ Jason S. McLellan[2]†

**Ebola virus causes hemorrhagic fever with a high case fatality rate for which there is no approved therapy. Two human monoclonal antibodies, mAb100 and mAb114, in combination, protect nonhuman primates against all signs of Ebola virus disease, including viremia. Here, we demonstrate that mAb100 recognizes the base of the Ebola virus glycoprotein (GP) trimer, occludes access to the cathepsin-cleavage loop, and prevents the proteolytic cleavage of GP that is required for virus entry. We show that mAb114 interacts with the glycan cap and inner chalice of GP, remains associated after proteolytic removal of the glycan cap, and inhibits binding of cleaved GP to its receptor. These results define the basis of neutralization for two protective antibodies and may facilitate development of therapies and vaccines.**

Ebola virus (EBOV) causes a rapidly fatal hemorrhagic fever for which there is currently no treatment (*1*–*3*). We recently isolated two monoclonal antibodies (mAb100 and mAb114) from a 1995 Kikwit Ebola survivor that potently neutralize multiple EBOV isolates spanning more than 40 years (*4*). When administered as a cocktail to rhesus macaques, these antibodies fully protected from clinical symptoms, viremia, and death. Furthermore, mAb114 monotherapy fully protected macaques from death and illness when given as late as 5 days after infection (*4*). In this study, we sought to identify the structural and molecular basis of neutralization for these protective antibodies.

The EBOV glycoprotein (GP) is a class I fusion protein comprising disulfide-linked subunits, GP1 and GP2, which associate to form a chalice-shaped trimer (*5*–*7*). The GP1 subunit binds to the EBOV receptor, Niemann-Pick C1 (NPC1), allowing GP2-mediated fusion of the viral and host-cell membranes (*5*, *8*–*11*). The GP1 subunit contains a core domain and a "glycan cap," which are shielded by the heavily glycosylated mucin-like domain (MLD) (Fig. 1A). The MLD is dispensable for virus entry but is a target for host antibody responses (*6*, *7*, *12*–*16*). Using immunoprecipitation (IP), we found that mAb100 and mAb114 recognized GP ectodomains lacking the MLD ($GP_{\Delta Muc}$), suggesting that their epitopes reside elsewhere on GP (Fig. 1B) (*17*).

To identify the epitopes recognized by these antibodies, crystal structures of their antigen-binding fragments (Fab100 and Fab114) were determined individually to 2.0 Å and in a ternary complex with $GP_{\Delta Muc}$ to 6.7 Å (table S1 and fig. S1, A and B). The complex structure was solved by molecular replacement using the refined structures of the unbound Fabs and the previously solved EBOV $GP_{\Delta Muc}$ structure (*6*) as search models and was refined to an $R_{work}/R_{free}$ of 26.0/34.3% (table S1). The crystal structure shows that Fab100 binds to the base of GP, parallel to the viral membrane, makes contacts with both GP1 and GP2, and cross-links two adjacent protomers (Fig. 1C and fig. S1C). In contrast, Fab114 binds within the GP chalice, perpendicular to the viral membrane, and makes contacts with both the glycan cap and the GP1 core (Fig. 1C and fig. S1C).

Because GP binds NPC1 in acidic late-endosomes and lysosomes (*8*–*12*, *16*), we compared antibody binding to $GP_{\Delta Muc}$ at neutral and low pH using cryogenic electron microscopy (cryo-EM). The structures of the ternary complexes at pH 7.4 and 5.0 were calculated to a resolution of 9 Å by single-particle reconstruction (fig. S2). The ternary-complex crystal structure fit well as a rigid body into the cryo-EM densities (Fig. 2). Further rigid-body refinement of the Fabs and GP did not change the overall structure substantially, indicating that the crystal structure closely resembles the cryo-EM structure. Comparisons of the cryo-EM structures at pH 7.4 and 5.0 revealed highly similar structures (Fig. 2 and fig. S2C), suggesting that these antibodies would remain associated with GP during trafficking of EBOV to low-pH compartments. Analysis of the cryo-EM structure also revealed a bulky density near the Fab100 interface that would be consistent with an *N*-linked glycan at residue Asn563 of GP (*6*, *7*) (fig. S3A). Enzymatic trimming of the glycans using endoglycosidase H (EndoH) did not appreciably alter Fab100 binding to GP, suggesting that *N*-linked glycans are not critical for Fab100 recognition (fig. S4, A to C).

Binding of Fab100 to the base of the GP trimer (Fig. 1C and fig. S1C) resembles that of KZ52, a prototypic neutralizing antibody that does not confer protection in macaques (*6*, *18*, *19*). However, Fab100 is rotated about the trimeric axis by ~60° with respect to KZ52 (fig. S3B). This rotation enables Fab100 to contact GP1 and GP2 of one protomer, as well as the internal fusion loop (IFL) of the neighboring protomer, whereas KZ52 contacts only a single protomer (fig. S3C). Fab100 is also in close proximity to the β13-β14 loop (Fig. 3A) (residues 190 to 213), which is disordered in the previous structure (*6*). Biochemical studies have shown that EBOV entry requires cleavage of this loop by cathepsins L and B (*11*, *12*, *20*–*23*), which releases the glycan cap and MLD, exposing the receptor-binding domain (RBD) within the GP1 core (*8*–*12*, *20*, *21*). Interestingly, the cryo-EM structure revealed additional electron density corresponding to portions of the β13-β14 loop in close proximity to the Fab100 light chain (Fig. 3A). The observed density would be expected to accommodate residues 190 to 197 and 209 to 213 and may accommodate additional residues depending on the conformation of the β13-β14 loop, which is difficult to determine given the weak electron density of this region. We therefore hypothesized that Fab100 would sterically block proteolysis by cathepsins. To test this, we used cathepsin L (Cat L) to digest $GP_{\Delta Muc}$ that was pretreated with mAb114, mAb100, KZ52, or control mAb. The amount of cleaved GP1 ($GP1_{20k}$) was similar in the control and mAb114 reactions (Fig. 3B). Consistent with previous reports, KZ52 delayed the appearance of $GP1_{20k}$ (*24*). For mAb100, the primary product was an intermediate form (GP1i) with only trace amounts of $GP1_{20k}$, indicating that mAb100 significantly reduced GP1 cleavage (Fig. 3B). Similarly, cleavage of GP1 by thermolysin, which mimics cathepsin B (Cat B) (*8*, *11*, *20*, *23*), was inhibited by mAb100 (fig. S4D). These data suggest that mAb100 neutralizes EBOV by sterically blocking cathepsin cleavage of the β13-β14 loop.

We next determined the affinity of Fab100 and KZ52 for $GP_{\Delta Muc}$ at neutral and low pH. The affinity of Fab100 was ~5 and ~10 times stronger than KZ52 at pH 7.4 and 5.3, respectively (Fig. 3C and fig. S4A), suggesting that mAb100 remains tightly associated with GP in low-pH compartments. Notably, the affinity of KZ52 for thermolysin-cleaved GP ($GP_{THL}$) at

[1]Vaccine Research Center, National Institute of Allergy and Infectious Diseases, National Institutes of Health, Bethesda, MD 20892, USA. [2]Department of Biochemistry, Geisel School of Medicine at Dartmouth, Hanover, NH 03755, USA. [3]Electron Microscopy Laboratory, Cancer Research Technology Program, Leidos Biomedical Research, Inc., Frederick National Laboratory for Cancer Research, Frederick, MD 21702, USA. [4]Centre for Infectious Diseases Research, Collaborative Innovation Center for Diagnosis and Treatment of Infectious Diseases, Beijing Advanced Innovation Center for Structural Biology, Department of Basic Medical Sciences, School of Medicine, Tsinghua University, Beijing 100084 China. [5]Department of Medicine, Brigham and Women's Hospital, Harvard Medical School, Boston, MA 02115, USA. [6]Institute for Research in Biomedicine, Università della Svizzera Italiana, CH-6500 Bellinzona, Switzerland. [7]National Institute for Biomedical Research, National Laboratory of Public Health, Kinshasa B.P. 1197, Democratic Republic of the Congo. [8]Division of Infectious Diseases, Boston Children's Hospital, Boston, MA 02215, USA. [9]Institute of Microbiology, ETH Zurich, CH-8093 Zurich, Switzerland.
*These authors contributed equally to this work. †These authors contributed equally to this work. ‡Corresponding author. E-mail: njsull@mail.nih.gov (N.J.S.); yxiang@mail.tsinghua.edu.cn (Y.X.)

Downloaded from on March 17, 2016

pH 5.3 was decreased by a factor of more than 1000 as compared with uncleaved GP. For Fab100, a modestly reduced affinity for $GP_{THL}$ was driven primarily by a faster dissociation rate (Fig. 3C and fig. S4A). However, the dissociation rate constant ($k_{off}$) of the bivalent mAb100 immunoglobulin G (IgG) was similar between uncleaved and $GP_{THL}$ (fig. S5), suggesting that mAb100 remains bound even after proteolytic cleavage at low pH. Due to the quaternary nature of the mAb100 epitope, which includes the internal fusion loop, mAb100 may also prevent conformational rearrangements of GP that occur downstream of proteolytic cleavage. Antibodies with quaternary epitopes have been recently identified that potently neutralize other viruses, suggesting that this mode of binding represents a powerful immunological solution to viral entry (*25*–*27*).

Unlike mAb100, mAb114 recognizes an epitope spanning both the glycan cap and the GP1 core (Figs. 4A and 1C). Most contacts appear to be made between the CDR H3 and L3 of Fab114 and the loop connecting β8 and β9 of the GP1 core (*6*). The importance of this region for mAb114 binding was confirmed by CLIPS (chemical linkage of peptides onto scaffolds) conformational-epitope mapping (*28*) (fig. S6A). Because the contacts within the GP1 core remain after cathepsin cleavage (fig. S7A), we investigated mAb114 binding to $GP_{THL}$ using IP and found that $GP_{THL}$ was recognized similarly to GP and $GP_{\Delta Muc}$ (Fig. 4B). Furthermore, negative-stain EM showed that the binding orientation of Fab114 to $GP_{THL}$ was similar to $GP_{\Delta Muc}$ (Fig. 4C), demonstrating that the glycan cap is dispensable for mAb114–GP interaction.

Because EBOV particles transit from neutral to low-pH compartments (*12*, *16*, *20*), we measured binding kinetics of Fab114 to $GP_{\Delta Muc}$ at pH 7.4 and 5.3 and observed similar subnanomolar affinities (Fig. 4D and fig. S6B). When compared with antibody 13C6, which competes with mAb114 for binding to GP (*4*) but is not protective in macaques (*15*, *29*), Fab114 has a significantly slower $k_{off}$, leading to an affinity that is tighter by factors of more than 250 and 40 at pH 7.4 and 5.3, respectively (Fig. 4D and fig. S6B). Importantly, 13C6 only makes contact with the glycan cap (*30*), whereas mAb114 bound GP after glycan cap removal (Fig. 4, B and C). The affinity of Fab114 for $GP_{THL}$ at pH 5.3 remained high [equilibrium dissociation constant ($K_D$) of 8.0 nM], consistent with our structural data showing that Fab114 primarily contacts residues within the GP1 core.

After cathepsin cleavage of GP1, a hydrophobic pocket is exposed on the GP1 core that is formed primarily by α1 and β4 and bordered by charged residues in β7, β8, and β9. These regions have been proposed to be the RBD of EBOV GP (*6*, *23*, *31*–*36*). Our data suggested that the interaction of mAb114 with residues in β7 to β9 might block NPC1 access to this pocket. To investigate this, we performed a competition assay with mAb114, $GP_{THL}$, and NPC1 domain C (NPC1-dC)—the domain responsible for engaging cleaved GP and mediating virus entry (*8*–*10*). Using biolayer interferometry, we found that when mAb114 was bound to $GP_{THL}$, NPC1-dC was unable to bind (Fig. 4E and fig. S6C). Similar results were obtained using IP (fig. S6D). These findings are consistent with the observation that both Fab114 and NPC1-dC have similar affinities for $GP_{THL}$ (Fig. 4D and fig. S6B) and indicate that mAb114 neutralizes EBOV infection by preventing binding of cathepsin-cleaved GP to its receptor NPC1.

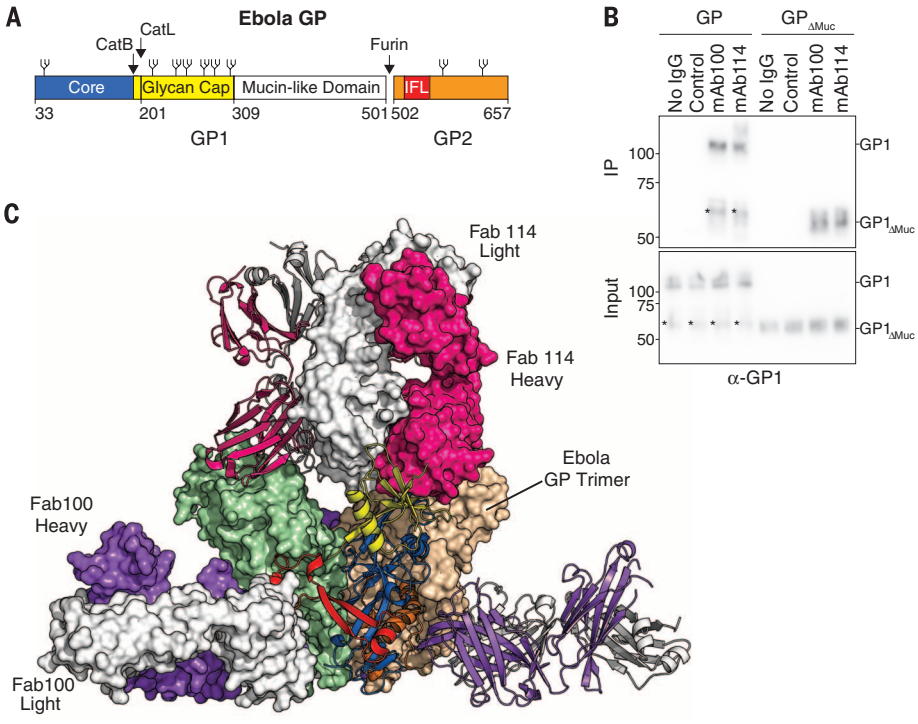



**Fig. 1. Binding requirements and structure of antibodies in complex with GP.** (**A**) Schematic representation of GP monomer, colored by domain. GP1 core region (33 to 190) is colored blue, GP1 glycan cap is colored yellow (201 to 308), and the mucin-like domain is uncolored (309 to 501). The GP2 IFL is colored red, and the remainder of GP2 is colored orange. Glycans are shown as branched lines, and proteolytic cleavage sites are labeled with arrows. Disulfide bonds within and between GP1 and GP2 are omitted for clarity. (**B**) IP of soluble GP ectodomain containing or lacking the mucin-like domain ($GP_{\Delta Muc}$) by mAb100, mAb114, or isotype control. Binding and input were analyzed using immunoblotting for GP1. *GP1 degradation product present only in mucin-containing GP. $n$ = 3 replicates; representative image shown. (**C**) Crystal structure of $GP_{\Delta Muc}$ in complex with Fab100 and Fab114. Fab100 is shown in purple (heavy chain) and white (light chain). Fab114 is shown in pink (heavy chain) and white (light chain). Molecular surfaces of two $GP_{\Delta Muc}$ protomers are colored in green and beige, whereas the third is shown as a ribbon representation and colored according to the schematic in (A).

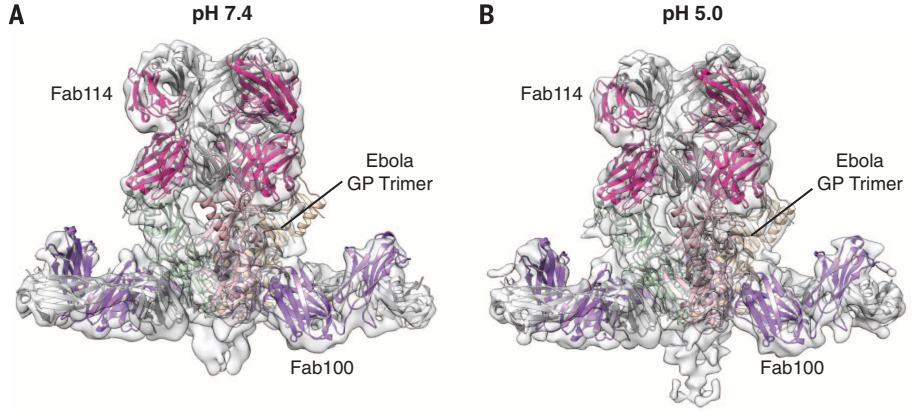



**Fig. 2. Cryo-EM of $GP_{\Delta Muc}$-Fab100-Fab114 complex.** Cryo-EM was performed on the ternary complex of $GP_{\Delta Muc}$ with Fab100 and Fab114 at (**A**) pH 7.4 and (**B**) pH 5.0. Shown are the superimpositions of the crystal structure (ribbon) into the cryo-EM density maps at their respective pH.

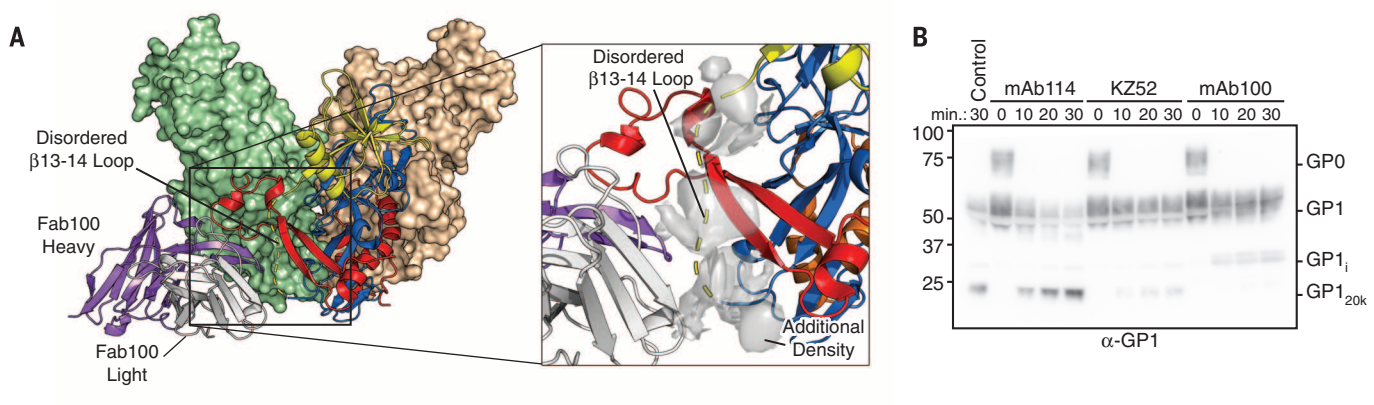
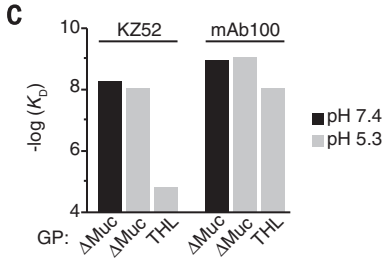



**Fig. 3. mAb100 inhibits cathepsin cleavage of GP.** (**A**) Fab100 binding occludes access to the β13-β14 loop of GP1. Protomers and Fab100 heavy and light chains are colored and oriented as in Fig. 1C. The variable domain of one Fab100 is shown in a ribbon representation, and all other Fabs are removed for clarity. Inset shows a zoomed view of the Fab100-GP interface with the difference map generated by masking out the cryo-EM densities of the fitted crystal structures shown as a gray transparent surface. The β13-β14 loop is shown as a dashed yellow line connecting the GP1 core (blue) and the glycan cap (yellow). (**B**) $GP_{\Delta Muc}$ was incubated with the indicated antibodies followed by cleavage at pH 5.5 by Cat L at 37°C. Samples were removed at 5-min intervals and analyzed by immunoblot for GP1. $n$ = 3 replicates; representative image shown. (**C**) Binding kinetics, as determined by biolayer interferometry, of $GP_{\Delta Muc}$ or $GP_{THL}$ (THL) with Fab100 or KZ52 at the indicated pH. $K_D$s are plotted on a negative log scale. $n$ = 2 replicates; representative experiment shown.



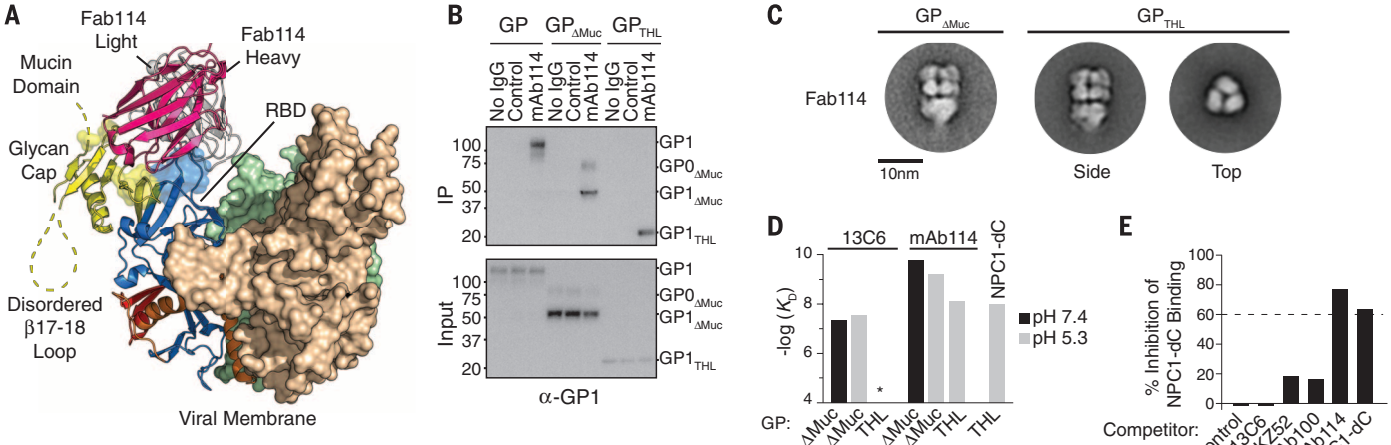




**Fig. 4. mAb114 blocks binding of NPC1 to the GP1 core.** (**A**) Fab114 binds to regions in the glycan cap and core of GP1. Protomers are colored as in Fig. 1C and viewed with a 100° rotation about the trimeric axis with respect to the orientation in Fig. 1C. The variable domain of a single Fab114 is shown in ribbons, and all other Fabs have been removed for clarity. GP residues predicted to make contact with Fab114 are shown as transparent surfaces. (**B**) Immunoprecipitation of $GP_{\Delta Muc}$ and $GP_{THL}$ by the indicated antibodies. Samples were analyzed by immunoblot for GP1. $n$ = 3 replicates; representative image shown. (**C**) Class averages of single particles from negative-stain electron micrographs of Fab114 in complex with $GP_{\Delta Muc}$ and $GP_{THL}$. (**D**) Binding kinetics, as determined by biolayer interferometry, of $GP_{\Delta Muc}$ or $GP_{THL}$ with Fab114, 13C6, or NPC1-dC at the indicated pH. $K_D$s are plotted on a negative log scale. *No binding. $n$ = 2 replicates; representative experiment shown. (**E**) Inhibition of NPC1-dC binding to $GP_{THL}$ by competitor proteins (NPC1-dC) or antibodies (mAb100, mAb114, 13C6, KZ52, or isotype control) was determined by biolayer interferometry. Dashed line represents 60% inhibition of binding. $n$ = 3 replicates; representative experiment shown.

Despite being in the same competition group as mAb114 (*4*), antibody 13C6 fails to neutralize EBOV due to its inability to remain bound to GP after cathepsin cleavage. Conversely, the Marburg GP-antibody MR78 recognizes an analogous receptor-binding domain on Marburg GP and also binds to cleaved EBOV GP, yet fails to neutralize EBOV due to its inability to recognize the native trimer (uncleaved GP) (*34*, *35*). The failure of MR78 to bind native EBOV GP led to the hypothesis that NPC1-blocking antibodies might not be elicited during Ebola virus infection (*34*). Strikingly, mAb114 overcomes these structural constraints by binding to the center of the GP1 chalice with a near-vertical angle of approach (85° with respect to the viral membrane) that allows access to the GP1 core. The recently published crystal structure of NPC1-dC bound to $GP_{THL}$ revealed that in addition to making contacts with the hydrophobic pocket exposed by removal of the glycan cap and MLD, NPC1 also contacts the surrounding charged region in β7 to β9 that is bound by mAb114 (fig. S7B) (*36*). Taken together, these data reveal a key site of vulnerability in the EBOV GP targeted by mAb114 and demonstrate that this class of antibodies can be elicited by natural infection.

The experiments herein reveal that mAb100 and mAb114 mediate virus neutralization by targeting independent essential steps in EBOV entry: exposure of the RBD by protease cleavage and receptor binding. Because these steps are required for the entry of all members of the *Filoviridae* family (*8*, *11*), our studies identify vulnerabilities targeted by the host immune system that could potentially be exploited in vaccine and therapeutic development.

## REFERENCES AND NOTES


1. J. Burke, R. Declerq, G. Ghysebrechts, *Bull. World Health Organ.* **56**, 271–293 (1978).
2. J. J. Muyembe-Tamfum *et al*., *Onderstepoort J. Vet. Res.* **79**, 1–8 (2012).
3. WHO Ebola Response Team, *N. Engl. J. Med.* **371**, 1481–1495 (2014).
4. D. Corti *et al*., *Science* **351**, 1339–1342 (2016).
5. S. C. Harrison, *Nat. Struct. Mol. Biol.* **15**, 690–698 (2008).
6. J. E. Lee *et al*., *Nature* **454**, 177–182 (2008).
7. S. A. Jeffers, D. A. Sanders, A. Sanchez, *J. Virol.* **76**, 12463–12472 (2002).
8. M. Côté *et al*., *Nature* **477**, 344–348 (2011).
9. E. H. Miller *et al*., *EMBO J.* **31**, 1947–1960 (2012).
10. J. E. Carette *et al*., *Nature* **477**, 340–343 (2011).
11. J. Misasi *et al*., *J. Virol.* **86**, 3284–3292 (2012).
12. K. Chandran, N. J. Sullivan, U. Felbor, S. P. Whelan, J. M. Cunningham, *Science* **308**, 1643–1645 (2005).
13. D. Olal *et al*., *J. Virol.* **86**, 2809–2816 (2012).
14. J. E. Lee *et al*., *J. Mol. Biol.* **375**, 202–216 (2008).
15. J. A. Wilson *et al*., *Science* **287**, 1664–1666 (2000).
16. J. Misasi, N. J. Sullivan, *Cell* **159**, 477–486 (2014).
17. Materials and methods are available as supporting material on *Science* Online.
18. W. B. Oswald *et al*., *PLOS Pathog.* **3**, e9 (2007).
19. T. Maruyama *et al*., *J. Infect. Dis.* **179** (suppl. 1), S235–S239 (1999).
20. K. Schornberg *et al*., *J. Virol.* **80**, 4174–4178 (2006).
21. M. Brecher *et al*., *J. Virol.* **86**, 364–372 (2012).
22. C. L. Hood *et al*., *J. Virol.* **84**, 2972–2982 (2010).
23. D. Dube *et al*., *J. Virol.* **83**, 2883–2891 (2009).
24. D. J. Shedlock *et al*., *Virology* **401**, 228–235 (2010).
25. Y. Iba *et al*., *J. Virol.* **88**, 7130–7144 (2014).
26. M. S. Gilman *et al*., *PLOS Pathog.* **11**, e1005035 (2015).
27. J. H. Lee *et al*., *Nat. Commun.* **6**, 8167 (2015).
28. P. Timmerman, W. C. Puijk, R. H. Meloen, *J. Mol. Recognit.* **20**, 283–299 (2007).
29. X. Qiu *et al*., *Nature* **514**, 47–53 (2014).
30. C. D. Murin *et al*., *Proc. Natl. Acad. Sci. U.S.A.* **111**, 17182–17187 (2014).
31. M. A. Brindley *et al*., *J. Virol.* **81**, 7702–7709 (2007).
32. B. Manicassamy, J. Wang, H. Jiang, L. Rong, *J. Virol.* **79**, 4793–4805 (2005).
33. O. M. Mpanju, J. S. Towner, J. E. Dover, S. T. Nichol, C. A. Wilson, *Virus Res.* **121**, 205–214 (2006).
34. T. Hashiguchi *et al*., *Cell* **160**, 904–912 (2015).
35. A. I. Flyak *et al*., *Cell* **160**, 893–903 (2015).
36. H. Wang *et al*., *Cell* **164**, 258–268 (2016).


## ACKNOWLEDGMENTS

We thank the 19-ID beamline staff at the Structural Biology Center at the Advanced Photon Source, Argonne National Laboratory. We thank W. Shi and M. Choe for preparation of antibodies, J. Mascola and K. Leigh for critical reading, M. Cichanowski for graphics, and B. Hartman for manuscript preparation. The data presented in this manuscript are tabulated in the main paper and in the supplementary materials. Atomic coordinates and structure factors for the crystal structures of Fab114, Fab100, and the ternary complex of these Fabs bound to Ebola virus GP have been deposited in the Protein Data Bank under accession codes 5FHA, 5FHB, and 5FHC, respectively. Cryo-EM maps and related materials have been deposited to the EM Data Bank under accession codes EMD-3310 and EMD-3311. This work was supported by the Intramural Research Program of the Vaccine Research Center, the National Institute of Allergy and Infectious Diseases, and the National Institutes of Health. J.M. received grant support from NIH-5K08AI079381 and a Boston Children's Hospital Faculty Development award. M.S.A.G. was supported by the National Institute of General Medical Sciences of the National Institutes of Health under award T32GM008704. Y.X. received grant support from the 973 program (2015CB14010102), the National Natural Science Foundation of China (81550001 and 31470721), and the Junior Thousand Talents Program of China (20131770418). This work was funded in part with federal funds from the Frederick National Laboratory for Cancer Research, National Institutes of Health, under contract HHSN261200800001E. We thank the Tsinghua University Branch of China National Center for Protein Sciences (Beijing) for providing the EM facility support. Argonne is operated by UChicago Argonne, LLC, for the U.S. Department of Energy, Office of Biological and Environmental Research, under contract DE-AC02-06CH11357. N.S., S.M., B.G., J.L., J.J.M.T., D.C., and A.L. are listed as inventors on patent applications related to antibodies to Ebola virus and their use. The content of this publication is solely the responsibility of the authors and does not necessarily represent the official views of the National Institutes of Health.

## SUPPLEMENTARY MATERIALS

www.sciencemag.org/content/351/6279/1343/suppl/DC1
Materials and Methods
Figs. S1 to S7
Table S1
References (*37*–*55*)

18 October 2015; accepted 17 February 2016
Published online 25 February 2016
10.1126/science.aad6117



# What if you could...

- use up to **44% less plastic** for your nucleic acid purification*
- **recycle ALL** of your packaging and plastics
- AND, still recover the same **highly pure DNA**?

## Now, you can.

NEW ENGLAND BioLabs® Inc.

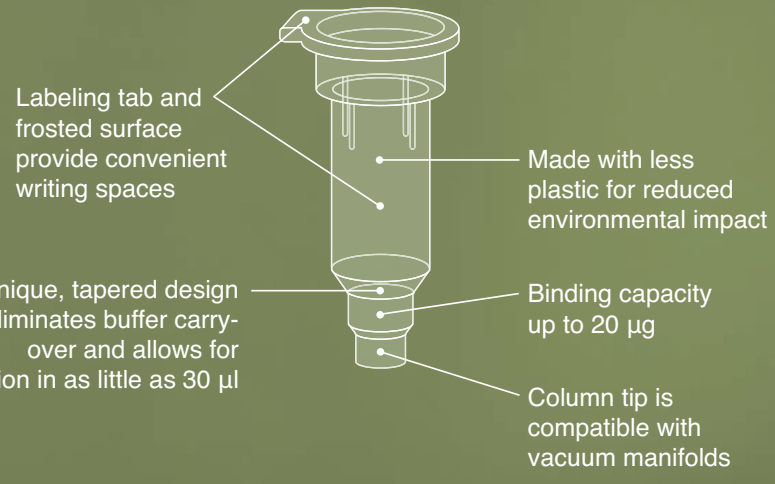
# It's time for change.

## Introducing Monarch™ Nucleic Acid Purification Kits

It's time to transform your DNA purification experience. NEB's Monarch Nucleic Acid Purification Kits are optimized for maximum performance and minimal environmental impact. With an innovative column design, buffer retention is prevented, eliminating risk of carryover contamination and enabling elution in smaller volumes. The result – highly pure DNA for your downstream applications.

Make the change and migrate to Monarch today.

### Optimized design of Monarch Miniprep Columns




Request your free sample at **NEBMonarch.com**

NEW ENGLAND BIOLABS® and NEB® are registered trademarks of New England Biolabs, Inc.
MONARCH™ is a trademark of New England Biolabs, Inc.
*Visit NEBMonarchPackaging.com for details.



Too young to win a prize
in Stockholm this December?

We don't think so.

Science & SciLifeLab
PRIZE
FOR YOUNG SCIENTISTS

Get published in *Science* and win $30,000 USD. Enter today: www.sciencemag.org/scilifelabprize

Cell and Molecular Biology | Ecology and Environment | Genomics and Proteomics | Translational Medicine

Science
AAAS

Knut och Alice Wallenbergs Stiftelse

SciLifeLab

BOYALIFE
博雅控股集团

# All about BIOTECHNOLOGY

## All for Human Development and Health Improvement

Boyalife Group is an enterprise centered on innovation in the biotechnology field covering stem cell technology and bio-pharm. Found in 2009, Boyalife Group has more than 30 wholly-owned subsidiaries and holding companies currently, becoming the leading brand in healthcare and pharmaceutical center in China.

Our operative segments all for better health are including:

- Stem Cell Technology
- Pharmaceutical
- Gene Harbor
- Cloning Factory
- Health Management
- Regenerative Medicine
- Disease Models

For more information, visit : www.boyalifegroup.com




# BOYALIFE & Science Science Translational Medicine Award in Stem Cells and Regenerative Medicine

## Stem cells and regenerative medicine is the new frontier in life sciences. Boyalife, Science and Science Translational Medicine jointly establish a global award to recognize significant contributions in advancing basic science to clinical applications in this field.

The award is to recognize and reward scientists in the fields of stem cells and/or regenerative medicine with a focus on developing cell-based treatments for cancer, degenerative disorders, immunotherapy and stem cells transplantation.

You could be next to win this prize and to receive

- ★ A Grand Prize of **$25,000** and a Runner-Up Prize of **$5,000** will be awarded.
- ★ The Grand Prize Winning Essay will be published in Science; a brief abstract of the Runner-Up Essay will be published in Science.

The 2016 Award is now open. The award ceremony will be held in San Francisco, on 23rd June, 2016.

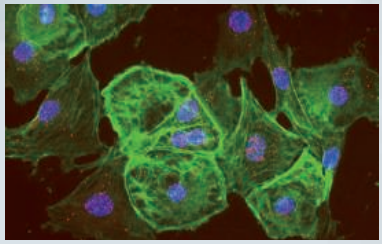
For more information, please visit: *http://www.sciencemag.org/prizes/boyalife*

BOYALIFE StemCell Science AAAS Science Translational Medicine AAAS

# DISCOVER PROTEIN–PROTEIN INTERACTIONS WITH DUOLINK® USING PLA® TECHNOLOGY

## Proximity Ligation Assay (PLA) Technology provides sensitive *in situ* detection of endogenous proteins

- Visualize individual interactions without overexpressing proteins
- Gain high specificity with dual binding of primary antibodies
- Increased sensitivity of single molecule due to signal amplification
- Analyze using standard immunofluorescence instruments



For more information, visit
**sigma-aldrich.com/duolink**

©2016 Sigma-Aldrich Co. LLC. All rights reserved. SIGMA and SIGMA-ALDRICH are trademarks of Sigma-Aldrich Co. LLC, registered in the US and other countries. Duolink and PLA are registered trademarks of Olink AB.
Sigma-Aldrich Corp. is a subsidiary of Merck KGaA, Darmstadt, Germany.

eppendorf

adVantage **New Promotion March 1 – June 30, 2016**



# Macro-offers for Microbiologists

**Premium solutions for your microbiological processes – now save up to 25 %!**

Our new Eppendorf Advantage™ special offers include Eppendorf premium products ideally suited for the most important steps of your microbiology workflow.

> Buy a Mastercycler® nexus gradient PCR cycler and save 25 %

> Purchase any Eppendorf Xplorer® or Xplorer plus electronic pipette with 20 % off

> Save 20 % on the ep*Motion*® 96

> Get the Eppendorf HeatSealer S100 with 20 % savings

www.eppendorf.com/advantage

Eppendorf®, the Eppendorf logo, epMotion®, Eppendorf Xplorer®, and Mastercycler® are registered trademarks of Eppendorf AG, Hamburg, Germany.
Eppendorf Advantage™ is a trademark of Eppendorf AG, Hamburg, Germany. U.S. Design Patents are listed on www.eppendorf.com/ip.
Offers may vary by country. All rights reserved, including graphics and images. Copyright © 2016 by Eppendorf AG.

# Don't miss the debut of *Science Immunology*.

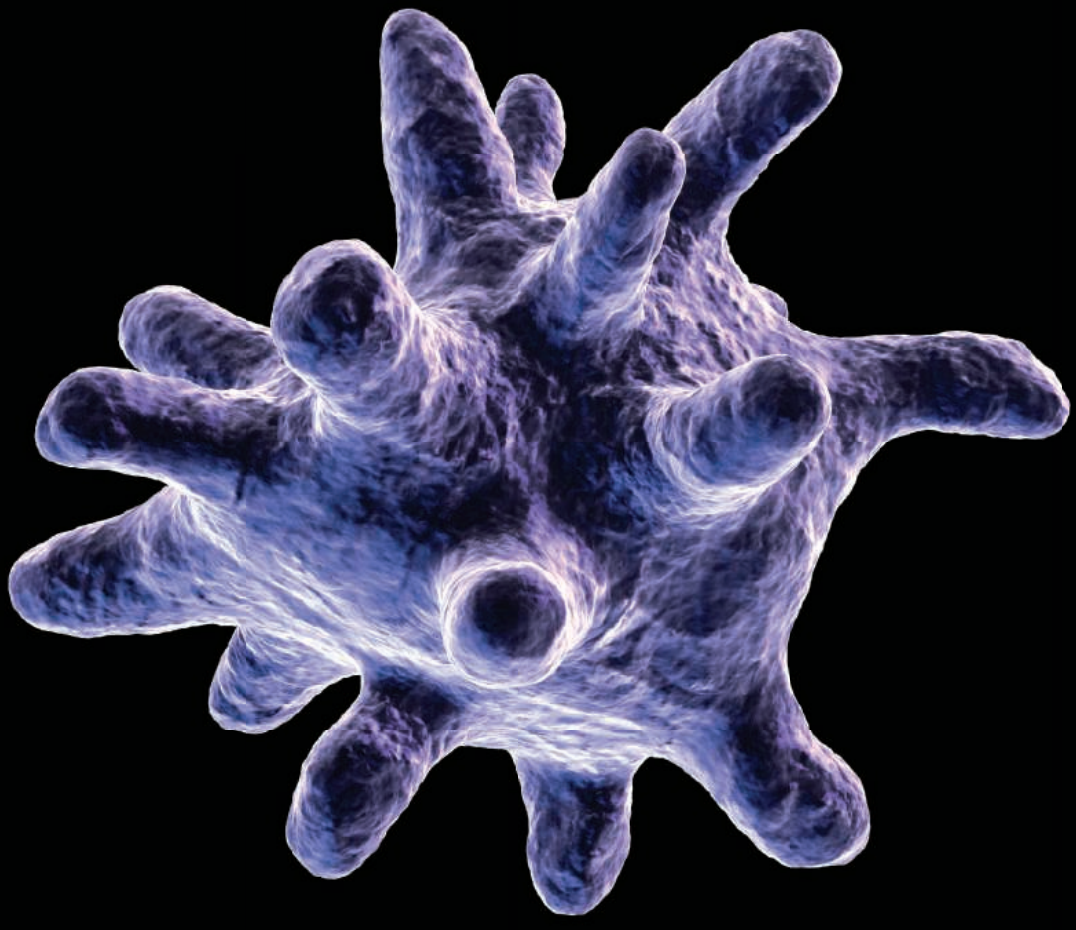


Image: Eraxion / iStockPhoto

## NOW ACCEPTING PAPERS

*Science* is expanding its reach into immunology—now offering the newest online-only, weekly journal in the *Science* family of publications. *Science Immunology* will provide original, peer-reviewed research articles that report critical advances in all areas of immunological research, including studies that provide insight into the human immune response in health and disease.

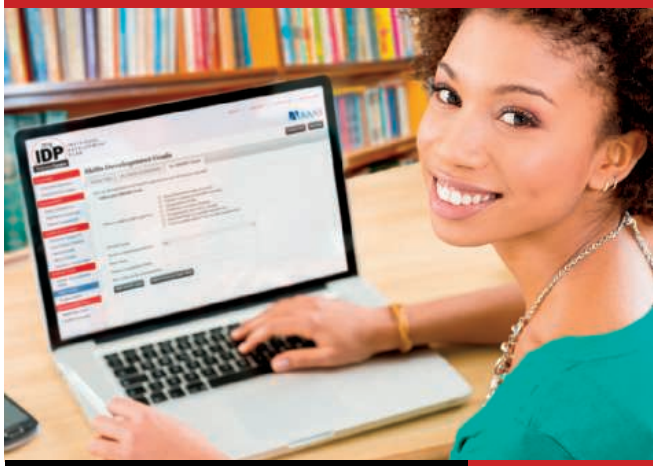
Be a part of the *Science Immunology* debut issue publishing Summer 2016!

Submit your manuscript today at **ScienceImmunology.org.**

Science Immunology

AAAS

# myIDP: A career plan customized for you, by you.



For your career in science, there's only one Science

my IDP ScienceCareers

Recommended by leading professional societies and the NIH

**Features in myIDP include:**

- Exercises to help you examine your skills, interests, and values.
- A list of 20 scientific career paths with a prediction of which ones best fit your skills and interests.
- A tool for setting strategic goals for the coming year, with optional reminders to keep you on track.
- Articles and resources to guide you through the process.
- Options to save materials online and print them for further review and discussion.
- Ability to select which portion of your IDP you wish to share with advisors, mentors, or others.
- A certificate of completion for users that finish myIDP.

Visit the website and start planning today!
myIDP.sciencecareers.org

ScienceCareers In partnership with:

advancing the life sciences 1912-2012 FASEB Federation of American Societies for Experimental Biology

Medical College of Wisconsin

UCSF University of California San Francisco

Burroughs Wellcome Fund

# HIV Cure Funding Opportunity

Gilead Sciences has spent 25 years working to improve treatments for people living with HIV, with an ultimate goal in mind: finding a cure.To that end, we've set aside fundingto support academic institutions,nonprofit organizations and communitygroups committed to HIV cure activities.

Visit www.gilead.com/HIV-Cure-FOA to learn more and apply for funding.

GILEAD

### Antibodies

Bio-Rad has expanded its new product line of Western blot-validated PrecisionAb Antibodies to include a vast collection of cancer targets (e.g., Bcl2, Bax, p53). These targets play central roles in the switch that turns a normal cell into a tumor cell. As part of the PrecisionAb line of primary antibodies, the new offerings have been validated against 12 biologically relevant cell lines that express endogenous levels of the targets. Only antibodies that detect these proteins with high sensitivity and specificity are included in the PrecisionAb product line. The high specificity prevents misidentification of proteins and helps detect proteins that are downregulated in cancer. The antibodies are sold in trial sizes to allow for economical in-house validation and a positive control lysate so researchers can benchmark the target molecular weight.

**Bio-Rad**
For info: 800-424-6723
www.bio-rad.com/getprecisionab

### UV-Vis Spectrophotometer

The NanoDrop One and NanoDrop One$^{C}$ UV-Vis microvolume spectrophotometers are designed to help life science researchers gain a more complete understanding of sample quality and avoid costly delays due to troubleshooting and repeating experiments. These new spectrophotometers introduce Acclaro sample intelligence technology, which enables researchers to identify sample contaminants and obtain corrected concentration results, receive instant feedback about sample quality with on-demand technical support and guided troubleshooting, and confidently measure samples with embedded sensor and digital image analysis. The NanoDrop One's high-resolution, touchscreen interface makes it easy to use as a compact, ergonomic instrument, while the powerful auto-range pathlength technology facilitates accurate measurements for concentrated samples with no need for dilutions. The NanoDrop sample-retention system measures 1–2 µL of sample in seconds without the need for cuvettes, making it a cost- and time-effective solution for busy labs. The NanoDrop One$^{C}$ instrument features both pedestal and cuvette measuring positions.

**Thermo Fisher Scientific**
For info: 877-724-7690
www.thermoscientific.com/nanodrop



### Microplate Reader

The new reference multimode high-throughput screening (HTS) reader PHERAstar *FSX* is the latest evolution in microplate reader instrumentation and combines high sensitivity, speed, and unmatched flexibility in plate formats up to 3,456 wells. Built on the successful PHERAstar *FS* platform, the PHERAstar *FSX* has improved features that make it superior to any microplate reader on the market. The PHERAstar *FSX* offers all the leading nonisotopic detection technologies and is unmatched in sensitivity and speed in fluorescence intensity (FI) and fluorescence polarization (FP). Moreover, the reader offers an ultrahigh dynamic range in luminescence, enabling greater flexibility and more precise measurement results. The outstanding sensitivity of the PHERAstar *FSX* is based on an innovative optical design including three independent light sources. To ensure best performance for any assay, the PHERAstar *FSX* comes with the next-generation laser for time-resolved fluorescence/time-resolved fluorescence energy transfer (TRF/TR-FRET).

**BMG Labtech**
For info: 877-264-5227
www.bmglabtech.com

### Western Blot Substrate

Chemi FP is the most sensitive horseradish peroxidase (HRP) substrate for Western blotting yet, with attomole sensitivity and a long-lasting signal output. The light emission is stable for 10 times longer than is possible with typical enhanced chemiluminescence (ECL) substrates. This enables the user to detect bands not usually visualized with other commonly used substrates. Importantly, the high signal-to-noise level and large dynamic range of the product makes it ideal for quantifying low-intensity bands. The chemifluorescence emission allows the Chemi FP to be imaged using chemifluorescence imaging techniques in addition to traditional charge-coupled device (CCD) imaging systems and film. Chemi FP is the perfect substrate to use when working with one of the Omega Lum Gel Documentation systems. The combination of one of Aplegen's three Western blotting applications with the Chemi FP guarantees superb results.

**Gel Company/Aplegen**
For info: 415-247-8760
www.gelcompany.com

### Mass Detector

The new control driver for the Microsaic 4000 MiD mass detector expands the portfolio of instruments managed by Clarity, a single-point control software platform. The Microsaic 4000 MiD control module includes both digital control and data acquisition for the detector. It includes MiDas compact interface module controls and allows performing detector calibration, maintenance, and service operations from the Device Monitor software window. Clarity Chromatography Software provides seamless integration of Microsaic 4000 MiD with a wide range of high-performance liquid chromatography (HPLC) systems that are already controlled by Clarity. Clarity MS Extension greatly extends Clarity capabilities. Clarity is able to evaluate spectral data from mass spectrometry (MS) detectors together with data from conventional HPLC detectors (including quantification) and add the third dimension for data analysis. Clarity Chromatography Software has a strong position in the chromatography data systems market. Clarity is highly regarded for its intuitive approach, excellent performance, cost effectiveness, and proficient technical support.

**DataApex**
For info: +420-251-013-403
www.dataapex.com

Electronically submit your new product description or product literature information! Go to www.sciencemag.org/about/new-products-section for more information.

Newly offered instrumentation, apparatus, and laboratory materials of interest to researchers in all disciplines in academic, industrial, and governmental organizations are featured in this space. Emphasis is given to purpose, chief characteristics, and availability of products and materials. Endorsement by *Science* or AAAS of any products or materials mentioned is not implied. Additional information may be obtained from the manufacturer or supplier.

ADVERTISEMENT



# Singapore's path to prosperity

Science and technology continue to be a cornerstone of Singapore's economy. Over the years the country has built a solid infrastructure to create a truly interdisciplinary research environment, becoming a hub for innovative research. An 18% boost in the country's research budget over the next five years is a clear nod to the success of this commitment and will continue to solidify Singapore's prominence as a global leader in science and technology innovation.

Today's supercomputers can perform a mind-boggling 10 quadrillion calculations per second, but they still can't match the cognitive capacity of the human brain: An experiment on one of the world's fastest supercomputers in 2013 was able to mimic only 1% of 1 second's worth of human brain activity—and even that took 40 minutes. The massive amount of hardware and power required to process complex information is one major roadblock in developing artificial intelligence. Comparatively, "the human brain consumes about 20 watts of power and is only about 1 liter in size," explains **Dim-Lee Kwong,** executive director of the Institute of Microelectronics (IME) at Singapore's Agency for Science, Technology and Research (A*STAR). Taking a cue from the human brain in which the left and right parts work in symphony to process information, what if engineers could increase the interconnections between a computer's central processing unit and its memory? "We could potentially reduce the power required and the time it takes to compute," says Kwong, "That is cognitive computing. . . and it's coming."

Developing such enabling technology is a cornerstone of IME and represents only one way that A*STAR aims to make a name for itself in the realm of groundbreaking science—it is also how A*STAR is strengthening Singapore's future economy. Over 15 years ago, the government declared science and technology to be an essential pillar of the nation's economic growth. Singapore has no natural resources. With a small population of only 5.5 million, it faces tough competition from neighboring countries to attract foreign investment. It was for these reasons that the government implemented an ambitious plan to capitalize on human knowledge, its most valuable asset.

A*STAR's predecessor, the National Science and Technology Board, was set up in 1991 to develop Singapore into a research hub in selected fields of science and technology, and thus make the nation more competitive globally. Early on, planners realized that truly innovative research is interdisciplinary. To be able to cross-pollinate ideas quickly, different research institutes should be located close to one another. The opening of Fusionopolis Two in fall 2015 marked another milestone in the development of Singapore's research and development hub for physical sciences and engineering. Fusionopolis One and Two, together with Biopolis—the nation's hub for biomedical sciences—comprise 650,000 square meters of office and laboratory space across 19 buildings, and are designed for both the public and private sectors to conduct activities in research, innovation, and enterprise.

"These campuses provide some of the best infrastructure and state-of-the-art facilities for research. They also create a very conducive environment for spontaneous collaborations across the disciplines along the innovation-value chain and between the public and private sectors," says **Lim Chuan Poh,** A*STAR's chairman.

Since Singapore's first National Technology Plan was implemented in 1991, the government has invested nearly S$42 billion (US$29 billion at today's rates) on research and innovation. The funding's purpose has been not only to boost basic research, but also to support mission-oriented research that would feed back into the country's economy in terms of job growth, exportable technology, and increased entrepreneurship. The investment has paid off so far. Over the last 10 years, the number of research scientists and engineers across both the public and private sectors has increased from a base of 15,600 in 2002 to 32,800 in 2014.

To capitalize on this momentum, early this year Prime Minister **Lee Hsien Loong,** chairman of the Research, Innovation and Enterprise Council (RIEC), announced an 18% increase in the nation's 2016–2020 research budget over the previous five-year







**Biopolis and Fusionopolis, creating an environment for interdisciplinary public-private collaborations (clockwise from top left: Biopolis, Fusionopolis Two, Fusionopolis One).**

budget—1% of the country's gross domestic product, and a percentage on par with that of other industrialized countries. The S$19 billion (US$13.5 billion) in funding includes a budget increase of more than 50% for emerging research, innovation, and enterprise activities. One key difference in the current budget, however, is the priority placed on four technology domains in which Singapore has either developed a competitive advantage or meets a national need: Advanced Manufacturing and Engineering, Health and Biomedical Sciences, Services and Digital Economy, and Urban Solutions and Sustainability.

## Interdisciplinary collaboration yields results

A*STAR has been successful in meeting the nation's research agenda because it has been able to build research capabilities ahead of industry trends, says Lim. For example, A*STAR is already building a strong capacity in fields that will contribute to what World Economic Forum founder and executive chairman Klaus Schwab has dubbed the "Fourth Industrial Revolution," brought on by a range of new technologies that will "fuse the physical, digital, and biological worlds."

The cognitive computing project now underway at IME, for example, could revolutionize not only research but also industry and society in the form of intelligent robots and devices that improve health. To move the research forward, physical proximity is a huge advantage, says Kwong.

In addition to IME, the newly christened Fusionopolis Two also houses the following A*STAR research institutes: the Data Storage Institute, the Institute of Materials Research and Engineering, and the Singapore Institute of Manufacturing Technology.

IME is working in collaboration with A*STAR's Institute for Infocomm Research ($I^2R$), where scientists are charged with developing the software that would be required for cognitive computing to succeed. $I^2R$ is located in Fusionopolis One, just across a bridge from Fusionopolis Two, where IME is housed. "Instead of writing an e-mail or making a phone call, we can just sit down together and hash out ideas," says Kwong.

IME's cognitive computing project will also require materials for new technology and innovations in data management. The meeting of minds fostered by institutes housed together makes it easier to move such ideas forward, says Kwong. Even a casual encounter in the elevator can spark a conversation about an idea that may have languished had it required more formal routes of communication. "We are duplicating the old Bell Labs model [of nurturing innovation through collaboration]," Kwong adds.

The proximity to industry that Fusionopolis affords also ensures that innovation is translated into the economy. Industry brings prototyping and optimization expertise, says Kwong. "They have the know-how to seamlessly transfer technology to the local manufacturing infrastructure, which is how you translate R&D into the economy." Two institutes located in Fusionopolis One have already established 19 joint labs with industry since 2008. A*STAR hopes that the additional institutes now located in the adjacent building will forge even more joint research to develop and bring to market the enabling technologies of the future in key areas such as advanced materials, silicon photonics, data center storage technologies, and nanofabrication.

"Being ahead of international industry trends will stand Singapore in good stead to adapt to the evolving global economy and to stay competitive and differentiated," says Lim. "Going forward, A*STAR will continue to place strategic bets on promising new areas of research and innovation to pave the way for Singapore's future."

## The Advanced Remanufacturing and Technology Centre

Cognitive computing is an example of the type of early stage, goal-oriented research that A*STAR will fund. However,

its primary role is "to bridge the gap between academia and industry," says Lim. "This requires us not only to work closely with the private sector to co-innovate, but also to look further ahead to invest in research that will position Singapore well for the future," he adds.

Manufacturing has been a pillar of Singapore's economy, contributing about 20% to the nation's gross domestic product. From 2004 to 2014, the sector has grown in productivity by 3.0% annually, outpacing the national average of 0.7%. To further fortify the nation's prominence as a leader in manufacturing technology, A*STAR officially opened the Advanced Remanufacturing and Technology Centre (ARTC) in January 2015, with the aim to "create bridges between public and private organizations to work together in solving manufacturing issues," says **David Low,** chief executive officer of ARTC.

Modeled on similar advanced manufacturing research centers in the United Kingdom, ARTC operates primarily through company membership. Each private member must pay an annual fee. In return, companies receive ARTC's research expertise, industrial space, and equipment to test out innovative ideas that improve or create new manufacturing processes. "ARTC aspires to be a catalyst for technical solutions and for creating business opportunities," says Low.

There are now 35 participating industry members, although nonmembers are also welcome to approach ARTC. The S$400,000 (US$285,000) annual membership fee for founding and Tier 1 members is hefty and the bar to qualify for membership is high, Low says, but members have priority access to ARTC brain capital, resources, and facilities. Members also get more out of the relationship because they tend to be more committed to solving specific issues. And because Singapore has a reputation for protecting and respecting intellectual property, corporate members can openly discuss ideas freely, without concern that trade secrets will be revealed.

Rolls-Royce, for example, is an ARTC founding member. The company is a major manufacturer of airplane engines. A gas turbine engine has a typical lifespan of about 25 years. Without a repair process, Rolls-Royce would have to replace many parts over an engine's lifetime, which costs money not just in materials but also in energy and in the man-hours required to manufacture them, Low explains.

Singapore is the largest aerospace maintenance, repair, and overhaul country in Asia, says Low. Rolls-Royce and its joint venture employ approximately 2,500 people in Singapore. So working with ARTC to improve the repair and maintenance process made practical sense. One of the 35 joint projects seeks to replace a chemical cleaning process with a dry-ice blasting method. The new method is less expensive than replacing or recycling parts and is more environmentally friendly.

For this project, ARTC brought in AmpTec Industrial Heating, a local manufacturer of dry-ice cleaning equipment. The cleaning process is carried out by a sophisticated robot supplied by ABB Singapore—a multinational manufacturer of power and automation technologies. ARTC integrated the dry-ice cleaning equipment with the robot, programming the robotic path as well as developing the key parameters for the cleaning process. Collaborating companies can benefit hugely, says Low. "If a project is successful, ARTC already has the suppliers ready and simply hands over the process. It bridges a gap and hastens the time to market, which accelerates economic growth for Singapore."

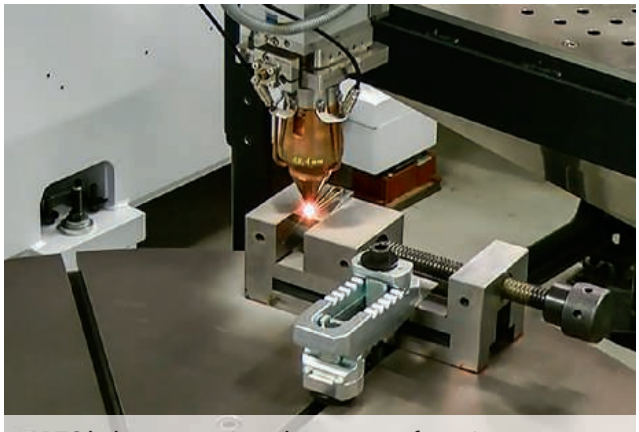
## New biomedical initiatives

Although research projects in computing and manufacturing are focused on developing enabling tools and objects, part of the nation's research strategy is also intended to improve quality of life at home. One key goal highlighted under the Health and Biomedical Sciences research domain is to support research that "advances the health of the people of Singapore." At Biopolis—a 13-building research campus adjacent to Fusionopolis that provides space for both public and private sponsored biomedical research—an A*STAR initiative launched in 2013 is already making progress toward that goal. The Personalized OMIC Lattice for Advanced Research and Improving Stratification (POLARIS) initiative has as its principal goal to implement genomic medicine. Thought leaders around the world have pointed to molecular medicine as playing an ever-increasing role in improving health care outcomes.

"We made a strategic decision to identify the barriers," says **Patrick Tan,** program director of POLARIS. Although funded by A*STAR, the initiative is actually a multiparty collaboration among hospitals, regulatory agencies, and universities, says Tan. The barriers can be bureaucratic, administrative, or logistical, he adds.

One project, for example, aims to study how next-generation sequencing could replace conventional genotyping methods for tuberculosis detection and potentially enable more rapid detection of drug-resistant strains. Another project involves creating a next-generation cancer-sequencing panel that could be used as a diagnostic tool. The key research findings coming out of these two projects, however, will be those showing how to speed up and deliver genomic tests to the clinic, says Tan. In other words, the research is not only about discovery but also about implementation. Consequently, POLARIS also works closely with Singapore's Ministry of Health.

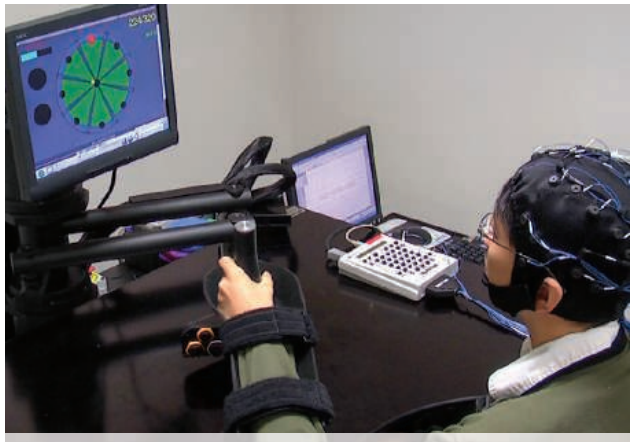
Still another project will potentially translate a research discovery into knowledge that could specifically help the local population. In 2012, a team that included researchers from Duke-NUS (National University of Singapore) Graduate Medical School



**ARTC helps companies advance manufacturing practices through technology.**




POLARIS translates genomics into clinical therapies for Singapore and beyond.



Technology helps stroke patients regain mobility.

in Singapore, A*STAR's Genome Institute of Singapore, Singapore General Hospital, and the National Cancer Centre Singapore discovered a common variation in the *BIM* gene in people of East-Asian descent that contributes to some cancer patients' failure to benefit from tyrosine-kinase inhibitor drugs. The research also pointed to a combination therapy that may be able to override drug resistance. The research clearly has clinical implications: POLARIS has developed a genomic test that can screen for the mutation.

To aid the transfer of diagnostic tests to the clinic, A*STAR also launched the Diagnostics Development (DxD) Hub in 2014, a national initiative that brings together clinicians, researchers, innovators, entrepreneurs, and industry professionals with the objective of quickly transforming intellectual property into clinically validated and marketable diagnostic devices. The DxD Hub is located in Biopolis and is led by A*STAR's commercialization division, Exploit Technologies.

Also in 2014, A*STAR, Nanyang Technological University, and the National Healthcare Group signed a memorandum agreeing to commit at least S$100 million (US$71.3 million) toward the new Rehabilitation Research Institute of Singapore (RRIS). The collaboration will leverage the expertise of scientists, clinicians, and engineers to develop innovative technology solutions to improve outcomes for stroke patients. The strategy employs clinical robotics and biomechanics as well as computer games as tools to aid rehabilitation. Researchers at A*STAR's $I^2R$ have developed a noninvasive technology, which works by building a direct interface between the human brain and the computer. Traditionally, stroke rehabilitation exercises involve human-to-human interaction between a therapist and patient. The ArtsBCI (Advanced rehabilitation therapy for stroke based on Brain-Computer Interface) technology uses a robotic machine to move a patient's arm, activated by electrical signals picked up by an electroencephalogram (EEG) netting. Clinical trials conducted at Tan Tock Seng Hospital and the National Neuroscience Institute demonstrated its use in helping stroke patients regain various degrees of mobility.

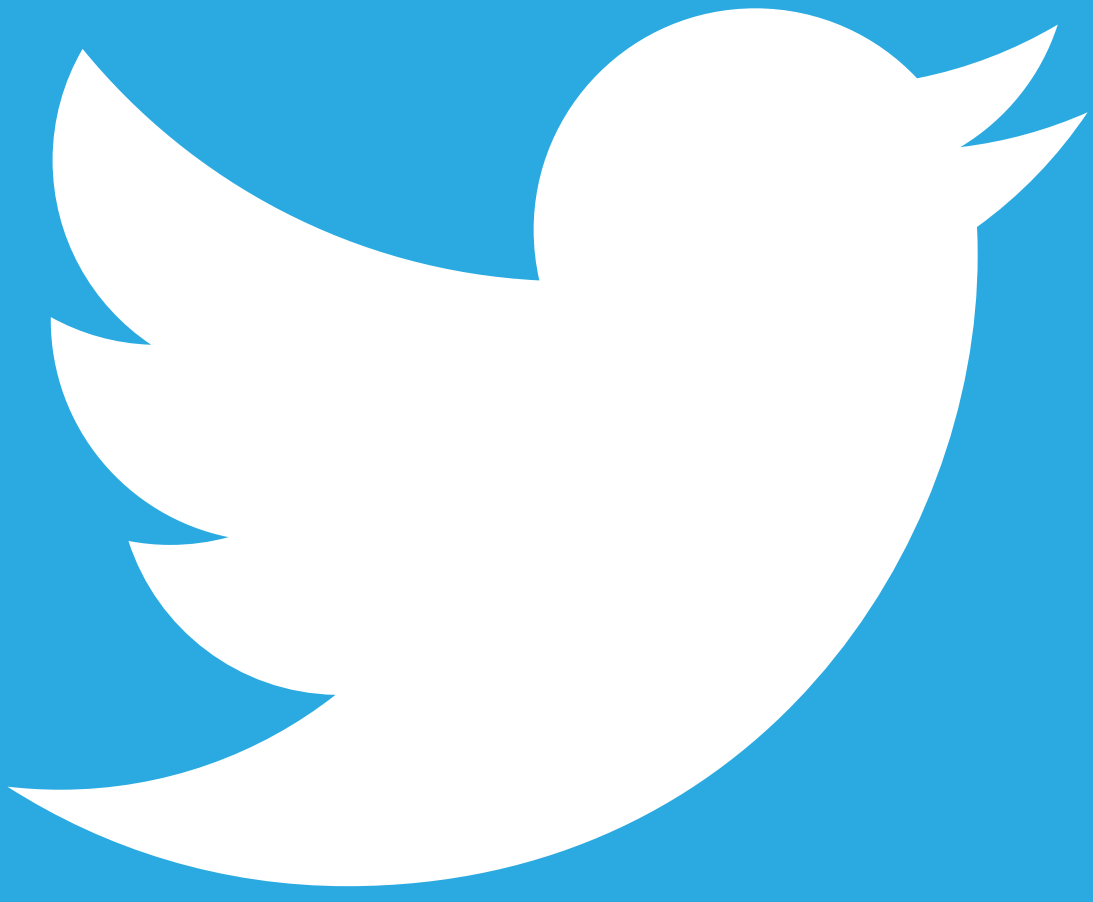
"A*STAR has played a critical role in connecting various research players thus far," says Lim. Going forward, it will intensify its role "as convener and orchestrator of nationwide programs to foster greater collaboration and integration between academia, the clinical community, and industry, so as to translate research into innovative medicines, medical devices, and value-based healthcare."

## The investment pays off

Singapore's gross domestic expenditure on research, innovation, and enterprise has grown from S$3.4 billion (US$2.4 billion) in 2002 to S$8.5 billion (US$6.06 billion) in 2014—a testament to the nation's growth strategy. "From a predominantly physical science and engineering research focus, we now have strong multidisciplinary capabilities in both the biomedical sciences and physical sciences and engineering," says Lim.

Other indicators also point to success: Singapore now has vibrant startup clusters such as the JTC LaunchPad @ one-north, located adjacent to Fusionopolis One, which will house about 750 startups by 2017, up from 500 in 2015 and 250 when it first began in 2011. A*STAR has also spawned about 60 startups from its research institutes since 2011. The translation of research and technology into potentially tangible benefits or advances for society has landed the nation high rankings in several international economic indicators. Singapore was ranked seventh in INSEAD Business School's Global Innovation Index 2015, and was recently ranked the world's second-most competitive economy in the World Economic Forum Global Competitiveness Report 2015–2016—a position it has held for five years consecutively. Singapore was also ranked the second-highest Asia-Pacific economy within the subcategory of innovation.

Singapore's ability to achieve its goals within a relatively short time is a reflection of "strong government commitment sustained over the last few funding cycles," says Lim. Also contributing to its success is the nation's (and hence the research community's) small size, which makes it easier for all parties to engage and work together to shape the research landscape, he adds. "This spirit of cooperation and collaboration for economic impact and societal benefits will be even more critical going forward in a much more challenging and uncertain global environment."



## Join the Conversation!

Twitter is a great way to connect with AAAS members and staff about the issues that matter to you most. Be a part of the discussion while staying up-to-date on the latest news and information about your personal member benefits.

**Follow us @AAASmember and join the conversation with #AAAS**

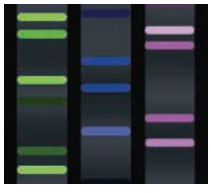
AAAS MemberCentral

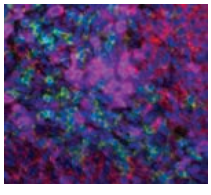
MemberCentral.aaas.org

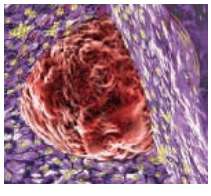
# want new technologies?

antibodies
apoptosis
biomarkers
cancer
cytometry
data
diseases
DNA
epigenetics
genomics
immunotherapies
medicine
microbiomics
microfluidics
microscopy
neuroscience
proteomics
sequencing
toxicology
transcriptomics









## watch our webinars

Learn about the latest breakthroughs, new technologies, and ground-breaking research in a variety of fields. Our expert speakers explain their quality research to you and answer questions submitted by live viewers.

**VIEW NOW!**
**webinar.sciencemag.org**

Science
AAAS

Brought to you by the *Science*/AAAS Custom Publishing Office

@SciMagWebinars

CELL SIGNALING TECHNOLOGY

# Deciphering Cancer

## Antibodies to evaluate key signaling networks in cell death and survival.






Download pathways at www.cellsignal.com/cancerpathways

**For Research Use Only. Not For Use In Diagnostic Procedures.**
© 2016 Cell Signaling Technology, Inc. Cell Signaling Technology and CST are trademarks of Cell Signaling Technology, Inc.
16PADCANR0005ENG

Cell Signaling TECHNOLOGY®




## *Science* Careers Advertising

For full advertising details, go to ScienceCareers.org and click For Employers, or call one of our representatives.

**Tracy Holmes**
Worldwide Associate Director
*Science* Careers
Phone: +44 (0) 1223 326525

THE AMERICAS

E-mail: advertise@sciencecareers.org
Fax: +1 (202) 289 6742

**Tina Burks**
Phone: +1 (202) 326 6577

**Nancy Toema**
Phone: +1 (202) 326 6578

**Online Job Posting Questions**
Phone: +1 (202) 312 6375

EUROPE / INDIA / AUSTRALIA / NEW ZEALAND / REST OF WORLD

E-mail: ads@science-int.co.uk
Fax: +44 (0) 1223 326532

**Sarah Lelarge**
Phone: +44 (0) 1223 326527

**Kelly Grace**
Phone: +44 (0) 1223 326528

**Online Job Posting Questions**
Phone: +44 (0) 1223 326528

JAPAN

**Katsuyoshi Fukamizu** (Tokyo)
E-mail: kfukamizu@aaas.org
Phone: +81 3 3219 5777

**Hiroyuki Mashiki** (Kyoto)
E-mail: hmashiki@aaas.org
Phone: +81 75 823 1109

CHINA / KOREA / SINGAPORE / TAIWAN / THAILAND

**Ruolei Wu**
E-mail: rwu@aaas.org
Phone: +86 186 0082 9345

All ads submitted for publication must comply with applicable U.S. and non-U.S. laws. *Science* reserves the right to refuse any advertisement at its sole discretion for any reason, including without limitation for offensive language or inappropriate content, and all advertising is subject to publisher approval. *Science* encourages our readers to alert us to any ads that they feel may be discriminatory or offensive.

ScienceCareers
FROM THE JOURNAL SCIENCE AAAS

ScienceCareers.org

Universität Konstanz

The University of Konstanz, with its "Institutional Strategy to promote Top-Level Research", has been receiving continuous funding since 2007 within the framework of the Excellence Initiative by the German Federal and State Governments.

The Movement Ecology Cluster is a joint venture of the University of Konstanz and the Max Planck Society to decode the general mechanisms and principles of movement and collective behavior from the cellular to the population level.

For this cluster, the University of Konstanz is filling **as soon as possible** the following positions:

### W3-Professor of Organismal Interactions
**(Job Offer 2016/054)**

### W3-Professor of Limnology / Aquatic Ecology
**(Job Offer 2016/055)**

### W3-Professor of Genetic Adaptations in Aquatic Systems
**(Job Offer 2016/056)**

We seek applicants who are internationally recognized for their research in the field of Organismal Interactions and who address fundamental questions in ecology, behaviour or evolution. We are particularly interested in researchers who have made important conceptual advances and have worked across, or integrated, levels of biological organisation and complexity (e.g. genes and social behaviour, individual interactions and group or population dynamics). This could involve behavioural studies, experimental evolution, microbiomics, co-evolution, plant-insect interactions or the study of mechanisms of interactions among organisms.

All application materials (curriculum vitae, publication list, a list of grants and awards, details of teaching experience, as well as statements of current research topics, future research directions and interests) should be sent as one pdf file and in English to Prof-2016-054@uni-konstanz.de, or Prof-2016-055@uni-konstanz.de or Prof-2016-56@uni-konstanz.de **until 15 April 2016**.

Further information is available on our website: http://www.uni-konstanz.de/stellen or by contacting Hanns Fahlbusch, phone +49(0)7531/88-2413, e-mail: hanns.fahlbusch@uni-konstanz.de.

University of Nebraska Lincoln

## Head
## Department of Animal Science

The University of Nebraska-Lincoln (UNL) Institute of Agriculture and Natural Resources (IANR) is seeking candidates for the position of Head, Department of Animal Science.

The Head, Department of Animal Science is directly responsible for oversight of the integrated research, teaching and extension/outreach programs of on-campus faculty in the Department. The Department has a tradition of excellence in undergraduate and graduate education, research and extension/outreach in animal sciences (http://animalscience.unl.edu/). The Department Head reports to the Deans of the Agricultural Research Division (ARD), College of Agricultural Sciences and Natural Resources (CASNR), and Cooperative Extension Division (CED) at UNL, and as such is part of the IANR Administrative Team working collaboratively with IANR Administration and all unit administrators.

Candidates must possess (1) a PhD or equivalent in animal science or a related discipline; (2) a record of achievements in their field of expertise and be qualified for appointment as a tenured, full professor in the Department of Animal Science; (3) a documented record of collaborative leadership experience including leadership of teams through the ability to envision, facilitate, develop, and coordinate innovative, interdisciplinary and collaborative research, teaching, extension, or training programs.

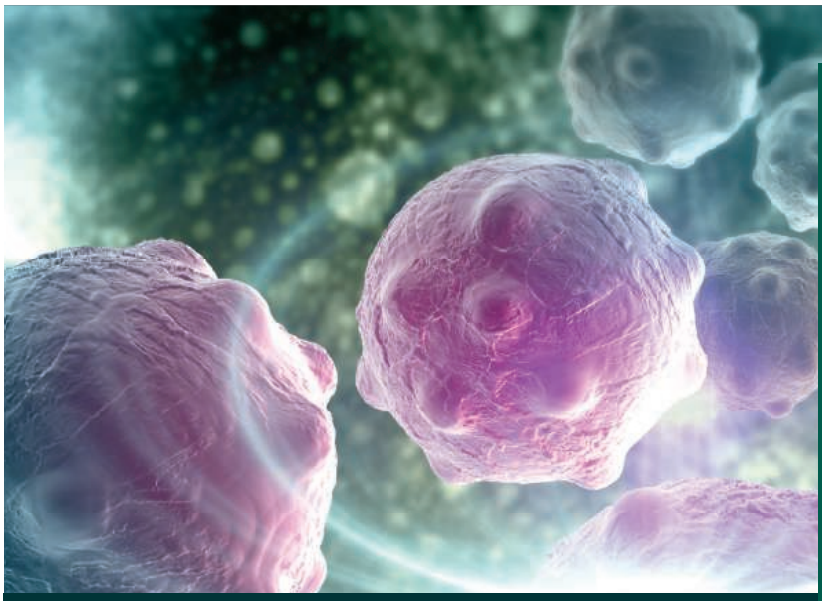
**Preferred qualifications include:** (1) experience building new partnerships to capitalize on emerging research, teaching or extension opportunities; (2) experience working with faculty and administrators to enhance capacity in animal science; (3) experience in mentoring undergraduate students, graduate students, or other professionals; (4) experience in creating meaningful research-based engagement with clientele and stakeholders; and (5) leading submission of competitive applications for large, extramural grants to support research, teaching, extension, or training efforts.

Nebraska ranks #4 in the US in total livestock receipts and livestock products account for about 2/3 of Nebraska's farm income. As of February 2016, Nebraska ranked #1 in cash receipts from meat animals, commercial read meat production, commercial cattle slaughter, and cattle on feed; #2 in ethanol production; #3 in corn grain production; #4 in beef cows; and #6 in hogs and pigs.

To view the details and make application, go to **http://employment.unl.edu**. Search for position **#F_160065**. Click on "**Apply to this job**." Complete the application and attach a letter of interest, curriculum vitae, contact information for three professional references, and a one-page statement of administrative philosophy (Other). Review of Applications will begin on **May 2, 2016**, and continue until the position is filled or the search is closed.

*The University of Nebraska-Lincoln is committed to a pluralistic campus community through Affirmative Action, Equal Opportunity, work-life balance, and dual careers. See http://www.unl.edu/equity/notice-nondiscrimination.*

ScienceCareers online @sciencecareers.org



Cancer Feature:

# Cancer Research

Issue date: April 8

Ads accepted until April 1 if space allows

**For recruitment in science, there's only one *Science*.**

**Looking to hire a cancer researcher?** Reach them through the pages of *Science*. Our upcoming cancer feature explores how major institutions are planning to prepare for the challenges involved in precision medicine. This hot research area is sure to draw the readers you need to reach.

## What makes *Science* the best choice for recruiting?

- Read and respected by 400,000 readers around the globe
- Your ad dollars support AAAS and its programs, which strengthens the global scientific community.

## Why choose this feature for your advertisement?

- Relevant ads lead off the career section with a special cancer research banner
- Bonus distributions:

  American Association for Cancer Research, April 16–20, New Orleans, LA

  AACR Career Fair, April 16, New Orleans, LA.

## Expand your exposure by posting your print ad online:

- Link on the job board homepage to a landing page for cancer research positions.

Produced by the *Science*/AAAS Custom Publishing Office.

**Deliver your message to a global audience of targeted, qualified scientists.**

**129,574**
subscribers in print every week

**352,966**
monthly unique browsers on ScienceCareers.org

**65%**
of our weekly readers are Ph.D.s




SCIENCECAREERS.ORG

ScienceCareers
FROM THE JOURNAL SCIENCE AAAS

To book your ad: **advertise@sciencecareers.org**

**The Americas**
+202 326 6582

**Japan**
+81 3 3219 5777

**Europe/RoW**
+44(0)1223 326500

**China/Korea/Singapore/Taiwan**
+86 186 0082 9345

Duke University School of Medicine

**Duke University Department of Ophthalmology**

**Faculty Position for Associate or Full Professor in Eye Research**

The Department of Ophthalmology at Duke University School of Medicine seeks applications for a faculty position as Associate or Full Professor with tenure. We are particularly interested in candidates with laboratory research programs exploring innovative approaches to understanding the biology of the visual system or pathobiology of vision loss. Applicants must hold a Ph.D. and/or M.D., demonstrate an outstanding record of research accomplishment, and maintain active NIH funding. An endowed chair may be available to qualified candidates. Please send a CV, a brief cover letter with career and research interests, and names of 3-5 references to **Search Committee, c/o Ashley Barnwell at: EyeCenterFacultyRecruitment@dm.duke.edu**.

*Duke University is an Affirmative Action, Equal Opportunity Employer.*

**IN SEARCH OF REMARKABLE SCIENTISTS**

**Molecular Technologist, Houston, Texas**

Do you have a PhD in microbiology or biochemistry with a strong desire to change the world to biofuels? Then we'd like you to help us pilot an exciting new project.

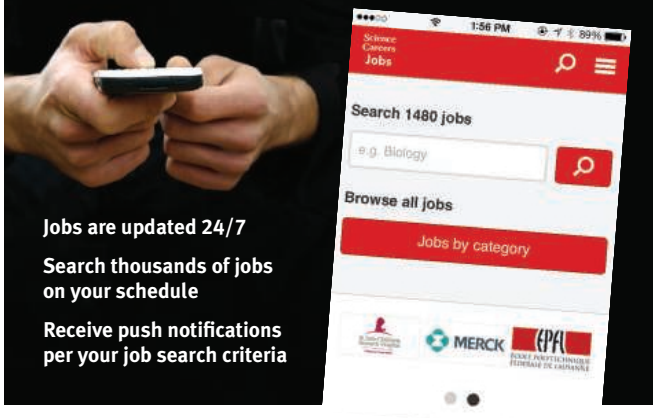
Joining our in-house microbial biofuels team, you'll be working with transformable host organisms to efficiently produce different biofuel components at both lab and pilot scale. You'll need experience in one or more of the following areas: metabolic pathway improvement via transformation, microbial/pathway evolution, transformation of non-standard hosts, solid or liquid fermentation (batch or continuous flow at pilot scale).

Find out more and apply online at **www.shell.com/careers**. In the "Students and Graduates" section, click on "Shell Recruitment Day" and then create an account. When entering your contact details, select "Other" in response to "Where you found out about this Shell opportunity," click "Next" and then type in "**Biofuels**."

**DISCOVER WHAT YOU CAN ACHIEVE AT SHELL**

*Minority, Female, Disabled and Veteran EEO/AA Employer.*

Download the *Science* Careers jobs app from Science




**Jobs are updated 24/7**

**Search thousands of jobs on your schedule**

**Receive push notifications per your job search criteria**

**Get a job on the go.**

Search worldwide for thousands of scientific jobs in academia, industry, and government. The application process is seamless, linking you directly to job postings from your customized push notifications.

Scan this code to download app or visit **apps.sciencemag.org** for information.

ScienceCareers | AAAS
FROM THE JOURNAL SCIENCE

ScienceCareers.org




L'INRA RECRUTE DES CHERCHEURS

**DEPUIS 70 ANS, LES CHERCHEURS ET COLLABORATEURS DE L'INRA TRAVAILLENT À TROUVER DES RÉPONSES AUX DÉFIS DU MONDE.**

L'Inra recrute des chargés de recherche, du chercheur en début de carrière ou expérimenté, et des ingénieurs de recherche débutants et confirmés en situation de handicap.

**LES CANDIDATURES SONT ATTENDUES JUSQU'AU 25 AVRIL 2016 SUR JOBS.INRA.FR**

INRA VOTRE AVENIR EST NOTRE CULTURE 70 ans

ScienceCareers online @sciencecareers.org

# myIDP: A career plan customized for you, by you.




For your career in science, there's only one Science

my IDP ScienceCareers

Recommended by leading professional societies and the NIH

**Features in myIDP include:**

- Exercises to help you examine your skills, interests, and values.
- A list of 20 scientific career paths with a prediction of which ones best fit your skills and interests.
- A tool for setting strategic goals for the coming year, with optional reminders to keep you on track.
- Articles and resources to guide you through the process.
- Options to save materials online and print them for further review and discussion.
- Ability to select which portion of your IDP you wish to share with advisors, mentors, or others.
- A certificate of completion for users that finish myIDP.

Visit the website and start planning today!
myIDP.sciencecareers.org

ScienceCareers In partnership with:

advancing the life sciences 1912-2012 FASEB Federation of American Societies for Experimental Biology

UCSF University of California San Francisco

Medical College of Wisconsin

Burroughs Wellcome Fund

Advance your career with expert advice from *Science* Careers.



**Download Free Career Advice Booklets!**
ScienceCcareers.org/booklets

**Featured Topics:**

- Networking
- Industry or Academia
- Job Searching
- Non-Bench Careers
- And More



ScienceCareers
FROM THE JOURNAL SCIENCE AAAS

ScienceCareers online @sciencecareers.org

*By* **Ahmed Waqas**

# How I made my own opportunities

Like many other medical students in Pakistan, during my first year of medical school I aspired to become a neurosurgeon to enjoy a lucrative lifestyle and high social status. But all that changed when I was diagnosed with depression during my second year. Although painful, the experience instilled in me a passion for psychiatry, a field that has yet to establish itself in Pakistan. Today, my dream is to improve mental health care for mothers and children in low- and middle-income countries. I want to take a combined academic and clinical approach, but I have found many obstacles to pursuing research in Pakistan. Persistence and an ability to leverage whatever resources I can find have been key to my success thus far.

At first, I found few research opportunities and mentors. In Pakistan, it is unusual for medical students to pursue research. At my university hospital, clinicians with a strong research background were rare, especially in a field like psychiatry. Also, I was not at the top of my class, and several faculty members I approached tried to discourage me from pursuing research by saying it would be overwhelming alongside my medical studies.

I finally found a mentor during my third year of medical school. Our lecturer in physical medicine and rehabilitation believed in the importance of research and invited me and other interested students to join him on a project investigating the attitudes of Pakistani medical students and faculty members toward plagiarism.

Through this lecturer I also learned about AuthorAID, an international development program coordinated by the U.K.-based charity INASP that aims to help researchers in developing countries publish their research. I used AuthorAID and its online library to learn about the scientific method, research design, and the writing and publishing processes. I deepened my biostatistics skills by reading books, taking free courses that I found online, attending webinars offered by research agencies in Pakistan, and teaching myself how to use statistics software packages.

Over time, I also learned to reach out to get more help. While working on the plagiarism project, I got in touch with the scientist at the University of Rijeka in Croatia who had developed the original survey questionnaire. I was thrilled when she agreed to teach me while she conducted the validation analysis and wrote up the results. A few months later, I was able to use what I had learned to survey the mental well-being of Pakistani health care professionals. With language help from AuthorAID in the Eastern Mediterranean (a separate AuthorAID project), I published a first-author paper about the work. Since then, I have been grateful to receive email supervision from researchers I have contacted in the United States, the United Kingdom, and Japan. This has helped me further expand my skills and pursue other scientific interests, which today include the psychosocial factors in Pakistan that affect anxiety and depression during pregnancy.



*"Over time, I also learned to reach out to get more help."*

I pay it forward by sharing my knowledge with junior students at my institution through workshops and collaborations. Challenges remain, however. In particular, there is little financial support for research in Pakistan, especially for undergraduates, and my co-authors and I have had to put in our own money while trying to be as frugal as possible.

I have a long way to go to fulfill my dream. After I graduate this summer, I plan to complete both my clinical and research training, ideally in the United States. In addition to establishing a clinical practice, I hope one day to set up an epidemiological research center in Pakistan that would help improve the standard of care for mothers and children with mental health issues. But my experiences so far have encouraged me to believe that if I work hard, persevere, and make the most of the resources available, I can reach my most far-fetched ambitions. ■

*Ahmed Waqas is in the final year of his Bachelor of Medicine and Bachelor of Surgery degree at the CMH Lahore Medical College and Institute of Dentistry in Pakistan. Send your story to SciCareerEditor@aaas.org.*

ILLUSTRATION: ROBERT NEUBECKER

Downloaded from on March 17, 2016



Published by AAAS